1 April 1985

APPENDIX II

FINAL REPORT: AFOSR 82-0020

SPECKLE IMAGE RECONSTRUCTION

P. A. STRITTMATTER and E. K. HEGE

(602)621-6524 (602)621-1049

STEWARD OBSERVATORY

UNIVERSITY OF ARIZONA

TUCSON, AZ 85721

STEWARD OBSERVATORY PROGRESS REPORT

This report contains results obtained from observations using the University of Arizona 2.3 meter telescope, the Kitt Peak National Observatory 4 meter telescope and the Multiple Mirror Telescope.

Kitt Peak National Observatory, a division of the National Optical Astronomy Observatories, is operated by the Association of Universities for Research in Astronomy, Inc., under contract to the National Science Foundation.

The Multiple Mirror Telescope is a joint facility of the University of Arizona and the Smithsonian Institution.

Security Classification: Unclassified

Distribution Unlimited:

Partial contents:

1. Size Measurement of a Geosynchronous Satellite Using the MMT (Multiple Mirror Telescope)
   Hege and Jensen

2. Pluto
   Hege and Drummond

3. Speckle Interferometry of Asteriods; I. 433 Eros
   Drummond, Cocke, Hege and Strittmatter

4. Speckle Interferometry of Asteroids. II. 532 Herculina
   Drummond, Hege, Cocke, Freeman and Christou

5. Speckle Interferometry of Asteriods. III. 511 Davida.
   Drummond and Hege

6. High-Speed Digital Signal Processing for Speckle Interferometry
   Hege, Cocke, Strittmatter and Worden

7. Knox-Thompson Phase Recovery Photon-by-Photon
   Eckart, Cocke and Hege

8. Use of "CLEAN" in Speckle Image Calibration
   Eckart, Hege, Christou and Shaklan

9. Seeing Calibration of Optical Astronomical Speckle Interferometric Data
   Christou, Cheng and Hege

10. Seeing Studies for Speckle Holographic Imaging
    Christou and Hege

11. A Self Calibrating Shift-and-Add Technique for Speckle Imaging
    Christou, Hege, Freeman and Ribak

12. The Physical Diameter of Alpha Orionis?
    Cheng, Strittmatter, Hege, Hubbard, Goldberg and Cocke

13. (and) Images of Alpha Orionis?
    Hebden, Christou, Cheng, Hege and Strittmatter

14. Image Reconstruction from Astronomical Speckle Interferometry
    AFOSR Conference Report

15. Recovery of Binary Star Orientation and Relative Intensity: A Comparison of Techniques
    Hege, Christou, Freeman, Cocke, Bagnuolo and Granrath

16. Image Restoration via the Shift-and-Add Algorithm
    Bagnuolo

17. Speckle Imaging with the PAPA Detector
    Papaliolios, Nisenson and Ebstein

18. Shift-and-Add Imaging through Partially Isoplanatic Seeing
Bates, Beckers, Christou, Hege and Sinton

19. Wavelength Dependent Scaling in Speckles
Szumilo and Hege

20. Betelgeuse and Eros Imaged by Fourier Phase Retrieval from Speckle Data
Bates, Christou, Cocke, Drummond, Fright, Hege, Mnyama, Roddier, Roddier and Sinton

21. Maximum Magnitude Estimation of the Object's Power Spectrum in Stellar Speckle Interferometry
Granrath

22. The Differential Speckle Interferometer
Beckers, Hege and Murphy

23. Statistical Analysis of the Self-Calibrating Shift-and-Add Image Reconstruction Technique
Freeman, Hege, Christou, Ribak and Roddier

24. The Versatile Array
Woolf

25. Adaptive Optics
Woolf

26. Gone with the Wind, or Sailing and Seeing with a Giant Telescope
Woolf and Ulich

27. Very Large Ground-Based Telescopes for Optical and IR Astronomy
Angel

28. Continued Development of a Proximity Focused Image Intensifier for Astronomical Applications
Cromwell

29. SPIE Abstracts
Hege et al.

SIZE MEASUREMENT OF A GEOSYNCHRONOUS EARTH SATELLITE USING THE MMT*

E. K. Hege

Steward Observatory
Tucson, AZ 85721

and

E. Jensen

Aerospace Corporation
Los Angeles, CA 90009

*The Multiple Mirror Telescope (MMT) is a joint facility of the University of Arizona and the Smithsonian Institution.

DRAFT: 03 June 1985

ABSTRACT

We have used the B-E mirror pair of the Multiple Mirror Telescope as a two-beam interferometer to produce a one-dimensional size estimate for a geosynchronous Earth satellite FLTSATCOM1 using speckle autocorrelation techniques. At the arbitrarily chosen vertical position angle, we find a diameter of 4.9±2.0 meters for the diameter of that synchroonouw object.

1. INTRODUCTION

Labeyrie (1970) first pointed out that the short exposure images (specklegrams) of the seeing perturbed telescope image contained information on the structure of the source up to resolutions corresponding to the diffraction limit of the telescope. During the past several years there has been a rapid development in speckle interferometry techniques for obtaining high resolution angular measurements through the earth's atmosphere using large ground based telescopes. Speckle interferometry (See review by Dainty,1984) produces diffraction limited results with spatial resolution gains of $\sim 10^2$ over that normally permitted by the earth's atmosphere. Our work has demonstrated the technique for asteroids (Drummond et al.,1985a,1985b,1985c), artificial satellites, bright, resolvable stars and other celestial objects (Hege, Strittmatter and Woolf, 1984). It has furthermore been applied to sources as faint as $m_v \sim 16$, (Hege et al., 1981,1982b).

In classical speckle interferometry, the specklegrams are recorded and then processed to yield the autocorrelation (AC) or power spectrum (PS) of the object. Thus the n^{th} specklegram (magnified, narrow-band, short-exposure image) $i_n(x,y)$ of the object is represented by the convolution (* implies convolution)

$$i_n(x,y) = o(x,y) * p_n(x,y) \qquad (1.1)$$

where $p_n(x,y)$ is the point-spread function of the atmosphere plus instrument for the n^{th} specklegram and $o(x,y)$ is the object as seen above the atmosphere. Using the Fourier transform notation $FT(i_n(x,y)) = I_n(u,v)$, taking Fourier transforms of many specklegrams and averaging the square modulus yields

$$\langle |I_n(u,v)|^2 = |O(u,v)|^2 \langle |P_n(u,v)|^2 \rangle \qquad (1.2)$$

This result may be inverted to yield the object power spectrum $PS_o = |O(u,v)|^2$ for those spatial frequencies (u,v) for which the speckle transfer function $STF = \langle |P_n(u,v)|^2 \rangle$ is bias free and non-zero.

In the ideal case the STF is non-zero to the diffraction limit of the telescope and is determined by making interspersed observations of a point source calibrator. In practice, the STF is not bias free and many other corrections, depending upon detector and observing conditions, are required: examples are correction of geometric distortion, removal of photon statistics bias, etc. Calibration of this speckle transfer function is fundamental to all of the procedures utilized in this study.

The calibration of simple speckle interferometric power spectrum observations requires

(i) integration of of individual frame power spectra, $PS = \langle |I_n(u,v)|^2 \rangle$, defined by 1.2; or equivalently integration of individual frame autocorrelation function

(ii) standardization of each observation with corresponding measurements of an unresolved point source, $PS_p = \langle |I_{pn}(u,v)|^2 \rangle$, suitably controlled for variable seeing conditions (discussed further in Christou et al., 1985)

(iii) measurement of the detector transfer function $DTF = |D(u,v)|^2$. DTF represents the photon point spread response of the detector, which for our intensified television video raster detector is variable over the image space (x,y) (Hege et al., 1980).

The resulting object power spectrum, calibrated for aperture and seeing effects, can then be estimated by computing (see Hege et al., 1982a).

$$|O(u,v)|^2 \propto \frac{(PS_o/|D_o(u,v)|^2 - N_o)}{(PS_p/|D_p(u,v)|^2 - N_p)} \qquad (1.3)$$

where N_p and N_o are the noise bias associated with the point source and the object power spectra, respectively, produced by the image sampling process. The detector transfer function DTF = $|D(u,v)|_i^2$ is measured by integrating the individual frame power spectra for random events detected subsequent to illumination of the detector with uniform, low intensity light, digitized in the same way as for the point source and the object, respectively.

The division by the point source calibration result removes the seeing bias as well as the residual mean speckle distortion. Division of the observed PS's (coadded - averaged - individual frame PS's) for both the object and the point source calibrator by the corresponding DTF's and subsequent subtraction of the corresponding N's (= mean number of photons per frame, if DTF's and PS's are normalized) removes the photon noise bias in the numerator and denominator of this object power spectrum estimator, eq 1.3.

2. OBSERVATIONS

On 30 March 1983 FLTSATCOM1 was observed for 30 minutes and again on 31 March 1983 for an additional 30 minutes using mirrors B and E (an opposite, verticle pair). The mirrors were cophased (Hege et al., 1985) using a bright star at similar elevation (within 2^o) as the satellite. The observing bandpass was 10 nm at 550 nm. The range of the object during both observations was approximately 37,000 Km.

The debiased power spectra, averaged along the direction corresponding to the mirror separation, for FLTSATCOM1 and for an SAO catalogue star near the same elevation (observed to similar statistics) are shown in Figures 1 and 2 respectively.

From the cut-off frequency in Figure 1, the size of the object is approoximately 1/50 aarcsecond. This corresponds to 3.6 m at the range of the object. It is impossible from this noisy, inadequately calibrated (i.e. poor bias correction) pair of results to produce a significant deconvolution by eq. 1.3. Such a measure would have required:

i) a longer integration.

ii) more accurate calibration of the photon point spread function (PSF), or better yet, a measurement with a true "photon counting" detector. The present scheme of localizing events in a video raster leads to non-"delta-function" photon responses and in fact to signal dependent DTF's, as noted above.

iii) Active pathlength monitoring to assure that the telescope MTF is stable during such extended integration and calibration measurements.

A second observation, with the same observing parameters, on 5 May 1983 was reduced in somewhat different manner. No effort was made to correct for noise bias. The measurements were taken from the raw autocorrelation functions. A gaussian model was used to correct for the

seeing distribution. Then a uniform disk profile was fit to the central residual, but at radii large comparaed to the size of the photon detection PSF. A siimilar measure of an SAO star was used to correct for the effects of convolution by the telescope diffraction size. Using

$$(\text{Diameter})^2 = (\text{Measured})^2 - (\text{Star})^2$$

to deconvolve, in Gaussian approximation, the diffraction-limited (stellar) response from the measured satellite response to give a value 6.1 m for the satellite diameter in the verticle direction.

These two values appear to disagree drastically, or they may agree well; but we cannot say which without further analysis. They were observed under different conditions of solar illuminatioin, and the results of our asteriod analyses (Drummond et al., 1985a,b,c) show conclusively that such large differences in the autocorrelation (or equivalently power spectrum) size can arise from illuminatioin effects. A model analysis of these results has not yet been attempted.

Clearly an image reconstruction, or better yet an image retrieval (the difference being whether image phase information is inferred or actually measured - Hege et al., 1985) is desireable. We have only begun to apply image reconstruction methods to asteroid data (c.f. figure 3 - Fienup 1979 method) and are only in preliminary stages of image phase retrieval (c.f. figure 4 - Nisenson and Papaliolios 1983 version of the Knox/Thompson 1974 method) for photon-statistics limited data.

Our best estimate presently available from these measurements is the average of the two.

Verticle Diameter (FLTSATCOM1) = 4.9 m ($\pm$2.0 m)

No measures have yet been obtained with the recently implemented six-beam interferometer acheived with the fully cophased MMT as described by Hege et al. (1985). With open loop control to compensate for temperature effects, and with discrete event Knox/Thompson phase retrieval methods, we are now in position to make a well calibrated two-dimensional measurement. By combining Knox/Thompson phase retrieval with Fienup image enhancement, we expect to be able to produce diffraction limited (75 nrad resolution) images of such objects.

3. TRACKING INTERMEDIATE- AND LOW-EARTH ORBIT OBJECTS

Several improvements to the MMT have enhanced its performance as a satellite tracking instrument. A new 24 bit D/A encoder and software to match has been installed for foth AZ and EL servos. There is no longer a requirement for separate gain settings for tracking and slewing, thus the glitches originally encountered in changing between tracking and slewing have been eliminated. Autoguiding software is now available in the Telescope Coalignment System which allows common mode tracking errors to be removed by the mount control and differential mode errors to to removed symmetrically by the secondaries. This is particularly important for maintaining the cophased condition when woperating the telescope as a multiple aperture interferometer. The present closed-loop operation of this autoguiding system at 4 Hz removes tracking errors at 1 Hz.

Pageos was acquired (about 1/2 degree from the predicted position) by executing a "squaare spiral" search around the predicted trajectory. No useful high-resolution observations were obtained:

i) The accuracy of the Aerospace supplied ephemeris was limited to 2 decimal places (36 arc seconds) for each point.

ii) The coordinates were spaced at one minute intervals. This caused tracking non-linearities beyond the capability of the guiding system (at that time) to compensate.

In order to track such an intermediate range object, we would require:

i) Ephemeris accuracy of 4 decimal places.

ii) Three or more points per minute.

Such an ephemeris should be supplied in machine readable format to be transferred to the MMT mount-control system without manual entry.

Space Shuttle was observed using coordinates acquired from Johnson Space Center. These were accurate only to three decimal places (3.6 arc

seconds) at 5 second intervals. The object was acquired in the Celestron wide field, and tracked in the MMT acquisition TV with tracking errors of 10 to 20 arc seconds. This was too imprecise to make spectroscopic observations (the purpose of that exercise), let alone to make high-resolution measurements in a 2" field of view. Nevertheless, it was encouragingly small for such a rapidly moving object, and withoud the aid of the new autoguiding capability. The range of Space Shuttle during this experiment was about 1000 Km.

The following improvements would make acquisition and tracking of objects at 1000 Km range possible using the MMT:

i) A machine-readable, 4 decimal place, 5 second interval ephemeris. On-line generation from the orbit elements would be better still.

ii) Further fine tuning of the autoguiding capabilities may improve tracking of these rapidly moving objects.

FIGURES

Figure 1. FLTSATCOM1 - Debiased power spectrum. No significant energy is seen above about 50 cycles/arc second.

Figure 2. SAO 137310 - Debiased power spectrum. Shows energy to 6.86 m aperture cut-off at 61 cycles/arc second.

Figure 3. Eros - Image by Fienup method. Shows evidence for non-symmetric object with non-uniform brightness.

Figure 4. Vesta - Image by Knox/Thompson method. Shows evidence for nearly spherical object with non-uniform brightness.

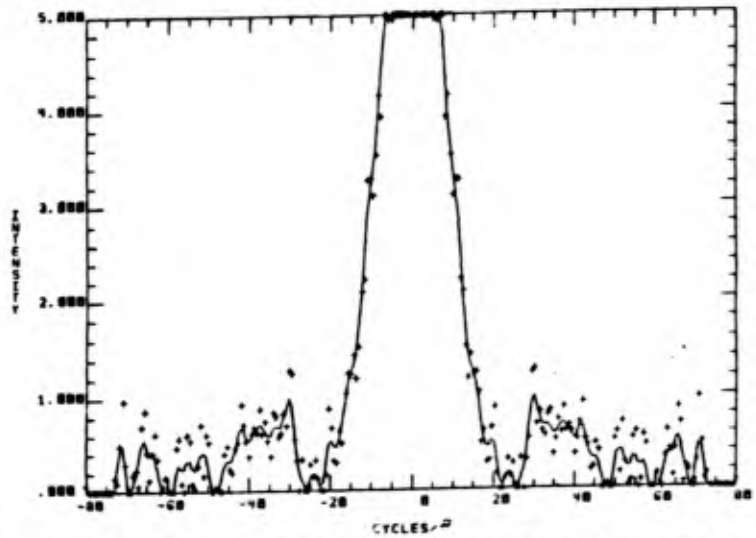

Figure 1 FLTSATCOM1 - Debiased power spectrum. No significant energy is seen above about 50 cycles/acrsecond.

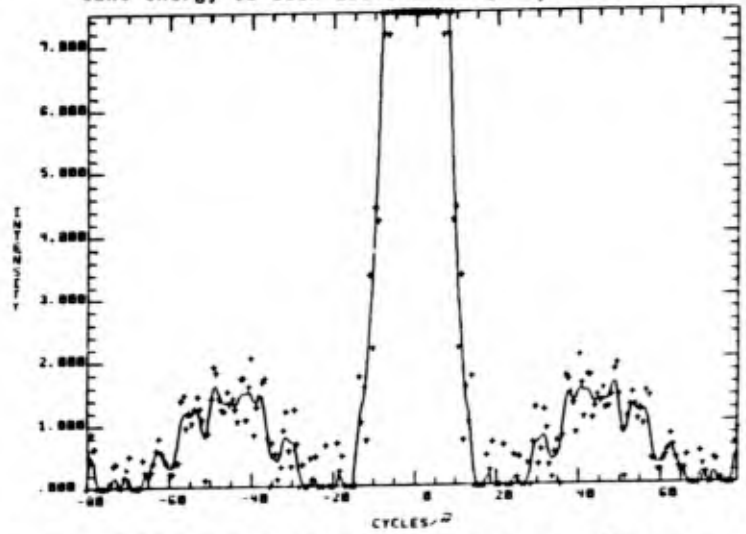

Figure 2 SAO 137310 - Debiased power spectrum. Shows energy to 6.86 m aperture cut-off at 61 cycles/arcsecond.

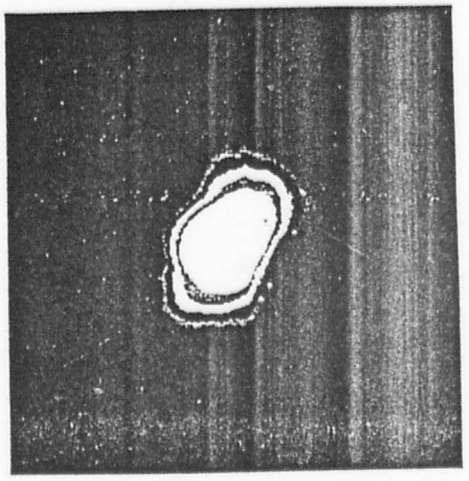

Figure 3

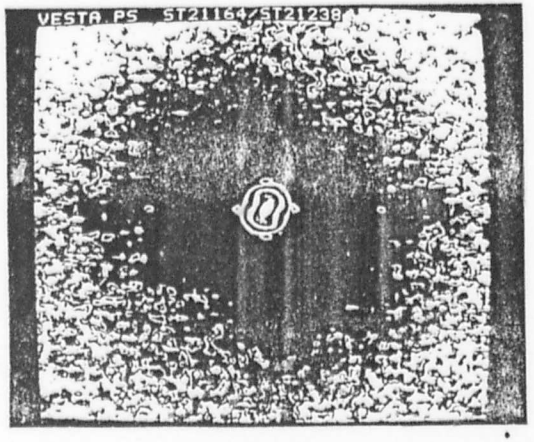

Figure 4

Circular No. 3986

Central Bureau for Astronomical Telegrams
INTERNATIONAL ASTRONOMICAL UNION

Postal Address: Central Bureau for Astronomical Telegrams
Smithsonian Astrophysical Observatory, Cambridge, MA 02138, U.S.A.

TWX 710-320-6942 ASTROGRAM CAM Telephone 617-495-7244/7440/7444

PLUTO

E. K. Hege and J. Drummond, Steward Observatory, write that a well-calibrated speckle interferometric observation made on Feb. 16.44 UT with the Harvard speckle camera at a single 1.8-m mirror of the Multiple Mirror Telescope showed the satellite 1978 P1 to be separated from the primary by 0".168 ± 0".01 in p.a. 179° ± 3°. The prediction by Harrington and Christy (1981, A.J. 86, 442) gave separation 0".36 in p.a. 7°3. The discordance in position angle confirms that found earlier (Hege et al. 1982, Icarus 50, 72) and shows the satellite's orbital inclination (with respect to the plane of the sky) to be 94° ± 1°, a decrease of 1° ± 1° over the prediction (and in contrast to a 3° ± 4° increase over prediction observed in 1980 June). This suggests that the expected eclipses of the system should be occurring when Pluto next becomes favorably placed, although events may be delayed by ~ 4 hr.

PERIODIC COMET SCHAUMASSE (1976 XV = 1984m)

J. Gibson reports his recovery of this comet as shown below. The indicated correction to the prediction on MPC 7660 is ΔT = −0.10 day. The recovery appears to confirm a single, hitherto unreported, observation of the comet by E. Roemer at the 1976 return (at ΔT = −0.03 day from the corresponding prediction).

UT	α_{1950}	δ_{1950}	m_1	Observer
1976 Dec. 27.54146	15^{h}48^{m}59^s.03	−14°06′42″.4	18.5	Roemer
1984 Sept. 5.48613	6 43 01.85	+20 42 28.2	19	Gibson
6.47909	6 46 10.85	+20 44 06.5		"

E. Roemer (Steward Observatory, Kitt Peak Station). 2.3-m reflector. The comet's image is a faint smudge, weak and diffuse in poor seeing at low altitude.

J. Gibson (Palomar Mountain Observatory). 1.2-m Schmidt telescope. Stellar condensation with very weak coma.

Computations by the undersigned show that linkage of the 1959-1960, 1976 and 1984 observations can be accomplished using the nongravitational parameter A_1 = −0.051. This compares with A_1 = −0.038 during 1911-1928 and A_1 = −0.041 during 1944-1960.

1984 September 12 Brian G. Marsden

ICARUS 61, 132–151 (1985)

Speckle Interferometry of Asteroids

I. 433 Eros

J. D. DRUMMOND, W. J. COCKE, E. K. HEGE, AND P. A. STRITTMATTER

Steward Observatory, University of Arizona, Tucson, Arizona 85721

AND

J. V. LAMBERT

Department of Astronomy, New Mexico State University, Las Cruces, New Mexico 88003

Received May 4, 1984; revised September 11, 1984

Analytic expressions for the semimajor and semiminor axes and an orientation angle of the ellipse projected by a triaxial ellipsoid (an asteroid) and of the ellipse segment cast by a terminator across the ellipsoid as functions of the dimensions and pole of the body and the asterocenteric position of the Earth and Sun are derived. Applying these formulae to observations of the Earth-approaching asteroid 433 Eros obtained with the speckle interferometry system of Steward Observatory on December 17–18, 1981, and January 17–18, 1982, the following dimensions are derived: (40.5 ± 3.1 km) × (14.5 ± 2.3 km) × (14.1 ± 2.4 km). Eros' north pole is found to lie within 14° of RA = 0^h16^m Dec. = +43° (ecliptic longitude 23°, latitude +37°). Other than knowing the rotation period of Eros, these results are completely independent of any other data, and in the main confirm the results obtained in the 1974–1975 apparition by other methods. These dimensions, together with a lightcurve from December 18, 1981, lead to a geometric albedo of 0.156 ± 0.010. A series of two-dimensional power spectra and autocorrelation functions of the resolved asteroid clearly show it spinning in space.

I. INTRODUCTION

While speckle interferometric observations of asteroids have been made in the past (Worden, 1979; Hege *et al.*, 1980a, b; Bowell *et al.*. 1981), they have been used mainly to demonstrate the high angular resolution capability of the technique. [For an introduction into astronomical speckle interferometry we recommend Dainty (1975), Worden (1979), and Hege *et al.* (1982a).] To obtain the most information from this powerful direct method, an asteroid needs to be followed throughout its rotational cycle. By assuming that the asteroid can be modeled as a rotating triaxial ellipsoid, we show in Section II that the changing semimajor axis, semiminor axis, and orientation of the projected ellipse theoretically lead not only to the three axial dimensions of the asteroid but to the location of its spin axis as well. We also include the case of a nonzero solar phase angle and take into account the terminator cast across the projected ellipse. These analytic expressions for obtaining the dimensions and pole of an asteroid as functions of quantities observable with speckle interferometry can also be used to interpret an entire photometric lightcurve not just the extrema or amplitude, if it is assumed that a lightcurve is generated by the visible illuminated portion of the projected ellipse.

With the speckle interferometry system at Steward Observatory (Hege *et al.*, 1982a), we have begun a program to observe asteroids of various taxonomic classes to provide a check of the assumptions and results obtained by radar, radiometry, photometry, polarimetry, etc., and to

0019-1035/85 $3.00

provide calibration asteroids for these methods. To demonstrate the ability of speckle interferometry to obtain useful results, we begin our program by applying our speckle technique to 433 Eros, since the various methods used to observe it in 1974–1975 have converged to well-agreed-upon dimensions and pole, summarized by Zellner (1976). Our observations of Eros with speckle interferometry in 1981–1982 and the subsequent analysis are presented in Section III, and in Section IV we display a spectacular series of power spectra and autocorrelation functions clearly showing Eros spinning in space.

In several cases, asteroids have been implicated as having satellites from speckle interferometric observations (Hege *et al.*, 1980b; Bowell *et al.*, 1981). If a satellite can be detected with speckle interferometry, then the proof of its existence will be in the ability of the technique to follow the satellite in its orbit about the asteroid, which will also lead to a determination of the mass of the system. Hege *et al.* (1982b) summarize speckle interferometric observations of such a system as represented by Pluto and Charon. We have in hand or have scheduled observations of several of the suspected binary asteroids, but Eros gives no indication of having a satellite by speckle observations.

II. THE FUNDAMENTAL EQUATIONS

A. Derivations

In matrix form, the equation for a point on the surface of a triaxial ellipsoid (asteroid) can be written as

$$\tilde{\mathbf{x}}'\mathbf{T}'\mathbf{x}' - 1 = (x'y'z')\begin{pmatrix} 1/a^2 & & \\ & 1/b^2 & \\ & & 1/c^2 \end{pmatrix}\begin{pmatrix} x' \\ y' \\ z' \end{pmatrix} - 1$$
$$= (x'/a)^2 + (y'/b)^2 + (z'/c)^2 - 1 = 0. \quad (1)$$

Let $a \geq b \geq c$ be the principal axial radii, c being the rotational axis. The projection of the ellipsoid onto the plane of the Earth's sky is an ellipse of the form $\tilde{\mathbf{y}}\mathbf{Q}\mathbf{y}$, where $\mathbf{y}$ is a two dimensional vector and $\mathbf{Q}$ is a 2×2 matrix. In an arbitrary coordinate system the equation for the ellipsoid is

$$\tilde{\mathbf{x}}\mathbf{T}\mathbf{x} - 1 = 0. \quad (2)$$

Let $\mathbf{x}' = \mathbf{R}\mathbf{x}$, where the transformation between coordinate systems $\mathbf{x}'$ and $\mathbf{x}$ is given by the rotation matrix $\mathbf{R}$. Then from (1) and (2)

$$\tilde{\mathbf{x}}\mathbf{T}\mathbf{x} = \tilde{\mathbf{x}}'\mathbf{T}'\mathbf{x}' = \tilde{\mathbf{x}}\tilde{\mathbf{R}}\mathbf{T}'\mathbf{R}\mathbf{x} \quad (3)$$

which implies that $\mathbf{T} = \tilde{\mathbf{R}}\mathbf{T}'\mathbf{R}$.

Writing (2) explicitly

$$\tilde{\mathbf{x}}\mathbf{T}\mathbf{x} - 1 = \sum_{ij} T_{ij}x_ix_j - 1$$
$$= T_{11}x^2 + 2T_{12}xy + T_{22}y^2 + 2T_{13}xz + T_{33}z^2 + 2T_{23}yz - 1 = 0.$$

Or, gathering terms in x

$$T_{11}x^2 + 2(T_{12}y + T_{13}z)x + (T_{22}y^2 + 2T_{23}yz + T_{33}z^2 - 1) = 0. \quad (4)$$

If we orient ourselves so that the yz plane is the plane of the sky and x lies along our line of sight to a triaxial ellipsoid asteroid, then for a point on the edge of the apparent ellipse not only must x satisfy (4), but since for a given y and z there is only one x which corresponds to the edge, the roots of (4) must be real and equal. Thus the discriminant of (4) must vanish:

$$4(T_{12}y + T_{13}z)^2 - 4T_{11}(T_{22}y^2 + 2T_{23}yz + T_{33}z^2 - 1) = 0$$

or gathering terms in y and z and multiplying by $-1/4T_{11}$

$$[1/T_{11}][(T_{11}T_{22} - T_{12}^2)y^2 + 2(T_{11}T_{23} - T_{12}T_{13})yz + (T_{11}T_{33} - T_{13}^2)z^2] - 1 = 0. \quad (5)$$

Now this equation is in itself quadratic and diagonalizable and can be expressed as

$$\tilde{\mathbf{y}}\mathbf{Q}\mathbf{y} - 1 = 0, \quad (6)$$

where $\tilde{\mathbf{y}} = (y, z)$ and

$$\mathbf{Q} = \frac{1}{T_{11}}\begin{pmatrix} T_{11}T_{22} - T_{12}^2 & T_{11}T_{23} - T_{12}T_{13} \\ T_{11}T_{23} - T_{12}T_{13} & T_{11}T_{33} - T_{13}^2 \end{pmatrix}.$$

Since (5) is the general equation for an ellipse in the yz plane of the sky, the presence of the cross term in yz indicates that the semimajor (semiminor) axis of the apparent ellipse makes an angle γ with the $y(z)$ axis, where γ is given by

$$\tan 2\gamma = 2Q_{12}/(Q_{11} - Q_{22}). \qquad (7)$$

To relate the matrix $\mathbf{Q}$ to the semiaxes of the apparent ellipse we need to find the eigenvalues q of $\mathbf{Q}$, where

$$\mathbf{Qy} = q\mathbf{y}.$$

The equation we need to solve then is

$$|\mathbf{Q} - q\mathbf{I}| = 0 = \begin{vmatrix} Q_{11} - q & Q_{12} \\ Q_{12} & Q_{22} - q \end{vmatrix}$$

or

$$q^2 - (Q_{11} + Q_{22})q + (Q_{11}Q_{22} - Q_{12}^2) = 0.$$

From the quadratic formula

$$q = \frac{(Q_{11} + Q_{22}) \pm [(Q_{11} + Q_{22})^2 - 4(Q_{11}Q_{22} - Q_{12}^2)]^{1/2}}{2} \qquad (8)$$

and q is related to the semimajor and semiminor axes α and β by

$$q^{\pm} = \begin{pmatrix} 1/\beta^2 & \\ & 1/\alpha^2 \end{pmatrix}.$$

Now in defining our coordinate system let us choose the y axis as coincident to the asteroid's largest axis (a) at the instant in the rotation when a lies unprojected in the plane of the Earth's sky perpendicular to our line of sight. This allows us to use Euler angles as defined and illustrated by Goldstein (1950). Thus the Euler angle θ is the angle between our z axis in the plane of the sky and z', the asteroid's spin axis. The Euler angle ϕ is the angle between the line of sight to the asteroid and the line of nodes (which lies in the plane of the Earth's sky), and by our chosen coordinate system is a constant $\pi/2$. The third Euler angle, ψ, is the rotational phase angle defined as the angle between x' (along which a lies) and the line of nodes; ψ is 0 when the longest body axis is perpendicular to our line of sight and occurs at maximum projected area. The transformation (3) leads to the symmetric T matrix, where

$$T_{11} = \frac{\cos^2\theta \sin^2\psi}{a^2} + \frac{\cos^2\theta \cos^2\psi}{b^2} + \frac{\sin^2\theta}{c^2}$$

$$T_{12} = T_{21} = -\frac{\cos\theta \sin\psi \cos\psi}{a^2} + \frac{\cos\theta \sin\psi \cos\psi}{b^2}$$

$$T_{13} = T_{31} = -\frac{\cos\theta \sin\theta \sin^2\psi}{a^2} - \frac{\cos\theta \sin\theta \cos^2\psi}{b^2} + \frac{\sin\theta \cos\theta}{c^2}$$

$$T_{22} = \frac{\cos^2\psi}{a^2} + \frac{\sin^2\psi}{b^2}$$

$$T_{23} = T_{32} = \frac{\sin\theta \sin\psi \cos\psi}{a^2} - \frac{\sin\theta \sin\psi \cos\psi}{b^2}$$

$$T_{33} = \frac{\sin^2\theta \sin^2\psi}{a^2} + \frac{\sin^2\theta \cos^2\psi}{b^2} + \frac{\cos^2\theta}{c^2}.$$

After simplification (8) can be written

$$q^{\pm} = \frac{-B \pm \sqrt{B^2 - 4AC}}{2A} \qquad (9)$$

where

$$A = a^2b^2c^2T_{11} = b^2c^2\cos^2\theta \sin^2\psi + a^2c^2\cos^2\theta \cos^2\psi + a^2b^2\sin^2\theta$$

$$-B = a^2b^2c^2T_{11}(Q_{11} + Q_{22}) = a^2(\sin^2\theta \sin^2\psi + \cos^2\psi) + b^2(\sin^2\theta \cos^2\psi + \sin^2\psi) + c^2\cos^2\theta$$

$$C = a^2b^2c^2T_{11}(Q_{11}Q_{22} - Q_{12}^2) = 1.$$

Therefore, the semimajor and semiminor axes of the ellipse projected by a triaxial ellipsoid are

$$\alpha = (q^-)^{-1/2} = \left[\frac{2A}{-B - \sqrt{B^2 - 4AC}}\right]^{1/2}$$

$$\beta = (q^+)^{-1/2} = \left[\frac{2A}{-B + \sqrt{B^2 - 4AC}}\right]^{1/2}$$

and γ makes an angle with the y axis

$$\gamma = \frac{1}{2}\tan^{-1}\left[\frac{2\sin\theta\cos\psi\sin\psi(b^2 - a^2)}{a^2(\sin^2\theta\sin^2\psi - \cos^2\psi) + b^2(\sin^2\theta\cos^2\psi - \sin^2\psi) + c^2\cos^2\theta}\right] \quad (10)$$

from (7).

Note that (9) is expressed as a quadratic solution which has some well-known properties. For instance, since the product of the roots of a quadratic equation are

$$q^+q^- = C/A,$$

we can easily express the projected area of the triaxial ellipsoid as

$$\pi\alpha\beta = \pi(q^+q^-)^{-1/2} = (A/C)^{1/2} = A^{1/2} = abcT_{11}^{1/2} \quad \text{since } C = 1.$$

Over a few rotations of the asteroid, we can regard θ as constant and $\phi = \pi/2$. Therefore we can find α, β, and γ as functions of only ψ, the rotational angle. If the latitude of the sub-Earth point is high enough, the projected ellipse will rotate smoothly through 360°. If, however, the latitude is low the ellipse will appear to reverse directions. Taking the derivative of γ with respect to ψ we can see that when the sub-Earth point lies in the body's northern hemisphere ($\theta > 0$), γ will increase monotonically, or decrease monotonically if in the southern hemisphere ($\theta < 0$), provided that $\cos^2\theta < (a^2 - b^2)/(a^2 - c^2)$. If $\cos^2\theta > (a^2 - b^2)/(a^2 - c^2)$ the projected ellipse will reverse directions when

$$\cos^2\psi = \{[\sec^2\theta(a^2 - b^2)/(a^2 - c^2)] - 1\}/\{[(a^2 - b^2)/(a^2 - c^2)] - 2\}.$$

Another consideration is that there is a twofold ambiguity in the determination of θ. The rotational axis can make either an angle θ or $180° - \theta$ with the plane of the sky, both corresponding to the same latitude in the same hemisphere for the sub-Earth point. The northern or southern hemisphere can easily be determined by the sense of rotation: if the apparent ellipse rotates through the y axis (through the maximum α) in a counterclockwise (north–east–south–west) direction, the sub-Earth point lies in the northern hemisphere, and vice versa. However, without some other piece of information, such as would be conveyed by a terminator, it is not possible to resolve the θ ambiguity.

We now have the equations relating the body dimensions and rotational pole direction to the observed size, shape, and orientation of the ellipses projected by a rotating triaxial ellipsoid. Using a nonlinear least squares technique we can solve for the six unknown parameters a, b, c, θ, and the zero points ψ_0 and γ_0, from measurements of the observables α, β, and γ as a function of time (or ψ) for a known rotational period. Thus far we have assumed, however, that we see the projected ellipse at full illumination, i.e., at a solar phase angle of 0. Particularly at large phase angles we must take the terminator into consideration. We will now outline the derivation for the size, shape, and orientation of the terminator ellipse segment as a function of the same parameters, with the added information of the known position of the Sun, but this time from a vector analysis approach rather than from the use of matrix transformations. The answers should converge for a solar phase angle of 0.

We first note that in body-centered coordinates, where a point on the surface of triaxial ellipsoid is given by (1)

$$f(x', y', z') = (x'/a)^2 + (y'/b)^2 + (z'/c)^2 = 1, \quad (11)$$

the unit vector to the Earth is given by $\mathbf{E} = (i, j, k)$ where

$$\begin{aligned} i &= -\cos\theta \sin\psi \\ j &= -\cos\theta \cos\psi \\ k &= \sin\theta \end{aligned} \quad (12)$$

and the unit vector to the Sun is given by $\mathbf{S} = (l, m, n)$ where

$$\begin{aligned} l &= -\cos\theta_\odot \sin\psi_\odot \\ m &= -\cos\theta_\odot \cos\psi_\odot \\ n &= \sin\theta_\odot. \end{aligned} \quad (13)$$

The body centered celestial coordinates of the Earth and Sun are θ, ψ, and $\theta_\odot$, $\psi_\odot$, where the θ's are latitudes of the sub-Earth and sub-Sun points and the ψ's are related to the longitudes of these points (L, measured in a right-handed coordinate system from the a axis) by $\psi = -(L + 90°)$.

Since the outward normal for a point on the surface of an ellipsoid described by f (Eq. (1)) is given by ∇f, and since the terminator is the locus of points whose outward normals are perpendicular to the direction to the Sun ($\mathbf{S}$), the terminator equation is $\mathbf{S} \cdot \nabla f = 0$, which leads to

$$-x'_T \cos\theta_\odot \sin\psi_\odot/a^2 - y'_T \cos\theta_\odot \cos\psi_\odot/b^2 + z'_T \sin\theta_\odot/c^2 = 0 \quad (14)$$

where from (1)

$$(x'_T/a)^2 + (y'_T/b)^2 + (z'_T/c)^2 = 1. \quad (15)$$

As before we rotate the yz plane of the Earth's sky so that the z axis coincides with the projection of the body's rotational axis. The obliquity, ρ, is the angle required to rotate about the line of sight to the asteroid (the x axis) until the spin axis is in the xz plane. If the Earth and Sun define the original xy plane, then ρ is also the angle between the position angle of the Sun (centered on the asteroid) and the y axis, measured counterclockwise (N–E–S–W) from the Sun (see Appendix I). We then get x'_T, y'_T, and z'_T in terms of the new coordinates x, y, z

$$\begin{aligned} x'_T &= -x \cos\theta \sin\psi + y \cos\psi + z \sin\theta \sin\psi \\ y'_T &= -x \cos\theta \cos\psi - y \sin\psi + z \sin\theta \cos\psi \\ z'_T &= x \sin\theta + z \cos\theta, \end{aligned} \quad (16)$$

and substituting into (14) and recombining, we obtain

$$x(il/a^2 + jm/b^2 + kn/c^2) + y(l \cos\psi/a^2 - m \sin\psi/b^2) + z(l \sin\theta \sin\psi/a^2 + m \sin\theta \cos\psi/b^2 + n \cos\theta/c^2) = 0. \quad (17)$$

Next we solve (17) for x, substitute this back into (16), and use x'_T, y'_T, z'_T in terms of only y and z in (14). This yields an expression for the terminator as seen projected onto the Earth's plane of sky, which we transform into an ellipse as we did in the solar phase = 0 case, except that the discriminant of (4) does not vanish, and therefore (4) must be solved fully.

It is advantageous to express the unit vector to the Sun in terms of known constraints, e.g., $\mathbf{E} \cdot \mathbf{S} = \cos\omega$, where ω is the known solar phase angle:

$$\begin{aligned} l &= -\cos\theta_\odot \sin\psi_\odot \\ &= -[\cos\omega \cos\theta \sin\psi + \sin\omega(\sin\rho \sin\theta \sin\psi - \cos\rho \cos\psi)] \\ m &= -\cos\theta_\odot \cos\psi_\odot \\ &= -[\cos\omega \cos\theta \cos\psi + \sin\omega(\cos\rho \sin\psi + \sin\theta \sin\rho \cos\psi)] \\ n &= \sin\theta_\odot = \cos\omega \sin\theta - \sin\omega \cos\theta \sin\rho. \end{aligned} \quad (18)$$

We finally get after solving (4) and (8) for the terminator as seen by the Earth, and simplifying, an expression analogous to (9)

$$q_T^{\pm} = \frac{-B_T \pm \sqrt{B_T^2 - 4A_T^2 C_T}}{2A_T^2}$$

where $A_T = b^2c^2il + a^2c^2jm + a^2b^2kn$

$$C_T = b^2c^2l^2 + a^2c^2m^2 + a^2b^2n^2$$

$$-B_T = -BC_T - a^2b^2c^2 \sin^2 \omega$$

and the expression analogous to (10)

$$\gamma_T = \frac{1}{2} \tan^{-1} \left[\frac{\sin \theta \sin 2\psi(a^2 - b^2) + \sin^2\omega \sin 2\rho a^2b^2c^2/C_T}{[\cos 2\psi(a^2 - b^2) + (a^2i^2 + b^2j^2 + c^2k^2) - c^2 - \sin^2\omega \cos 2\rho a^2b^2c^2/C_T]} \right].$$

B. Implications for Lightcurves

Since the cusps are points that lie on the edge of both the projected ellipse and the terminator ellipse, since the terminator ellipse is internally tangent to the projected ellipse, and since a line connecting the cusps passes through the common center of both ellipses, it can be shown that the illuminated visible area (A_i) of a smooth ellipsoid seen at some phase angle is given by

$$A_i = (\pi\alpha\beta + \pi\alpha_T\beta_T)/2 = \pi/2[A^{1/2} + A_T/C_T^{1/2}] \quad (19)$$

and the area in shadow is

$$A_s = \pi/2[A^{1/2} - A_T/C_T^{1/2}]. \quad (20)$$

The area in shadow is larger than the illuminated area when $A_T < 0$ (and therefore β_T is negative). Derivations of the lightcurve equations for a geometrically scattering triaxial ellipsoid are given by Barucci and Fulchignoni (1982) and by Ostro and Connelly (1984). The latter authors correct some of the equations of the former and note that the area in shadow can be larger or smaller than the illuminated area depending, respectively, on whether or not "the plane of the terminator intersects the solar phase angle."

Equations (19) and (20) lead to some interesting considerations with regard to information gathered from photometry. Assuming that a lightcurve is generated by only the changing illuminated area as a function of rotation, then (19) is our analytic expression for a lightcurve. In reality, (19) may only be proportional rather than equal to the observed intensity as a function of time, but the proportionality factors should be expressible as functions of not only ω, the solar phase angle (the usual phase function), but also of the obliquity ρ and the aspect $(90° - \theta)$. In fact, any attempt to deduce microscopic or macroscopic properties of asteroids should include the geometrical effect that a terminator has on the amount of area in shadow. The usual phase function does not completely describe the behavior or the brightness of an asteroid over time. Especially at larger phase angles, completely different lightcurves or extrema of brightness can result from a different θ or ρ at the same ω (Dunlap, 1971; Surdej and Surdej, 1978; Barucci *et al.*, 1982).

The three methods of rotational pole determination, the lightcurve amplitude/aspect relation, the brightness/aspect relation (Zappalà *et al.* 1983; Zappalà and Knežević 1984), and photometric astrometry (Taylor, 1979; Taylor and Tedesco, 1983), are all affected by improper consideration of the area in shadow bounded by the terminator and the dark limb. The amplitude and brightness of lightcurves should be judged taking the location of the terminator into effect. Photometric astrometry, which relies on a comparison of extremal timings over long intervals, will lead to spurious results if the terminator is not considered, because the epoch of maximum and minimum light shift with respect to the maximum and minimum projected total area as a function of ω *and* θ *and* ρ. Taylor and Tedesco (1983) are aware of this and restrict lightcurve comparisons to observations made at the same ecliptic longitude and solar phase angle, which eliminates the dependence of lightcurve shifts with respect

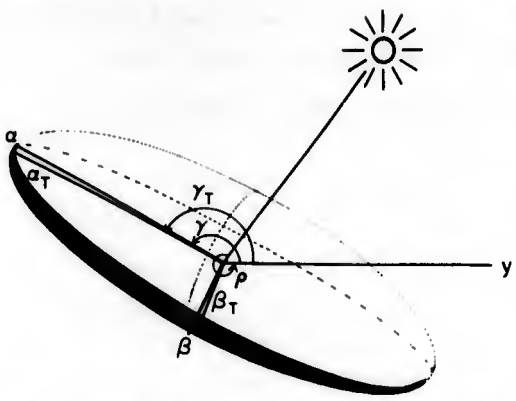

FIG. 1. The ellipse projected by a triaxial ellipsoid. $\alpha, \beta, (\alpha_T, \beta_T)$ are the semimajor and semiminor axes of the projected body (terminator) ellipse, and $\gamma(\gamma_T)$ is the position angle of $\alpha(\alpha_T)$ measured from y in the yz plane of the Earth's sky. The x axis lies along the line of sight to the asteroid. The obliquity ρ is defined in Appendix I.

to θ and ω, but not to ρ. We define an amplitude of a predicted lightcurve as the maximum illuminated area divided by the minimum over a rotation, a phase lag as the epoch of maximum illuminated area minus the epoch of maximum total projected area, and list these quantities in the results of each model fit for Eros in Section III.

C. Summary

Recapitulating, with reference to Fig. 1, to Appendices I and II, and to the unit vectors (12) and (18), the semiaxes of the ellipse of the body seen in projection for solar phase angle $\omega = 0$ are (from Eq. (9) *et seq.*)

$$(\alpha^-)^2, (\beta^+)^2 = \frac{2A}{-B \pm \sqrt{B^2 - 4AC}}, \quad (21)$$

where superscript signs specify the corresponding eigenvalues and

$$A = (bci)^2 = (acj)^2 + (abk)^2$$

$$-B = a^2(1 - i^2) + b^2(1 - j^2) + c^2(1 - k^2)$$

$$C = 1,$$

and

$$\tan 2\gamma = [\sin\theta \sin 2\psi(a^2 - b^2)]/\{\cos 2\psi(a^2 - b^2) + [(ai)^2 + (bj)^2 + (ck)^2] - c^2\}. \quad (22)$$

We note that γ reverses direction if

$$\cos^2\theta > \frac{a^2 - b^2}{a^2 - c^2}.$$

For solar phase angle $\omega \neq 0$ the semiaxes of the ellipse due to the terminator (subscript T) are

$$(\alpha_T^-)^2, (\beta_T^+)^2 = \frac{2A_T^2}{-B_T \pm \sqrt{B_T^2 - 4A_T^2 C_T}}, \quad (23)$$

where the sign convention for the roots is as for Eq. (21) and

$$A_T = (bc)^2 il + (ac)^2 jm + (ab)^2 kn$$

$$C_T = (bcl)^2 + (acm)^2 + (abn)^2$$

$$-B_T = C_T(-B) - a^2b^2c^2 \sin^2\omega, \text{ and}$$

$$\tan 2\gamma_T = \frac{[\sin\theta \sin 2\psi(a^2 - b^2) + \sin^2\omega \sin 2\rho a^2b^2c^2/C_T]}{\{\cos 2\psi(a^2 - b^2) + [(ai)^2 + (bj)^2 + (ck)^2] - c^2 - \sin^2\omega \cos 2\rho a^2b^2c^2/C_T\}}. \quad (24)$$

Note that as the solar phase angle goes to 0, $C_T \to A$, $A_T \to A$, $B_T \to AB$, and, thus, α_T, $\beta_T \to \alpha, \beta$, and $\gamma_T \to \gamma$. The illuminated area is given by (19) and the area in shadow by (20).

III. 433 EROS

A. Speckle Interferometry

To inaugurate our speckle interferometry studies of minor planets, treated as smooth,

featureless, geometrically scattering triaxial ellipsoids, rotating about their shortest (c) axis, we chose the asteroid 433 Eros since it is perhaps the best studied asteroid of all, with well-agreed-upon rotational pole coordinates and axial dimensions. With a 300-Å-wide filter at 5500 Å, we made seven 10-min observations of Eros over the two consecutive nights of December 17 and 18, 1981, and again over January 17 and 18, 1982, using the 2.3-m telescope and speckle camera and equipment (Hege *et al.*, 1982a) of Steward Observatory. Each Eros observation was preceded and followed by a similar observation of a nearby (<1°) star. The unbiased two-dimensional speckle image power spectrum of Eros was divided (deconvolved) by the unbiased power spectrum of the stars observed before and after to remove the modulation transfer function of the telescope and the seeing (Hege *et al.*, 1982*a*). The adopted parameters of the projected ellipse for each observation are the averages of four independent measurements of α, β, and γ; each deconvolution (one with a star observed before and one with a star observed after Eros) was examined over two regions (one at high spatial frequencies and one at low frequencies). The semimajor axis, semiminor axis, and relative position angle of the long axis were determined by finding the best fit to the power spectrum of a uniformly bright ellipse.

We assume that the measured ellipse will be well approximated by an ellipse that is a mean between the ellipse due to the terminator and the projected ellipse. To form this mean we calculate the ellipse that has the same area and the same ratios of moments as does the visible illuminated part of the asteroid as found with the equations derived in Section II. Assuming uniform illumination, a y moment, z moment and cross moment can be calculated for the illuminated figure as

$$\int y^2 dydz, \qquad \int z^2 dydz, \qquad \int yzdydz,$$

respectively. We include a "photometric constraint" by requiring that the mean ellipse have the same area as does the visible illuminated portion of the asteroid, in addition to having the same ratio of y, z, and yz moments. We then compare these calculated mean ellipses to our observations using sets of measured α, β, and γ, as functions of rotational phase, by means of a nonlinear least-squares program adapted from Jefferys (1980). To put the dimensionless γ on equal footing in the least-squares program with α and β we weight each γ by $(\alpha^2 - \beta^2)^{1/2}$. This makes sense because the more eccentric the ellipse, the easier it is to determine its position angle, and the greater the weight assigned to γ.

Table I lists the results of a five-parameter (biaxial) fit for the December 1981 run, while Tables II and III list the biaxial and triaxial results for January 1982. Biaxial fits yield the diameters 2a and 2b ($c = b$), the asterocentric sublatitude of the Earth, θ, a

TABLE I

LEAST-SQUARES RESULTS FOR EROS DECEMBER 17–18, 1981: BIAXIAL CASE $\omega = 40°$

	2a	2b	θ	ψ_0	ρ
2a = 38.9 ± 2.5 km	2.5 km				
2b = 14.0 ± 1.9 km	0.11	1.9 km			
θ = −75° ± 26°	0.66	−0.02	26°		
ψ_0 = −7° ± 106°	−0.05	0.14	−0.19	106°	
ρ = 69° ± 105°	0.06	−0.14	0.20	−1.00	105°

Note. Pole (1950): RA = 48° DEC = +48°; (±31°). Phase lag of maximum: +64°; minimum: +66°. Amplitude: 1.094. Standard error of fit: 4.8 km.

TABLE II

LEAST-SQUARES RESULTS FOR 433 EROS JANUARY 17–18, 1982: BIAXIAL CASE $\omega = 52°$

	2a	2b	θ	ψ_0	ρ
2a = 43.8 ± 4.3 km	4.3 km				
2b = 14.6 ± 3.0 km	0.08	3.0 km			
θ = −58° ± 12°	0.51	−0.15	12°		
ψ_0 = 48° ± 14°	0.09	0.56	0.24	14°	
ρ = −59° ± 14°	−0.08	−0.54	−0.25	−0.94	14°

Note. Pole (1950) RA = 5° DEC = 37°; (±10°). Phase lag of maximum: −4°; minimum: −2°. Amplitude: 1.369. Standard error of fit: 7.9 km.

TABLE III

LEAST-SQUARES RESULTS FOR 433 EROS JANUARY 17–18, 1982: TRIAXIAL CASE $\omega = 52°$

	2a	2b	2c	θ	ψ_0	ρ
2a = 46.7 ± 4.5 km	4.5 km					
2b = 18.8 ± 3.7 km	0.21	3.7 km				
2c = 13.3 ± 13.3 km	0.01	−0.17	13.3 km			
$\theta = -51° \pm 9°$	0.56	0.03	0.35	9°		
$\psi_0 = 30° \pm 15°$	0.08	0.50	−0.01	−0.01	15°	
$\rho = -43° \pm 15°$	−0.08	−0.49	−0.00	−0.02	−0.94	15°

Note. Pole (1950) RA = 356° DEC = +46°; (±10°). Phase lag of maximum: −8°; minimum: +4°. Amplitude: 1.365. Standard error of fit: 8.3 km.

rotational zero point, ψ_0, and the obliquity, ρ. Triaxial fits also yield c, but near a polar aspect c is so foreshortened that it becomes indeterminate and only a biaxial fit becomes possible. This was the case in December and a triaxial solution could not be found.

The θ, $180° - \theta$ ambiguity exists only for a solar phase angle of 0. In theory, the effect of the terminator should resolve the ambiguity, but in practice the difference may not always be significant enough to provide a solution. For every model, we examined fits for both counterparts of the θ ambiguity, but near a polar aspect only one global minimum in the χ^2 hyperspace is to be expected since the ambiguity disappears when $\theta = \pm 90°$. Thus, between the two solutions for January, the one most closely matched to the single December solution is chosen.

In each table are listed the results and the 1σ (standard deviation) errors determined from the fit. The full correlation matrix, where the diagonal elements are these same formal errors and the off-diagonal elements are the normalized correlation coefficients, is given in each table as well. The 1950 celestial coordinates of the pole derived from θ, ρ, the position of the asteroid, and the position of the Sun are then given, followed by the phase lags and lightcurve amplitudes as previously defined, with the phase lag for maximum listed first. Finally, the value of the standard error (in kilometers) from the fit is listed, i.e.,

$$\mathrm{SE} = \left[\frac{\text{residuals}^2}{N - n}\right]^{1/2} \tag{25}$$

where $N = 21$ equations of condition, $n = 5$ or 6 parameters, and the residuals are between the measured and predicted α, β, and $(\alpha^2 - \beta^2)^{1/2}\gamma$. To mitigate, to some extent, the model dependence of our final determination of the dimensions and pole of Eros, we first form weighted averages of the parameters from Tables II and III for January using $c = b$ from biaxial fits, and using the $1/\sigma^2$ as weights. Then we find weighted averages between January and December.

The determination of the error in the location of the pole depends only on the errors of θ and ρ. The area of uncertainty on the sky surrounding each pole is wedge shaped, but we quote the radius of a circle with the same area for convenience. When finding the weighted pole between two determinations (for example, between the December and January poles), we weight each according to the area of error and locate the pole between the two.

Our best estimate of the dimensions and pole are given in Table IV, along with a consensus model from Zellner (1976), who used photometric, polarimetric, spectroscopic, radiometric, radar, and occulation results from the 1974–1975 apparition of Eros to synthesize a coherent model. His pole is based on the results of Millis *et al.* (1976) and Scaltriti and Zappalà (1976), who used an amplitude/aspect relationship to

TABLE IV

COMPARISON OF RESULTS FOR 433 EROS

Dimensions	
Speckle interferometry (this paper)	
2a = 40.5 ± 3.1 km	Pole (1950) RA = 4 ±14°
2b = 14.5 ± 2.3 km	
2c = 14.1 ± 2.4 km	DEC = +43
Consensus model (Zellner, 1976)	
2a = 36 ± 1 km	
2b = 15 ± 1 km	Pole (1950) RA = 10 ± 2°
2c = 13 ± 1 km	DEC = +16 ± 2°
Radar (Jurgens and Goldstein, 1976)	
2a = 37.2 ± 0.3 km	
2b = 15.7 ± 0.3 km	Assumed Pole
2c assumed = 14 km	
Radiometry (Lebofsky and Rieke, 1979)	
2a = 39.3 ± 2.0 km	
2b = 16.1 ± 0.8 km	Assumed Pole
2c assumed = 2b	

Pole Coordinates

	1950 Ecliptic	
	Longitude	Latitude
This paper	23° (± 14°)	+37°
Scaltriti and Zappalà (1976)	17° ± 1°	+10° ± 4°
Millis *et al.* (1976)	15.4° ± 2.2°	+9.3° ± 3.8°
Dunlap (1976)	16° ± 3°	+12° ± 1°
Lumme *et al.* (1981)	15°	+20°
Taylor (1984) from 1974–1975	18° (± 2.0°)	+7°
from 1981–1982	21° (± 3.3°)	+13°

find a pole, and of Dunlap (1976), who used photometric astrometry. Table IV also shows the results of the radar study of Eros by Jurgens and Goldstein (1976), who assumed a c axis diameter of 14 km and from Dunlap's pole a sublatitude of 20° (although according to our calculations with Dunlap's pole it should have been 6°). A detailed thermal modeling of Eros was compared to radiometric observations by Lebofsky and Rieke (1979), who assumed $b = c$ and Zellner's pole; their results are also shown in Table IV. The ecliptic coordinates of Eros' pole as determined since Vesely's (1971) summary of the subject complete Table IV. Taylor (1984) has used photometric astrometry for the 1974–1975 apparition of Eros, and independently for the 1981–1982 lightcurves to find the poles listed in Table IV.

Figure 2 shows our weighted model (solid line) prediction and the measured major axes (upper symbols) and minor axes (lower) points for the December (solar phase angle = 40°) run. The upper dashed

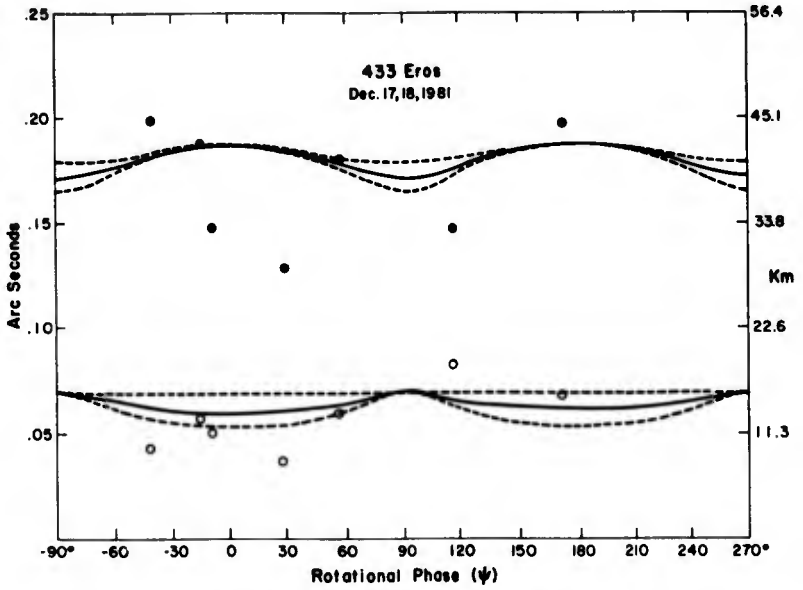

FIG. 2. Major diameter (upper part of figure) and minor diameter of 433 Eros as a function of rotational phase over Dec. 17–18, 1981. The measured diameters are shown as dots (solid for major and open for minor diameters), the solid lines are the predicted measured diameters using our results from Table IV, the dashed line above each solid line is the predicted projected body diameter, and the dashed line below is the predicted terminator diameter.

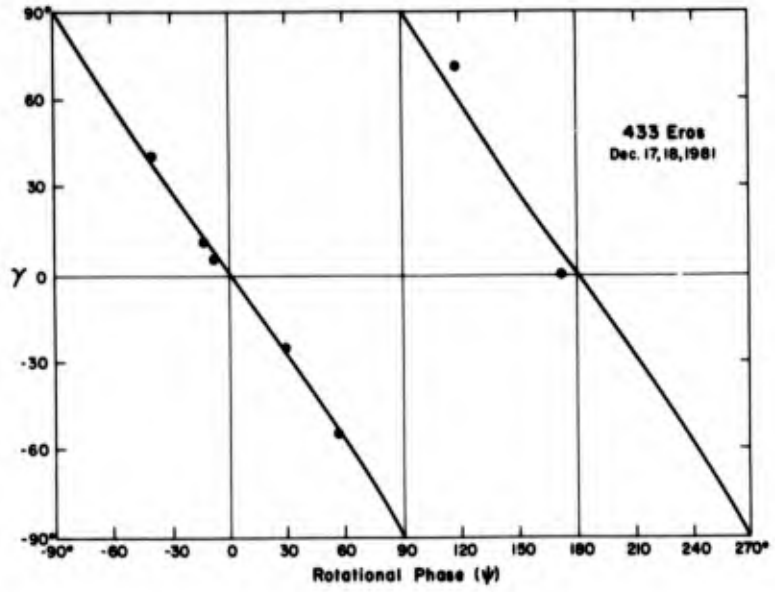

FIG. 3. γ as a function of rotational phase over Dec. 17–18, 1981. Measured γ's are dots; the solid line is the predicted position angle of the illuminated ellipse using our parameters in Table IV. The position angle of the projected ellipse and the terminator fall within the width of the solid line. The negative slope indicates that the sub-Earth point lies in the asteroid's southern hemisphere.

line through each set of points is due to the projected body ellipse while the lower dashed line is due to the terminator ellipse; the actual model fit always falls between the two. Figure 3 shows the fit to γ. Figures 4 and 5 are for the January (52°) run, but this time the nonlinear, least-squares program tended to values of 0 for the minor

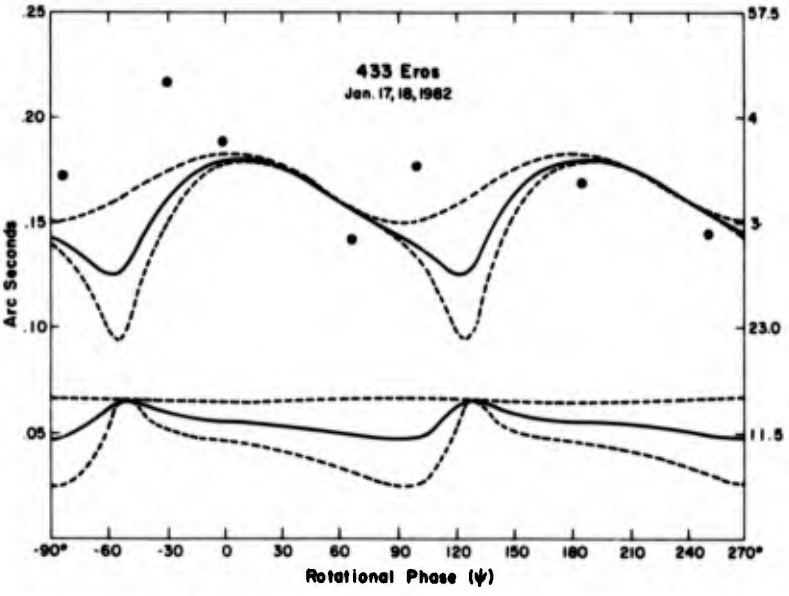

FIG. 4. Same as Fig. 2, but for Jan. 17–18, 1982. Because the minor diameter was apparently unresolved, we do not plot the measured minor diameters. The nominal resolution limit of the 2.3-m telescope is 0".05.

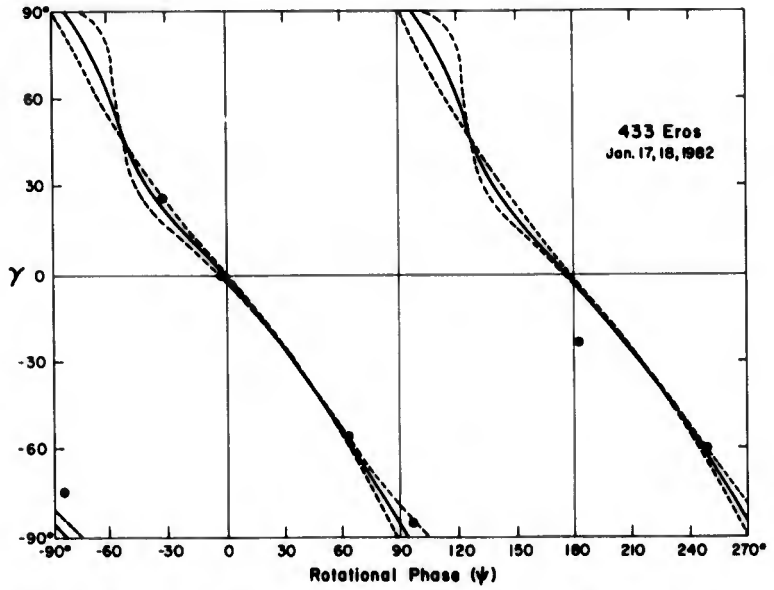

FIG. 5. Same as Fig. 3, but for Jan. 17–18, 1982. The dashed line through (0,0) is the position angle of the projected ellipse. The other dashed line is the position angle of the terminator.

axes, implying that the short dimension of the projected body ellipse, made even smaller by the terminator, was 0, i.e., was not resolved. We, therefore, set the "measured" minor axes equal to 0".05 (=11.5 km), the nominal resolution limit of the 2.3-m telescope, but did not use the β residuals in finding SE, set $N = 14$ instead of 21 in Eq. (25), and did not plot measured β's in Fig. 4. While the scatter is rather large for α and β (with some systematic trend evident in the residuals for January), it is small for the γ curve. This is to be expected since the viewing geometries during these runs is rather polar, with latitudes of the sub-Earth point being $-74°$ in December and $-57°$ in January. Such situations create little change in α or β and a nearly linear change in γ as a function of rotational phase. It is immediately obvious that the Earth lies in the asteroid's southern hemisphere because for our coordinate system a $\theta < 0$ yields a negative slope for the γ curve, and for $\theta > 0$, a positive slope, as a function of ψ. The sense of rotation is undoubtedly the easiest piece of information to obtain from speckle interferometry, whereas neither photometric astrometry nor radiometry (Matson, 1971; Morrison, 1977) can determine this in less than several months.

Figures 6 and 7 illustrate the lightcurve for December and January generated by (19), again with the upper dashed line representing the area of the projected ellipse, the lower dashed line that of the terminator ellipse, and the solid line that of the total illuminated area.

B. Eros' Lightcurve and Albedo

On December 18, 1981, D. Tholen obtained the lightcurve of Eros shown in Fig. 8 with the 154-cm telescope at the Catalina station of the University of Arizona. A minimum of $B = 10.96$ occurred at 4.517 UT and a maximum of 10.59 at 5.955 UT. With a rotational period of 5.2703 hr from Tedesco (1979), which is the mean of the sidereal periods determined by Millis *et al.* (1976) and Dunlap (1976) during the 1974–1975 apparition, we note that the difference between the maximum and minimum is 1.438 hr or 98° in rotational phase. A comparison of Tholen's lightcurve characteristics with one predicted from Zellner's

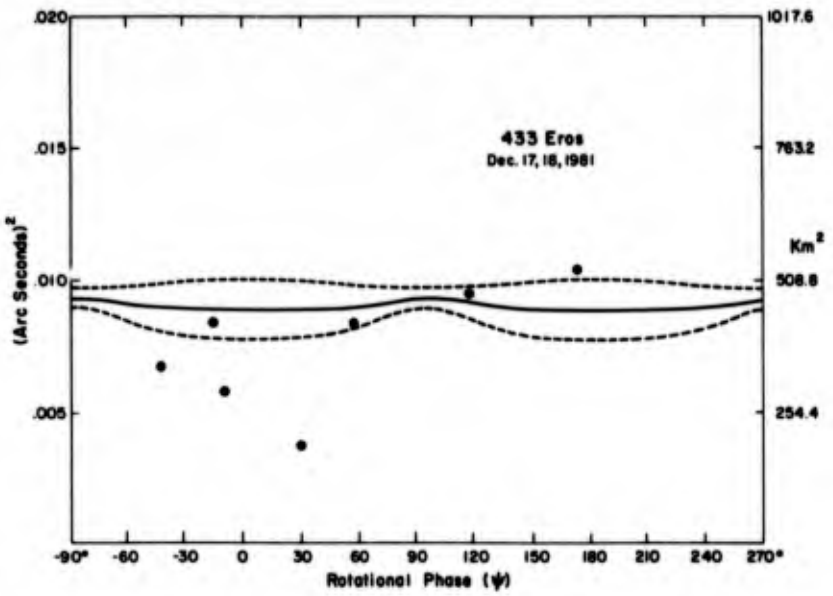

FIG. 6. Predicted "lightcurve" of Eros for Dec. 17–18, 1981. Assuming that the lightcurve is generated by the illuminated area, the upper dashed line is the predicted area of the projected body ellipse, the lower dashed line is the area of the terminator ellipse, and the solid line is the illuminated area, all from our model for Eros given in Table IV. The dots in the figure are the products of our measured α and β.

model, one from the December fit, and one from our weighted model (Fig. 6) is listed in Table V. (Note that the ordinate of Fig. 6 is area, which if assumed proportional to intensity, leads to the superimposed lightcurve in Fig. 8.)

Specification of the positions of the Sun, the asteroid, and the asteroid's pole does

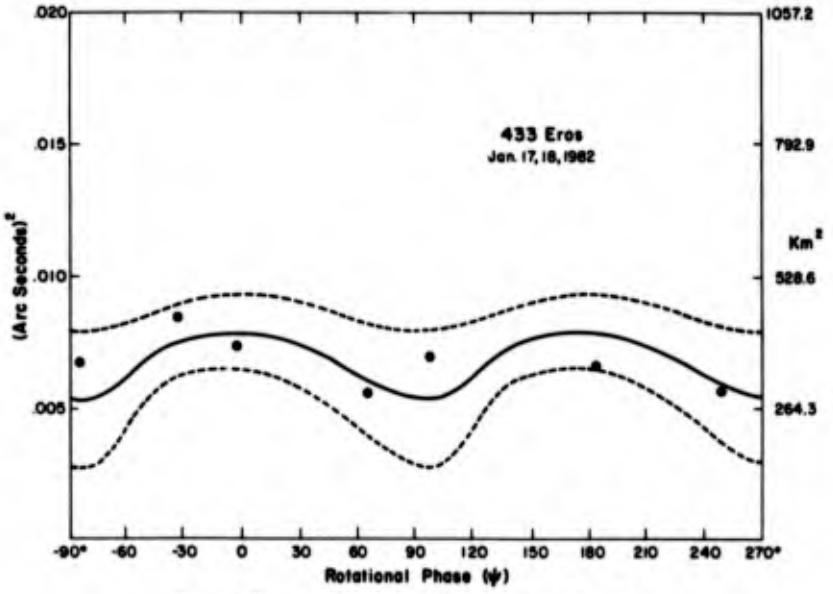

FIG. 7. Same as Fig. 6, but for Jan. 17–18, 1982.

TABLE V

COMPARISON OF OBSERVED AND THEORETICAL LIGHTCURVE CHARACTERISTICS

	Tholen	Zellner	Dec. fit only	Dec. + Jan. model
Rotational phase difference max − min	98°	100°	88°	112°
Rotational phase difference of max from Tholen's max	0	−24°	−33°	−36°
Rotational phase difference of min from Tholen's min	0	−22°	−43°	−22°
Amplitude in mag	0.37	0.23	0.10	0.07

not lead to predictions of the times of extrema unless an epoch and period are also known. In other words, even if the pole is known it is not possible to predict the lightcurve for a given night without a time reference. Therefore, in order to compare the observed lightcurve to the predicted ones we proceed as follows. With the position of the pole it is possible to predict the position angle of maximum elongation (the location of the y axis). Then it is merely a matter of noting the time that the rotating ellipse attains this position angle, which establishes rotational phase zero. For high sub-Earth latitudes, γ varies nearly directly with ψ, as can be seen by the slope of nearly -1 for the γ curve in Fig. 3 and the cross correlation of -1 for ψ_0 and ρ in Table I. Thus the sum of ψ_0 and ρ is nearly a constant, and if ρ is known then ψ_0 can be obtained from the measured value of the constant. From Table I the value for the constant is 62°, from the adopted pole ρ is −98°, and ψ_0, then, is −20° relative to the time of our first mea-

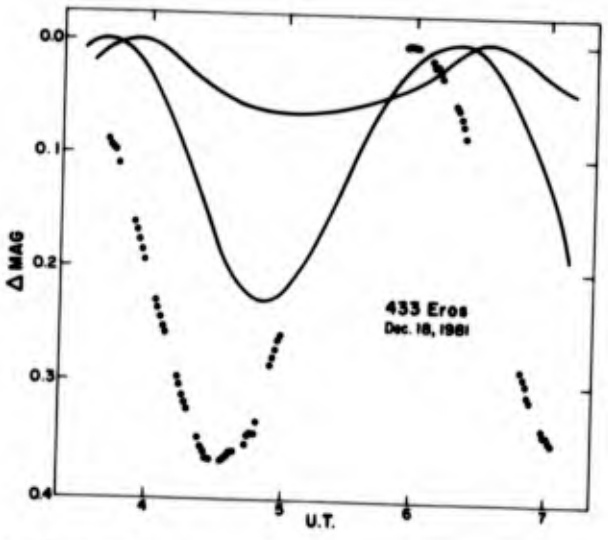

FIG. 8. Lightcurve of Eros obtained by D. Tholen with the 154-cm telescope at the Catalina station of the University of Arizona. Solid dots constitute the lightcurve measured by Tholen, the shallow curve represents the lightcurve predicted from our model, assuming that intensity is proportional to illuminated area as discussed in the text, and the deeper curve is the lightcurve from the consensus model with the same assumption. The maximum for Tholen's lightcurve is $B = 10.59$ and the minimum is $B = 10.96$.

surement point (the fourth point in Fig. 6). Using the same constant, but ρ as predicted from Zellner's pole, we can also make a predicted lightcurve for Zellner's model, all of which leads to Table V and Fig. 8.

At first it might appear that the agreement between the observed and theoretical lightcurves is poor. However, since both Dunlap (1976) and Millis *et al.* (1976) found that lightcurve amplitudes from models must be scaled up, especially at larger solar phase angles, in order to match Eros' observed amplitudes, the amplitude discrepancies are not worrisome to our results for the size and shape of the asteroid. In addition, it should be recalled that our predicted "lightcurves" are only the total projected area in illumination and do not include any particular scattering law, although at lower solar phase angles (<20°), assuming that the intensity is proportional to the illuminated area is tantamount to assuming Lommel–Seeliger scattering. In fact, the poor phase and amplitude match between the observed and predicted lightcurves could result from any one or combination of the following: high sub-Earth latitudes produce low-amplitude lightcurves containing relatively little phase information, making it difficult to establish a zero phase point accurately; no scattering laws are included; and Eros may depart from a smooth triaxial ellipsoid. Indeed, Jurgens and Goldstein (1976) noted that not only was Eros rough on the scale of 3.5 and 12.6 cm, as well as 70 cm (Campbell *et al.*, 1976), but that the projected axis of rotation did not equally divide the projected area, as would be the case for an ellipsoid. For these reasons we place little importance in the phase discrepancies, attributing them to the microscopic properties of Eros. The gross features (size, shape, and pole) are well established by speckle interferometry.

Using the phase coefficient of 0.024 mag/deg, the reddening of 0.001 mag/deg, and the B − V of 0.88 for Eros from Zellner (1976), together with the maximum B of 10.59 from Tholen's lightcurve and our determination of the illuminated area at lightcurve maximum, we find a $V_0(1,0)$ (magnitude at maximum light corrected to unit distance and zero solar phase angle) of 10.85 and a geometric albedo of 0.156 ± 0.010. This $V_0(1,0)$ is somewhat fainter than Zellner's 10.78 ± 0.04 from the 1974–1975 apparition of Eros, which was 0.5 mag brighter than that found in earlier apparitions. The error in our albedo covers the extreme range induced by assigning maximum or minimum illuminated area, from the December results or from the combined January/December model, to the observed maximum in Tholen's lightcurve. The albedo stands between Zellner's 0.19 ± 0.01 and Lebofsky and Rieke's (1979) radiometric determination of 0.125 ± 0.025.

IV. A VISUAL COMPARISON

Figure 9 is a summary of the actual speckle data for the 17–18 December 1981 observations after processing to correct for atmospheric seeing effects. The principal result of this analysis is the set of debiased seeing-corrected power spectra [see Hege *et al.* (1982a,b) for further details of speckle data reductions] shown in the center row. On the left is the result for an unresolved star showing energy, nearly uniformly, to the diffraction limit of the measurement. The next seven frames show results for Eros at different lightcurve phases. These are characteristically different from the result for an unresolved star in two ways: the energy falls off more rapidly than the diffraction-limited result (i.e., the object is resolved) and it does not fall off uniformly (the object is more highly resolved—longer—in a particular direction). Unfortunately, instrumental effects are also present, notably vertically (N–S), and especially near the center (at lowest spatial frequencies). Nevertheless, the two significant attributes of these data sets, those showing the object to be resolved and elongated, are sufficient to support the further analysis described in this paper.

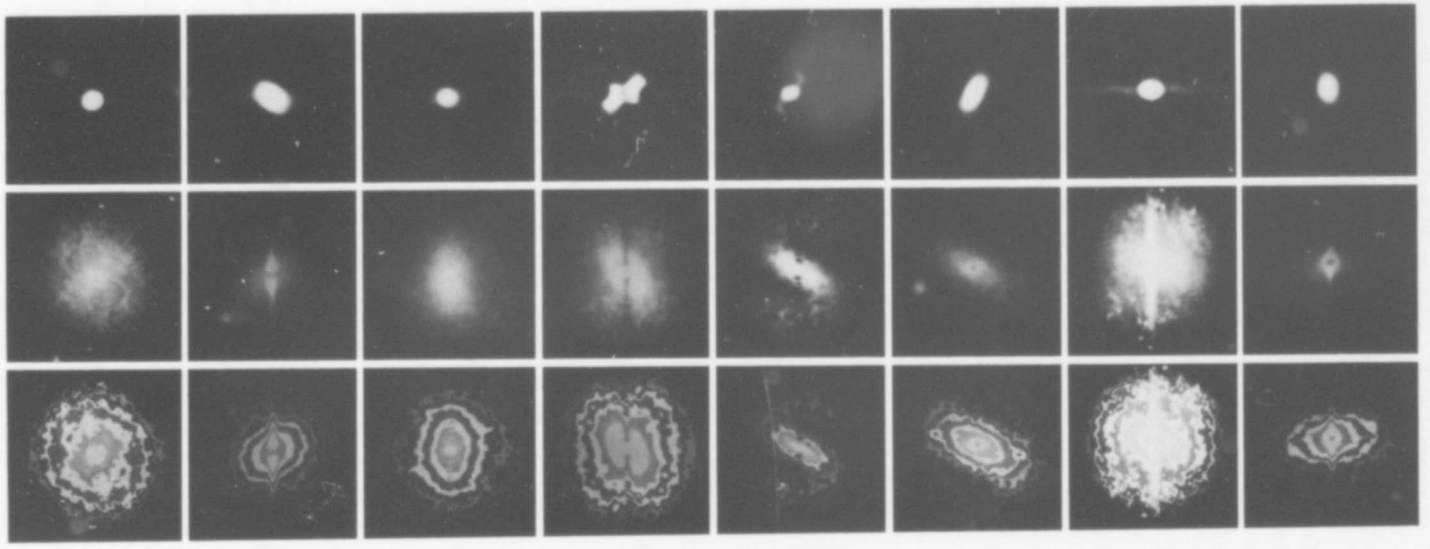

FIG. 9. The actual data for the Dec. run. The first frame in each row is an unresolvable source (a star). The remaining frames in the top row are the seven autocorrelation functions of Eros, those in the middle row are the two-dimensional power spectra for the same Eros points, and those in the bottom row are these same power spectra but with contours of intensity. The order of the frames is not in the same sequence as in Fig. 2, but can be matched to the following sequence of points in Fig. 2: 5, 6, 1, 2, 3, 7, 4. Measurements yielding α, β, and γ were made in power spectrum space (the middle row). Data from the central region, and along the verticle axis, of the power spectrum were excluded from our least-squares analysis in order to avoid fitting instrumental artifacts at those frequencies.

In order to help the reader better visualize these attributes, intensity contours (shown as brighter regions) are superimposed on the power spectra in the bottom row. The intensity is maximum at (or near) the center. Each energy contour is a factor of 2 less than its neighbor toward the center. Typically five contours are visible indicating a signal-to-noise of about $2^5 = 32$. Although not exactly elliptical, the generally *oblong* character of these contours is easily noted. Our first least-squares parameterization fits elliptical contours to each of these energy distributions in order to extract three characteristic primary parameters, the semimajor and semiminor axes, and the position angle for each observation. This set of α, β, and γ values is analyzed using a second least-squares procedure to determine the actual body parameters and pole as previously described.

The top row of frames is the same set of data, presented as autocorrelation functions (Fourier transforms of the power spectra in the middle row). These are more directly comparable to the actual diffraction-limited telescopic images in that they preserve both the ratio of length to width and the orientation of the object itself. The stellar (unresolved) autocorrelation shows a strong, symmetric Airy minimum and a faint (if asymmetric) first Airy maximum surrounding a central diffraction disk. The results for the asteroid all show, to a greater or lesser degree, evidence for an elongated object at a characteristic position angle. The instrumental artifacts, seen vertically in the power spectra, are now (by the properties of the Fourier transform) seen horizontally and mainly at larger distances in these autocorrelation functions. We have made no attempt in this work to analyze the significance of the obvious departures from simple elliptical shape (e.g., particularly in the third and fourth Eros frames) which are caused in part by details on the surface of the asteroid. We have limited this analysis, as noted above, to considerations *only* of overall shape (length and width of projected image) and orientation (position angle).

Figures 10 and 11 are side-by-side comparisons of our measured ellipses superim-

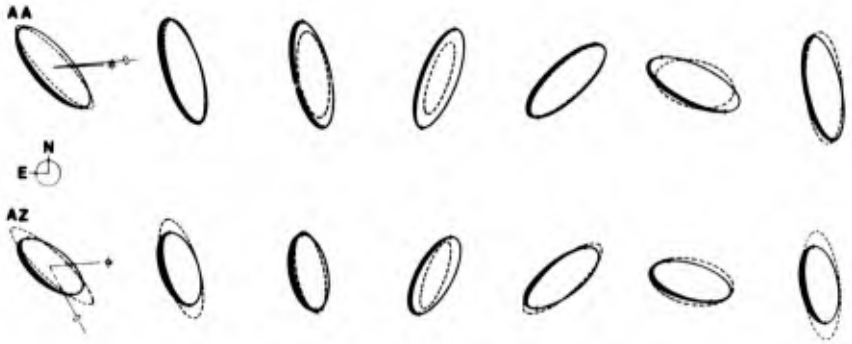

FIG. 10. Comparison of predicted projected ellipses and measured ellipses for Dec. 17–18, 1981. Our adopted solution for the dimensions and pole of Eros (Table IV) results in the upper series (AA) of projected ellipses (solid line figures). The dashed ellipses are our measured ellipses at the same rotational phase. The lower series (AZ) are the projected ellipses from the consensus solution (Table IV), and again superimposed are our measured ellipses at the same rotational phase. From our solution the sub-Earth latitude during this run was −74° and the sub-Sun latitude was −34°. The difference between the sub-Earth and sub-Sun longitudes was +6°. For the consensus model the sub-Earth latitude was −58°, the sub-Sun latitude was −30°, and the difference between the longitudes was +43°. The solar phase angle was 40°, Eros' position was 1^h44^m, and +40′ and its distance from the Earth was 0.311 AU. On the 0.″05 diameter circle, which corresponds to the minimum resolution disk of the 2.3-m telescope, north and east are indicated. On the first ellipse of each series, the direction to the Sun and to Eros' north pole are shown according to each solution.

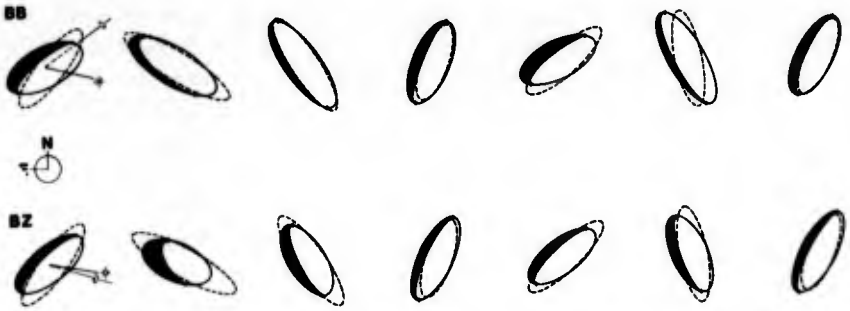

FIG. 11. Comparison of predicted projected ellipses and measured ellipses for Jan. 17–18, 1982. As in Fig. 10, the upper series (BB) of solid line ellipses are from our solutions, and the lower series (BZ) are from the consensus solution. The sub-Earth latitude from our model during the Jan. run was −57°, the sub-Sun latitude was −11°, and the difference between the sub-Earth and sub-Sun longitudes was −32°. For the consensus model the sub-Earth latitude was −56°, the sub-Sun latitude was −4°, and the difference between longitudes was +6°. The solar phase angle was 52°, Eros' position was 2^h57^m, +32° and its distance from the Earth was 0.317.

posed on our model and on the consensus model of Eros for December 1981 and January 1982, respectively. Presented in this manner the agreement between the two models is indeed convincing. Judging from the agreement between earlier works and the current speckle interferometric efforts for Eros, it appears that speckle is capable of obtaining the same information for asteroids as several other methods in concert, but in only one or two nights, provided the rotational period is known.

APPENDIX I

In an attempt to avoid any possible confusion of the term obliquity as used in this paper and as used by Dunlap (1971) and Barucci and Fulchignoni (1982), or Taylor (1979), we present Fig. 12, which shows the position of the Sun projected onto the plane of the Earth's sky, centered on the asteroid, for each possible quadrant. The z axis is the projection of the asteroid's spin axis and the y axis is the line of nodes (the intersection of the asteroid's equator and the plane of the Earth's sky). Both Dunlap and Taylor define obliquity as a positive quantity, the former restraining the obliquity to lie between 0 and $\pi/2$ and the latter between 0 and π. We define obliquity as a position angle with the normal convention that the angle measured in a counterclockwise direction (N–E–S–W) is positive and varies between 0 and 2π.

Define three position vectors in the asteroid's coordinate system (Section IIA), one for the Earth, one for the Sun, and one for the line of nodes:

$$\mathbf{E} = (i, j, k)$$

$$\mathbf{S} = (l, m, n)$$

$$\hat{\mathbf{Y}} = (\cos\psi, -\sin\psi, 0).$$

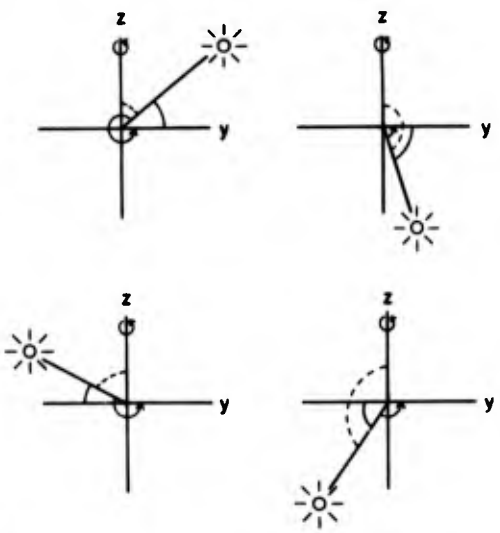

FIG. 12. Obliquity as defined by Dunlap (1971), —; by Taylor (1979), – – –; and this paper (Appendix I), →.

The cosine of the solar phase angle, ω, is given by $\mathbf{E} \cdot \mathbf{S}$. Our obliquity, ρ, measured from the projection of $\mathbf{S}$ onto the plane of the Earth's sky to y, can be found from

$$\cos \rho = \hat{\mathbf{Y}} \cdot \mathbf{S}/\sin \omega = (l \cos \psi - m \sin \psi)/\sin \omega$$

$$\sin \rho = \hat{\mathbf{Y}} \cdot \mathbf{E} \times \mathbf{S}/\sin \omega = (k \cos \omega - n)/(\sin \omega \cos \theta).$$

APPENDIX II: NOMENCLATURE

A, B, C	terms used in quadratic formula for projected ellipse
A_i	illuminated area of projected ellipse, bounded by terminator and bright limb
A_s	area of projected ellipse in shadow, bounded by terminator and dark limb
A_T, B_T, C_T	terms used in quadratic formula for terminator ellipse
$a \geq b \geq c$	semidiameters of triaxial ellipsoid rotating about c
$\mathbf{E} = (i, j, k)$	position vector of Earth in asterocentric coordinates [see Eq. (12)]
L	asterocentric longitude measured positive in a right-handed coordinate system, from the longest body axis (a); $L = -(\psi + 90°)$
$\mathbf{S} = (l, m, n)$	position vector of Sun in asterocentric coordinates [see Eq. (18)]
$\hat{\mathbf{Y}}$	position vector of line of nodes: the intersection of the asteroid's equatorial plane and the plane of the Earth's sky
x, y, z	asterocentric rectangular coordinates with the x axis pointed toward the Earth, and the y axis coincident with the line of nodes
x', y', z'	asterocentric rectangular coordinates rotating with the asteroid, with a, b, c lying along x', y', and z'
$\alpha \geq \beta$	semidiameters of ellipse projected by ellipsoid
$\alpha_T \geq \beta_T$	semidiameters of terminator ellipse
γ	position angle measured in the plane of the sky, between the y axis and α
γ_T	position angle measured in the plane of the sky, between the y axis and α_T
θ ($\theta_\odot$)	asterocentric latitude of sub-Earth (sub-Sun) point, or equivalently the Euler angle between the asteroid's rotation axis and the Earth's (Sun's) sky plane
π	3.1416 . . .
ρ	obliquity (see Appendix I)
ϕ	the Euler angle between the line of sight and the line of nodes; by our selected coordinate system this angle is a constant $\pi/2$
ψ ($\psi_\odot$)	the Euler angle equivalent to the rotational phase angle measured from the line of nodes, with $\psi = 0$ when the longest body axis (a) is perpendicular to the line of sight and lies unprojected in the plane of the sky; $\psi = -(L + 90°)$, $\psi_\odot = -(L_\odot + 90°)$
ω	solar phase angle, the angle between the Sun and Earth as seen by the asteroid; $\mathbf{E} \cdot \mathbf{S} = \cos \omega$

ACKNOWLEDGMENTS

We are grateful to D. Tholen for obtaining the lightcurve of Eros on our behalf and for providing ephemerides for our asteroid observations. J. Freeman digitized the data, and unbiased and deconvolved the power spectra. His diligent efforts were essential to the science garnered from the observations and are greatly appreciated. This work was supported in part

by NASA Grant NAGW-224, by AFGL Contract F19628-82-K-0025, and by AFOSR Grant 82-0020.

REFERENCES

BARUCCI, M. A., R. CASACCHIA, M. FULCHIGNONI, R. BURCHI, A. D. PAOLOANTONIO, C. GIULIANI, L. MILANO, F. SCALTRITI, AND V. ZAPPALÀ (1982). Laboratory simulation of photometric light curves of the asteroids. *Moon Planet* **27,** 387–395.

BARUCCI, M. A., AND M. FULCHIGNONI (1982). The dependence of asteroid lightcurves on the orientation parameters and the shapes of asteroids. *Moon Planet* **27,** 47–57.

BOWELL, E., B. L. MORGAN, K. LUMME, J. C. DAINTY, H. A. VINE, AND M. POUTANEN (1981). Speckle interferometric observations of Ceres, Vesta, Hebe, and Victoria. *Bull. Amer. Astron. Soc.* **13,** 719.

CAMPBELL, D. B., G. H. PETTENGILL, AND I. I. SHAPIRO (1976). 70-cm radar observations of 433 Eros. *Icarus* **28,** 17–20.

DAINTY, J. C. (1975). Stellar speckle interferometry. In *Laser Speckle and Related Phenomena* (J. C. Dainty, Ed.), pp. 255–279. Springer-Verlag, Berlin.

DUNLAP, J. L. (1971). Laboratory work on the shapes of asteroids. In *Physical Studies of Minor Planets* (T. Gehrels, Ed.), pp. 147–154. Univ. of Arizona Press, Tucson.

DUNLAP, J. L. (1976). Lightcurves and the axis of rotation of 433 Eros. *Icarus* **28,** 69–78.

GOLDSTEIN, H. (1950). *Classical Mechanics*. Addison–Wesley, Reading, Mass.

HEGE, E. K., W. J. COCKE, E. HUBBARD, M. GESHAM, P. A. STRITTMATTER, R. RADICK, AND S. P. WORDEN (1980a). Speckle interferometric observations of Pallas. *Bull. Amer. Astron. Soc.* **12,** 509.

HEGE, E. K., W. J. COCKE, E. N. HUBBARD, J. CHRISTOU, AND R. RADICK (1980b). Possible secondaries of asteroids found by speckle interferometry. *Bull. Amer. Astron. Soc.* **12,** 662.

HEGE, E. K., E. N. HUBBARD, P. A. STRITTMATTER, AND W. J. COCKE (1982a). The Steward Observatory speckle interferometry system. *Optica Acta* **29,** 701–715.

HEGE, E. K., E. N. HUBBARD, J. D. DRUMMOND, P. A. STRITTMATTER, AND S. P. WORDEN (1982b). Speckle interferometric observations of Pluto and Charon. *Icarus* **50,** 72–81.

JEFFERYS, W. H. (1980). On the method of least squares. *Astron. J.* **85,** 177–181.

JURGENS. R. F., AND R. M. GOLDSTEIN (1976). Radar observations at 3.5 and 12.5 cm wavelength of asteroid 433 Eros. *Icarus* **28,** 1–15.

LEBOFSKY, L. A., AND G. H. RIEKE (1979). Thermal properties of 433 Eros. *Icarus* **40,** 297–308.

LUMME, K., M. POUTANEN, AND E. BOWELL (1981). Photometric determinations of asteroid shapes and spin axial directions. *Bull. Amer. Astron. Soc.* **13,** 719.

MATSON, D. L. (1971). Infrared observations of asteroids. In *Physical Studies of Minor Planets* (T. Gehrels, Ed.), pp. 45–50. NASA SP-267, Washington, D.C.

MILLIS, R. L., E. BOWELL, AND D. T. THOMPSON (1976). UBV photometry of asteroid 433 Eros. *Icarus* **28,** 53–67.

MORRISON, D. (1977). Asteroid sizes and albedos. *Icarus* **31,** 185–220.

OSTRO, S. J., AND R. CONNELLY (1984). Convex profiles from asteroid lightcurves. *Icarus* **57,** 443–463.

SCALTRITI, F., AND V. ZAPPALÀ (1976). Photometric lightcurves and pole determination of 433 Eros. *Icarus* **28,** 29–31.

SURDEJ, A., AND J. SURDEJ (1978). Asteroid lightcurves simulated by the rotation of a three-axes ellipsoidal model. *Astron. Astrophys.* **66,** 31–36.

TAYLOR, R. C. (1979). Pole orientations of asteroids. In *Asteroids* (T. Gehrels, Ed.), pp. 480–493. Univ. of Arizona Press, Tucson.

TAYLOR, R. C. (1984). The pole orientation of asteroid 433 Eros by applying photometric astrometry. Submitted for publication.

TAYLOR, R.C., AND E. F. TEDESCO (1983). Pole orientation of asteroid 44 Nysa via photometric astrometry, including a discussion of the method's application and its limitations. *Icarus* **54,** 13–22.

TEDESCO, E. F. (1979). Lightcurve parameters of asteroids. In *Asteroids* (T. Gehrels, Ed.), pp. 1098–1107. Univ. of Arizona Press, Tucson.

VESELY, C. D. (1971). Summary on orientations of rotation axes. In *Physical Studies of Minor Planets* (T. Gehrels, Ed.), pp. 133–140. NASA SP-267, Washington, D.C.

WORDEN, S. P. (1979). Interferometric determinations of asteroid diameters. In *Asteroids* (T. Gehrels, Ed.), pp. 119–131. Univ. of Arizona Press, Tucson.

ZAPPALÀ, V., AND Z. KNEŽEVIĆ (1984). Rotation axes of asteroids: Results for 14 objects. *Icarus* **59,** 436–455.

ZAPPALÀ, V., M. DI MARTINO, P. FARINELLA, AND P. PAOLICCHI (1983). An analytical method for the determination of the rotational direction of asteroids. In *Asteroids, Meteors, and Comets* (C.-I. Lagerkvist and H. Rickman, Eds.), pp. 73–76. Astronomiska Observatorium, Uppsala, Sweden.

ZELLNER, B. (1976). Physical properties of asteroid 433 Eros. *Icarus* **28,** 149–153.

ICARUS 61, 232–240 (1985)

Speckle Interferometry of Asteroids

II. 532 Herculina

J. D. DRUMMOND, E. K. HEGE, W. J. COCKE, J. D. FREEMAN, AND J. C. CHRISTOU[1]

Steward Observatory, University of Arizona, Tucson, Arizona 85721

AND R. P. BINZEL

Department of Astronomy, University of Texas, Austin, Texas 78712

Received May 21, 1984; revised October 5, 1984

Speckle interferometry of 532 Herculina performed on January 17 and 18, 1982, yields triaxial ellipsoid dimensions of (263 ± 14) × (218 ± 12) × (215 ± 12) km, and a north pole for the asteroid within 7° of RA = 7^h47^m and DEC = −39° (ecliptic coordinates $\lambda = 132°$ $\beta = -59°$). In addition, a "spot" some 75% brighter than the rest of the asteroid is inferred from both speckle observations and Herculina's lightcurve history. This bright complex, centered at asterocentric latitude −35°, longitude 145–165°, extends over a diameter of 55° (115 km) of the asteroid's surface. No evidence for a satellite is found from the speckle observations, which leads to an upper limit of 50 km for the diameter of any satellite with an albedo the same as or higher than Herculina.

INTRODUCTION

Assuming that an asteroid is a smooth triaxial ellipsoid rotating about its shortest axis, the resolved asteroid will project onto the plane of the Earth's sky as an ellipse. Even at low to moderate solar phase angles (<45°), the illuminated portion of an asteroid can still be approximated by an ellipse. At low solar phase angles, a smooth, airless dark body tends to suffer little or no limb darkening (French and Veverka, 1983). Even for objects similar in albedo to Herculina, French and Veverka (1983) found that what limb darkening may exist is nearly (but not totally) reduced by macroscopic surface roughness. Thus, treating an asteroid as a smooth triaxial ellipsoid uniformly bright from the terminator to the opposite limb appears to be a useful approximation and is indeed what is traditionally used (e.g., Ostro and Connelly, 1984). As the asteroid rotates it presents a series of ellipses that change in size, shape, and orientation. There is a transformation from each ellipse to actual body parameters that involve six variables, three dimensions and three (Euler) angles. The asteroid's axial dimensions and the direction of its spin axis, including the sense of rotation, can then be found from a least-squares analysis of this ellipse series. The derivation of the relevant equations was given by Drummond *et al.* (1985, Paper I) and applied to speckle interferometric observations of 433 Eros. In the present paper we use the same technique to study 532 Herculina.

THE DATA AND RESULTS

Four observations of Herculina were made on January 17, 1982, and another four on January 18, at the 2.3-m telescope of Steward Observatory, using the equipment as described by Hege *et. al.* (1982). Each observation was a 10-min videotape of Herculina taken at 30 Hz. Each 10-min observation was later Fourier transformed, and the power spectra were coadded. In order to remove the modulation transfer function

[1] Visiting Astronomer from Department of Astronomy, New Mexico State University, Las Cruces, N.M.

0019-1035/85 $3.00

of the telescope and the seeing (Hege *et al.*, 1982), the unbiased two-dimensional speckle image power spectrum accumulated from each 10-min observation was divided (deconvolved) by the two-dimensional power spectrum of a star observed immediately before and again by the power spectrum of a different star observed immediately after Herculina. Each deconvolved power spectrum of Herculina was then fit over two regions of spatial frequencies to the power spectrum of a uniformly bright ellipse. The major axis, minor axis, and position angle of the major axis for the asteroid's elliptical power spectrum were taken as the average of two measurements from both of the deconvolved power spectra. The average standard deviation from the mean of the four measurements of each Herculina observation ranged between 0".002 and 0".018 for the long axis dimension, between 0".003 and 0".043 for the short axis dimension, and between 1 and 6° for the position angle. Image scale and absolute orientation were calibrated with a mask placed over the secondary mirror at the end of the run. The diffraction limit of the 2.3-m telescope is 0".05 at 5500 Å and the scale was 0".01 per pixel.

On a "poor" night seeing may not be a statistically stationary process during observations of the first nearby standard, the asteroid, and the second nearby standard. However, since the observation of the asteroid is always sandwiched between the two standards, and the results are the average between the two deconvolutions, any trend in the seeing should be compensated. Furthermore, even if a change in seeing is not entirely compensated, the remaining "error" will simply be manifest as noise on the measurements when all observations are fit simultaneously, resulting, perhaps, in increased errors for the final parameters. (See below.)

Table I gives pertinent data regarding the observing circumstances for Herculina, which moved less than one-third of 1° between the first observation on the first night and the last observation on the second night. Because the solar phase angle was only 6°, the terminator was virtually coincident with one edge of the projected ellipse.

TABLE I

ASPECT DATA FOR SPECKLE OBSERVATIONS

DATE	RA (1950)	DEC
January 17 and 18, 1982	8^h58^m	+25°41′
Distance from Earth 1.495 AU	Distance from Sun 2.459 AU	
Solar phase angle 6°.0	Position angle of Sun, centered on Herculina 74°	

Three independent quantities are measured for each of the eight observations of the projected ellipse: a major axis dimension α, a minor axis dimension β, and a position angle γ of the long axis. Altogether, then, there are 24 equations of condition to solve for six unknown parameters. However, as discussed later, four measurements were not used in the analysis, leaving 20 equations of condition. A nonlinear least-squares (Jeffreys, 1980) routine was used to solve for the dimensions of the three axes a, b, c, the latitude of the sub-Earth point θ, a zero point for the rotational phase ψ_0 (corresponding to maximum light), and the obliquity ρ (as defined in Paper I). With θ, ρ, and the position of Herculina, we calculate the location of the pole directly. The error in the position of the pole arises from the errors in θ and ρ, and corresponds to the radius of a circle with the same area as the area enclosed by the various poles calculated by varying θ and ρ by their errors. Table II lists the least-squares solution for each of the parameters and presents the matrix of normalized correlation coefficients for the full six-parameter fit, Table III lists the same for a five-parameter fit, where b is assumed equal to c (the prolate spheroid biaxial case), and Table IV shows the information for the biaxial fit using all the points, including the four discrepant ones. A triaxial solution could not be found

TABLE II

TRIAXIAL SOLUTION AND CORRELATION MATRIX (WITHOUT FOUR LOWEST β's)

$a = 261 \pm 14$ km $\quad \psi_0 = -35 \pm 13°$
$b = 222 \pm 16$ km $\quad \theta = -29 \pm 23°$
$c = 213 \pm 18$ km $\quad \rho = 30 \pm 8°$

Standard error of fit = 0.019 = 21 km

RA	Pole (1950)	DEC
7^h59^m		$-33°$
	$\pm 14°$	
13^h39^m		$+77°$

	a	b	c	ψ_0	θ	ρ
a	—					
b	−0.60	—				
c	0.33	−0.35	—			
ψ_0	−0.12	0.11	−0.15	—		
θ	0.63	−0.80	0.79	−0.14	—	
ρ	0.08	−0.07	0.09	−0.90	0.07	—

TABLE III

BIAXIAL SOLUTION AND CORRELATION MATRIX (WITHOUT FOUR LOWEST β's)

$a = 265 \pm 15$ km $\quad \psi_0 = -38 + 9°$
$b = c = 216 \pm 10$ km $\quad \theta = -23 + 5°$
$\rho = 32 + 7°$

Standard error of fit = 0.018 = 20 km

RA	Pole (1950)	DEC
7^h42^m		$-39°$
	$\pm 6°$	
15^h22^m		$+75°$

	a	b	ψ_0	θ	ρ
a	—				
b	−0.35	—			
ψ_0	−0.01	−0.04	—		
θ	0.13	0.04	−0.02	—	
ρ	0.01	0.03	−0.87	−0.01	—

TABLE IV

BIAXIAL SOLUTION AND CORRELATION MATRIX (INCLUDING FOUR LOWEST β's)

$a = 278 \pm 17$ km $\quad \psi_0 = -37 + 9°$
$b = c = 181 \pm 11$ km $\quad \theta = -24 + 6°$
$\rho = 32 + 7°$

Standard error of fit = 0.030 = 33 km

RA	Pole (1950)	DEC
7^h45^m		$-38°$
	$\pm 7°$	
15^h14^m		$+76°$

	a	b	ψ_0	θ	ρ
a	—				
b	−0.22	—			
ψ_0	−0.03	−0.01	—		
θ	0.21	0.04	0.01	—	
ρ	0.02	0.005	−0.82	−0.05	—

in the latter case if these four points were included in the analysis. Table V gives our adopted weighted (by the inverse errors squared) solution between Tables II and III. For each case the standard error of fit is listed and both poles for the θ, $\pi - \theta$ ambiguity (see Paper I) are given. However, based on the available published lightcurves (next section), the first listed pole is the correct one. From occultation (Bowell *et al.*, 1978), radiometric (Morrison and Lebofsky, 1979), and polarization (Bowell *et al.*, 1979) results, the diameter of Herculina has been found to be 217, 219, and 220 km, respectively. No published pole has been noted in the literature.

Figure 1 shows our measured major axis (diamonds) and minor axis (filled circles; open circles are not used in the analysis) plotted against rotational phase ψ. The upper line is the predicted major axis dimension from Table V, while the lower curve is the predicted minor axis. Figure 2 shows the predicted position angle (γ) of the major axis as a function of rotational phase. At rotational phase $\psi = 0$, maximum light occurs, the long body dimension a is perpendicular to our line of sight, and γ is zero.

TABLE V

ADOPTED SOLUTION (WEIGHTED MEAN OF TABLES II AND III)

$a = 263 \pm 14$ km
$b = 218 \pm 12$ km
$c = 215 \pm 12$ km
$\psi_0 = -37 \pm 10°$
$\theta = -23 \pm 7°$
$\rho = 31 \pm 7°$

RA	Pole (1950)	DEC
7^h47^m	$\pm 7°$	$-39°$

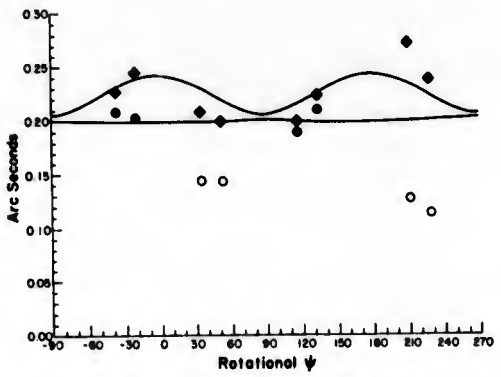

FIG. 1. Major (diamonds) and minor (circles) axis dimensions (0".01 = 10.84 km) plotted against rotational phase over Jan 17 and 18, 1982. Because of the effect of the bright spot on measuring the minor axes, open circles were not used in finding the solution. The upper (lower) line is the predicted major (minor) axis dimension from our adopted weighted solution (Table V).

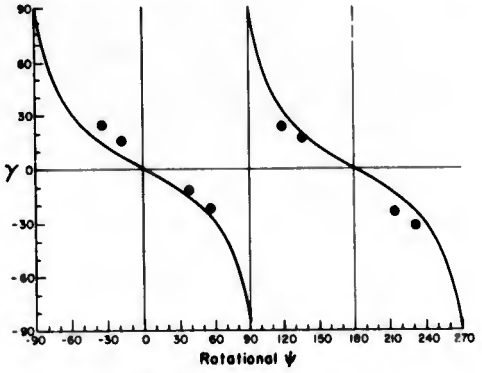

FIG. 2. The position angle (γ) of the major axis plotted as a function of rotational phase over Jan 17 and 18, 1982. At $\psi = \gamma = 0$, maximum light would occur, and Herculina's longest axis would lie in the plane of the Earth's sky perpendicular to our line of sight. The line is the position angle predicted from the results listed in Table V and is superimposed on our measured γ's, the solid dots.

HERCULINA'S LIGHTCURVES

Including the 1982 apparition, lightcurves have been obtained at four oppositions (Table VI): in 1954 (Groeneveld and Kuiper), in 1963 (Chang and Chang), in 1978 (Harris and Young, 1979), and in 1982 (independently by M. Di Martino (1984, private communication) by Cunningham (1983) and by R. P. Binzel—see Table VII and below). The four oppositions are summarized in Table VI. For all but the 1978 opposition, Herculina displayed one maximum and one minimum in ~9 hr, implying an 18-hr rotational period. However, in 1978, Harris and Young found two (and perhaps even three)

TABLE VI

SUMMARY OF PREVIOUS LIGHTCURVES

DATE	RA (1950)	DEC	Solar phase angle	Amplitude (mag)	Sub-Earth[a] latitude	Comments
Jan 2, 1954[b]	6^{h}07^m	+17°30′	4°.5	0.08	−29°	
Jan 19–22, 1963[c]	4 24	+11 47	17	0.18	−21	
Jun 25, 1978[d]	14 52	+ 2 08	20	0.15	+14	Second min. 0.12 mag. lower than primary max.
Mar 20–25, 1982[e]	8 21	+32 46	21.5	0.15	−18	

[a] Based on pole location of 7^{h}47^m, −39°.

[b] Groeneveld and Kuiper (1954).

[c] Chang and Chang (1963).

[d] Harris and Young (1979). Lightcurves were obtained from May 29 through August 1 by Harris and Young at Table Mountain and by E. Bowell and L. Martin at Lowell. All lightcurves are quite similar, and the Jun 25 aspect data are chosen as representative of the middle of the period.

[e] R.P.B. (this paper). M. Di Martino (1984, personal communication) obtained a similar 0.15-magnitude amplitude lightcurve for Jan 29–31, 1982, as did Cunningham (1983) for Feb 26–Mar 29, 1982, but with a slightly higher amplitude of 0.18 magnitude.

TABLE VII

ASPECT DATA FOR 1982 LIGHTCURVE

DATE (0^h UT)	RA (1950)	DEC	Earth distance (AU)	Sun distance (AU)	Phase angle	Ecliptic	
						Long.	Lat.
1982 Mar 20	8^h21^m	32^d45^m	1.710	2.374	21°2	120°	13°
Mar 21	21	32 46	1.719	2.373	21.4	120	13
Mar 22	21	32 46	1.729	2.372	21.7	120	13
Mar 25	22	32 46	1.757	2.368	22.3	120	13

maxima and minima in 9 hr, and convincingly demonstrated that a 9.406-hr period was correct.

Figure 3 shows the lightcurve constructed from four nights of data obtained by R.P.B. in March 1982, assuming a 9.406-hr period. A two-channel photometer was used on the 0.91-m telescope at McDonald Observatory. The second channel of the photometer which is described in Nather (1973) was offset to a nearby star to monitor the photometric constancy of the night. The observations were made differentially with respect to a second nearby comparison star SAO 060790, spectral Type F5. All observations were made using an uncooled RCA 8850 photomultiplier tube and a standard B filter (Schott 385 and BG 12) and were transformed to the Johnson B system using solar-type standards from Landolt (1973). The small delta B − V between all of the objects allowed second-order color terms to be ignored in the reduction.

Each measurement is the average of at least 100 sec of integration time on the asteroid and on the comparison star. Differential extinction was accounted for in the reduction using nightly determined extinction coefficients. The resulting error for each of the observations is less than 0.01 magnitude.

The observing circumstances for each of the four nights are presented in Table VII. Phase angle and distance corrections were applied in order to place the observations from the four nights on the vertical scale. No correction for light time was applied.

A SPOT ON HERCULINA

In Fig. 1 it is obvious that the lowest four β measurements are unreasonably low and should be excluded from a fit of a uniform smooth ellipsoid model. If they are not excluded, Table IV suggests a maximum lightcurve amplitude of nearly 0.5 magnitude—unrealistically large. In order to assess the effect of what a dark spot would have on the power spectrum of an asteroid, we cal-

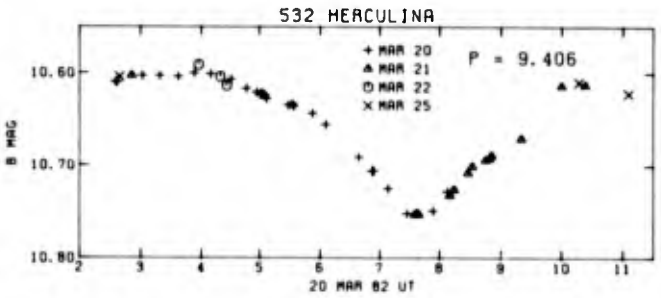

FIG. 3. The lightcurve of 532 Herculina as measured with a B filter at the 0.91-m telescope at McDonald Observatory. (See text.)

culated the two-dimensional power spectrum of an ellipse with a dark or bright spot at various locations. It turned out that the biggest effect is caused by a *bright* spot. In fact, the easiest way to cause an underestimate of the size of the *minor* axis in image space (from measurements made in power spectrum space) is to place a bright spot at the end of the *major* axis.

After several such numerical experiments we were able to locate a bright spot on Herculina that not only qualitatively explains the speckle interferometric measurements, but to a large extent explains the lightcurves observed. A spot with the following characteristics is suggested:

Asterocentric latitude	−35°
Asterocentric longitude (measured in a right-handed system from the longest axis in the equatorial plane)	145°
Diameter	55° = 115 km
Albedo relative to non-spot surface	1.75

When such a spot is located on the limb, midway between the major and minor axes, it causes us to severely underestimate the minor axis (the first two low β's in Fig. 1) and slightly underestimate the major axis. When the spot is on the tip of the major axis it not only causes an underestimation of β, but also causes a small overestimation of α (as in the second set of low β's). When the spot is near the center of the ellipse, it has the least effect (the two measurements at $\psi \approx 125°$). Moreover, when the latitude of the sub-Earth point lies in Herculina's southern hemisphere (as in 1954, 1963, and 1982), the bright spot "fills in" one of the lightcurve minima, and when the sub-Earth latitude is in the northern hemisphere (1978), two minima should be seen. Harris and Young (1979) correctly interpreted the lightcurve data by concluding that "the pole orientation of 532 Herculina is such that the two aspects (1963 and 1978) were both at midlatitudes but opposite hemispheres from one another." This is essentially what we find from our speckle observations.

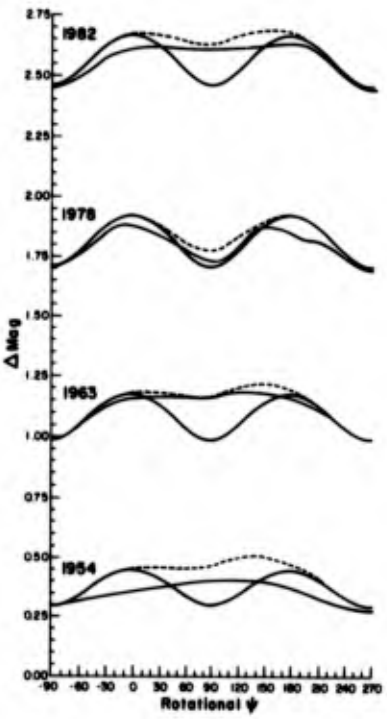

FIG. 4. Theoretical lightcurves for four oppositions. Using the model from Table V, lightcurves for the four epochs considered in Table VI are shown as sinusoidal solid lines. The dashed line is the lightcurve with the contribution from the bright spot included. Note how the spot raises one of the minima to the level of the maxima in three of four cases. The 1978 lightcurve was the only one obtained when the sub-Earth point was in the asteroid's northern hemisphere (the spot is at latitude −35°). We urge the reader to compare these lightcurve shapes with the actual ones from the references listed in Table VI, but for convenience we have sketched in the observed (lower amplitude) lightcurves.

We were able to reproduce the shape of the observed lightcurves listed in Table VI quite well by placing the spot at longitude 165 instead of 145°, a difference that is allowed by the simplistic approach (a single, uniform, circular spot). Figure 4 shows the lightcurves generated with this spot, and we urge comparison to the observed ones. Our computer-generated lightcurves include the visible illuminated area of the asteroid, plus the contribution of the illuminated area of the spot (75% brighter than

the rest of the asteroid), and takes into account foreshortening of the spot. It is also necessary to include a Lambertian term for the spot in order to even remotely match the observed lightcurves, i.e., the foreshortened illuminated area of the spot was multiplied by the cosine of the angle between the asteroid's radius vector to the spot and the asterocentric position of the Sun. Although the shapes of the lightcurves agree well, the computer-generated lightcurves are an average of 0.08 magnitude greater than those observed. But again this may be due to our simplistic approach to what is undoubtedly a complex albedo structure, especially in the southern hemisphere of Herculina. If the spot and the solar phase angle are ignored in our calculated lightcurve, then the discrepancy is reduced to 0.04 magnitude. A 0.08-magnitude amplitude discrepancy is also less than the range in amplitudes calculated by varying the dimensions of Herculina by the errors in Table V.

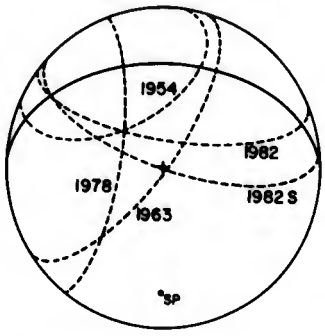

FIG. 5. A graphical representation of the amplitude/aspect analysis for Herculina. On the celestial sphere (note the south celestial pole and the solid equator), tipped so that our pole at 7^h47^m, $-39°$, is directly beneath us (the plus), each curve (derived from the amplitudes in Table VI and the dimensions in Table V) is drawn centered on the position of the asteroid at the time of the observations. The 1982S curve comes from our own speckle observation. Note the intersection of the 1963 curve with our pole, and the intersection of the 1954, 1978, and 1982 curves some 20° away at 6^h48^m, $-24°$.

AN AMPLITUDE/ASPECT CHECK

As a check of the consistency of our estimates for the dimensions and pole of Herculina, we performed a simple amplitude/aspect analysis. Using the dimensions from Table V of 263 × 218 × 215, ignoring the effect of the solar phase angle, and disregarding the spot, the amplitude can be expressed as the ratio of maximum to minimum projected area and is a function of aspect ($90° - \theta$) only. For amplitudes (A) converted to a linear scale, the sub-Earth latitude (θ) can be found from

$$\tan^2\theta = c^2(A^2b^2 - a^2)/[a^2b^2(1 - A^2)],$$

where a, b, and c are the triaxial diameters. From observed amplitudes (Table VI) and our dimensions, we convert each lightcurve amplitude to a θ. We then plot the position of the asteroid on the celestial sphere and draw a circle around it of radius $90° - \theta$. Ideally, since the pole must lie somewhere on each circle, all the circles should intersect at the location of the pole. Figure 5 shows four circles from the four lightcurves of Table VI, as well as the circle from our own speckle observations.

In fact, the speckle results not only give a circle but indicate where on the circle the pole lies. We have tipped the celestial sphere so that the location of this pole at 7^h47^m, $-39°$, lies at the center (a plus). The circle from the 1963 lightcurve intersects the speckle (1982S) curve at precisely this point, while the three other lightcurves intersect at 6^h48^m, $-24°$, a difference of 20°. We feel this is good agreement and adds confidence to our results for Herculina.

A SATELLITE?

The possibility of a satellite orbiting Herculina was suggested by a secondary event observed during a stellar occultation in 1978 (Bowell *et al.*, 1978; Van Flandern *et al.*, 1979). However, no indications of a satellite could be found at any rotational phase from our speckle observations (i.e., no interference fringes were seen in the power spectra). According to the diameter and orbital radius of the hypothetical satellite

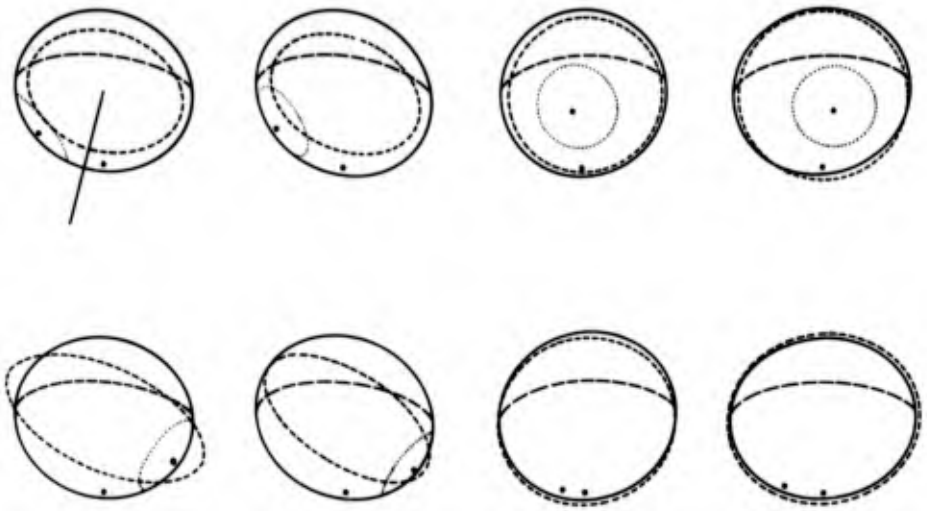

FIG. 6. 532 Herculina on Jan 17 and 18, 1982. North is indicated on the first "frame." Each frame shows Herculina's south pole and equator, the ellipse (dashed) as measured by speckle interferometry, and the location of the bright spot (dotted) with its center denoted by a large dot. In the last two frames the bright spot is on the other side of the asteroid. The spot is slightly larger than the resolution disc of 0".05 for the 2.3-m telescope. The order of the frames in this figure is chronological. The last two frames here correspond to the first two in Figs. 1 and 2, the first frame here is point 3 in the earlier figures, frame 2 is point 4, etc.

(50- and 1000-km separation), it should have been continuously within our 2".5 field of view. We can therefore set an upper limit for the diameter of an object with the same albedo as Herculina at 0".05 = 50 km, and for a satellite with an albedo 75% brighter, corresponding to the albedo of the bright spot, an upper limit of 40 km. Our observations, then, lead to the conclusion that if a satellite exists for Herculina, it is probably smaller than previously suggested.

SUMMARY

By modeling Herculina as a triaxial ellipsoid with a large bright spot in its southern hemisphere, we have been able to explain its lightcurves and its speckle interferometric observations. Figure 6 summarizes our results by combining the information from Figs. 1 and 2. At the rotational phase of each speckle measurement, the predicted projected ellipse from the ellipsoid in Table V is shown (solid line ellipse), as well as the measured ellipse (dashed), the bright spot (dotted) and its center, and the asteroid's south pole and equator. In the last two frames the bright spot is not visible but its center is shown on the other side of the asteroid. Note the correlation between the location of the bright spot and, in particular, the size of the minor axis of the measured ellipse; the greatest effect occurs when the spot is on the limb.

We predict that if colorimetry or polarimetry had been performed during any of the lightcurves from Table VI, except 1978, there would have been variation with rotation because of the spot. By the same token we predict one maximum and minimum during one rotational cycle and variations in color and polarization over the rotational cycle when the sub-Earth point lies in the southern hemisphere of Herculina. This will occur around the November 1985 opposition when θ will be $-25°$. During the July 1988 opposition, since the sub-Earth point will lie in Herculina's northern hemisphere ($+23°$), two maxima and two minima will be seen, and little if any color or polarization variation with rotation will be seen.

In 1987 and 1989, the latitudes will be +7 and −8°, respectively, and the situation will be intermediate.

ACKNOWLEDGMENTS

This work was supported by NASA Contract NAGW-224, AFGL Contract F19628-82-K-0025, and AFOSR Grant 82.0020. The observations by R. P. Binzel were supported by NASA Grant NGR 44-012-152.

REFERENCES

Bowell, E., J. McMahon, K. Horne, M. F. A'Hearn, D. W. Dunham, W. Penhallow, G. E. Taylor, L. H. Wasserman, and N. M. White (1978). A possible satellite of Herculina (abstract). *Bull. Amer. Astron. Soc.* **10**, 594.

Bowell, E., T. Gehrels, and B. Zellner (1979). Magnitudes, colors, types, and adopted diameters of the asteroids. In *Asteroids* (T. Gehrels, Ed.) pp. 1108–1129. Univ. of Arizona Press, Tucson.

Chang, Y. C., and C. Chang (1963). Photometric observations of variable asteroids. II. *Acta Astron. Sin.* **11**, 139–149.

Cunningham, C. (1983). Photoelectric photometry of asteroid 532 Herculina. *Minor Planet Bull.* **10**, 4–5

Drummond, J. D., W. J. Cocke, E. K. Hege, P. A. Strittmatter, and J. V. Lambert (1985). Speckle interferometry of asteroids. I. 433 Eros. *Icarus* **61**, 132–151.

French, L. M., and J. Veverka (1983). Limb darkening of meteorites and asteroids. *Icarus* **54**, 38–47.

Groeneveld, I., and G. P. Kuiper (1954). Photometric studies of asteroids II. *Astrophys. J.* **120**, 529–546.

Harris, A. W., and J. Young (1979). Photoelectric lightcurves of asteroids 42 Isis, 45 Eugenia, 56 Melete, 103 Hera, 532 Herculina and 558 Carmen. *Icarus* **38**, 100–105.

Hege, E. K., E. N. Hubbard, P. A. Strittmatter, and W. J. Cocke (1982). The Steward Observatory speckle interferometry system. *Opt. Acta* **29**, 701–715.

Jeffreys, W. H. (1980). On the method of least squares. *Astron. J.* **85**, 177–181.

Landolt, A. U. (1973). UBV photoelectric sequences in celestial equatorial Selected Areas 92–115. *Astron. J.* **78**, 959–981.

Morrison, D., and L. A. Lebofsky (1979). Asteroid radiometry. In *Asteroids* (T. Gehrels, Ed.) pp. 184–205. Univ. of Arizona Press, Tucson.

Nather, R. E. (1973). High speed photometry. *Vistas Astron.* **15**, 91–111.

Ostro, S. J., and R. Connelly (1984). Convex profiles from asteroid lightcurves. *Icarus* **57**, 443–463.

Van Flandern, T. C., E. F. Tedesco, and R. P. Binzel (1979). Satellites of asteroids. In *Asteroids* (T. Gehrels, Ed.) pp. 443–465. Univ. of Arizona Press, Tucson.

SPECKLE INTERFEROMETRY OF ASTEROIDS

III. 511 Davida

J. D. Drummond and E. K. Hege

Steward Observatory

University of Arizona

Tucson, Arizona 85721

Running title: Interferometry of Davida

Send proofs to: J. D. Drummond
Steward Observatory
University of Arizona
Tucson, Arizona 85721

Subm. Hcd to Icarus 21 May 1985

36 manuscript pages
6 figures
9 tables

ABSTRACT

511 Davida was observed with the technique of speckle interferometry at Steward Observatory's 2.3m telescope on May 3, 1982. Based on 5 ten minute observations, its dimensions were found to be (465 $\pm$ 33) x (358 $\pm$ 39) x (258 $\pm$ 52) km. Such a shape falls close to an equilibrium figure of a "rubble pile," suggesting a density of 1.4 $\pm$ 0.4 gm/cm^3. Simultaneous with the determination of the size and shape of Davida, we find its north pole to lie within 26° of RA = 19^{h}08^m, Dec = 15° (λ = 291 °, β = +37°).

We derive and apply to Davida a new simultaneous amplitude magnitude (SAM) aspect method for finding, from photometric data only, axial ratios and rotational pole coordinates. We also employ various weightings in a linear form of the amplitude aspect relation to find axial ratios and a pole. Precise albedos follow from speckle and photometry, but they depend on the form of the phase function (the Gehrels and Tedesco or Lumme and Bowell treatments) and the photometric method used to find the pole and axial ratios.

An alternative interpretation of the photometric data which cannot be excluded, is that rather than suggesting a change to the axial ratios found from speckle observations, the photometry could indicate albedo structure over the surface of Davida. The precision of our present autocorrelation/power spectrum result does not force a choice between a uniform albedo or an albedo gradient. Image reconstruction techniques presently under

development may, however, permit such discriminations.

Introduction

In order to find its triaxial dimensions and the direction of its angular momentum vector (its spin axis) we have obtained five speckle interferometric observations of the sixth largest (Zellner, 1979) minor planet, 511 Davida. Zappala and Knezevic (1985) have applied the amplitude-magnitude-aspect relationship (Zappala et al. 1983; Zappala and Knezevic 1984) to lightcurves of Davida extending back to 1952. We, too, derive and apply a new simultaneous amplitude-magnitude-aspect, and a weighted amplitude-aspect, method to the photometric data of Davida. These photometric methods lead to an independent check of the location of Davida's spin axis and its axial ratios as found through speckle interferometry, which, being a high angular resolution technique, follows the changing projected size, shape, and orientation of the asteroid to derive its pole and dimensions.

For image modelling purposes, an asteroid is assumed to be a triaxial ellipsoid rotating about its shortest axis ($a \geq b \geq c$), smooth (no large craters, mountains, etc.), featureless (no albedo variations), and uniformly bright (scatters geometrically). Such an ellipsoidal model asteroid projects as an apparent ellipse of uniform brightness on the plane of the Earth's sky. The two-dimensional image autocorrelation function of a uniformly bright ellipse has the same shape and orientation (but twice the size) as the ellipse itself. The corresponding image power spectrum also has the same elliptical shape, but

appears rotated 90° because of the reciprocal relation between image extent and spatial frequency. The projected figure of the real asteroid on the plane of the Earth's sky is thus characterized by the fit of an elliptical model to the observed image autocorrelation function or image power spectrum data. This yields the observed major axis dimension (α), minor axis dimension (β), and position angle of the major axis (γ) for a particular time in the asteroid's rotational cycle. The equations relating the observed elliptical parameters (α,β,γ) for a series of rotational phase angles, Ψ, to the three axes dimensions and pole direction of the triaxial ellipsoid are given by Drummond et al. (1985a). Thus, a non-linear least squares routine is applied to a series of (α,β,γ) and yields simultaneously six parameters: the three axes dimensions, two Euler angles (θ, the sub-Earth point latitude, and Ψ_o, the zero point in the rotational cycle) and the obliquity φ, the projected angle between the asteroid's north pole and the ecliptic north pole; see Appendix I of Drummond et al. 1985a).

Observations and Results

On May 3, 1982, with the 2.3m telescope of Steward Observatory and the speckle camera and equipment described by Hege et al. (1982), five ten-minute speckle observations of Davida were made, each observation being preceded by an observation of one nearby star, and followed by another observation of a second star. The co-added power spectra of Davida for each ten minutes were divided by the power spectra of the flanking stars in order to remove the telescope modulation transfer function and the seeing (Hege et al. 1982; Drummond et al. 1985a,b). The aspect data for Davida on May 3, 1982, is given in Table I.

Table II gives the six parameter fit to the fifteen equations of condition (five α's, five β's, and five γ's). As for most non-linear least squares routines, our program (adopted from Jefferys 1980, 1981) linearizes about the residuals. The errors for the parameters can then be computed directly during the solution of the equations of condition. For 433 Eros (Drummond et al. 1985a) and 532 Herculina (Drummond et al. 1985b), the errors so computed appear to be reasonable. However for Davida they are unreasonably large, especially for the smallest dimension, c, because at certain orientations of the asteroid, the residual space (or χ-squared hyperspace) is quite convoluted and even discontinuous. As explained by Drummond et al. (1985a), at certain configurations the asteroid will appear

to suddenly reverse directions as it rotates. Near this configuration a small change in any of the six parameters during the iterations will result in a large change in the predicted position angles, and thus in the residuals. The errors computed in such a situation are not realistic. For instance, the minimum in the χ-squared hyperspace results in the solution that appears in Table II, but the formal error for c of $\pm$386 km implies that our data allows c to be negative.

Since this unphysical possibility is caused by the warped residual space, we compute the errors, instead, by considering the five solution sets of observations taken four at a time. For each of the six parameters we find the mean (μ) and standard deviation (δ) of the five sets, and calculate the error (σ) of p (the parameter solution given in Table II) by $\sigma^2 = (p-\mu)^2 + \delta^2$. (For two of the five sets only a 5 parameter fit [b=c] converged to a solution.)

Table III gives the 5 parameter solution, the prolate spheroid case (b=c) using all five observations. Since this biaxial ellipsoid never reverses direction of rotation, the χ-squared hyperspace is not warped, and there are no problems finding the solutions or computing the errors. However, the fit to α, β, and γ (none illustrated), are much worse than the triaxial case, and, furthermore, the triaxial solution does not allow a biaxial situation $(b - \sigma_b) > (c + \sigma_c)$. Therefore, unlike our treatment of Eros and Herculina, we do not consider a weighted average between the biaxial and triaxial solutions, and only use the latter (Table II), rejecting the biaxial solution

(Table III).

In Figure 1 we show the measured α's (upper filled circles) and β's (lower open circles), as a function of rotational phase. The upper line is the predicted α from the solution in Table II, and the lower line is the predicted β. Figure 2 shows the measured (circles) and predicted (line) γ's for our triaxial solution of Table II. To illustrate the problem caused by the weird shape of the residual space, Figure 3 results from using the adopted solution of Table II, but changing the latitude of the sub-Earth point, θ, by 1° from -39°.6 to -40°.6. In Figure 2 $\cos^2\theta > (a^2-b^2)/(a^2-c^2)$ and the condition for rotation reversal of the projected ellipse is satisfied. In Figure 3 $\cos^2\theta < (a^2-b^2)/(a^2-c^2)$ and the ellipse does not reverse directions.

Davida as a Rubble Pile

A particular sub-set of triaxial ellipsoid figures is allowed if a body is in hydrostatic as well as gravitational equilibrium. The shape of such objects is maintained by gravity only since they have no internal strength (Chandrasekhar 1969; Weidenschilling 1981). If an asteroid suffers a catastrophic collision it is possible that reaccumulation could occur among the ejecta with relative velocities less than the escape velocity of the largest remnant (Zappala et al. 1984). Such rubble piles (Davis et al. 1979) would form a particular triaxial ellipsoid equilibrium figure that is a function only of its angular momentum.

Within the errors, our determination of the shape of Davida suggests the possibility that it could be such an equilibrium figure, and since we know its volume and rotation period, it is possible to find its mean density as was suggested by Farinella et al. (1981). Following their lead, we note that for the equilibrium figure of 465x377x244, which falls within the errors of our observations, and has the same long dimension and volume as the solution from Table II, a rotational period of 5.1297 hours (Zappala and Knezevic, 1985) leads to a mean density of 1.4 $\pm$ 0.4 gm/cm^3. This density is rather low and could mean that there is substantial void space within the asteroid, or for that matter, may suggest that Davida is not a rubble pile after all.

Photometry

When the solar phase angle (ω) is less than substantial, there is a two-fold ambiguity in determining the pole direction from the changing size, shape, and orientation of the projected ellipses. However, this θ, $\pi-\theta$ ambiguity (Drummond et al. 1985a) which is manifest as a choice between two obliquities, and therefore two poles, can easily be resolved by considering lightcurve data. In Table IV we compare the observed lightcurve amplitudes (taken from Zappala and Knezevic, 1985 and from Vesely and Taylor, 1985) to our predicted amplitudes using pole 1 in Table II. The RMS deviation from the observed amplitudes is .04 mag, whereas with pole 2 it was found to be .18 mag. The choice between the two pole solutions is obvious.

Next we derive and apply yet another magnitude-amplitude-aspect relation. Several versions of the principle are currently used, e.g., Zappala's amplitude-magnitude (AM; Zappala et al. 1983, Zappala and Knezevic 1984), or Tedesco and Taylor's (1985) magnitude-amplitude-shape-aspect (MASA), relationships. To distinguish our new technique we dub our method the simultaneous amplitude-magnitude (SAM) relation. Adopting the assumptions from the introduction of this paper, the square of the amplitude (converted from magnitudes to a linear scale) of an asteroid's lightcurve is given as the ratio of maximum to minimum projected area squared

$$R^2 = (A + B \cos^2\theta)/(A + C \cos^2\theta) \qquad (1)$$

where $A = a^2b^2$, $B = a^2c^2 - a^2b^2$, and $C = b^2c^2 - a^2b^2$. The latitude of the sub Earth point, θ, comes from

$$\sin\theta = -[\cos(\lambda-\lambda_p)\cos\delta\cos\delta_p + \sin\delta\sin\delta_p],$$

where λ, δ and λ_p, δ_p are the known celestial or ecliptic coordinates of the asteroid and the unknown coordinates of the asteroid's pole, respectively.

Unlike photometric astrometry (Taylor and Tedesco, 1983), which takes advantage of the movement of the sub-Earth point across lines of longitude on the asteroid to derive a pole direction, the amplitude-magnitude-aspect relation, which takes advantage of the movement of the sub-Earth point across lines of latitude on the asteroid, is model-dependent in that it is a function not only of the location of the pole but of the axial ratios as well. Thus a non-linear least squares solution of equation (1) for ab, ac, bc, λ_p, and δ_p, (or A, B, C, λ_p, and δ_p) would result in finding simultaneously $a^2/b^2 = (A+B)/(A+C)$, $b^2/c^2 = A/(A+B)$, and $a^2/c^2 = A/(A+C)$ and λ_p, δ_p. A separate solution of the numerator in (1), using $V_o(1,\theta)$ converted to intensity (the magnitude-aspect relation), would yield only $b^2/c^2 = A/(A+B)$ and a pole position, if the amplitudes are not available. Thus two separate determinations of b^2/c^2 and the pole are made with eq. (1) and the magnitude-aspect method.

Another way of attacking the problem is to use a grid of poles and axial ratios to find the combination that minimizes the residuals between observed and predicted amplitudes and maximum intensities. Our new method, however, uses a linear least squares technique to find the axial ratios from a grid of possible poles, thus eliminating the necessity of sampling a grid of axial ratios. First, if only amplitudes are considered, then

by manipulating (1) we can form a linear amplitude aspect relation

$$(R^2-1)^{-1} = k + l\tan^2\theta \qquad (2)$$

and solve for k and l for each trial pole where $k = (A+C)/(B-C)$ and $l = A/(B-C)$, and thus $a^2/b^2 = (k+1)/k$, $b^2/c^2 = l/(k+1)$, and $a^2/c^2 = l/k$. The pole and the resulting k and l that minimize the residuals between "observed" and predicted $(R^2-1)^{-1}$ is chosen as the best solution. The drawbacks to this method are that it is a non-linear relation between the observable quantity R and the independent variable θ, and that it gives more weight to observations at higher θ. However, (2) is the simplest statement of the amplitude-aspect relation.

If both V_o and an amplitude for a given epoch are provided then it is possible to convert the maximum and minimum light to intensities squared, X^2 and N^2, respectively. Two linear combinations of these quantities yield two equations to solve for three unknowns. Adding and subtracting the numerator and denominator in (1) yields

$$X^2 + N^2 = K + L\cos^2\theta \qquad (3)$$

$$X^2 - N^2 = M\cos^2\theta \qquad (4)$$

A linear least squares solution of these equations for each trial pole is made, and again the pole giving the lowest vector sum of the residuals in (3) and (4) is chosen. The corresponding K, L, and M give the axial-ratios:

$$\frac{a^2}{b^2} = \frac{K+L+M}{K+L-M} = \frac{A+B}{A+C}$$

$$\frac{a^2}{c^2} = \frac{K}{K+L-M} = \frac{A}{A+C}$$

$$\frac{b^2}{c^2} = \frac{K}{K+L+M} = \frac{A}{A+B}$$

The advantage of this amplitude magnitude aspect method is that a linear least squares estimate is made for the unknowns, which yield axial ratios for the pole giving the lowest residuals for all the available information simultaneously.

We now apply this new method (SAM) by selecting the seven amplitudes in Table IV for Davida that have a corresponding V_o in Table V, an accumulation of $V(1,\omega)$'s by Zappala and Knezevic (1985) and Vesel, and Taylor (1985) from original sources contained therein. But first, we use all the $V(1,\omega)$'s in Table V to construct the standard solar phase function plot of $V(1,\omega)$ vs ω, and show this as Figure (4). Using the eight points observed at $\omega > 6.5°$ we find $V(1,\omega) = 6.445(\pm.042) + .048(\pm.004)$. Using the opposition effect as formulated by Gehrels and Tedesco (1979), we then calculate the RMS deviation from the solid line in Figure (4) for all eleven points as 0.035 mag. If we choose the Lumme and Bowell (1981a,b; Bowell and Lumme 1979) phase function description, we derive $m(0) = 6.132(\pm.063)$ and $Q = 0.045(\pm.028)$ with an RMS scatter of 0.033 mag. Both methods describe the data adequately but we will proceed in our analysis by using the residuals from the Gehrels and Tedesco formulation.

Implicit in the standard phase plot, Figure (4), is that b/c = 1, that the maximum area does not change with θ. But let us attribute the residuals in Figure 4 to differences in θ at

various oppositions, and convert each residual to an intensity. Then using the seven residuals that have corresponding amplitudes in Table IV we can derive seven (X^2, N^2) pairs. The only data that is excluded is the 1962 amplitude for which a V_o was not found; also, only one amplitude and V_o from 1979 is chosen so as not to bias the results toward one opposition. Next we construct a grid of pole positions at 1° intervals in both ecliptic longitude and latitude in the region of the poles found by speckle and by Zappala and Knezevic (1985).

We find solutions for our SAM method (equations (3) and (4)), and for the amplitude-aspect relation as given by (2). Bevington (1969) suggests that when a non-linear equation is transformed to a linear equation, the equations of condition should be weighted. In our case (2) should be weighted by

$$\left[\frac{d(R^2-1)^{-1}}{dR^2}\right]^{-2} = (R^2-1)^4.$$

This seems rather severe, so in addition to finding the unweighted least squares solution to (2), we also find two weighted solutions, one using the suggested $(R^2-1)^4$ as weights and one using $(R^2-1)^2$. Table VI gives the pole and axial ratios for the four methods, along with the errors as found by a formal analysis of the propagation of the uncertainties in the coefficients K, L, and M, or k and ℓ, generated from the linear least squares routines. For instance the error in the a/c ratio using (2) is

$$\sigma_{a/c} = \frac{\partial a/c}{\partial a^2/c^2}\,\frac{\partial (a^2/c^2)^{1/2}}{\partial (a^2/c^2)}\,\sigma_{a^2/c^2} = .5(a/c)^3\,\ell^{-2}\left(k^2\sigma_\ell^2 + \ell^2\sigma_k^2\right)^{1/2}.$$

The RMS error for the location of the pole arises from the differences between the θ's calculated from the given pole and

from inverting (2):

$$\theta = \tan^{-1}\left[\frac{(R^2 l)^{-1} - k}{l}\right]^{1/2} = \tan^{-1}\left[\frac{c^2/b^2 - R^2 c^2/a^2}{R^2 - 1}\right]^{1/2}$$

The RMS amplitudes (converted back to magnitude from intensities) arises from comparing the observed amplitudes to a rearranged (1)

$$R^2 = \frac{\frac{c^2}{b^2}\cos^2\theta + \sin^2\theta}{\frac{c^2}{a^2}\cos^2\theta + \sin^2\theta}$$

Rounding out Table VI are the equivalent results from the entirely independent method of speckle interferometry based on the May 3, 1982 obeservations. Note that the 8° RMS error for the speckle pole in Table VI is determined from photometric data, whereas the 26° uncertainty in Table II derives from speckle observations.

In Table VII we show the solar phase functions for each of the solutions in Table VI, using both the Gehrels and Tedesco phase function and the Lumme and Bowell formulation, although the residuals to the b/c = 1 phase function (Figure 4) were determined from the Gehrels and Tedesco fit for input into the SAM method. For the cases where b/c≠1, the observed $V(1,\omega,\theta)$'s were corrected to the polar view $V(1,\omega,90^\circ)$ using the appropriate b/c and pole.

Of the photometric solutions for the pole and axial ratios in Tables VI and VII, we prefer the results from the simultaneous-amplitude-magnitude method because it uses both V_o and amplitudes simultaneously and is a simple combination of linear equations. The vector sum of the RMS scatter in

magnitudes from the predicted and observed amplitudes from Table VI, column 7, and from the predicted and observed $V(1,\omega,\theta)$ from Table VII, column 3, is ~~.036~~ .023 mag. ~~Nearly~~ N_2+ as good is the amplitude-aspect relation (eq. 2) weighted by $(R^2-1)^2$, which gives a vector sum of RMS scatter of .837. The unweighted amplitude-aspect method, and the amplitude-aspect method weighted by $(R^2-1)^4$, give RMS scatters of .849 and .896 magnitudes, respectively, and we do not consider them serious contenders for possible models of Davida. Figures 5 and 6 show the aspect corrected solar phase functions for the SAM results and for the preferred weighted amplitude aspect method (WAA), respectively, although the latter method uses only amplitudes as input and does not use V_o data at all.

Other salient points from this analysis of photometric data are 1) Regardless of the method, the a/b ratio seems to be well determined at 1.24. 2) The location of the pole is also well determined and is not very sensitive to the method. 3) On the other hand, the a/c and b/c ratios vary dramatically with the location of the pole and the method of analysis. 4) The uncertainties in the axial ratios increase with increased weighting. 5) The Lumme-Bowell formulation of the phase function appears to give slightly (but perhaps insignificantly) lower residuals in the fits to the data than the Gehrels and Tedesco method. 6) None of the axial ratios derived from photometry are equilibrium figures.

Combining Speckle and Photometry

One of the most useful applications of speckle and photometric data is in the derivation of rather precise albedos, especially for dark objects where the polarization slope-albedo law saturates (Dollfus and Zellner 1979). For each of the fits for Davida in Table VI we find the figure requiring the least change (in an RMS sense) in the speckle dimensions to meet the axial ratios found from the photometry. These dimensions are listed in Table VIII along with the uncertainties, where the latter are calculated as the vector sum of the uncertainty in the speckle dimension plus the difference between the speckle and photometric dimension. Also listed in the table are the visual albedos calculated with the V(1,0)'s and m(0)'s of Table VII according to eq. (3) of Dollfus and Zellner (1979), where the errors in the albedos follow from the propagation of the uncertainties in a, b, and V(1,0) or m(0).

Table VIII

Comparisons and Summaries

In one night, speckle interferometric observations yield a triaxial ellipsoid figure for Davida, and two pole solutions. A simple inspection of the lightcurve history of the asteroid easily distinguishes between the two. The pole lies within 26° of ecliptic coordinates (291°; +37°), and the axial ratios are a/b = 1.38 ± .17 and b/c = 1.39 ± .32. This compares favorably to Zappala and Knezevic's (1985) results from their amplitude-magnitude-aspect (AM) method, which give a pole some 18° from ours at (303°±4°; +34°±5°) or taking into account scattering, 12° away at (302°±6°; +29°±6°). Their axial ratios also agree with ours to within our errors: a/b = 1.26 and b/c = 1.18 (or 1.19 and 1.13 with scattering corrections).

We derive a new simultaneous amplitude-magnitude-aspect (SAM) technique that for Davida yields a pole within 2.°3 of (308°; +38°), 16° away from the speckle pole, and axial ratios of a/b = 1.24±.03, and b/c = 1.12±.03, both within the uncertainties of the values found from speckle. If only amplitudes are considered, then our version of a weighted amplitude-aspect relation gives a pole at (311°; +32°), with an uncertainty of 2.°6. The axial ratios for this method are a/b = 1.24±.09 and b/c = 1.24±.09.

Although Taylor (Vesely and Taylor, 1985) was not able to achieve a totally satisfactory result with photometric astrometry

of Davida, by considering only pairs of observations at the same longitudes a pole within 22° of (285°; +45°) was suggested, which is only 9° from the speckle pole. Chang and Chang (1963), from only four lightcurves, found a pole at (306°, + 34°) with an early version of the amplitude-aspect relation, superseding the one Gehrels and Owings (1962) found at (172°, +10°) from three lightcurves.

The radiometric diameter of Davida is listed as 323 km by Morrison and Zellner (1979) and 335 km by Bowell et al. (1979). The mean diameter from speckle $(abc)^{1/3}$ is 350 ± 28 km, from speckle and SAM is 361 ± 35 km, and from speckle and WAA is 359 ± 30 km, all in reasonable agreement.

The albedo computed for the speckle dimensions is p_v = 0.036 ± .005, or from either of our favored photometric models p_v = .033 ± .005 with the Gehrels and Tedesco phase function. With the Lumme and Bowell phase relation p_v is (0.041-.042+0.006-.007).

While the photometric SAM and WAA results for the pole and axial ratios are consistent with the results from speckle interferometry, in the sense that they fall within the tolerances of the speckle measurements, it is nevertheless tempting to try to explain the 16-17° difference between the speckle and photometric poles, and the differences between the axial ratios, because the speckle shape implies an equilibrium figure and the photometric ratios do not. (In this connection it should be noted that although neither the SAM nor any of the amplitude-aspect ratios are equilibrium figures, the mean of the two weighted methods, $A/A(R^2-1)^2$ and $A/A(R^2-1)^4$ in Table VI, are very close to the suggested equilibrium figure of 465x377x244.) It is

possible to reconcile the differences between the speckle and photometric results by invoking an albedo structure over the asteroid.

If the speckle rotational pole and axial ratios are considered correct, then a photometric pole some 16-17° away from the rotational pole implies that the brightest point on the asteroid is off-axis and would lead to asymmetric lightcurves. If the photometric ratios and pole are considered correct than the discrepancy in the speckle results is probably due to the fact that they are based on only 5 ten-minute observations at one aspect on one night, whereas the photometry was gathered over 28 years at various aspects. Between these two independent solutions are many possible albedo structures that would bridge the two results. For instance, with the speckle dimensions and the photometric rotational pole, the albedo structures listed in Table IX for both phase functions and each photometric method would produce exactly the photometric history of Davida. Thus for the SAM method, a 23% decrease in albedo from the view along the a axis to the view from over the pole, and a decrease of 5% from the view along the a axis to the view along the b axis, would produce, with the speckle dimensions and photometric pole, the same photometric behavior as would the SAM model in Tables VI-VIII. For the WAA results a decrease of 15% and 4%, respectively, would produce the same photometric history as the WAA model in Tables VI-VIII. While the photometric axial ratios in Table VI do not allow an equilibrium figure, the speckle dimensions, with or without the albedo structures given in Table

IX, do, of course, lead to the equilibrium figure density of 1.4 gm/cm^3.

With the photometric data available, then, there is no way to choose between a uniform albedo, non-equilibrium figure, and an equilibrium figure with albedo gradients. However, we are developing an image reconstruction program, which is the ideal use of speckle interferometric data, and perhaps a successful image reconstruction will shed light on the matter.

ACKNOWLEDGEMENTS

We thank Eugene Perlman and Gary Schmidt for helpful discussions regarding the properties of least squares fitting procedures. This work is supported under NASA contract NAGW-224.

References

Birch, P. V., E. F. Tedesco, R. C. Taylor, R. P. Binzel, C. Blanco, S. Catalano, P. Hartigan, F. Scaltriti, D. J. Tholen, and V. Zappala (1983). Lightcurves and phase function of asteroid 44 Nysa during its 1979 apparition. Icarus 54, 1-12.

Bowell, E., T. Gehrels, and B. Zellner (1979). Magnitudes, colors, types, and adopted diameters of the asteroids. In Asteroids (T. Gehrels, Ed.) 1108-1129, University of Arizona Press, Tucson.

Bowell, E. and K. Lumme (1979). Colorimetry and magnitudes of asteroids. In Asteroids (T. Gehrels, Ed.) 132-169, University of Arizona Press, Tucson.

Chandrasekhar, S. (1969). Ellipsoidal Figures of Equilibrium. Yale University Press, New Haven, Conn./London.

Chang, Y. C., and C. Chang (1963). Photometric observations of variable asteroids. II. Acta Astron. Sin. 11, 139-149.

Davis, D. R., C. R. Chapman, R. Greenberg, S. J. Weidenschilling, and A. W. Harris (1979). Collisional evolution of asteroids: populations, rotation, and velocities. In Asteroids (T. Gehrels, Ed.) 528-557, University of Arizona Press, Tucson.

Dollfus, A. and B. Zellner (1979). Optical polarimetry of asteroids and laboratory samples. In Asteroids (T. Gehrels, Ed.) 170-183, University of Arizona Press, Tucson.

Drummond, J. D., W. J. Cocke, E. K. Hege, P. A. Strittmatter, and J. V. Lambert (1985a). Speckle interferometry of asteroids. I. 433 Eros. Icarus 61, 132-151.

Drummond, J. D., E. K. Hege, W. J. Cocke, J. D. Freeman, J. C. Christou, and R. P. Binzel (1985b). Speckle interferometry of asteroids. II. 532 Herculina. Icarus 61, 232-240.

Farinella, P., P. Paolicchi, E. F. Tedesco, and V. Zappala (1981). Triaxial equilibrium ellipsoids among the asteroids? Icarus 46, 114-123.

Gehrels, T. and D. Owings (1962). Photometric studies of asteroids. IX. Additional lightcurves. Astrophys. J. 135, 906-924.

Gehrels, T. and E. F. Tedesco (1979). Minor planets and related objects. XXVIII. Asteroid magnitudes and phase relations. Astron. J. 84, 1079-1087.

Hege, E. K., E. N. Hubbard, P. A. Strittmatter, and W. J. Cocke (1982). The Steward Observatory speckle interferometry system. Optica Acta 29, 701-715.

Jeffreys, W. H. (1980). On the method of least squares. Astron. J. 85, 177-181.

Jeffreys, W. H. (1981). On the method of least squares. II. Astron. J. 86, 149-155.

Lumme, K. and E. Bowell (1981a). Radiative transfer in the surfaces of atmosphereless bodies. I. Theory. Astron. J. 86, 1694-1704.

Lumme, K. and E. Bowell (1981b). Radiative transfer in the surfaces of atmosphereless bodies. II. Interpretation of

phase curves. Astron. J. 86, 1705-1721.

Morrison, D. and B. Zellner (1979). Polarimetry and radiometry of the asteroids. In Asteroids (T. Gehrels, Ed.) 1090-1097, University of Arizona Press, Tucson.

Taylor, R. C. (1979). Pole orientations of asteroids. In Asteroids (T. Gehrels, Ed.) 488-493, University of Arizona Press, Tucson.

Taylor, R. C. and E. F. Tedesco (1983). Pole orientation of asteroid 44 Nysa via photometric astrometry, including a discussion of the method's application and its limitations. Icarus 54, 13-22.

Vesely, C. D. and R. C. Taylor (1985). A survey of asteroid lightcurves. Submitted to Icarus.

Weidenschilling, S. J. (1981). How fast can an asteroid spin? Icarus 46, 124-126.

Zappala, V., M. DiMartino, P. Farinella, and P. Paolicchi (1983). An analytical method for the determination of the rotational directions of asteroids. In Asteroids, Comets, Meteors (C. I. Lagerkvist and H. Rickman, Eds.) 73-76, Uppsala Universitet Repocentralen HSC, Uppsala.

Zappala, V. and Z. Knezevic (1984). Rotation axes of asteroids: Results for 14 objects. Icarus 59, 436-455.

Zappala, V. and Knezevic (1985). Pole coordinates of the asteroid 511 Davida via amplitude-magnitude method. In preparation.

Zappala, V., P. Farinella, Z. Knezevic, and P. Paolicchi (1984). Collisional origin of the asteroid families: Mass and velocity distributions. Icarus 59, 261-285.

TABLE I.

Aspect Data for Speckle Observations

Date	RA	Dec
3 May 1982	15^h56^m	-2° 08'

Distance from Earth	Distance from Sun
2.655 AU	3.604 AU

Solar Phase Angle	Position Angle of Sun centered on Davida
8°3	53°

TABLE II.

Triaxial Solution

a	=	465 ± 33 km
b	=	358 ± 39 km
c	=	258 ± 52 km
ϕ_0	=	-10° ± 44°
θ	=	-40° ± 28°
ρ_1	=	285° ± 26°
ρ_2	=	105° ± 26°

Pole 1

RA = 19^h08^m Dec = +15°

Ecliptic Long = 291° Lat = +37°

Pole 2

RA = 12^h40^m Dec = -18°

Long = 196° Lat = -12°

The error radius around each pole solution is 26°.

TABLE III.

Rejected Biaxial Solution

a	=	512 ± 100 km
b = c	=	334 ± 39 km
ϕ_0	=	-24° ± 14°
θ	=	-14° ± 13°
ρ_1	=	324° ± 17°
ρ_2	=	144° ± 17°

Pole 1

RA = 20^h56^m Dec = +16°

Ecliptic Long = 322° Lat = +32°

Pole 2

RA = 10^h52^m Dec = -17°

Long = 171° Lat = -23°

The error radius around each pole solution is 16°.

TABLE IV.

Date	λ	β	Amplitudes Observed Amplitude	θ_1	Speckle Predicted Amplitude	O-C
Jan. 26, 1952	112	+3	0.06	+50	0.06	0.00
April 8, 1953	200	+22	.25	-12	.25	.00
Jan. 26, 1958	147	+12	.09	+30	.15	-.06
Dec. 5, 1962	63	-17	.12	+43	.09	.03
Dec. 30, 1968	100	-4	.07	+55	.05	.02
Mar. 21, 1970	195	+22	.22	-9	.27	-.05
Aug. 7, 1972	304	-7	.06	-44	.09	-.03
Dec. 6, 1979	52	-18	.18	+35	.13	.05

TABLE V.

V(1,ω,θ)

Date	λ	β	ω	V(1,ω)	θ_1	Speckle V(1,ω, 90)
Jan. 26, 1952	112	+3	5.0	6.55	+50	6.43
April 8, 1953	200	+22	6.6	6.72	-12	6.39
Jan. 26, 1958	147	+12	8.1	6.72	+30	6.48
Dec. 29/30, 1968	100	-4	1.65	6.35	+55	6.26
Mar. 21, 1970	195	+22	7.8	6.82	-9	6.48
Aug. 7, 1972	304	-7	3.6	6.48	-44	6.32
Oct. 31, 1979	60	-20	10.7	6.86	+43	6.70
Nov. 12, 1979	59	-20	7.9	6.73	+42	6.56
Dec. 7, 1979	52	-18	10.0	6.83	+35	6.62
Dec. 17, 1979	51	-17	12.8	6.96	+34	6.74
Jan. 3, 1980	50	-14	17.2	7.13	+31	6.89

Table VI. Pole and Axial Ratio Solutions

	Ecliptic Pole Coordinates λ	β	θ RMS	a/b	a/c	b/c	RMS Amplitudes (mag) (n=7)
Speckle	291	+37	8.8	1.38±.17	1.88±.39	1.39±.32	.044
SAM (eq. 3 & 4)	302	+38	2.3	1.24±.03	1.39±.07	1.12±.03	.011
Amplitude/Aspect, eq. 2; wt=$(R^2-1)^2$	311	+32	2.6	1.24±.09	1.54±.13	1.24±.09	.011
Amplitude/Aspect unweighted	309	+25	3.6	1.23±.04	1.17±.04	0.95±.02	.015
Amplitude/Aspect wt=$(R^2-1)^4$	316	+42	2.1	1.25±.11	2.20±.56	1.76±.44	.009

Table VII Phase Functions

	Gehrels and Tedesco			Lumme and Bowell		
	V(1,0,90)	Phase Coefficient	RMS Mag (n=11)	m(o)	Q	RMS Mag.
b/c=1	6.445(±.042)	.048(±.004)	.035	6.132(±.063)	.045(±.028)	.033
Speckle	6.177(±.029)	.043(±.003)	.059	6.030(±.117)	.172(±.047)	.057
SAM	6.353(±.026)	.039(±.002)	.022	6.189(±.041)	.116(±.017)	.022
Amplitude/Aspect wt=$(R^2-1)^2$	6.295(±.031)	.036(±.003)	.035	6.084(±.055)	.102(±.022)	.029
Amplitude/Aspect unweighted	6.479(±.052)	.041(±.005)	.047	6.145(±.076)	.018(±.034)	.041
Amplitude/Aspect wt=$(R^2-1)^4$	6.846(±.078)	.038(±.007)	.096	5.938(±.171)	.362(±.078)	.072

Table VIII Diameters and Albedos

	a	b	c	p_V(G&T)	p_V(L&B)
Speckle	465±33	358±39	258±52	.036±.005	.041±.007
SAM	432±47	349±48	312±75	.033±.005	.042±.007
$A/A(R^2-1)^2$	445±39	358±39	291±62	.033±.005	.041±.006
A/A	409±65	332±47	349±185	.033±.007	.045±.010
$A/A(R^2-1)^4$	470±33	376±43	214±68	.038±.006	.042±.009

33

Table IX Orthogonal Albedos for Speckle Dimensions and Photometric Pole

	Gehrels and Tedesco			Lumme and Bowell		
	P_c	P_b	P_a	P_c	P_b	P_a
SAM	.030	.038	.039	.038	.047	.049
$A/A(R^2-1)^2$	.032	.036	.038	.039	.044	.046
A/A	.027	.039	.0042	.037	.054	.056
$A/A(R^2-1)^4$	.040	.032	.033	.045	.035	.037

29
34

Figure Captions

Fig. 1. Measured major (α) and minor (β) axis dimensions (solid and open dots, respectively) as a function of rotational phase for 511 Davida on May 3, 1982. The upper line is the least squares fit to the major axis dimensions and the lower line in the simultaneous fit to the minor axis dimensions. Maximum area (maximum light) occurs at rotational phase 0° and 180°.

Fig. 2. Measured relative position angles (dots) of the major axis and the simultaneous (along with the data in Fig. 1) least squares fit to the measured position angles (γ) as a function of rotation on May 3, 1982. At rotational phase 0° and 180°, maximum area is reached, and $\underline{a}$ is perpendicular to our line of sight, lying unforeshortened in the plane of the Earth's sky. Note that the position angle reverses direction near minimum light at rotational phases -90° and 90°.

Fig. 3. Same as Fig. 2, but the latitude of the sub-Earth point (θ) has been changed by one degree. Unlike in Fig. 2, for this aspect the asteroid would not appear to reverse directions during rotation. The one degree change in θ results in a large change to the structure of the residuals. See text.

Fig. 4. Standard (b assumed equal to c) solar phase plot of V_o (from Table V) vs solar phase angle. The linear portion of the Gehrels and Tedesco phase function is calculated from the eight points observed at greater than 6.5°. The intercept of this line is at $V_o(1,\theta) = 6.445$, while the intercept for the Lumme and Bowell fit is $m(\sigma) = 6.132$. See Table VII.

Fig. 5. Solar phase function for the simultaneous-amplitude-magnitude (SAM) aspect results given in Tables VI and VII. Here the brightness $V(1,\omega,\theta)$ is corrected to $V(1,\omega,90)$, the view from above the pole. The Gehrels and Tedesco phase function formulation is used and a line is fit to the eight points observed at greater than 6.5°.

Fig. 6. Same as Fig. 5, but for the weighted, by $(R^2-1)^2$, linear amplitude-aspect results. The line is a fit to the seven points observed at greater than 7°.

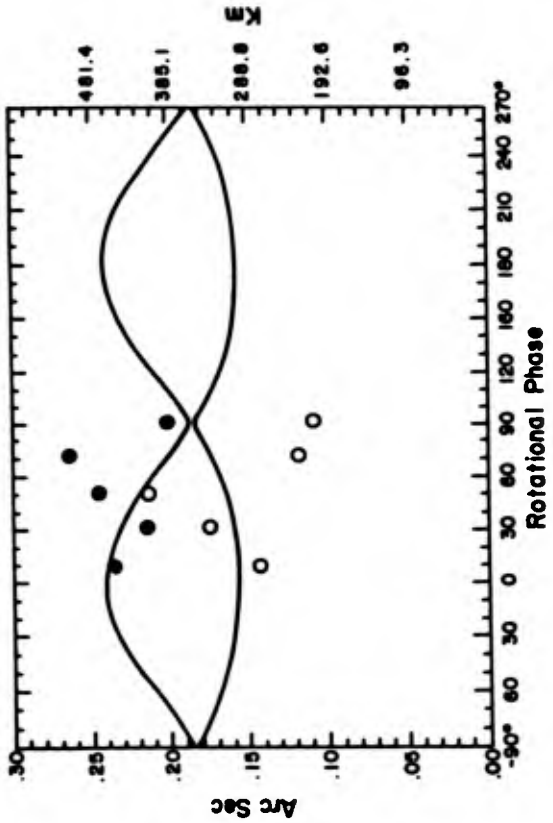

Fig 1
Drummond
Hase

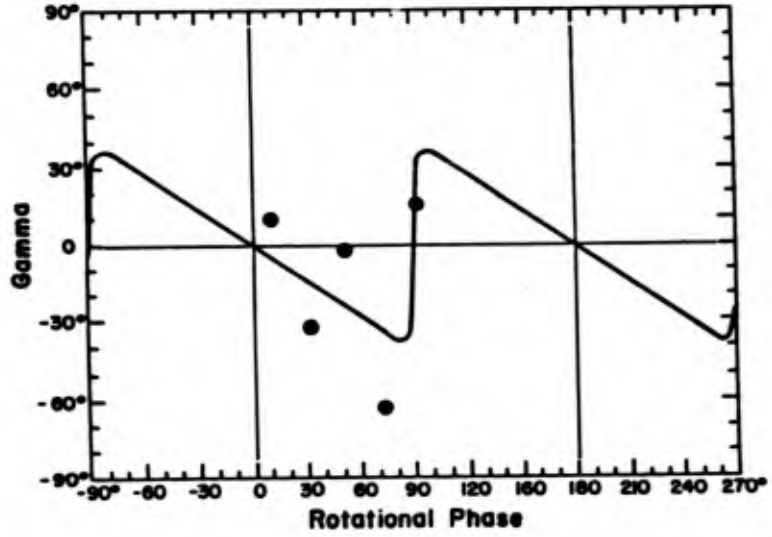

Fig 2
Drummond
Hase

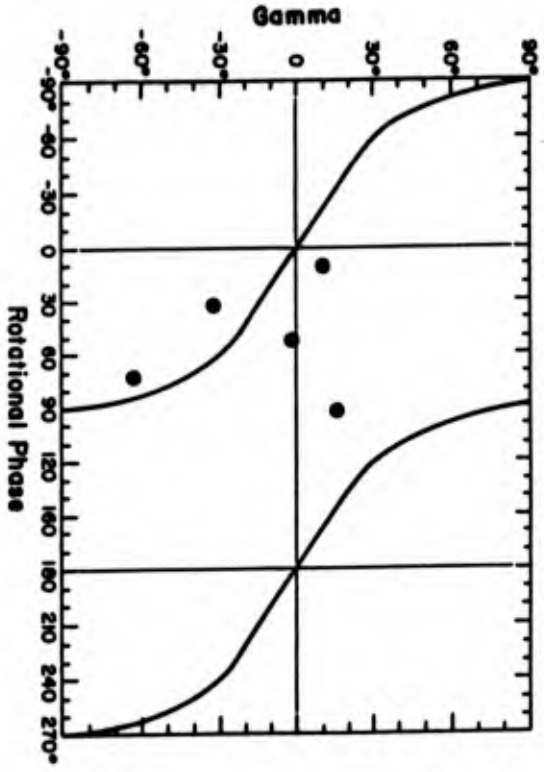

Fig. 3
Observed
Phase

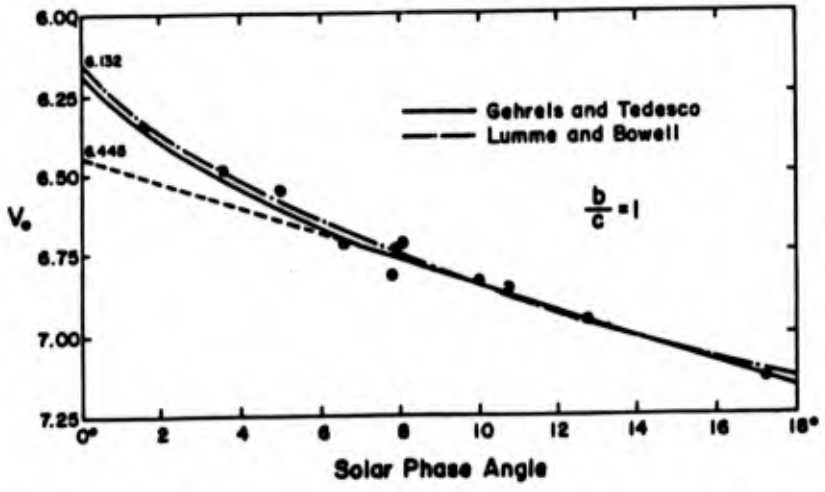

Fig. 4
Observed
Phase

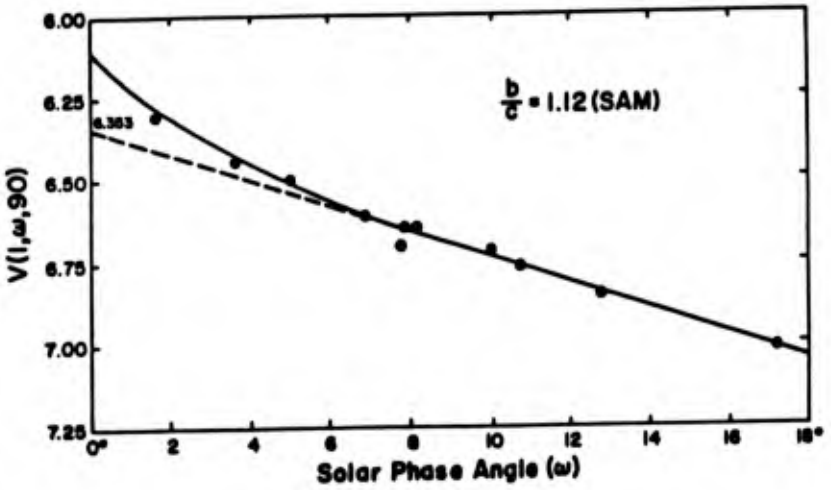
6.00
6.25
6.50
6.75
7.00
7.25
V(1,ω,90)
6.383
b/c = 1.12 (SAM)
0°
2
4
6
8
10
12
14
16
18°
Solar Phase Angle (ω)

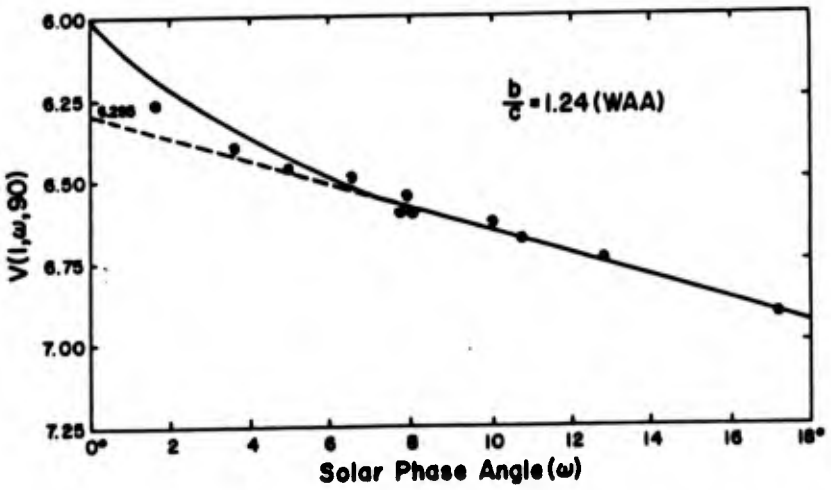
6.00
6.25
6.50
6.75
7.00
7.25
V(1,ω,90)
6.286
b/c = 1.24 (WAA)
0°
2
4
6
8
10
12
14
16
18°
Solar Phase Angle (ω)

445-64

HIGH-SPEED DIGITAL SIGNAL PROCESSING FOR SPECKLE INTERFEROMETRY

E. K. Hege, W. J. Cocke, P. A. Strittmatter, S. P. Worden

Steward Observatory
Tucson, AZ 85721

William C. Booth

Signal Processing Systems
Waltham, MA 02154

Abstract

Speckle Interferometry has now been shown capable of yielding diffraction limited information on objects as faint as visual magnitude 16. Research in progress at Steward Observatory is aimed at improving (a) the resolution, (by using the Multiple Mirror Telescope* with its 6.9 meter baseline), (b) the accuracy of the derived results (by implementing better recording devices and reduction algorithms), and (c) the efficiency and speed with which the information can be provided (by means of high-speed digital signal-processing hardware).

The instrumentation proposed here will improve spatial resolution at visible wavelengths to approximately 15 milliarc-seconds (75×10^{-9} radians, the best possible for any existing telescope), reduce detector induced image distortion to less than 1% and increase the throughput to essentially real-time complex Fourier transform amplitude and phase integrations at the telescope.

Introduction

Speckle interferometry[1-3] is a post-detection image processing technique for producing diffraction limited images using large astronomical telescopes in the presence of Earth's turbulent atmosphere which otherwise limits the imaging resolution.

Since 1978 the basic design of the Steward Observatory digital video speckle camera has evolved, as reported in a series of publications [4-7], to comprise three basic subsystems: a) video digitization of an intensified, magnified focal-plane image; b) Fourier transform (or vector autocorrelation) signal processing; and c) image analysis to produce the final interpreted results of speckle interferometry. Experience gained with these systems has shown the need for further refinements of these basic elements. a) Improved detectors are required to provide better spatial resolution and geometric fidelity as well as better linearity and dynamic range; b) real-time signal processing is required to permit the primary data compression to be accomplished at the telescope while the observations are in pro-gress; and c) image processing systems (in addition to general-purpose computational capabilities) are required to efficiently reduce the speckle interferometric results. This basic speckle interferometry system design is shown schematically in Figure 1.

The present realization of this camera [6], consisting of first generation electrostatic inverters (4 stages of Varo 8605), a plumbicon camera and a Grinnell digital video memory system for video digitization and general-purpose minicomputers of very limited capabilities (Data General Nova class) for both the signal processing and the image processing functions, has been applied successfully to observations of asteroids [8], the Pluto-Charon system [9] and the $15^m.7$ QSO PG115+080 [10] as well as to observations of bright supergiants [11-13] and binary stars [14-15]. These observations and results have revealed both the capabilities and the limitations of this system. Among the demonstrated capabilities are included a) observations of structure as faint as m_v=18 in an m_v=16 system[10], b) obser-vations of structure at the diffraction limit of the Multiple Mirror Telescope[13,16], c) astrometric observations[8-10,14-15] and d) mapping of faint envelopes around bright supergiants[12].

Among the limitations of this system, the most severe are a) detector limitations including large geometric distortions, limited linearity and low dynamic range; b) extremely limited signal processing throughput in which the primary signal processing time ranges up to 100 times that required for the observations at the telescope; and c) no special purpose array processing capability for image analysis. We anticipate upgrading of observatory computational capabilities to include array-processing image analysis.

* The Multiple Mirror Telescope is a joint facility of the University of Arizona and the Smithsonian Institution.

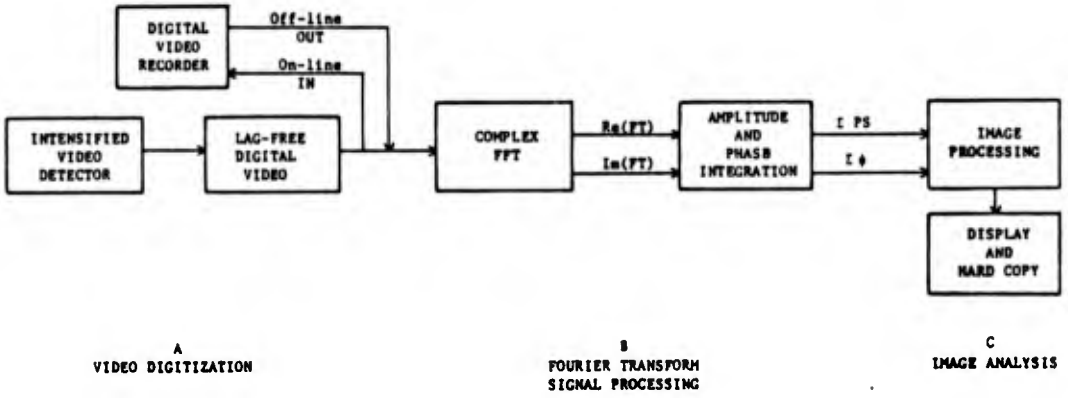

Figure 1. The Digital Speckle Interferometry System.

It is the purpose of this paper to propose instrumentation, specifically detectors and real-time Fourier signal processors, to aleviate limitations of present detectors and signal processors, in order to a) exploit the 75 nanoradian (15×10^{-3} arc seconds) full resolution of the Multiple Mirror Telescope[17] over a distortion-free field at least 10 microradians (2 arc seconds) square, and b) provide the required primary signal processing, with at least 256-pixel resolution in each direction, in real time at the telescope.

Detector Requirements

Experience with our present intensified plumbicon video system[6], together with evidence from other workers[18], estab-lishes rather strong criteria for detector performance. In order to have single-photon detection, detector-lag elimination[5] is required to remove frame-to-frame correlation. This can be accomplished by frame-subtraction[6] for analogue detection or video-raster event-localization schemes[7], as shown in Figure 2. Event-localization using newly developed time-tagging detector readout schemes[19,20] are intrinsically lag-free. For bright-object work, these readout systems must be highly linear and have a large dynamic range (at least 8-bits deep for analogue intensities) or very fast (10^6 events/sec for photon-counting schemes). For astrometric work, or for multiple specklegram differential work[12], very low geometrical distortion (less than one pixel in a 512 x 512 primary raster) is required.

Proximity focused electrostatic image intensifiers[21], configured in a system with sufficient gain for good photo-electron pulse discrimination, as represented schematically in Figure 3, provide greatly improved geometrical fidelity and geometrical stability compared to either electrostatic inverters or magnetic focused devices. High quantum efficiency (>20%) and low dark current ($<10 e.cm^{-2}.sec^{-1}$ at -30C) are required in order to obtain useful specklegrams of m_v=15 or fainter objects, although these levels of dark-emission are difficult to achieve for proximity focused devices with good red response. Also, very fast (1 microsecond) output phosphors are required if event detection at 10^6/sec is to be achieved.

The geometrical fidelity and stability and the linearity and dynamic range of the system cannot be better than that of the image intensifier readout system. This immediately rules out electron-gun video systems in the changing environments of an instrument mounted on an astronomical telescope. Solid-state (CCD or Photodiode) cameras[22], as well as the event localizing schemes noted above, appear to meet the requirement that the performance of the primary detector (the first stage image intensifier photocathode) not be degraded.

Although the majority of speckle interferometry to date has used exposures of 20-50milliseconds (we typically use 33ms as defined by the 30Hz video framing rate), we have experienced atmospheric conditions on many occasions when speckle interferometry could not be effectively accomplished with exposures greater than 1 to 10ms. In this case rapid shuttering with frame-subtraction (with subsequent loss of duty-cycle in a standard video raster scheme), or time tagging schemes (with sub-sequent increase in specklegram rate) are required. The time-tagging, photoelectron-localization schemes of Timothy et al. and Papaliolios et al. appear very attractive as means of introducing variable (and therefore

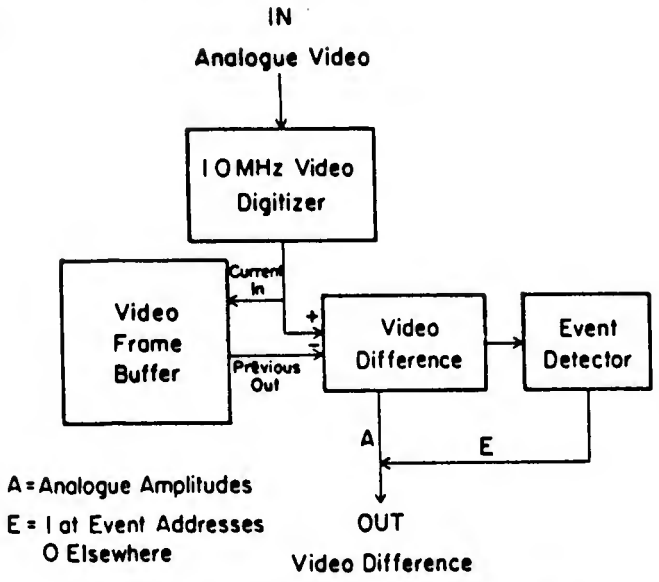

Figure 2. Lag-free Digital Video.

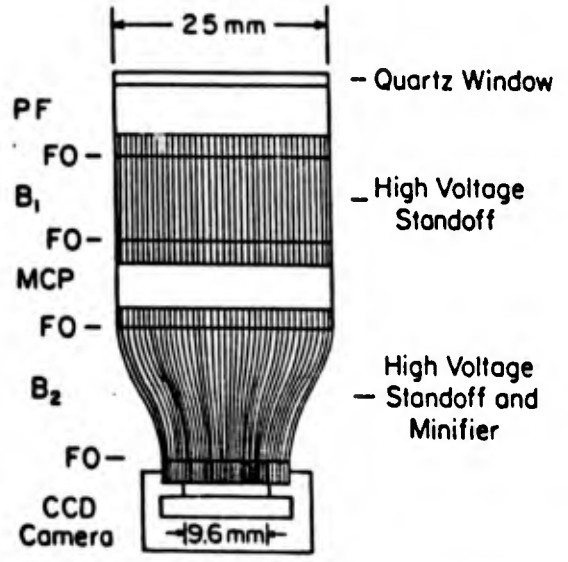

Figure 3. A low-distortion, high-gain multi-stage image intensifier. a CCD camera can provide standard video readout, or a time-tagging event detector readout may be used. PF = proximity focus image intensifier. FO = fiber optics. MCP = micro-channel plate image intensifier.

optimizable) frame rates. However, particularly for short correlation times, this places even greater demands upon subsequent signal processor bandwidths. It may be desirable to have both time-tagging and conventional video detectors.

Our experience with analogue video data-logging has also revealed severe limitations, both in dynamic range and bandwidth of U-matic 3/4inch video cassette recorders. This same experience has, however, proven the value of archiving the primary data domain, which should be preserved even as on-line data-reduction capabilities are implemented. Archived data can subsequently be reduced by different algorithms to extract different information (or to correct prior procedural or parametric errors) if it is preserved in its original form.

Since certain aspects of the data reduction process are applied to nearly all data sets (complex FFT, co-addition of power spectra or autocorrelation functions, co-addition of image phases or phase differences, co-addition of centroided frames), we considered the possibility of moving one step away from the primary video domain, namely logging the (possibly "super-resolved") complex FFT for each video frame on standard digital magtape. A simple calculation quickly revealed that conventional 9-track digital techniques are quite inadequate. The compressed format of time-tagged event addresses is the best contender for a high-fidelity pimary data archive, especially for fainter objects where recording only non-zero pixels is a considerable advantage. Although quite expensive, digital video recording techniques can maintain the speeds required if full-format recording of amplitudes for bright objects is required.

Speckle Data Processing Algorithms

All Speckle Interferometry proceeds from the accumulation of co-added power spectra (or equivalently for photoelectron limited observations, co-added autocorrelation functions). Since this processing looses all image phase information, it is also desirable to include some image phase integration method as well. No single method has yet proven superior to any other, so we wish to specify a system with sufficient flexibility to accomodate several possible image phase retrieval (as contrasted to image phase "reconstruction") methods[12,23-28].

The differential method[12] requires co-addition of the complex deconvolution of two speckle grams obtained simultaneously in two different wavelengths. Cocke's[24] phase unwrapping method requires super-resolution (i.e. increased size of input raster) and neighborhood processing to recover missing multiples of 2π (Figure 4.).

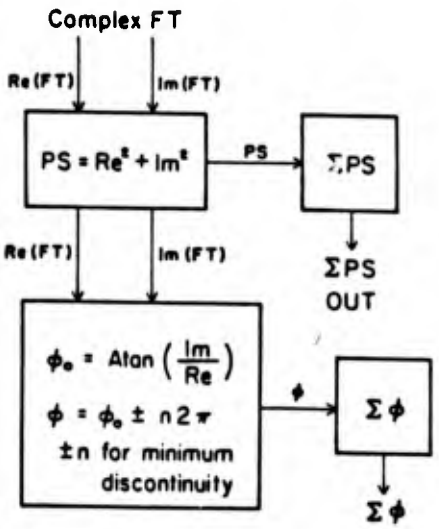

Figure 4. The Phase-unwrapping method.

The shift-and-add[28] methods (derivative of that used originally by Lynds, Worden, and Harvey[25]) require neighborhood processing to extract a sampling function which is cross-correlated with the original specklegrams to produce image estimates which are co-added. A variant[26] of the LWH method extracts a weighted sampling function by which the specklegrams are deconvolved frame-by-frame to produce seeing-corrected image estimates (a la the differential method) which are co-added.

Nisenson, et al.[27] have proposed a scheme based upon the accumulation of four arrays, each of which is derived from the complex Fourier transform and summed over the ensemble of specklegrams, which can be the basis for an integration yielding the Fourier phases. We propose in this paper a hardware realization of that procedure.

Given $FT(i(x,y)) = I(u,v) = A(u,v)e^{if(u,v)}$, the four arrays which are to be accumulated are:

(1)	$\langle I(u,v) \rangle$	Equivalent to the Long Exposure.
(2)	$\langle \lvert I(u,v) \rvert^2 \rangle$	The usual Power Spectrum.
(3)	$\langle I^*(u,v) I(u+\Delta u,v) \rangle$	An X-phase array.
(4)	$\langle I^*(u,v) I(u,v+\Delta v) \rangle$	A Y-phase array.

Nisenson, et al. show that (3) and (4) effectively yield phase differences which can be integrated to yield the desired transform phases for a Knox-Thompson style two-dimensional image reconstruction. In a subsequent paper[29], Nisenson et al. have shown that this method can also be corrected for the effects of photon noise bias. Hence it is our method of choice for both bright objects as well as faint objects for which the photon noise bias becomes dominant.

In practice, we have found that ordinary computational methods are prohibitively slow for even the usual power spectrum processing and that ordinary array processors of the AP-120B class would not provide the through-put to implement the above four-array algorithm on a sufficiently fine grid to sample the diffraction limit of the MMT in a real-time integration at 60Hz (or even 30Hz). We require the accumulation of the four arrays noted above for 8-bit video data digitized on a 256 x 256 raster for every 16.7ms (60Hz) video field in order to utilize the full duty cycle of the observation for faint objects. In searching for a technology capable of this task, we found that the special-purpose signal-processing hardware optimized for radar and sonar signal processing appears to satisfy our requirements. Hence we propose a Signal Processing Systems SPS-1000 based system.

Real-time Video Fourier Transform Signal Processing

The configuration of the proposed SPS-1000 signal processing subsystem for digital speckle interferometry is illustrated in figures 5 and 6. The system is shown in minimum, and maximum configurations. The minimum system provides a modest but acceptable level of performance at a minimum cost. The maximum system can be incrementally expanded to improve

throughput until an optimum configuration is reached. The maximum configuration uses a different basic processor and therefore would involve a more extensive modification if a smaller configuration is built first. However, since all models of the SPS-1000 use the same byte sliced building block modules, the smaller processor can be converted, at the factory, to the larger one. Thus the proposed system provides a systematic means whereby the performance of the digital speckle interferometry system can be increased over a period of time.

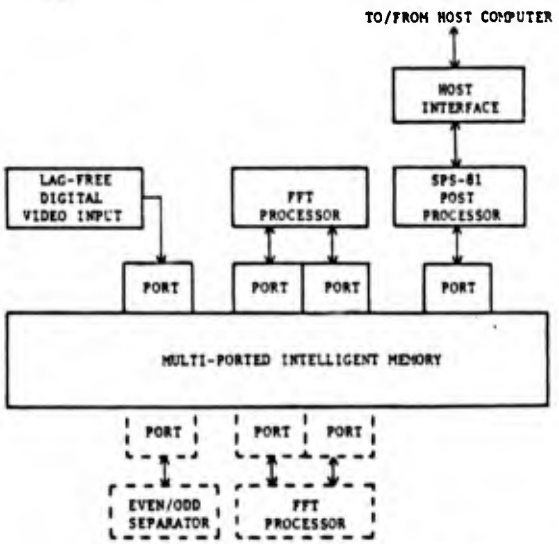

Figure 5. Minimum system.

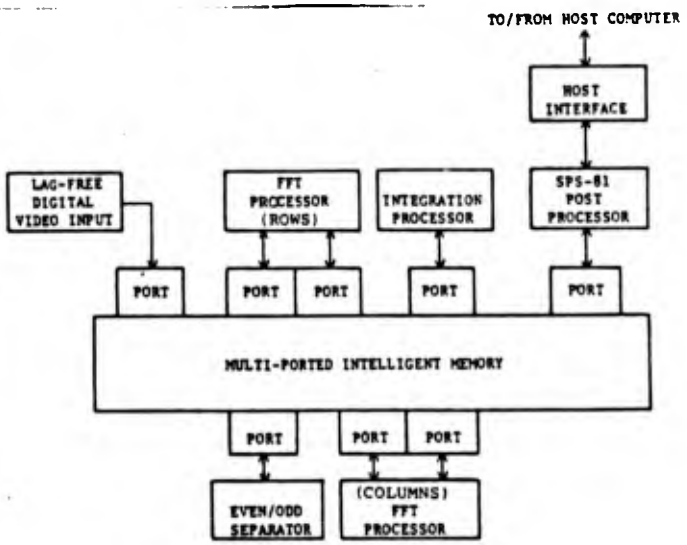

Figure 6. Maximum system.

As mentioned previously, the use of a conventional programmable processor such as a general purpose computer and/or an array processor is precluded by the high computational rates required by the algorithms used. At the same time, it is desired that the system be programmable to some reasonable level to permit modification of the techniques used. This desire, coupled with the high cost and schedule risk associated with development of a special purpose hard-wired processor, motivated the selection of the SPS-1000 for the signal processor.

The SPS-1000 is a memory centered multi-processor system which was developed to facilitate implementation of high speed real-time signal processing systems such as radar and sonar. It uses a multi-ported intelligent memory to provide attachment points for a variety of processors each optimized for a specific part of the overall signal processing task. These processors may be general purpose computers, array processors, microprocessors, hard-wired modules, etc. For applications which involve Fourier Transforms, the manufacturer offers an imbedded Fast Fourier Transform (FFT) processor which attaches to two of the ports of the memory. A general purpose programmable signal processor (the SPS-81) with throughput comparable to that of a high speed array processor is also offered as an imbedded processor.

The use of intelligent memory as the system integration medium, coupled with a manufacturer supported block diagram compiler, permits the system to operate under program control by application oriented high level language statements.

For the minimum system we selected a small SPS-1000 processor designated the SPS-1016-15. This system includes an imbedded FFT processor which will perform continuous FFTs of up to 1024 complex points at sample rates up to 1.9 megahertz. FFTs larger than 1024 points are accomplished at one half that rate. Two dimensional FFTs are accomodated by using the same pipeline for both the row and column FFTs. The throughput of the system can be doubled by adding a second FFT processor so that the row and column FFTs are accomplished concurrently. The SPS-1000 can be prewired to accept the second FFT processor as a plug-in option to facilitate future expansion.

For the maximum system we selected a faster version of the SPS-1000 designated the SPS-1016-45 with an additional FFT processor. This system can perform continuous two-dimensional FFTs on complex data input at over 6 megahertz.

Both the minimum and maximum systems use an SPS-81 imbedded processor as a post FFT processor. In the case of the minimum system, the SPS-81 can perform the integration of the transformed data as well as the post integration processing. For the maximum system, the SPS-81 is not fast enough to do the integration. Therefore, for this version a specialized

imbedded processor will be used to accomplish the integrations and the SPS-81 will be required to perform only the post integration processing.

Both the minimum and maximum systems are programmable, so that a variety of application software packages can be developed to provide tradeoffs between various performance parameters. For example, Table I indicates the tradeoff between frame size and frame rate for each of the two configurations discussed in this paper.

Table I System Performance Tradeoffs

	Minimum System		Maximum System	
Frame Size (pixels)	Frame Rate (Hz)	Pixel Rate (MHz)	Frame Rate (Hz)	Pixel Rate (MHz)
128 x 128	70	1.15	270	4.42
256 x 256	18	1.17	84	5.51
512 x 512	4.6	1.21	23	6.03

The frame rates and corresponding pixel rates indicated in the table are the maximums which can be accomodated by the system. Since the system is data driven, the data can be input at any rate up to the maximum for the particular frame size used with no change to the software. The maximum frame rates given above for the minimum system can be approximately doubled by adding the second FFT processor which is indicated by broken lines in Figure 5. The performance numbers for the maximum system already include the second FFT processor. All of the above numbers presume maximum utilization of the capability of the hardware. Prudence dictates, however, that some 5% to 10% reduction of these numbers be applied to allow a performance margin as in all programmable digital processors.

The reader will note that the input data to the system are real whereas the FFT operation is inherently a complex number algorithm and the outputs from the FFT are complex. Although several algorithms exist for performing real to complex FFTS, the FFT processor of the SPS-1000 does only complex to complex FFTs. For the minimum system, the input data will be made complex by inputting zeros in the imaginary parts of the complex input words. This makes for some inefficiency in the first (row) FFT operation but is in keeping with the concept of a minimum system. The result of a complex FFT on real input data is a conjugate symmetric array, one half of which is the desired result. Therefore, one half of these results can be ignored in doing the column FFTs and no further inefficiency results. Thus, the processing of an N X N input array results in an N/2 X N intermediate array and a similar output array.

For the maximum system, advantage is taken of an option offered by the manufacturer of the SPS-1000 to efficiently perform real to complex FFTs. This option, called an even-odd separator unscrambles the results obtained by performing an FFT on a pseudo-complex input array which is obtained by packing successive even and odd input samples as the real and imaginary parts of complex words. This technique reduces the input rate and the size of the row FFTs by half and results in increased system performance. The even-odd separator can also be included in the minimum system to provide a further performance improvement over and above that which can be achieved by a second FFT processor.

The implementation of the signal processing functions for the minimum and maximum systems are illustrated by Figures 7 and 8. The two implementations are identical except for the packing on input and the even-odd separate between the row and column FFTs. In the minimum system the four integrations will be performed by the SPS-81 processor whereas in the maximum system these will be done by a specialized processor attached to a separate port. In both cases the image reconstruction will be done by the SPS-81 processor.

The entire signal processor is attached to a host computer which provides the application program files and the downloading function. The host computer can be connected directly to a port or can interface to the system through the SPS-81 processor. We have chosen the latter since the SPS-81 requires a host interface in any case and thus one port can be saved.

Since the basic concept for this system is an intelligent, multi-ported memory system, considerable flexibility in implementation of and variants to the basic speckle processing algorithm are possible. We have discussed only the requirements for Knox-Thompson based image reconstruction in order to limit the scope of this discussion. However, the flexibility of the system is adequate to allow implementation of other image retrieval methods such as the complex deconvolution of differential speckle imaging or the neighbor-

hood processing required by phase-following approaches. By employing more integration buffers and simple first-moment calculations one could implement "r_o-monitoring"[30] as proposed by Mariotti *et al.* to improve the precision of seeing calibrations, for example.

We believe this type of system provides an optimal compromise between hard-wired signal processors (the ultimate in speed) and conventional, floating-point processors (the ultimate in algorithmic flexibility).

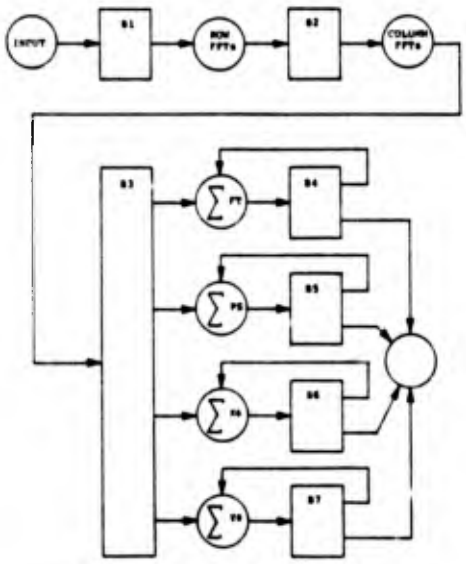

Figure 7. Minimum processing.

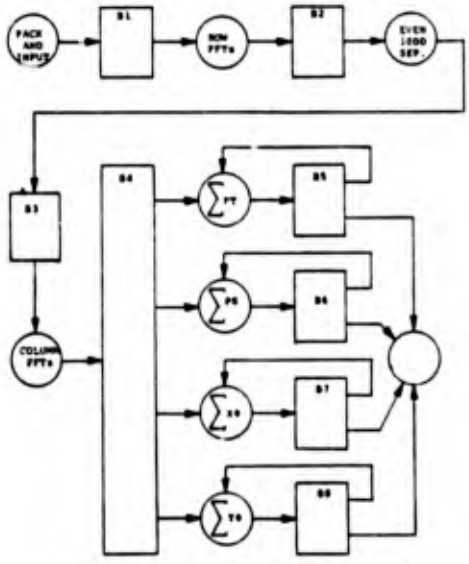

Figure 8. Maximum processing.

Conclusions

Present detector limitations appear to be surmountable by implementation of currently available proximity-focused image intensifiers suitably coupled to solid-state video readout devices. The data-processing requirements, which now make speckle image reconstruction computationally impractical, can be met by implementation of currently available signal-processing technology. The raw data sets from which true image reconstructtion can be achieved can be accumulated in real-time (image power spectra and image phase arrays) at the telescope just as optical spectra (in raw form) are presently integrated in real-time while the observation progresses. No serious implementation of diffraction limited astronomical optical image reconstruction can settle for less.

Acknowledgements

We thank P. Nisenson and C. Papaliolios for several useful discussions about signal processing and R. Cromwell for the basic outline for the proximity focused image intensifier system.

References

1. Labeyrie, A. "Attainment of Diffraction-Limited Resolution in Large Telescopes by Fourier Analysing Speckle Patterns in Large Telescopes", Astron. and Astrophys. 6, 85, 1970.

2. Labeyrie, A. "Stellar Interferometry Methods", Ann. Rev. Astron. Astrophys. 16, 77, 1978.

3. Worden, S. P. "Astronomical Image Reconstruction", Vistas in Astron. 20, 301, 1977.

4. Hubbard, G., E.K. Hege, M. Reed, P.A. Strittmatter, and N. Woolf, "The Steward Observatory Speckle Camera", Astron. J., 1437, 1979.

5. Hege, E.K., E.N. Hubbard and P.A. Strittmatter, "An Intensified Event-Detecting Television System for Astronomical Speckle Interferometry" SPIE Proceedings 264, 29, 1980.

6. Hege, E.K., E.N. Hubbard, P.A. Strittmatter, and W.J. Cocke, "The Steward Observatory Speckle Interferometry System" Optica Acta, 29, 70, 1982.

7. Macklin, R. H., E.K. Hege, and P.A. Strittmatter, "A Real-time Photoelectron Event-detecting Video System" SPIE Proceedings 359, , 1982.

8. Drummond, J.D., W.J. Cocke, E.K. Hege, and P.A. Strittmatter, "Speckle Interferometry of Asteroids. 433 Eros" Submitted to Icarus, 1983.

9. Hege, E.K., E.N. Hubbard, J.D. Drummond, P.A. Strittmatter, S.P. Worden, and T. Lauer, "Speckle Interferometric Observations of Pluto and Charon" Icarus 50, 72, 1982.

10. Hege, E.K., E.N. Hubbard, P.A. Strittmatter, and S.P. Worden, "Speckle Interferometric Observations of the Triple QSO PG1115+08" Astrophys. J. (Letters) 248, L1, 1981.

11. Goldberg, L., E.K. Hege, E.N. Hubbard, P.A. Strittmatter, and W.J. Cocke, "Speckle Interferometry of a Ori: Preliminary Results" SAO Special Reports 392, 131, 1982.

12. Beckers, J.M., E.K. Hege, and H.P. Murphy, "The Differential Speckle Interferometer" SPIE Proceedings 445, 1983.

13. Beckers, J.M., E.K. Hege, and P.A. Strittmatter, "Optical Interferometry with the MMT" SPIE Proceedings 444, 1983.

14. Cocke, W.J., E.K. Hege, E.N. Hubbard, P.A. Strittmatter, and S.P. Worden, "An Image Reconstruction for Capella" Lowell Observatory Reports, In press, 1983.

15. Hege, E.K., E.N. Hubbard, W.J. Cocke, P.A. Strittmatter, S.P. Worden, and R.R. Radick, "Recovery of Intensity Information from Speckle Data" Lowell Observatory Reports, In Press, 1983.

16. McCarthy, D.W., P.A. Strittmatter, E.K. Hege, and F.J. Low, "MMT as an Optical-infrared Interferometer and Phased Array" SPIE Proceedings 332, 57, 1982.

17. Beckers, J.M., E.K. Hege, F.J. Low, D.W. McCarthy, and P.A. Strittmatter, "The use of the Multiple Mirror Telescope as a Phased Array" SPIE Proceedings 440, 1983.

18. Nisenson, P., J. Apt, R. Goody, and C. Papaliolios, "Speckle Imaging for Planetary research" Icarus 53, 465, 1983.

19. Timothy, J. G., C.L. Joseph, and S.C. Wolff, "High resolution spectroscopy with the multi-anode microchannel array detector systems" SPIE Proceedings 331, 301, 1982.

20. Papaliolios, C., and L. Mertz, "New Two-dimensional Photon Camera" SPIE Proceedings 331, 1982.

21. Cromwell, R.H., H.W. Funk, K. Frank, P.A. Strittmatter, R.G. Allen, E.K. Hege, and H. Kuhr "A Proximity Focused Image Intensifier for Astronomy" Eighth Symposium on Photoelectronic Image Devices, London, 1983.

22. McAlister, H.A., W.G. Robinson, and S.L. Marcus "Development of a Dual Microchannel Plate Intensified CCD Speckle Camera" SPIE Proceedings 331, 113, 1982.

23. Knox, K.T. and B.J. Thompson "Recovery of Images from Atmospherically Degraded Short-exposure Photographs" Astrophys. J. 193, L45, 1974.

24. Cocke, W.J. "Computer Simulation Comparisons of Speckle Image Reconstruction Techniques" SPIE Proceedings 231, 99, 1980.

25. Lynds, C.R. S.P. Worden and J.W. Harvey "Digital Image Reconstruction Applied to Alpha Orionis" Astrophys. J. 207, 174, 1976.

26. Christou, J. and J. Freeman (Private communication) are currently developing and evaluating a self-calibrating deconvolution variant of the original Lynds-Worden-Harvey method.

27. Nisenson, P. and R. Statchnik, C. Papaliolios, and P. Horowitz, "Data Recording and Processing for Speckle Image Reconstruction" SPIE Proceedings 243, 88, 1980.

28. Bates, R.H.T., and F.M. Cady "Towards True Imaging by Wideband Speckle Interferometry" Opt. Commun. 32, 365, 1980.

29. Nisenson, P., and C. Papaliolios "Effects of Photon Noise on Speckle Image Reconstruction with the Knox-Thompson Algorithm" Opt. Commun., In Press, 1983.

30. Mariotti, J.M., A. Chelli. R. Foy, P. Lena, F. Sibille, and G. Tchountonov "Infrared Speckle Imaging: Improvement ofk the Method; Results on Miras and Protostars" Astron. Astrophys. 120, 237, 1983.

Knox-Thompson Phase Recovery Photon-by-Photon

A. Eckart, J. Cocke and K. Hege

ABSTRACT

To obtain reliable maps from speckle interferometry data using amplitude and phase information, Nisenson and Papaliolios proposed to use a set of three arrays, two of which contain the phase information. The phases used to Fourier transform the amplitude data (obtained from the autocorrelation) are given implicity as phase differences between adjacent grid points in the x- and y-directions. We have implemented a discrete photon version of this algorithm in which cosine and sine modulated sums over the photon coordinate lists are accumulated.

In the photon limited case the n-th specklegram becomes

$$i_n(L) = \sum \delta(L - L_i) \qquad (1)$$

where $\{L_i\}_n$ = the list of photon addresses (x_i,y_i) for the n-th frame. The discrete Fourier transform of this is

$$I(K) = \sum_L \exp\{(2\pi i/N)(K-1)(L-1)\} \cdot i(L) \qquad (2)$$

The desired quantities to be integrated are of the form, for shift s,

$$Q_s(K) = I^*(K) \cdot I(K+s). \qquad (3)$$

The inverse Fourier transform of this is

$$q(L) = \sum_K \exp\{(-2\pi i/N)(K-1)(L-1)\} \cdot Q(K), \qquad (4)$$

which is an image-plane expression reducing to

$$q(L) = \sum_{L'} \sum_K \exp\{(2\pi i/N)(K-1)[L'_n - (L-1)]\} \times \exp\{(2\pi i/N)\, s\, (L_n - 1)\}. \qquad (5)$$

This reduces to an autocorrelation-function-like quantity with a complex modulation term:

$$q(L) = N \sum_L \exp\{(2\pi i/N)\, s\, (L'_n - 1)\} \times \delta(L'_n - L_n - L + 1), \qquad (6)$$

This expression is essentially only a weighted summation over the photon list coordinates. Therefore, it allows us to accumulate the Fourier transforms of the phase difference files in a very efficient way. A final Fourier transform provides the actual phase differences.

As proposed by Knox (1976) a first estimate of the actual phases is achieved by assuming their continuity and averaging the sums of the phase differences via two different paths from the orgin to each point in the grid (Figure 1). The phase in the origin can be set to zero. This procedure is subject to errors (O'Donnell, 1983) especially in the case of weak signals where the phase differences are poorly determined. In order to distribute the errors uniformly over the u-v-plane a well known (e.g. Hardy et al., 1977) method of phase averaging is applied:

$$N = 0.25 \cdot (A+a + B-b + C-c + D-d) \qquad (7)$$

We use this method of phase averaging in an interative way: Starting at the origin we spiral outwards, replacing each phase by the average given above. For each executed spiral each phase (except for the origin) is therefore determined by 1 to 3 phases already averaged in the course of the current spiral. Therefore with an increasing number of interations the intially obtained estimates of the phases become more and more dominated by the actual phase differences to the adjacent grid points. Figure 2 shows the convergence of the process. A standard derivation for the iteration defined as:

$$O_k = \text{sqrt}\left(\frac{1}{m-i} \sum_{i}^{m} \sum_{j}^{m} (N_{k-1}(i,j) - N_k(i,j))^2 \right) \qquad (8)$$

is plotted against the number of iterations.

Nisenson, P. Stachnik, R., Papaliolios, C., Horiwitz, P.: 1980, SPIE Vol. 243, 88.

O'Donnell, Thesis, 1983, University of Rochester.

Knox, K. T., 1976, J.O.S.A., Vol. 66, 1236.

Hardy, J. W., Lefebvre, J. E., Koliopoulos, C. L., 1977, J.O.S.A., Vol. 67, 360.

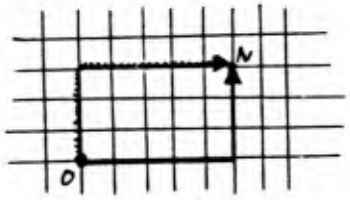

PATH A

PATH B

O : Origin

N : grid Point

Figure 2

USE OF "CLEAN" IN SPECKLE IMAGE CALIBRATION

A. Eckart, K. Hege[+], J. Christou, and S. Shaklan

ABSTRACT

In order to deconvolve images of program sources with images of point like calibrator sources, attempts were made to use the "clean" procedure implemented in the Advanced Image Processing System (AIPS). This algorithm is applied to radio interferometric data in order to remove structural features due to the synthesized interferometer beam. We have recently applied it to remove residual PSF effects in speckle interferometry, using images of an unresolved source, observed and reduced commensurately, to remove systematic artifacts from images of resolved sources.

[+]Visiting astronomer, Kitt Peak National Observatory, a division of the National Optical Astronomy Observatories, operated by the Associated Universities for Research in Astronomy, Inc., under contract with the National Science Foundation.

Description of the "CLEAN" Algorithm

Both the image of the program source, as well as the image of the calibrator, are in terms of "CLEAN" uncleaned. That means they still contain features due to post processing and, in the case of unfilled apertures, due to incomplete coverage in the Fourier transform (u,v)-plane. Therefore the images are denoted as "dirty map" and "dirty beam". Using CLEAN, a large fraction of these artificial structural features can be removed.

CLEAN is an interative process which looks for the peak in the brightness distribution of the dirty map and subtracts at this location the dirty beam pattern having a peak of g*100% of the current peak in the dirty map. This process is subsequently repeated on the residual dirty map. The loop gain g and the number of iterations n determine the quality of the cleaned map and the duration of the process.

In this way a set of values $c_i(x_i)$, where $1 < i < n$ and x_i are coordinates in the dirty map, is created so that the dirty map I_d can be written as a sum of weighted dirty beam patterns B_d and the final residual map I_R:

$$I_d(x) = \sum_i c_i \cdot B_d(x-x_i) + I_R$$

The number of iterations must be sufficiently large so that either the noise in the residual map equals the calculated noise, or so that only a certain number of values c_i are negative.

The cleaned map I_c is obtained by replacing the dirty beam pattern B_d with the restored beam pattern B_c which is commonly obtained by fitting a gaussian component to the central component of the dirty beam.

Using CLEAN for Speckle Interferometry

In the case of speckle interferometry, the following restrictions must be made on the dirty beam and the dirty map measurements:

i) Both should have a comparable coverage in the (u,v)-plane. In the ideal case, it should be exactly the same. This is especially important in the case of unfilled apertures such as that of the Multiple Mirror Telescope (MMT).

ii) They should be of comparable dynamic range.

iii) The data sets should be postprocessed in exactly the same way.

iv) The measurements should cover almost the same time. Our speckle calibration procedures, which to first order correct for variable seeing conditions, make this a weak requirement.

Points i and ii are important to achieve a high dynamic range in the final cleaned map, and to correct for features due to incomplete (u,v)-plane coverage - i.e. for MMT results. By fulfilling iii structural features due to post processing can be removed by the CLEAN algorithm.

Fulfilling iv makes sure that the long term atmospheric variations (variable seeing) are contained similarly in both data sets. Frequent, alternate observations of the program source and a nearby calibrator are the prefered observation mode to obtain optimal results by using the CLEAN procedure.

Our Attempts to use CLEAN

We applied the cleaning technique to dual frequency (6563A and 6500A) observations of the supergiant Alpha Orionis - an extended program source - and the unresolved calibrator source Gamma Orionis made at the Kitt Peak 4m telescope. The cleaning was done using (arbitrarily) 50 iterations and a loop gain of 0.7 which seemed to give reasonable residuals.

Both the peak and the integral intensity of the dirty and the final cleaned maps were within less than 3%, and always in good agreement. This data set was by no means ideal for using clean since the data were not obtained quasi-simultaneously as required. Both data sets were, however, preprocessed to remove seeing effects (Christou et al., 1985). The results obtained show some of the capabilities of this process. Figure 1 demonstrates the results for the two pairs of observations noted above.

The cleaned images of Alpha Orionis, at both wavelengths, show the clearly extended star surrounded by diffuse halo emission. a) The cleaning process obviously removed the artificial NW,SE extensions of the uncleaned star image that are prominent at the 4% to 16% contour levels. b) Furthermore, the CLEAN procedure revealed features, the N and W extensions of the halo emission, that were probably infered by the post processing of the Alplha Orionis 6563A data. c) The cleaning of Alpha Orionis at 6563A with Alpha Orionis at 6500A reveals a NE,SW extension that, if confirmed by further data analysis, contains spectral index information of the halo emission. d) The cleaning of Gamma Orionis at 6563A with Gamma Orionis at 6500A shows that in the N and S there are still some artifacts left on the 2% level in the 6563A map.

References

Hogbom, J.A. 1974, Astr. Ap., Suppl. 15, 417.

Christou, J.C., E.K. Hege, J.D. Freeman and E. Ribak 1985, Submitted to J. Opt. Soc. Am.

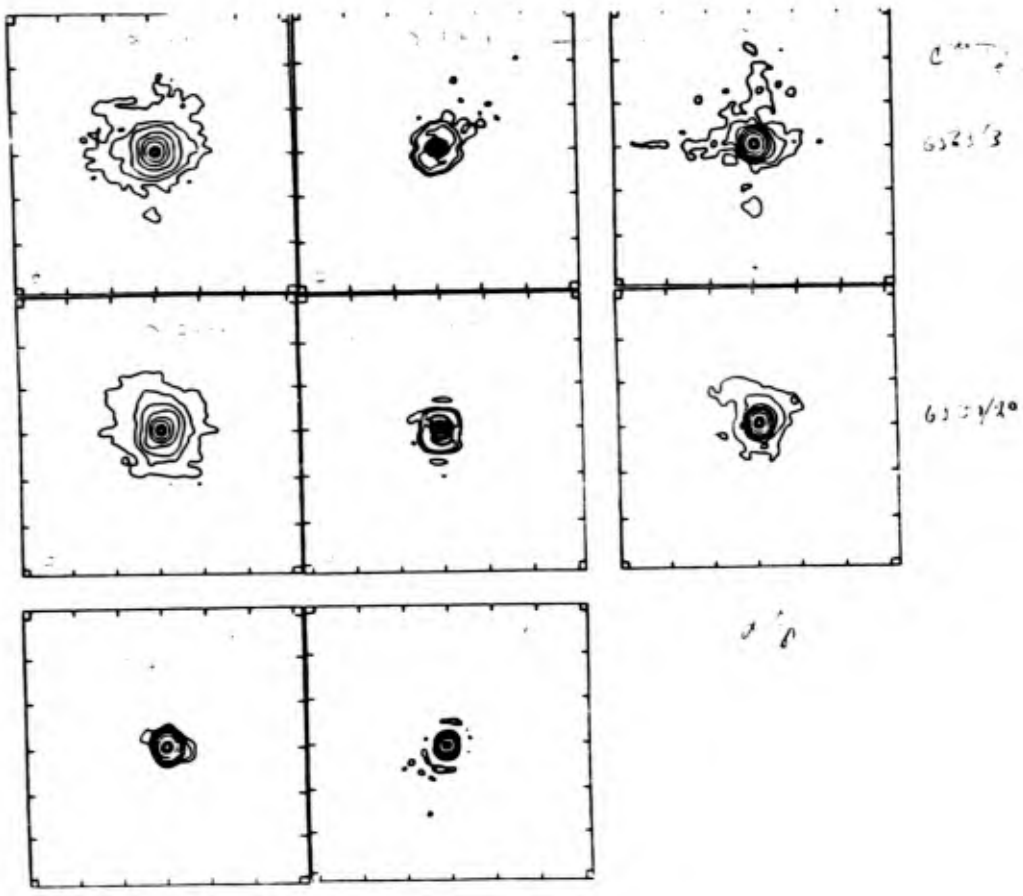

Figure 1

Seeing Calibration Of Optical Astronomical Speckle Interferometric Data

Julian C. Christou*, Andrew Y.S. Cheng, E. Keith Hege+

Steward Observatory, University Of Arizona

Tucson, Az 85721

&

C.Roddier

National Optical Astronomy Observatories

Tucson, Az 85726

To be submitted to: **The Astronomical Journal**

* Visiting Astronomer from Department of Astronomy, New Mexico State University, Las Cruces, NM 88003

+ Visiting Astronomer, Kitt Peak National Observatory, National Optical Astronomy Observatories, operated by the Association of Universities for Research in Astronomy Inc., under contract to the National Science Foundation.

Abstract

In this paper we show the effect of different seeing conditions, as parameterized by the atmospheric coherence scale r_o, upon standard Labeyrie (1970) analysis for independent observations of both a resolved object and its point source calibrator. Atmospheric dependent effects are shown by using both models and data. We show how to sort the data into like seeing bins in order to produce a calibrated image power spectrum estimate. We also justify using a stronger weighting of intermediate spatial frequencies in the image power spectrum estimator when fitting physical parameters constrained by image models to characterize the object. The use of data editing techniques to eliminate bad speckleograms, thus improving the image power spectrum estimate, is also discussed.

I. Introduction

An intensified video camera with digital readout has been used at Steward Observatory since 1979 (Hubbard et al., 1979) to obtain high angular resolution information about a number of astronomical objects (Hege et al., 1981,1982ab, Drummond et al.,1985ab, Cheng et al., 1985, Hege et al.,1985). The standard reduction process for Speckle Interferometry (SI) is that first proposed by Labeyrie (1970) and involves computing the unbiased power spectrum for data sets of both a resolved object and an unresolved point source. A seeing compensated image power spectrum estimator of the resolved object is obtained by taking the quotient of the two. A full description of this process is given by Hege et al. (1982a) and is further discussed in section II.

If the time-dependent statistics of the atmosphere are different between the resolved object and the unresolved object then this power spectrum estimator quotient is not properly calibrated for the variable seeing effects. Because of this, an image power spectrum estimator, computed as a simple quotient as above, will contain spurious power which can lead to misinterpretation of the final results. This problem has been previously discussed by Aime et al. (1978) for application to speckle measurements of the solar granulation and by Mariotti et al. (1983) for application to infrared speckle imaging. We have studied this problem using both normal and log-normal models for the statistics of the complex wavefront after passing through the turbulent atmosphere. A procedure has been implemented which, (i)

locates and omits "bad" speckiegrams from a data set and (ii) sorts the good speckiegrams into bins of like seeing as determined from the second-order moment of the speckie cloud.

The final power spectrum estimators are then computed by using data from the same seeing bins for each object. The results produced for the resolved red supergiant Alpha Orionis by this improvement to the reduction procedure are reported in another paper (Cheng et al.,1985) whereas this paper concentrates upon the theory and technique of seeing calibration.

II. Experimental Determination of the Object Power Spectrum.

An individual speckiegram is conventionally represented as a convolution of the object distribution, o(r) with the instantaneous point spread function of the telescope-atmosphere combination, s(r). i.e.

$$i(r) = o(r) * s(r) \qquad 1$$

where * denotes convolution and r implies a two-dimensional spatial domain. The time averaged power spectrum can be written as

$$PS = \langle |I(f)|^2 \rangle = |O(f)|^2 . \langle |S(f)|^2 \rangle \qquad 2$$

where I(f) is the Fourier transform of i(r), etc. in the corresponding two-dimensional spatial frequency domain, f. In Labeyrie's theory of SI (Labeyrie 1970) the measured power spectrum for the resolved object is deconvolved by dividing it by

the power spectrum of an unresolved object taken under similar seeing conditions as implied by Roddier (1981). The power spectrum of the unresolved object should give the Speckle Transfer Function (STF), $\langle|S(f)|^2\rangle = PS_\delta$, so that the desired object power spectrum can be recovered by the following relation

$$|O(f)|^2 = PS/PS_\delta \qquad 3$$

The measured power spectra in equation 2 also include noise bias terms due to photon statistics which must be removed before the quotient (3) is computed (Hege et al. 1982a).

III. Modeling the Speckle Transfer Function

Equation 2 represents the time-averaged power spectrum of a set of speckiegrams as the product of the object power spectrum with the time-averaged STF given also by equation 2 for an unresolved (point) source. The quality of the measurement of the STF determines the ability of SI to obtain diffraction limited information in the presence of the turbulent atmosphere. This function contains terms representing both the telescope and atmospheric transfer functions and has been well studied with excellent descriptions of its derivation given by Korff (1973), Fried (1979) and Roddier (1981). They show that the STF has no simple analytical expression when log-normal statistics are used, but that it can be represented approximately by a two component model for the normal statistics case. The first component is for spatial frequencies up to the atmospheric cut off $f_0=r_0/\lambda$ and the second for frequencies lying between f_0 and the telescope

diffraction limit $f_c=D/\lambda$, where λ is the wavelength of observation, r_0 is the coherence length of the atmosphere as defined by Fried (1966) and D is the diameter of the telescope aperture. Fried (1979) has shown that this two component model is a valid approximation especially for large values of the ratio of D/r_0 (notably large telescopes or poor seeing).

The low frequency ($0<f<f_0$) component is approximated by the transfer function of a long exposure with the wavefront tilt removed, as for a rapid guided image, i.e.

$$\langle|S(f)|^2\rangle_{LF} = |T(f)|^2.\exp[-6.88(\lambda f/r_0)^{5/3}.[1-(\lambda f/D)^{1/3}]] \qquad 4$$

where T(f) is the telescope transfer function given by the autocorrelation of the aperture. The high frequency ($f_0<f<f_c$) component is approximated by the relation

$$\langle|S(f)|^2\rangle_{HF} = 0.435\ (r_0/D)^2.T(f) \qquad 5$$

The above approximations describe a STF dependent upon three parameters. Two of these, D and λ, can be controlled by the observer but the third, r_0, is determined from the random nature of the seeing. It is therefore important to consider the effect of varying r_0 upon the STF. Figure 1a shows the STF, as computed using equations 4 and 5, for a range of values of r_0 from 10 cm to 35 cm for a telescope of aperture D = 4m and an observing bandpass centered at λ= 650 nm. Figure 1b shows the same but computed using the log-normal model. It can be seen in both sets of plots that as r_0 decreases in value then both the width of the low frequency component and the amplitude of the high frequency

component decrease. The telescope transfer function T(f) is also shown. Comparison of figures 1a and 1b shows that as r_o increases the difference between the two models also increases especially over the intermediate frequency range. However, the normal model is shown to be a good approximation when the ratio D/r_o is large.

The object power spectrum estimator (3) can be rewritten as

$$PS_o = |O(f)|^2 \, PS'_s / PS_s \qquad 6$$

where PS'_s represents the STF for the object data set and PS_s is the STF of the point source. If the seeing is the same for both objects then $PS'_s = PS_s$ and PS_o is in fact a good estimate of the object power spectrum. However for different seeing conditions the power spectrum will be contaminated by the term PS'_s / PS_s. In order to study the effect of this contamination we computed quotients of the STF at different values of r_o. This effect is seen in figure 2 which shows the quotients for different values of r_o relative to two different "worst cases" of 10 cm (figure 2a) and 39 cm (figure 2b) respectively as computed using the normal model. For the latter case when $D/r_o = 10$ the quotients are also shown computed for the log-normal model (figure 2c). Figures 2b and 2c agree very well at spatial frequencies $>.3f_c$. At lower spatial frequencies however, the log-normal model has a greater range over which the the differences in seeing effect the slope of the quotient. The frequency of greatest difference is at a lower frequency in the log-normal model than in the other. These figures demonstrate the seeing statistics dominated domain at the lowest spatial frequencies ($f<f_c$) modelled by (4). Over

the seeing dominated region of the quotient there is a sharp increase in excess power as the seeing degrades. For higher spatial frequencies, where the telescope transfer function dominates, the excess power is frequency independent and goes as the square of the ratio of the two different r_o's. The greater the relative difference in r_o the more pronounced are those effects and the more sensitive the quotient becomes to the differences in seeing. It can also be seen that the worse the seeing the larger the quotient becomes for the same absolute difference in r_o although the width of the low frequency spike is reduced comensurate with the larger seeing disk. The effect of an inadequate seeing calibration is therefore to multiply the object power spectrum by a function resembling those shown in the two panels of figure 2. For the case of the point source having poorer seeing then the energy at frequencies in the seeing domain will be increased and significant spurious unresolved energy will be introduced. A correct deconvolution therefore requires that observations of the resolved and unresolved objects with <u>similar seeing statistics</u> be accumulated before attempting the calibration given by (3).

IV. Data Selection

The arguements of the preceding section imply a requirement that the data be binned according to the seeing. Besides being affected by the seeing, the speckiegrams are also contaminated by a variety of processes after detection due to the nature of the detector and signal processing hardware. We have implemented a

data editing algorithm which inspects every speckiegram to identify and exclude any bad frames, including those (i) where the speckles are saturated such that they become "clipped", (ii) which contain anomalously low signal due to a shutter malfunction or to passing clouds and (iii) which contain only part of the speckle cloud due to guiding errors within the detector field of view (typically 0.5-5 arc-seconds).

For high-precision work, we have also found it useful to correct for calibratable systematic detector-induced artifacts including (i) geometric (pincushion) distortion, (ii) detector vignetting and flatfield response, and (iii) signal-dependent video pedestal ("black-level") due to the video cassette recorder response characteristics. When seeing conditions and choice of detector image scales are such that the speckiegram at the instrumental focal plane is larger than the detector field of view, additional apodizing to force the data smoothly and continuously to zero at its boundaries is also neccessary.

Our speckiegrams are digitized into 128 X 128 arrays of 8bit pixels. The saturated speckiegrams are located as those which have the greatest number of pixels with values $\geq$ 250. The limit is chosen by visual inspection of a sample of the speckiegrams. The low power frames are simply found by summing all the power within a speckiegram and comparing to some threshold. The poorly guided frames are located by computing the first-order moment of the speckiegram to obtain the frame centroid. If this lies outside a certain range then the frame is omitted.

The second-order moments about the centroid of the well-guided speckiegrams are also computed, giving the dispersion of power within the frame, and thus the size of the speckle cloud. This size parameter is then used to sort the data according to the instantaneous seeing. In order to relate this size parameter, σ, to an estimate of the seeing as defined by the Fried parameter r_o, we assume the speckle cloud to obey (in first approximation) a Gaussian distribution. i.e.

$$I(r) = A \exp[-(r^2/2\sigma^2)] \qquad 7$$

The Fourier transform of 7 is

$$I(t) = \sqrt{2\pi}\, A \exp[-2(\sigma\pi t)^2] \qquad 8$$

where the exponent can be compared to the term $\exp[-(t/t_1)^2]$ such that

$$t_1 = 1/\sqrt{2}\,\pi\sigma \qquad 9$$

Seeing theory (Woolf,1982) predicts that the seeing disc has no analytic expression but is the Fourier transform of a function of the term $\exp[-(t/t_1)^{5/3}]$ (cf. equation 4). The difference between this and a Gaussian is non-negligible but small with the Gaussian having greater amplitude at low frequencies and falling far below at higher frequencies. The RMS difference between the two functions is approximately 2% of the peak amplitude. Thus the Gaussian represents a good first-order approximation. Since $t_1 = r_o/2.1\lambda$ (Woolf, 1982) we obtain the r_o estimator

$$r_e = \lambda/2\sigma \qquad 10$$

Theoretically it is not strictly possible to interpret the measurement of r_e as being an estimate of r_0 because the latter is defined only for a long exposure image. Equation 10 is however an expedient estimate of the equivalent aperture size for which the speckle cloud represents the instantaneous angular resolution of the atmosphere.

V. Experiments

We have analyzed speckiegrams for the resolved supergiant Alpha Orionis (object) and an unresolved star Gamma Orionis (comparison) taken February 2 and 3, 1981 with the 4m Mayall telescope (with an effective aperture of 3.8m) operated at Kitt Peak National Observatory, National Optical Astronomy Observatories (NOAO). Observations at a number of different wavelengths with integration times of approximately ten minutes for the program object and five minutes for the comparison were made. The data were acquired with the Steward Observatory speckle camera and recorded onto 3/4" U-Matic video tape using the system as described by Hege et al. (1982a). The video speckiegrams were digitized later using the Grinnell and EDS Point 4 systems at Steward Observatory and the data reduction was accomplished using the Cyber 720/172 at NOAO.

Before the power spectra were computed we ran the data through a selection algorithm to flag the good and bad frames and to tag the good ones according to the seeing estimate, r_e. We found that the selection algorithm could throw out as much as 70% of the data mostly because of saturated speckles (there was

considerable, variable, high cirrus), indicating the need for careful monitoring of the detector gain while observations are in progress. Seeing bins of width r_e = 1.5 cm were chosen.

The power spectrum reduction routines then computed average power spectra for the data in each of the seeing bins. The interpretation and analysis of this successful reduction of the Alpha Orionis power spectra, yielding the first ever set of stellar limb-darkening measures, is discussed by Cheng et al. (1985).

The mean values of the seeing estimates for three data sets of Alpha and Gamma Orionis are presented in table 1. This also gives the mean measurements of the speckle cloud size indicating the spectacular sub arc-second seeing for this observing run. (it can happen at Kitt Peak). The seeing estimates, r_e, are also shown corrected for zenith angle, z, and computed for the standard wavelength of 500 nm using the relation

$$r_0 = \lambda^{6/5} \cos^{3/5} z \qquad 11$$

Figure 3 shows histograms for the distribution of the instantaneous seeing estimates r_e, for all six data sets. For the 650 nm data set the seeing distribution for the two is very similar with mean values of approximately 42 cm for each. The 354.2 nm data set however represents the other extreme where the tails of the two distributions barely overlap. At 656.3 nm there is more of an overlap but the mean of the two distributions are

seperated by more than 4 cm. Based on the model calculations these plots manifestly demonstrate the need for seeing dependent calibrations.

The shapes of these histograms differ somewhat from each other, but all appear superficially to resemble a normal distribution. However, it is important to note that both tails of the distribution have been clipped due to the data selection algorithm. The exclusion of the saturated data sets affects the high r_e tail because for good seeing there is a greater average power per speckle and therefor a greater probability of saturation. The low r_e tail is effected by the exclusion of speckiegrams whose effective width was equivalent to the frame size thus making difficult to obtain an estimate of r_e.

The data presented here was not taken with the usual obvious observing disciplines and techniques which the models imply. This in part explains the differences in the seeing distribution between Alpha and Gamma Orionis. The objects are not close in the sky and no attempt was made to chop back-and-forth between them to minimize the differences of the seeing statistics.

We have since begun an observing technique similar to that used for photometry. Two comparisons are observed bracketing the program object and for bright objects the integration times are kept short (≈ 2 minutes) whereas they are longer for fainter objects (≈ 10 minutes) in order to increase the photon SNR. This allows for a greater probability of similar seeing but r_o has been observed to vary substantially within a 5 to 10 minute

interval. Thus the specific observing program must optimize the competing opposite tendencies, a not unusual physical circumstance.

Figure 4 illustrates the nature of such variable seeing. This shows the variation of r_e, as estimated for 1 second data bins, as a function of time. The data set was of one of the components of ζ^2 Lyrae taken with the Steward Observatory 2.3 meter at Kitt Peak. The seeing estimate varies from ~11 cm to ~17 cm with a ~14 cm mean value. There is ~90 second period in the variability of the seeing indicating that even with such short integration times it would be possible to have quite different mean seeing values. Hence there is still need for the seeing calibration of the speckle data.

The effects of seeing stability has not yet been thoroughly investigated and the statistics of the variation of r_e as a function of time as well as the effects of atmosphere correlation time variability are beyond the scope of this paper, although they are currently under investigation.

The curves presented in figure 2 show the model predicted appearences of the STF quotients at different values of r_o. Figure 5 shows observations of the same effects using the data for Gamma Orionis at = 650 nm. The quotients are computed with respect to the worst seeing (smallest r_e) case. Qualitatively the models (figure 2) and the data are very similar showing two components, a constant bias at high spatial frequencies and a sharp excess in the seeing dominated domain. The quantitative

differences can be explained as being due in part to values of r_e not having been properly calibrated to r_o and also to errors caused by the fitting and removal of the photon noise bias and detector transfer function. The curve for r_e=39 cm was computed by splitting the data set into two halves and taking the quotient of the two debiased power spectra. This gives a measure of the inherent noise in these quotients. The amplitudes of the low frequency spikes of the seeing dominated component are similar, however the models predict a greater discrepency than observed for the high frequency component. The qualitative behavior of the curves is the same in that the closer the two values of r_e the nearer unity is the frequency independent component ($f_o<f<f_c$). For frequencies below, but near f_c, the effects of signal statistics and small number divisions dominate.

Because of the binning of the power spectra, the number of frames in each bin is less than the total thus decreasing the apparent Signal-to-Noise Ratio (SNR) for each of the binned power spectra compared to the usual ensemble summed power spectrum, especially at the tail ends of the distribution of r_e. The number of speckles in a speckle cloud depends upon the ratio $(D/r_o)^2$. For good seeing (large r_o) there are fewer speckles with more power per speckle than for poorer seeing. Thus the SNR per specklegram is greater for the better seeing. The curves of the STF in Figure 1 support this: the higher frequencies carry relatively greater power for larger r_o. However, in the data set there are only a few speckleograms with the very best seeing. Thus the data from the two tails of the seeing distribution should not

be weighted equally in combining the bin-calibrated power spectrum estimators. Of course the SNR of the final power spectrum is determined by the number of speckleograms in each of the corresponding bins for the object and the point source. In practice each of the bins yields an independent reduction for the object power spectrum and the final power spectrum will be a weighted average with the weighting proportional to the number of observations in each bin and proportional to r_e^2 corresponding to the bin. The first weight is suggested by Poisson statistics (assuming the same number of photons in each observation) and the second by the seeing model.

VI. Conclusions

We have presented models and data to show the importance of a detailed seeing calibration of speckle data sets reduced by the standard SI power spectrum analysis. Both the models and the data show the same effect, that for the case of poor or no calibration the resultant object power spectrum will be contaminated in different, and unpredictable, ways at the low frequencies ($0<f<f_o$) and at the highest frequencies ($f<f_c$). We suggest that for all such analyses the possible differences in seeing between the object and the point source must be taken into account. In this we support the conclusions of Mariotti _et al_. (1983) who considered similar problems for intra-red speckle data.

It is reassuring, however, for the work reported in Drummond _et al_. (1985ab) and Cher _et al_. (1985) that this same model analysis predicts that the shape of such a power spectrum

estimate, if not its frequency independent bias, is largely unaffected by these seeing effects. In these reductions, the parameterization of the physical model was accomplished by fits to the intermediate spatial frequency range, avoiding the seeing dominated region, of the power spectrum estimates. In both of these studies the physical models produced a measurable amount of unresolvable power. For Drummond's asteroid work this could be interpreted as being due to unresolvable surface structure and for Cheng's analysis the binning evidence also indicates the unresolved power was real. The r_e=39 cm curve in figure 5, having a mean value of ~1, implies that the Poisson noise bias (Hege et al. 1982a) is consistent up to .9 t_c and therefore does not lead to an extra bias in the object power spectrum.

Our new (albeit more computationally intensive than ever!) SI reduction procedures sort the data sets of both the object and point source into seeing bins to obtain a set of seeing weighted, deconvolved power spectra. In order to do this sorting we have developed a technique to obtain an expedient estimate of the instantaneous value of the atmospheric coherence length, r_o, from the second-order moment of the speckle cloud. We have also implemented editing schemes to ignore bad speckleograms which can also contaminate the final results and to correct for detector systematics which can distort them. The importance of this refined analysis is apparent especially when considering subsequent processing, including various schemes of image reconstruction which use the Fourier modulus such as Fienup (1978), Knox-Thompson (1974) and Phase-Unwrapping (Cocke 1979),

or which invoke model fitting procedures to constrain physical image parameters.

There is a need for chopping between the point-source calibrators and the resolved object in order to minimize the seeing differences. Binning of the data sets for seeing calibration is still required because the variations in r_e can be greater than the integration time. We believe that, even with improved observing and data acquisition protocol, the accuracy of power spectral analysis is significantly improved by careful processing of the data to take into account the seeing variations and bad speckleograms within the data set and worth the additional computation overhead.

VII. Acknowledgements

This work was supported in part by the NSF (grants AST-8113212 and AST-8201092 and access to the Cyber 720/172 at NOAO), the AFGL (contract F19628-82-K-0025) and the AFOSR (contract 82-0020). We also acknowledge the contributions of A. Szumilo for support and revisions to the data reduction software, and, together with J.Freeman and S.Shakian, for many long hours of tedious data digitization and computer babysitting. We also thank P.A. Strittmatter, N.J. Woolf and F. Roddier for many useful discussions and advice.

We particularly thank the NOAO staff and visitors for enduring any inconveniances caused by these extensive data reductions, and the support staff at Kitt Peak who made the

installation and use of our visitor instrument at the 4 meter telescope a successful delight.

References

Aime C.,G.Ricort,C.Roddier & G.Lago,(1978),J.Opt.Soc.Am.,68,1063

Cheng A.Y.S.,P.A.Strittmatter,E.K.Hege,E.N.Hubbard, L.Goldberg & W.J.Cocke,(1985),in preparation.

Cocke W.J.,(1980) in "International Computing Conference" ed. W.T.Rhodes, SPIE Proc.,231,39

Drummond J.D., W.J.Cocke, E.K.Hege, P.A.Strittmatter & J.V. Lambert,(1985a), Icarus,61,132

Drummond J.D.,E.K.Hege,W.J.Cocke,J.D.Freeman,J.C.Christou & R.P. Binzel,(1985b),Icarus,61,232

Fienup J.R.,(1978),Opt.Lett.,3,27

Fried D.L.,(1966),J.Opt.Soc.Am.,56,1372

Fried D.L.,(1979),Optica Acta,26,597

Hege E.K., E.N.Hubbard, P.A.Strittmatter & S.P.Worden, (1981), Astrophys.J.,248,L1

Hege E.K.,E.N.Hubbard,P.A.Strittmatter & W.J.Cocke,(1982a),Optica Acta,29,701

Hege E.K.,E.N.Hubbard,J.D.Drummond,P.A.Strittmatter,S.P.Worden & T.Lauer,(1982b),Icarus,50,72

Hege E.K., J.M.Beckers, P.A.Strittmatter & D.W.McCarthy, (1985), Appl.Opt., in press.

Hubbard E.N.,E.K.Hege, M.A.Reed, P.A.Strittmatter & S.P.Worden, (1979),Astron.J.,84,1437

Knox K.T. & B.J.Thompson,(1974),Astrophys.J.,193,L45

Korff D.,(1973),J.Opt.Soc.Am.,63,971

Labeyrie A.,(1970),Astron.Astrophys.,6,85

Mariotti J.M., A.Chelli,R.Foy,P.Lena,F.Sibille & G.Tchountonov, (1983),Astron.Astrophys.,120,237

Roddier F.,(1981),"The Effects Of Atmospheric Turbulence in Optical Astronomy" in Progress in Optics 19,ed. E.Wolf.

Woolf N.J.,(1982),"High Resolution Imaging From The Ground",Ann.Rev.Astron.Astrophys.,20,367

Table 1. Measured Seeing Parameters

Object	Wavelength λ(nm)	Speckle Cloud Size 2σ (as)	Seeing Parameters $\langle r_o \rangle$ (cm) (λ,z)	$(500nm,0^\circ)$	Zenith Angle $z(^\circ)$
Gamma Ori.	650	.31	42.8	34.5	32
	656.3	.41	33.0	27.8	39
	854.2	.42	41.7	24.5	34
Alpha Ori.	650	.31	42.9	33.6	27
	656.3	.36	37.5	30.6	35
	854.2	.35	50.6	28.4	26

Figure Captions

Figure 1: (a) Models of the Speckle Transfer Function using the two components as described in the text. a is the seeing dominated component and b is the high frequency term which allows information recovery to the diffraction limit. The parameters were chosen for an obscured aperture corresponding to the 4m and for r_0 equal to 10,15,20,25,30 and 35 cm. The telescope transfer function, T(f), is also shown for D=3.8m with an obscuration ratio of .3. (b) STF models for the same range of r_0 with the log-normal statistical model.

Figure 2: Quotients of the Speckle Transfer Function for different values of r_0 chosen so that the denominator has poorer seeing. (a) (using the normal model) represents quotients for r_0 values of 14,13,12,11 and 10 cm with the STF at r_0 = 10 cm, (b) represents the quotients at r_0=44,43,42,41,40 and 39 cm with r_0=39 cm for the the normal model and (c) as b but for the log-normal model.

Figure 3: Histograms of the estimate of the seeing, r_e, for three different data sets of Alpha and Gamma Orionis. (a)is at 650nm, (b)is at 656.3nm and (c)is at 854.2nm.

Figure 4: Variation of r_e for 1 seconds bins as a function of time showing periodic variability of the seeing.

Figure 5: Measured quotients of the Speckle Transfer Function for Gamma Orionis at 650nm. Note that the SNR is given by splitting bin 1 into two and taking the quotient. Because the SNR is fairly

small (=8), especially at the highest frequencies, the quotients overlap making it difficult to distinguish them from each other.

Fig. 1a

SPECKLE TRANSFER FUNCTION

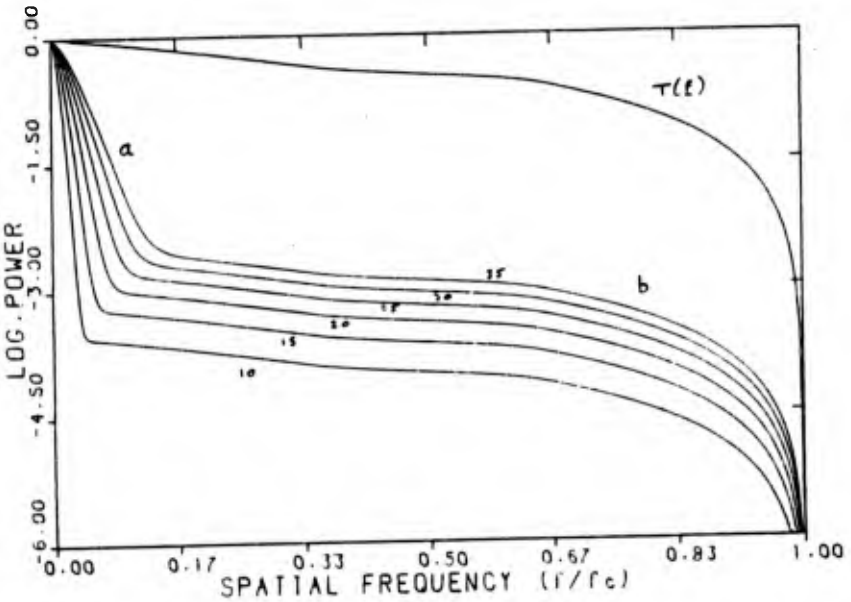

1b

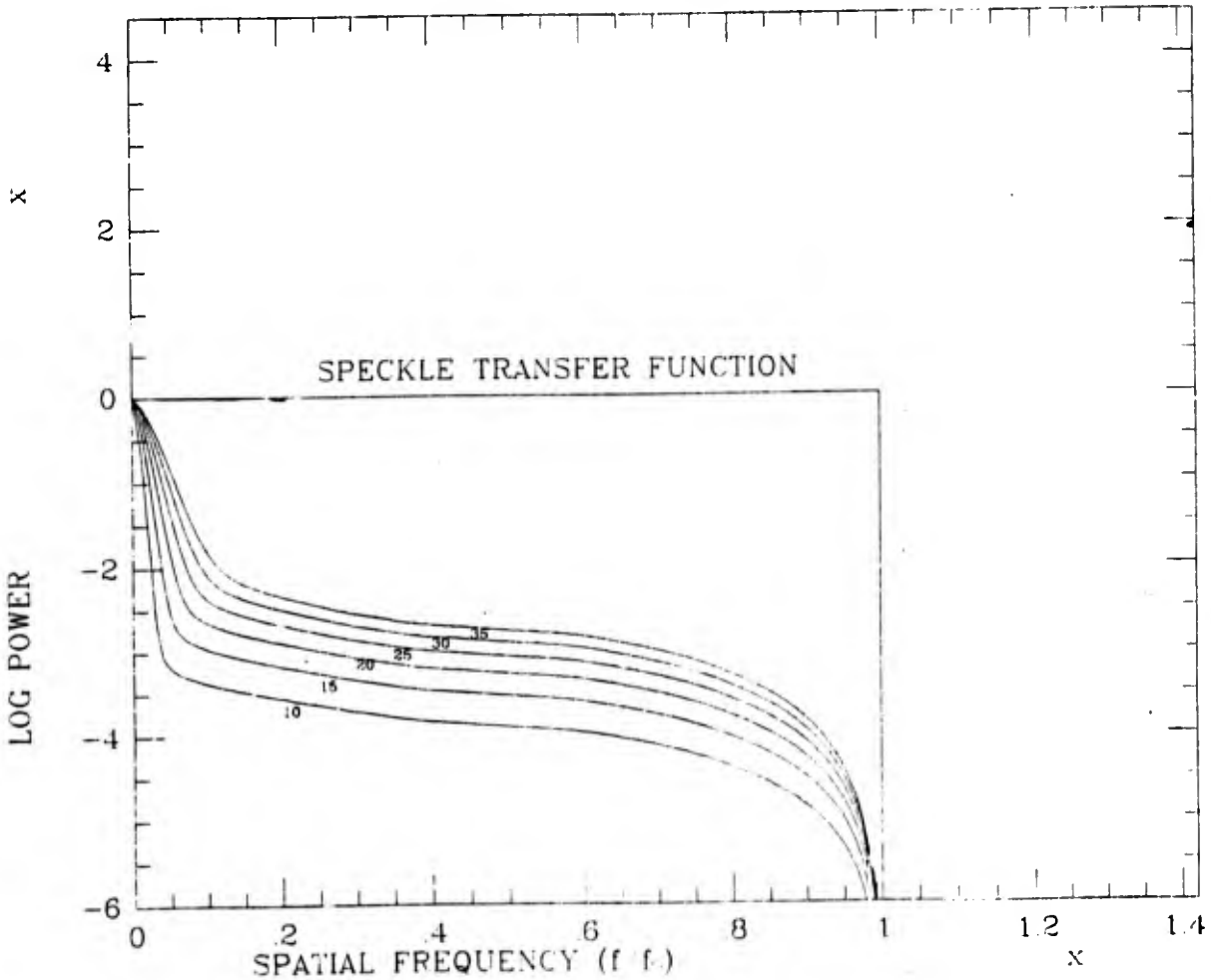

Fig 2a.

10 cm

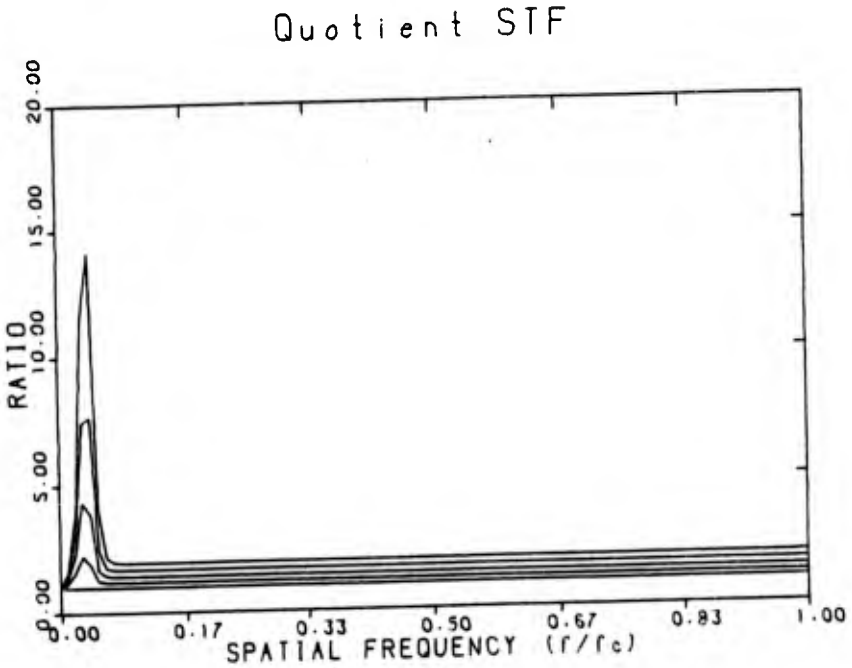

Fig 2b.

3 cm

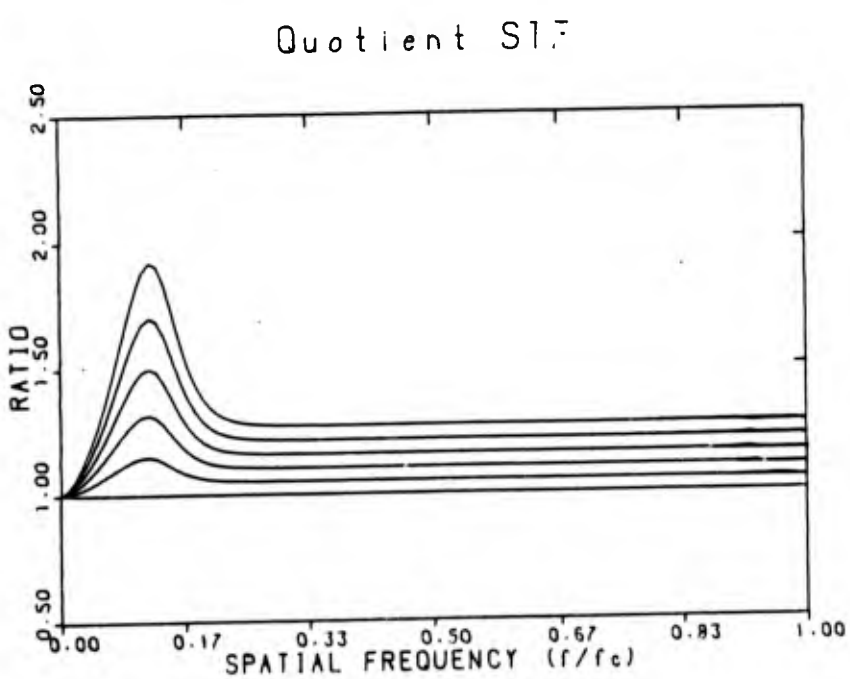

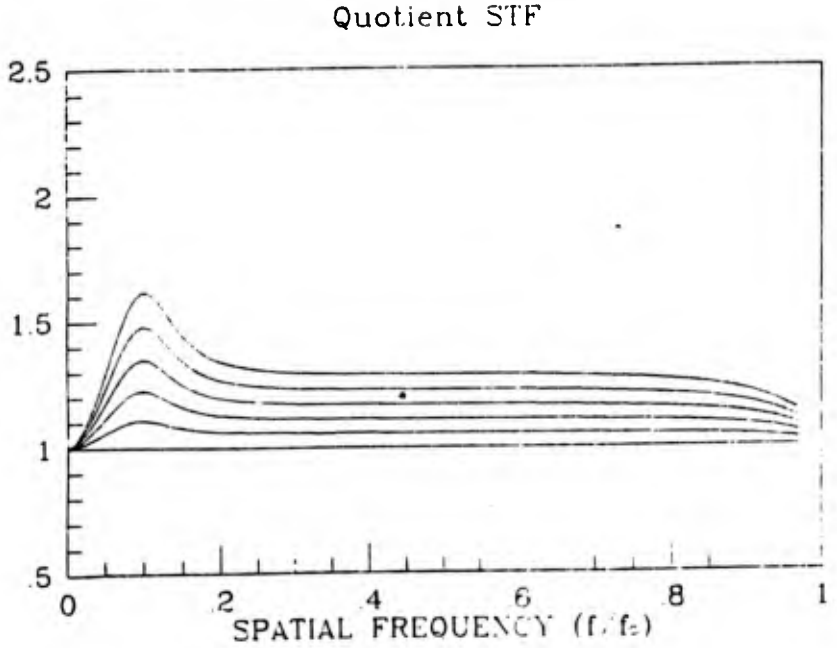
Quotient STF
2.5
2
1.5
1
.5
0
2
4
6
8
1
SPATIAL FREQUENCY (f/fc)

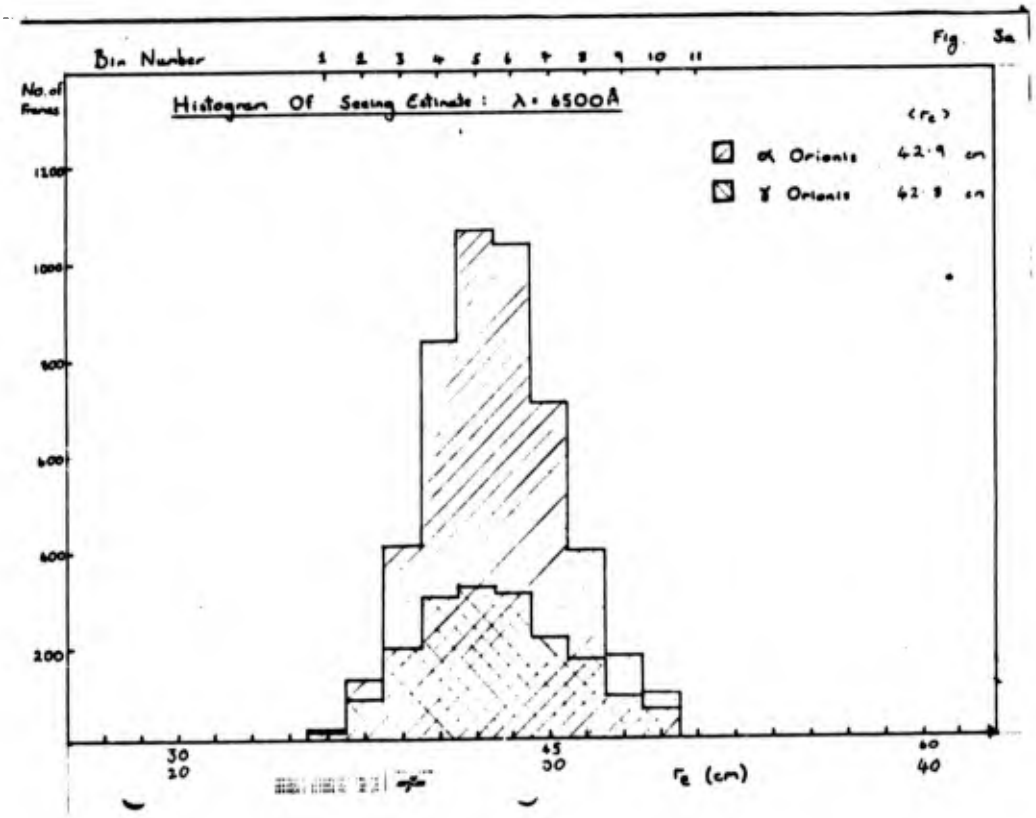
Fig. 3a
Bin Number 1 2 3 4 5 6 7 8 9 10 11
No. of Frames
Histogram Of Seeing Estimate : λ = 6500Å
⟨rε⟩
α Orionis 42·9 cm
β Orionis 42·8 cm
1200
1000
800
600
400
200
30
20
45
30
60
40
rε (cm)

Fig 4b

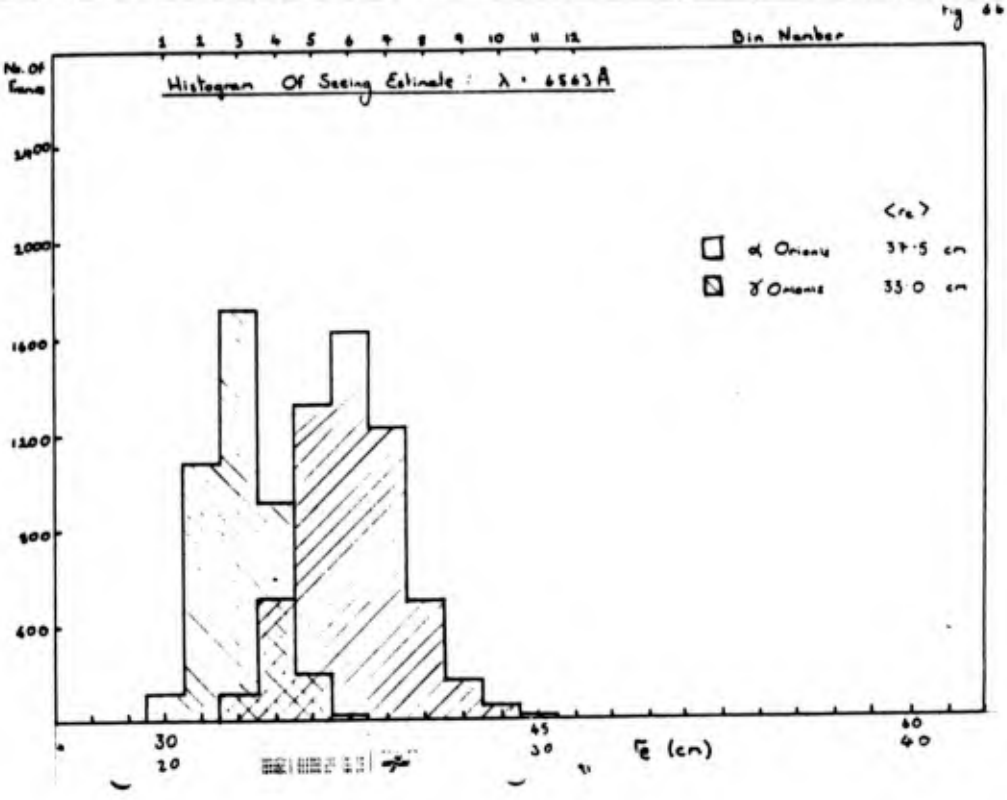
Bin Number
1 2 3 4 5 6 7 8 9 10 11 12
No. Of Frames
Histogram Of Seeing Estimate : λ = 6563 Å
<r_e>
α Orionis 37·5 cm
β Orionis 33·0 cm
2000
1600
1200
800
400
30
20
45
30
60
40
r_E (cm)

Fig. 3c

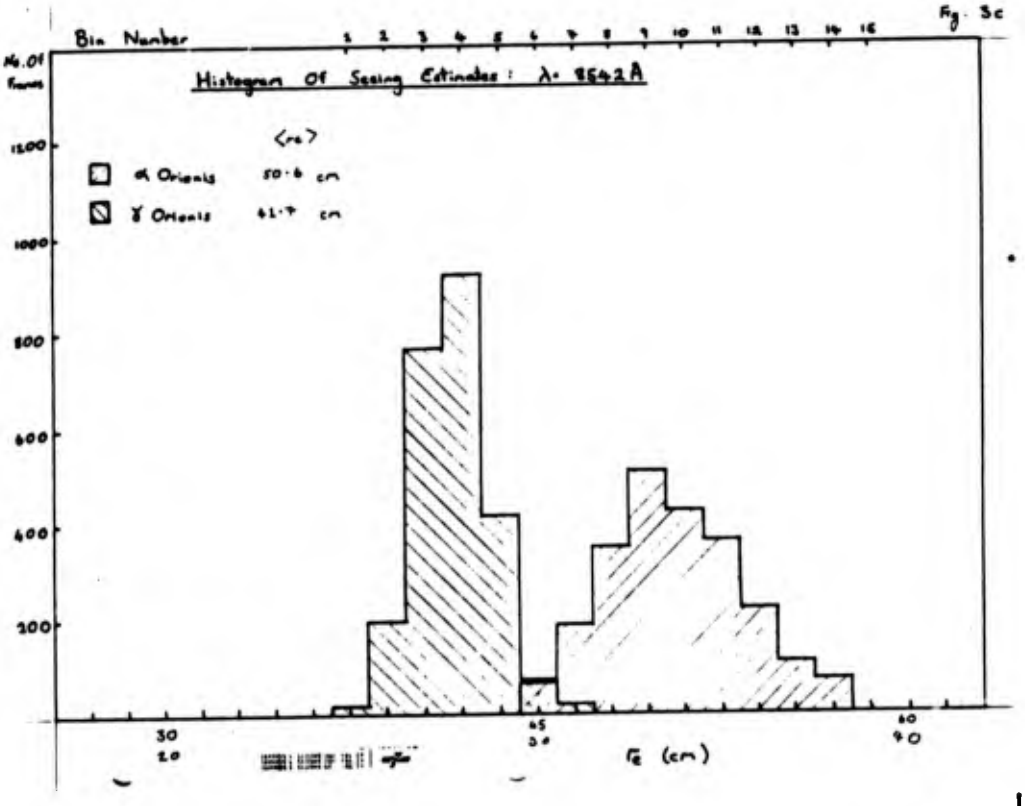
Bin Number
1 2 3 4 5 6 7 8 9 10 11 12 13 14 15
No. Of Frames
Histogram Of Seeing Estimates : λ = 8542 Å
<r_e>
α Orionis 50·6 cm
β Orionis 41·7 cm
1000
800
600
400
200
30
20
45
30
60
40
r_E (cm)

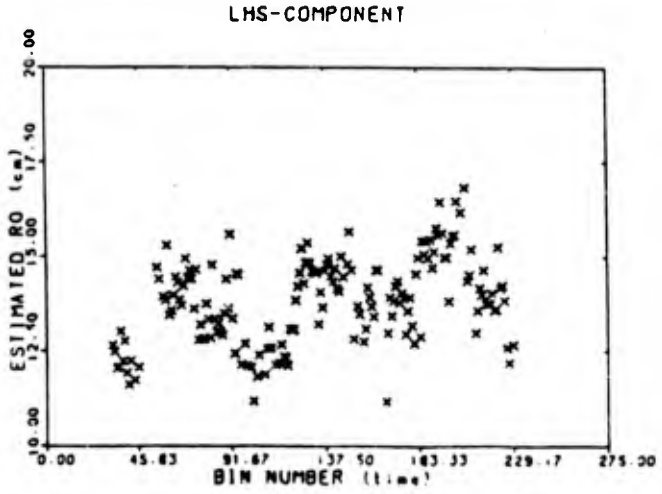
LHS-COMPONENT
ESTIMATED RO (cm)
20.00
17.50
15.00
12.50
10.00
0.00
45.83
91.67
137.50
183.33
229.17
275.00
BIN NUMBER (time)

Fig 4

Fig. 5

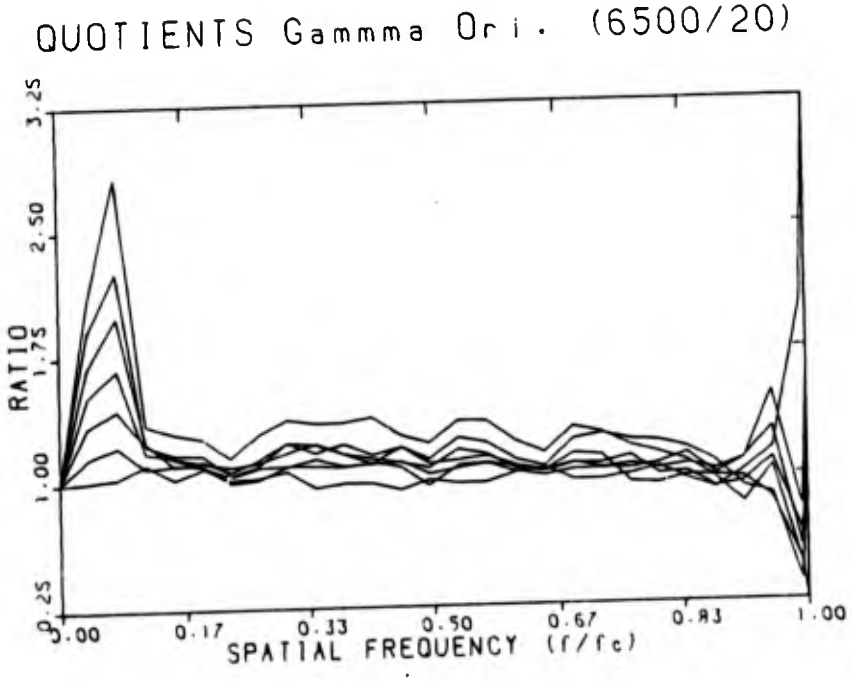
QUOTIENTS Gammma Ori. (6500/20)
RATIO
3.25
2.50
1.75
1.00
0.25
0.00
0.17
0.33
0.50
0.67
0.83
1.00
SPATIAL FREQUENCY (f/fc)

Seeing Studies for Speckle Holographic Imaging

J. Christou and K. Hege

ABSTRACT

The two-fold purpose of this study is to quantitatively evaluate the degree of isoplanicity in a particular speckle holographic measurement and to propose a technique for reweighing speckle holographic cross-spectrum amplitudes in order to recover quantitatively correct, diffracton limited speckle holographic images.

Seeing Studies

a. Introduction

We are currently investigating the effects of seeing upon speckle interferometric methods. We define seeing as the process which distorts the incoming, above atmosphere, complex wavefront. It is parameterized by the correlation length of the atmosphere, r_c, and the correlation time, τ_o, as defined by Fried (1966). Our analysis presently is concerned with measurements of r_o but we are ready to begin studying the effects of τ_o.

We define seeing quality as r_o. It is this parameter which affects the size of the conventional seeing disc, or in the speckle interferometric case the average size of the speckle cloud. We assume that the exposure time of a typical speckiegram is less than the atmospheric correlation time.

b. Labeyrie Analysis

The attached preprint, "Seeing Calibration of Optical Astronomical Speckle Interferometric Data" by Christou, Cheng and Hege discusses the theoretical and observational effect of different r_o's on the standard Labeyrie power spectrum analysis. It shows that the high-frequency tail of the Speckle Transfer Function (power spectrum of a point source) can be approximated by a function which varies as r_o^2 indicating that the better the seeing (high r_o) the greater the signal-to-noise ratio of the power spectrum. That paper also stresses the need for careful point source seeing calibration for the deconvolution of the

object power spectrum.

c. Determination of the Instananeous Seeing Estimate r_e

Strictly speaking r_o is defined only for a long exposure which averages over the instantaneous seeing. We have defined a quantity related to r_o which defines the instantaneous seeing for a single speckle cloud. This quantity, r_e, is introduced by Christou et al. is computed from the second-order moment about the centroid of the speckle cloud.

Figure 1 shows a time series of averaged values of r_e, over one second bins, determined independantly for the two components of the 2.3" binary ξ^2 Lyrae. The data was taken with the Steward Observatory 2.3m telescope at Kitt Peak using the Steward Speckle Camera. It is clearly seen from the curves that the seeing was the same for both data sets. This isoplanaicity is understandable because the seeing cells, which determine r_o, will be basically the same size over the telescope aperture and especially so for a small angular separation of 2 arc-seconds. The 90 second periodicity in both curves appears to be real because of the independant determination of r_e. Figure 2 shows the corresponding power spectrum for one of the components compared to a two component model for the speckle transfer function. The validity of the r_e measures are borne out as the differences between the model values and the measurments are less than a couple of centimeters.

The statistics of the time variation of r_e is currently under investigation for several data sets for detailed comparison

with the theory predicted log-normal distribution.

c. Isoplanaticity and Speckle Holography

Since the instantaneous gross structure (i.e. size) between two seeing clouds is very strongly correlated, it is also of interest to look at the correlation of the fine structure between the clouds. As both components of ξ^2 Lyrae are unresolved, the speckle clouds represent the instantaneous combined point spread function (PSF) of the telescope and atmosphere. If isoplanaticity exists then the PSF is spatially invariant and so the two speckle clouds should be the same except for Poisson statistics. Measurements by a number of workers using both adaptive optics and speckle interferometry imply that the size of the isoplanatic patch is typically less than 3 arc-seconds (Nisenson and Stachnik, 1978, Schneidermann and Karo, 1978, Lohmann and Weigelt, 1979, Weigelt, 1979 and Poillaine et al., 1979). This is because the complex wavefront passes along different paths through the atmosphere which have different turbulence profiles. It is these turbulence profiles which determine the fine structure of the speckle cloud.

Bates et al. (1985) and Bagnuolo (1984) have reported that the effects of non-isoplanaticity on Shift-and-Add analysis is not as great as for other speckle reduction techniques (e.g. Knox-Thompson analysis). Because of this Bates et al. have proposed using Simple Shift-and-Add images of point sources, as seeing calibrators, to search nearby regions (up to ~ 1 arc-minute) for resolvable detail. However, this technique is also

limited by the size of the isoplanatic patch and therefore measurements of the degradation due to non-isoplanaticity will improve this technique.

Visual inspection of speckle clouds of closely separated stars shows that they are qualitatively very similar. Because of this, speckle holographic techniques (Bates, 1973) have been proposed by which a resolved structure can be imaged by using a nearby unresolved object as a measure of the instantaneous PSF.

A speckle image can be represented as

$$i(x) = o(x) * p(x) \qquad 1$$

where $o(x)$ is the object, $p(x)$ is the combined instananeous PSF and * denotes convolution. Thus the object distribution can be obtained by deconvolution. This assumes that the PSF is the same to good precision for both the object and the point source. It does not take into account non-isoplanatic effects. Thus the realization of the speckle holographic techniques relies upon the validity of the isoplanatic assumption. In order to study this assumption we have defined an isoplanatic parameter, T(u) (after Nisenson and Stachnik who investigated this problem for binary star power spectra) where u represents the spatial frequency domain,

$$T(u) = \frac{\langle P_1(u) P_2^*(u) \rangle}{\langle |P(u)|^2 \rangle} \qquad 2$$

and $P_i(u)$ is the Fourier transform of the i'th component of the

close binary. P(u) is the mean of the two values of P(u) and where $\langle \ldots \rangle$ denotes an ensemble average over a set of speckleograms. Because the numerator is the cross-spectrum and the denominator is the power spectrum, T(u) represents a correlation coefficient between the two speckle clouds as a function of the spatial frequency u.

The same ϵ^2 Lyrae data set was used to compute a value for T(u). The results of this analysis are shown in figures 3 and 4. Figure 3 shows the two power spectra and the cross-spectrum of the two components of ϵ^2 Lyrae. The power spectra are essentially the same which is expected as the seeing statistics, shown in figure 1, are the same. Notice that the cross-spectrum shows a definate fall-off, compared to the power spectra, for frequencies greater than the seeing limit ($u > r_o/\lambda = u_o$). This effect is better represented in figure 4 which shows cuts through the isoplanatic parameter parallel and perpendicular to the separation vector between the two components. For frequencies dominated by the seeing (i.e. $< u_o$) the curves are essentially unity as expected from the r_o analysis. However at greater spatial frequencies the correlation falls off drastically to a value of .5 at $u = .15u_o$ for the perpendicular component and at $u = .1u_o$ for the parallel component. Both curves then settle down to a 10% correlation up to the diffraction limit. The difference between the two orthogonal components is due to the correlation of frequencies across the width of the speckle cloud along the separation vector.

These curves represent, in the mean, the relative

differences between the PSF's corresponding to a set of observational parameters. These are r_0, τ_0 and θ, the separation angle. The aim of this study is to investigate the variability of T(u) as a function of these variables in order to generate a family of such curves which can be used as weights for the speckle holography deconvolutions. The weighting function will be the inverse of T(u) which will correct the point source PSF to the object PSF in order to accurately recover the required high-spatial frequency information.

We are currently modifying the speckle camera by adding a 'Star-Shifter' which will allow us to place in the same field objects which have a greater separation than the acquisition field (typically <2°). This will therefore allow us to use point sources up to 15 arc seconds away from object as a deconvolution key for the speckle holography experiments. We will then also be able to measure the effects of partial isoplanicity up to greater separations which is important for any sort of wide-field high resolution imaging. Weigelt (1979) has measured partial isoplanicity up to separations of 22 arc-seconds and Beckers (private communication) has suggested that the high frequency tail of T(u) extends out to even larger angular separations indicating that there is nearly always some correlation between the time ensemble of speckle clouds at <u>all</u> spatial frequencies. The use of the 'Star-Shifter' will enable us to make quantitative measures to see over how large a separation angle the high frequency correlation extends as this will be of great importance to wide-field (≈1 arc-minute) speckle holographic imaging.

Speckle Holographic Imaging

Consider two discrete sources, $o_1(r)$ & $o_2(r)$, close together. Then the speckle image of each will be

$$i_1(r) = o_1(r) * p_1(r)$$
$$i_2(r) = o_2(r) * p_2(r) \qquad (1)$$

and the Fourier Transform becomes

$$I_1(f) = O_1(f) \cdot P_1(f)$$
$$I_2(f) = O_2(f) \cdot P_2(f) \qquad (2)$$

Now, if $o_2(r)$ is unresolved, then

$$I_2(f) = P_2(f)$$

and for the isoplanatic case $P_1(f) = P_2(f) = P(f)$ so that (2) becomes

$$I_1(f) = O_1(f) \cdot P(f)$$
$$I_2(f) = P(f) \qquad (3)$$

Therefore, $I_2(f)$ will be a simultaneous measurement of the P.S.F., $P(f)$. Thus the object transform can be recovered from the complex quotient

$$O_1(f) = \frac{I_1(f)}{I_2(f)} \qquad (4)$$

or taking a data set on N speckleograms, then

$$\text{Estimate of } O_1(\underline{f}) = \left\langle \frac{I_1(\underline{f})}{I_2(\underline{f})} \right\rangle \tag{5}$$

where $\langle \cdots \rangle = \frac{1}{N} \sum_i^N (\cdots)$

Following the approach of DSI (à la Beckers) this quotient is reduced to a "weighted" quotient, i.e.

$$E\left[O_1(\underline{f}) \right] = \frac{\sum_i^N \left(\frac{I_1(\underline{f})}{I_2(\underline{f})} \right)_i . W_i(\underline{f})}{\sum_i^N W_i(\underline{f})} \tag{6}$$

where $W_i(\underline{f}) = |I_2(\underline{f})|^2_i$, so that (6) now becomes

$$E[O_1(\underline{f})] = \frac{\sum_i^N \left(I_1(\underline{f}) . I_2^*(\underline{f}) \right)_i}{\sum_i^N |I_2(\underline{f})|^2_i} \tag{7}$$

If isoplanicity is not true, then $P_1(\underline{f}) \neq P_2(\underline{f})$ so that (4) becomes

$$\frac{I_1(\underline{f})}{I_2(\underline{f})} = O_1(\underline{f}) . \frac{P_1(\underline{f})}{P_2(\underline{f})} \tag{8}$$

Thus the object transform is modified by a term, $M(\underline{f})$ equal to

$$M(\underline{f}) = \frac{P_1(\underline{f})}{P_2(\underline{f})} \tag{9}$$

The Question now occurs – "What is the form of (9) and how can you calibrate it?"

Consider two point-sources, then (assuming non-isoplanatism)

$$I_1(\underline{f}) = P_1(\underline{f}) \qquad I_2(\underline{f}) = P_2(\underline{f}) \tag{10}$$

so that (7) becomes

$$E[M(\underline{f})] = \frac{\sum_i \left(P_1(\underline{f}) . P_2^*(\underline{f}) \right)_i}{\sum_i |P_2(\underline{f})|^2_i} \tag{11}$$

But $\langle |P_1(\underline{f})|^2 \rangle . \langle |P_2(\underline{f})|^2 \rangle = \langle |P(\underline{f})|^2 \rangle$

so that (11) becomes

$$E[M(\underline{f})] = \frac{\langle P_1(\underline{f}) . P_2^*(\underline{f}) \rangle}{\langle |P(\underline{f})|^2 \rangle} \tag{12}$$

which is simply the Isoplanatic Parameter.

But this is a measure of $P_1(\underline{\epsilon})$ deconvolved by $P_2(\underline{\epsilon})$ [cf. (5) & (6)] so that it measures $M(\underline{\epsilon})$ Thus

$$E[O_1(\underline{\epsilon})] = \frac{\langle I_1(\underline{\epsilon}) . I_2^*(\underline{\epsilon}) \rangle}{\langle |I_2(\underline{\epsilon})|^2 \rangle} . \langle M(\underline{\epsilon}) \rangle^{-1} \qquad (13)$$

$$= \frac{\langle I_1(\underline{\epsilon}) . P_2^*(\underline{\epsilon}) \rangle}{\langle |P_2(\underline{\epsilon})|^2 \rangle} . \frac{\langle |P'(\underline{\epsilon})|^2 \rangle}{\langle P_1'(\underline{\epsilon}) . P_2'^*(\underline{\epsilon}) \rangle}$$

$$= \frac{\langle I_1(\underline{\epsilon}) . P_2^*(\underline{\epsilon}) \rangle}{\langle P_1'(\underline{\epsilon}) . P_2'^*(\underline{\epsilon}) \rangle} \qquad (14)$$

where the P's refer to measurements of two point sources taken under similar (almost identicle) seeing conditions.

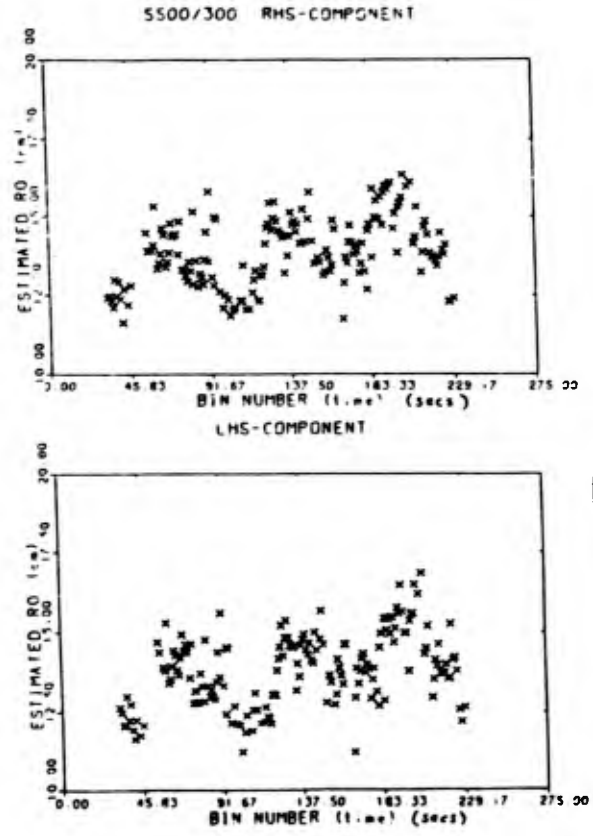

Fig 1

Epsilon Lyr. + STF models (90")

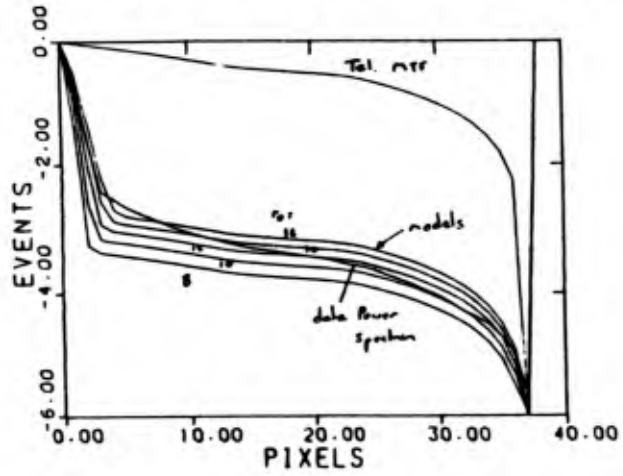

Data power spectrum shows response characteristic of slight telescope mirfocus. It is consistent with $r_o \approx 14$ cm.

Fig. 2

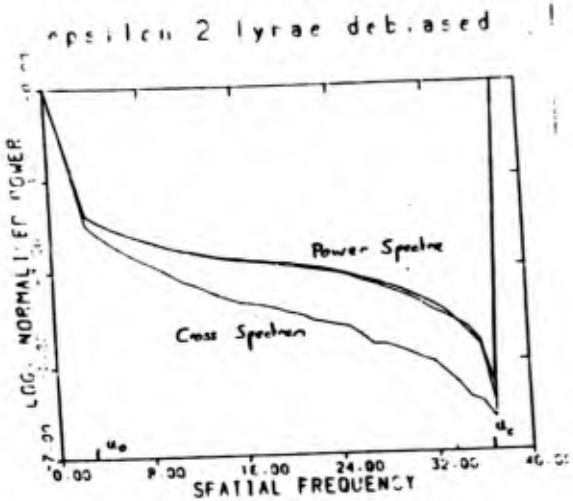

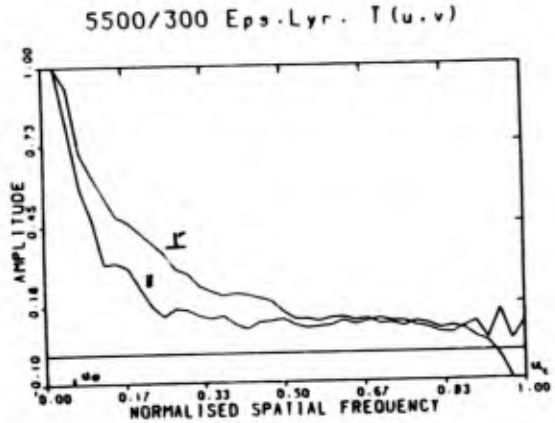

A Self Calibrating Shift-and-Add Technique for Speckle Imaging**

Julian C. Christou*, E. Keith Hege+, Jonathan D. Freeman & Erez Ribak

Steward Observatory, University of Arizona
Tucson, Az 85721

To be submitted to: Journal Of The Optical Society Of America-A

* Visiting Astronomer from Department of Astronomy, New Mexico State University, Las Cruces, NM 88003.

+ Visiting Astronomer, Kitt Peak National Observatory**.

** Observations reported here were obtained at the Multiple Mirror Telescope Obervatory, a joint facility of the University of Arizona and the Smithsonian Institution, and at Kitt Peak National Observatory.**

** Kitt Peak National Observatory is a division of the National Optical Astronomy Observatories, operated by the Association of Universities for Reseach in Astronomy, Inc., under contract to the National Science Foundation.

Abstract

We describe an image reconstruction technique for astronomical speckle interferometric data. This variant of the Shift-and-Add algorithm originally developed by Lynds, Worden and Harvey utilizes a weighted impulse distribution of speckle positions to extract an average speckle for a data set. This is done by means of a weighted deconvolution procedure, similar in form to a Weiner filter, which deconvolves the speckiegram by the impulse distribution. Results show that this method appears to be self-calibrating for seeing effects. It yields point spread functions, for observations of an unresolved star, which compare quatitatively with computed Airy patterns for both simple apertures and the fully phased Multiple Mirror Telescope array. Images of the resolved object Orionis agree with power spectrum measurements.

I. Introduction

Since its introduction by Labeyrie[1], speckle interferometry has been used to obtain diffraction-limited information about astronomical objects. In its original form the technique yielded the object distribution power spectrum estimate of a series of short-exposure (~60ms) images (speckiegrams). This power spectrum estimate contains only information about the modulus of the Fourier transform of the object distribution and, without the phases of the Fourier transform, cannot be used to reconstruct the object. A number of techniques have been developed to reconstruct these phases and therefore the object by assuming that there is a unique phase solution[2,3,4]. These techniques, however, rely on no input phase information. There are uncertainties about the uniqueness of the reconstructed phases and also whether the algorithm used actually converged to these phases. A number of other imaging techniques exist which recover the phases from the original speckiegrams. Among these are the Shift-and-Add algorithms[5,6] and the Knox-Thompson[7] approach. Comprehensive reviews of speckle imaging techniques can be found in Bates[8] and Dainty[9].

The pretered imaging techniques are those which use the phase information available in the speckiegrams. One such set of methods make use of the intuitive interpretation of a speckle as being a highly distorted version of the diffraction-limited image. Variations of this form of analysis were proposed by Lynds, Worden and Harvey[5] and Bates and Cady[6] and a theoretical study by Hunt *et al.*[10] has shown that diffraction-limited

information is preserved. The latter method, known as Shift-and-Add (SAA) has been further developed by Bagnuolo[11,12]. SAA is accomplished by first locating the brightest pixel in each speckiegram, then shifting to place this pixel at the center of image space and coadding to average over a set of shifted speckiegrams. The result is a diffraction-limited image sitting on top of a seeing produced background, caused by averaging over the remaining speckles of the speckiegram. Thus, the SAA image is dependent upon the seeing conditions and contains a seeing-dependent bias (background). The Lynds, Worden & Harvey (LWH) technique utilizes those speckles whose intensities lie above some threshold (typically the brightest 10%) and uses them to generate an impulse distribution of delta functions having unit amplitude at the speckle positions. The LWH image is built up by cross-correlating the speckiegram with the impulse distribution to shift these brightest speckles to the center of image space. The final result is obtained by averaging over the whole data set. Like the SAA image, the LWH image also comprises two components, the diffraction-limited image on top of a broader seeing background. For both methods the extraction of the diffraction-limited image is dependent upon the seeing conditions and this is made more difficult when the size of the object approaches that of the seeing disc.

II. Method

The technique we have used is derived from that of LWH, but utilizes *all* speckles in the speckiegram above a background noise

level. The speckiegram, i(r) is assumed to be approximated by a convolution of the object, o(r), with the telescope point spread function, a(r) all convolved with a set of weighted delta functions (impulse distribution), imp(r) corresponding to the amplitudes and positions of the speckles. i.e.

$$i(r) = [o(r)*a(r)] * imp(r) \qquad 1$$

where * denotes convolution and r represents the image domain. This simple model takes into account that the speckiegram is formed by random phase shifts in the complex wavefront due to refractive index variations in the atmosphere. Thus a speckiegram can be considered to be a set of highly distorted diffraction limited images within a region defined by the seeing disk. Therefore, if this assumption is true, the diffraction limited image can be obtained by deconvolving the speckiegram by the impulse distribution. The impulse distribution can be obtained by locating all the speckle maxima and setting the amplitudes of the delta functions equal to that of the corresponding speckle amplitudes. Thus, when the speckiegram (1) is deconvolved by the impulse distribution the result is, to a first approximation, the diffraction-limited image of the object. In this analysis we used the local maxima in the speckiegrams to define the amplitude and position of the impulses.

To avoid the problems inherent in regular deconvolution techniques, i.e. division by zero or small numbers in the complex quotient, we have implemented a weighted deconvolution procedure similar in form to a Wiener filter. Denoting the Fourier

transform by uppercase, then the complex quotient can be written as

$$FT[o(r)*a(r)] = \frac{\sum_n [I_n(f)/Imp_n(f)]\, W_n(f)}{\sum_n W_n(f)} \qquad 2$$

where f is the spatial frequency domain corresponding to r, n repesents the n'th speckiegram and W(f) is the weighting function.

In order to minimize the number of complex divisions and to obtain a function which is always non-zero we chose the weighting function to be the power spectrum of the impulse distribution, i.e. $W_n(f)=|Imp_n(f)|^2$. The numerator in (2) then becomes the cross spectrum between the speckiegram and the impulse distribution thus reducing the number of complex quotients to one, that of the ensemble average (sum) of the cross spectra and the impulse power spectra so that (2) can be rewritten as

$$FT[o(r)*a(r)] = \frac{\sum_n I_n(f)\, Imp_n^*(f)}{\sum_n |Imp_n(f)|^2} \qquad 3$$

The averaged impulse distribution power spectrum contains a bias term due to the effects of Poisson statistics and is therefore non-zero at all frequencies. Because we use a weighted impulse distribution and a weighted deconvolution technique we call this analysis Weighted Shift-and-Add/Weighted Deconvolution (WSA/WD).

It is interesting to note that the numerator of (2) is the Fourier transform of the cross-correlation of the speckiegram

with the weighted impulse distribution and therefore is a minor modification to LWH which we denote by WSA/XC.

III. Results

The WSA images, as well as the images from other Shift-and-Add techniques, contain a photon spike at the center due to the photon noise in the speckiegrams. This can be removed by a correction applied in the Fourier plane. At the same time, the effects of the detector transfer function can also be removed. Hege et al.[13] have reported that the detector response is a sharp Gaussian. In the spatial frequency domain this becomes a broad Gaussian which is a multiplicative term because of the convolution of the detector response with the signal. A Gaussian is fit to frequencies beyond the telescope cut off $f=D/\lambda$, where D is the diameter of the aperture and λ is the observing wavelength. This Gaussian is divided out and the remaining bias of unity is subtracted. This effectively removes the photon noise biased induced photon spike from these images.

Figure 1 shows the radial averaged profiles for the SAA, WSA/XC and WSA/WD images for the point source γ Orionis observed at the Kitt Peak National Observatory (KPNO) 4 meter Mayall telescope with a bandpass of 2.0 nm centered on 650.0 nm using the Steward Observatory (SO) speckle camera[13]. Comparison of these profiles clearly shows the seeing produced background in both the SAA and WSA/XC reductions to be substantially reduced to the flat background shown in the WSA/WD profile. Figure 2

compares the same WSA/WD result to that of an Airy profile for a 3.3 meter aperture with a central obscuration ratio of 1:3 which is the case for the Mayall telescope. These two profiles compare very favorably: the width of the central lobe and the position and amplitude of the first Airy ring agree to within a few percent. Figure 3 shows the theoretical Airy pattern and the reconstructed Airy pattern image from which the radial averaged profiles were computed. The RMS difference between these two images is ~ .2% that of the peak for radii greater than the first Airy ring (the region where the seeing is dominant in the SAA and WSA/XC images). The effects of a non-uniform Airy pattern give an RMS difference of ~1.9% for radii within the first Airy ring.

WSA/WD radial profiles for the extended object α Orionis and the unresolved point sources γ and ε Orionis, taken with the SO 2.3 meter are shown in figure 4. The observing bandpass of .3 nm was centered on 854.2 nm. The point source observations of γ and ε Orionis bracketed the measurements of α Orionis. They give very similar profiles, the difference indicating a residual sensitivity of the technique to differences in the data sets. At λ = 850 nm the diffraction limit of the 2.3 m is 76 milli-seconds of arc (msa) so that the ~50 msa disc of α Orionis[14] remains unresolved as is seen in the figure. The α Orionis profile shows an extension, most probably due to the presence of a circumstellar gaseous envelope, up to a radius of ~300 msa. This measurement is commensurate with power spectrum analysis of a 4m data set at the same wavelength as reported by Goldberg et al.[15].

Reconstructed images of both α Orionis and β Orionis, are shown in figure 5. These observations were made with the KPNO 4 m with bandpasses of 656.3/.3 nm and 650.0/2.0 nm. The images of β Orionis show a lumpy Airy ring at a NE-SW position angle (figures 5b & 5d). By comparison to the point source, α Orionis is clearly resolved by this larger telescope (figures 5a & 5b) and the images also show structure at the same position angle as the lumpy Airy ring.

In order to remove the effects of the lumpy PSF from these α Orionis images, we used the CLEAN[16] algorithm. CLEAN has been successfully applied in the past to radio interferometric observations in order to remove artifacts and systematics due to the interferometer beam. It is an iterative process which locates the brightest pixel in the 'dirty map' (resolved object image) and at this location it subtracts the 'dirty beam' (point source image) which is set to be a factor (loop gain, G) of the current peak in the dirty map. The process is repeated on the residual. The algorithm generates an array of delta functions of varying intensities in such a way that the dirty map can be considered to be the weighted sum of the dirty beam at the delta function locations plus the final residual. The iterations stop when either the intensity of the final residual is at the image noise level or when a certain number of negative delta functions is reached. The 'clean map' is generated by convolving the delta function array with a 'clean beam' which is usually obtained by fitting a Gaussian to the central component of the dirty beam. The quality of the final clean map depends upon both the value of

G and the number of iterations.

The 'cleaned' images of α Orionis are shown in figures 5c and 5e. The loop gain was set at 70% and 50 iterations were used. These images show the removal of the lumpy Airy ring and indicate a non-uniform structure of the stellar envelope.

The use of CLEAN is further demonstrated in the next figure. A data set of α Orionis and ε Orionis taken with the SO 2.3 m at a wavelength of 650 nm was reduced using the WSA/XC algorithm. These images are shown in figures 6a and 6b respectively. They still include the photon spike but the seeing background was removed by approximating it by a Gaussian and then subtracting. Both of these images contain, in addition to the noise spike, a video artifact due to the non-linear response of the TV camera. This 'undershoot' is produced by the video cassette recorder electronics after scanning across a bright speckle. The ε Orionis image was used as a 'dirty beam' to CLEAN the Orionis image (figure 6c) as described above. The loop gain was also set to 70% for 50 iterations. This clean image shows the removal of the undershoot artifact and also shows the presence of a probable stellar envelope with a position angle similar to that seen in the 4m data set. The astrophysical interpretation of these and other α Orionis images is currently in preparation for publication elsewhere.[17]

Finally, figure 7 shows the PSF of the fully phased Multiple Mirror Telescope (MMT) at a bandpass of .3 nm centered on 656.3 nm using Orionis as an unresolvable source. The FWHM of the

central lobe = 20 mas which is consistent with that of an Airy pattern for a 6.9 m aperture at the same wavelength. The sidelobes show the six-fold symmetry expected but non-uniform amplitudes indicate imperfect phasing. The computed response published by Angel[18] can be compared favorably to this result. The potential utility of the MMT as a phased array high resolution imaging telescope is discussed further by Hege et al.[19].

IV. Discussion

The WSA technique appears to produce realistic PSF's for three telescopes, the SO 2.3m, the KPNO 4 m and the fully phased 6.9 m MMT. The results for the extended object, α Orionis, agree between the 2.3m and the 4m. when the different resolution limits are taken into account. The disc size and envelope presence agree well with other measurements. The major improvement of this technique over other SAA analyses is that it appears to be self calibrating for seeing and produces a flat background (i.e. no residual seeing bias) thus enabling realistic interpretation of extended low-power structure such as stellar envelopes. This self calibration is due to the selection of all speckles and the weighting of the impulses so that there is no residual when a speckle is deconvolved by its corresponding impulse. The use of the CLEAN algorithm allows the systematics of the telescope PSF (and even serious video artifacts) to be removed when an unresolved point source (dirty beam) is observed.

The results presented here represent a preliminary analysis of a larger data base being studied for astrophysical content[17].

Currently the technique is limited to bright objects (atmospheric statistics dominated), but it is hoped to extend it to the faint object domain (photon limited) by using a matched filter[20] to locate the speckle maxima.

V. Acknowledgements

We wish to thank Andreas Eckart for the application of the CLEAN algorithm. E. Ribak, is supported by a Weizmann Fellowship. This work was supported in part by AFGL contract F19628-82-0025, AFOSR grant 82-0020 and NSF grants AST-8201092 and AST-8312976.

VII. References

1. A.Labeyrie, 'Attainment of Diffraction Limited Resolution In Large Telescopes by Fourier Analyzing Speckle Patterns in a Star Image', Astron.Astrophys.,6,85,(1970).

2. J.R. Fienup, 'Phase Retrieval Algorithms: A Comparison', Appl.Opt.,21,2758,(1982).

3. R.H.T.Bates, 'Fourier Phase Problems are Uniquely Solvable in More Than 1 Dimension:I',Optik,61,247,(1982).

4. S.F.Gull & G.J.Daniell, 'Image Reconstruction From Incomplete and Noisy Data, Nature,272,686,(1978).

5. C.R.Lynds, S.P.Worden & J.W.Harvey, 'Digital Image Reconstruction Applied to Alpha Orionis', Astrophys.J.,207,174,(1976).

6. R.H.T.Bates & F.W.Cady, 'Towards True Imaging by Wideband Speckle Interferometry', Opt.Commun.,32,365,(1980).

7. K.T.Knox & B.J.Thompson, 'Recovery Of Images From Atmospherically Degraded Short-Exposure Photographs', Astrophys.J.,193, L45,(1974).

8. R.H.T.Bates, 'Astronomical Speckle Imaging', Phys.Rep., 90,203,(1982).

9. J.C.Dainty, 'Stellar Speckle Interferometry' in Laser Speckle and Related Phenomena, Vol. 9 of Topics in Applied Physics (Springer-Verlag, Berlin Heidelberg 1984), Chap. 7.

10. B.R.Hunt, W.R.Fright & R.H.T.Bates, 'Analysis of the Shift-and-Add Method for Imaging Through Turbulent Media', J.Opt.Soc.Am.,73,456,(1983).

11. W.G.Bagnuolo, 'The Application of Bates' Algorithm to Binary Stars', Mon.Not.R.Astron.Soc.,200,1113,(1982).

12. W.G.Bagnuolo, 'Image Restoration by the Shift-and-Add Algorithm', Opt.Lett.,10,200,(1985).

13. E.K.Hege, E.N.Hubbard, P.A.Strittmatter & W.J.Cocke, 'The Steward Observatory Speckle Interferometry System', Optica Acta, 29,701,(1982).

14. A.Y.S.Cheng,P.A.Strittmatter,E.K.Hege,E.N.Hubbard,L.Goldberg & W.J.Cocke, 'The Physical Diameter of Alpha Orionis?', in preparation.

15. L.Goldberg, E.K.Hege, E.N.Hubbard, P.A.Strittmatter & W.J.Cocke, ' Speckle Interferometry of Alpha Orionis: Preliminary Results', in Second Cambridge Workshop on Cool Stars, Stellar Systems & the Sun, ed. M.S.Giampapa & L.Golub, SAO Special Report 392 Vol 1, 131, (1982).

16. J.A.Hogbom, 'Aperture Synthesis With A Non-Regular Distribution Of Interferometer Baselines', Astron.Astrophys. Supp.,15,417,(1974).

17. J.C.Hebden,J.C.Christou,A.Y.S.Cheng,E.K.Hege,P.A.Strittmatter & J.M.Beckers, 'Two Dimensional Imaging of Alpha Orionis', in preparation.

18. R.P.Angel, 'Very Large Ground-Based Telescopes for Optical & IR Astronomy', Nature,295,651,(1982).

19. E.K.Hege, J.M.Beckers, P.A.Strittmatter & D.W.McCarthy, 'The Multiple Mirror Telescope as a Phased Array Telescope', Appl.Opt.,in press.

20. E.Ribak,E.K.Hege & J.C.Christou, 'Identification of Speckles by Matched Filtering', Bull.Am.Astron.Soc.,16,385,(1984).

Figure Captions

Figure 1: Radial average profiles for Gamma Orionis, (i) SAA, (ii) WSA/XC and (iii) WSA/WD at λ=650.0/.2 nm using the KPNO 4 meter.

Figure 2: Radial averaged profiles for (i) WSA/WD Gamma Orionis and (ii) Airy pattern of 3.8 meter aperture with a 1:3 central obscuration at λ=650.0/.2 nm.

Figure 3: (a) Theoretical and (b) Measured Airy patterns of the KPNO 4 meter. (See figure 2 for parameters). Scale = 7.2 mas/pixel.

Figure 4: WSA/WD radial averaged profiles of (i) Alpha Orionis, (ii) Epsilon Orionis and (iii) Gamma Orionis taken with the Steward Observatory 2.3 meter at λ=854.2/.3 nm.

Figure 5: Reconstructed images of Alpha and Gamma Orionis. (a) WSA/WD Alpha Orionis (=656.3/.3 nm), (b) WSA/WD Gamma Orionis (λ=656.3/.3 nm), (c) a cleaned by b as described in text., (d)-(f) as before but at λ=650.0/2.0 nm. All observations at KPNO 4 meter.

Figure 6: Reconstructed images of Alpha and Gamma Orionis. (a) WSA/XC Alpha Orionis, (b) WSA/XC Gamma Orionis, (c) a cleaned by b as described in text. Observations at SO 2.3 meter at λ=650.0/2.0 nm.

Figure 7: WSA/WD image of Gamma Orionis taken with the fully phased MMT at λ=656.3/.3 nm. The artifacts are a result of the

apodizing window caused by the the video digitizer. This is the MMT point spread function. Scale = 5 msa/pixel.

Figure 1

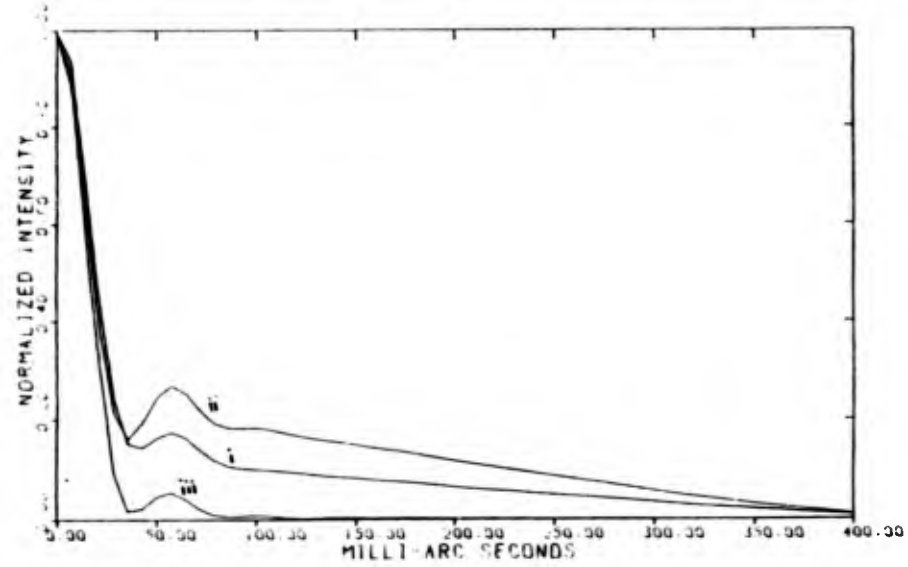

Figure 2

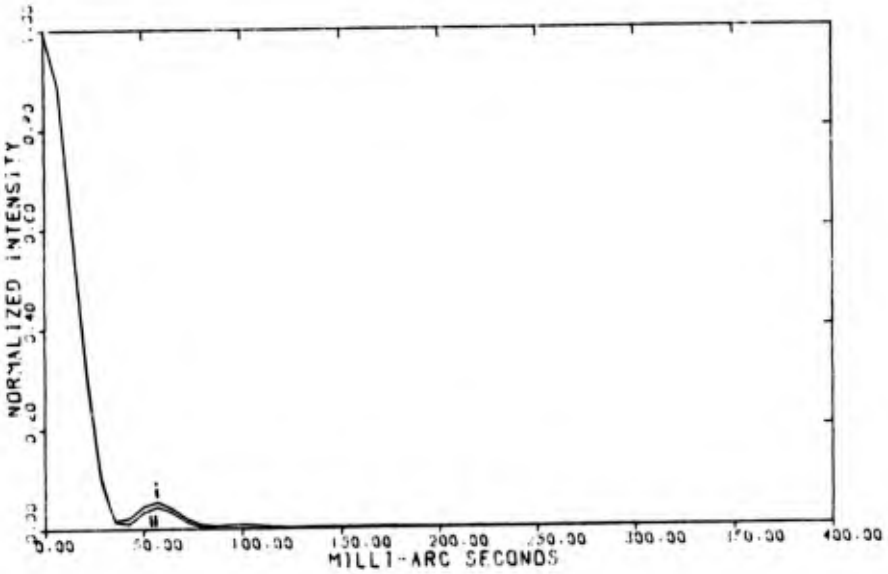

a)

(b)

Fig. 3

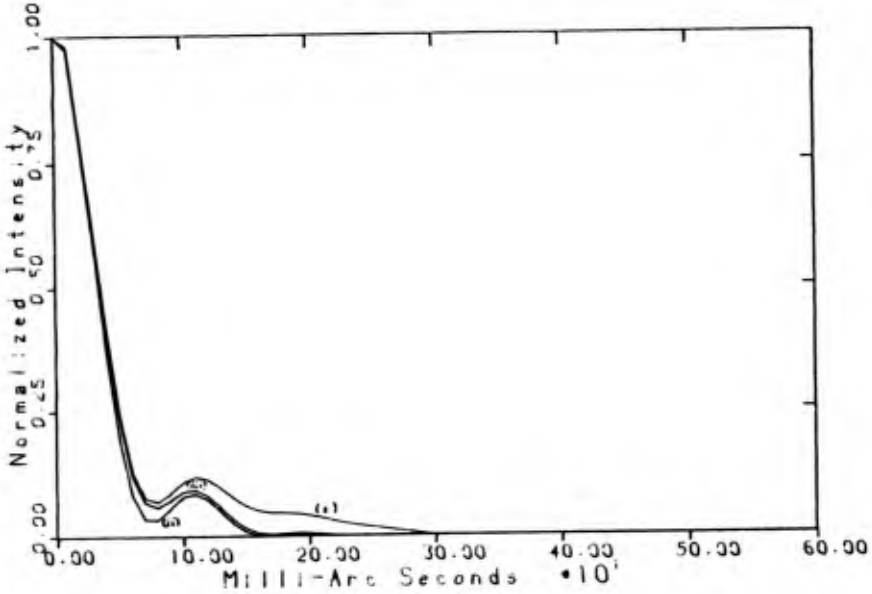

Figure 4

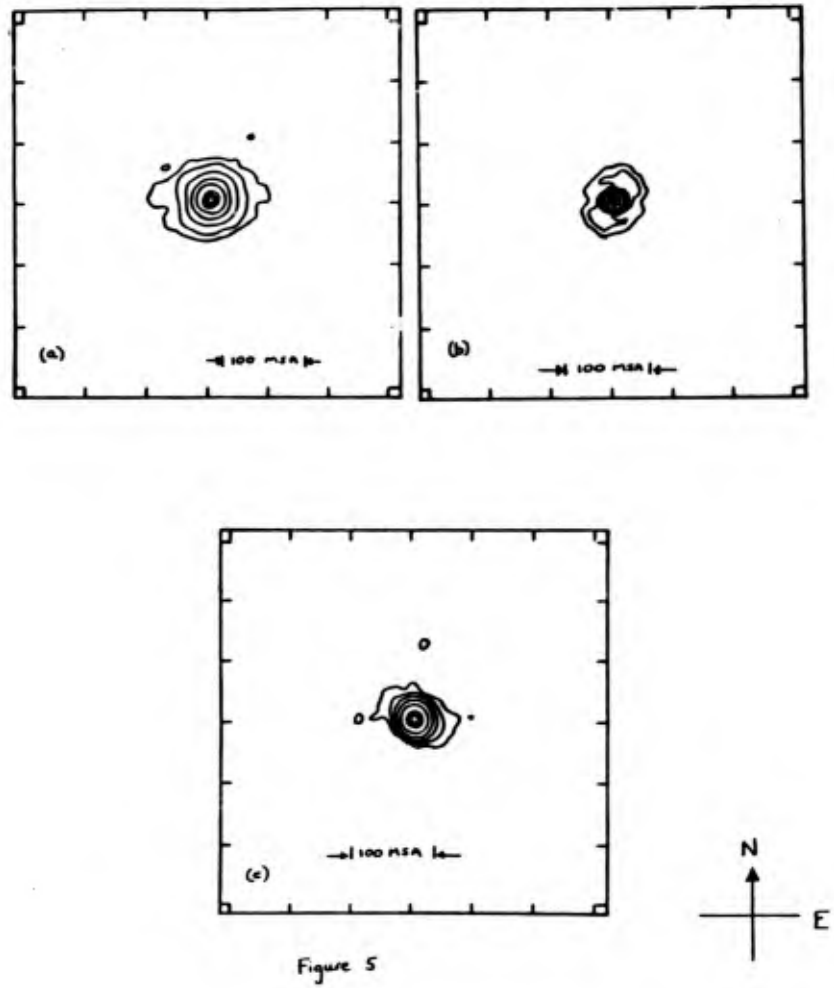

Figure 5

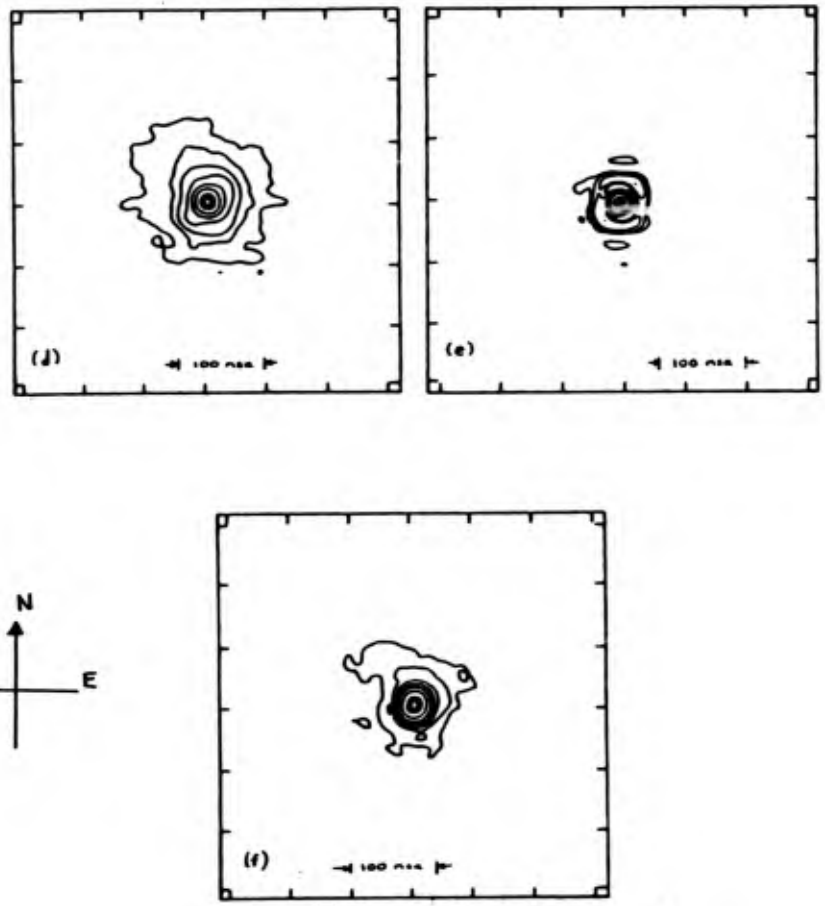

Figure 5

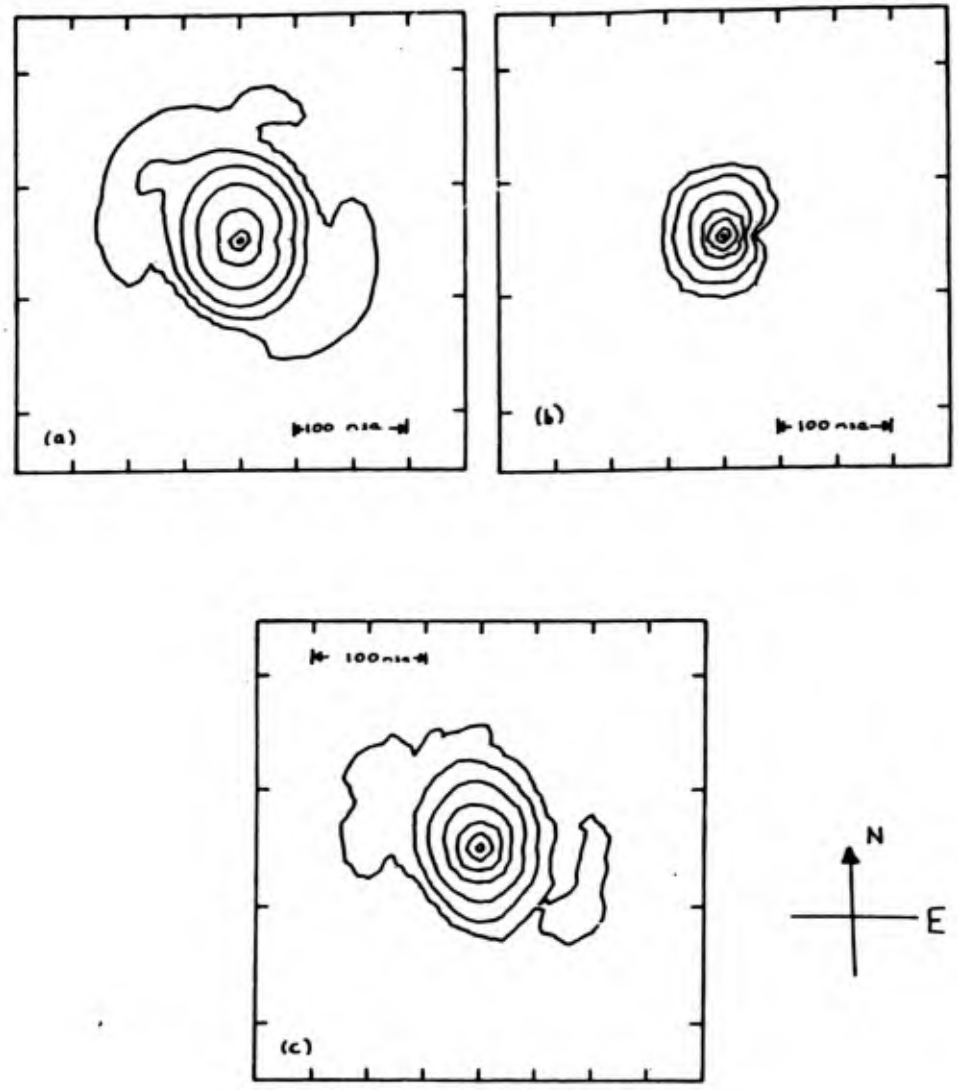

Figure 6

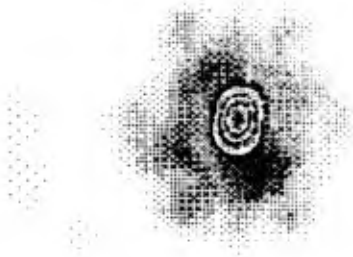

Figure 7

THE PHYSICAL DIAMETER OF ALPHA ORIONIS?

BY

A. Y. S. CHENG

P. A. STRITTMATTER*

E. K. HEGE*

E. M. BURBAIL* **

L. GOLDBERG+

AND

W. J. COCKE

JANUARY, 1985

SUBMITTED TO ASTROPHYSICAL JOURNAL (LETTERS)

Steward Observatory, The University of Arizona, Tucson, Arizona 85721.

* Visiting Astronomer, Kitt Peak National Observatory, National Optical Astronomy Observatories, operated by the Association of Universities for Research in Astronomy Inc., under contract to the National Science Foundation.

+Kitt Peak National Observatory, Tucson AZ ... .

++Present Address: ... .

ABSTRACT

Previously reported speckle interferometric measurements of the angular diameter of Alpha Orionis are widely scattered and apparently inconsistent, ranging from 79 ± 1 to 30 ± 4 mas. Stellar atmosphere models predict a stellar disk to be limb-darkened differently for different spectral features. Upon analysis of well-calibrated speckle observations of Alpha Orionis obtained at various wavelengths with the KPNO 4 meter telescope, we are able to account for both the scattering of the previous speckle measurements as well as our new results in terms of a fixed physical stellar diameter with spectral feature dependent limb-darkening coefficients. We find the angular diameter of Alpha Orionis is 65 mas with limb-darkening (cosine model) coefficients ranging from about 1 in TiO absorption bands to about 0.4 in CaII absorption lines.

I. INTRODUCTION

Alpha Orionis is an M2Iab,SRc late type supergiant star with mass loss rate about $10^{-6\pm1}$ $M_\odot$/year. High resolution speckle interferometric observations have the potential capability of measuring the photospheric sizes, the inner mass flow sizes and the extended mass flow geometries for a number of late type supergiant stars of known mass loss rates. Yet there is a large variation in the values previously reported for the angular diameter, obtained by speckle interferometry, of Alpha Orionis .

We find evidence that such scattering can be resolved by using an appropriate stellar model, a limb-darkened stellar disk instead of a uniform disk, with a limb-darkening coefficient which vaires as a function of the spectral features spanned by the observing bandpass, and further that the data forces a particular choice from the ensemble of possible models.

In this paper, we discuss only the photospheric radius, since we fit the speckle data to image model power spectra only in the range of spatial frequency where any extended structure is expected to have very low spectral power. This is to avoid confusing the detection of large extended structure with a slight miss calibration of the seeing, although we have been particularly careful about seeing calibrations. The required seeing calibrations are discussed in a companion paper, Christou et al. (1985). A full two-dimensional analysis using a combination of techniques is being pursued. Other non-spherically symmetric details of the object, which we have previously reported (Colberg et at. 1981) are being studied further in our continuing work.

The physical diameters inferred by speckle interferometry angular diameters disagree with those inferred by other photometric techniques by about a factor of 1.5 to 2 (see, e.g. Tsuji 1976). We do not intend to account for such discrepancy here. That discrepancy would only be resolved with very careful modelling of the temperature structure of the star, the effect of larger scale dust shell scattering (see, e.g. Tsuji 1978, Roddier and Roddier 1983) and precise knowledge of the distance. In sections II, III and IV we will discuss the observations, the speckle interferometry data reductions and the interpretation of speckle image power spectra respectively. In section V we discuss the results and their interpretations. In the conclusion, We offer a possible explanation for the wide variation in previously reported speckle interferometry results.

II. OBSERVATIONS

Alpha Orionis was observed with unusually good seeing at the KPNO 4 meter telescope on 2nd and 3rd February, 1981 using the Steward Obsevatory intensified video speckle camera (Hege et al. 1982). The seeing on the first night was about half arc-second, and less than one arc-second on the second night. Various band-passes (see Table 1) were used to observe both Alpha and Gamma Orionis (the object and the calibration star respectively). Video specklegrams for each band-pass were recorded for about 10 to 15 minutes on the object and about 5 minutes on the calibration star. The specklegrams were recorded with 15 ms exposures at the rate of 7.5 Hz (every fourth video frame). At this shutter frequency the afterglow of the image intensifier has sufficiently

decayed between exposures that it can be removed by means of video subtraction of consecutive frames during data digitization. The 15 ms exposure time is short enough to freeze the turbulence in the Earth's atmosphere, so that the speckleograms retain image details up to the full diffraction limit of the telescope.

The video speckleograms were digitized 8 bits deep in a 128 by 128 pixels array with a Grinnell digital television system, yielding a detector image scale of 7.22 mas/pixel, and written on 9-track tapes using the Steward Observatory Point 4 minicomputer system.

It has been shown theoretically that the point spread function calibration in speckle interferometric analysis is very sensitive to the seeing, characterized by Fried's parameter r_0. We adopted a new and more careful reduction procedure (which is unfortunately, much more computer time consuming), to calibrate the seeing and instrumental point spread function (Christou et al. 1985).

The relevant essentials of our new reduction procedure include specific measures (1) to edit the data, (2) to remove known systematic detector-induced artifacts, and (3) to bin the speckleograms according to instantaneous seeing.

The image power spectra of the digitized speckleograms, edited, corrected and binned, were accumulated using the NOAO CDC Cyber 720/170 and the fast Fourier transform algorithm. The power spectra were then written on 9-track tapes, and transported back to the Steward Observatory computing facilities (at that time Point 4 and Eclipse minicomputers) for analysis. Since we now

separate out good seeing data, we find that they often give better signal to noise. (e.g. 100 frames of good seeing data and 1000 frames of moderate seeing data give similar signal to noise ratio in the final results.)

III. POWER SPECTRUM ANALYSIS

The detector colored noise bias (see, Hege et al. 1982) was removed from each binned, summed power spectrum by fitting a two dimensional anamorphic Gaussian at spatial frequencies larger than the diffraction limit cut-off frequency.

The effects of seeing and of the combined instrumental and telescope optical transfer functions were corrected, giving clean, deconvolved power spectra of the object, by dividing the debiased power spectrum of the object (Alpha Orionis) by that of a point source (Gamma Orionis) of comparable seeing (same r_0, i.e. corresponding bin). These calibrated image power spectra were then analyzed by fitting model image power spectra to the averaged radial profiles to extract the physical parameters, radius R and limb-darkening coefficient U. A typical averaged radial power spectrum profile, together with a typical model fit, are shown in figure 1.

The model image power spectrum was computed for a limb-darkened stellar disk image intensity profile $I(r;R_*,U)$:

$$I(r;R_*,U) = I_0 [(1 - U) + U * \cos (r/2R_*)], \quad \text{for } r < R_*$$
$$= 0, \quad \text{for } r > R_*$$

with R_* being the radius of the star and U being the limb-darkening coefficient. We computed normalized intensity profiles, $I_0 = 1$. A uniform disk corresponds to U = 0. For a spherically

symmetric disk, the corresponding model power spectra $P(u;R_*,U)$ are given by:

$$P(u;R_*,U) = \pi^2 \left| \int_0^r dr\ r\ I(r;R_*,U)\ J_0(2\pi ru) \right|^2,$$

where J_0 is the zeroth order Bessel function and u is the spatial frequency. For a uniform disk, namely U = 0, $P(u;R_*,0)$ reduces to:

$$P(u;R_*,0) = \left| J_1(2\pi ru)/u \right|^2,$$

with J_1 being the first order Bessel function. The computed model power spectrum and its first partial derivatives, $\partial P(u;R_*,U)/\partial R_*$ and $\partial P(u;R_*,U)/\partial U$ (computed as first differences) were tabulated for use in an iterative non-linear least square fitting procedure (Jeffreys 1960,1981).

The observed power spectra $P_o(u)$ were then fitted by the linear combination

$$P_o(u) = A * P(u;R_*,U) + B,$$

with A and B being constant parameters which allow the normalized model to be scaled to the data and with B/(A+B) the amount of unresolved power in the observation.

Figure 2 displays two different models which are indistinguishable, over the spatial domain investigated and at the statistical precision achieved, with regard to their ability to fit a typical radial profile. This illustrates the ambiguity in the models: we could not simultaneously fit both parameters R_* and U uniquely to any single observed power spectrum profile. Therefore, we fixed the limb-darkening parameter U and fitted the data by only the three parameters R_*, A and B. The limb-darkening parameter U was varied between 0 and 1, with $\Delta U = 0.1$, and different R_*, A and B values are obtained for each of the

corresponding three-parameter fits. The results together with the statistics from those fits, are listed in Table 1. The unresolved power and RMS error of the fits for U = 0 are typical for all values of U, and therefore are useless in themselves as discriminators of goodness of fit.

The results in Table 1 are shown in figure 3. This illustrates the wide scattering of the inferred radii for each spectral bandpass and for a fixed limb-darkening coefficient. This figure also shows the extremes of how different models give different measured radii for our data sets. Presented this way, the ensemble of fits suggests the physical key for selecting the most appropriate model from the ensemble of possible models.

Since the limb-darkening coefficient is expected to be a function of the spectral feature, an interpretation of these results which we have depicted graphically in figure 3, is possible if we require a single fixed physical stellar radius. Our choice is represented by the horizontal line in figure 3. If we assume that the limb-darkening can be no greater than U = 1, nor less than U = 0, our measurements actually set upper and lower limits of the physical diameter of Alpha Orionis (the dot-dash lines in figure 3). When a radius is fixed for the star, the limb-darkening coefficients for each of the spectral bandpasses can be predicted from the intersections of the radius and the fitted curves. Possible values are tabulated in Table 2. Alternatively if limb-darkening coefficients are known from other sources (e.g., model atmosphere calculations), then the radius of the star is measured.

The limb-darkening coefficients for an M2 supergiant star have been computed by Tsuji (1976) to be about 0.9 to 1.0 for TiO bands, and 0.4 to 0.7 for CN and CO bands which are generated in deeper layers of the stellar atmosphere. In our measurements, the bands at 6500/20, 5500/10Å and 5200/10Å fall into strong TiO bands, and they are highly limb-darkened with U at about 0.9 to 1. Therefore, we predict the radius of Alpha Orionis to be about 32.5 mas, based on figure 3.

Other values for the limb-darkening coefficients are tabulated in Table 2. These values are due to the combined result of all of the spectral features included within the particular observing bandpass. In late-type supergiant stars, numerous features are usually present even in bandpasses as narrow as 20 to 3 Å, depending upon the spectral region. In the lower panel of figure 4 we have inserted a typical M2 supergiant spectrum (HD13136,M2I) taken by Jacoby, Hunter and Christian 1984.

IV. CONCLUSIONS

We suggest that the scattering of past speckle interferometric angular diameter measures for Alpha Orionis, summarized in Table 3 and plotted as the scatter diagram in figure 4, can be resolved by assuming a simple stellar disk intensity profile, namely a limb-darkened disk with variable coefficients for different spectral features and with a single, physical radius. We find this to give reasonably good fit to all the observed data. Our measured angular diameter, 65 mas, is consistent with all previous measurements if the limb-darkening effect has been properly taken into account.

Our measured limb-darkening values are also consistent with those predicted from model atmosphere calculations. Refined model atmosphere calculations of the particular limb-darkening coefficients for our observed spectral bands are required, to further pin down the exact radius of Alpha Orionis. If speckle interferometry is to be a direct probe to the atmosphere of resolvable late-type supergiant stars, very careful choice of spectral regions for observation is required.

The effective temperature of Alpha Orionis remains an open question (see review in Tsuji 1976). The higher temperature predicted by Tsuji (T_e 4000°K) is due to the smaller angular diameter chosen. With our new measured larger angular diameter, this temperature decreases to about 3600°K. A lower effective temperature favours formation of silicate dust in its circumstellar envelope, which has been observed in the past (see e.g. Woolf and Ney 1969). This will require further study of theoretical model atmospheres of late-type supergiant stars, their circumstellar envelopes and related mass loss mechanisms.

V. ACKNOWLEDGEMENTS

This work was supported in part by the NSF (grants AST-8113218 and AST-8201692 and access to the CDC64xx at NCAO), the AFGL (contract F19628-82-K-0025) and the AFOSR (contract 82-0010). We also acknowledge the contributions of A. Szumillo for support and revisions to the data reduction software, and together with J. Freeman and S. Shaklan, many long hours of tedious data digitization and computer babysitting.

We particularly thank the NCAO staff and visitors for

enduring any inconveniances caused by these extensive data reductions, and the support staff at Kitt Peak who made the installation and use of our visitor instrument at the 4 meter telescope a successful delight. We also thank D[illegible] N. J. Woolf for many interesting and helpful discussions and suggestions.

REFERENCES

Beckers, J. M. 1982, Optica Acta, 29, 361.

Beckers, J. M., Hege, E. K., and Murphy, H. P. 1983, in SPIE Proceedings, 445, Instrumentation in Astronomy V, 462.

Bonneau, D., and Labeyrie, A. 1973, Ap. J. (Letters), 181, L1.

Christou, J. C., Cheng, A. Y. S., and Hege, E. K. 1985, in preparation.

Currie, D. G., Knapp, S. L., and Liewer, K. M. 1974, Ap. J., 187, 131.

Goldberg, L., Hege, E. K., Hubbard, E. N., Strittmatter, P. A., and Cocke, W. J. 1981, in Second Cambridge Workshop on Cool Stars, Stellar Systems, and the Sun,(Vol. I), ed. M. S. Giampapa and L. Golub (SAO Special Report 392), p.131.

Gezari, D. Y., Labeyrie, A., and Stachnik, R. V. 1972, Ap. J. (letters), 173, L1.

Hege, E. K., Hubbard, E. N., Strittmatter, P. A., and Cocke, W. J. 1982, Optica Acta, 29, 721.

Jacoby, G. H., Hunter,D. A., and Christian, C. A. 1984, Ap. J. Suppl., 65, 257.

Jeffreys, W. H. 1980, A. J., 85, 177.

-----, 1981, A. J., A. J., 86, 149.

Lynds, C. R., Worden, S. P., and Harvey, J. W. 1976, Ap. J., 207, 174.

McConnel, M. J., and Lutes, R. H. T. 1975, Computer Graphics and Image Processing, 4, 25.

McGregor, P. J. 1981, in Second Cambridge Workshop on Cool Stars, Stellar Systems, and the Sun, Vol. I, ed. M. S. Giampapa and L. Golub (SAO Special Report 392) p.83.

Pease, F. G. 1931, Ergebn. Exacten. Naturwis., 10, 84.

Ricort, G., Aime, C., Vernin, J., and Kadiri, S. 1981, A. A., 9, 232.

Roddier, C., and Roddier, F. 1983, Ap. J.,270, L22.

Tsuji, T. 1976, P. A. S. J., 28, 567.

Tsuji, T. 1978, P. A. S. J., 30, 435.

Welter, G. L., and Worden, S. P. 1980, Ap. J., 242, 673.

Woolf, N. J., and Ney, E. P. 1969, Ap. J., 155, L181.

TABLE 1

Summary of Models Fit to Alpha Orionis Image Power Spectra

Lamda (Å) / Band-pass (Å)	8542 / 3	8500 / 100	6563 / 3	6500 / 20	5500 / 100	5200 / 100	4100 / 100
Limb-darkening			Radius (mas)				
U = 0.0	31.2 ±0.7	28.9 ±0.4	28.4 ±0.2	26.6 ±0.1	26.9 ±0.2	26.5 ±0.2	28.3 ±0.6
U = 0.1	31.5 ±0.7	29.1 ±0.4	28.8 ±0.2	26.8 ±0.1	27.2 ±0.2	26.8 ±0.2	28.9 ±0.6
U = 0.2	31.8 ±0.7	29.4 ±0.4	29.1 ±0.2	27.2 ±0.1	27.5 ±0.2	27.1 ±0.2	29.2 ±0.6
U = 0.3	32.1 ±0.7	29.8 ±0.4	29.4 ±0.2	27.5 ±0.1	27.9 ±0.2	27.6 ±0.2	29.7 ±0.6
U = 0.4	32.6 ±0.7	30.2 ±0.4	29.9 ±0.2	27.9 ±0.1	28.3 ±0.2	28.0 ±0.2	30.2 ±0.6
U = 0.5	33.3 ±0.8	30.7 ±0.4	30.5 ±0.2	28.4 ±0.1	28.8 ±0.2	28.7 ±0.2	31.0 ±0.7
U = 0.6	33.9 ±0.8	31.5 ±0.4	31.1 ±0.2	29.1 ±0.1	29.4 ±0.2	29.3 ±0.2	31.7 ±0.7
U = 0.7	34.7 ±0.8	32.2 ±0.4	32.0 ±0.2	29.8 ±0.1	30.2 ±0 2	30.2 ±0.2	32.7 ±0.7
U = 0.8	35.8 ±0.8	33.2 ±0.4	33.0 ±0.2	30.7 ±0.1	31.1 ±0.2	31.2 ±0.2	33.8 ±0.7
U = 0.9	37.2 ±0.9	34.6 ±0.5	34.4 ±0.2	32.0 ±0.1	32.4 ±0.2	32.6 ±0.2	35.3 ±0.8
U = 1.0	39.2 ±0.9	36.4 ±0.5	36.2 ±0.2	33.7 ±0.1	34.2 ±0.3	34.4 ±0.2	37.3 ±0.8
	Unresolved Power B/(A+B)						
U = 0.0	.274 ±.008	.201 ±.006	.101 ±.003	.064 ±.002	.095 ±.004	.056 ±.002	.370 ±.001
	Standard Error (RMS) in the Fit						
U = 0.0	.103 ±.093	.050 ±.069	.042 ±.023	.017 ±.026	.011 ±.010	.025 ±.018	.118 ±.068

Table 2

Predicted Radius and Limb-darkening Coefficient of Alpha orionis

Wavelength (Å)	8543	8500	6563	6500	5500	5200	4100
Band-pass (Å)	3	100	3	20	100	100	100
Radius (mas)	Limb-darkening Coefficient U						
Lower Limit 31.2	0.00	0.56	0.61	0.84	0.81	0.80	0.53
Mean 32.5	0.38	0.73	0.74	0.93	0.90	0.89	0.68
Upper Limit 33.7	0.55	0.84	0.86	1.00	0.98	0.96	0.80

Table 3

Previous Measured Radius of Alpha Orionis

	Wavelength (Å)	Diameter (mas)	Reference
a)	5750	34 - 47	Pease 1931
b)	5000±125	> 50	Gezari et al. 1972
c)	4220	69 ± 5	Bonneau & Labeyrie 1973
	4880	67 ± 5	
	5700	55 ± 5	
	7190	52 ± 5	
	10400	< 50	
d)	4213±34	62 ± 17	Currie et al. 1974
	5025±35	47 ± 6	
	5823±46	57 ± 9	
	5992±15	57 ± 6	
	6336±16	44 ± 13	
e)	5100±50	49 ± 1 (U = 0)	Lynds, Worden & Harvey 1976
		74 ± 1 (U = 1)	
	5180±50	53 ± 1 (U = 0)	
		79 ± 1 (U = 1)	
f)	5100±50	66 ± 6 (U = 0.6)	McDonnel & Bates 1976
g)	5300±80	35 ± 10 (core)	Ricort et al.1981
		100 ± 40 (halo)	
h)	6000±50	45 ± 1 (U = 0)	Welter & Worden 1980
		50 ± 2 (U = .5)	
		62 ± 2 (U = 1)	
	6500±50	45 ± 2	
		49 ± 2	
		61 ± 3	
	7000±50	42 ± 1	
		45 ± 1	
		55 ± 2	
	7400±50	30 ± 4	
		32 ± 4	
		39 ± 4	
i)	5350±90	37 ± 3	Roddier & Roddier 1983

FIGURE CAPTIONS

1. Typical data and model normalized radial averaged power spectra. The dotted line is from data at 6500/20Å, and the solid line is for a best fit to the data of a selected model. The shaded region is either due to seeing calibration error or to large extended structures (or both).

2. Two typical power spectra. The solid line is for R = 24 mas and U = 0, while the dashed line is for 38 mas and U = 1.

3. Best fit models vs limb-darkening parameter U for each observing bandpass. The shaded region delimits the range of radius values, R = 32.5 ± 0.7 mas, permitted by the sets of fits to the data. The uncertainty is that allowed by $0 \leq U \leq 1$.

4. Summary of the results of speckle interferometry measures of the diameter of Alpha Orionis. Our result is represented by the line at 61 mas. A spectrum of a typical late-type M2 supergiant (HD13136), with our observed bandpasses indicated, is shown at the bottom.

Figure 1

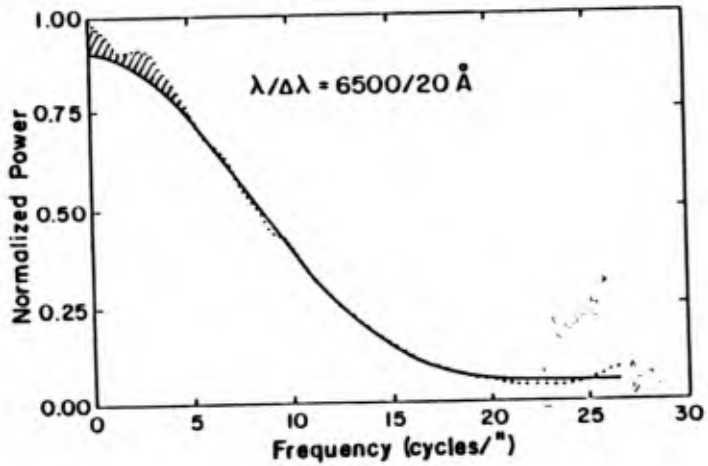

Fig 2

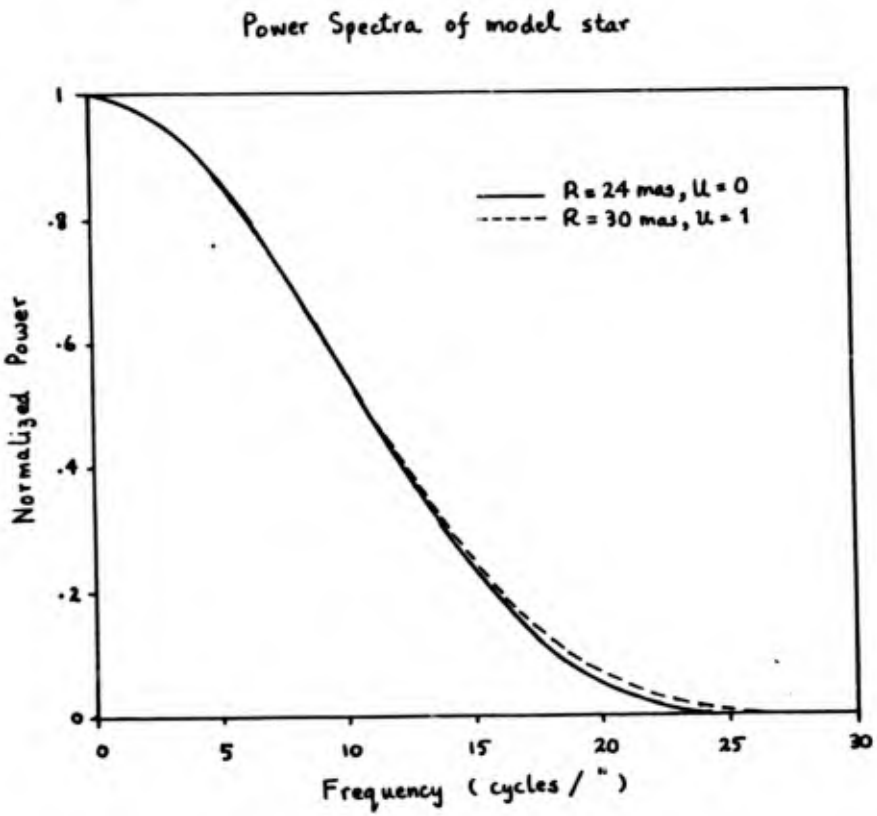

Figure 3

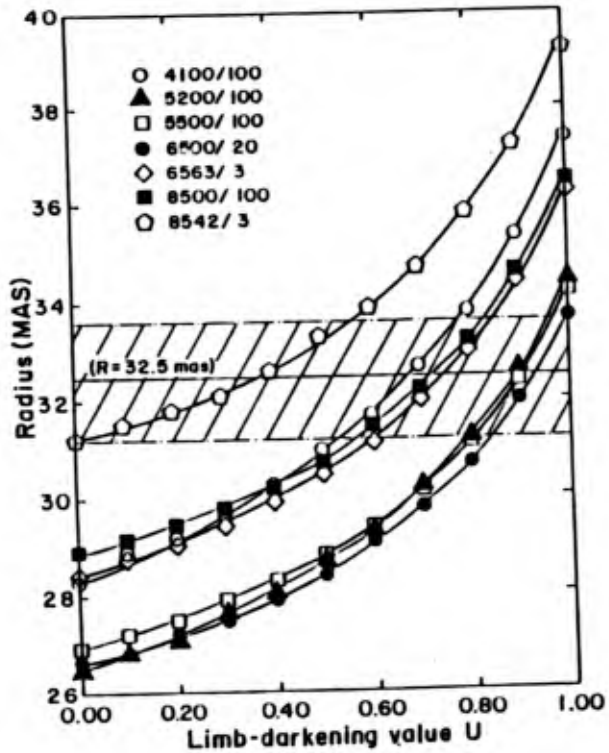

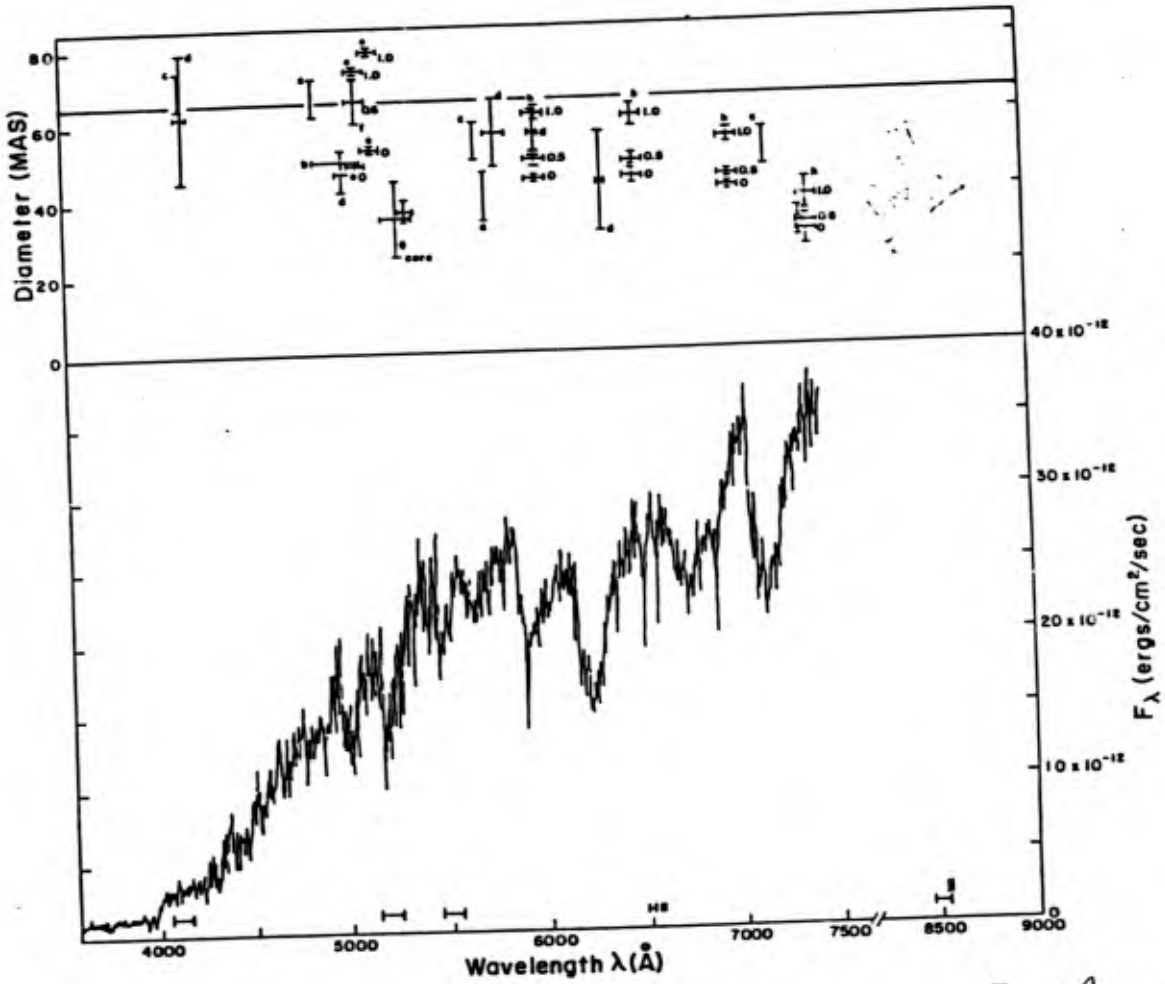
Diameter (MAS)
80
60
40
20
0
40 x 10⁻¹²
30 x 10⁻¹²
20 x 10⁻¹²
10 x 10⁻¹²
0
F_λ (ergs/cm²/sec)
4000
5000
6000
7000
7500
8500
9000
Wavelength λ(Å)

Figure 4

The versatile array

N. J. Woolf, J. R. P. Angel, and D. W. McCarthy, Jr.

Steward Observatory, University of Arizona
Tucson, Arizona 85721

Abstract

We discuss a four element non-degenerate array telescope-interferometer for ground use. The elements are 8 meter mirrors, and the maximum array spacing and two element spacing are 75m and 10.8m respectively. The array may be used as three separate telescopes, one 11.3m and two 8m for work not requiring highest angular resolution. We discuss the problems of making speckle measures to high enough precision for synthetic images to be produced. We conclude by showing that the high resolution presents opportunities to make types of observation that are neither possible with VLBA nor NNTT.

Introduction

Since the introduction and development of new interferometric speckle techniques by Labeyrie and his collaborators[1], there has been a surge of interesting observational results. These results encourage the design of interferometers of higher resolution and sensitivity. However, the very large change in quality of interferometric data, with modest changes in observing conditions suggests that interferometry makes a poor sole justifier for a giant facility at optical and IR wavelengths. One would like to have a facility in which extraordinary conditions were used for interferometry, and yet the facility provided for alternate high interest work for the, say 2/3 of the time when conditions are more ordinary.

There has been some recent confusion as to the value of using large apertures in interferometers, though they are clearly preferred for the other types of observation. The value of a large aperture in increasing interferometric sensitivity is not very great when the image is enlarged beyond the diffraction pattern by seeing. In that case, the speckle interference patterns add incoherently, and sensitivity increases linearly with aperture diameter, whereas in the diffraction limited case, sensitivity increases as $(\text{diameter})^2$.

In the visible, the apertures may be made coherent by adaptive optics if the object is bright enough (~ 10th magnitude), which is not usually helpful. However beyond a few microns the isoplanatic patch is so large, and the speckle change time so long that the telescope can be made coherent in the IR by using adaptive optics working with the visible light of the object, or a faint field star. For these cases the interferometer with large primary mirrors becomes a very powerful tool, because the sensitivity is increasing as $(\text{diameter})^2$.

A study of the optimum use of collecting area in a visible or IR interferometer shows that greatest sensitivity is obtained by dividing the area into two equal apertures, and moving one so as to sequentially explore the U-V plane. For a practical interferometer, there is a benefit from reducing the types of motion needed for a large aperture, and in keeping the moved apertures to manageable dimensions. In this paper we have chosen to balance these needs by considering an array of four 8m mirrors, in which the exploration of the U-V plane is done by an azimuth motion of the array, coupled with the diurnal apparent motion of the sky.

Eight meter mirrors make good building blocks. They are the largest individual mirrors likely to be available in the near future. In the 0.3 to 1 micron range, CCD spectrographs on this size telescope are limited by photon noise of sky background for resolving powers up to a few times 10^4. With mirrors this large, it is possible to make a few element interferometer with high angular resolution, and with no holes in the U-V plane.

This article breaks into four further sections. First, there is a description of the Versatile Array concept. Second, is a discussion of the expected optical performance of the concept, with estimates of a few of the design parameters. Third, is a discussion of the problem of making interferometric measures with sufficiently small systematic errors that good image reconstruction is possible. Finally, there is a discussion of the application of this device to two major problem areas in astronomy. The first concerns the nature and structure of the innermost regions of energetic extragalactic objects such as quasars and Seyfert galaxies. The second concerns the structure of solar-system-like objects in formation.

Fig 1

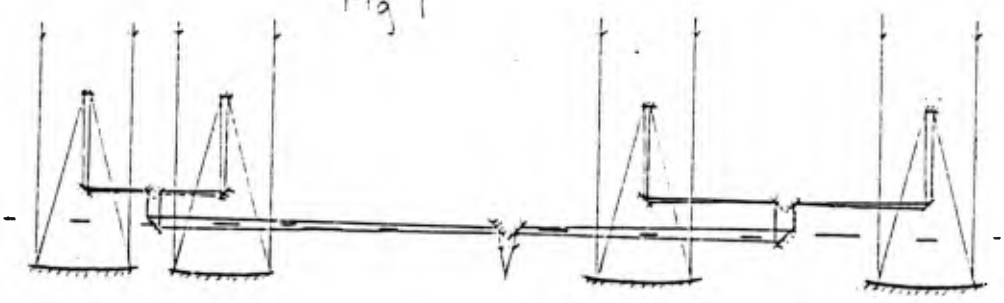

Fig 2

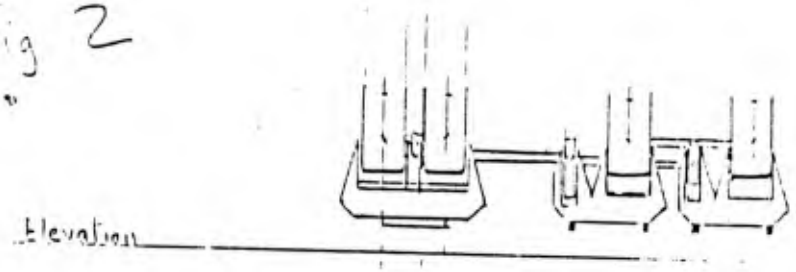

Elevation

0 Meters 50 100

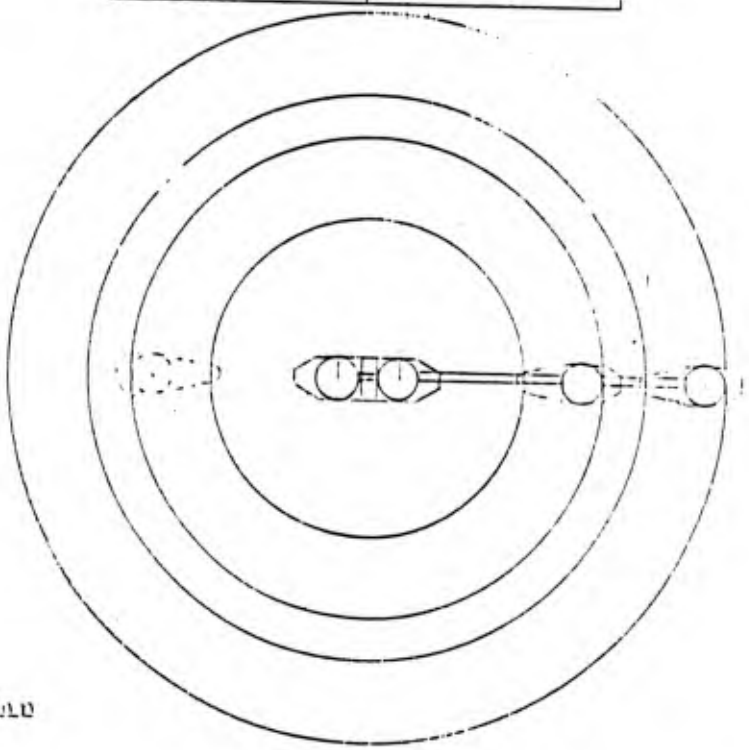

Plan

IMAGES OF ALPHA ORIONIS ?

By

J.C.Hebden
J.C.Christou
A.Y.S.Cheng
E.K.Hege
P.A.Strittmatter

Steward Observatory, University of Arizona, Tucson, AZ 85721

and
J.M.Beckers

NOAO, 950 N.Cherry, Tucson AZ 85726

Preliminary Draft

April 1985

To be submitted to Astrophysical Journal Letters

Abstract

Between February 1981 and December 1983 a series of speckle interferometric observations were made of the M-type supergiant Alpha Orionis in an attempt to produce two-dimensional images of the star at the hydrogen-alpha line. The telescopes employed include the Steward Observatory 2.3 meter and NOAO 4 meter telescopes at Kitt Peak and the fully-phased six-mirror Multiple Mirror Telescope at Mount Hopkins, Arizona. Various data reduction techniques were applied which divide into two main catagories : i) Shift-and-Add methods applied to conventional speckle interferometric observations, and ii) Differential speckle interferometry. Data reduction also included the application of the CLEAN algorithm to calibrate the images produced by the Shift-and-Add technique with data reduced similarly for a point source. The images produced are encouragingly consistent in suggesting the atmospheric structure they exhibit and a possible observed evolution of the structure over the three year period of observations is proposed.

1. Introduction

The low surface gravity and absence of strong magnetic field lines causes the surrounding envelopes of red supergiant and giant stars to be very extended and relatively cool. This makes them visible in the light of the hydrogen Balmer lines (e.g. H-alpha 6563Å) and the singly ionized calcium lines (e.g. CaII 8582Å). Occultation measurements by White et al. (1982) and speckle observations by Goldberg et al. (1982) have presented evidence for spatially extended H-alpha emission surrounding several M-type supergiants. Asymmetry discovered in the cores of several strong resonance lines in M stars (Adams and MacCormack 1935) suggests that these giant stars are surrounded by huge circumstellar shells moving away from the central star at velocities of the order of 5 km/s. Furthermore it has been shown (Deutsch 1956) that such shells are responsible for considerable mass loss.

The most thoroughly studied of all red-giant stars has been Alpha Orionis, an M2 Iab late type supergiant. Like most red-giant and supergiant stars Alpha Orionis is an irregular variable and displays a high mass loss rate, typically calculated as about 10^{-6} $M_\odot$/year. Numerous observations have also identified variability in both the visual brightness and radial velocity of the supergiant star on timescales of a few weeks or months. The mean amplitudes are about half a magnitude and 6km/s respectively. For a review see Goldberg (1984). The variability roughly satisfies the phase relation for a pulsating star, i.e. maximum brightness coinciding with minimum radius (Sanford 1933). In addition Hayes (1984) has produced results showing variation in the polarization of Alpha Orionis on timescales of months. Possible temporal irregularity and spatial inhomogenity are in accordance with the suggestion of Schwarzchild (1975) that the surfaces of supergiants may be irregular due to the presence of very large convective cells.

Since 1920 when Michelson and Pease (1921) first determined the angular diameter of Alpha Orionis, the star has become one of the most frequently observed objects using high resolution interferometric techniques. However it was not until 1976 that the first attempt at image reconstruction of this star (or indeed of any star other than our own sun) was published, by Lynds, Worden and Harvey (1976). The breakthrough in ground based high resolution methods which led to this and subsequent results came when Labeyrie (1970) proposed the technique of stellar speckle interferometry (SI). This technique enables diffraction limited resolution to be obtained from large optical telescopes, despite the effects of atmospheric turbulence, by utilising single short exposure narrow bandwidth images (specklegrams). Since Labeyrie's original work many extensions have been made to the theory and application of speckle interferometry and, in particular, to the recovery of diffraction limited images. One such image reconstruction technique which is relevent to the work described here is known as Shift-and-Add (SAA). This is an extension by Bates and Cady (1980) of the method used by Lynds et al. which

produced that first stellar map. SAA is discussed in more detail in section 3. Another recent modification of SI is a technique called Differential Speckle Interferometry (DSI) as proposed by Beckers (1982). DSI utilises two simultaneously acquired narrow band images (see section 4).

Diffraction limited imaging of the resolved disk and extended atmosphere of Alpha Orionis and other giant stars may become an invaluable aid to the understanding of stellar mass loss processes and to the study of stellar evolution. In addition, as Hartmann (1982) suggests, the combination of high resolution images with radio measurements should yield a much clearer picture of electron densities and temperatures in the inner regions of the stellar wind.

In this paper we present the results obtained from a series of speckle interferometric observations of Alpha Orionis made over a three year period. The resolved disc and H-alpha envelope of the star has been imaged using a variety of techniques. We attempt to define asymmetrical features consistent with each result and we tentatively propose how such structure may have changed visually during the period between observations.

2. Observations

Between February 1981 and December 1983 Alpha Orionis was observed on four separate occasions with the purpose of obtaining information on the structure of the star's disk and extended envelope at the H-alpha waveband. Two basic speckle interferometric techniques were employed: conventional SI, and DSI. The implementation of each method is discussed separately below.

i) Conventional Speckle Interferometry

Observations of Alpha Orionis were made at the NOAO 4 meter telescope on 2/3 February 1981 and also on the Steward 2.3 meter telescope at Kitt Peak on 5/6 November 1982 using the Steward Observatory intensified video speckle camera as described by Hege et al. (1982). The instrumental and observational parameters for both runs were essentially the same. H-alpha (6563Å/3Å) and red continuum (6500Å/20Å) bandpass filters were employed to observe the supergiant as well as point-source calibration stars Epsilon and Gamma Orionis. Video specklegrams were recorded for about 15 minute intervals for Alpha Orionis, interspersed with 5 minute observation of the calibration stars. The specklegrams were recorded with 15ms exposures at the rate of 7.5 Hz, equivalent to every fourth video frame. Excluding light from three out of every four frames enables the image intensifier afterglow to decay sufficiently between exposures so that unevenness in the background signal can be removed by on-line subtraction of consecutive frames. The 15ms exposure time is sufficiently short to effectively freeze the atmospheric turbulence so that specklegrams retain information at frequencies up to the diffraction limit of the telescope. Post-observational data

processing begins with digitization of the specklegrams 8 bits deep in a 128x128 pixel array by a Grinnell digital television system. The digitized data is stored on 9-track tapes using the Steward Observatory Point 4 minicomputer system.

ii) Differential Speckle Interferometry

DSI observations of Alpha Orionis were made using the Steward 2.3 meter telescope on 5/7 March 1982 and on the fully-phased six-mirror Multiple Mirror Telescope (MMT) on 16/17 December 1983. This new technique utilizes the Differential Speckle Camera (Beckers et al. 1983) which enables an object to be observed at two wavebands simultaneo sly. This is achieved by passing the light from the star through a solid Fabry-Perot etalon, which has a different narrow passband at two orthogonal polarizations, and then shifting one polarized image with respect to the other using a Wollaston Prism. In this way two specklegrams are produced, separated by about 7.38mm in the image plane. Adjustment of the etalon temperature shifts the bandpasses for the two polarizations. The bandpass separation and full width at half maximum at peak transmission are dependent on the choice of mica spacer in the etalon. The March 1982 observations were obtained at H-alpha (bandwidth 0.45Å) and simultaneously in the nearby continuum about 4Å away. The December 1983 MMT observations produced specklegrams at H-alpha (bandwidth 1.2Å) and continuum about 6Å away. Once again Gamma Orionis was used as a point-source calibration star. Data was obtained for the supergiant at two distinct sky position angles separated by about 80 degrees. Identification of image features which rotate correspondingly would be a very strong validation of the technique. Video specklegram pairs were recorded in an identical manner to that described for conventional speckle observations. Each video frame was digitized as two 128x128 pixel arrays and stored consecutively on 9-track magnetic tape.

3. CLEAN Shift and Add images

The principal concept behind the imaging technique used by Lynds, Worden and Harvey (as mentioned in section 1 and hereafter referred to as LWH) is that each individual bright speckle in a specklegram may be considered as a photon-noise limited representation of a randomly distorted but nearly diffraction limited image of the star. Thus LWH realised that they might be able to form a useful image of a resolvable astronomical object by superimposing the brighter speckles obtained from a series of specklegrams, thus averaging the random distortions and building an average which approximates the true image as more and more data is added. This was, as mentioned earlier, later developed into the technique known as Shift-and-Add by Bates and Cady. This idea of stacking all the speckles from a large number of frames was applied to the H-alpha data of Alpha and Epsilon Orionis obtained on the 2.3 meter telescope in November 1982. In practice the stacking up procedure consisted of cross-correlating the specklegram with an array containing a series of delta functions whose position and amplitude correspond to the position and peak

height of the speckles. This process produces an image which is situated upon a broad background which is subtacted to a high degree by comparison to a suitable Gaussian function. Figures 1a and 1b show the results for 1000 specklegram frames of Alpha and Gamma Orionis respectively. The general elongation in the vertical direction is due to the pixels having a smaller scale in the N-S direction than in the E-W direction. The Gamma Orionis image, as well as the Alpha Orionis image to a much lesser degree, contains an artifact due to non-linear effects of the TV camera. As the TV camera scans across very bright speckles the automatic gain control (AGC) of the camera causes the effective intensity of the scan to "undershoot" as illustrated in figure 2. Thus the images appear compressed on one side, in the scan line direction adjacent to the part of the image at which the speckles are brightest (i.e. the center). The brighter, more point-like, Gamma Orionis speckles cause more severe "undershoot" to occur.

In order to produce an image of Alpha Orionis freefrom the effects of the telescope PSF and from spurious systematic effects like those described above, attempts were made to deconvolve the image with the Gamma Orionis image using the CLEAN algorithm. The CLEAN procedure (Högbom 1984) has been successfully applied in the past to radio interferometric data in order to remove structural features due to the synthesized interferometer beam.

Conventionally the pre-processed image is referred to as the "dirty map" and the image with which the deconvolution is performed as the "dirty beam". CLEAN is an iterative process which locates the point of greatest intensity in the dirty map and subtracts at this location the dirty beam whose peak intensity is G% of the current peak in the dirty map. This process is repeated on the residual after subtraction. The quality of the final "cleaned map" is dependent on both the value of the loop gain G and the number of iterations. In this way a set of delta functions of varying intensities are generated such that the dirty map can be considered as a weighted sum of dirty beams plus the final residual. The number of iterations is selected so that either the intensity in the final residual is equal to the expected noise level or that only a certain number of delta functions have negative intensities. The cleaned map is then obtained by convolving the array of delta functions with an estimate of the "clean beam", commonly obtained by fitting a Gaussian to the central component of the dirty beam.

Thus the CLEAN algorithm was applied to Alpha Orionis using figure 1a as the dirty map and figure 1b as the dirty beam. The cleaning was performed by using 50 iterations and a loop gain of 70%. The cleaned image of Alpha Orionis is shown in figure 1c. The outer 2% contour shows significant elongation in the N-W, S-E direction at a position angle of about 120 degrees (mod 180°). However, the inner contours exhibit an elongation at a position angle of about 169 degrees (mod 180°). The 4% contour extends over a diameter of about 120 msa.

A recent modification of the SAA technique has been implemented

which enables speckles to be co-added without producing the Gaussian-like background. Weighted Shift-and-Add (WSA), as described by Christou et al. (1985), produces an array of impulses in an identical manner to that described above and then deconvolves each specklegram by its corresponding impulse array. Performing a complex deconvolution, a quotient in Fourier space, normally introduces spurious effects associated with the presence of small numbers in the denominator. WSA avoids this by weighting each complex quotient by the power spectrum of the impulse array, and summing over a large number of frames. This technique was applied to the 6500Å/20Å and 6563Å/3Å observations of Alpha and Gamma Orionis obtained using the NOAO 4 meter telescope in February 1981. Figures 3a and 3b show the WSA reconstructed images for 1500 specklegrams of Alpha and Gamma Orionis at H-alpha wavelengths, and figures 3c and 3d show similar images for 1500 specklegrams of the same stars using a 6500Å/20Å bandpass filter.

Using the Gamma Orionis images as the dirty beams, the images of Alpha Orionis were cleaned as described above. Fifty iterations were performed using a loop gain of 70%. The results of this cleaning process are shown in figures 3e (6563Å) and 3f (6500Å). Once again the cleaned H-alpha image exhibits significant N-W, S-E elongation. The outermost contour yields a position angle of about 117 degrees (mod 180°) whereas the inner contours suggest an elongation at about 160 degrees (mod 180°). However, the cleaned 6500Å image of Alpha Orionis shows practically no such elongation above the level of the noise.

4. Differential Speckle Imaging

As mentioned in section 1 Differential Speckle Interferometry is a technique which involves recording two speckle images simultaneously. By observing an astronomical object at two distinct but nearby wavelengths, image information relating to the differences in the object as results from the difference in wavelength (e.g. Stellar emission or absorption lines, Doppler shifts, Zeeman effects) can be derived. One inherent benefit of DSI is that information at very narrow (e.g. emission, absorption line) wavebands can be derived at a far greater signal-to-noise ratio (SNR) than that achievable using single image (conventional) SI alone. Petrov et al. (1985) show that the overall SNR for DSI is equal to the geometric mean of the two component specklegram SNRs. Thus it is beneficial to use a reference specklegram as bright as possible. Unfortunately at the moment we are constrained to the use of a single detector so the line/reference brightness ratio can not become too large without sacrificing single photon detection in the line specklegram. Note that it is always true that a unique unambiguous image of an object at either wavelength can only be derived using the DSI techniques described here if the object intensity distribution at the other wavelength is known: this is a comparative technique.

Since the first measurements by Michelson and Pease (1921), most experimental estimates of the disc diameter of Alpha Orionis have

suggested that the star is practically unresolved at continuum wavelengths on a 2.3 meter telescope. Thus, by assuming the DSI reference specklegrams obtained in March 1982 to be those of a nearly unresolved source, reconstruction of the image of the star at H-alpha was attempted using essentially the same method as that known as Speckle Holography (Bates et al. 1973). Each H-alpha specklegram was cross-correlated with its corresponding reference specklegram and the cross-correlations were co-added. In practice the physical separation between specklegrams is not exactly equal to the separation between the centers of the two digitized 128x128 arrays. Consequently crosscorrelation produces two peaks situated on a broad Gaussian-like seeing background. Having assumed the continuum image to be unresolved, each of these peaks represents an image of Alpha Orionis at the H-alpha waveband. Isolation of these images was achieved by subtracting a least-squares fit Gaussian model from the seeing background. One image is orientationally correct with respect to the sky and the other has the E-W direction reversed. The former image is shown in figure 4. In accordance with the other H-alpha images of Alpha Orionis described so far, there is a very significant elongation in the N-W, S-E direction, this time even at high contour levels. The position angle is about 118 degrees (mod 180°).

The fully-phased six-mirror MMT has an effective aperture of 6.86 meters. At the H-alpha waveband this corresponds to a diffraction limit of about 20mas and thus Alpha Orionis, which most measurements show to have a continuum diameter of between 50mas and 60mas, is quite easily resolved by the MMT. Whereas reference specklegrams obtained in the continuum with the MMT can not be used to deconvolve the corresponding line specklegrams so as to produce an actual image, performing such a deconvolution can still enable information relating to the physical differences at the different wavelengths to be derived.

The data reduction procedure implemented for the December 1983 MMT observations consisted of performing frame-by-frame complex deconvolutions of the H-alpha specklegrams by their simultaneously acquired counterparts. In a similar manner to that described for WSA in section 3, each complex quotient is weighted by the reference power spectrum and summed over a large number of frames. The resulting "Differential Image" may be expressed as

$$FT^{-1}\left\{\frac{\sum_N \frac{h(u,v)}{c(u,v)}\,|c(u,v)|^2}{\sum_N |c(u,v)|^2}\right\} = FT^{-1}\left\{\frac{\sum_N h(u,v)\,c^*(u,v)}{\sum_N |c(u,v)|^2}\right\} \qquad (1)$$

since $|c(u,v)|^2 = c^*(u,v).c(u,v)$ and where N is the ensemble of DSI specklegram pairs, h(u,v) is the Fourier transform of the line specklegram and c(u,v) is the Fourier transform of the reference specklegram.

Figure 5 shows a differential image of the point source Gamma Orionis. 1000 frames of data were used. Since it is assumed that

Gamma Orionis is unresolved at both wavebands, its differential image is essentially equivalent to the (inverse) Fourier transform of a cylindrical (top-hat) function with radius equal to the frequency cut-off of the telescope (D/λ). The differential image is therefore a Jinc function ($J_1(r)/r$) whose half-power width is expected to be about $0.61\lambda/D$ radians, or about 12mas for the 6.86m aperture of the MMT at the H-alpha waveband. The image scale in figure 5 is equal to about 5.2mas per pixel and hence the half-power width (about 3 pixels) agrees well with the expected result. The rather non-uniform brightness of the first secondary maxima suggests that there was possibly less than perfect optical coherence between the six constituent mirrors of the MMT. A region of a second ring is also apparent.

Figure 6 shows a differential image of Alpha Orionis obtained from an identical number of frames. The overall SNR looks poorer, even though the supergiant is brighter in the bandpass used, because the object is resolved (more photons per speckle but considerably larger speckles). Further differential images of Alpha Orionis were generated using about 7000 frames of data for each sky position angle. Though radial average measurements confirmed the existence of structure over a diameter of at least 150mas, very little evidence of the expected 80 degree image rotation was observed, due to the relatively poor SNR. A detailed analysis of the reduction technique revealed that the weighted deconvolution quotient (equation 1) contains a form of inherent Wiener-type filter which suppresses the signal at high spatial frequencies. It can be shown that the power-spectra in the denominator contain a noise bias term constant for all frequencies (subject to detector photon PSF considerations), whereas the cross-spectra in the numerator are bias free. Consequently signals at high spatial frequency below the diffraction limit are suppressed as the noise term becomes significant compared to the power-spectrum signal. In order to prevent this inherent filtering effect, attempts were made to debias the co-added power-spectra in the denominator of equation 1. The power-spectrum plus noise term is already multiplied by the Fourier transform modulus of the detector photon PSF. By assuming this response to be Gaussian, removal of the noise bias was achieved by subtraction of a Gaussian model which was fitted to the data at spatial frquencies greater than the telescope cut-off frequency.

Figures 7a and 7b show the differential images of Alpha Orionis at the two sky position angles after removal of the noise bias terms. About 7000 frames were used for each image. At large radii there appears to be no evidence of asymmetrical structure which is not still noise dominated. There are several possible reasons for this. Firstly the MMT sky-rotator was not employed due to technical difficulties and consequently the image was permitted to rotate by about 9 degrees, blurring the image at large radii, during each of the two observations. Secondly imperfect coherence between the six mirrors may be responsible for the systematic fringes apparent in the images. Finally, the absence of any gross N-W, S-E elongation evident in the conventional SI results is

easily explained should the structure be visible in both the H-alpha waveband and the nearby continuum. However, at small (< 30mas), high SNR, radii there is considerable evidence that an elongated asymmetric feature in the image having a position angle of about 20 degrees is observed to rotate exactly as predicted.

5. Discussion

The very first image reconstruction of Alpha Orionis by LWH exhibited only marginal evidence of surface structure detected above the noise level. Further data reduction using the LWH technique and image enhancement (Worden et al. 1976, Wilkerson and Worden 1977, Welter and Worden 1980) consistently demonstrated asymmetry in the image of Alpha Orionis at a variety of wavebands, though no quantative measurements were produced. Digital restoration techniques applied to the LWH 5000Å data by McDonnell and Bates (1976) also confirmed a departure from circular symmetry in the disc features of Alpha Orionis.

Observations of the supergiant were also made by Roddier and Roddier (1983) in November 1980. Their study of fringe visibility at 5348Å/90Å suggested an elongation at 22 degrees (mod 180°) at large spatial frequencies (small radii) and a N-W, S-E elongation at small spatial frequencies (large radii). Preliminary results obtained from SI observations by Goldberg et al. (1982) also indicate the presence of elongated structure in the N-W, S-E direction. Measurements obtained in the H-alpha waveband suggested a position angle of about 157 degrees (mod 180°) for November 1980 and about 176 degrees (mod 180°) for February 1981. These latter observations were also used by Goldberg et al. to reconstruct an image using the Fienup (1978) phase retrieval method. An image was produced which once again showed a significant elongation in the N-W, S-E direction. However, a position angle of only 110 degrees was derived. Red continuum (6500Å) observations indicated a position angle asymmetry at 28 degrees (mod 180°). Fienup reconstruction at the singly ionized calcium line (8542Å) showed some, though significantly less, evidence of asymmetry, again at 110 degrees.

Combining the above past measurements with the results presented in this communication produces overwhelming evidence for the existance of an elongated "cloud" of H-alpha emission around Alpha Orionis, up to 3 times the estimated continuum diameter in length, in a N-W, S-E direction. Our results would suggest a position angle of 118 +/- 5 degrees, with no apparent rotation of the feature relative to the sky over the 3 year period. However we tentatively suggest that the extension may have increased in the N-W direction while being reduced in the S-E direction. It is feasible, at least, that such variability would be produced by a cloud (possibly annular) rotating perpendicularly to the line of sight in a N-W, S-E oriented plane. The fact that there is generally less evidence of asymmetry in the continuum would suggest that the cloud was predominantly gaseous rather than dust. One also might expect a dominant and temporally invariant (on the timescale of months at least) polarization angle if such

a nearby, optically thin, asymmetric dust cloud were present.

Jones (1928) derived a period of 5.781 years for the mean radial velocity variation of the photosphere of Alpha Orionis. Comparatively recent observations by Goldberg (1979) confirm this result to within 0.5 percent. This periodicity might be associated with a stellar rotation period of that duration, which corresponds to a surface (tangential) velocity of about 20 km/s. The possible rotation of extended features that we might have detected would imply a period of the order of the 6 year variability, though the tangential velocities would be correspondingly higher, perhaps higher than the upper limit suggested by line profile studies.

Three of the four observations reported here produced images which exhibited evidence for an additional asymmetrical position angle at radii comparable with the estimated continuum disc size (60 msa), where the SNR is highest. The measured position angles are 160 degrees (mod 180°; February 1981), 169 degrees (mod 180°; November 1982) and 20 degrees (December 1983). It is not yet evident that these results could be consistent with a rotation period of about 6 years. Perhaps more likely is that each feature represents small scale structure on the surface of the star that exists only on the time scale of months. Goldberg et al. (1982) attributed the presence of asymmetry in November 1980 and February 1981 to the existance of a "hot-spot" on the surface of the star. This same feature would not be inconsistent with our February 1981 WSA result described in section 3.

Hayes (1980) has suggested that the observed changes in polarization are consistent with the growth of a surface feature followed by changes in its orientation. Goldberg et al. (1982) find that their observations lend general support to this suggestion. In a comprehensive review of linear polarization variation of Alpha Orionis between 1979 and 1983, Hayes (1984) concludes that large-scale convective cells fullfil the necessary requirement for production of the observed incessant polarization activity. He further suggests that ordered polarization changes, a manifestaion of the waxing and waning of the cells, implies that only a few cells would be present at any one time, at variance with the rudimentary estimates of Schwarzchild (1975). Incidentally, it is very improbable that the polarization variation occurs through scattering of light from matter around the star since the observed short term variation requires rotation or radial velocities inconsistent with current estimates. Unfortunately there appears to be little correlation between our observed asymmetry position angles and the polarization angles as measured by Hayes (1984). Similarly the changes in the intensity of polarized light appears unassociated with the occurance or otherwise of central asymmetrical features.

6. Conclusions

The results of this study may be summarized as follows. The presence of a large scale asymmetric elongation in the H-alpha

envelope has been verified by implementing several speckle interferometric techniques. It extends over at least 3 stellar radii and corresponds to a position angle of about 118 degrees (mod 180°). Though this position angle appears effectively constant over the three year period of observation, extension in the N-W direction may have increased at the expense of the S-E extension. Smaller scale asymmetries have also been identified within the diameter of the stellar disc. Evolution of these features appears to be consistent only with random fluctuations of surface structure on the timescale of months. No correlation has been established between their behaviour and position, and polarization variations over the same period.

An accurate determination of the relationship between temporal variation in the radial velocity, magnitude and polarization of Alpha Orionis and optical features on the surface and in the extended envelope of the star, will require further extensive study using these high resolution optical imaging techniques. Ultimately such study of Alpha Orionis and other rapid mass-loss objects will enable stellar evolution to be better understood (since giant stars which shed sufficient mass will avoid ending their existance in the form of supernovae), and may provide valuable information on the important question of "missing mass" in the universe. We have demonstrated that speckle interferometry is now producing useful unambiguous images and we are confident that a wide variety of speckle imaging methods will continue to provide valuable astronomical data with steadily increasing quality.

References

Adams,W.S. and MacCormack,E.,Astrophys.J.,81,119.1935
Bates,R.H.T. and Cady,F.M.,Opt.Commun.,32,365.1980
Bates,R.H.T.,Gough,P.T. and Napier,P.J.,Astron.Astrophys.,22,319.
1973
Beckers,J.M.,Opt.Acta,29,361.1982
Beckers,J.M.,Hege,E.K. and Murphy,H.P.,Proc.SPIE,vol.445,Intsr.in
Astron.,p462.1983
Christou,J.C.,Hege,E.K.,Ribak,E. and Freeman,J.,Astrophys.J.Lett.
(to be submitted)
Deutsch,A.J.,Astrophys.J.,123,210.1956
Fienup,J.R.,Opt.Lett.,3,27.1978
Goldberg,L.,Pub.Astron.Soc.Pac.,96,366.1984
Goldberg,L.,Qu.J.R.Astron.Soc.,20,361.1979
Goldberg,L.,Hege,E.K.,Hubbard,E.N.,Strittmatter,P.A. and Cocke,
W.J.,SAO Special Reports 392,131.1982
Hartmann,L.,Highlights in Astronomy,vol.6,IAU.1982
Hayes,D.P.,Astrophys.J.Lett.,241,L165.1980
Hayes,D.P.,Astrophys.J.Sup.Ser.,55,179.1984
Hege,E.K.,Hubbard,E.N.,Strittmatter,P.A. and Cocke,W.J.,Opt.Acta,
29,701.1982
Högbom,J.A.,Astron.Astrophys.Supp.,15,417.1974
Jones,H.Spencer,Mon.Not.R.Astron.Soc.,88,660.1928
Labeyrie,A.,Astron.Astrophys.,6,85.1970
Lynds,C.R.,Worden,S.P. and Harvey,J.W.,Astrophys.J.,207,174.1976
McDonnell,M.J. and Bates,R.H.T.,Astrophys.J.,208,443.1976
Michelson,A.A. and Pease,F.G.,Astrophys.J.,53,249.1921
Petrov,P.,Roddier,F. and Aime,C.,Submitted to J.Opt.Soc.Am.A
Roddier,C. and Roddier,F.,Astrophys.J.,270,L23.1983
Sanford,R.F.,Astrophys.J.,77,110.1933
Schwarzchild,M.,Astrophys.J.,195,137.1975
Welter,G.L. and Worden,S.P.,Astrophys.J.,242,673.1980
White,N.M.,Kreidl,T.J. and Goldberg,L.,Astrophys.J.,254,670.1982
Wilkerson,M.S. and Worden,S.P.,Astron.J.,82,642.1977
Worden,S.P.,Lynds,C.R. and Harvey,J.W.,J.Opt.Soc.Am.,66,1243.1976

Figure 1 : 90" observations LWH November 1982

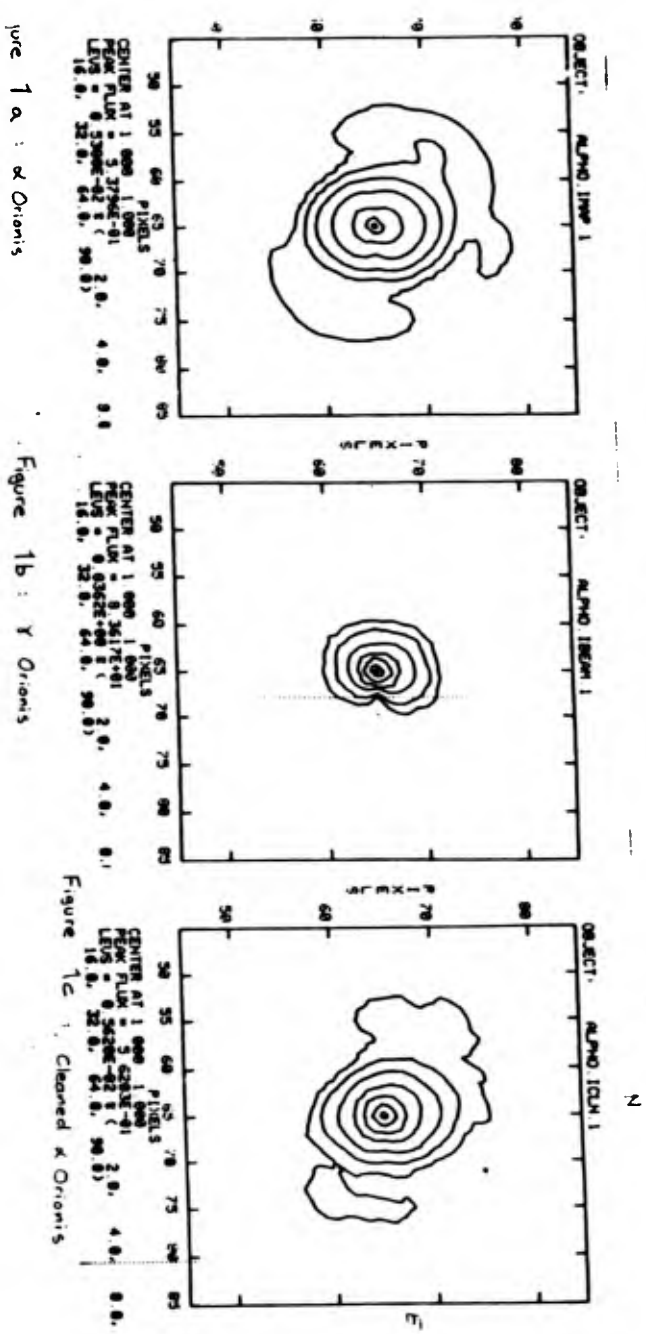

Figure 1a : α Orionis

Figure 1b : γ Orionis

Figure 1c : Cleaned α Orionis

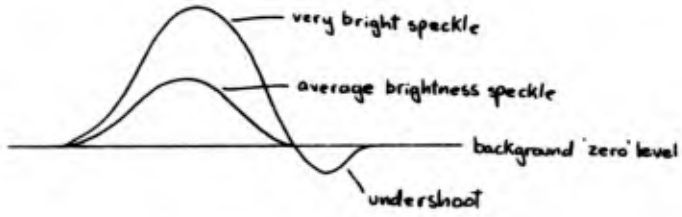

Figure 2

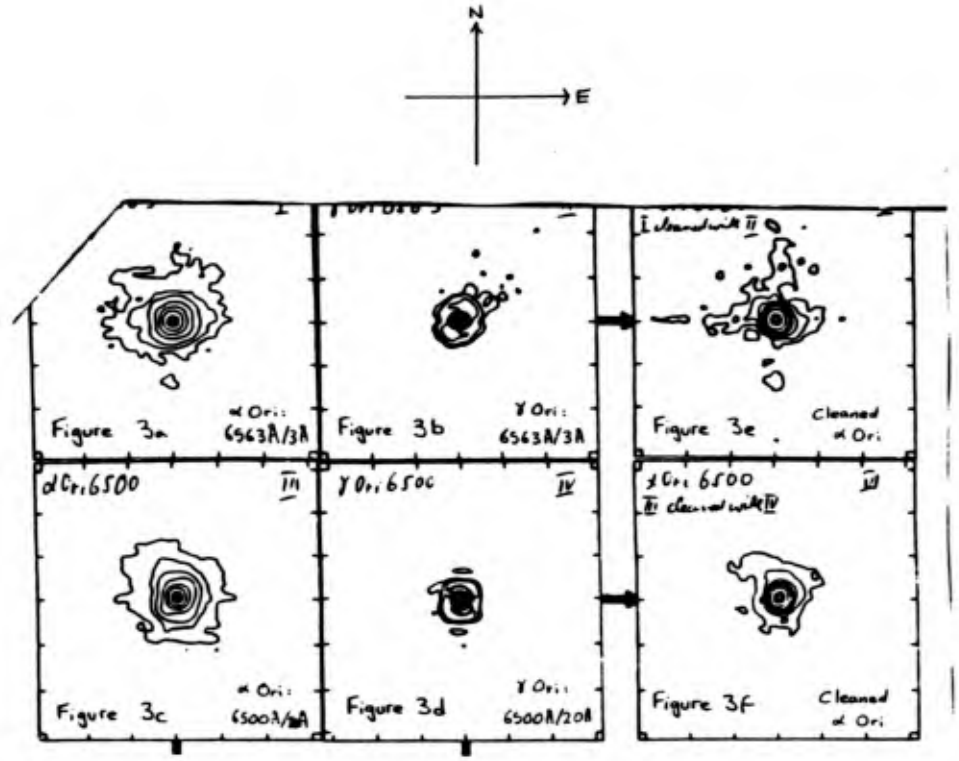

Figure 3 : 4m observations WSA February 1981

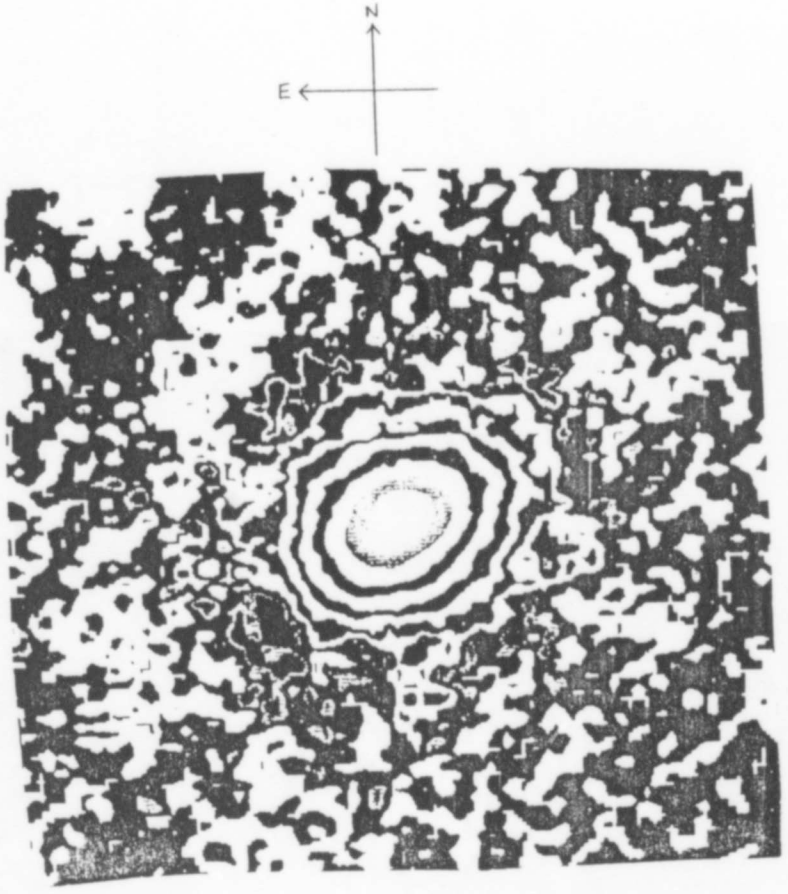

Figure 4: DSI XC 2.3m observations March 1982

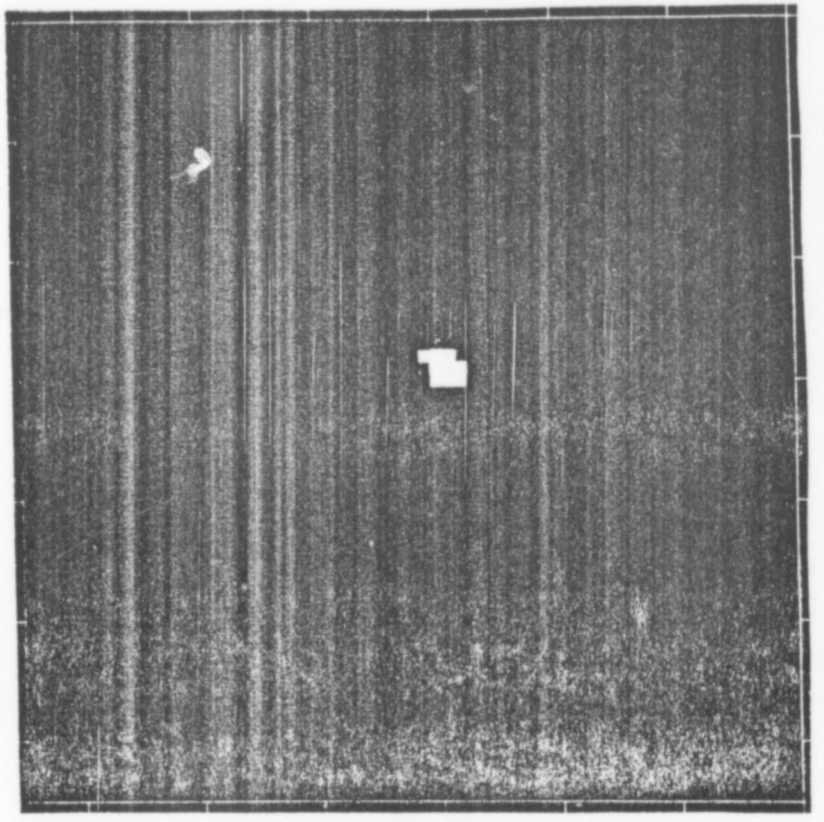

Figure 5 : Differential image of γ Ori : MMT December 1983

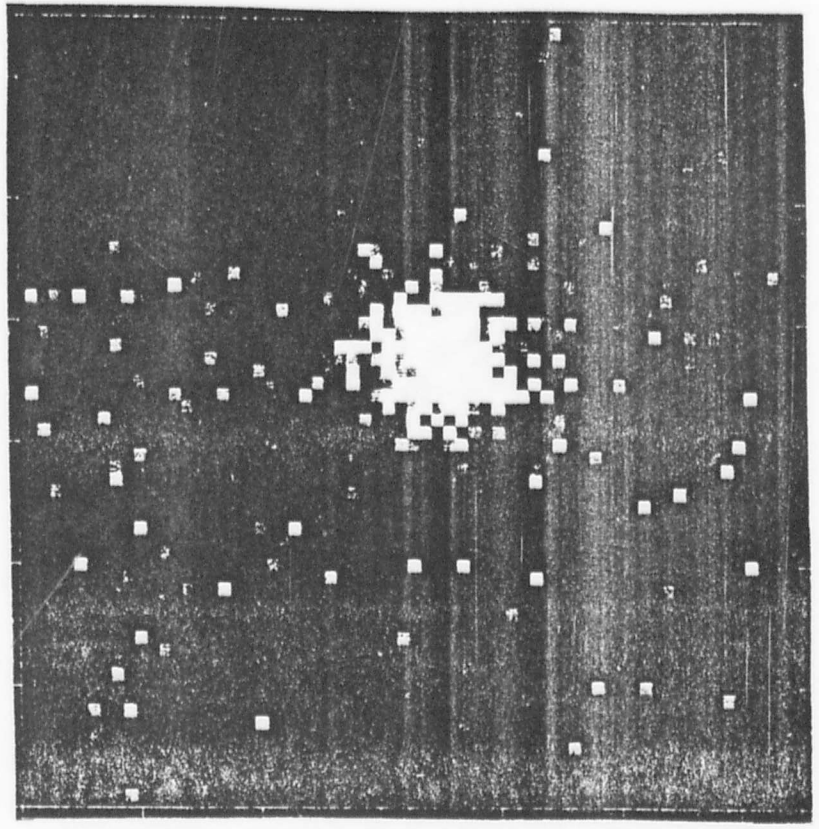

Figure 6: Differential image of α Ori : MMT December 1983

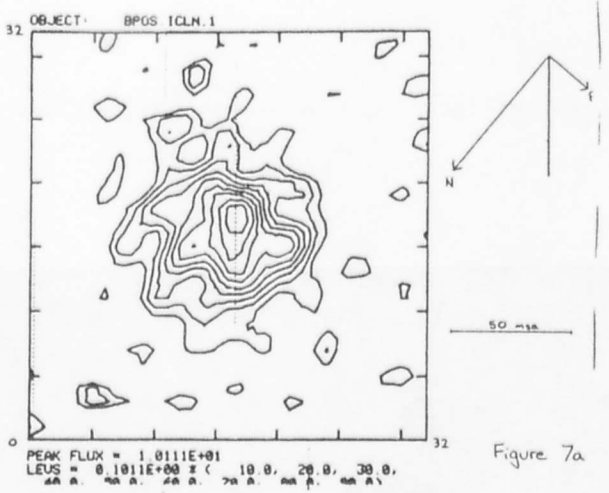

Figure 7a

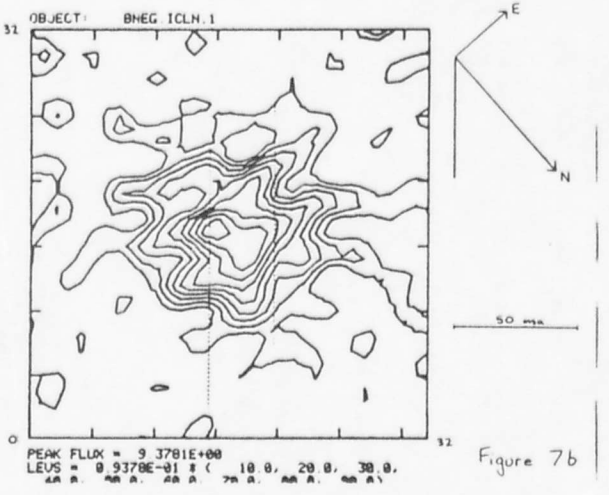

Figure 7b

Figure 7: Differential images of α Ori after removal of filtering effects

IMAGE RECONSTRUCTION
from
ASTRONOMICAL SPECKLE INTERFEROMETRY
(Theory and Practice)

Sponsor: Air Force Office of Scientific Research
Dr. Henry Radoski
Bolling Air Force Base
AFOSR/NP
Washington, D.C. 20332

Abstract

The goal of achieving diffraction limited images from specklegrams obtained at ground-based telescopes now appears to be within reach. A number of groups in several countries have contributed to this advance. We therefore organized an informal workshop on the subject with participation limited to those actively involved in the field. Fifty participants presented an overview of their work and discussed problems and progress.

Dates: 10-13 April 1983

Location: The University of Arizona Conference Center
Oracle, Arizona

Conference Hosts: Keith Hege
University of Arizona

Christopher Dainty
University of Rochester

Costas Papaliolios
Harvard University
and
Smithsonian Astrophysical
Observatory

Nature of the Conference

The goal of the conference was to work on the definition of the next stages of research towards the solution of the problem of diffraction limited imaging through the turbulent atmosphere. This was a working conference/seminar for those currently active in the field and, through a natural process of self-selection, was kept small. A residential conference setting was provided to encourage productive exchange of ideas. No proceedings will be published. All presentations were made as informal exchanges not to be referred to as published material. Only this brief report, intended for private use by the participants, exists.

The sessions included invited papers, contributed reports, spontaneous presentations, and questions with ample time for discussion. Poster presentations were also encouraged. This workshop was specifically arranged, to allow spontaneous organization of informal working sessions on topics raised by the scheduled sessions. Each attendee was expected to make a contribution, formal or informal, especially emphasizing the particular limitations and problems encountered in the work being presented.

A synopsis of the actual events, as recorded by Chris Dainty follows. A group photograph, courtesy of Jim Fienup, is appended together with the conference attendance roster. A longer list of people who have been identified as having interests related to the subject of this conference is available upon request from Keith Hege, Steward Observatory, Tucson, AZ 85721.

IMAGE RECONSTRUCTION FROM ASTRONOMICAL

SPECKLE INTERFEROMETRY - THEORY AND PRACTICE

A Workshop held at Oracle, Arizona, 10 - 13 April, 1983.

Co-hosts: Keith Hege, Chris Dainty, Costas Papaliolios

Sponsored by the Air Force Office of Scientific Research

Program

1. Experience : Astronomical Results (Chairmen: K. Hege, P. Nisenson)
2. Experience : Systems (Chairman: H. McAlister)
3. Image Reconstruction : General Methods (Chairman: C. Dainty)
4. Image Reconstruction : Modulus - Only Methods (Chairman: J. Fienup)
5. Arrays and Future Techniques (Chairman: Peter Strittmatter).

This workshop was a relatively informal gathering of about 50 specialists in astronomical high angular resolution imaging, including the visible, IR and radio wavelengths. Approximately 2/3 of the time was allocated to 44 "formal" presentations, the remaining time being for free discussion.

Peter Strittmatter, the Director of Steward Observatory, welcomed those present, and introduced the subject by reviewing the astronomical achievements of speckle interferometry in the decade or so since the invention by Antoine Labeyrie. These achievements include measurements of asteroids, planets, the Sun, binary stars, giant and variable stars, protostars, and extra-galactic objects.

I. Experience : Astronomical Results

There were 13 presentations describing astronomical results obtained using speckle interferometry, with many speakers concentrating on problems that arise in getting results from speckle data. Bob Stachnik (Harvard) reported measurements on Io, Uranus, Neptune, Titan and the Sun. For extended objects (low contrast speckle), an ISIT detector has a small dynamic range, a poor pulse height distribution, and other features that make it inadequate for speckle imaging. His opinion is that a CCD detector is best for high light levels (10 bit grey levels are needed) and a true photon counter for low light levels. A problem in their solar work is that there is no atmospheric MTF available, so that the absolute contrast of features cannot be determined.

Jack Drummond (Steward Observatory) described measurements on asteroids, particularly Eros. By parameter fitting, its properties have been extracted from sets of speckle data and these agree well with other predictions. About 15 asteroids per quarter brighter than 12 magnitude are observable.

Hal McAlister (Georgia State University) summarized binary star speckle interferometry. Currently there exist about [illegible] measurements on approximately 600 binaries (about 60% by McAlister). The maximum magnitude difference detectable by speckle appears to be only $\Delta m_v = 3$, and no-one routinely determines Δm due to system nonlinearities. He stressed the importance of accurate calibration of the plate scale and the need for a large telescope to obtain lower errors. A slide showing the contribution of speckle observations to the mass-luminosity curve was also shown.

Gerd Weigelt (Univ. of Erlangen-Nurnberg) presented two measurements of Pluto-Charon, showing Charon moving around Pluto; only 15,000 frames gave useful data on this 16th magnitude system. He has also reduced data on NGC 1068 and the triple quasar (using a 1.5 m telescope). He showed images of binary stars obtained by the speckle masking (triple correlation) method, stressing that the magnitude difference is obtainable to less than ±.2 in this initial data. He briefly described the technique of speckle spectroscopy.

Jacques Beckers (Steward Observatory) presented an image of Betelgeuse in H-α emission obtained by "speckle spectroscopy"; this assumes a form for the continuum image, which is used as a reference for the H-α emission data. He is using tunable filters of $\Delta\lambda = \frac{1}{2} - 1\frac{1}{2}$ Å with bands 1-8 Å apart for both this and for differential speckle interferometry. This latter technique is proposed for measuring the position angle of binaries and the axis of rotation of rotating stars.

Jon Freeman (Steward Observatory) showed speckle spectroscopy data on α-Tau and γ-Cas, obtaining diameter v wavelength in the range 520-700 nm.

François Roddier (Univ. of Nice) showed energy spectra of Betelgeuse obtained by pupil plane interferometry using his rotation-shearing interferometer. This type of interferometer requires less calibration (or none?) than speckle as regards the atmosphere and has a higher SNR at very high light levels. It appears to require a higher resolution detector, due to the fact that (like a hologram) the information is carried on fringes; a factor of two was suggested.

C. Perrier (ESO) described IR image reconstruction at 5 μm on η-Car. According to Fried, the probability of a "good" ($\Delta\varphi \leq 1$ rad) image is $\exp\ (-.15(D/r_o)^2)$, and with r_o proportional to $\lambda^{6/5}$ this looks good at 5 μm. He compared Knox-Thompson, Wiener restoration, Biraud restoration (all positive) and maximum entropy (MEM) on short exposure data; tentatively, the MEM seemed to be most reliable.

Alain Chelli (Observatoire de Lyon), in an IR study of the Orion-KL region, used the BN object as a reference to reconstruct an image of RC2, 9 arc sec distant. The result confirms that RC2 is the primary source in the cloud.

Bob Howell (Univ. of Hawaii) presented the power spectra of T-Tauri at K, L and M, clearly showing its duplicity. He stressed two problems: first that variable seeing makes calibration by a reference extremely difficult (variable seeing is worse than conventionally "poor" seeing) and second that it was easy to pick up a 60 cycle component from the chopping secondary. He also showed image reconstruction on Mon R2IRS 3 using the Knox-Thompson algorithm.

Don McCarthy (Steward Observatory) gave some results from his extensive study of astrometric binaries (stars with variable proper motion); his table of results included Ross 614, Wolf 1062, CC986, α-Oph, μ-Cas and many others. the largest Δm being approximately 3.7 (all were observed at K). He mentioned the difficulty of finding good reference stars (i.e. finding stars known to be point sources). The need for images was illustrated by the data on χ-Uma, a complicated object containing at least four sources. The BN object (assumed unresolved by Chelli) is resolved and he has applied a modified version of Walker's algorithm (takes the average of each "half" of the Walker method) to BN, which has an East-West diameter at K of .8 arc sec.

Bill Bagnuolo (Aerospace Corp.) has applied Bates' "shift-and-add" algorithm to Capella speckle data; it appears that the orbit as published by McAlister and others should be rotated 180°.

Finally in this session, Ron Ekers (NRAO), addressing those who were not necessarily "black belt interferometricists", discussed some problems in radioastronomy, in particular the use of closure phase and of techniques such as CLEAN and MEM.

2. Experience : Systems

Hal McAlister described the Georgia State University speckle camera for binary star speckle. It uses a dual microchannel plate (ITT, $17,000 in 1980) coupled to a CCD (244x248 pixels). The image tube can act as the shutter; an RCA videotape recorder, modified by the addition of stepper motors for still frame analysis, is used to record data, which is analyzed after the observing run. The image tube is currently not cooled, and has about 50 dark counts/sec at room temperature over the field.

Costas Papaliolios (Harvard) described his photon event counting system. The counting rate is limited by the P47 phosphor (τ = 200 ns) to about 10^6sec, although currently they can only handle 10^5/sec. The x and y 8-bit coordinates of photons are sequentially recorded on modified videotape recorder for processing after observations. The system described in the SPIE Proceedings (Vol. #331) had problems (but still worked): field curvature, vignetting, exponential pulse height distribution and low quantum efficiency. These are overcome by a new optical system and the use of a variable threshold on the photomultiplier signals. He pointed out that Koechlin's method of implementing the Knox-Thompson algorithm is easy with the output of this device; bias corrections are also straightforward.

Jeremy Hebden (Imperial College) reported observations of R136a, NGC 1068, 1 ZW 1, NGC 3372, NGC 4151 and the binary in the Red Rectangle with a photon correlator system. The problem of the photon noise spike is still not satisfactorily resolved.

Kenneth Jason (Imperial College) described a 4-channel IR speckle system (J or H, K, L and M wavelengths) under construction; since the design uses a single slit (or grating), there is a problem in making simultaneous observations at all

four wavelengths.

Chris Dainty (Univ. Rochester) illustrated the practical problem of using a reference star for atmospheric calibration in the IR; possible solutions are (a) model fitting using r_o estimated from the object scans, for barely resolved objects, (b) ad hoc polynomial fitting and statistical analysis of the data, (c) only observe in stable conditions. He was also advised to stick to theory.

J.M. Mariotti (Observatoire de Lyon) presented measurements of the variation of r_o with time at 4.6 μm. The parameter r_o appears to be distributed with a log normal low, the scatter being a function of r_o. The power spectrum of r_o was also shown; it appeared to consist of a "DC" component (white noise) with low frequency peaks (periodic components of r_o).

François Roddier described how his rotation-shearing interferometer works; it forms an incoherent hologram. He described how the polarization properties of it were made constant. Achromatic fringes can be formed with a finite field of view, unlike the speckle case, but there is a centering problem. Gerd Weigelt commented that, in the laboratory, he had used this type of interferometer to get the modulus (roughly independent of the "atmosphere") and used speckle masking to get the phase.

Keith Hege (Steward Observatory) briefly described the Steward Observatory speckle camera. It uses an ISIT, with a photon centering algorithm and software vector autocorrelation (all off-line). They have had moderate success using Worden's algorithm to reduce the sensitivity to seeing.

Pete Worden (USAF) discussed some US Air Force objectives in their support (since ~ 1976) of astronomical speckle interferometry. Particular interests are imaging the solar surface and nearby objects such as satellites. The

requirement of 1 m resolution of satellites implies 10 m diameter Earthbased telescopes; he emphasized the potential cost-effectiveness of ground-based observations, using either adaptive optics or interferometry.

3. Image Reconstruction I : General Methods

Pete Nisenson described the Harvard Group's implementation of the Knox-Thompson algorithm. He stressed the problem of the photon spike, the use of the average image to calibrate the photon noise, and the need for a good camera. The first stage of the algorithm consists of the bootstrap process; the second stage involves averaging using the four nearest neighbors, with perhaps 20 iterations. The results of a signal-to-noise analysis show that the SNR is essentially the same as normal speckle interferometry. He showed a demonstration on a (laboratory?) 11 magnitude/pixel object (5 magnitude when integrated), showing the importance of the quantization of gray levels (20 → 100 → 500 → 1000).

At 9.52 a.m., the session chairman noted that outside a blizzard was blowing; although some Arizonians lost their cool, most participants remained calm.

Jim Sherman (Analytic Information Processing) discussed the importance of noise correction and illustrated this for additive, Poisson and multiplicative noises. He also described the effect of non-isoplanicity.

Richard Barakat (Harvard) described the effect of aberrations on the Knox-Thompson algorithm. On-axis (symmetrical) aberrations have little effect, but off-axis aberrations, such as coma, have a strong effect. He also briefly described the interaction of turbulence and aberrations via time-integration.

John Walker (RSRE), who discovered the exponential filter method, gave a description of it; the exponential slope should be chosen to attenuate the object by about

a factor of 4 at one edge. He stressed the practical aspects : trying six starts of the Fienup algorithm gave six different images (computer simulation) but six starts of the exponential filter algorithm always gave the correct result.

Richard Bates (Univ. of Canterbury) started by describing what a Wiener filter was (there had be n some confusion earlier about this). He then described t.. shift-and-add method, pointing out that it was insensitive to aberrations (like ordinary speckle interferometry). The background fog is a result of the incoherent nature of the imaging, and is not obtained in the coherent case, which was illustrated by some ultrasonic speckle results that he showed.

Jim Fienup (ERIM) reviewed the iterative algorithms that have become attached to his name. There are several, the most useful two being the "error reduction" and the "hybrid input-output". He showed the effect of photon noise of the object on reconstructions; 100 photons / pixel gives good results, 10 photons/pixel was bearable and even 1 photon/pixel on average gave something recognizable in the given example. He discussed the "bands" or "stripes" that are sometimes obtained and suggested that these could be eliminated by adding known noise at the start and subtracting it at the end (Ron Ekers said that the radioastronomers also do this technique to get rid of artifacts). The iterative algorithms can fail, particularly on objects with symmetries.

Alan Greenaway (RSRE) and Nigel Arnot (Queen Elizabeth College) described an interferometric technique, based on phase closure and similar to the method of Rhodes and Goodman, that recovered images from a single frame of object data. One needs 10^4 - 10^6 photons/pixel, so it would only work on the Sun.

4. Image Reconstruction : Modulus-only Methods

Richard Bates, in an after-dinner entertainment with a message, stressed the importance of using a combination of methods to solve the phase problem. He gave the example of using the following combination; defogging, the Canterbury interpolation/phase closure algorithm, Fienup, refogging. The interpolation/phase closure algorithm uses oversampling of the power spectrum to estimate the absolute values of phase differences and phase closure to decide the signs. Chris Dainty commented on aspects of the method where improvement was needed for complicated objects.

Bryan Brames (Univ. Rochester) showed how Eisenstein's criterion could be used to test whether an object was guaranted to have an unique solution to the phase problem. Fienup's algorithm coverges much faster for such objects, which have a reference point (similar but not identical to holography).

Jim Fienup showed how, for objects of convex support, it was possible to reconstruct from the support of the autocorrelation. He also presented a recursive algorithm for reconstruction of Eisenstein objects. The reference points in such objects sift out one or more rows, which can be used as a starting point for the recursive algorithm.

John Cocke (Steward Observatory) described how Bochner's theorem (which concerns the positive definiteness of functions) can be used to incorporate the positivity constraints in practical algorithms. For example, the power spectrum of a positive object must satisfy $P(0) + 1/3\ P(2f) \geq 4/3\ P(f)$.

Alan Greenaway discussed uniqueness in modulus-only reconstruction, stressing that different starts in the Fienup algorithm could give different "converged" images in certain cases involving symmetry.

Finally in this session, Richard Barakat, said that he had found necessary conditions for uniqueness of the n-dimensional continuous (not discrete) phase problem and that they indicated that the solution in two or more dimensions would always be unique in practice. An algorithm to find the phase from the modulus had been written for one dimension (which is non-unique) and the two dimensional algorithm should be written this summer.

5. Arrays and Future Techniques

Bob Stachnik described a tentative design for a space interferometer comprising three free-flying spacecraft (two telescopes and a beam-combining station). The baseline would vary in the range 0-10 km as they circled the Earth, giving resolution of up to 10^{-5} arc sec at 15-20th magnitude with 1 m collectors. He also reviewed possible astronomy that could be done with such a system. Gerd Weigelt commented on a similar European design, indicating a limiting magnitude of 24.

J. Mariotti described the current status of the CERGA interferometers. The small system, with two 25 cm apertures, is being used at baselines up to 60 m both in the visible and IR. A large variation of fringe visibility with time was reported. Measurements of the phase differences at intervals of .1s were described, these being greater at a 16 m baseline than at an 8 m baseline. In the large telescope system, the second 1.5 m tel scope is almost ready; there has been some problems with the novel mounts. A limiting magnitude of at least $m_v = +7$ is expected.

Jacques Beckers reported on the status of the "Very Small Array" (VSA), more commonly known as the Multiple Mirror Telescope (MMT), as regards interferometry. Three mirrors have been phased in the optical region. With all six mirrors, the spatial frequency plane is full and optical systems to phase this in both the visible and IR are

under construction (IR system by Low and McCarthy).

Nick Woolf (Steward Observatory) presented some Optical/IR/Radio parallels that appeared to point to working in the diffraction-limited regime with a filled, background limited array. The compromise between speckle interferometry and adaptive optics was discussed.

Richard Bates, commenting on optical synthesis telescopes, made the point that complexity (yielding redundant data) may be preferable to a simple but highly toleranced system in VLBI; he stressed how VLSI electronics will influence the reduction of complex data. Oversampling for the phase is also important. Similar arguments apply in space as well.

Gerd Weigelt talked about the "speckle" in the space telescope images. This is essentially deconvolution, and an optical system for the faint object camera has been built to ensure that the image is sampled sufficiently finely.

Chris Dainty discussed possible techniques of using the time information in imaging through turbulence. A SNR analysis by himself and O'Donnell has shown no significant advantage over normal speckle, but there may be useful information for object reconstruction techniques.

Charles Kenknight (Univ. of Arizona) suggested using both pupil and image plane data to obtain object reconstructions to 10 magnitude. He suggested a grating shearing interferometer for pupil plane measurements.

This summary would not be complete without an expression of thanks on behalf of all the participants to Keith Hege who put it all together, to the projectionist for his patience, and to the staff of the University of Arizona Conference Center at Oracle for their hospitality.

Chris Dainty

April 20, 1983

CONFERENCE ATTENDANCE ROSTER

1. Aizenman, Morris
(202) 357-7643
Astronomy Section
National Science Foundation
Washington, D.C. 20550
U.S.A.

2. Arnot, Nigel
(01) 937-5411
Queen Elizabeth College
Physics Dept.
Campden Hill Road
W/8 London
ENGLAND

3. Bagnuolo, William
Aerospace Corporation
Building D8 M/4 939
P.O. Box 92957
Los Angeles, CA 90009

4. Bates, Richard H. T.
(03) 588-4781
Dept. of Electrical Engineering
University of Canterbury
Christchurch 1
New Zealand

5. Barakat, Richard
(617) 495-4781
Aiken Computation Lab
Harvard University
Cambridge, MA 02138

6. Beckers, Jacques
(602) 621-1812
Multiple Mirror Telescope Obs.
University of Arizona
Tucson, AZ 85721

7. Beckwith, Steve
(607) 256-4807
Dept. of Astronomy
Space Sciences Bldg.
Cornell University
Ithaca, NY 14853
U.S.A

8. Bracewell, Ron
(415) 857-9263
836 Santa Fe Avenue
Stanford, CA 94305
U.S.A.

9. Brames, Bryan
Institue of Optics
University of Rochester
Rochester, NY 14627
U.S.A.

10. Cady, Frederick
(406) 944-2501
Dept. of Electrical Engineering
Montana State University
Bozeman, MT 59717
U.S.A.

11. Chelli, Alain
856-0705
Observatoire de Lyon
69230 St. Genis-Laval
FRANCE

12. Christou, Julian
(602) 621-1049
Dept. of Astronomy NMSU
Steward Observatory
University of Arizona
Tucson, AZ 85721
U.S.A.

13. Cocke, John
(602) 621-6540
Steward Observatory
University of Arizona
Tucson, AZ 85721
U.S.A.

14. Dainty, J. C.
(716) 275-2323
Institute of Optics
University of Rochester
Rochester, NY 14627
U.S.A.

15. Drummond, Jack
(602) 621-1459
Steward Observatory
University of Arizona
Tucson, AZ 85721
U.S.A.

16. Ebstein, Steve
(617) 495-7459
CEPP Harvard University
29 Oxford Street
Cambridge, MA 02138
U.S.A.

17. Ekers, Ron
(505) 772-4297
National Radio Astronomy Obs.
P.O. Box 0
Socorro, NM 87801
U.S.A.

18. Fienup, Jim
(313) 994-1200
ERIM, Box 8618
Ann Arbor, MI 48107
U.S.A.

19. Fraser, Don
Steward Observatory
University of Arizona
Tucson, AZ 85721
U.S.A.

20. Freeman, Jon
(602) 621-1049
Steward Observatory
University of Arizona
Tucson, AZ 85721
U.S.A.

21. Greenway, A. H.
06845-2733+3342
RSRE
St. Andress Road
Great Malorn
WR/4 3PS U.K.

22. Hanson, Don
(315) 330-1110

RADC
Griffiss ARB
New York 13441
U.S.A.

23. Harvy, J. W.
(602) 327-5511

Kitt Peak National Observatory
Box 26732
Flagstaff, AZ 85726
U.S.A.

24. Hebden, Jeremy
(589) 5111-2543

Dept. of Physics
Imperial College
Prince Consort Road
London, SW7 2BZ
ENGLAND

25. Hege, Keith
(602) 621-1049

Steward Observatory
University of Arizona
Tucson, AZ 85721
U.S.A.

26. Howell, Robert
(808) 948-8534

Institute for Astronomy
2680 Woodlawn Drive
Honolulu, HI 96822

27. Jason, Kenneth
349-1466

Dept. of Physics
Imperial College
Prince Consort Road
London, SW7 2BZ
ENGLAND

28. Kenknight, Charles

29. Lynds, Roger
(602) 327-5511

Kitt Peak National Observatory
Tucson, AZ 85726
U.S.A.

30. Mariotti, J. M.
7-856-0705

Observatoire de Lyon
F-69230 Saint-Genis-Laval
FRANCE

31. McAlister, Hal
(404) 658-2932

Dept. of Physics
Georgia State University
Atlanta, GA 30303

32. McCarthy, Don

Steward Observatory
University of Arizona
Tucson, AZ 85721

33. Nisenson, Peter
(617) 495-2829

Center for Astrophysics
60 Garden Street
Cambridge, MA 02139

34. Papaliolios, Costas
(617) 495-7459

Dept. of Physics
Harvard University
Cambridge, MA 02138
U.S.A.

35. Perrier, C.
(89) 320-06-245

European Southern Observatory
Karl Schwarzschild Stra/22
D-8044 Garching bei 7 unchen

36. Ponsonby, John
0477-71321

University of Manchester
Jodrell Bank
Macclesfield, Cheshire
ENGLAND

37. Radick, Richard
(505) 434-1390

Sacramento Peak Observatory
Sunspot, New Mexico 88349
U.S.A.

38. Radoski, Henry
(202) 767-4906

AFOSR/NP
Building 140
Washington, D.C. 20332
U.S.A.

39. Ridgeway, Steve
(602) 327-5511

Kitt Peak Observatory
Box 26732
Tucson, AZ 85726
U.S.A.

40. Roddier, Francis
(33-93) 84-09-66

Dept. of Astrophysique
de 1' I.M.S.P
Universite de Nice
Parc Valrose
X 06034 Nice-Cedex
FRANCE

41. Sherman, Jim
(415) 837-2803

Analytic Information Processing
Box 966
Danville, CA 94526
U.S.A.

42. Shough, Dean
(415)493-4411 Ext. 45164

Lockheed
3251 Hanover
Palo Alto, CA 94304

43. Stachnik, Bob
(617) 495-2829

Center for Earth & Planetary Sci.
Harvard University
Cambridge, MA 02214
U.S.A.

44. Strittmatter, Peter
(602) 621-6524

Steward Observatory
University of Arizona
Tucson, AZ 85721
U.S.A.

45. Van Citter, Wayne

National Science Foundation
1800 G. Street N.W.
Washington, D.C. 20550

46. Von der Luhe, Oskar
0-761-32864

Kiepenheuer-Institute
for Sonnenphysik
Schoneck Strasse G
D-7800 Freilburg

47. Walker, J. G.
06845-2733 Ext. 3031

Royal Signals & Radar Est.
Malvern
Worcs. WR14 3PS
ENGLAND

48. Weigelt, Gerd
0-131-857204

Physikalisches Institut
Univ. Erlangen-Nurnberg
8520 Erlangen
WEST GERMANY

49. Woolf, Nick
(602) 621-4897

Steward Observatory
University of Arizona
Tucson, AZ 85721
U.S.A.

50. Worden, Simon (Pete)
(213) 643-0676

Chief, Advanced Tech. Div. (SDIYBA)
Box 92960 Worldway Postal Center
Los Angeles, CA 90009
U.S.A.

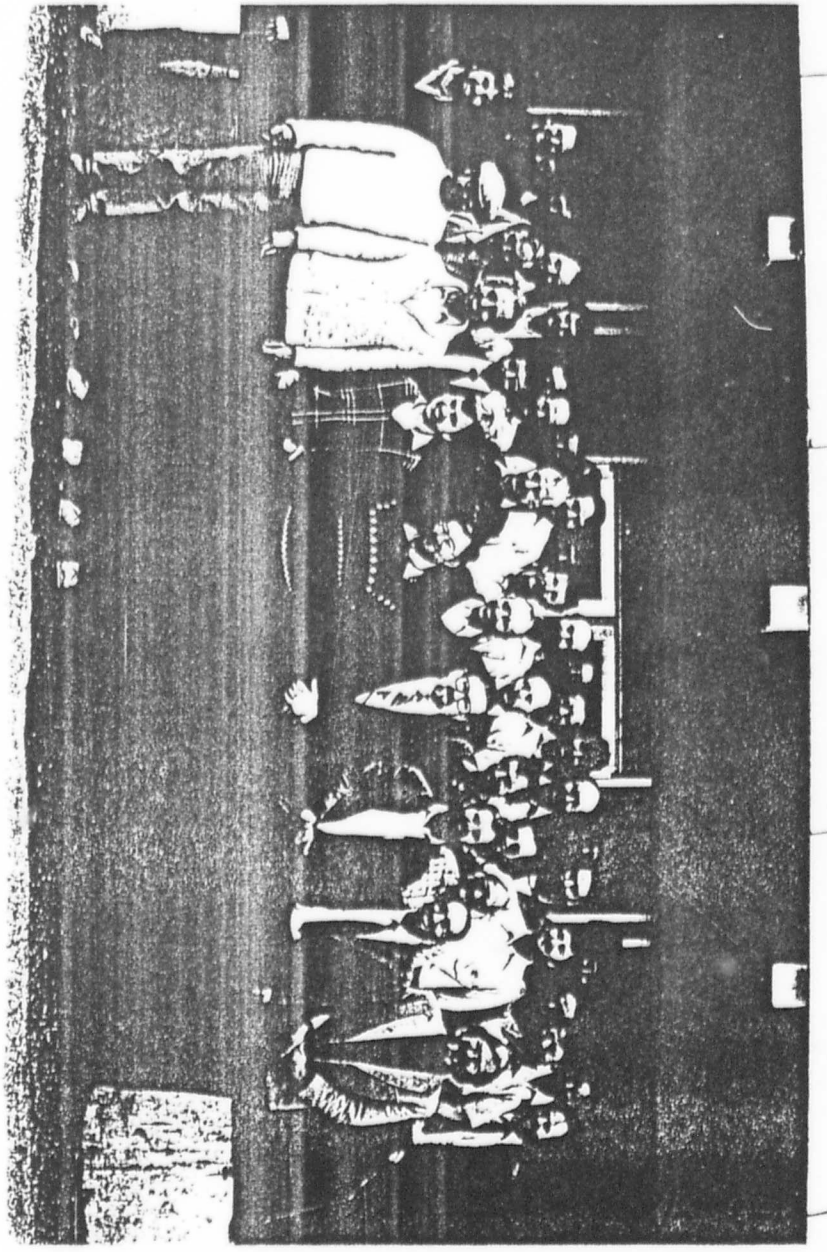

RECOVERY OF BINARY STAR ORIENTATION AND RELATIVE INTENSITY
A Comparison of Speckle Techniques[+]

E.K. Hege*, J.C. Christou, J.D. Freeman and W.J. Cocke

Steward Observatory
Tucson, AZ 85721

W. Bagnuolo

Aerospace Corporation
Los Angeles, CA 90009

and

D. Granrath

Science Applications International Corporation
Tucson, AZ 85711

*Visiting Astronomer Kitt Peak National Observatory[++]

[+]Some of the data reported here were obtained using the Multiple Mirror Telescope, a joint facility of the University of Arizona and the Smithsonian Institution.

[++]Kitt Peak National Observatory is a division of the National Optical Astronomy Observatories, operated by the Association of Universities for Research in Astronomy, Inc., under contract to the National Science Foundation.

To be Submitted to **Astroomical Journal**

DRAFT 1 Jun 85

ABSTRACT

Astronomical speckle interferometry data sets for Capella and for the Lunar occultation binary 115 Tau obtained with various telescopes, and a set of simple, photon noise free simulated specklegrams for a triple star have been analyzed using several image reconstruction processes in order first to check their ability to retain quantitative relative amplitude information and second to compare the computational efficiency of the algorithms. Well calibrated, simple Labeyrie power spectrum analysis can give reliable intensity estimates in addition to (ρ,Θ) measures, but orientation information (mod 180°) is lost. An amplitude squared weighted shift-and-add cross-correlation gives the relative amplitudes and orientation but contains a strong seeing bias. A weighted shift-and-add deconvolution gives that as well as a seeing self-calibration. This analysis can be applied to fainter objects when matched filter techniques are used to locate individual speckles. A screened shift-and-add method is also quantitative, although non-linear and like the amplitude squared cross-correlation includes a seeing bias. For the weighted shift-and-add cross correlation and the screened shift-and-add the seeing bias can be effectively modelled with a Gaussian profile and subtracted away. The Knox-Thompson technique, and a phase unwrapping scheme also are quantitative, and when combined, using the Fienup iterative method, with amplitude calibration given by contemporaneous observation of a point source calibrator give good amplitude fidelity and seeing compensation. This last combination of methods is the most computationally expensive, but the best understood theoretically. All of the methods appear to give equivalent fidelity to the original source when analyzing the same data. A maximum norm power spectrum method was also applied to the Capella data set

and found to produce good relative amplitude recovery, but (because it is a power spectrum technique) it does not give quadrant resolution. Applications in differential speckle interferometry, (α ORI) and speckle holography (α SCO), which use binary star techniques, are also presented.

1. INTRODUCTION

Labeyrie (1970) first pointed out that the short exposure images (specklegrams) of the seeing perturbed telescope image contained information on the structure of the source up to resolutions corresponding to the diffraction limit of the telescope.

During the past several years there has been a rapid development in speckle interferometry techniques for achieving high resolution imaging through the earth's atmosphere using large ground based telescopes. Speckle interferometry (See review by Dainty,1984) produces diffraction limited results with spatial resolution gains of $\sim 10^2$ over that normally permitted by the earth's atmosphere. Our work has demonstrated the technique for asteroids (Drummond et al.,1985a,1985b,1985c), artificial satellites, bright, resolvable stars and other celestial objects (Hege, Strittmatter and Woolf, 1984). It has furthermore been applied to sources as faint as m_v - 16, (Hege et al., 1981,1982b). Although we make no attempt to exhaustively review the subject, others have had similar successes, notably McAlister's extensive binary star program (e.g. McAlister and Hartkopf, 1984), the Harvard group (e.g. Nisenson and Papaliolios, 1983 and Papaliolios, Nisenson and Ebstein, 1985), Weigelt, et al. (Angewandte Optik, 1983) and the Imperial College group (e.g. ----------).

Past successes have relied heavily upon autocorrelation function or power spectrum analysis for binary star research, as this method gives a simple, accurate measure of separation (ρ) and position angle (θ - Mod 180°). Determination of quadrant (e.g. Bagnuolo and McAlister, 1983) and of relative magnitudes (e.g. Bagnuolo, 1982, Hege et al.,1983, [Imp. Coll. ref.], McAlister, ----) has been a more difficult problem, especially in optical wavelengths (for IR experience, see e.g. McCarthy, ----). Recent

detector developments (e.g., Papaliolios, et al, 1985) and advances in image reconstruction methodology, being evaluated in this work, appear to allow resolution of these last two deficiencies.

In classical speckle interferometry, the specklegrams are recorded and then processed to yield the autocorrelation (AC) or power spectrum (PS) of the object. Thus the n^{th} specklegram (magnified, narrow-band, short-exposure image) $i_n(x,y)$ of the object is represented by the convolution (* implies convolution)

$$i_n(x,y) = o(x,y) * p_n(x,y) \qquad (1.1)$$

where $p_n(x,y)$ is the point-spread function of the atmosphere plus instrument for the n^{th} specklegram and $o(x,y)$ is the object as seen above the atmosphere. Using the Fourier transform notation $FT(i_n(x,y)) = I_n(u,v)$, taking Fourier transforms of many specklegrams and averaging the square modulus yields

$$\langle|I_n(u,v)|^2 = |O(u,v)|^2\langle|P_n(u,v)|^2\rangle \qquad (1.2)$$

This result may be inverted to yield the object power spectrum $PS_o = |O(u,v)|^2$ for those spatial frequencies (u,v) for which the speckle transfer function $STF = \langle|P_n(u,v)|^2\rangle$ is bias free and non-zero.

The methods we report here fall into two groups, depending upon the degree to which they are self-calibrating for the seeing bias introduced by the speckle transfer function STF. We discuss first the more conventional techniques in which both the seeing bias and aperture/detector effects must be calibrated by reference to a set of observations of an unresolvable source.

In the ideal case the STF is non-zero to the diffraction limit of the telescope and is determined by making interspersed observatioins of a point source calibrator. In practice, the STF is not bias free and many other corrections, depending upon detector and observing conditions, are required: examples are correction of geometric distortion, removal of photon statistics bias, etc. Calibration of this speckle transfer function is fundamental to all of the procedures utilized in this study.

The limitation to power spectrum information is in some applications a serious one; direct image information is clearly preferable. For this purpose it is necessary to obtain (or retain) both the phase and the amplitude of the Fourier components. Direct phase information can be integrated from individual specklegrams using the Knox-Thompson (1974) algorithm (or variations thereon, e.g., Nisenson and Papaliolios 1983) or by the imageplane shift-and-add techniques (again including many variations) developed by Bates and Cady (1980), Hunt, Fright and Bates (1982), Bates and Fright (1983), Bagnuolo (1983), the original method of Lynds, Worden and Harvey (1976), and a new self-calibrating procedure developed at Steward Observatory (Christou, Ribak, Hege and Freeman, 1985). These methods provide phase information for either direct use or for input to the Fienup (1978,1979) or related procedures (e.g., Bates and Fright 1983) for image touchup. These amplitudes-only techniques seek to derive phase information from the Fourier amplitudes alone, without startup phase information, but would be ambiguous mod 180^o.

The calibration of simple speckle interferometric power spectrum observations requires

(i) integration of of individual frame power spectra, $PS = \langle|I_n(u,v)|^2\rangle$, defined by 1.2; or equivalently integration of individual frame autocorrelation function

(ii) standardization of each observation with corresponding

measurements of an unresolved point source, $PS_p = \langle |I_{pn}(u,v)|^2 \rangle$, suitably controlled for variable seeing conditions (discussed further in Christou et al., 1985)

(iii) measurement of the detector transfer function $DTF = |D(u,v)|^2$. DTF represents the photon point spread response of the detector, which for our intensified television video raster detector is variable over the image space (x,y) (Hege et al., 1980).

The resulting object power spectrum, calibrated for aperture and seeing effects, can then be estimated by computing (see Hege et al., 1982a).

$$|O(u,v)|^2 \quad \frac{[PS_o/|D_o(u,v)|^2 - N_o]}{[PS_p/|D_p(u,v)|^2 - N_p]} \qquad (1.3)$$

where N_p and N_o are the noise bias associated with the point source and the object power spectra, respectively, produced by the image sampling process. The detector transfer function $DTF = |D(u,v)|_i^2$ is measured by integrating the individual frame power spectra for random events detected subsequent to illumination of the detector with uniform, low intensity light, digitized in the same way as for the point source and the object, respectively.

The division by the point source calibration result removes the seeing bias as well as the residual mean speckle distortion. Division of the observed PS's (coadded - averaged - individual frame PS's) for both the object and the point source calibrator by the corresponding DTF's and subsequent subtraction of the corresponding N's (= mean number of photons per frame, if DTF's and PS's are normalized) removes the photon noise bias in the numerator and denominator of this object power spectrum estimator, eq 1.3.

Some of our recently developed techniques produce results which, to first order, are free of the seeing bias component of the speckle transfer function. There remains, in this second approach, the problem of removal of aperture and detector effects, but as these are, also to first order, time independent. These also require observation of an unresolvable source for their calibration, which can be accomplished by application of, e.g., the algorithm CLEAN as used in radio astronomy.

2. THE DATA BASE

In this study we evaluated, by comparisons using both a simulated data set and real astronomical data, several methods for diffraction limited reconstruction of speckle image data including the phase retrieval method of Knox and Thompson and several variations on shift-and-add methods, as well as conventional Labeyrie power spectrum analysis.

Our speckle interferometry system (Hege et al., 1982a) uses an intensified plumbicon camera with sufficient gain and dynamic range to observe either image amplitude (Analog - bright object, atmospheric statistics dominated) or photon coordinate (Event - faint object, photon statistics dominated) data. In regular use at the 2.3m and KPNO 4m telescopes and at the MMT, it produces frame subtracted data (to suppress detector lag), digitized 8-bits deep, at standard video frame rates corresponding to a bit-rate of approximately 60 MHz at full resolution, sufficient to sample the 6.9m diffraction limit of the MMT over a 1 arc second field of view. The 4 stages of Varo image image intensifiers can be operated as a variable attenuator, to allow observations of objects of all brightnesses, so that the digital video system has maximum detective quantum efficiency at the gain required for photoelectron event detection. We use a video recorder to archive the data at the telescope , with a duty cycle of unity. Using a Grinnell digital television system, data from the ideo recordings is again digitized (8-bits) and logged on 9-track magtape for subsequent reduction.

Data acquired in differential speckle interferometry mode (DSI - Beckers, 1982) was obtained using the differential speckle camera described by Beckers, Hege and Murphy (1983) in conjunction with the digital video procedures described here.

The simulated triple star specklegrams were generated in a very simple

(atmospherically unrealistic but computationally useful) approximation which placed randomly weighted (uniform distribution $0 < w < 1$) perfect, diffraction images of a triple point source at random locations (normal distributioin about frame center) in the specklegram frame. Ten frames of about 100 speckles per frame were generated for these studies. Our very limited computing capabilities (at that time) limited us to this statistically modest sample.

3. IMAGE RECONSTRUCTION

The development of fundamental capabilities for speckle image reconstruction and of a basic understanding of the atmospheric processes involved in high resolution imaging procedures has been the central objective of our work. Only recently has this effort come to fruition in the development of methods which yield valid point spread functions (aperture diffraction patterns) for point sources (Christou et al., 1985). That was the first crucial step in validation of these methods. This work focuses on further validation and optimization of procedures for reconstructing images of binary stars, the next simplest case.

A vocabulary of image reconstruction (image phase recovery) techniques has been implemented. These include: i) the methods of image phase reconstruction using image amplitudes only, developed by Fienup (1978,1979) and by Bates et al, (1983). ii) The methods for integrating image phases proposed by Knox and Thompson (1974) and by Cocke (1982), with realilzations of the Knox/Thompson method suitable for either frequency plane (u,v) (as originaloly developed) or image plane (x,y) integrations (as extended by Nisenson and Papaliolios, 1983) for atmospheric statistics dominated or photon statistics dominated observations, respectively. iii) Three variants on the shift-and-add image retrieval method originally proposed by Lynds, Worden and Harvey (1976) and by Bates and Cady (1980), applicable to atmospheric statistics dominated observations. iv) A matched filter image retrieval method recently developed at Steward Observatory by Ribak, Christou and Freeman (1985) applicable at least to the intermediate domain where photon statistics are important, and possible to the extreme photon statistics domain. And v) Differential speckle imaging (DSI), in which two simultaneous image plane observatioins in different wavelengths

are compared, developed by Beckers, Hege, and Murphy.

3.1 The Knox-Thompson Method

Nisenson et al., (1980) show that simple cross spectrum analysis with phase shifts in x and y effectively yield phase differences which can be integrated to yield the desired transform phases for a Knox-Thompson style two-dimensional image reconstruction. In a subsequent paper, Nisenson and Papaliolios (1983) have shown that this method can also be corrected for the effects of photon noise bias. Hence it is applicable to both bright objects as well as faint objects for which the photon noise becomes dominant. They have proposed a scheme based upon the accumulation of three arrays, each of which is derived from the complex Fourier transform and summed over the ensemble of specklegrams, which can be the basis for an integration yielding the Fourier phases.

Given $FT(i(x,y)) = I(u,v) = A(u,v)e^{i\phi(u,v)}$, the arrays which are to be accumulated in order to recover the amplitudes A(u,v) and phases $\phi(u,v)$ are:

$\langle|O(u,v)|^2\rangle$ The calibrated image amplitudes given by 1.3.

$\langle I^*(u,v)\cdot I(u+\Delta u,v)\rangle$ An X-phase array. (3.1.1)

$\langle I^*(u,v)I^*(u,v+\Delta v)\rangle$ A Y-phase array. (3.1.2)

In the photon limited case, the n^{th} specklegram, eq. 1.1, becomes

$$i_n(L) = \sum \delta_i(L - L_i) \qquad (3.1.3)$$

where $(L_i)_n$ = the list of photon addresses (x_i,y_i) for the n^{th} frame. The image plane equivalents to (3.1.1) and (3.1.2) reduce to autocorrelation-function-like quantities of the form

$$q(L) = N \sum_{L'} \exp[(2\phi i/N)\, s\, (L'_n - 1)] \times \delta(L'_n - L_n - L + 1), \qquad (3.1.4)$$

i.e., the autocorrelation function with a complex modulation term.

2.2 Shift-and-Add Methods

These algorithms utilize from one to "all" of the speckles in a single specklegram to obtain a "mean speckle" for that particular specklegram. The average of these mean speckles over a number of specklegrams is then taken to represent diffraction-limited information which, in certain circumstances, can be considered to be a high resolution image of the object irradiance. A simplistic model for a specklegram is that it is the sum of a number of discrete speckles. If p(x,y) is the profile of a point source speckle, then the specklegram is, in a very simplistic approximation, the convolution of such a profile with an impulse distribution imp(x,y) representing the amplitude (impulse amplitudes) and phase (impulse locations) distortions of the atmosphere during exposure n. For a point source, the observed specklegram is then the convolution

$$i_n(x,y) = p(x,y) * imp_n(x,y) \qquad (3.2.1)$$

where * represents convolution.

For a resolved object, in this same approximation, each "speckle" is the convolution of the point source speckle with the resolved object irradiance o(x,y). Then the specklegram of a resolved object is

$$i_n(x,y) = [p(x,y)] * imp_n(x,y)] * o(x,y). \qquad (3.2.2)$$

For both resolved and unresolved objects, (3.2.2) and (3.2.1) respectively produce a "mean speckle" o(x,y) superimposed upon a broad,

seeing induced background. By comparing the resolved object result to that of the point source, for example by Wiener filtering (as suggested by Bates ----), the object irradiance o(x,y) can then be recovered. This approach was first applied by Lynds, Worden and Harvey (1976).

In order for this method to yield results it is essential that the individual speckles in a specklegram should have well defined maxima. If this is not so, then the "mean speckle" would blur out the diffraction-limited information needed to define the impulse function $imp_n(x,y)$ and thus (3.2.1) and (3.2.2) could not be used. The seeing bias, of the form $\langle[p(x,y) * imp_n(x,y)]\rangle$, is closely related to $\langle|p(x,y)|^2\rangle$, the Fourier transform of the speckle transfer function STF since imp(x,y) contains similar amplitude information.

This analysis is also limited to bright object data where individual bright analogue speckles are visible. On the Steward system this translates to objects with apparent magnitudes less than approximately m=6 to 8 depending upon seeing and observing bandwidth. We have implemented several variations of this basic theme.

3.2.1 Simple Shift-and-Add

SAA was first proposed by Bates and Cady (1980) and consists of locating the brightest speckle within a specklegram and co-adding on a specklegram-by-specklegram basis. This is the most straightforward of the analyses implemented. In this case, the impulse function is simply a unit delta-function located at the position of the brightest speckle, which in turn is defined to be the local maximum of the specklegram. To suppress effects of Poisson noise (photon statistics), which blurr the positions of the local speckle maxima, we explored the use of various filter functions which may be applied to (convolved with) the individual specklegrams, in

order to estimate $Imp_n(x,y)$ before further processing. This technique, when optimized, is called matched filtering, and is discussed further in section 3.4.

3.2.2 Screened Shift-and-Add

One of the major drawbacks of this form of analysis is that only one speckle per specklegram contributes to the final image. A variation on this technique, screened shift-and-add (SSA), developed (Bagnuolo 1982,3) to include more signal from each specklegram has also been evaluated. SAA analysis has the advantage of its simplicity but has the disadvantages (i) that the brightest pixel can be due to a photon noise spike (or an ion event), (ii) it could be saturated and therefore not linearly related to the object intensity and (iii) more specklegrams are required to reach the same signal-to-noise ratio (S.N.R.) as the SSA technique. The screened shift-and-add technique therefore appears to be the SAA method of choice.

3.2.3 Weighted Shift-and-Add Methods

We have implemented algorithms for two further variants on these shift-and-add ideas, weighted shift-and-add (WSA) and deconvlved shift-and-add (WSA/D). WSA/D has the further advantage of "flattening" the seeing-noise background upon which all shift-and-add results are superimposed, in effect achieving a seeing self-calibration.

The S.N.R. can be increased tremendously if the majority of speckles in a specklegram can be used. This was the advantage of the Lynds, Worden and Harvey (1976) method, hereafter referred to as LWH. In their analysis of Alpha Orionis they created an impulse function, $imp_n(x,y)$ in equation 3.2.2, to represent the distribution of the speckles in an individual specklegram. This was then cross-correlated with the original specklegram to produce the mean speckle $p(x,y)*o(x,y)$ for that particular specklegram. Their impulse function is comprised of a set of Dirac delta functions of

uniform height. Thus all the speckles contributed the same weighting to the mean speckle. The actual algorithms used to create p(x,y) in fact calculated the cross correlation between the speckle and impulse frames so as to avoid problems of small number diviions in the complex quotient of any deconvolution process.

This technique is non-linear because of a thresholding of the data to locate only the brightest speckles and also because of the (artificially) uniform impulse distribution imp(x,y). To avoid these non-linearities we weight the impulse distribution by setting the amplitude of the delta function to that of the speckle which they represented and use all of the speckles with no thresholding. Thus all the speckles in the specklegram were being utilized thereby increasing the S.N.R. compared to the SAA or SSA technique. This defines our Weighted Shift and Add (WSA) method.

We investigated weighting other than simply the corresponding speckle amplitudes for the components $imp_n(x,y)$. One particularly interesting weighting, use of the squares of the corresponding amplitudes, yields the particularly interesting result for binary star research that, when cross-correlated with the corresponding specklegram, the averaged response yields quasi autocorrelation function sidelobes preserving the relative amplitudes and orientation of binary objects. This is discussed further in section 4.1.

3.3 Self-calibrating Deconvolution and Holographic Methods

Implicit in deconvolution and holographic methods is some technique for sampling the instantaneous speckle modulation transfer function (MTF), the quantity $P_n(u,v)$ whose modulus is averaged to produce STF the second term in eq. 1.2. We have experimented with two methods for obtaining this information which use variants on speckle interferometry, the first made

possible with the differential speckle camera (Beckers, 1982), and the second utilizing the data reductions methods invented for it.

If the object is essentially unresolved in one wavelength and well resolved in an adjacent wavelength (i.e., the continuum near an emission or absorption feature vs. a sample centered on that feature), or if the observation can be arranged so that a sufficiently bright, unresolved source is in the field, then a complex deconvolution consisting of the complex quotient

$$O'(u,v) = \langle I_{rn}(u,v)/I_{un}(u,v) \rangle, \qquad (3.3.1)$$

where $I_{rn}(u,v)$ and $I_{un}(u,v)$ are respectively the complex Fourier transforms of the n^{th} specklegrams for the resolved and unresolved components obtained simultaneously, yields a useful approximation $O'(u,v)$ of the desired complex object intensity distribution upon averaging a sufficient number of observations. Not surprisingly, there is a "division by small numbers" problem with this quotient.

There is, also, a <u>crucial</u> detector distortion problem in this method using our present Varo electrostatic inverter intensified video camera. There is sufficient geometrical distortion (principally "pincushion") that it is necessary to correct the data frame-by-frame. We have implemented a simple grid re-mapping algorithm which is calibrated by observing a calibrated, square-grid reticle in the speckle camera (telescope) focal plane.

This Weighted Shift-and-Add with deconvolution (WSA/D) is an extension of the method proposed by Lynds, Worden and Harvey (LWH). This method creates an impulse frame for each specklegram which consists of zeros everywhere except at the loci corresponding to the local maxima of the

specklegram. At these loci the impulse frame takes on the values of the specklegram. Letting the specklegram be $d_i(x,y)$ and the weighted impulse frame be $imp_i(x,y)$ then we compute

$$I_i(x,y) = [FT\{d_i(x,y)\}/FT\{imp_i(x,y)\}]\ FT\{imp_i(x,y)\}^2 \qquad (3.3.1)$$

(where FT denotes the complex Fourier Transform) and sum $I_i(x,y)$ over the ensemble $\{i\}$ of specklegrams. Dividing this sum by the sum of the weighting moduli $|FT\{imp_i(x,y)\}|^2$ and inverse transforming produces the WSA image. The advantage of this method over that of LWH and Bates' conventional shift-and-add analysis, or of SSA, is that it eliminates the residual "seeing" produced background which remains in those methods. This defines the method we call weighted shift-and-add with deconvolution, WSA/D.

4. IMAGE RECONSTRUCTION RESULTS

We have investigated a computer generated set of "triple star" simulated specklegrams and real binary star data obtained at i) the Steward Observatory 2.3m, ii) the Kitt Peak 4m telescope and iii) the 6.9m Multiple Mirror Telescope.

4.1 Triple Star Simulation

The ten specklegram triple star noise-free simulation was analyzed by the simple shift-and-add (SAA) method. The ratio of the three components was 16:8:1. Figure 1 shows the reconstruction. The two brighter components are clearly visible with the correct separation and position angle. The third component, however, is lost in the noise of this process. This noise is introduced from the remainder of the specklegram when the whole specklegram is translated to put the bright speckle at the specklegram center. As only ten specklegrams were used in this analysis there was not enough signal in the third component to induce a significant response compared to the noise background. The measured ratio of the two brighter components is 1:0.504. Since the known input signal can be used to analyze the output, one can see the expected response (otherwise lost in the noise) at the position of the third component as shown in the cuts in figure 2.

The weighted shift-and-add (WSA) was applied to the ten specklegram triple-star simulation and the results can be seen in figure 3. Notice that unlike the SAA image this shows a triple peak for a two body system. This is easily explained because the cross-correlation between the speckle and weighted impulse frames mimics an autocorrelation procedure. As in an autocorrelation a binary object will produce a triple response, as the autocorrelation looks at only the spacing in the original distribution and

not its sense. This cross-correlation differs from the autocorrelation in that a speckle cross-correlates with a delta function rather than itself. The peaks in the cross-correlation are therefore of the speckle size instead of twice the size as for the autocorrelation case: this cross-correlation is a type of "quasi-autocorrelation".

Thus for the case of a binary system, or any multiple system, the ambiguities of the orientation which exist in an autocorrelation will also exist in the cross-correlation. However, for a resolvable single object, e.g., a supergiant, where there is only one maximum per speckle then the cross-correlation peak will represent the "mean" speckle for the specklegram. In figure 3 there is a background due to the cross-correlation of the speckles with the delta functions representing other speckles which create a "seeing" hump similar to that for both the SAA (as in Figure 1) and the SSA methods as well as in the regular autocorrelation.

In order to use this weighted analysis on binary star data so that the orientation information can be extracted, the impulse function must be replaced by the square of itself before computing the cross-correlation. This has the effect of removing the amplitude symmetry in the "quasi-autocorrelation". If for example a binary star with components of brightness A1 and A2 respectively, then the secondary peaks in the "quasi-autocorrelation" will have amplitudes each of A1*A2. However, when the impulse function is squared the amplitudes now become A1*A1*A2 and A1*A2*A2 respectively giving a ratio of A1:A2, the ratio of the actual component brightnesses. Figure 4 shows the cross-correlation for the squared impulse distribution for the triple star simulation data. The amplitude symmetry is no longer present and the NE secondary is brighter agreeing with the results for the SAA case as to the orientation of the system. Of course, if we have the case of identically equal components then this case too

would degenerate into a "quasi-autocorrelation": no technique could recover an "orientation" if the two components had identical brightness. This could only be done if their spectral types were different so that observations could be made at wavelengths and bandpasses chosen to emphasize the difference. Analysis shows that the original intensity ratio is preserved in the ratio of the sidelobes (secondary to tertiary) and that the orientation is given by the orientation of the secondary with respect to the primary (central) response. Thus, unlike strict (or "quasi-") autocorrelation, this non-linear method preserves phase and amplitude information for binary star research.

An alternative to computing the cross-correlation is actually computing the full complex deconvolution WSA/D. The full complex FFT of both the specklegram and the (linear weighted) impulse frame are computed and the complex quotient is calculated (eq. 2.2.11). These are summed to provide the average deconvolved object transform. This is then inverse transformed using an FFT to give the full deconvolution.

For every speckle maximum in the specklegram there is an impulse with a corresponding weight. From equation (2.2.1) it can be seen that the deconvolution will give the "mean speckle" for the specklegram. In fact this is the mean speckle maximum. If the object is a binary system with both components unresolved, then each speckle has two maxima and therefore each speckle is represented by two impulses. The deconvolution then removes all duplicity giving a single peak. This is not the desired result! Thus as a method for studying multiple systems the deconvolution version of the Weighted Shift-and-Add (WSA/D) needs some modification. However for a point source or single resolvable source meeting the deconvolution requirement, specifically that individual speckles are

characterized by a single maximum, this technique produces a well defined mean speckle. An advantage to this form of analysis is that all speckles are deconvolved with their respective impulses. This places the mean speckle at the origin (center) of the specklegram. Thus there is no "seeing" background unlike the SAA, SSA and WSA methods. This therefore allows a better determination of any intensity information as the background does not have to be fit and removed. In fact, this is a "seeing" independent technique which only depends upon the existence of speckles with such specific properties.

Figure 5 is the deconvolved WSA (WSA/D) image for the triple star simulation data set. Notice the bright central maximum and the flat background. As expected no other structure is significant. Figure 6 is also a WSA/D image but this time the impulse frame was generated from a smoothed specklegram. The original specklegram was smoothed with a low pass filter to "blur" the maxima from the two brighter components to produce just one maximum. This filtered impulse frame was then deconvolved with the original specklegram, the sum of ten of these providing the image. The secondary component is now clearly visible with the correct orientation, separation and ratio of the two intensities. The flat "no-seeing" background is apparent. In effect, a matched filter has allowed proper identification of the components of $imp_n(x,y)$ for each specklegram.

Another way to properly identify the components of $imp_n(x,y)$ for multiple systems is to edit the impulse function. The regular Labeyrie autocorrelation or SAA or SSA analysis determines the spatial information about the object, i.e., its separation and position angle. For a binary system the two components produce two maxima for each speckle giving two impulses for each speckle. Knowing the spatial information, it is then possible to look for impulse pairs with the same vector separation. Either

the left or right impulse from the pair can now be edited out of the impulse frame and the deconvolution calculated. Figure 7 shows the effect of doing this for the triple star simulation. The secondary is now detected although there is more structure in the otherwise flat background. As for all of the reconstruction tests for this data set the tertiary component is not visible being lost in the noise of the background. This is just an effect of small number statistics. The tertiary would become readily apparent, e.g., 100 frames.

The triple star simulation data set was also analyzed by the Knox-Thompson and the phase-unwrapping (Cocke, 1980) techniques. The results are shown in Figure 8. For this "noise-free" simulation, the Knox-Thompson method gives superior results. It is not clear that this will be the case for the Poisson statistics limited data.

4.2 Telescope Speckle Point Spread Function Measurements

Figure 9 shows the WSA/D images for unresolved stars for the 2.3m and 4m telescopes. The flat background is very much in evidence as well as the Airy ring. Figure 10 shows a similar result obtained for the fully cophased, 6-beam Multiple Mirror Telescope showing the expected response for its 6.9m diameter unfilled pupil.

4.3 Alpha Aurigae (Capella)

Capella was observed with the Steward Observatory speckle camera using a 100A bandpass centered at 5200A on 2 Feb 81 with the Kitt Peak 4m telescope. Capella is a well studied system composed of two G III giants of similar magnitude. The SAA image of Alpha Auriga is shown in figure 11. Unlike for the photon statistics free simulation, this image suggests three components. Each speckle has two maxima, one for each component of the

binary system. The brightness ratio of these maxima will be equal to that of the two components modified by Poisson statistics. As the two components have similar magnitudes it is possible, occasionally, for the maximum due to the fainter component to be larger than the other. When this happens the spurious third component of the SAA image is created. If a binary system consisted of two very nearly equal components (to within measurement limits), thentheSAA image would be similar in form to an autocorrelation and SAA analysis would conceal the correct orientation of the system. For the more common unequal component case, the maximum due to the brighter component should occur more frequently, and therefore the correct orientation can be ascertained as the brighter of the two secondaries of the SSA image. The ratio of the intensities of the two secondaries is therefore related to the magnitude difference between the two components (Bagnuolo, 1982). Referring again to figure 11 it can be seen that the NW component appears to be the brighter. An estimate of the brightness difference can be made by removing the background from the SSA image. To do this a twelve parameter non-linear 2-D least squares fit was applied to the center 30 square pixels of the image. The three peaks were modelled by gaussians and a gaussian "seeing" background sitting atop a tilted term (a*x+b*y+c*x*y) was also assumed. The central five pixels of the image were omitted in the fit because of the photon spike (noise bias). The intensity ratio of the two secondaries was found to be r=0.66 which corresponds to a true intensity ratio fo f=0.80. This model image is also shown in figure 11.

4.4 The Occultatic~ Binary 115 Tau

Relative magnitude estimates for the components of 115 Tau have been obtained from Lunar occultation photometry (Africano, et al. 19--), which

was observed with speckle interferometry on 18 December 1981 at the 2.3m telescope using a 300A wide filter centered at 5500A.

Figure 14 shows the SAA images for 115 Tauri and the comparison 113 Tauri. At the epoch of observation the separatioan of the two components of 115 Tauri was approaching the diffraction limit of the 2.3m telescope as can be seen by comparing the images in figure 14. The Airy ring is clearly visible in this image and the secondary component can be seen overlapping the Airy ring to the east in the resolved object. Notice a smaller blurring westward of the central peak due to the fainter (statistically induced) tertiary response. For 113 Tauri no secondary peaks can be seen. The Airy ring in both images shows very non-uniform structure. This seems to be a characteristic of these data sets, and, in fact, we attribute it to the OTF of the system: telescope + camera, etc.

These two images were seeing corrected using a Gaussian model and then Fourier transformed. The complex quotient of the two was then computed and inverse transformed to produce a deconvolved "image", figure 15. We can now see the two secondary peaks more clearly as the Airy ring has also deconvolved. There is no indication of a third component as suggested by "lumpy" Airy rings. The magnitude ratio is not correct, appearing to be greater in the deconvolved result than occultation measures show. This is partly due to inadequacies in the seeing model correction, but mostly due to photon noise bias which isnot compensated in this method.

The "ringing" in these results is typical of any attempts to apply linear deconvolution techniques to noisy data such as this. Because we need a non-linear technique to apply the OTF calibration to the resolved object, and because the radio astronomical algorithm CLEAN (Hogbom, 1974) was invented for this purpose, we applied it to the results in figure 14, using the seeing corrected and noise debiased SAA image for 113 Tau as the

"dirty beam" to restore the data for 115 Tau. Figure 16 shows the result when restored with a clean beam also derived from the 113 Tau data.

4.5 Holographic Deconvolution Method

Simultaneous speckle grams of α_1 and α_2 Sco were recorded. Since α_2 Sco is a fainter B-type companion to α_1 Sco, it can be used as a holographic reference for a complete image reconstruction of α_1 Sco. In order to balance the relative intensities of these objects, we placed a neutral density filter in front of the intensified video camera (speckle) focal plane so that it just intercepted the image of α_1 but not α_2. The simple SAA results for both objects were accumulated separately, and the results are shown in figure 17. The resolved nature of α_1 Sco, and possibly evidence for extended structure, is clearly seen. Initial efforts to perform the holographic deconvolution using eq. 2.2.11 were not convincing due to insufficient data to produce good S.N.R. The statistics in the quotient are, of course, limited by the fainter object. A longer integration should produce good results.

Better results have been achieved with the two bandpass DSI approach. Figure 18 shows results for α_1 Sco obtained by the integration 2.2.11 applied frame-by-frame to DSI data in which the Fourier transform of the data on line center is divided by the data off line for which α_1 Sco is only partially resolved. In order to restore an image which should more nearly represent the true appearance of the object, the integrated quotient transform was multiplied by the Fourier transform of a uniform disk of the size corresponding to the continuum disk size of α_1 Sco from conventional speckle interferometry. This may not be exactly correct, as α_1 may not be a perfect, symmetric uniform disk in the continuum. The results are nevertheless encouraging, and show definite evidence for an elongated

gaseous envelope.

Differential Speckle Interferometry (DSI) (Beckers, 1982) produces an instrumentally sheared "binary", the brightest speckles of which correlate at the known instrumental separation in each specklegram of the simultaneous DSI specklegram pair. The SAA result is then accumulated separately for each component of the pair. This will then allow a comparison of the two results for which the seeing effects should be identical. An example for α Ori observed with the Mica Fabry-Perot with two bandpasses 0.125 nm wide separated by 0.5 nm is shown in Figure 19. Both images show evidence for a faint, elongated cloud oriented South-East to North-West. The bandpass in the red wing of the line shows this effect to be weaker, but somewhat surprisingly not altogether absent.

Figure 20 shows a similar pair of Correlated SAA images obtained for the unresolved (Optically) star α Lyr (Vega). The curious elongation in the raster direction (on instrumental artifact) is due to a bright-speckle video raster non-linearity. It does show (cf. Figure 19) an object with angular size smaller than α Ori, and comparable to the telescope PSF.

5. COMPARISON OF RESULTS

FIGURE CAPTIONS

Figure 1. Triple star simulation. Simple shift-and-add. Third component response, just at noise level, is marked by arrows. Because the data set is noise free, and because only one, brightest speckle coordinate is used for each frame, no reflection "ghosts" are seen.

Figure 2. Horizontal cut through centers of expected responses in triple star simulation SAA result. The recovered intensity ratios are 1:0.504:0.08 compared to input 1:0.5:0.0625 (=16:8:1).

Figure 3. Triple star simulation. Weighted SAA (WSA).

Figure 4. Squared Impulse WSA for Triple Star simulation. The phase and relative amplitudes are preserved for a binary system.

Figure 5. Deconvolved WSA image for triple star simulation (WSA/D). The most notable feature here is the "flattened" seeing background.

Figure 6. Filtered deconvolved WSA for triple star simulation. Note that now the phase and relative intensity are preserved. This matched filtering forced the speckles to have only a singel maximum.

Figure 7. Edited deconvolved WSA for triple star simulation. Again the orientation and relative magnitudes are preserved, but the background is noisier since only half of the speckles are used.

Figure 8. Triple star image reconstruction. Knox-Thompson (left) and phase unwrapping (right).

Figure 9. Alpha Lyrae by deconvolved WSA (WSA/D) showing unresolved object on flattened background. This demonstrates the seeing self-calibration implicit in this method. KPNO 4m Telescope. 7.22 msa/pixel.

Figure 10. Gamma Ori. MMT Point spread Function

Figure 11. Capella by simple SAA. Left is raw result. Right is 12 parameter model fit (see text).

Figure 12. Residual to SAA Model-fit to Capella shown in Figure 11.

Figure 13. Capella by Squared Impulse WSA. The relative intensity of the components is preserved.

Figure 14. 113 Tau (unresolved -- left) and 115 Tau (resolved -- right) by Simple SAA.

Figure 15. 115 Tau deconvolution results from simple SAA after crude model-fit seeing correction. An "aperture" filter is required before the inverse transformation. Left -- Filter corresponds to telescope aperture. Right -- Filter corresponds to .7x telescope aperture.

Figure 16. 115 Tau SAA result after CLEAN.

Figure 17. Simultaneous SSA results for α Sco. α_2 Sco left. α_1 Sco right. MMT mirror A, a 72" Telescope, was used.

Figure 18. DSI Holographic Deconvolution of α_1 Sco (left). The superimposed circle represents the continuum disk size. The results for α Lyr (right) are shown for comparison. KPNO 4m Telescope.

Figure 19. Correlated SAA α Ori. Left -- line center. Right -- off line.

Figure 20. Correlated SAA. Vega.

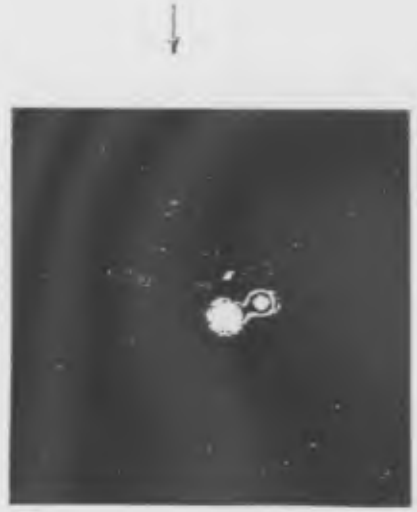

Figure 1 Triple star simulation. Simple shift-and-add. Third component response just at noise level, is marked by arrows.

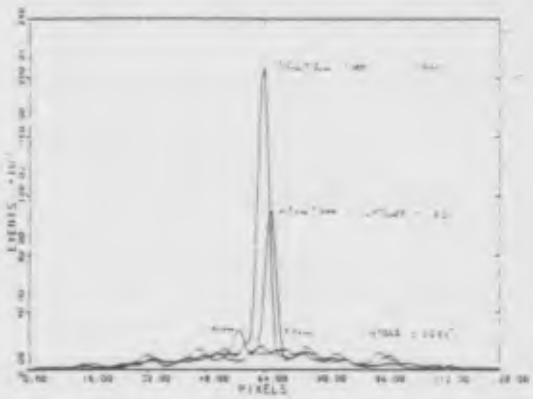

Figure 2 Horizontal cut through centers of expected responses in triple star simulation SAA result. The recovered intensity ratios are 1 : 0.504 : 0.08 compared to input 1 : 0.5 : 0.0625.

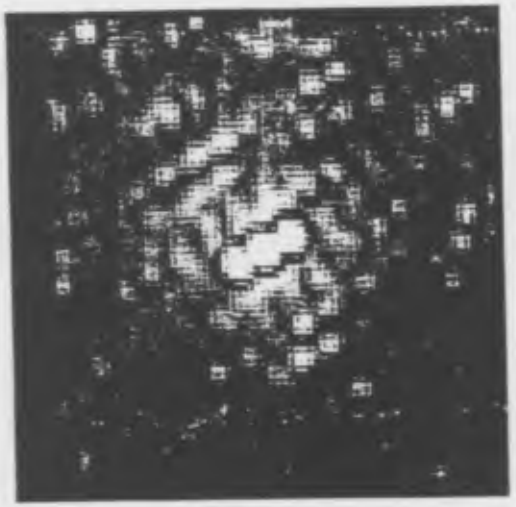

Figure 3 Triple star simulation. Weighted SAA (WSA).

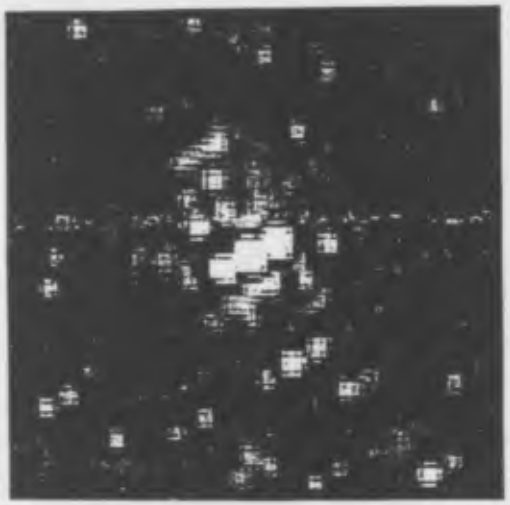

Figure 4 Squared Impulse WSA for Triple Star simulation. The phase and relative amplitudes are preserved for a binary system.

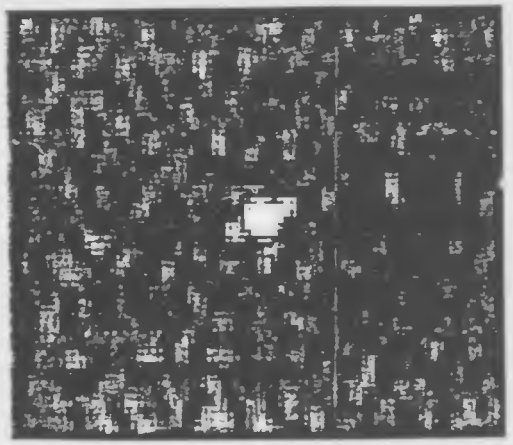

Figure 5 Deconvolved WSA image for triple star simulation. The most notable feature here is the "flattened" seeing background.

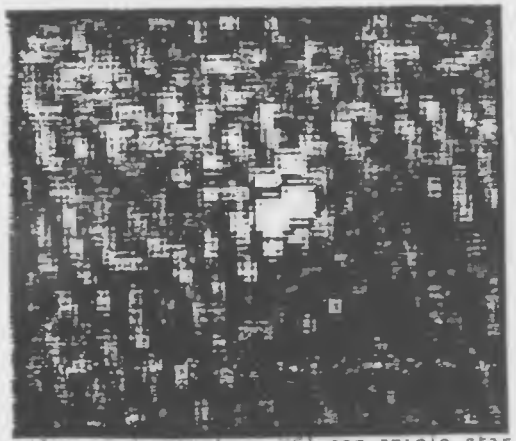

Figure 6 Filtered deconvolved WSA for triple star simulation. Note that now the phase and relative intensity are preserved. Filtering forced the speckles to have only a single maximum.

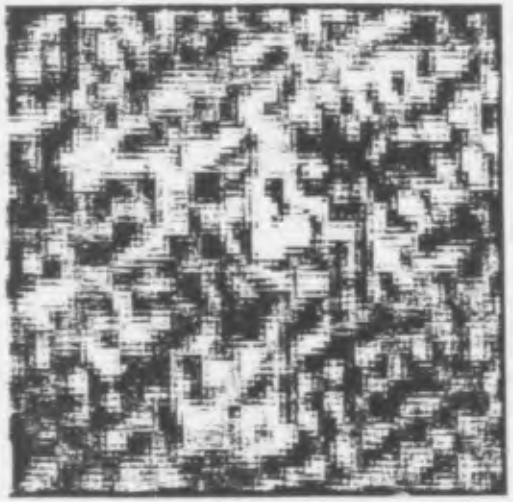

Figure Edited deconvolved WSA for triple star simulation. Again the orientation and relative magnitudes are preserved, but the background is noiser since only half of the speckles are used.

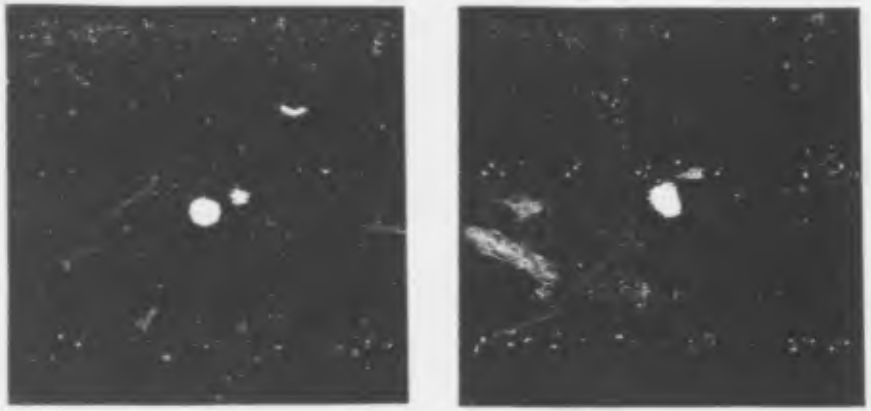

Figure 9 Triple star image reconstruction. Knox-Thompson (left) and phase unwrapping (right).

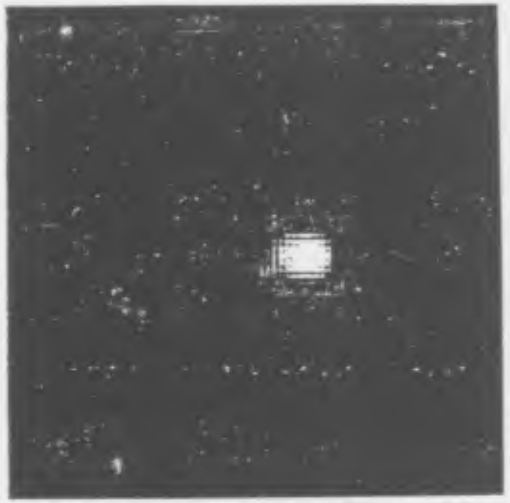

Figure Alpha Lyrae by deconvolved WSA showing unresolved object on flattened background.

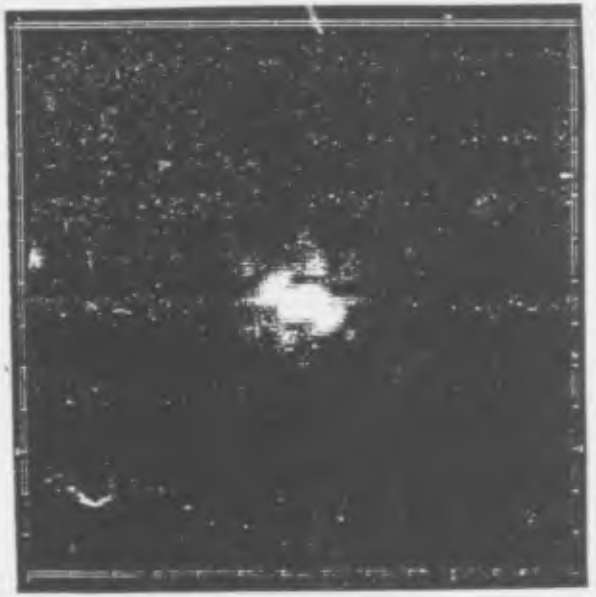

Fig 10

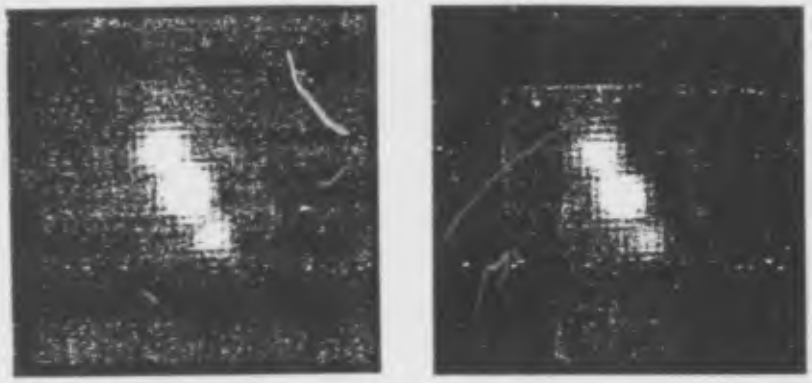

Figure : Capella by SSA. Left is raw result. Right is 12 parameter model fit (see text).

Figure 12 Residual to SSA Model-fit to Capella.

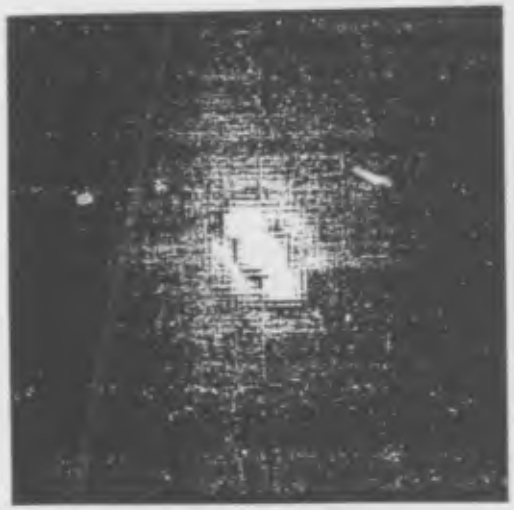

Figure : Capella by Squared Impulse WSA.

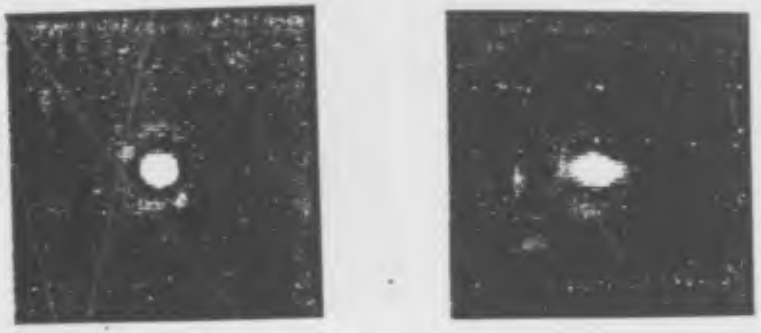

Figure 14 113 Tau (unresolved - left) and 115 Tau (resolved - right) by SSA.

Figure 115 Tau deconvolution results from SSA after crude model-fit seeing correction. An "aperture" filter is required before the inverse transformation. Filter corresponds to telescope aperture (left) and to .7 x telescope aperture (right).

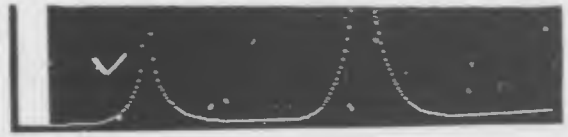

Fig 17.

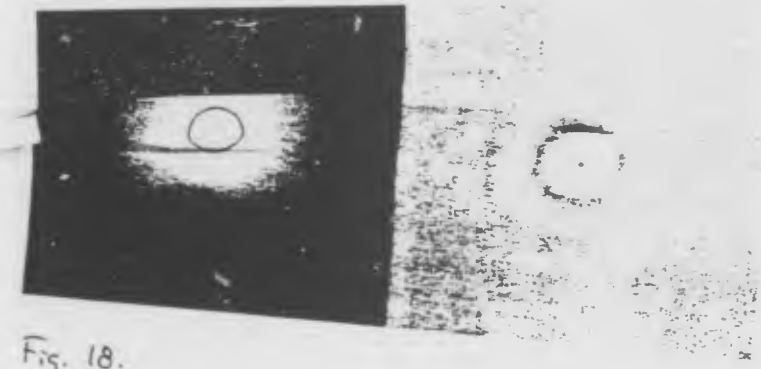

Fig. 18.

Fig 16

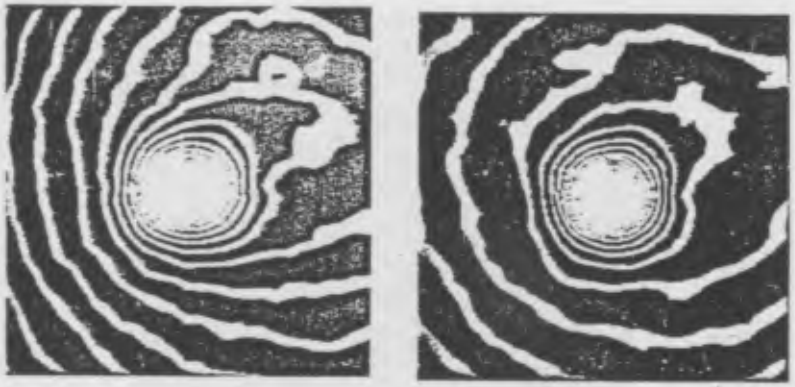

Figure [illegible] Correlated SAA % Ori. Left - line center. Right - off line.

Figure [illegible] Correlated SAA. Vega.

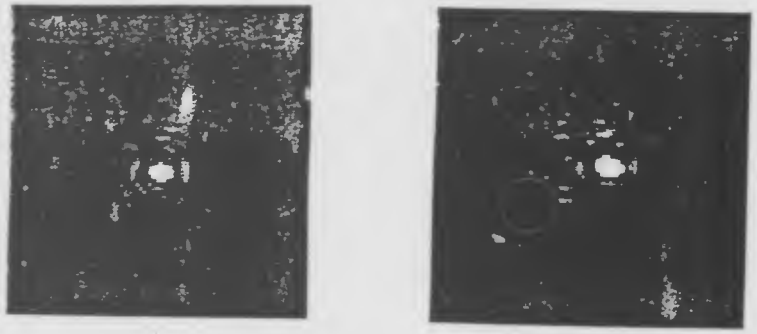

Figure 115 Tau deconvolution results from SSA after crude model-fit seeing correction. An "aperture" filter is required before the inverse transformation. Filter corresponds to telescope aperture (left) and to .7 x telescope aperture (right).

Fig 16

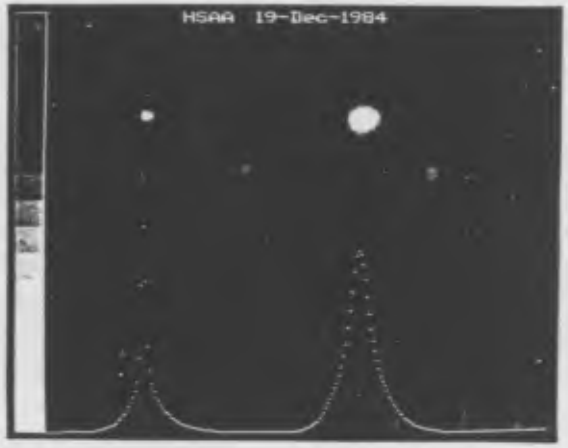

Fig 17.

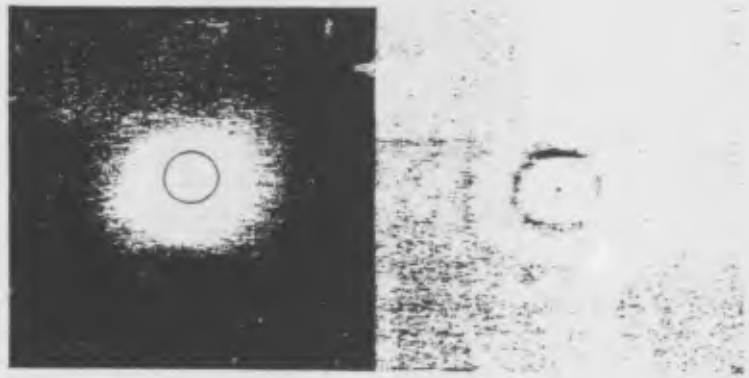

Fig. 18.

IMAGE RESTORATION VIA THE SHIFT-AND-ADD ALGORITHM

by

William G. Bagnuolo, Jr.

The Aerospace Corp.
M4/939
P.O. 92957
Los Angeles, CA 90009

ABSTRACT- A new method for image restoration based on the shift-and-add algorithm is presented, the main advantages of which appear to be speed and simplicity. The shift-and-add pattern produced by an object is given by the object correlated by a non-linear replica of itself whose intensity distribution is strongly weighted toward the brighter pixels. A method of successive substitutions analogous to Fienup's algorithm can then be used to "decorrelate" the SAA pattern and recover the object. The method is applied to the case of the extended chromosphere of Betelgeuse.

Optics Letters, 10, 200 May '85

INTRODUCTION

The original version of shift-and-add (SAA) proposed by Bates and Cady[1] involved superimposing areas centered about the brightest pixel of each speckle interferometry frame to produce a composite image. Applied to double stars this procedure results in a pattern consisting of three spots, the intensities of which can be used[2,3,4] to determine the relative intensities of the stars. However, the SAA pattern of an extended object cannot be so easily interpreted.

This paper considers first the calculation of the SAA pattern produced by a given object, then considers the inverse problem of interpreting a given SAA pattern in terms of a reconstructed object, and finally presents results of image restoration with simulated speckle frames and actual Betelgeuse data.

THE SAA PATTERN PRODUCED BY A GIVEN OBJECT

Let us assume that the object consists of n "pixels", with the intensity of the ith pixel given by r_i. For convenience set $r=1$ for the brightest pixel. Assume also that the point spread function caused, e.g. by atmospheric turbulance, is given by an exponential distribution.[5] (The problem of assuming a different distribution could be handled by one of the approximation methods discussed later.) It is also assumed that the object is bright enough so that the photon noise is unimportant (e.g. a bright star). The intensity distribution of a speckle interferometry frame is given by the instantaneous point-spread function convolved with the object. Thus, at any given pixel of the frame the intensity is given by the sum of n exponential functions:

look up Goodman, pg 7.

Error would disagree with this one

(1) $I = \sum_{i=1}^{n} I_i$, where $p(I_i) = \exp(-I_i/r_i)/r_i$

is the probability density of I_i. (i.e. at any given pixel the total intensity is "caused" by the sum of n overlapping object distributions, the contributions being weighted by r_i.

the entire paper stands or falls.

the part of the object for the ith object distribution overlapping the pixel in question. Note that we have assumed that the separation of the pixels comprising the object is approximately the resolution size, so that these distributions are essentially independent.)

The probability density resulting from the sum of independent random variables $X_1 \ldots X_n$ with densities $f(x_i)$ that are zero for $x_i<0$ is given[6] by the inverse Laplace Transform of the product of the Laplace Transforms for f_1 to f_n. The Laplace Transform of $p(I_i)$ is given by $1/(1+b_i)$, where $b_i=1/r_i$. Therefore, the probability density of the pixel intensities of the frame may be calculated (using the Residue Theorem to evaluate the inverse transform):

$$(2)\quad p(I) = \left(\prod_{i=1}^{n} b_i\right) \sum_{i=1}^{n} \frac{e^{-b_i I}}{\prod_{\substack{j=1 \\ j\neq i}}^{n} (b_j - b_i)}$$

To consider the SAA pattern resulting from superposition about pixels above a given intensity level, w, (2) can be integrated from w to infinity giving the distribution:

$$(3)\quad P(I) = p(I \geq w) = \left(\prod_{i=1}^{n} b_i\right) \sum_{i=1}^{n} \frac{e^{-b_i w}}{b_i \prod_{\substack{j=1 \\ j\neq i}}^{n} (b_j - b_i)}$$

Next, it is useful to calculate the average contribution, $\bar{I}_m$, from the m th overlapping object to the total intensity $I (\geq w)$ of a bright pixel that is used for SAA superposition.

By Bayes' Theorem we know that:

$$(4)\quad p(I_m | I \geq w) = p(I_m)\, p(I \geq w | I_m)/P(I)$$

The probabilities $p(I_m)$ and $P(I)$ are known from (1) and (3). The conditional probability $p(I \geq w | I_m)$ can be calculated in the same way as in (3), but this time with only n-1 pixels. Thus:

$$(5)\quad P_m(I) = p(I_m | I \geq w) = \left(\prod_{\substack{i=1 \\ i\neq m}}^{n} b_i\right) \sum_{\substack{i=1 \\ i\neq m}}^{n} \frac{e^{-b_i (w - I_m)}}{b_i \prod_{\substack{j=1 \\ j\neq i,m}}^{n} (b_j - b_i)} \qquad \text{if } I_m \leq w$$

$$= 1, \quad \text{if } I_m = w$$

Now, $\bar{I}_m = \int I_m\, p(I_m | I \geq w)\, dI_m$, and by substituting (5) and (1) into (4) and integrating we get:

$$(6)\quad \bar{I}_m = \sum_{\substack{i=1 \\ i\neq m}}^{n} \frac{\left[e^{-b_i w} - e^{-b_m w}\left(1 + (b_m - b_i) w\right)\right] \prod_{\substack{j=1 \\ j\neq i}}^{n} \left(\frac{b_j}{b_j - b_i}\right)}{(b_m - b_i)\, Q} + \frac{(1 + b_m w)}{b_m Q} e^{-b_m w}$$

$$\text{where} \quad Q = P(I) \Big/ \prod_{i=1}^{n} b_i$$

Now, if the average contribution of the m th overlapping object to the pixel in question is $\bar{I}_m$, its intensity at its brightest pixel location is $b_m \bar{I}_m$ (ignoring the contributions of other overlapping objects). Thus, we can define the average intensity of the m th overlapping object to be $b_m \bar{I}_m$, and the intensity contribution of this object to any given pixel (not necessarily the pixel to be shifted-and-added about) can be easily found by multiplying $b_m \bar{I}_m$ by the appropriate r_k. Figure 1 schematically shows the relationship between $\bar{I}_m$ and the m th overlapping object.

It is convenient to deal with the background-subtracted intensities in computing the pattern made with the n overlapping objects. Thus, those pixels "unreached" by any of the overlapping objects have intensity zero. Consider a given pixel at a location which is overlapped by the k th pixel of the m th overlapping object. The net intensity contribution from this object to the given pixel is $(b_m \bar{I}_m - 1) r_k$. Or, more compactly, the background-subtracted pattern (S) is given by the cross-correlation of the original object (O) and a weight (Q), where the k th pixel of Q is given by $Q_k = b_k \bar{I}_k - 1$, i.e. $S = O \star Q$.

For superpositions about the brightest pixels (i.e. for high w) Q is a distorted nonlinear replica of O, in which the brightest pixels of O are enhanced. As $w \to \infty$, Q becomes pointlike (the brightest pixel of the original image) and S becomes more like O. (There is of course a tradeoff between the goodness of the image S and the frequency of its occurrence.)

The case where the shift-and-add has been taken about the lowest pixels has been considered previously for double stars.[2,4] In this case an analogue to (6) may be calculated by considering p(I=w), etc.

For the case of more than 25-30 pixels, (6) becomes cumbersome. Accordingly, several approximation methods have been developed to compute the weighting function Q for this case. The most straightforward is to approximate a number of smaller pixels by a single larger "artificial pixel" whose mean and standard deviation are the same as that produced by the sum of the smaller pixels. Thus, to approximate k pixels by a single shifted exponential, $p(I_x)$, we have:

(7) $p(I_x) = \exp(-I_x/R)/R$ if $I_x \geq r_{off}$

$= 0$ otherwise,

where $R=(\sum_{i=1}^{k} r_i^2)^{1/2}$, and $r_{off}=\sum_{i=1}^{k} r_i - R$

Substitutiong these larger "pixels" leads to values of $\bar{I}_m$ in (6) with the summation over remaining "real" and artificial pixels and cutoff w replaced by $w-\sum_{j=1}^{K} r_{off}(j)$ for K artificial pixels. (This results from the shifted exponential distributions assumed.

Another way is to regard each exponential distribution as a X^2 distribution with 2 degrees of freedom. The sum of these exponential distributions is therefore the sum of X^2 distributions, and following Ref. 7 it can be shown that the distribution of (3) is given approximately by a scaled X^2 distribution with a mean of $\sum r_i$ and $f=2(\sum r_i)^2/\sum r_i^2$ degrees of freedom. A X^2 distribution with f degrees of freedom can be approximated by the Wilson-Hilferty transformation[7] of the standard error function. Thus (3) may be approximated by:

(3') $P(I) \propto 1-ERF(x)$, where $x = \left[\left(\frac{w}{\bar{I}}\right)^{1/3} - \left(1-\frac{2}{9f}\right)\right] \Big/ \sqrt{\frac{2}{9f}}$

and the error function may be approximated[8] by:

(8) $ERF(x) = \frac{1}{2} + \frac{1}{\pi}\left[\frac{x}{3\sqrt{3}} + \sum_{n=1}^{12} n^{-1} e^{-n^2/9} \sin\left(\frac{nx\sqrt{2}}{3}\right)\right]$

The analogue to (5) for $p_m(I)$ can be readily found from the X^2 distribution for the n-1 pixels, and the same argument leading up to (6) can be followed, except that numerical integration is used to calculate $\bar{I}_m$.

Table I shows the relative weights (sum of weights=1.00) for a 25-pixel object calculated by means of the "exact" result of (6), the X^2 approximation of (6'), and a shifted Gaussian approximation (created by a similar method). The X^2 approximation thus seems satisfactory for this case.

Some advantages of the X^2 approximation are that: 1) for large objects only a limited number of r_i values are required to create a weighting function curve, and 2) the effects of SAA sampling at intervals smaller than the diffraction-size spacing could be taken into account by changing the effective number of degrees of freedom. (This will not be considered here, but will hopefully be incorporated in a later paper.)

SAA RECONSTRUCTION

The results of the previous section can be used for the inverse problem of estimating the object, given the SAA pattern. For small objects one can simply use a non-linear least-square fitting procedure to create a reconstructed image. Figure 3 contains an example of a 3x3 object (top) that is convolved with a number of exponentially distributed "point-spread functions" resulting in a series of 62x62 pixel speckle frames. The object is satisfactorially recovered from 200 speckle frames using the top 0.32% and

bottom 3.0% pixel SAA superpositions and a least-square gradient search fitting procedure.

For larger objects such a procedure becomes unattractive. A better approach is to use the repeated substitution method shown in Figure 4. An initial guess of the object distribution is made, the corresponding weighting function is calculated, and the next estimate of the object is "decorrelated" from the observed SAA pattern. The new object estimate is constrained to be non-negative and within the assumed support of the object (which can be estimated initially from the SAA pattern.) For objects with some brighter concentrations (e.g. Betelgeuse-like objects) convergence appears to be rapid.

The advantages of decorrelating a SAA pattern instead of an autocorrelation appear to be: 1) The resultant object is "nearly unique" due to the concentrated nature of the weighting function, thus avoiding any possible ambiguities obtained by using the autocorrelation, 2) a simpler algorithm than Fienup's[9] may be used for the image reconstruction (e.g. no conditioning in the spatial frequency domain is necessary). The principal disadvantage is that the weighting function must be calculated; but as was noted previously there are several reasonable methods of doing this. (For the autocorrelation, the weights are just the object itself.)

Figure 4 represents the results of a digital simulation of a "Betelgeuse-type" object which has a resolved core (with slight asymmetries) and an extended "chromosphere". A faint chromospheric banana-shaped (10 o'Clock to 3 o'Clock) feature has been added. For each simulated speckle frame the object was convolved with a point-spread function produced by a simulated circular aperture[10]. The simulated Airy pattern of the latter resulting from perfect "seeing" had a peak-to-first-null distance of 2.24 pixels (i.e. 25% of the power in the central pixel). Four hundred 64 x 64 frames were generated, and a SAA superposition was performed on the brightest pixel of each frame. The background, estimated by correlating the SAA brightest pixel locations with the long-term exposure made up of all the frames, was subtracted out.

The bottom of Figure 4 shows the results of a reconstruction from the SAA pattern sampled at spacings of 2 pixels (the distance between "independent" pixels due to the diffraction pattern size.) It appears that the main features of the object, including the "chromosphere" are recovered. To facilitate comparison between the original and recovered objects, the middle of Figure 4 shows the original object with similarly degraded pixel resolution.

Figure 5 shows reconstructed images of Betelgeuse obtained by SAA superpositions on some 1700 frames taken by K. Hege et al. (Steward Obs.) at the 8542A Ca II line) with the KPNO 4 m. telescope. As with the simulated data above, the SAA pattern was sampled at intervals of 2 pixels (as indicated by the pixel spacing (about .014 arcsec) and the SAA pattern for Gamma Orionis, a point star[3].) This result is preliminary and will hopefully be integrated into a further understanding of the star's chromosphere; however, it does illustrate the use of the SAA algorithm for a practical case.

CONCLUSION

This paper has tried to illustrate how image reconstruction can be done by means of the SAA algorithm, data for which would be simple to collect and to analyze even in real time. For some applications, for example, the two-parameter set of x^2 approximation weighting functions could be stored as look-up tables. For other applications, the algorithm should provide a check on existing reconstruction procedures at a modest cost.

REFERENCES

1. R.H.T. Bates and F.W. Cady, Opt. Comm. 32, 365 (1980).

2. W.G. Bagnuolo, M.N.R.A.S. 200, 1113 (1982).

3. B.R. Hunt, W.R. Fright, and R.H.T. Bates, J.O.S.A., 73, 456 (1983).

4. W.G. Bagnuolo and H.A. McAlister, P.A.S.P. 95, 992 (1983).

5. J.W. Goodman, in Laser Speckle and Related Phenomena, J.C. Dainty, ed. (Springer-Verlag, New York, 1975), p.9.

6. M.D. Springer, The Algebra of Random Variables (John Wiley & Sons, New York, (1979).

7. M.R. Chernick and V.K. Murthy, Am. J. of Math. and Mgt. Sci., 3, 145 (1983).

8. P.A.P. Moran, Biometrika, 67, 675 (1980)

9. J.R. Fienup, Opt. Lett., 3, 27 (1978).

10. W.G. Bagnuolo, Opt. Lett. 9, 65 (1984).

Table 1. Weights of a 25-Pixel Object.

(Top 0.1% SAA)

i	r_i	Relative Weights (exact)	(χ^2)	(Gauss.)
1	1.00	.1062	.1051	.0952
2	0.96	.0971	.0967	.0903
3	0.92	.0887	.0887	.0853
4	0.88	.0809	.0812	.0800
5	0.84	.0737	.0741	.0747
6	0.80	.0670	.0675	.0693
7	0.76	.0609	.0613	.0639
8	0.72	.0552	.0556	.0585
9	0.68	.0499	.0502	.0533
10	0.64	.0450	.0453	.0482
11	0.60	.0405	.0407	.0433
12	0.56	.0363	.0364	.0386
13	0.52	.0325	.0324	.0342
14	0.48	.0288	.0288	.0301
15	0.44	.0255	.0254	.0263
16	0.40	.0223	.0222	.0227
17	0.36	.0194	.0193	.0195
18	0.32	.0167	.0166	.0165
19	0.28	.0141	.0140	.0137
20	0.24	.0117	.0116	.0112
21	0.20	.0095	.0094	.0089
22	0.16	.0073	.0074	.0068
23	0.12	.0053	.0053	.0049
24	0.08	.0035	.0035	.0031
25	0.04	.0017	.0017	.0015

CAPTIONS FOR FIGURES

Figure 1. Intensity contributions from m th "Overlapping Object".

Figure 2. SAA image restoration from top .32% and bottom 3.0% of pixels.

Figure 3. Image reconstruction algorithm of object (0) from SAA pattern (5).

Figure 4. Image reconstruction of Betelgeuse-like object. Top: Original object, Middle: Original object, degraded resolution, Bottom: Restored object from 400 frames of data. Note: Grey-scale level increased by factor of 3.33 on left pictures to show fainter detail, centers are accordingly "burnt out".

Figure 5. Image Reconstruction from actual Betelgeuse data. Grey-scale level on left pictures increased by factor of 5.0 to show fainter detail.

Fig. 1

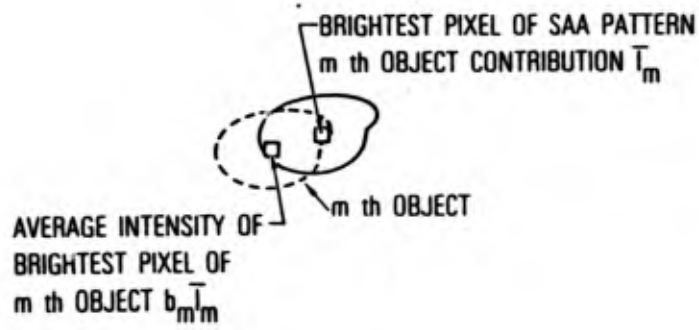

Fig 2

0.25	0.60	0.70
0.79	1.00	0.91
0.30	0.65	0.28

ORIGINAL OBJECT

0.275	0.623	0.710
0.790	1.030	0.883
0.268	0.662	0.240

RECONSTRUCTED OBJECT
FROM TOP 0.32% SAA

0.253	0.611	0.714
0.783	0.973	0.896
0.286	0.701	0.263

RECONSTRUCTED OBJECT
FROM BOTTOM 3.0% SAA

Fig. 3

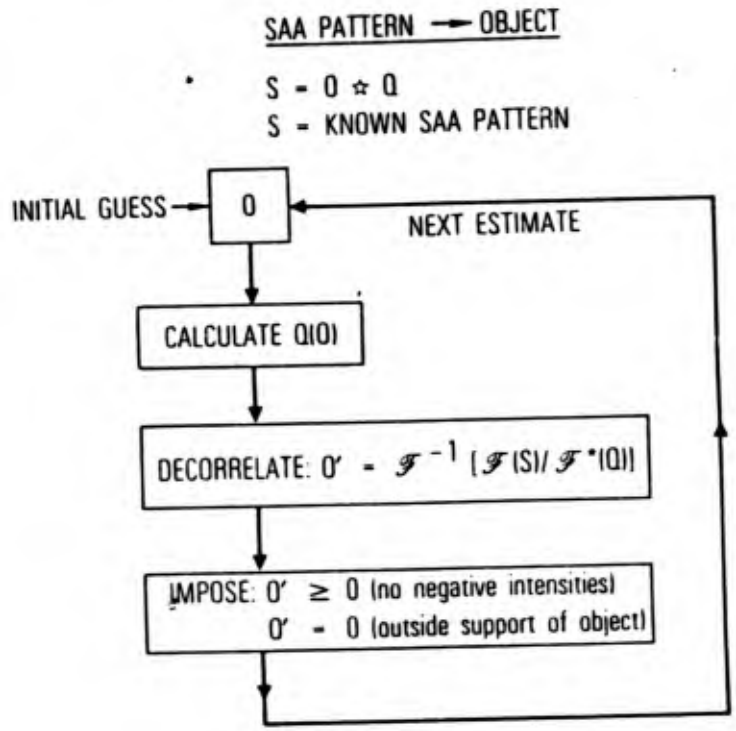

Fig. 4

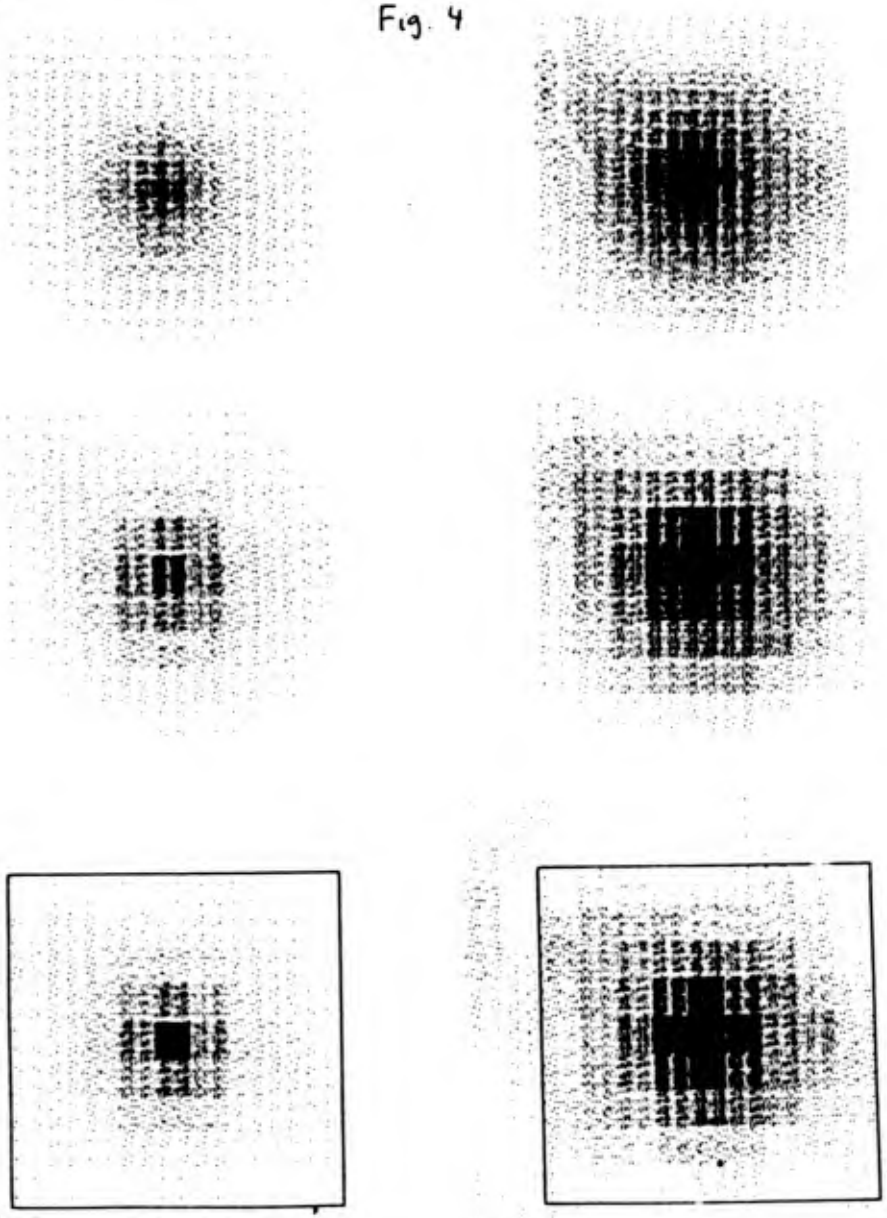

Fig 5

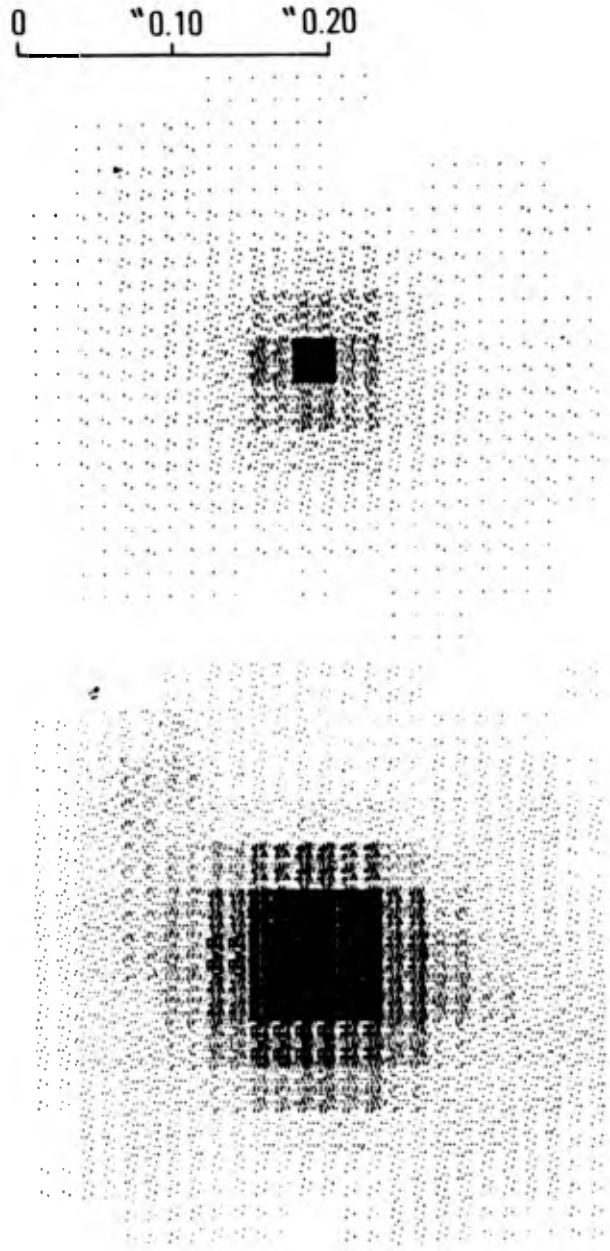

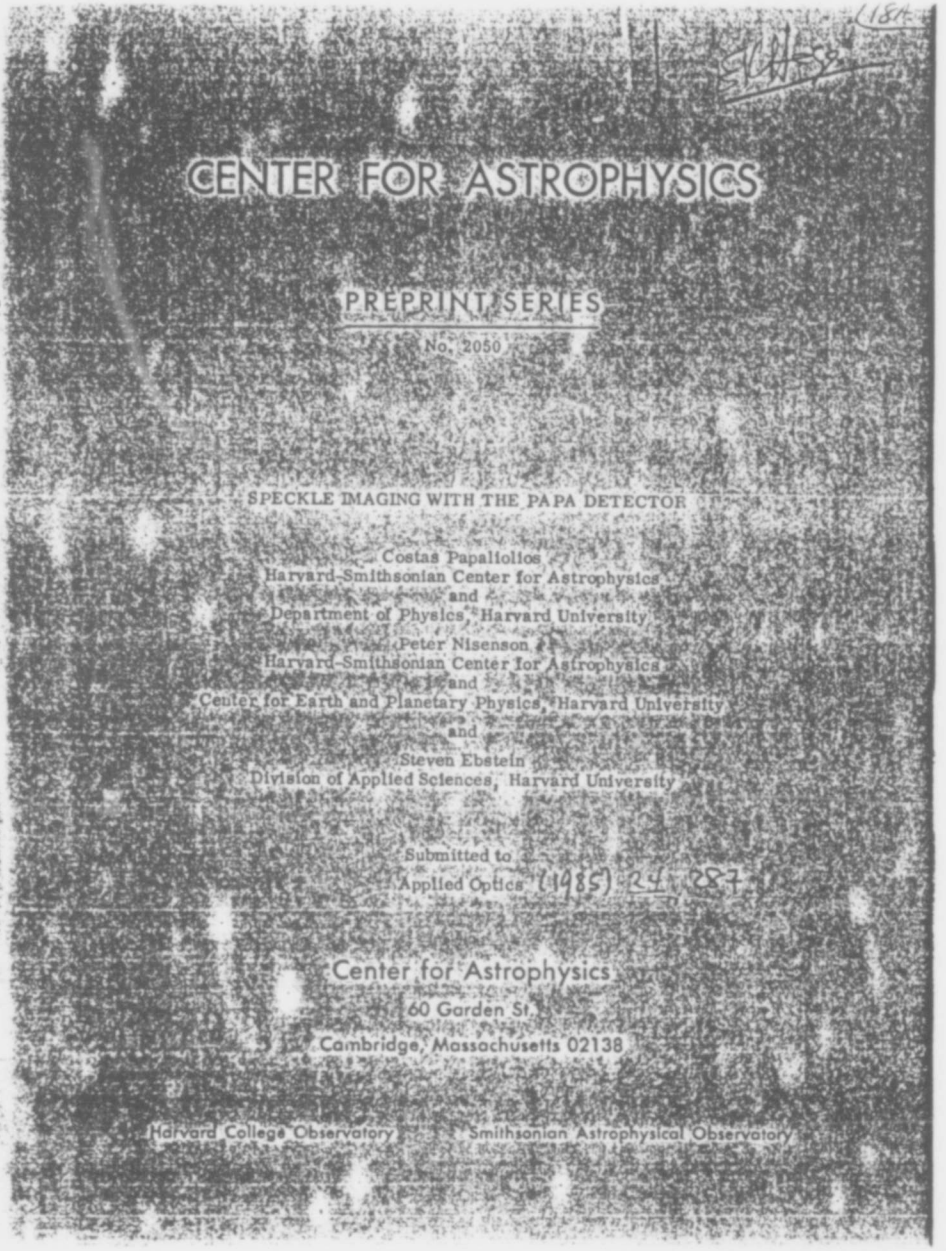

Center for Astrophysics
Preprint Series No. 2050

Speckle Imaging with the PAPA Detector

Costas Papaliolios
Harvard-Smithsonian Center for Astrophysics
and Department of Physics,
Harvard University, Cambridge, MA 02138

Peter Nisenson
Harvard-Smithsonian Center for Astrophysics
and Center for Earth and Planetary Physics,
Harvard University, Cambridge, MA 02138

Steven Ebstein
Division of Applied Sciences,
Harvard University, Cambridge, MA 02138

Abstract

A new two dimensional photon-counting camera, the PAPA (Precision Analog Photon Address) detector has been built, tested and used successfully for the acquisition of speckle imaging data. The camera has 512x512 pixels and operates at count rates of at least 200,000 per second. In this paper, we present technical details on the camera, and include some of the laboratory and astronomical results which demonstrate the detector's capabilities.

1. Introduction

A new two dimensional photon-counting camera has been built and successfully used for speckle imaging. The PAPA (Precision Analog Photon Address) detector works well at count rates of at least 200,000/sec and has 512x512 pixels of resolution. It provides a list of photon addresses in the order of their detection and can supply their arrival times to a precision of about 1 microsecond. An earlier version of this camera[1] was built and provided the experience that enabled the construction of the present highly successful model. The camera has been tested in the laboratory and now has been used on three telescope observing runs.

The properties that make this camera particularly useful for speckle work are: 1) The individual photon positions are recorded making it possible to do exact photon noise bias corrections that arise from the quantization of the detected signal[2]. 2) The time information allows tailoring of the frame time (equivalent to the exposure time for a conventional camera) to match the atmospheric correlation time when the data is being computer processed, resulting in an optimized signal-to-noise ratio. 3) Recording the addresses of the detected photons is much more efficient than recording the number of photons in each pixel position (as with an array detector), since there are only a few photons detected per frame, for faint objects.

In this paper, we present a status report on the current state of the PAPA detector, along with results of tests in the laboratory

and speckle data acquisition at the telescope. Potential improvements in the maximum count rate and spatial resolution of the camera are discussed as well as its application to other areas.

2. Speckle Imaging

Speckle interferometry is a technique, first used by Labeyrie[8] that eliminates the atmospherically caused degradation in resolution which plagues all ground based telescopes with apertures larger than about 10cm in diameter. Speckle imaging, an extension of this technique[9-11], results in full image reconstruction at the diffraction limit of the telescope. The data taking requirements for both imaging and interferometry are quite similar. A sequence of short exposure photographs taken with a large telescope provides the basic input data. The exposure time is set to approximately match the atmospheric correlation time, typically 10 msec, but which may vary by an order of magnitude depending on the site and the atmospheric conditions. Because of this short exposure time and the narrow spectral bandwidths (about 100 angstroms) that are needed there are very few photons per exposure. The number of photons becomes even smaller for fainter objects, which always seem to be the most interesting ones to study. Although the processing of the data in the pioneering work of Labeyrie was done photographically using analog methods, these methods are inadequate and not very flexible for the present objects of interest. The information in each exposure is now entered into a digital computer which performs the speckle processing.

We initially tried to provide the data required for our speckle program with an intensified film camera, and later with an intensified video camera (an ISIT). Both cameras were only partially successful in providing data on the faint objects we were most interested in. It became apparent that the ideal camera for our purposes would be one that would detect individual photons as "delta" functions (i.e. their positions would be precisely specified, to the resolution of the camera), and would preserve the timing information down to about 1 msec. In this case the photon noise bias associated with the quantized signal could be completely removed[8]. In addition, the ability to easily transfer this information into a computer would be very important. At low count rates, several cameras could easily be built, such as a video system with digital centroiding. The camera we required would have to function at least at a rate of 100,000/sec.

3. Principle of Operation

Each photon detected at the photocathode of a high-gain image intensifier produces a bright spot at the output face of the intensifier. The measurement of the spot position consists of a series of binary decisions. A photomultiplier looking at an image of the intensifier output face determines that a photon has been detected, somewhere in the field. Another phototube looking at an identical image but through a mask that is clear on the left half and opaque elsewhere determines whether the detected photon is in the left

half of the field if it sees it or in the right half if it doesn't. Each succeeding phototube, looking through an appropriate mask at its image of the intensifier, determines one more bit in the x or y address of the photon. In this way 9 phototubes determine the position in the x direction to one of 512 locations, and 9 more phototubes can similarly determine the y position. The resulting 18-bit x-y address is recorded on tape for later entry into a computer. The sequence of addresses thus generated is recorded in the same order as the arrival time of the photons.

4. Description of the camera

The optical layout of the camera is shown in Fig. 1. A photon detected at the photocathode of the high-gain image intensifier produces a bright spot at the intensifier output. The light from this spot is collimated by the large lens and an array of identical small lenses, each picking off a small bundle of collimated light, forms its own image in its focal plane. The image formed by each small lens is a copy of the output face of the intensifier. A mask is placed in each of these image planes, except for one which we call the strobe channel. In order to uniformly illuminate the phototube, a field lens immediately follows each mask.

The masks used in the camera are Gray-coded rather than binary-coded. Gray code has the property that only one bit changes in the digital address from one pixel to the next (Fig. 2). Since only one bit of the Gray code changes between adjacent pixels, ambiguities associated with a photon crossing pixel boundaries can cause only a one pixel error in the decoded position. The contrast with a binary coded system is dramatic. A photon crossing the center of the field causes a change in all binary bits. If the bits do not switch simultaneously, the decoded position can yield an address that is anywhere in the field.

5. Photon camera electronics

For each detected photon event, the pulse outputs from the photomultipliers are integrated by fast, gated integrators. Since the intensifier has a finite spot size (though smaller than one pixel in diameter), a threshold for deciding whether a photon has landed in the clear or opaque area of a mask is set to half the strobe channel pulse height. This comparison is valid for pulses of a wide range of amplitudes, so the exponential pulse height distribution of the image intensifier does not present a problem. The result of all the comparisons is the Gray-coded x-y position for the event.

After each event is detected, the address of the photon is latched and the integrators are reset. The stream of addresses, converted digitally from a Gray to a binary code, are encoded on a video carrier and recorded serially onto a videocassette tape. The binary address is also D/A converted to provide a real time display on an x-y scope. In addition, a microcomputer samples the data stream, allowing for some processing and image integration at the telescope.

Back in the laboratory, the data is stripped from the video tape onto computer magnetic tape, allowing digital processing at the integrating computer.

6. Basic laboratory tests

Fig. 3 contains two direct integrated images recorded with the PAPA detector. Each was recorded at a count rate of 60,000 counts/sec and contains about 3.6 million detected photons. While the camera does have 512x512 pixels, the current data recording technique is limited to only 8 bits x 8 bits (256x256 pixels). Using only the lower 8 bits in the x and y photon addresses, we have imaged targets which demonstrate resolution at the 512x512 scale. At the scale normally used (256x256 pixels), integrated images of flat fields (uniformly illuminated fields) indicate pixel-to-pixel variations of about 30% rms. These non-statistical variations, which are presumed to be due to mask misalignments and imperfect optics, seem to be stable and are eliminated by standard flat-fielding operations in the computer. The flat fielding operation, important when the camera is used to produce accurate integrated images, is relatively unimportant for speckle applications since the artifacts fall almost entirely along the axes in frequency space. However, since the flat field correction is done so easily in an array processor, we routinely perform it on all of the data acquired.

7. Speckle results

The PAPA camera has now been used on three speckle observing runs on three different telescopes: the Steward Observatory 90" on Kitt Peak, the Smithsonian Astrophysical Observatory - University of Arizona Multiple Mirror Telescope, and the University of Hawaii 88". On each run, the camera worked without any problems and produced many usable data sets of technical and scientific value. We demonstrate the quality of the results with a few examples from the first data obtained with PAPA on the Steward 90" speckle run in November.

Fig. 4 shows a long exposure, a reconstruction, a power spectrum and a representation of the recovered transform phase for a 0.5 arcsecond separation binary SAO 93840. The two components are magnitude 8 and 9, and the recording data rate was 40,000 photons/sec. This star was not known as a double prior to this run. Fig. 5 shows a direct integration of a data set on the same star for various exposure times. Figs. 6 and 7 demonstrate the effect of the frame time (relative to the atmospheric correlation time) on the reconstructed power spectra and images, respectively. The time ordered photon list recorded with the PAPA allows partitioning the data in arbitrary time bins. The data was processed for equal signal to noise, ie. the number of frames varied inversely as the square of the number of photons per frame. It is suprising that even for frame times as long as 360 msec, there is still substantial correlation at low angular frequencies. Figs. 8 and 9 show the influence of the length of the integration on the quality of the recovered power spectra and images.

Fig. 10 contains the image, autocorrelation and power spectra for Delta Ori, a bright star with a faint companion (3 magnitudes difference). Fig. 11 shows another star, Gamma Ori, with a previously undetected companion. The two components have a magnitude difference of 5 with separation of 0.8 arcsecond. Because of the brightness of both Delta and Gamma Ori, neutral density filters had to be used to reduce the signals to a level within range of our data recording capabilities. Fig. 12 shows the image, autocorrelation and power spectrum for Vesta, a 0.3 arcsecond diameter asteroid. While this is only a small sample of the data recorded and processed the results demonstrate the linearity and dynamic range of the camera and its potential for speckle data recording.

3. Camera Properties

The PAPA detector, made from easily available off-the-shelf parts, is a two-dimensional photon camera that provides a time ordered list of photon positions. Currently, it can handle count rates of at least 200,000/second and it provides 512x512 pixel resolution.

The spatial resolution can certainly be increased by going to a larger diameter intensifier (the present version uses a 25mm diameter tube), or by using interpolation of the measured pulse height in each channel to obtain the extra bits of resolution. Unlike the resistive anode type of detectors which use centroiding and interpolation to provide the entire address information, most of the address information would still be provided by the masks and only the last few bits would come from the interpolation procedure. We think it is possible to build a camera with up to 4000x4000 pixel resolution, and requiring only a modification of the analog electronics.

The maximum count rate can also be increased somewhat just by improving the pulse electronics that follow the phototubes. The phosphor rise time of 20 nsec and decay time of 200 nsec, measured for the P-47 phosphor that is used on our intensifier, should allow the construction of a camera that could handle 1,000,000 counts/sec and lose only about 20% of the photons due to overlap.

The present version of the camera uses a single Generation II microchannel-plate intensifier with an extended-red S-20 photocathode which has a peak quantum efficiency of 4% . The camera electronics are set at a level in which 3/4 of the pulses are accepted, so the actual detector efficiency is 3%. We plan to couple a diode intensifier to the front of the microchannel-plate tube to increase the overall quantum efficiency to an expected 15% . The one potential problem with a two intensifier system is the increased geometric distortion in the conventional electron optics. However, this distortion can be corrected with a field lens located near the input face of the first intensifier, which introduces an inverse distortion compensating for the measured intensifier characteristic.

There are many applications for which this camera is of obvious value. It provides data that is in a convenient format for computer processing and the data rate is set by the number of photons detected, not by the number of resolvable pixels. The arrival time of the detected photons is preserved and can be recorded to a precision of under a microsecond. In addition to the speckle applications

already discussed, it could serve as the camera for a high spectral resolution echelle spectrometer with crossed dispersion , as has earlier been suggested[4], or as a star guider or tracker in a sparse field of faint stars.

9. Discussion

A new camera has been built to record the x-y positions of individually detected photons. It appears to approach the ideal low light level camera for our speckle work and preliminary data taken on three recent observing runs confirms this. For the first time we can make the essential photon noise bias correction that is always required for analysis of low light level speckle data. This camera has opened up a new field that we plan to exploit.

Acknowledgements

We wish to acknowledge the many useful discussions and supportive interest of Lawrence Hertz, Richard Goody, Robert Stachnik, Robert Noyes, and Keith Hege. We also wish to thank Joseph Lehar for help in the data reduction, Louis DeFeo for aid in the camera construction and Richard Cromwell for help in measuring the camera quantum efficiency. This work was partially supported by Grant No. NGL-22-007-228 of the National Aeronautics and Space Administration and by Grant No. AFOSR-81-0055 from the Air Force Office of Scientific Research. It gives us great pleasure to thank Dr. William Brunk (NASA) and Dr. Henry Radoski (AFOSR) who have been extremely supportive throughout the development of this detector.

References

1. C. Papaliolios and L. Hertz, Proc. Soc. Photo Opt. Instrum. Eng. 331, 360 (1982)
2. P. Nisenson and C. Papaliolios, Opt. Comm. 47, 91 (1983)
3. A. Labeyrie, Astron. Astrophys. 6, 85 (1970)
4. K.T. Knox and B.J. Thompson, Astrophy. J. 193 L45 (1974)
5. P. Nisenson, J. Apt, R. Goody and C. Papaliolios, Icarus 53, 465 (1983)
6. T. Gonsiorowski, App. Opt. 23, 1060 (1984)

Figure Captions

Fig. 1. Diagram of the PAPA two dimensional photon detector.

Fig. 2. Principle of Gray-coded masks for photon position detection.

Fig. 3. Direct images recorded with the PAPA detector at a data rate of 50,000 counts/sec.

Fig. 4. Reconstruction of SAO 93840 using 6000 frames at 60,000 counts/sec: a) direct sum b) image c) power spectrum d) recovered transform phase.

Fig. 5. Direct images of SAO 93840 for different integration times: a) .001 sec b) .01 sec c) .1 sec d) 100 sec.

Fig. 6. Effect of frame (exposure) time on the power spectrum for SAO 93840: a) 20 ms b) 80 ms c) 180 ms d) 360 ms

Fig. 7. Effect of frame (exposure) time on the reconstructed image for SAO 93840: a) 20 ms b) 80 ms c) 180 ms d) 360 ms.

Fig. 8. Convergence of the power spectrum for SAO 93840 as a function of number of frames: a) 6000 b) 1600 c) 400 d) 100.

Fig. 9. Convergence of the reconstructed image for SAO 93840 as a function of number of frames: a) 6000 b) 1600 c) 400 d) 100.

Fig. 10. Delta Orionis and its companion. Binary separation = 0.3 arcsecond, Δ V(magnitude difference) = 3: a) image b) autocorrelation c) power spectrum.

Fig. 11. Gamma Orionis and its companion. Binary separation = 0.8 arcsecond, Δ V(magnitude difference) = 5: a) image b) autocorrelation c) power spectrum.

Fig. 12. Reconstruction of the resolved (0.3 arcsecond) asteroid Vesta (data rate of 70,000 counts/sec): a) image b) autocorrelation c) power spectrum.

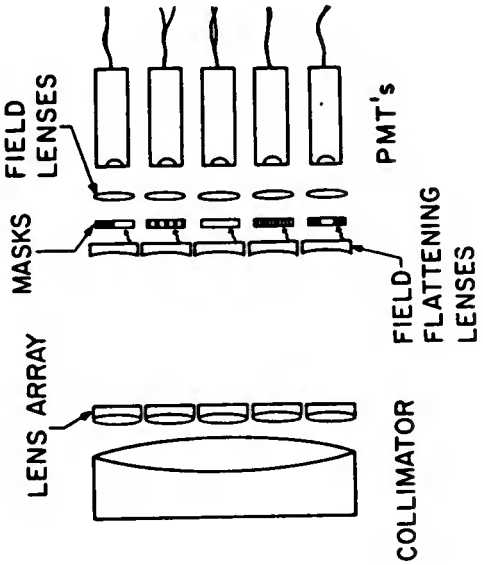

Fig. 1

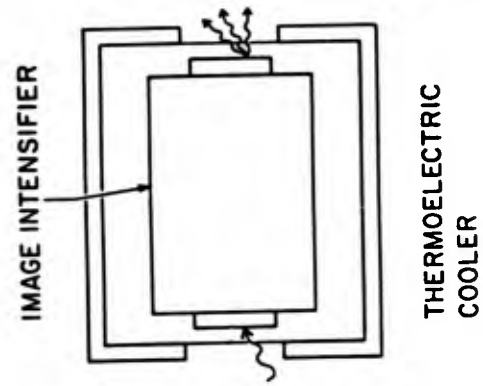

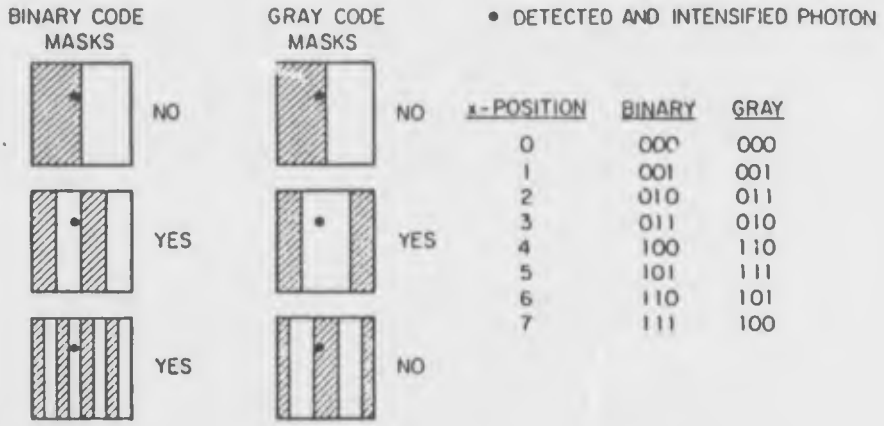
BINARY CODE MASKS
GRAY CODE MASKS
• DETECTED AND INTENSIFIED PHOTON
NO
YES
YES
NO
NO
YES
YES
NO
x-POSITION BINARY GRAY
0 000 000
1 001 001
2 010 011
3 011 010
4 100 110
5 101 111
6 110 101
7 111 100

Fig. 2

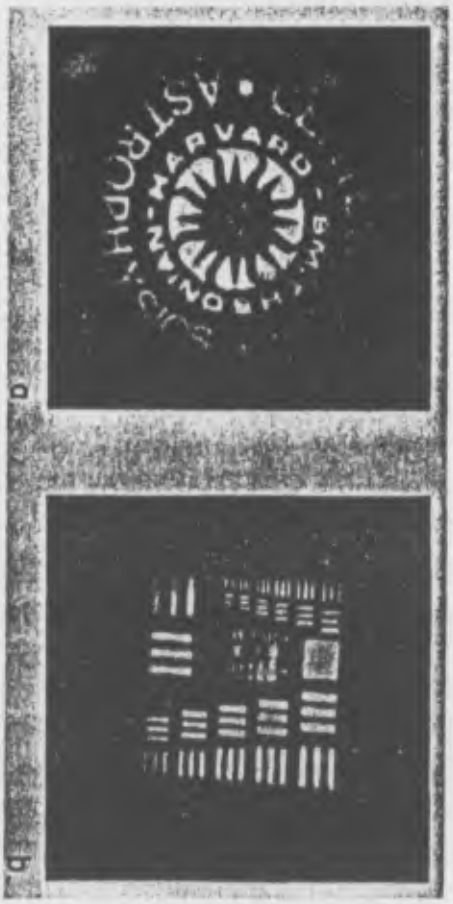
HARVARD-SMITHSONIAN ASTROPHYSICAL

Fig. 3

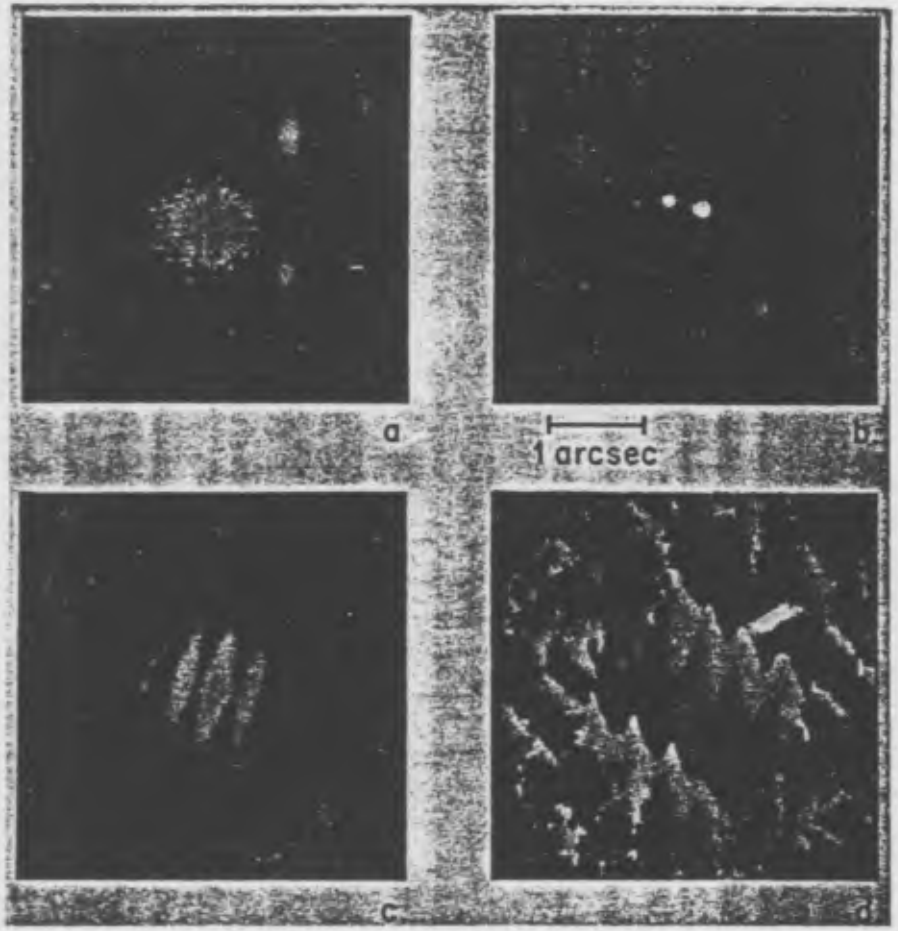

Fig. 4

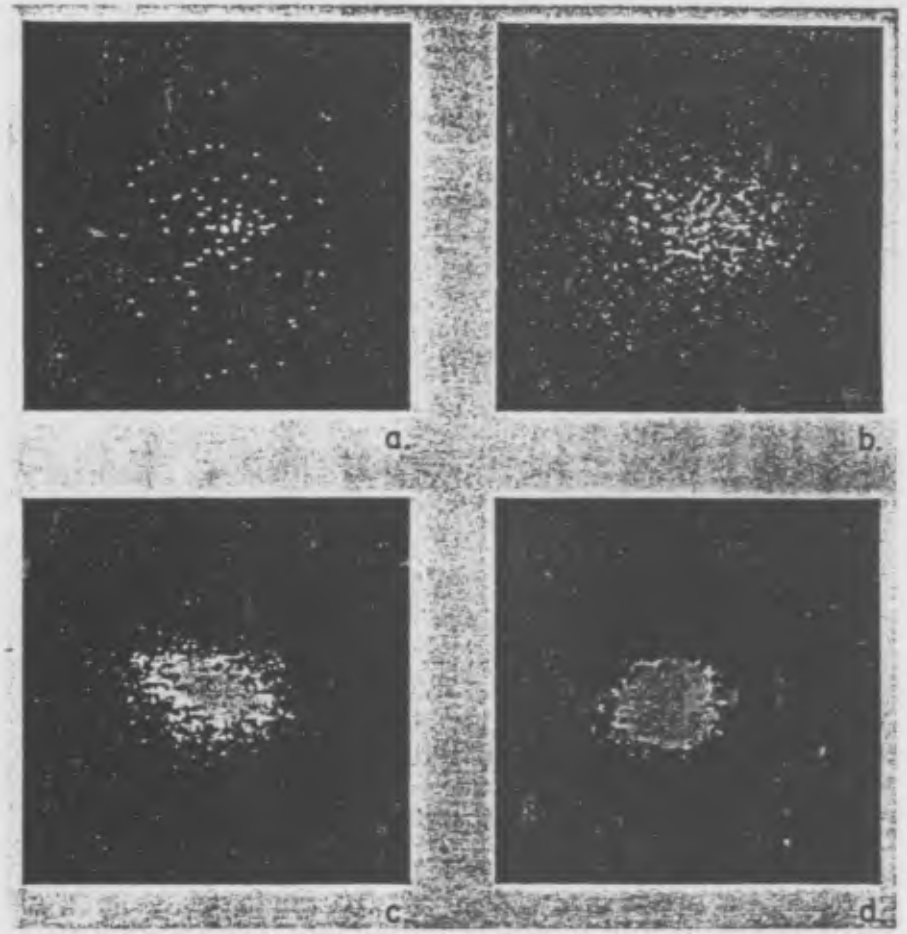

Fig. 5

SAO 73740

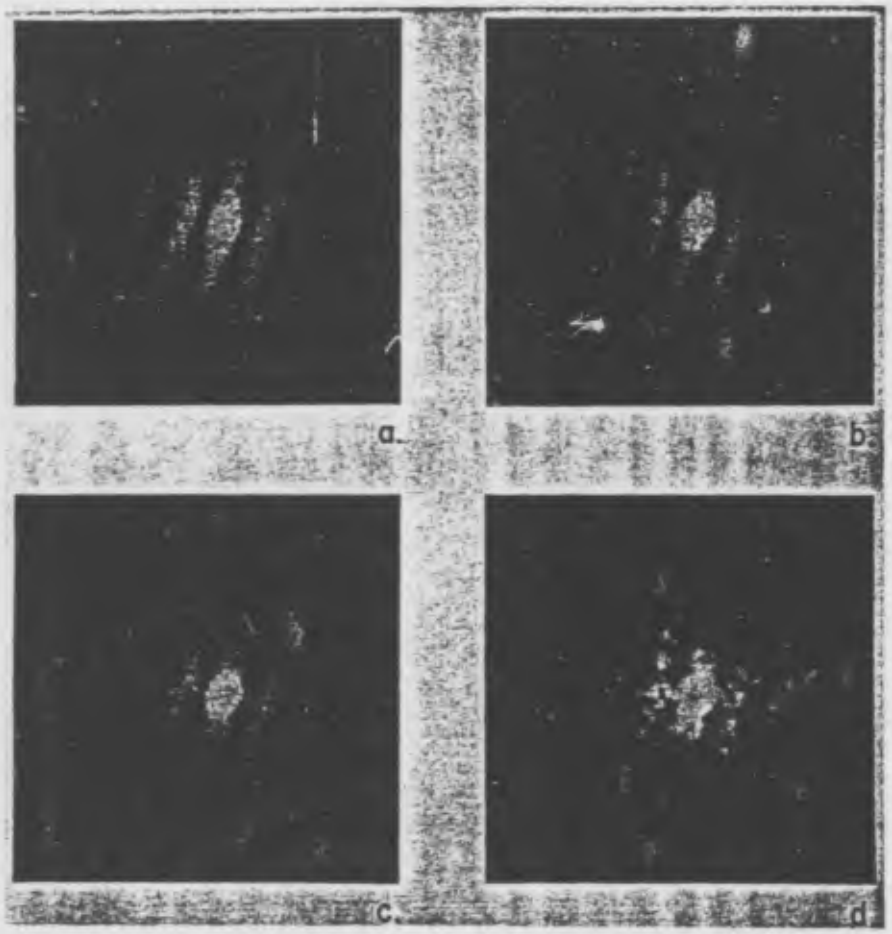

Fig. 6

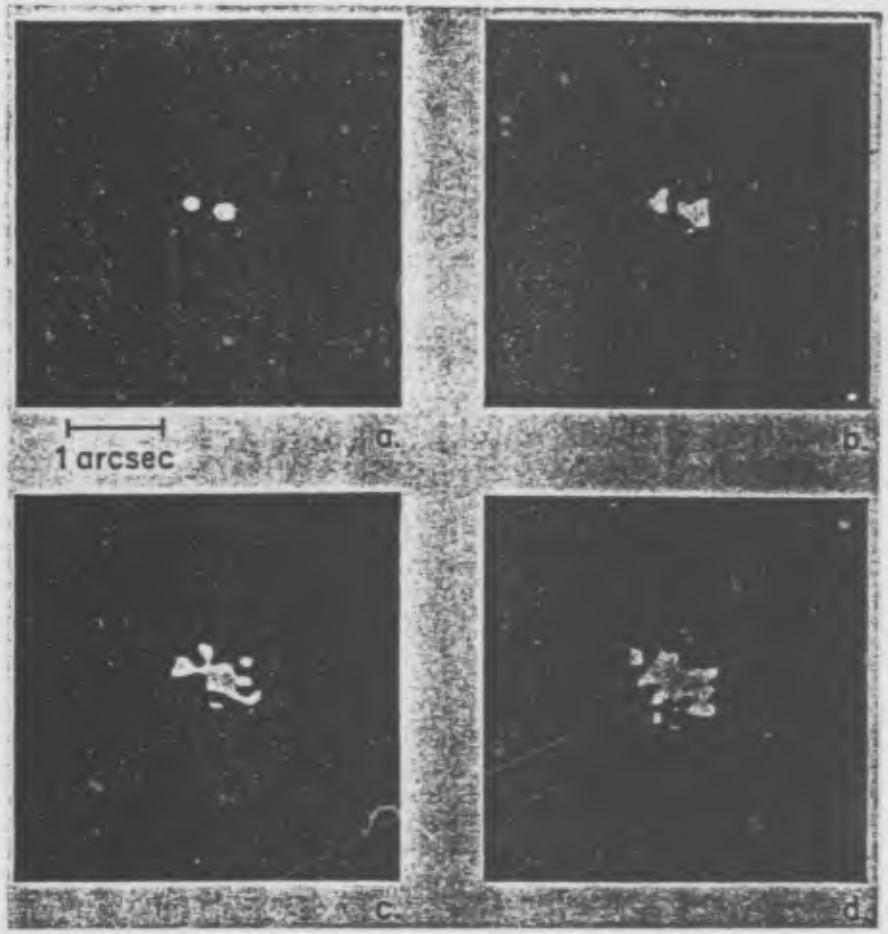

Fig. 7

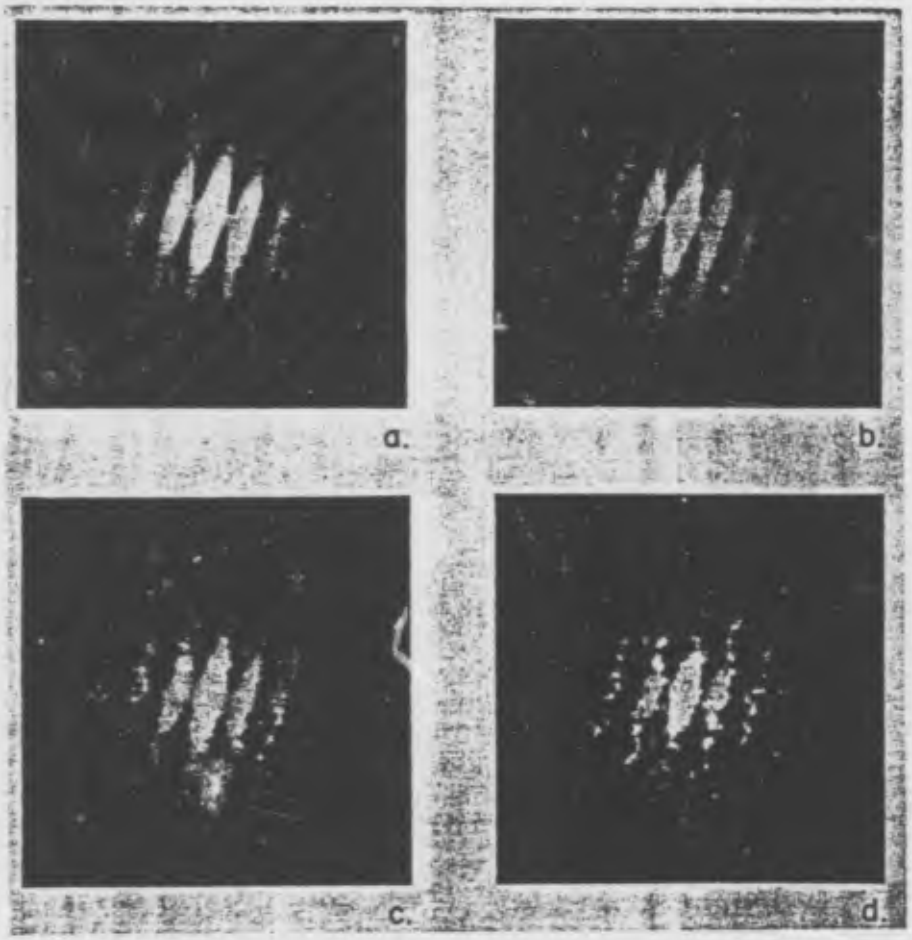

Fig. 8

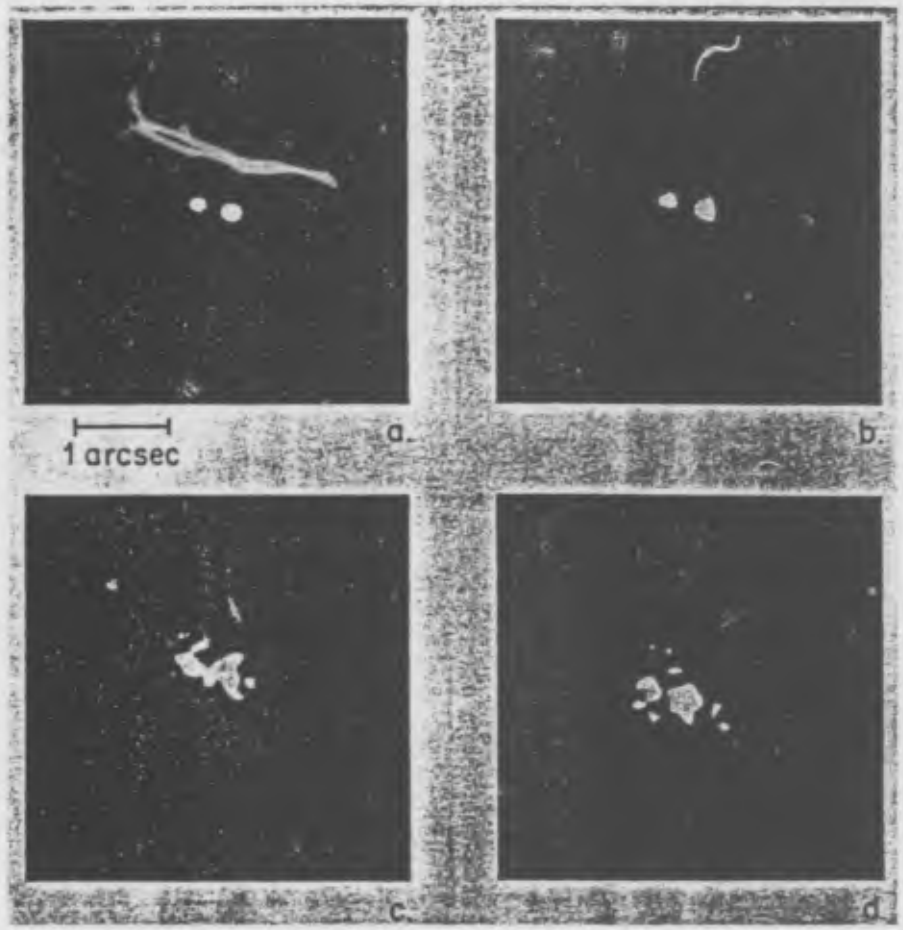

Fig. 9

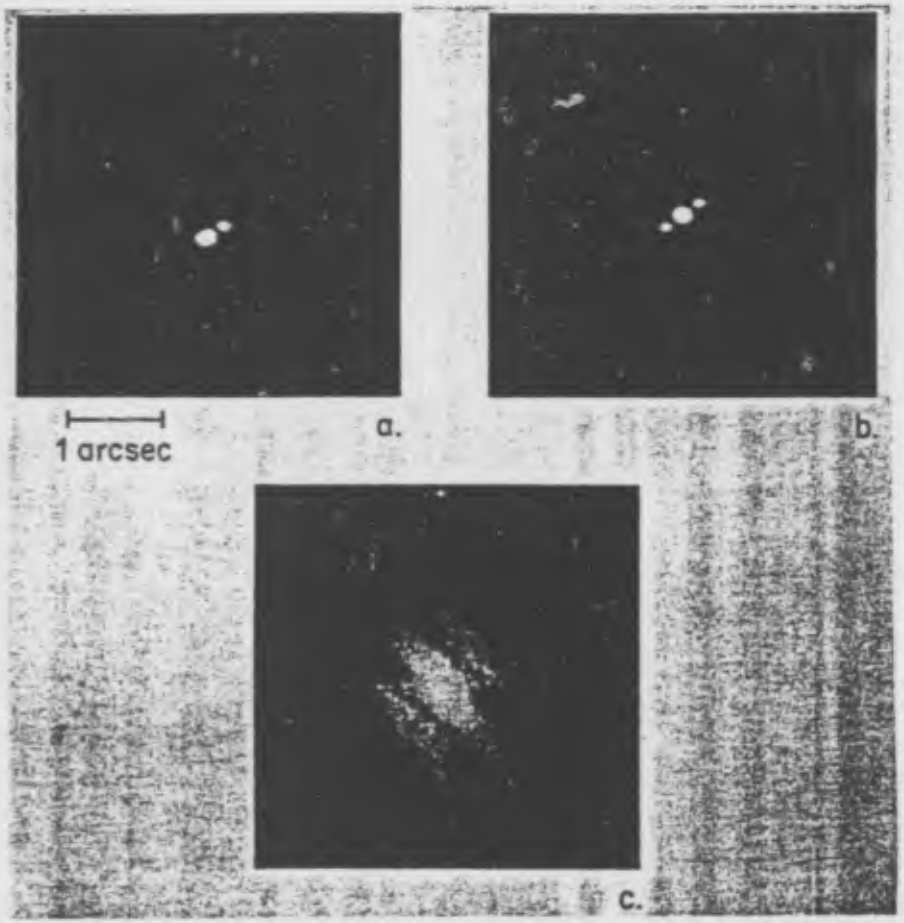

Fig. 10

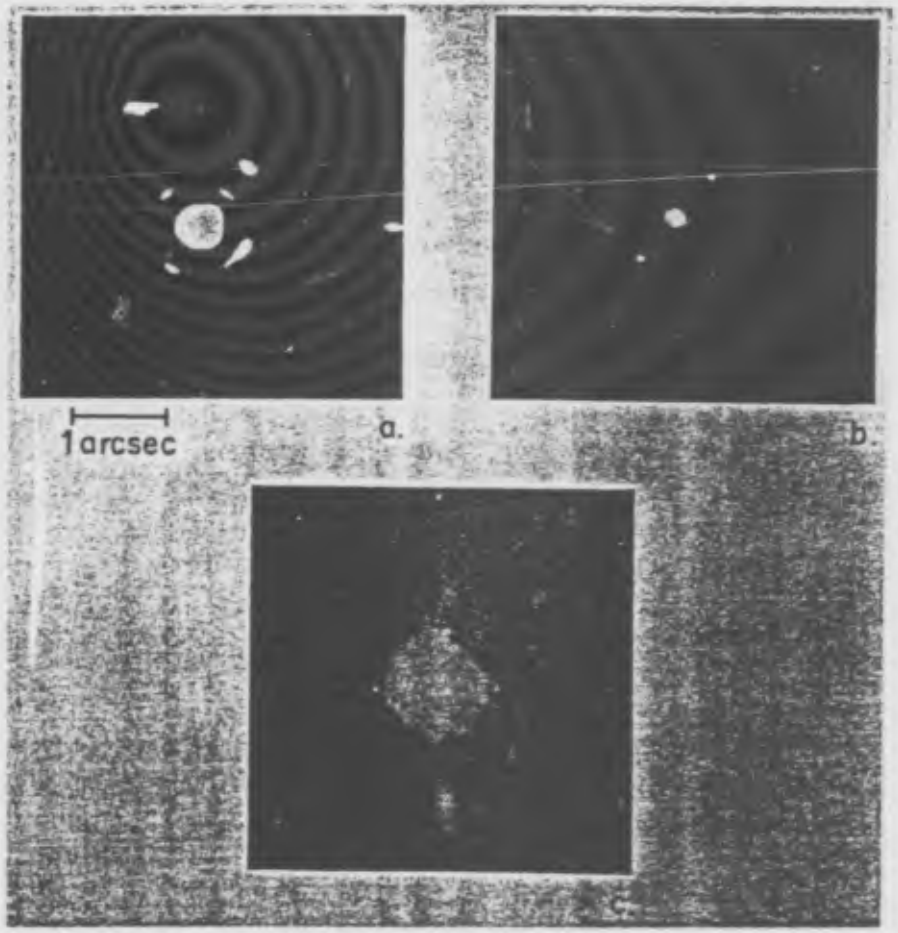

Fig. 11

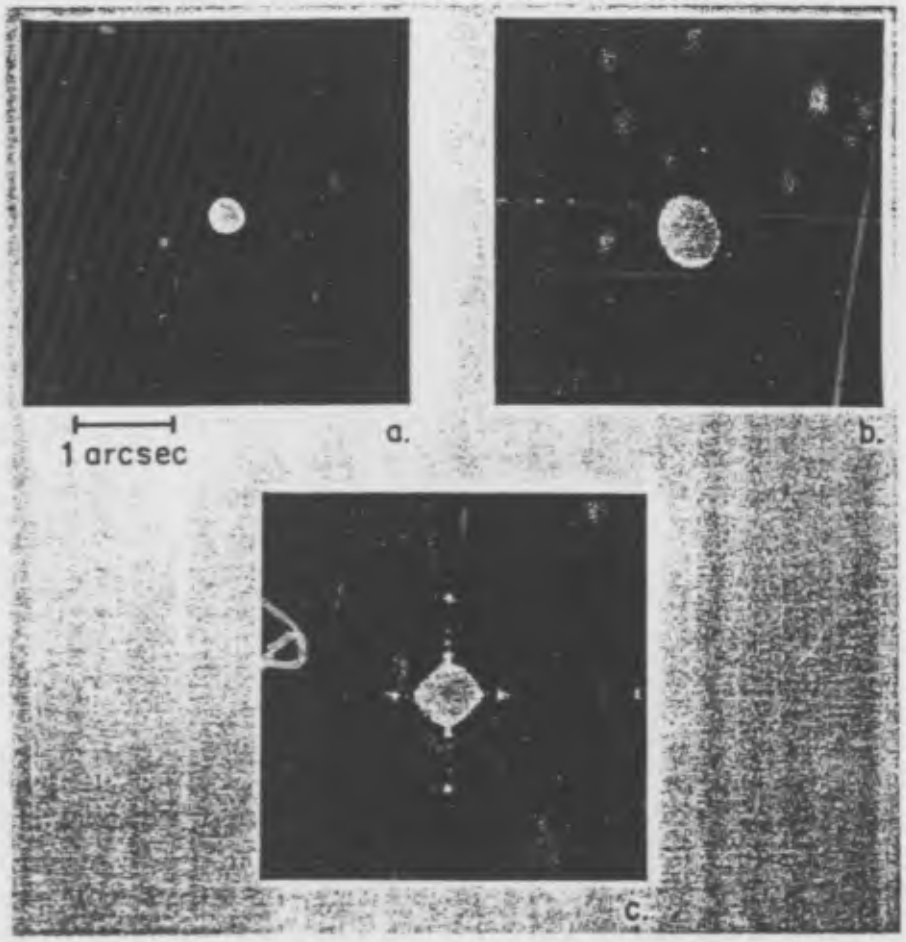

Fig. 12

SHIFT-AND-ADD IMAGING THROUGH PARTIALLY ISOPLANATIC SEEING

R.H.T. Bates*, J.M. Beckers†, J.C. Christou††, E.K. Hege††
and A.M. Sinton*

To be eventually Submitted to: MONTHLY NOTICES OF THE ROYAL ASTRONOMICAL SOCIETY

Summary A simplified theoretical approach to the effect of partial isoplanatism on shift-and-add suggests that the main degradation is loss of contrast rather than image distortion. This is illustrated by computer-generated results and by the processing of speckle images of Alpha Scorpius recorded with a single mirror of the Multiple Mirror Telescope. The apparent angular diameter of α_1 Scorpii is shown to be significantly greater than that of α_2 Scorpii (whose speckle images always provided the shift-and-add reference) even though the former is only just resolvable and the separation of the two components of Alpha Scorpius is greater than what is generally accepted as the (usual) diameter of the isoplanatic patch.

*Electrical & Electronic Engineering Department, University of Canterbury, Private Bag, Christchurch, New Zealand.

†? ? ? ?

††Steward Observatory, University of Arizona, Tucson, AZ 85721, USA.

1 INTRODUCTION

We argue that the shift-and-add technique (Bates and Cady 1980; Cady and Bates 1980; Bates and Robinson 1981; Bates and Fright 1982; Hunt et al 1983) for imaging objects viewed through severe seeing is relatively insensitive to departures from perfect isoplanatism. Our analysis complements Bagnuolo's (1982, 1984) statistical approach. Support for the theoretical arguments is provided by analysing shift-and-add images formed from speckle data obtained by Christou and Hege (1977) from observations of the pair of stars known as α_1 and α_2 Scorpii.

The relative insensitivity of shift-and-add to departures from perfect isoplanatism has three further implications, all of which are examined herein. The first is that conventional speckle interferometry (cf. §§6 and 8.4 of Bates 1982 - this reference is henceforth identified as B) is more adversely affected than is shift-and-add. The second implication is that shift-and-add permits a resolvable object (of arbitrary brightness) to be imaged to the diffraction limit, provided it is not overly removed from an adequately bright, isolated unresolved star. The third implication is that shift-and-add can be a suitable image processing technique for searching for faint detail in comparatively dark regions of the celestial sphere.

Certain preliminaries are established in §2. Theoretical consequences of imperfect isoplanatism are examined in §3. Two new adaptations of shift-and-add are proposed in §4, which includes supporting evidence in the form of results of a computational study. In §5 we show, by appropriate processing of recently recorded speckle images of Alpha Scorpius, that the first of the suggested adaptations of shift-and-add is indeed capable of generating useful astronomical data. We assess in §6 the significance of the work reported here.

2 PRELIMINARIES

We map the region of the celestial sphere in which we are interested onto image space. An arbitrary point in the latter is identified by the position vector x. The true image $f(x)$ of an observed object is what would be recorded by a perfectly figured telescope operating under ideal seeing conditions. So, the only imperfection contemplated for $f(x)$ is that it is diffraction limited by the finite pupil (of diameter D) of the telescope.

The object is partitioned into N sub-objects, occupying N non-overlapping sub-regions each of which is no larger than the isoplanatic patch. The true image of the n^{th} sub-object is denoted by $f_n(x)$, so that the whole true image is expressed in the form

$$f(x) = \sum_{n=1}^{N} f_n(x) \qquad (1)$$

In observational practice, the seeing is very rarely ideal, so that the diffraction limit is virtually never achieved with large telescopes (D>0.5m) operated conventionally. An image, which is recorded within a sufficiently brief interval that the state of the seeing does not change significantly during the exposure, is appropriately called instantaneous (see §3 of B). We denote by $h_{n,m}(x)$ the point spread function (psf) which describes the blurring of $f_n(x)$ during the m^{th} instant. Note that the ensemble average over m (here identified by angular brackets) of the $h_{n,m}(x)$ (for m running from 1 to M, with M being appropriately large) is equivalent to a long exposure image of an unresolvable object (i.e. an object smaller than the diffraction limit) of unit brightness. This is called the seeing disc (see §2.1 of B), which we write as

$$sd(x) = \langle h_{n,m}(x) \rangle \qquad (2)$$

The m^{th} speckle image (or specklegram, which is an instantaneous image, as defined above) of $f(x)$ can thus be written as (see §4 of 8)

$$s_m(x) = \sum_{n=1}^{N} \left(f_n(x) \,\theta\, h_{n,m}(x) \right) + c_m(x) \qquad (3)$$

where θ denotes convolution and $c_m(x)$ is the inevitable contamination (i.e. generalised noise).

Given an ensemble of speckle images, the brightest point (identified by x_m for the m^{th} image) in each is determined. Each image is shifted without rotation until its brightest point is at the centre of image space, and is then added to those of its fellows which have been similarly processed. After dividing by the number of images in the ensemble we obtain the shift-and-add image

$$f_{sa}(x) = < s_m(x + x_m) > \qquad (4)$$

For each m, we call the shift-and-add reference the point in $f(x)$ which is associated with x_m. Note that this reference can only be the same for all m if the brightest part of $f(x)$ is both unresolvable and much brighter than all other parts of $f(x)$. Even though $f_{sa}(x)$ is not in general a faithful version of $f(x)$, we emphasise that means have been developed (Minard et al 1985) for generating, from $f_{sa}(x)$, a significantly more faithful replica of $f(x)$.

3 IMPERFECT ISOPLANATISM

If the whole object lies within the isoplanatic patch, the images of all of the sub-objects are similarly blurred, implying that $h_{n,m}(x)$ equals some $h_m(x)$ for all N values of n. The form of $h_m(x)$ changes with m of course. When the blurring is only partially isoplanatic, which is the concern in this section, the forms of the $h_{n,m}(x)$ depend noticeably upon n as well as m.

A purely mathematical characterisation of partial isoplanatism is presented in §3.1. The level of agreement between this and a more physical model of the blurring process is discussed in §3.2. The theoretical consequences, for shift-and-add and for conventional speckle interferometry, of the formulas developed in §3.1, are examined in §§3.3 and 3.4 respectively.

3.1 Mathematical Model of Partial Isopanatism

We assume that each $h_{n,m}(x)$ can be expressed in terms of $h_{\ell,m}(x)$, for all ℓ different from n, by

$$h_{n,m}(x) = \left(1 - \alpha_{n,\ell,m}\right) h_{\ell,m}(x) + \beta_{n,\ell,m}\, g_{n,\ell,m}(x) \qquad (5)$$

where $\alpha_{n,\ell,m}$ and $\beta_{n,\ell,m}$ are independent real random numbers, in the range 0 to 1, with $\alpha_{n,n,m} = \beta_{n,n,m} = 0$, $\alpha_{n,\ell,m} = \alpha_{\ell,n,m}$, $\beta_{n,\ell,m} = \beta_{\ell,n,m}$ and

$$< \alpha_{n,\ell,m} > = < \beta_{n,\ell,m} > = \alpha_{n,\ell} = \alpha_{\ell,n} \qquad \text{with } \alpha_{n,n} = 0$$

It is appropriate to call $\alpha_{n,\ell}$ the degree of nonisoplanatism of the n^{th} sub-region with respect to the ℓ^{th}. We also take $h_{n,m}(x)$ and $g_{n,\ell,m}(x)$, for all ℓ, n and m, to be independent members of the same statistical ensemble.

3.2 Simplified Physical Model of Partial Isoplanatism

The formulas (5) and (6) are convenient for computational studies of partial isoplanatism, as we indicate in §4. It is important, however, to enquire whether these formulas are physically acceptable.

Atmospheric seeing is caused by random spatial variations of the refractive index of the atmosphere. One can think of "blobs" of air, each having a different refractive index. These blobs are moved by air currents. Their sizes, shapes and refractive indices vary with time.

3.4 Effect of Partial Isoplanatism on Speckle Interferometry

Since Labeyrie's speckle interferometry (cf. §6 of B) can be regarded as a special case of Knox-Thompson imaging (cf. §8.4 of B), we concentrate on the latter here.

The Knox-Thompson technique involves computing the Fourier transform $S_m(u)$ of each $s_m(x)$, where u is the position vector of an arbitrary point in Fourier space, and forming the quantity

$$T(u,w) = < S_m(u)\, S_m^*(u + w) > \qquad (11)$$

where the asterisk denotes complex conjugation and w is a fixed vector shift, with $|w|$ being a fraction of the effective width of the Fourier transform of the seeing disc. It is also necessary to carry out the same processing on an ensemble of speckle images of an unresolvable object. We denote by $T_o(u,w)$ the result of this latter processing. It transpires that $T(u,w)$ is the product of $T_o(u,w)$ and the quantity

$$\Phi(u,w) = F(u)\, F^*(u + w) - \sum_{n,\ell=1}^{N} \alpha_{n,\ell}\, F_n(u)\, F_\ell^*(u + w) \qquad (12)$$

where $F(u)$ and $F_n(u)$ are the Fourier transforms of $f(x)$ and $f_n(x)$ respectively. In practice, of course, the deconvolution (see §5.4 of B) of $T(u,w)$ is unavoidably contaminated - it can, however, provide a useful estimate of $\Phi(u,w)$.

The second term on the right hand side of (12) represents the effects of partial isoplanatism. If this second term is negligible, the standard Knox-Thompson algorithm (cf. §8.4 of B) permits $F(u)$ to be evaluated recursively at a grid of points in Fourier space. When the $\alpha_{n,\ell}$ are appreciable, they must contribute significantly to the overall noise level. The goal of Labeyrie's original version of speckle interferometry is to generate $\Phi(u,0)$, which corresponds to estimating $|F(u)|^2$. The available estimate of the latter is unavoidably contaminated significantly by the presence of the second term on the right hand side of (12), if the $\alpha_{n,\ell}$ are appreciable. Fried (1979) remarks similarly on speckle interferometry's sensitivity to imperfect isoplanatism.

Whereas the additional contamination due to imperfect isoplanatism merely raises the "fog level" for shift-and-add, it actually alters the information implicit in the quantities generated by conventional speckle interferometric processing. This distinction seems significant to us.

4 NEW IMAGING CAPABILITIES OF SHIFT-AND-ADD

It is seen from (8) that shift-and-add imaging remains useful until all of the $(1 - \alpha_{n,1})$ are so small that no part of the summation exceeds the level of the composite contamination. This suggests new adaptations of shift-and-add, which are described in the following two sub-sections.

Both adaptations involve an unresolved star and a resolvable object, close enough together that the blurring of their images is partially isoplanatic, but sufficiently separated that their seeing discs do not overlap. The unresolved star must be bright enough that each of its short exposures exhibits the typical mottled appearance of a speckle image (cf. §2.1 of B). The resolvable object need only be sufficiently bright that each of its short exposures record a few photon impacts.

There are two particular kinds of situation, discussed below, in which shift-and-add can be invoked to form diffraction-limited images of the resolvable object.

The blobs furthest from the telescope pupil are the chief cause of loss of isoplanatism. It is convenient to imagine these blobs arranged as a thin screen, parallel to the pupil plane at some height above it. If one draws rays from all points in the object to any particular point in the pupil, the reason for partial isoplanatism is made immediately apparent. Not all of these rays pass through the same blob, in general.

Even though the above physical picture does not (seem to) lead to such convenient formulas as (5) and (6), it can be straightforwardly transformed into a computer program. We have compared computational results obtained with such a program and with the mathematical model introduced in §3.1. The differences appear negligible, even for degrees of nonisoplanatism as large as 0.5. Accordingly, for the purposes of this paper, we think the approach introduced in §3.1 adequately accounts for the effects of partial isoplanatism. However, one of us (A.M.S.) intends to critically examine this assumption elsewhere.

3.3 Effect of Partial Isoplanatism on Shift-and-Add

For definiteness we take $f_1(x)$ to contain the shift-and-add reference. It is important to understand that this does not ensure that $f_{sa}(x)$ is a faithful replica of $f(x)$, because the diameter of the circle circumscribing the image of any sub-object may be appreciably larger than the Airy disc. It does, however, ensure that the shift-and-add reference always lies within the same isoplanatic patch (refer to second paragraph of §2). While this restricts the generality of our results, we doubt whether shift-and-add can be useful when the reference can hop about arbitrarily within speckle images which span several isoplanatic patches.

Since we are requiring $f_1(x)$ to always contain the shift-and-add reference, it is only the part of $s_m(x)$ depending upon $h_{1,m}(x)$ that contributes to the reconstruction of $f(x)$. As far as each $g_{n,1,m}(x)$ is concerned, the shift x_m is effectively random. So, averaging the $g_{n,1,m}(x + x_m)$ over m produces, for each n and 1, a smoothly varying disc similar to, although slightly larger than, the seeing disc. Since it makes essentially no difference to the present discussion, we assume it (for convenience) to be identical to the seeing disc, i.e.

$$< g_{n,1,m}(x + x_m) > = sd(x) \tag{7}$$

Combining (1) through (7) gives

$$f_{sa}(x) = f_{1,1sa}(x) + \sum_{n=2}^{N} \left((1 - \alpha_{n,1}) f_{n,1sa}(x) \right) + \bar{c}(x) \tag{8}$$

where

$$f_{n,1sa}(x) = f_n(x) \; \theta < h_{1,m}(x + x_m) > \tag{9}$$

and the <u>composite contamination</u> $\bar{c}(x)$ comprises all the "noisy" parts of $f_{sa}(x)$, i.e.

$$\bar{c}(x) = \sum_{n=2}^{N} \left(\alpha_{n,1} f_n(x) \; \theta \; sd(x) \right) + < c_m(x \quad x_m) > \tag{10}$$

The final term on the right hand side of (8) represents the familiar background "fog" (§8.7 of 8) on top of which the reconstructed image is revealed by shift-and-add. The first two terms indicate that all parts of $f(x)$ are recovered, to the same degree of faithfulness as for perfect isoplanatism, but the contrast of the n^{th} sub-image is reduced by the <u>contrast factor</u> $(1 - \alpha_{n,1})$. If an independent assessment of the variation of the degree of isoplanatism across the field of view were available then all parts of $f_{sa}(x)$ could be formed with equal contrast (but not with equal contamination levels, of course).

§4.1 Bright Resolvable Object

Suppose the speckle images of the resolvable object reveal the typical mottled appearance (see the right hand image in Fig. 4 for example). These speckle images could be subjected directly to shift-and-add. A faithful replica of the object would not be obtained, however, because in successive speckle images the shift-and-add reference can be expected to correspond to different parts of the object.

If the speckle images of the unresolved star are subjected to shift-and-add, a diffraction limited image of this star is formed. Furthermore, provided there is a reasonable degree of partial isoplanatism between the speckle images of the star and the resolvable object at any instant, the brightest point in the speckle image of the star can serve as a useful reference for both speckle images. The same parts of the resolvable object can be expected to be superimposed, each time a speckle image is added to those which have been previously processed, if the speckle images of the star and the object are both shifted identically, the shift being derived from the speckle image of the star.

The value of this suggestion is confirmed by the processing of observational data reported in §5. It is also supported by the computational results presented in §4.3.

§4.2 Searching Dark Regions for Faint Detail

Suppose the resolvable object introduced in §4.1 is so faint that its presence is only suspected before performing the processing suggested in this sub-section.

We imagine that one speckle camera occupies the part of the focal plane whereon impinges the light from the bright, unresolved star. Another speckle camera is positioned to capture photons from the suspected resolvable object. A diffraction-limited image of the latter could be formed by carrying out processing identical to that proposed in §4.1. The computational results presented in §4.3 indicate that this suggestion might be useful in observational practice.

§4.3 One-Dimensional Computational Simulation

We here illustrate the suggestion made in §4.2 with computationally generated one-dimensional speckle images. The reason for using one-dimensional images is that they make it easier, than two-dimensional images do, to display the effects of partial isoplanatism. The results presented in this section also provide support for the suggestion introduced in §4.1. Furthermore, the processing of two-dimensional images reported in §5 complements the present discussion and confirms that our proposals have practical value.

In terms of the notation introduced in §2, we here set $N = 2$ and replace the position vector x with the scalar Cartesian coordinate x. Fig. 1(a) shows a particular $f(x)$, for which $N = 2$. The coordinate x identifies the position of an arbitrary point in one-dimensional image space. The left hand part - i.e. $f_1(x)$ - of $f(x)$ is to be thought of as a one-dimensional resolvable object. The reader is asked to imagine that the right hand part $f_2(x)$ has been magnified many times, because we are envisaging that $f_2(x)$ represents a faint object. Fig. 1(b) is an ideal speckle image of $f(x)$ - i.e. $h_{1,m}(x) = h_{2,m}(x)$. It is worth emphasising that the right hand part of Fig. 1(b) could be expected to consist in practice of only a few photon impacts. This need not adversely affect the quality of the finally processed image, provided the observation is continued for long enough to generate a

useful signal-to-noise ratio (see references quoted in §13 of B).

Our suggested processing involves identifying the brightest point in each speckle image (Fig. 1(b) being a typical one) and shifting the whole of it (i.e. both the left and right hand parts - this is the crux of our suggestion) until its brightest point is at the origin of the x-axis (this origin is taken to be where the single peak comprising the left hand part - i.e. $f_1(x)$ - of Fig. 1(a) lies). Fig. 1(c) shows the shift-and-add image formed from *200* independent speckle images (we generated our psfs by taking the squared magnitudes of the one-dimensional Fourier transforms of functions of unit amplitude but pseudo-random phase). All the detail present in Fig. 1(a) is revealed in Fig. 1(c), as is of course to be expected since the speckle images from which Fig. 1(c) was formed were all ideal. The smooth curves on which the details are superimposed are the seeing discs for the sub-regions.

Fig. 2(a) shows a typical speckle image (computed as explained above) for partially isoplanatic seeing. The quantities $\alpha_{2,1,m}$ and $\beta_{2,1,m}$ - see (5) -, which should ideally be random, were chosen independently for *200* speckle images from a pseudo-random distribution ranging from *0* to *1*, so that $\alpha_{2,1} = 0.5$ (we write α instead of $\alpha_{2,1}$ from now on). Careful comparison of Figs. 1(b) and 2(a) confirms that, in the former both $f_1(x)$ and $f_2(x)$ are blurred similarly, whereas in the latter the two parts of the true image are blurred significantly differently. Fig. 2(b) shows the shift-and-add image formed from *200* speckle images statistically akin to the one shown in Fig. 2(a), which has been contaminated (as has each of its fellows) by adding pseudo-ransom noise, uniformly distributed between zero and the peak amplitude of the seeing disc due to $f_1(x)$.

Note that the amplitude of the version of $f_2(x)$ revealed in Fig. 2(b) is reduced compared to that seen in Fig. 1(c) by the contrast factor $(1 - \alpha) = 0.5$. The amplitude of the seeing disc appears to be increased, by comparison with Fig. 1(c), because of both the contamination and the degree of nonisoplanatism. The crucial aspect of Fig. 2(b) is, however, that the form of $f_2(x)$ is faithfully revealed even though $f_2(x)$ itself does not belong to the class of images which can be faithfully reconstructed by shift-and-add. It must be emphasised that we are able to reconstruct $f_2(x)$ successfully because the shifts are derived from the parts of the speckle images which are due to $f_1(x)$.

Fig. 2(c) shows the result of deconvolving (see §5.4 of B) the left hand part of Fig. 2(b) from the whole of Fig. 2(b). The form of $f(x)$ is revealed, with noise superimposed upon it and with the amplitude of $f_2(x)$ reduced by the contrast factor.

3 SHIFT-AND-ADD PROCESSING OF ALPHA SCORPIUS SPECKLE DATA

The two components α_1 and α_2 of Alpha Scorpius have an angular separation of about 3 arc-seconds. Fig. 3 shows the seeing discs (which are well separated) of these two components as viewed by Christou and Hege (1977) under quite favourable seeing conditions. Note how much brighter α_1 Scorpii is than α_2 Scorpii, and keep this in mind when looking at Figs. 4, 5, and 6.

Fig. 4 shows a typical speckle image recorded with the Steward Observatory speckle camera (Hege et al 1982). While the forms of the left and right hand parts of Fig. 4 are far from identical, the two speckle structures are alike in some significant particulars, such as the diagonal alignment of speckles from bottom left to top right. Also, the relative juxtaposition of bright features is quite similar in both parts of the image.

There are three ways in which shift-and-add can be employed. In the first, the speckle images from α_1 and α_2 Scorpii are treated as independent sets and are processed separately. We call this separate-shift-and-add. In the second and third ways of employing shift-and-add, simultaneously observed speckle images of α_1 and α_2 Scorpii are combined in pairs (Fig. 4 shows a typical pair) and the reference is chosen always from the left, or always from the right, hand speckle image. We call the resultant images, the left-shift-and-add image (Fig. 5) and the right-shift-and-add image (Fig. 6) respectively. Note that the separate-shift-and-add image consists of the left hand part of Fig. 5 and the right hand part of Fig. 6. All these shift-and-add images were formed by processing 2000 different (pairs of) speckle images.

We have radially averaged the six images shown in Figs. 3, 5 and 6. In each case, we took the "centre" of the image to be its brightest point, which then became the origin of polar coordinates r and θ. Denoting any of the images by $q(r;\theta)$ we define the normalised radially-averaged profile $q(r)$ by

$$q(r) = \left(1/2\pi q(0;0)\right) \int_0^{2\pi} q(r;\theta)\, d\theta \qquad (13)$$

with the radial coordinate being itself normalised to the interval $0 < r < 1$. The point of dividing through by $q(0;0)$ is to facilitate comparison of the shapes, or forms, of images whose amplitudes are significantly different.

Fig. 7(a) confirms that the forms of the two seeing discs are virtually identical.

The apparent angular diameters of the two components of Alpha Scorpius are thought to be different, with α_2 Scorpii being indubitably unresolvable. This is substantiated by Fig. 7(b) because the dotted curve is significantly narrower than the solid curve. However, the relative widths of the two curves cannot equal the relative angular diameters of the two components, for the following reason. The shift-and-add image of a resolvable object is usually more "spread out" than the original but with a narrower peak. In fact, the shape of the peak tends towards the autocorrelation of those parts (of the original) each of which are bright enough to constitute the shift-and-add reference in a significant fraction of the speckle images. We have both theoretical and experimental evidence for this (Hunt et al 1983; Minard et al 1985), which of course fits in with the obvious deduction that the shift-and-add image can only be a faithful replica of the original when the brightest point in the latter is unresolvable and is significantly brighter than any other point.

Since the apparent angular diameter of α_2 Scorpii is less than that of α_1 Scorpii, we would expect the two curves in Fig. 8(a) to be effectively identical under conditions of perfect isoplanatism. Since the reference is always chosen from the wider component's speckle image, the narrower component should exhibit the same "spread" in the finally processed image. So, the differences between the curves shown in Fig. 8(a) must characterise the degree of partial isoplanatism existing during the observations. On the other hand, the differences between the two curves shown in Fig. 8(b) should reflect both the partial isoplanatism and the greater apparent angular diameter of α_1 Scorpii as compared with α_2 Scorpii. To facilitate assessment of these speculations we show in Fig. 9 the dotted curve from Fig. 8(a) and the solid curve from Fig. 8(b).

The separations of the dotted and solid curves in Figs. 7(b) and 9 are merely indications of the relative

diameters of α_1 and α_2 Scorpii. The resolving power of a single mirror of the MMT is too small for us to estimate the diameter of Scorpii reliably. The fact that both separations are so similar does, however, strongly support our claim that the use we have made of shift-and-add processing confirms that the apparent angular diameter of α_1 Scorpii is indeed significantly larger than that of α_2 Scorpii.

6 CONCLUSIONS

Perhaps the most encouraging feature of the results reported here is that shift-and-add can reveal small differences in the apparent angular diameters of objects, even when both are close to being unresolvable (as is the case here). A disappointing aspect of our results is that the resolving power of a single mirror of the MMT is insufficient to separate "image" from "fog". It seems, however, that it should be possible to make an accurate estimate of the diameter of α_1 Scorpii from speckle data gathered from all 6 mirrors of the MMT operating in unison, even under conditions of appreciably imperfect isoplanatism.

Since the isoplanatic patch can be several arc-seconds in diameter (cf. §2.4 of B), it seems reasonable to suppose that the method proposed in §4.2 could be invoked to search regions (each centred on a particular unresolvable star) having diameters of at least 10 arc-seconds.

It should be noted that the separation of $f_1(x)$ and $f_2(x)$ is generally adequate for speckle holography (cf. §8.2 of B) to be invoked for processing the data gathered during a search of the kind suggested in §4.2. Conventional speckle interferometric processing (on which speckle holography relies) is much more complicated than shift-and-add imaging (which must perform at least as well as speckle holography under the envisaged circumstances). In order to have a chance of completing the proposed search reasonably expeditiously, it will be essential to carry it out by as simple processing as can be devised. Since it is difficult to imagine a processing scheme simpler than shift-and-add, and because the results presented in this paper are distinctly encouraging, we feel that it could be worthwhile implementing our suggested search procedure.

REFERENCES

Bagnuolo, W.J., 1982, Mon. Not. R. astr. Soc., 200, 1113.

Bagnuolo, W.J., 1984, Opt. Lett., 9, 65.

Bates, R.H.T., 1982, Phys. Rep., 90, 203.

Bates, R.H.T. & Cady, F.M., 1980, Opt. Commun., 32, 365.

Bates, R.H.T. & Fright, W.R., 1982, Mon. Not. R. astr. Soc., 198, 1017.

Bates, R.H.T. & Robinson, B.S., 1981, Ultrasonic Imaging, 3, 378.

Cady, F.M. & Bates, R.H.T., 1980, Opt. Lett., 5, 438.

Christou, J.C. & Hege, E.K., 1977, ? ?, ? ? ?.

Fried, D.L., 1979, Optica Acta, 26, 597.

Hege, E.K., Hubbard, E.N., Strittmatter, P.A. & Cocke, W.J., 1982, Optica Acta, 29, 701.

Hunt, B.R., Fright, W.R., & Bates, R.H.T., 1983, J. Opt. Soc. Am., 73, 456.

Minard, R.A., Robinson, B.S. & Bates, R.H.T., 1985, Proc. IEE, A132, 50.

Please let me know what references you want quoted here.

FIGURE CAPTIONS

Fig. 1 One-dimensional shift-and-add imaging for perfectly isoplanatic seeing (computer-generated results): (a) true image $f(x)$, where x denotes distance along axis representing one-dimensional image space; (b) typical uncontaminated speckle image: (c) shift-and-add image.

Fig. 2 One dimensional shift-and-add imaging for partially isoplanatic seeing (computer generated results applying to the $f(x)$ shown in Fig. 1): (a) typical contaminated (see text for details) speckle image ($\alpha = 0.5$); (b) shift-and-add image: (c) deconvolved shift-and-add image.

Fig. 3 Seeing discs for Alpha Scorpius (averages of 2000 observationally recorded speckle images): α_1 Scorpii on right, α_2 Scorpii on left.

Fig. 4 Typical observationally recorded speckle images of α_1 (on right) and α_2 (on left) Scorpii.

Fig. 5 Left-shift-and-add image of Alpha Scorpius (α_2, which is on the left, always provided the reference).

Fig. 6 Right-shift-and-add image of Alpha Scorpius (α_2, which is on the right, always provided the reference).

Fig. 7 Normalised radially-averaged profiles for α_1 (solid curves) and α_2 (dotted curves) Scorpii: (a) seeing discs: (b) separate-shift-and-add images.

Fig. 8 Normalised radially-averaged profiles for α_1 (solid curves) and α_2 (dotted curves) Scorpii: (a) right-shift-and-add image: (b) left-shift-and-add image.

Fig. 9 Normalised radially-averaged profiles for α_1 Scorpii from left-shift-and-add (solid curve) and α_2 Scorpii from right-shift-and-add (dotted curve).

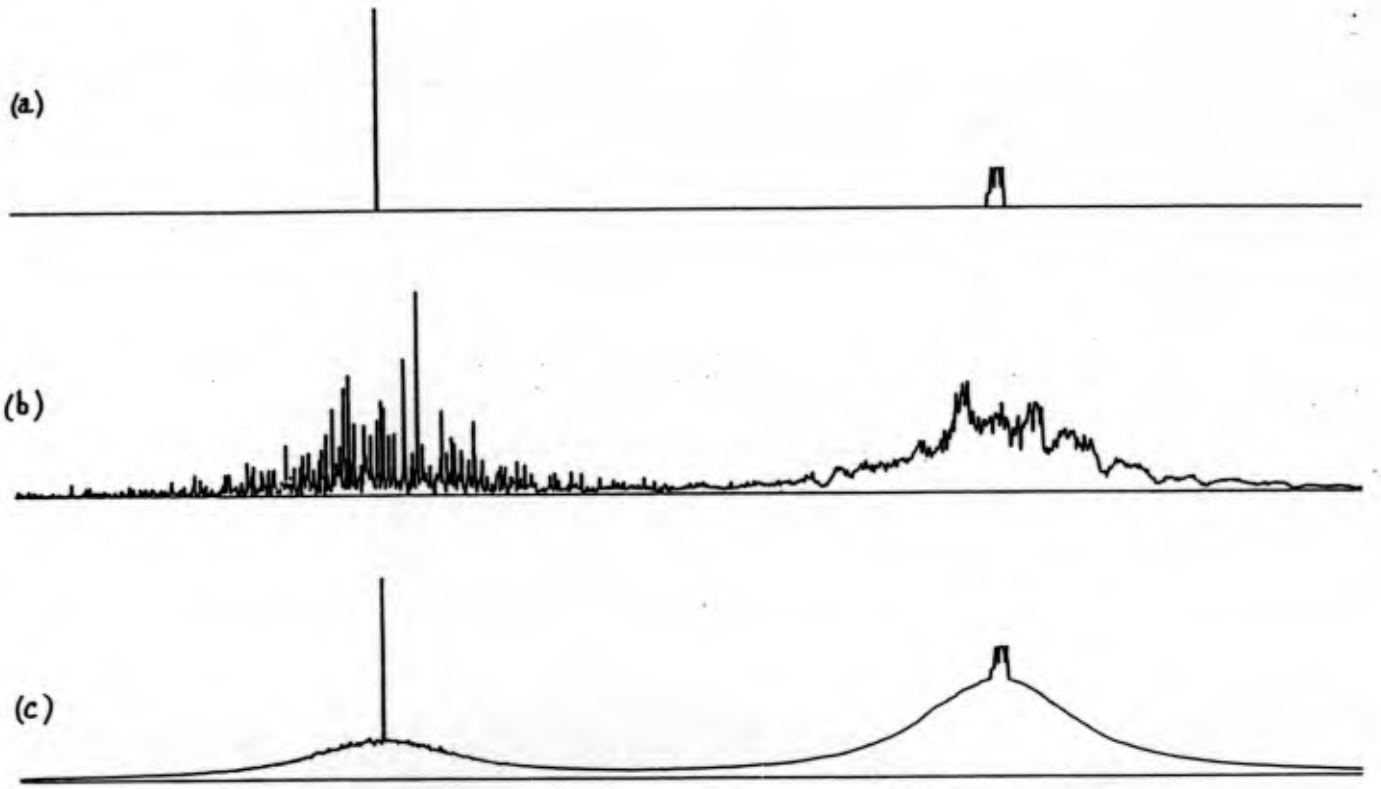

Figure 1 One-dimensional shift-and-add imaging for perfectly isoplanatic seeing: (a) true image $f(x)$ where x denotes distance along the axis representing one-dimensional image space; (b) typical uncontaminated speckle image; (c) shift-and-add image.

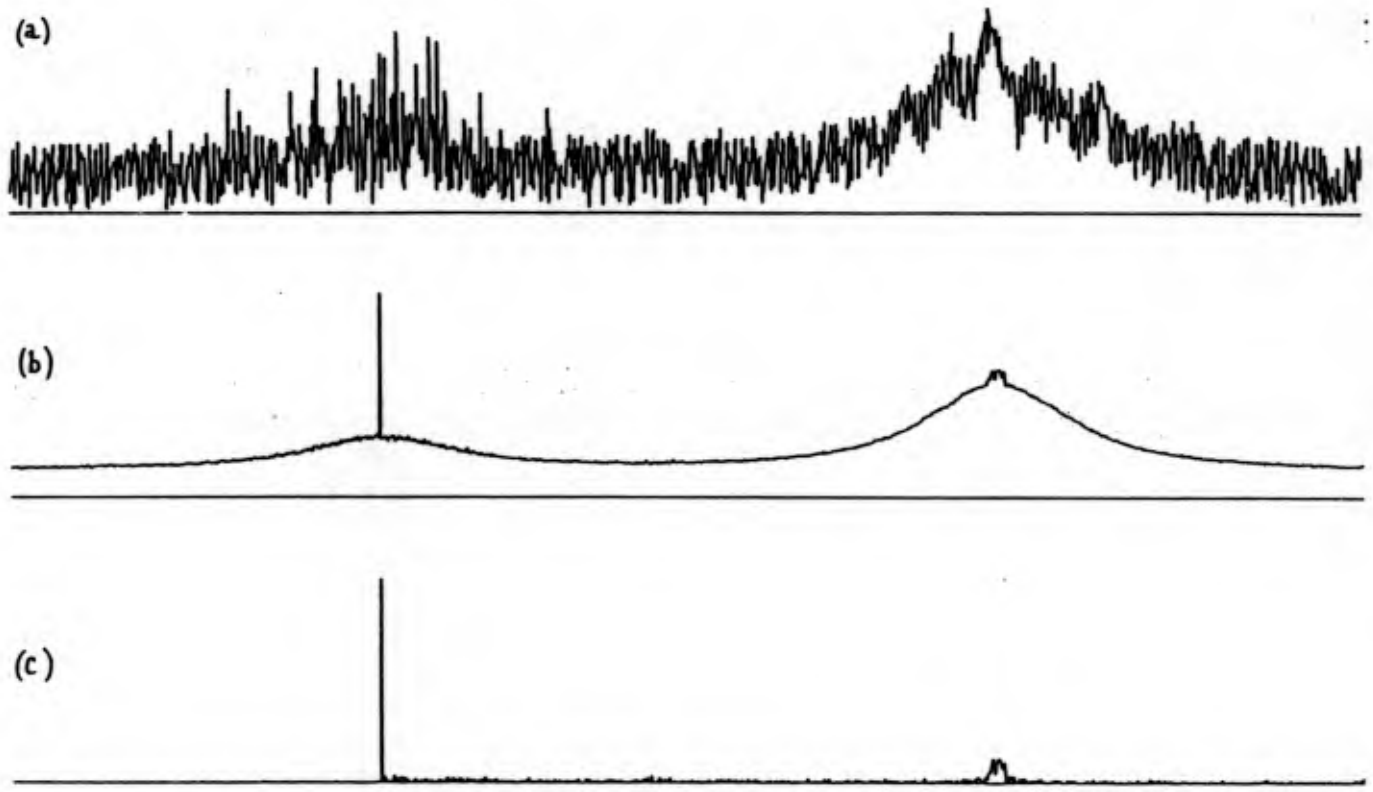

Figure 2 One-dimensional shift-and-add imaging for partially isoplanatic seeing: (a) typical contaminated (see text for details) speckle image ($\alpha = 0.5$); (b) shift-and-add image; (c) deconvolved shift-and-add image.

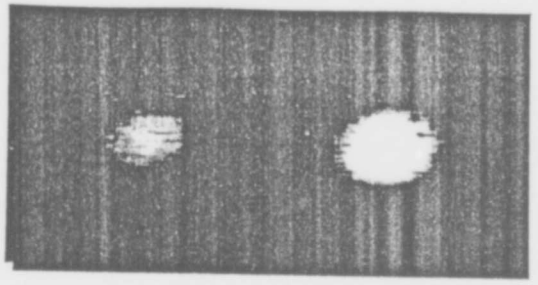

Figure 3

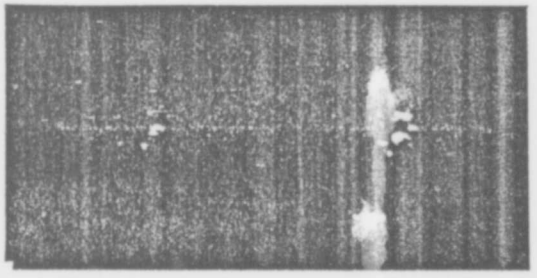

Figure 4

Note that we are preparing better versions of these figures (especially Fig. 4, which is almost invisible at present) - our photo lab is in even greater chaos than usual at the moment!

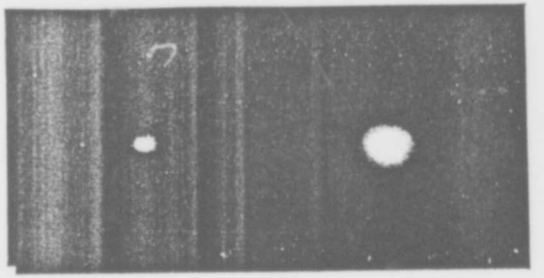

Figure 5

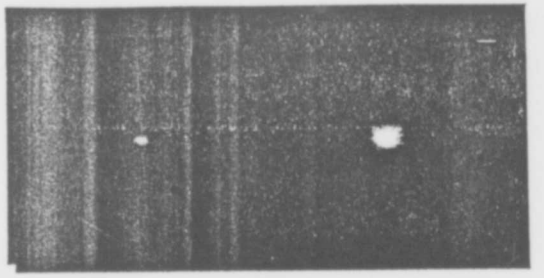

Figure 6

Note that we are preparing better versions of these figures (our photo lab is in even greater chaos than usual at the moment!)

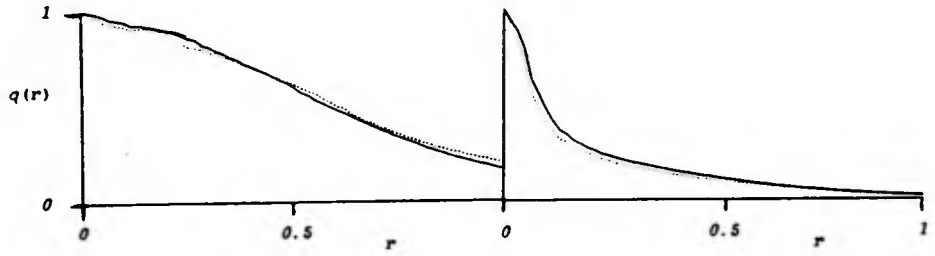

Figure 7

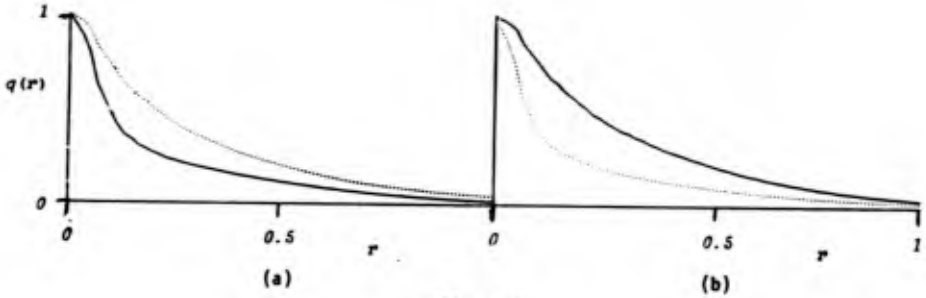

Figure 8

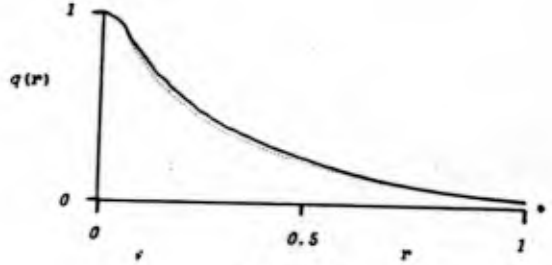

Figure 9

WAVELENGTH DEPENDENT SCALING IN SPECKLES

by Anthony Szumilo and E. Keith Hege

This research used the Multiple Mirror Telescope,
a joint facility of the University of Arizona
and the Smithsonian Institution.

WAVELENGTH DEPENDENT SCALING IN SPECKLES

by Anthony Szumilo and E. Keith Hege

Speckleg ns of star images arise from the interference of wavefronts distorted by cells of atmospheric turbulence. As products of interference, we then expect speckle characteristics to scale proportionally to the wavelength they are observed in. However, because there are also some refractive effects involved, all of the energy cannot scale with wavelength. The purpose of this experiment is to determine if th fraction of the total energy in specklegram features which scales with wavelength is measurable and significant.

This can be done by comparing the information in two speckle interferograms taken in different wavelengths. The same results, with much simpler one-dimensional calculations, are achieved by comparing two lines from a speckle spectrogram.

We assume the wavefronts from a point source entering at the top of the Earth's atmosphere are plane waves. The atmospheric turbulence gives rise to local areas of differing indices of refraction. This changes the phase of the incoming wave as a function of position (x,y) in the aperature plane. This induced phase delay is wavelength dependent, and for a point source, the point spread function in the image plane scales as the wavelength. The Fourier developement for this is given in Appendix 1.(J. Christou, Two Wavelength Speckle Imaging, unpub.).

Obtaining the Data

We obtained the dispersed specklegrams with a Differential Speckle Camera (DSC) (Beckers, et al, SPIE Vol 445, 1983). See figure 1. Light

DIFFERENTIAL SPECKLE CAMERA

Figure 1. Diagram of the Differential Speckle Camera used as a speckle spectrometer.

from opposite mirrors, B and E, of the Multiple Mirror Telescope is passed through a reflecting slit (at the telescope focal plane) to a zero deviation prism. The light then passes through a collimator/ camera lens system where it is imaged onto the intensified video system at 45x magnification. The slit used was 10 μm wide (about equal to the single mirror speckle size), and the prism was made of BK7 and F4 glass with a range of 430 to 860 nm. The spectrograph was calibrated using stars with known spectral features (in this case α Tau and γ Cas were used). A calibration curve (Figure 2) was obtained by fitting a cubic equation to the observed features. From this we determined the 750 nm and 500 nm lines to be used in the analysis corresponded to the 46th and 157th lines of the digitized spectrogram. The specklegrams were recorded on a Vidicon system (Hege, et al, Optica Acta, 1982) and later transferred to magnetic tape.

The object used was γ Cas (3rd magnitude, type B0). It is a small (unresolved) object, bright enough so that the atmospheric statistics dominated the photon statistics in the detected specklegram, and at the same time has spectral features which are weak, insuring comparable energies at the two wavelengths used. A sample spectrogram appears in figure 3 with the relevant frequencies indicated.

The analysis consisted of taking a profile of the star image (via the specklegram) in the two wavelengths. To compare the two, the dispersion scale of the 750 nm line was reduced to that of the 500 nm line. This effectively converts the interference information to the same scale. Care was taken to preserve phase information in

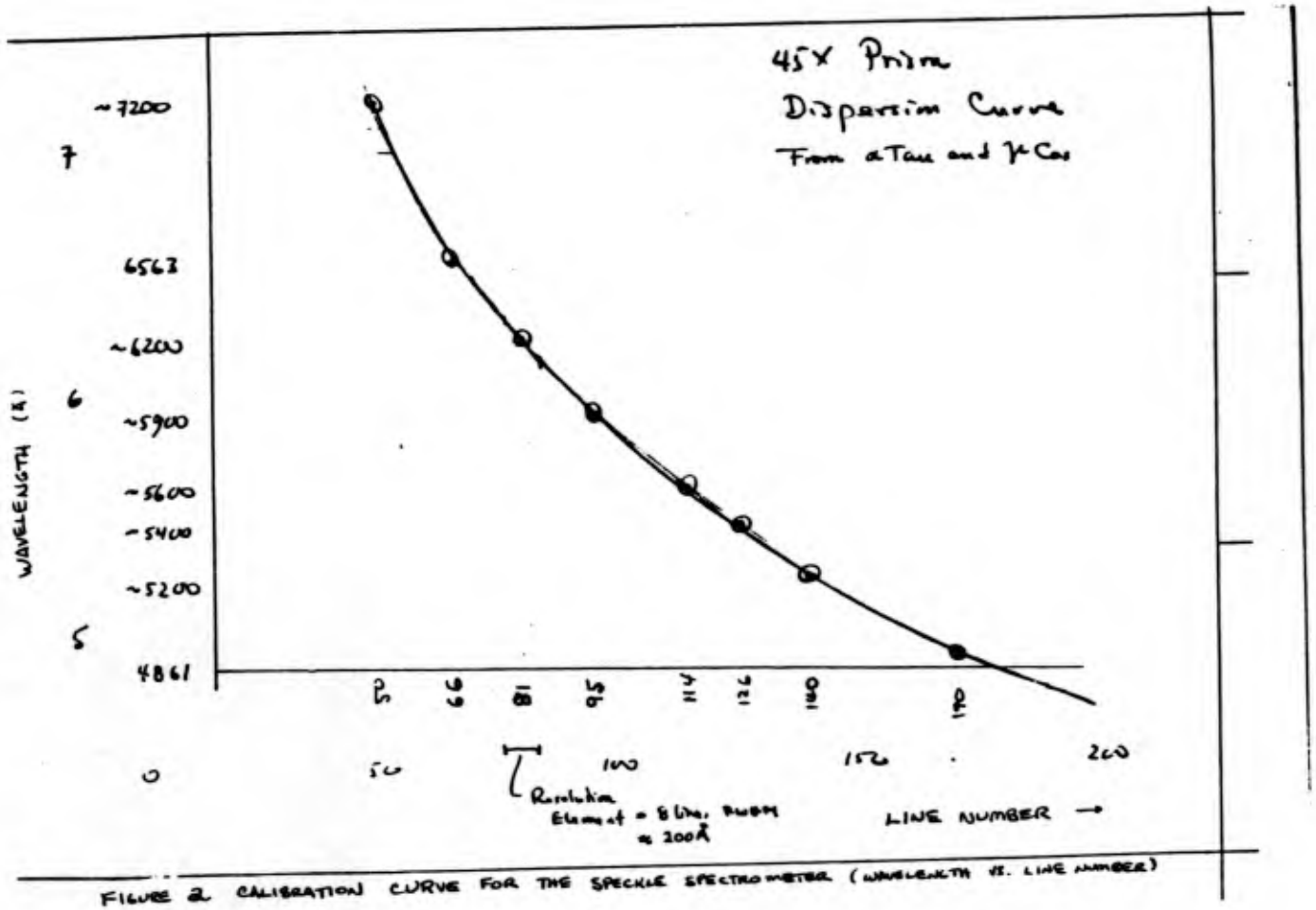

FIGURE 2 CALIBRATION CURVE FOR THE SPECKLE SPECTROMETER (WAVELENGTH VS. LINE NUMBER)

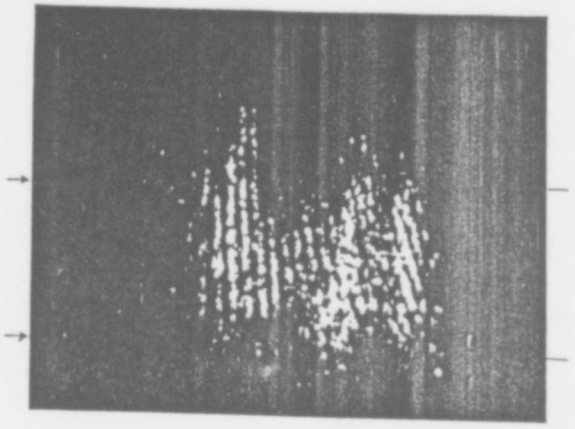

Figure 3. A speckle spctrogram obtained from the DSC. The verticle bands are the interference fringes, and run perpendicular to the prism slit. The two marked lines denaote the 750 nm (lower) and 500 nm lines used in the calculations.

this 'shrinking'. A cross correlation was then taken, as well as an autocorrelation of both lines for reference. The same was repeated for the next frame on the tape, and the respective correlations co-added. Interference fringes scale exactly as wavelength, and so we expected the autocorrelations to have substabtial power in the 4 pixel period, corresponding to the interference fringe frequency. Furthermore, the autocorrelations are modulated by the speckles. Thus if speckles scale poorly with wavelength, the modulation in the cross spectrum (with the 'shrunken' line) would be low compared to the AC. Modulation in the XC similar to that of the AC would imply speckles depend strongly on wavelength.

Data Processing

The algorithm, using the procedure described above, was implemented on a CDC CYBER, and a flowchart appears in Appendix 2. To improve the signal statistics and yet preserve spectral resolution (see calibration curve in fig. 2), 3 lines around the 750 nm line and 5 around the 500 nm line were co-added before the dispersion shrinking. Prior to taking the correlations, a gaussian filter was multiplicatively applied in Fourier Transform space at the fringe frequency corresponding to the 5m B-E mirror separation on the MMT. In addition, we assumed there may have been a drift in the relative pathlength in the interferometer. This would result in a slope in a graph of XC maximum vs. observation number. To correct for this possibility, a section was added to the algorithm which determined the maxima for the cross correlations. The implementation of this was two-fold: the XCs could be shifted so

that co-adding would occur at their maxima, and a plot of maxima vs. frame number (time) would show any temporal dependence of the interferometer phasing. No systematic drifts were observed. (See figure 4).

For controls in this experiment, cross correlations were taken between two lines of a frame where no dispersion scaling was used. Also, cross correlations were taken between the 500 nm line of one frame, and the (scaled) 750 nm line of the following frame. These frames correspond to about two seconds real time. Speckles produced by atmospheric turbulence shift on the order of 1/20th sec., so the two second difference should show no correlation.

Results/Conclusions

As expected, the autocorrelation sum showed a secondary maximum at the 4-pixel period. This is the interference fringe frequency and is readily seen in figures 3, 5, and 6. The AC sum for the 750 nm line showed a stronger peak at the fringe frequency than the AC for the 500 nm line. This is due to the fact that both the detector and the spectral resolution were degraded at the blue wavelength. We found the cross correlations which had been co-added on their maxima (for the temporally equal lines) to have a power which lay between the power found for the two ACs. Surprisingly, we also found the same type of correlation at the fringe frequency for the temporally uncorrelated frames, also having a power between the two ACs. We also found modulation at multiples for the 4-line periodicity. This in effect validates the algorithm. From the correlation in the

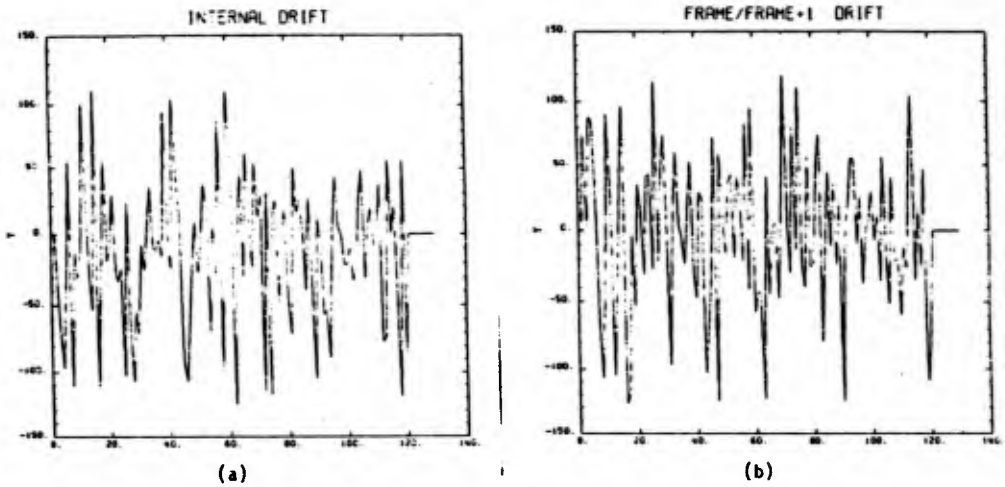

Figure 4. Plots of cross correlation maxima versus observation number. Plot (a) shows the maxima for the 750 nm and 500 nm lines within the same frame, and (b) shows the maxima for cross correlations taken between the red line of one frame and the blue of the next. The horizontal lines in each mark the mean. The maxima are grouped randomly about the mean lines, indicating no systematic drift in the interferometer phasing.

temporally independent frames, we can conclude that we are measuring a local effect and not an atmospheric one. The spectrometer behaves as a Young's double slit interferometer; phase is preserved along lines parallel to the slit.

From the modulation in the unshifted coadded cross correlations for the temporally dependent lines (Figure 7), we see that a fraction of the speckle energy does indeed scale with wavelength. The secondary maximum in figure 7 shows modulation on the order of 6% (compared to the value of the maximum itself). As a comparison, the secondary maximum for the temporally independent cross correlation sum (Figure 8) is barely visible (est. 2-3%). The greater modulation in figure 7 is due to the scaling nature of the speckles, and we conclude the amount of energy scaling with wavelength is on the order of the modulation. (Perfect modulation would have resluted in the minimum between the primary and secondary maxima being at zero.) Further experimentation is necessary to determine the accuracy of these results.

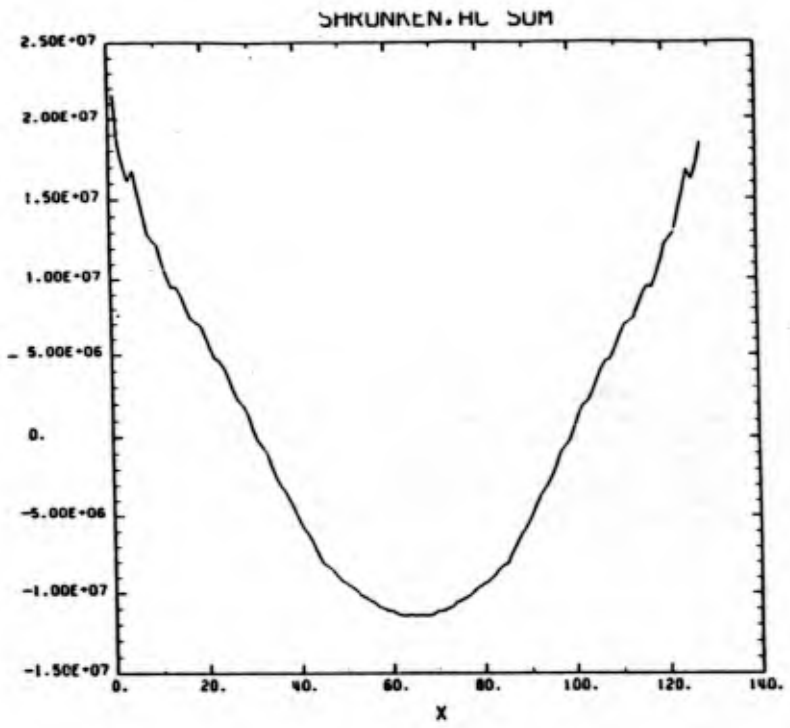

Figure 5. The coadded autocorrelations for the 750 nm lines. The secondary maximum occurs at the 4 pixel frequency, equal to the fringe frequency. The autocorrelations were taken after the dispersion scale shrinking.

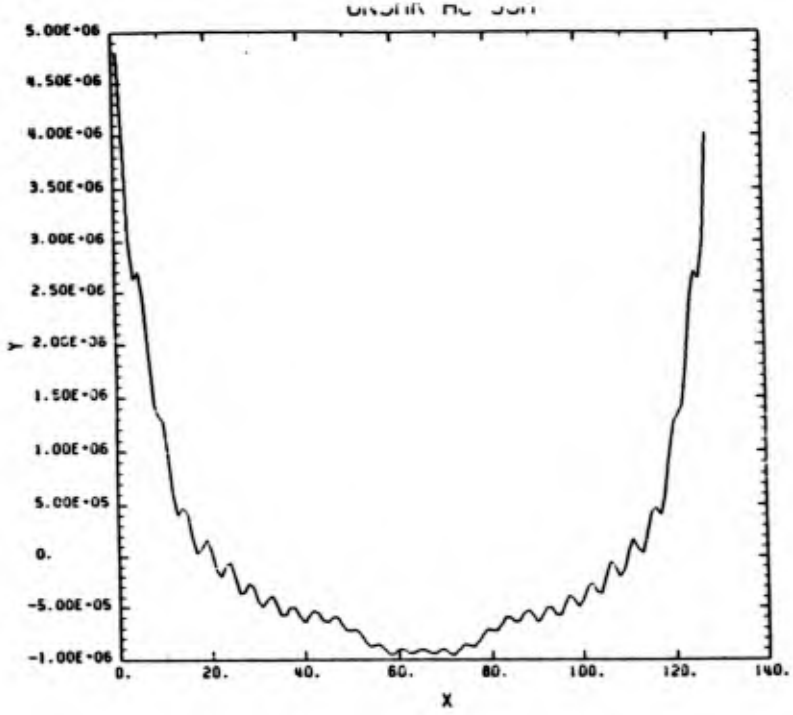

Figure 6. The coadded autocorrelations for the 500 nm lines.

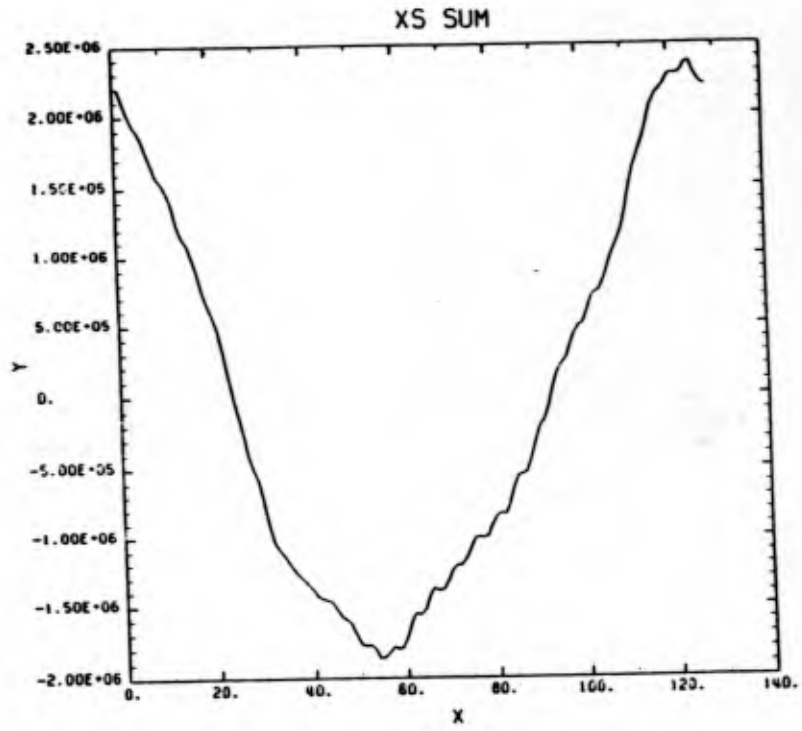

Figure 7. The unshifted cross correlation sum for the temporally correlated lines. The maximum occurs at a shift of -4 pixels (see figure 4a). The secondary maximum (4 pixels away from the maximum) and is evidence for the scaling nature of the speckles. The secondary maximum is barely visible for the temporally uncorrelated lines (cf. figure 8).

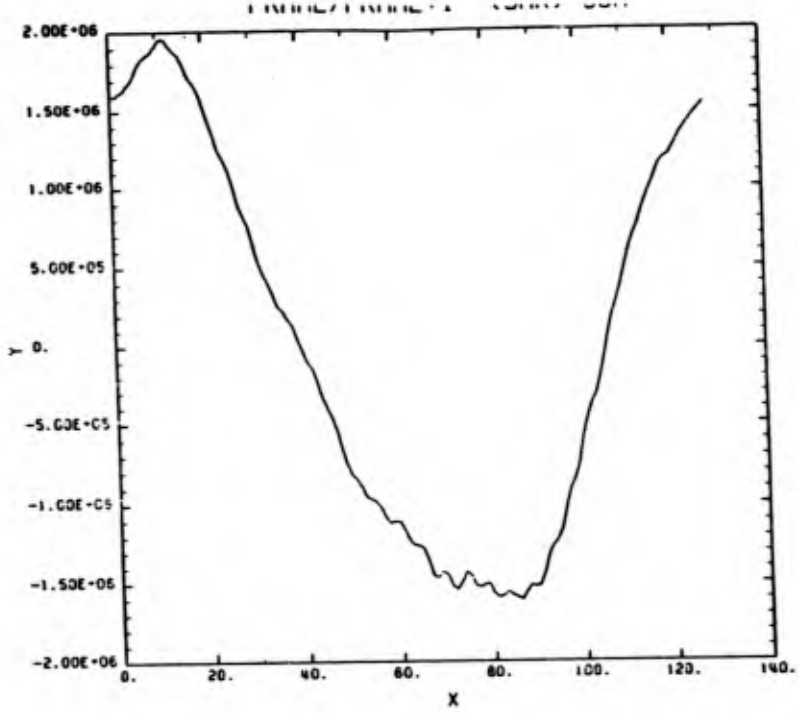

Figure 8. The coadded, unshifted cross correlations between the 750 nm line of one frame and the 500 nm line of the next (temporally uncorrelated). Notice the relatively low amount of power in the secondary maximum (which corresponds to the fringe frequency), and compare with figure 7.

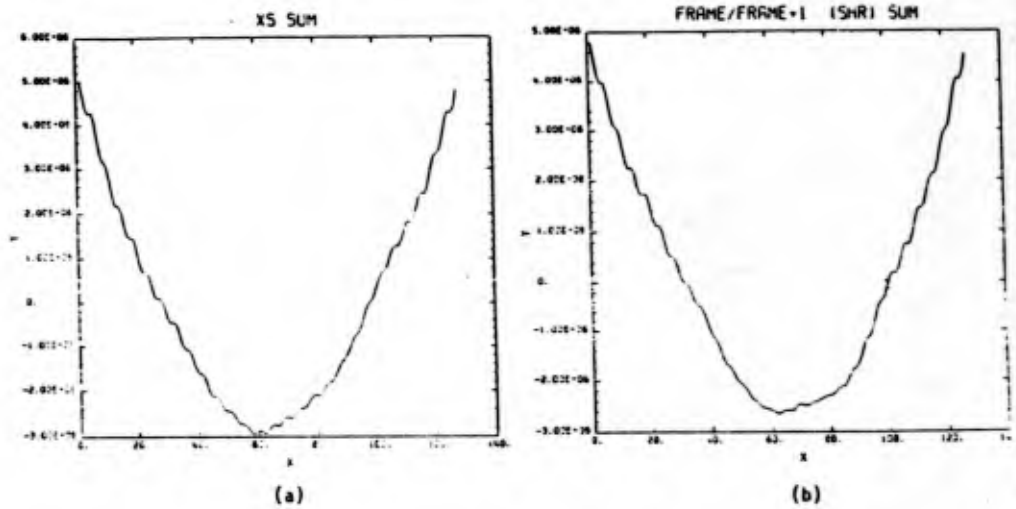

Figure 9. The sum of the cross correlations shifted on their maxima. (a) coadded cross correlations for the temporally correlated 750 nm and 500 nm lines, and (b) coadded XCs for the temporally uncorrelated lines. These retain a nature of a mean of the two autocorrelations in both cases.

APPENDIX 1 Mathematical derivations for wavelength denpendent scaling in speckle phenomena.

I. Image Formation - Point Spread Function

The formation of a single speckle image (speckle gram) is a complex procedure. Due to the distance of an astronomical object we can consider that plane - waves from the object are incident at the top of the earth's atmosphere. The turbulent structure of the atmosphere then distorts this plane wave due to random changes of its refractive index. The distorted wavefront is now imaged from the aperture - plane of the telescope to the focal plane. This can be seen in the following figure.

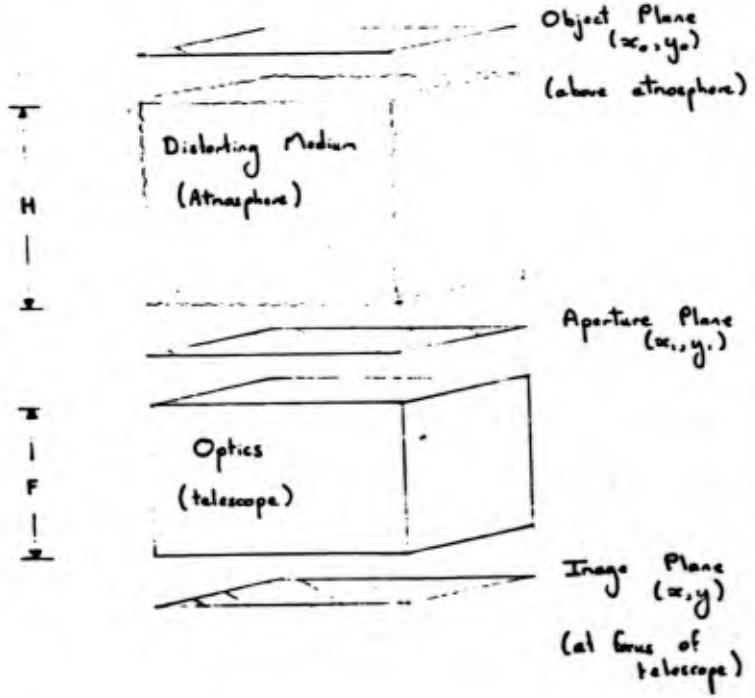

The distorting medium only affects the phases of the incoming wave. Thus, the spatial information is unchanged such that $(x_o, y_o) \rightarrow (x_1, y_1)$. Let the complex amplitude in the object plane be given as

$$U_o(x_1, y_1) = A \tag{1.1}$$

for a stationary state as the wave propagates perpendicular to the object plane.

After passage through the atmosphere, the complex amplitude suffers phase shifts of the form

$$U_1(x_1, y_1) = U_o(x_1, y_1) \cdot \exp\left[i \phi(x_1, y_1) \right] \tag{1.2}$$

where $U_1(x_1, y_1)$ is the complex amplitude in the aperture plane
ϕ $\phi(x_1, y_1)$ - - phase delay

The latter is related to the instantaneous refractive - index structure of the atmosphere by

$$\phi(x_1, y_1) = \frac{2\pi}{\lambda} \int_0^H dz \cdot n(x_1, y_1, z) \tag{1.3}$$

Thus, the complex amplitude at the aperture plane becomes

$$U_1(x_1, y_1) = A \exp\left[i \phi(x_1, y_1) \right] \tag{1.4}$$

(Note that ϕ is wavelength dependent).

The relation between the complex amplitude at the aperture plane & the complex amplitude at the focal plane is given by a Fourier transform representing the Fraunhofer diffraction formula.

i.e.

$$U(x,y) = \frac{\exp\left[ikF\right].\exp\left[i\frac{k}{2F}(x^2+y^2)\right]}{i\lambda F} \cdot \iint_{-\infty}^{\infty} dx_1 dy_1 \cdot \left[U_1(x_1,y_1).W(x_1,y_1)\right] \cdot \exp\left[-i\frac{2\pi}{\lambda F}.(xx_1+yy_1)\right] \quad (1.5)$$

where F is the distance between the aperture & image, i.e. the focal length.

$W(x_1,y_1)$ is the aperture function defined such that

$$W(x_1,y_1) : \begin{matrix} 1 & \text{for } (x_1^2+y_1^2)^{1/2} \leq D/2 \\ 0 & \text{elsewhere} \end{matrix}$$

D being the aperture diameter.

The P.S.F. of the optical system defined is the intensity in the focal plane.

i.e. $P(x,y) = |U(x,y)|^2 = U^*(x,y).U(x,y)$

$$\therefore P(x,y) = \frac{1}{\lambda^2 F^2} \cdot \left| \iint_{-\infty}^{\infty} dx_1 dy_1 \cdot \left[U_1(x_1,y_1).W(x_1,y_1)\right].\exp\left[-i\frac{2\pi}{\lambda F}(xx_1+yy_1)\right]\right|^2 \quad (1.6)$$

Equation (1.6) contains a Fourier Transform. The analytic form of an F.T. is

$$F(u,v) = \iint dx dy \cdot f(x,y).\exp\left[-i2\pi(xu+yv)\right] \quad (1.7)$$

where u & v are the frequencies for which the transform is evaluated.

Comparing (1.7) with (1.6) it is obvious to see that the frequencies for which the P.S.F. is calculated are given as

$$u = \frac{x}{\lambda F} \quad ; \quad v = \frac{y}{\lambda F}$$

so that the P.S.F. has a dependancy which should be written as the following :-

Let u & v have the definitions above, then

$$P(u,v) = \frac{1}{\lambda^2 F^2}\left| \iint_{-\infty}^{\infty} dx_1 dy_1 \cdot \left[U_1(x_1,y_1).W(x_1,y_1)\right]\exp\left[-i2\pi(x_1u+y_1v)\right]\right|^2 \quad (1.8)$$

where u & v are both λ-related.

If we leave it as in (1.8) then the P.S.F. is general as the arguments are now non-dimensional. Thus, (1.7) should now imply that

$$P(x,y) = P(x,y:\lambda) = P\left(\frac{x}{\lambda},\frac{y}{\lambda}\right)$$

II. Wavelength Effect

The wavelength dependance for point source imaging as described in § I arises that this is a scaling factor in the P.S.F., (eq. 1·8). The effect of the atmosphere is to introduce a wavelength-dependant phase delay in the plane wave as the plane is inversely proportional to the wavelength.

Considering only the scaling-effect we can consider the imaging equation of the system. This is in the form of a standard convolution, i.e.

$$I(x,y) = \iint dx_1 dy_1 \; O(x_1,y_1)\, P(x-x_1, y-y_1) \qquad (2\cdot1)$$

$$= O(x,y) * P(x,y)$$

Let us now assume that the object irradiance, $O(x,y)$, is grey, i.e. has no colour dependance and is therefore the same to look at at different wavelengths. Thus, for observations at a monochromatic wavelength, λ, we can rewrite (2·1) as

$$I(x,y;\lambda) = O(x,y) * P(x,y;\lambda) \qquad (2\cdot2)$$

But it was shown in § I that

$$P(x,y,\lambda) \Rightarrow P\left(\tfrac{x}{\lambda}, \tfrac{y}{\lambda}\right).$$

$\therefore$ (2·2) becomes

$$I(x,y;\lambda) = O(x,y) * P\left(\tfrac{x}{\lambda}, \tfrac{y}{\lambda}\right) \qquad (2\cdot3)$$

For a grey-object which is a point source, i.e. $\delta(x,y)$, then (2·3) reduces to

$$I(x,y;\lambda) = \delta(x,y) * P\left(\tfrac{x}{\lambda}, \tfrac{y}{\lambda}\right) \qquad (2\cdot4)$$

$$= \iint dx_1 dy_1 \; \delta(x_1,y_1)\, P\left(\tfrac{x-x_1}{\lambda}, \tfrac{y-y_1}{\lambda}\right)$$

Now, the delta function has the following property

$$\delta(ax, by) = \frac{1}{|ab|}\,\delta(x,y)$$

$$\therefore \quad \delta\left(\tfrac{x}{\lambda}, \tfrac{y}{\lambda}\right) = \lambda^2\, \delta(x,y)$$

$\therefore$ (2·4) becomes

$$I(x,y;\lambda) = \frac{1}{\lambda^2} \iint_{-\infty}^{\infty} dx_1 dy_1 \; \delta\left(\tfrac{x_1}{\lambda}, \tfrac{y_1}{\lambda}\right) P\left(\tfrac{x}{\lambda} - \tfrac{x_1}{\lambda}, \tfrac{y}{\lambda} - \tfrac{y_1}{\lambda}\right)$$

& letting $x_1' = \frac{x_1}{\lambda}$ & $y_1' = \frac{y_1}{\lambda}$

$$\therefore dx_1 = \lambda\, dx_1' \;\&\; dy_1 = \lambda\, dy_1'$$

$$\therefore I(x,y;\lambda) = \frac{\lambda^2}{\lambda^2} \iint_{-\infty}^{\infty} dx_1' dy_1' \; \delta(x_1', y_1')\, P\left(\tfrac{x}{\lambda} - x_1', \tfrac{y}{\lambda} - y_1'\right)$$

$$= P\left(\tfrac{x}{\lambda}, \tfrac{y}{\lambda}\right) = I\left(\tfrac{x}{\lambda}, \tfrac{y}{\lambda}\right) \qquad (2\cdot5)$$

Thus, for a point source, the image is, as one would expect, scaled by the wavelength. It is now possible to write by a general expression,

$$I\left(\tfrac{x}{\lambda}, \tfrac{y}{\lambda}\right) = O(x,y) * P\left(\tfrac{x}{\lambda}, \tfrac{y}{\lambda}\right)$$

APPENDIX 2: FLOWCHART OF ALGORITHM USED

The algorith, was implemented on a CDC CYBER, and the digitized speckle spectrograms were stored on magnetic tape in 128x256 arrays.

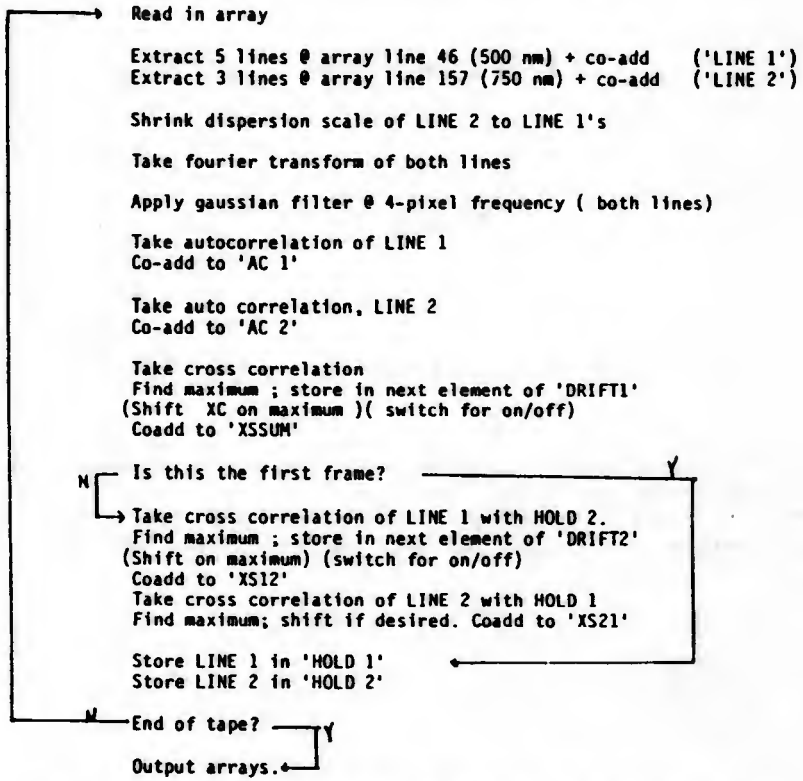

Two runs were performed, one with shifting on the maxima, the other without.

Acknowledgements

We express our gratitude to the National Optical Astronomical Observatories for the use of their computer facilities. Also, many thanks go to Julian Christou, Stuart Shaklan, and the entire Speckle Interferometry group at Steward Observatory. This work was supported in part by the Air Force Office of Scientific Research, AFOSR 82-0020.

References

Beckers, SPIE Vol 445
Hege, High Resolution using Speckle Interferometry
Hege, Optica Acta paper
Christou, Speckle Imaging Paper

BETELGEUSE AND EROS IMAGED BY FOURIER PHASE RETRIEVAL FROM SPECKLE DATA

R.H.T. Bates*, J.C. Christou†, W.J. Cocke†, J.D. Drummond†, W.R. Fright*, E.K. Hege†, D. Mnyama*, F. Roddier††, C. Roddier†† and A.M. Sinton*

Draft: May 1985

Submitted to: Ap.J.?
Astron. J.?
???

ABSTRACT: Recently developed phase retrieval algorithms are applied to visibility intensities formed from speckle data gathered from observations of Alpha Orionis (Betelgeuse) and Asteroid 433 (Eros). Diffraction limited images of both objects are reconstructed. Direct evidence is obtained that Betelgeuse possesses a "halo" and that Eros is an elongated body.

* Electrical & Electronic Engineering Department, University of Canterbury, Christchurch, New Zealand.

† Steward Observatory, University of Arizona, Tucson, AZ 85721, USA.

†† ?????

1. INTRODUCTION

We present images of the red giant star Alpha Orionis (Betelgeuse) and the asteroid 433 (Eros) reconstructed from speckle data with the aid of our Fourier phase retrieval procedure (Bates and Fright, 1983, 1984; Won et al 1985). The Betelgeuse data were gathered by Roddier and Roddier (1984) with a rotation shearing interferometer. Hege et al (19??) made conventional speckle interferometric observations (cf. Bates, 1982 §§6.1 and 9.7) of Eros with a single mirror of the Multiple Mirror Telescope (MMT). Observations were also made on unresolved stars, viewed under statistically similar seeing conditions.

For both Betelgeuse and Eros, it must be understood that the data, whose processing we describe in this paper, have been previously corrected by incorporating the observations on unresolved stars into the standard compensatory procedures (cf. Bates, 1982 §6.2).

Section 2 explains our image processing. The results for Betelgeuse and Eros are presented in Sections 3 and 4 respectively. In Section 5 we assess the quality of these results and suggest what is needed to improve them.

2. IMAGE PROCESSING STRATEGY

We introduce a pair of two-dimensional spaces, called image space and visibility space, arbitrary points in which are accorded Cartesian coordinates (x,y) and (u,v) respectively. The image f(x,y), here required to be positive (i.e. real and non-negative) and to have finite support (i.e. to occupy a finite region of image space - it is <u>not</u> necessary to

know the size and shape of the region a priori), and its visibility F(u,v) form a two-dimensional Fourier transform pair, which we indicate by

$$F(u,v) \leftrightarrow f(x,y) \tag{1}$$

The data constitute an estimate, here written as $|\tilde{F}(u,v)|^2$, of $|F(u,v)|^2$. However good this estimate is, it must be imperfect to some degree and it is likely to be increasingly corrupted the further one goes from the origin of visibility space. Because of this we claim that the form of the best available estimate of $|F(u,v)|^2$ must be

$$\begin{aligned} |F(u,v)|^2 &= |\tilde{F}(u,v)|^2 \text{ for } \rho<R \\ &= E(u,v) \quad \text{for } \rho>R \end{aligned} \tag{2}$$

where $\rho = (u^2 + v^2)^{\frac{1}{2}}$, and R and E(u,v) are defined later in this section.

It is a matnematical theorem that (cf. Bates, 1982 §6.3)

$$|F(u,v)|^2 \leftrightarrow ff(x,y) \tag{3}$$

where ff(x,y) is the autocorrelation of f(x,y). Since the latter is positive then so is ff(x,y). As a consequence of imperfections present in the data, however, g(x,y) is unlikely to be wholly positive, where

$$|\tilde{F}(u,v)|^2 \leftrightarrow g(x,y) \tag{4}$$

We therefore think it worthwhile to perform certain pre-processing.

The first step is to estimate the size of the region of image space occupied by the support of ff(x,y), which is necessarily finite because the support of f(x,y) is finite. We give the name autocorrelation box to the function bb(x,y) which is unity inside, and zero outside, the convex envelope obtained by applying a threshold (set by the available estimate of the "noise" level) to g(x,y). This envelope is that convex curve just enclosing all points in image space where g(x,y), which is obtained by computing the Fourier transform of the data, exceeds the threshold. Note that the Fast Fourier Transform (FFT) algorithm (cf. Brigham, 1974) is implied throughout this paper wherever there is mention of actual computation of Fourier transforms.

Our image processing actually refines the shape of bb(x,y). So, the Fourier transform of the data merely provides the first estimate of bb(x,y). At any stage in the processing the assumed shape of bb(x,y) is, of course, only the current estimate of that quantity. Because no confusion need be caused thereby, we always use the same symbol to denote a quantity and its current estimate. On defining

$$\varepsilon^2 = \iint_{-\infty}^{\infty} |e(x,y)|^2 \, dx \, dy \tag{5}$$

we call ε the error, where e(x,y) consists of all g(x,y) outside bb(x,y) and the negative parts of g(x,y) inside bb(x,y). The positive parts of g(x,y) inside bb(x,y) constitute the current estimate of the autocorrelation and are therefore denoted by ff(x,y).

Having chosen a particular value of R, we generate (the current estimate of) $|F(u,v)|^2$ by setting E(u,v) equal to the positive part (for $\rho > R$) of the Fourier transform of ff(x,y). The next estimate (which of course becomes the current estimate, as soon as it is computed) of ff(x,y) is then generated by Fourier transforming $|F(u,v)|^2$. An iterative

loop is thus set up and is continued until ε ceases to decrease (i.e. starts to oscillate). This procedure is repeated for several different values of R. The one resulting in the lowest final value for ε is assumed optimum. The whole of this above procedure is repeated with several different autocorrelation boxes, the lengths of their sides being slightly different from the original ones. The overall optimum versions of bb(x,y) and $|F(u,v)|^2$ are taken to be those corresponding to the smallest value obtained for ε. This completes our pre-processing.

Once the overall optimum version of $|F(u,v)|$ is obtained, we embark on generating (a current estimate of) the phase $\Psi(u,v)$ of $F(u,v)$. It is convenient to redefine g(x,y) by

$$|F(u,v)| \exp(i\,\Psi(u,v)) \leftrightarrow g(x,y) \qquad (6)$$

We emphasise that $|F(u,v)|$ must be sampled twice as finely, in both the u and v directions, as would be necessary if $\Psi(u,v)$ was given a priori (note that this sampling constraint must be satisfied if the above-described pre-processing is to be possible). Consequently, g(x,y) can have value throughout bb(x,y). Because f(x,y) is positive, its support is just enclosed by the image box b(x,y), whose linear dimensions are necessarily half those of bb(x,y) (Bates, 1984). The current estimate of the image, denoted by f(x,y), is the positive part of g(x,y) inside b(x,y). The formula (5) can be used for the phase retrieval error, provided the domain of integration is the autocorrelation box, and e(x,y) consists of all of g(x,y) outside b(x,y) and the negative part of g(x,y) inside b(x,y).

We employ our composite phase retrieval procedure (Bates and Fright, 1983, 1984; Won et al 1985) to refine $\Psi(u,v)$. We begin with crude phase

estimation then perform ten iterations of Fienup's error-correction (sometimes called error-reduction) algorithm and continue with Fienup's hybrid-input-output algorithm until the error ceases to fall (or starts to oscillate).

To generate the results presented in the two following sections, we performed this image processing entirely interactively. We chose the values of the thresholds, and varied the values of R and of the gain factors (typically 0.2) for the hybrid-input-output algorithm, by "eye" and by making "educated guesses" based on our computational experience.

3. BETELGEUSE

Fig. 1 shows what, in our opinion, are the optimum versions of $|F(u,v)|$, ff(x,y) and f(x,y) which our processing can generate from the data available for Betelgeuse.

The structure evident within the central bright region of Fig. 1a is prominent enough, we think, to represent physical structure. This is mirrored by the fringes exhibited by the autocorrelation (Fig. 1b). Consequently, while the fainter blotches in Fig. 1c are probably artefactual, the three brighter blobs contiguous to the main bright disc may well correspond to the cloud or "halo" which we would expect to be associated with the red giant. To identify unambiguously which detail in Fig. 1c we are referring to, we ask the reader to imagine the bright disc to be the body of a "duck". The three brighter blobs then constitute its "tail", "head" and "beak".

4. EROS

Fig. 2 displays the same optimised quantities for Eros as Fig. 1 does for Betelgeuse. We feel that the only unequivocal information is represented by the patent lack of circular symmetry exhibited by all three parts of Fig. 2. All detail, apart from the bright central blob, is artefactual in Fig. 2c in our opinion. However, it seems we can be confident that Eros is an elongated body.

5. CONCLUSIONS

The results presented in Sections 3 and 4 confirm that quantifiable images can be generated from observed visibility intensity data with the aid of the latest Fourier phase retrieval algorithms. We assert that Figs. 1c and 2c explicitly reveal detail concerning Betelgeuse and Eros, respectively, which could previously only be inferred indirectly.

There is a detail of our preprocessing which is mentioned here, rather than in Section 2, because it relates to the quality of our data. Even after completing all the processing described in the paragraph in between those containing equations (5) and (6) respectively, $ff(x,y)$ still contains some negative parts. This indicates that the data must be appreciably noisy. It also reflects the disquiet that seems to permeate the astronomical image processing community (but is nowhere stated explicitly, for lack of concrete evidence) concerning the faithfulness of results generated by conventional speckle interferometric processing. It may be that the effects of partial isoplanatism are more severe than people have hitherto thought (refer to (B) in §1.2 of Bates 1982). If this is so then we should be paying more attention to first-order interferometric

processing methods (cf. Bates et al 1985), which should be less noise sensitive than second-order methods. Conventional speckle interferometry is of second-order (Bates and Gough 1975). Whatever the cause of the errors in the visibility data, it must be identified and corrected before the promise of the image processing revolution initiated by Labeyrie (1970) can be fully realised.

To complete our preprocessing we set to zero the negative parts of $ff(x,y)$ which remained after the final iteration. The autocorrelations shows in Figs. 1b and 2b are versions of $ff(x,y)$ which are wholly positive (i.e. their negative parts have been truncated). The visibility intensities, to which the composite phase retrieval procedure are applied, are the Fourier transforms of the wholly non-negative autocorrelations. The $|F(u,v)|$ shown in Figs. 1a and 2a are the square-roots of such intensities. In order to check that the artefacts present in Figs. 1c and 2c did not depend upon the details of the image processing procedure, we repeated it, but with crude phase estimation replaced by a psuedo-random starting phase, and we used several different pseudo-random distributions. In each case the same artefacts were reconstructed, indicating that they must indeed have been due to errors in the data.

REFERENCES

Bates, R.H.T. (1982) "Astronomical speckle imaging", Physics Reports, 90, 203-297.

Bates, R.H.T., Beckers, J.M., Christou, J.C., Hege, E.K. & Sinton, A.M. (1985) "Shift-and-add imaging through partially isoplanatic seeing", Mon. Not. R. astr. Soc., submitted.

Bates, R.H.T. (1984) "Uniqueness of solutions to two-dimensional Fourier phase problems for localized and positive images", Computer Vision, Graphics, and Image Processing, 25, 205-217.

Bates, R.H.T. & Fright, W.R. (1983) "Composite two-dimensional phase-restoration procedure", J. Opt. Soc. America, 73, 358-365.

Bates, R.H.T. & Fright, W.R. (1984) "Reconstructing images from their Fourier intensities", in Advances in Computer Vision and Image Processing (T.S. Huang ed.), Vol. 1 Image Reconstruction from Incomplete Observations, Greenwich, CT: JAI Press, pp. 227-264.

Bates, R.H.T. & Gough, P.T. (1975) "New outlook on processing radiation received from objects viewed through randomly fluctuating media", IEEE Trans. on Computers, C-24, 449-456.

Brigham, E.D. (1974) Fast Fourier Transform, Englewood-Cliffs, N.J.: Prentice-Hall.

Hege, E.K., ??.....?? (19??)

Labeyrie, A. (1970) "Attainment of diffraction limited resolution in large telescopes by Fourier analysing speckle patterns in star images", Astron. Astrophys., 6, 85-87.

Roddier, C. & Roddier, F. (1984) "High resolution observation of Alpha Orionis with a rotation shearing interferometer", Astron. J., 270, 123-126.

Won, M.C., Mnyama, D. & Bates, R.H.T. (1985) "Improving initial phase estimates for phase retrieval algorithms", Optica Acta, in press.

FIGURE CAPTIONS

Fig. 1 Reconstruction of Betelgeuse. Optimum versions of: (a) $|F(u,v)|$, (b) $ff(x,y)$, (c) $f(x,y)$.

Fig. 2 Reconstruction of Eros. Optimum versions of: (a) $|F(u,v)|$, (b) $ff(x,y)$, (c) $f(x,y)$.

MAXIMUM MAGNITUDE ESTIMATION OF THE OBJECT'S POWER SPECTRUM IN STELLAR SPECKLE INTERFEROMETRY

Douglas J. Granrath
Science Applications, Inc.
5151 E. Broadway
Suite 1100
Tucson, AZ 85711

ABSTRACT

The maximum Fourier magnitude taken over a set of speckle images is proposed as a replacement for the standard power spectrum average. This new statistic estimates the diffraction-limited object-times-telescope magnitude values in a statistically unbiased and sufficient fashion, and has a variance that decreases with sample size faster than the average magnitude's variance. Simultaneous imaging of a nearby point source is unnecessary with this technique, and any object that lies within a single isoplanatic patch of the atmosphere can be estimated. Magnitude estimation results of the double star Capella are shown to corroborate these claims.

The classical means of stellar speckle interferometry invented by Labeyrie[1] involves the averaging of power spectra. In particular, the power spectrum of the object is estimated by dividing the averaged power spectra of the speckle images of the object by the averaged power spectra of speckle images from a nearby known point source. Since the fixed transfer function due to the telescope is known, the sole use of the reference star is to estimate the effect of the atmosphere upon the power spectral averaging process. Ideally, with a reference star within the same isoplanatic patch as the object (usually $\leq$ 20 arc. sec. away) the actual atmospheric transfer functions that acted upon the object are read out for each speckle frame. If a bright nearby star is unavailable, the speckle interferometry transfer function can be estimated with a reference star 10^0 or even 20^0 away, or by using an entirely theoretical estimate.[2] Since these are approximations to the actual transfer function that acted on the object, artifacts could arise in the result. This Letter will show that these ancillary atmospheric estimates are unnecessary, because it is possible to directly estimate the object-times-telescope magnitude values without distortion by the atmosphere.

Within an isoplanatic region of the sky the atmosphere can be modeled as being linear and shift-invariant.[3] Thus,

$$I_\ell(f_x,f_y) = O(f_x,f_y) \times H_\ell(f_x,f_y) \qquad (1)$$

where 'O' signifies the Fourier transform of the stationary object, 'H_ℓ' is the ℓ-th transfer function due to the atmosphere and the telescope, and 'I_ℓ' is the Fourier transform of the ℓ-th speckle image. When the power spectra of the speckle images are averaged we therefore have that

$$L^{-1}\sum_{\ell=1}^{L} |I_\ell(f_x,f_y)|^2 = |O(f_x,f_y)|^2 \times L^{-1}\sum_{\ell=1}^{L} |H_\ell(f_x,f_y)|^2 \ , \qquad (2)$$

for L frames. The last factor in Equation (2) is the speckle interferometry transfer function. A well-known result for incoherent imaging is that the magnitude of an aberrated optical transfer function is always less-than-or-equal-to its unaberrated counterpart at each spatial frequency other than DC:[4]

$$|H_a(f_x,f_y)| \leq |H_u(f_x,f_y)|. \qquad (3)$$

This immediately tells us that any average of aberrated transfer functions will be biased downward at each spatial frequency except DC. No matter how many speckle frames are used in the average, the speckle interferometry transfer function will never converge to the true (unaberrated) modulation transfer function with atmospheric phase distortion present.

If, instead of averaging, we take the maximum magnitude value, then we can avoid this downward bias in the magnitude estimate. To see this we write

$$\underset{\text{w.r.t.}\,\ell}{\text{MAX}} \{|I_\ell(f_x,f_y)|\} = |O(f_x,f_y)| \times \underset{\text{w.r.t.}\,\ell}{\text{MAX}} \{|H_\ell(f_x,f_y)|\} \quad (4)$$

which indicates that we take the maximum value with respect to the set of speckle frames independently at each spatial frequency. In practice, the total number of photon events per frame will vary, and we should normalize each frame by this value before applying Equation (4). We can think of this maximum magnitude statistic as an image quality metric which finds the least aberrated magnitude value at each frequency location via Equation (3).

An interesting question concerning this statistic is whether or not it uses all of the information in the entire set of speckle images. Heuristically, the average power may at first seem better because it explicitly uses all of the available data values, whereas the maximum magnitude uses only 1/L of the data in an explicit manner. In statistical theory this question translates into one concerning the sufficiency of the statistic. This theory tells us that for a family of parent distributions with the characteristic that they have a maximum allowable value, θ, the maximum value of a random sample from such a distribution is a sufficient statistic for estimating θ.[5] Since each new magnitude value is considered by testing it against the existing maximum, each one in fact conveys some information whether it becomes the maximum value or not. In other words, we have more confidence concerning the accuracy of the maximum value from a set of 100 measurements than we do if it came from only a few measurements.

We would like to determine whether our maximum magnitude statistic is unbiased relative to the theoretical maximum value of $|O(f_x,f_y)| \times |H_u(f_x,f_y)|$. Since at any spatial frequency, we know that the data values must occur betweeen zero and some unknown maximum value, we hypothesize a uniform distribution of the form

$$f(y;\theta) = 1/\theta, \quad (5)$$

with $0 < y \leq \theta < \infty$. Assuming a random sample of size L, the probability distribution of the sample set's maximum value, y_L, is [5]

$$g(y_L) = \frac{L}{\theta^L} y_L^{L-1}. \quad (6)$$

The expected value of y_L is easily found:

$$E[y_L] = \frac{L}{L+1}\theta. \quad (7)$$

Thus, the maximum magnitude is asymptotically unbiased as $L \to \infty$. Since the sample size is known, however, it is simple to unbias the statistic:

$$\hat{\theta} = \frac{L+1}{L} y_L, \quad (8)$$

where $\hat{\theta}$ is our estimate of θ. Similarly, the variance of the maximum value is readily found to be

$$\mathrm{Var}[y_L] = \frac{L}{(L+2)(L+1)^2}\,\theta^2. \qquad (9)$$

And the variance of our unbiased estimator,

$$\mathrm{Var}[\hat{\theta}] = \frac{1}{L(L+2)}\,\theta^2, \qquad (10)$$

decreases with increasing sample size at a rate that is faster than the 1/L rate of an average value estimator.

It is important to recognize that the uncertainty being modeled by the foregoing analysis is due solely to the perturbations induced into the data by atmospheric turbulence. Other noise sources, such as photon and sensor noises, for example, have not been included and would be present in actual data. With a state-of-the-art sensor and high light level imaging (number of photons per frame >> 1), the uncompensated "noise" due to the atmosphere would far surpass these other sources, however. The photon SNR level of a maximum magnitude estimate would exceed that of any single frame, but would be less than that of a power spectrum average. The power spectrum average, as we shall see, may give a smoother result, but the wrong spatial frequency values are being estimated.

The maximum magnitude estimator was tried on an actual set of speckle data. This data consisted of 135 frames of the double star Capella taken with the 4-meter Kitt Peak National Observatory

telescope.[6] The data was recorded on video tape, digitized, and then transformed with an array-processor-based Fast-Fourier-Transform routine. Each transformed speckle frame was converted to magnitude and phase form, and the magnitudes were normalized by the DC coefficient value to counteract photon count variations between frames. The result was then obtained by simply searching the individual frames for the largest magnitude value in each spatial frequency bin. For comparison purposes the same data set was power-spectrum averaged as well.

Figure 1 shows the results based on the first 16 speckle frames. The maximum magnitude result was multiplied by 17/16 everywhere except DC as per Equation (8). The square root was taken of the average power values to obtain magnitude units. Since the maximum magnitude routine normalized each speckle transform by its DC value, the final result was multiplied everywhere by the average DC value taken over all the frames. Both results were then log transformed, displayed with identical DC intensity values, and photographed equivalently in a side-by-side manner. Visual inspection of Figure 1 clearly shows the downward bias of the power-averaged result compared to the maximum magnitude result. Figure 2 compares these two methods after the entire set of 135 speckle frames has been used in both estimations. Since the average power result clearly retains its bias here, it is not converging towards the true magnitude (or power) values with an increasing number of speckle frames.

Col. 1 of Figure, ... National Observatory 4 meter telescope using the Steward Observatory speckle camera[7].

In conclusion, results presented in this Letter demonstrate that, for high intensity speckle imaging, maximum magnitude estimation can be used instead of power spectrum averaging. The maximum Fourier magnitude taken at each spatial frequency extracts all of the statistical information relevant to the true object magnitudes. More importantly, the maximum magnitude statistic can be simply unbiased and provides an increasingly accurate estimate with more speckle frames. This method "looks" through the atmospheric distortions and converges directly on the object-times-telescope magnitude values. Since its primary assumption was linear imaging, maximum magnitude estimation is also applicable to extended objects that lie within a single isoplanatic patch of the atmosphere.

REFERENCES

1. A. Labeyrie, "Attainment of Diffraction Limited Resolution in Large Telescopes by Fourier Analysing Speckle Patterns in Star Images," Astron. Astrophs. 6, 85-87 (1970).
2. D. Korff, "Analysis of a method for obtaining diffraction-limited information in the presence of atmospheric turbulence," J. Opt. Soc, Am., 63, No. 8, 971-980 (1973).
3. G.P. Weigelt, "Stellar speckle interferometry and speckle holography at low light levels." SPIE Proc., 243, 103-111 (1980).
4. J.W. Goodman, Introduction to Fourier Optics (McGraw-Hill, New York, 1968), p. 122.
5. R.V. Hogg and A.T. Craig, Introduction to Mathematical Statistics (Macmillan, New York, 1970).
6. Data was supplied thanks to Otto Franz (Lowell Observatory), Hal McCallister (Georgia State), and Keith Hege (Steward Observatory).
7. Hege, E.K., E.V. Hubbard, P.A. Strittmatter and W.J. Cocke "The Steward Observatory Speckle Interferometer System" Optica Acta 29, 70 (1982).

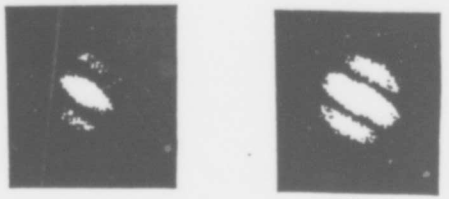

(a) (b)

Fig. 1. Fourier magnitude estimation results of Capella obtained via power spectrum averaging (a) and maximum magnitude estimation (b), using the first 16 speckle frames

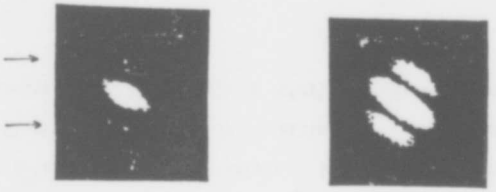

(a) (b)

Fig. 2. Fourier magnitude estimation results of Capella obtained via power spectrum averaging (a) and maximum magnitude estimation (b), using 135 speckle frames.

FIGURE CAPTIONS

Figure 1. Fourier magnitude estimation results of Capella obtained via power spectrum averaging (a) and maximum magnitude estimation (b) using the first 16 speckle frames.

Figure 2. Fourier magnitude estimation results of Capella obtained via power spectrum averaging (a) and maximum magnitude estimation (b) using 135 speckle frames.

The Differential Speckle Interferometer

Jacques M. Beckers

Multiple Mirror Telescope Observatory
Tucson, AZ 85721

E. Keith Hege, H. Patrick Murphy

Steward Observatory, University of Arizona
Tucson, AZ 85721

Abstract

We describe a new technique called "Differential Speckle Interferometry" (DSI) which uses simultaneous narrow band images of astronomical objects to study their structure. Simultaneous specklegrams of red supergiant and giant stars taken in the hydrogen lines and in the nearby continuum allow us to reconstruct the image of the extended chromospheres of these stars at resolutions of 100 nanoradians and better. We describe the instrumentation, analysis techniques, and results related to DSI.

Introduction

Refractive index variations associated with turbulence in the earth atmosphere cause severe distortions in the wavefront of astronomical objects observed by telescopes. Spatial phase variations in the wavefront amount to many cycles thus resulting in a major deterioration of the image quality. For exposure times short enough to freeze the temporal changes of the wavefront the broadened stellar images show the so-called speckle structure, each speckle being of a size near the theoretical diffraction limit of the telescope. Spatial analysis of the speckle image (specklegram) by means of power spectrum or autocorrelation techniques results therefore in some information on the size of the object in case of a resolved star or on the separation and orientation of the stars in a close binary system. To derive more detailed image information requires more sophisticated analysis or observing techniques[1].

We previously described[2,3] a technique called Differential Speckle Interferometry (or DSI) in which simultaneous speckle images taken in two nearby wavelengths are compared to derive image information which relates to the differences in the object as results from the difference in wavelength (e.g. due to Doppler shifts, stellar emission, or absorption lines, Zeeman effects). The DSI technique uses narrow band (0.04-0.16 nm) solid etalons with mica spacers to permit study of image differences in two spectral bands simultaneously. We have used DSI to image the envelopes of cold supergiant and giant stars, and to study stellar rotation and spectroscopic binaries. The DSI camera was built so that it can easily be converted into a so-called speckle spectrograph using prisms or grisms as spectral dispersers. We have used Speckle Spectroscopy to study stellar size variations over wavelength regions larger than allowed by the etalons across spectral features like TiO bands and hydrogen lines. The DSI system can also, of course, be operated as a conventional speckle camera. It is, consequently, a very flexible and powerful instrument. In this paper we describe details of the instrumentation, the data analysis, and some of the astronomical results.

The differential speckle camera

Figure 1 shows a diagram of the differential speckle camera (DSC) as it has been constructed. The DSC has been constructed for use with the Multiple Mirror Telescope (MMT), the Steward Observatory 2.3 meter telescope, and the KPNO 4 meter telescope, and has been successfully used at all three telescopes. The basic layout is very straightforward. After a reflecting prime focus stop which feeds the field viewing optics and the Telescope Coalignment System of the MMT, the light passes through a collimator-camera lens arrangement which images the star onto a four stage electrostatic image intensifier which is lens-coupled to a plumbicon®. The collimator is a 24.5 mm (10x) or 13.8 mm (5x) microscope objective which together with the 622 mm focal length camera lens give magnifications of 25x and 45x respectively. Table 1 summarizes the image scales so obtained at the three telescopes. They are well matched to the detector and the digitizer pixel size. The area between the collimator and camera lens is described as the "instrument bay" in which various optical configurations can be inserted as shown to the right in Figure 1. The DSC is a completely modular system in which optical components are mounted on metal inserts which can easily be exchanged in a closed-in optical bench mounted in the cassegrain focus. In a few minutes it is therefore possible to modify the optical configurations between the

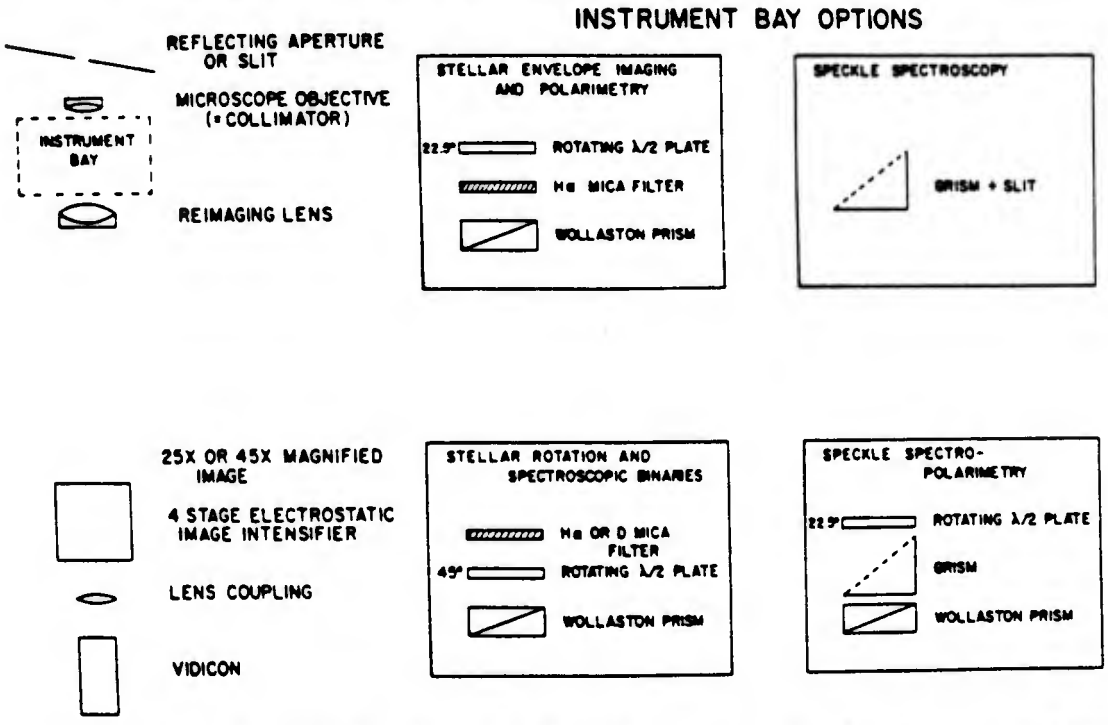

Figure 1. Diagram of the Differential Speckle Camera. On the left is shown the optical configuration of the instrument. In the middle and right are shown the different configurations of the instrument bay used for different types of observations.

Table 1. Image scales of the DSC at various telescopes*

Telescope	Cass. Focus Scale	Speckle Size**	Final Image Scale† (5x/10x)	Pixel Size†† (5x/10x)
MMT	278 μm/arcsec	98 nrad	7.1/12.5	36/20
KPNO 4^m	160 μm/arcsec	178 nrad	4.1/7.2	62/35
Steward 2.3^m	100 μm/arcsec	300 nrad	2.5/4.5	100/56

ones shown in Figure 1 and variants thereof, including conventional speckle interferometry, in which case a microprocessor controlled anti-dispersion system[4] is placed ahead of the entire DSC system.

In the differential speckle imaging mode (DSI) the optics bay contains the following components:

(a) A Solid Fabry-Perot Etalon with mica as its spacer, also called Dobrowolski filter[5]. Since mica is birefringent such an etalon has two passbands at different spectral locations for orthogonal linear polarization directions. The spectral separation of these two passbands is determined by the mica thickness. The filters that are part of the DSC are listed in Table 2. The mica filters are manufactured by the Daystar Corporation. The 3 and 4 period blocking filters are manufactured by the Andover Corporation. All optics, including lenses, waveplates, etc., are high efficiency antireflection coated to reduce possible effects resulting from multiple reflections.

(b) A Wollaston Prism separates the two specklegrams corresponding to the two polarization directions (and therefore to the two wavelengths). The Wollastons, manufactured by the Continental Optical Corporation, separate the images by 1.52 and 7.38 mm in the image plane. The former creates the artificial double star used in the stellar rotation and spectroscopic binary studies, the latter separates the two specklegrams completely. Figure 2 is an example of such simultaneous specklegrams of α TAU, one in the Hα line and one in the nearby continuum.

*When referring to our speckle observations we will use the angular scale of radians (1 μrad = 200 milliseconds of arc; 1 nrad = 0.2 millisecond of arc). When referring to focal scale we have used mm/arc second in reverence to custom.
**In nrad at Hα, taken as λ/d where d = the telescope aperture. d = 690 cm for MMT, 380 cm for KPNO 4^m, and 230 cm for Steward 2.3^m.
†In mm/arcsec
††In nrad for 240x256 video digitizer. Pixel size corresponds to 50 μm.

Table 2. Filters Used in DSC

	λ(nm)	$\lambda_{\parallel} - \lambda_{\perp}$(nm)	FWHM(nm)	Peak Transmission	Note
MICA:					
	589.0(D_2)	0.053	0.037	28%	
	656.3(Hα)	0.38	0.045	24%	
	656.3(Hα)	0.02	0.12	74%	
	656.3(Hα)	0.09	0.09	>65%	on order
	656.3(Hα)←	0.55←	0.12←	78%←	
	656.3(Hα)	0.80	0.16	78%	
	854.2(Ca^+)	0.5	0.09	>65%	on order
BLOCKER:					
	587.5(He D_3)	N/A	1.47	82%	
	589.0(D_2)	N/A	1.38	66%	
	656.3(Hα)	N/A	1.26	70%	
	854.2(Ca^+)	N/A	1.3	>60%	on order

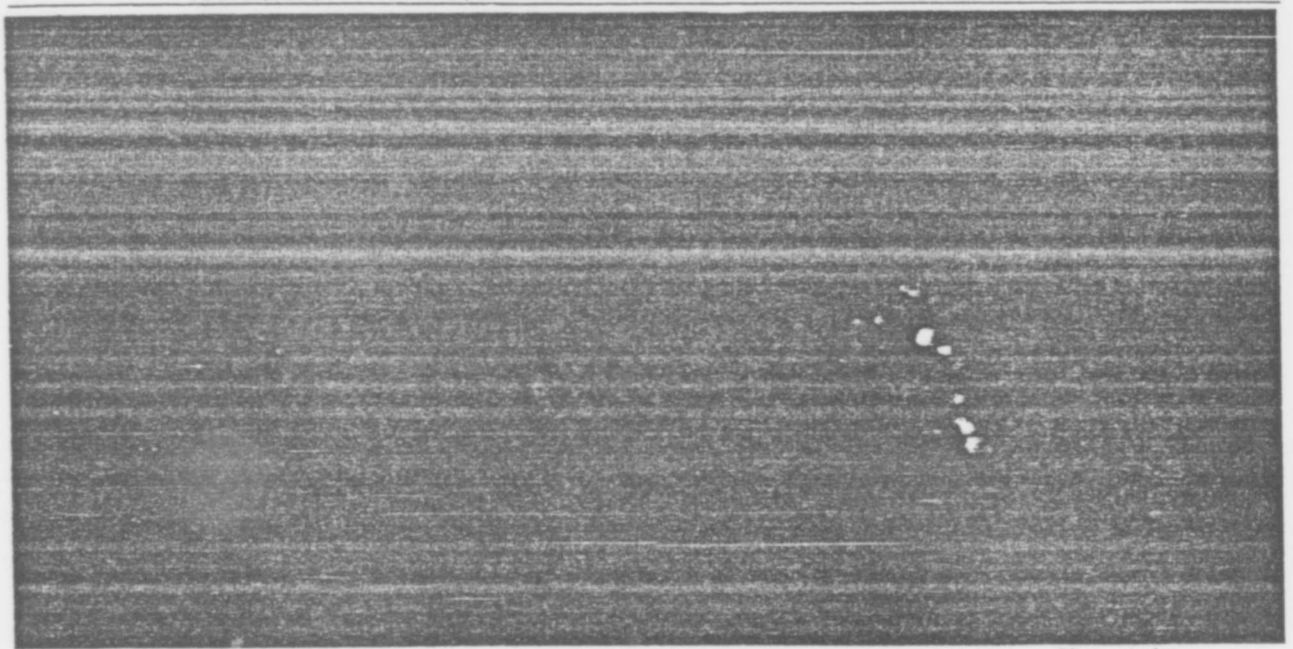

Figure 2. Double image formed by DSC using Wollaston prism beamsplitter. The right, brighter image is taken in the continuum 0.55 nm to the red of the Hα absorption line in α TAU. The left image is taken at the center of the Hα line.

(c) A rotating Half-Wave Plate driven by a computer controlled stepper motor in increments of 22.5° or 45°. When located in front of the mica filter it makes the DSC a full-fledged linear polarimeter if rotated at 22.5°. When located between the mica filter and Wollaston prism and rotated at 45° steps it swaps the wavelengths of the two images, a feature that is used for the stellar rotation and spectroscopic binary studies.

(d) In speckle spectroscopy the entrance aperture is replaced by a 5 μm or 10 μm wide slit (about equal to the speckle size) and the optics bay contains a GRISM (Carpenters Prism) or a zero deviation refractive disperser made of BK7 and F4 glass. The part of the speckle image intersected by the narrow slit is therefore spectrally dissected and recorded by the detector. Figure 3 shows a low dispersion speckle spectrogram taken with two opposite phased MMT telescopes. The baseline between the two telescopes runs parallel to the spectrograph slit so that the interference fringes are at right angles to the slit. The spectral behavior of both speckles and interference fringes are clearly shown. Both speckles and fringes separate linearly as a function of wavelength as they should, being interference phenomena. Table 3 lists the four spectrum dispersers now available for the DSC. Again, as with all DSC optics, they are modular so that they can be interchanged among themselves within a minute. In addition they can be replaced by the filter setup in a similar time. By using the rotating (22.5° steps) half waveplate and the Wollaston prism, the speckle spectroscopy can be combined with polarimetry, a feature which is of interest for certain stellar observations where polarization in lines is known to exist.

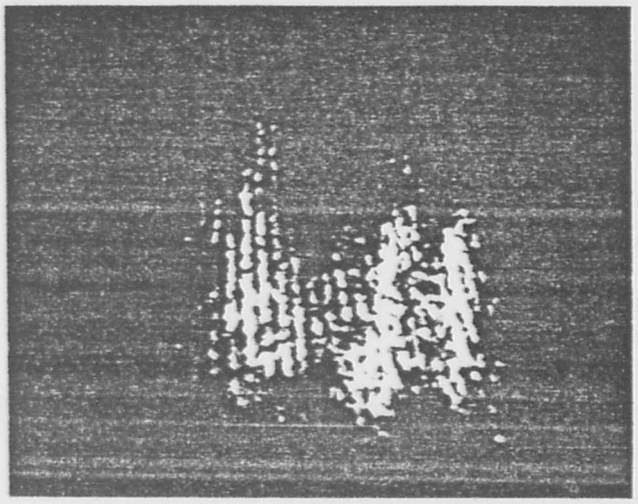

Figure 3. Speckle spectrogram taken with two phased MMT telescopes (separation = 5 meters). Wavelength runs from 450 nm on top to 850 nm on the bottom. The fringes are caused by the interference between the two telescopes. The larger scale inhomogeneities are due to the intersection of the combined speckle patterns of the two telescopes.

Table 3. Spectrum Dispersers Used in DSC

Type	Wavelength Range (nm)	Spectrum Resolution (5 μm slit; 5
Prism	430 - 860	~ 4nm
Grism	470 - 535	0.6 nm
Grism	580 - 605	0.25 nm
Grism	825 - 885	0.6 nm

Observations using differential speckle interferometry have produced images of late supergiant and giant Hα envelopes and measures of the spectroscopic binary α VIR and of the rotation of γ CYG. These observations, obtained at different telescopes with a variety of filters, are now being analyzed using a variety of software programs. The analysis software is quite different for the photon-limited case where the location of the individual photoelectrons are used than for the "bright" objects where the specklegrams are digitized as a whole maintaining the pixel to pixel brightness variation[5].

Red supergiant and giant star envelopes.

Because of their low surface gravity, the envelopes of these stars are very extended and rather cold making them, for example, visible in the light of the hydrogen Balmer lines (e.g. Hα) and of the singly ionized calcium lines (e.g. λ8542). In March 1982 observations were obtained with the Steward 2.3m telescope of α ORI with the 0.45 Å Hα filter at seven different wavelength positions centered around the Hα line (Hα + 1.5 Å; Hα + 1.0 Å; Hα + 0.5 Å, and Hα + 0.0 Å) selected by adjusting the filter temperature. Because of the low filter transmission these observations are photon-limited. The data was analyzed by cross correlation of the continuum specklegram with the line specklegram. Figure 4 (left) shows a cross section of the cross correlation so obtained both for a wavelength at the line center (Hα + 0.0 Å) and in the far Hα wings (Hα + 1.5 Å). The continuum image of α ORI is in fact close to the speckle image of a point source since the continuum size (~ 250 nrad) is somewhat less than the speckle size of the telescope (300 nrad). This cross correlation is therefore close to what has been called speckle holography[6], giving Hα images of the s... Superposed on the image is, however, a large background due to the cross correlation of the average atmospheric seeing disks. Subtraction of this background is tricky since it is continuously variable and since it is not exactly known. Assuming a gaussian shape for this background and adjusting it to the far wing of the cross correlation profile, we arrive at the image cross section after background subtraction shown in Figure 4 (right). The extended envelope around the star is clearly visible having a diameter of 1-2 μrad or 4-8 R_* (R_* = stellar radius) at the Hα center and disappearing in the far Hα wings. In the blue wing of the line (Hα - 0.5 Å) the Hα envelope is larger and better visible than in the red wing (Hα + 0.5 Å) probably because of the expansion of the optically thick envelope with ~ 20 km/s expansion which obscures the stellar disk in the blue wing but not in the red wing where the small stellar disk speckles therefore dominate the cross correlation.

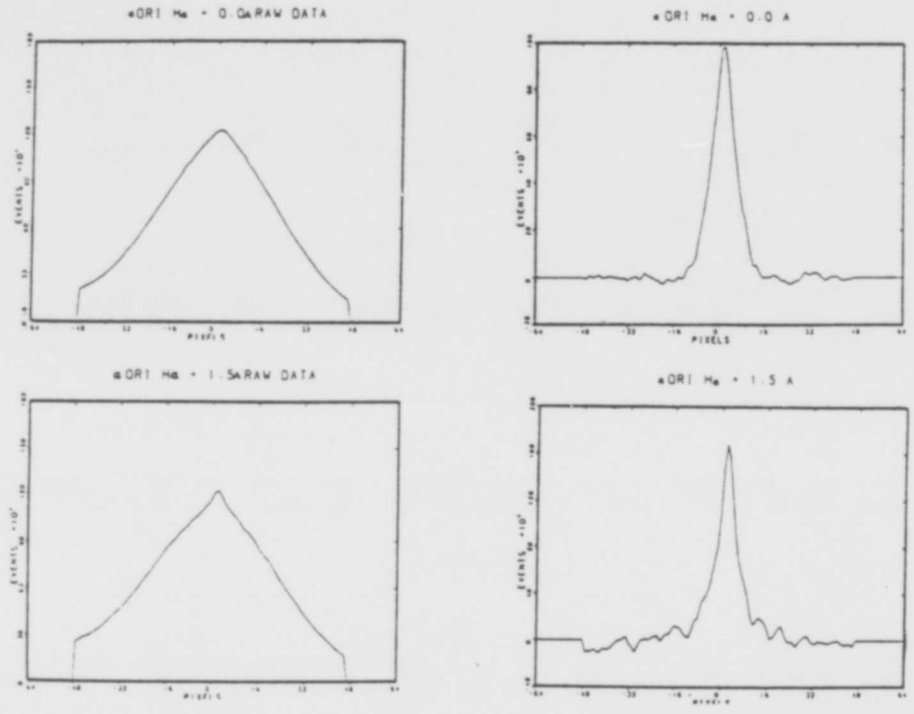

Figure 4. Cross section of Hα line and nearby continuum speckle images of α ORI taken with the Steward Observatory 2.3 meter telescope. Left before background subtraction, right after. Scale Abcissa: 1 division = 16 pixels = 0.4 arcsec.

Figure 2 is an image obtained with the 1.2 Å Hα mica filter at the KPNO 4^m telescope. It is a bright speckle image at Hα + 0.0 Å and in the continuum 5.5 Å away. The latter is an image of what we assume to be a known limbdarkened stellar disk with a diameter determined from interferometry, occultation, or other means. It is used to determine the atmosphere-telescope-instrument apparatus function which is then used to deconvolve the Hα + 0.0 Å image. This technique appears to work exceedingly well. Figure 5 shows an image of a point source (α LYR) and of a resolved red supergiant (α HER). The point source has a profile close to theoretical whereas the red supergiant image shows resolved structure.

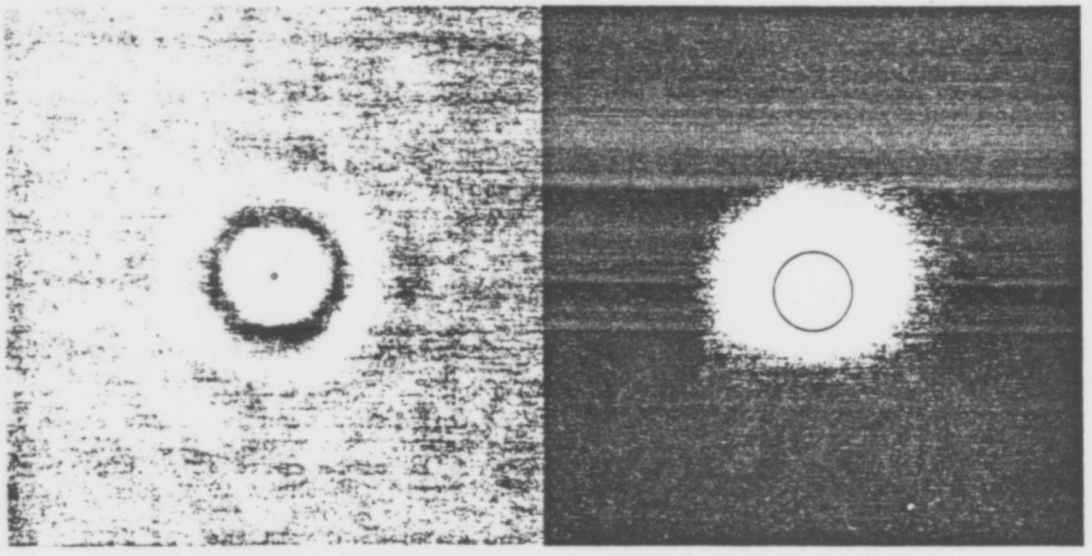

Figure 5. Hα images of the unresolved star α LYR (left) and of the resolved red supergiant α HER (right). Angular resolution is ~ 100 nrad. Size of each area is 0.285 x 0.285 arc seconds.

Spectroscopic binaries

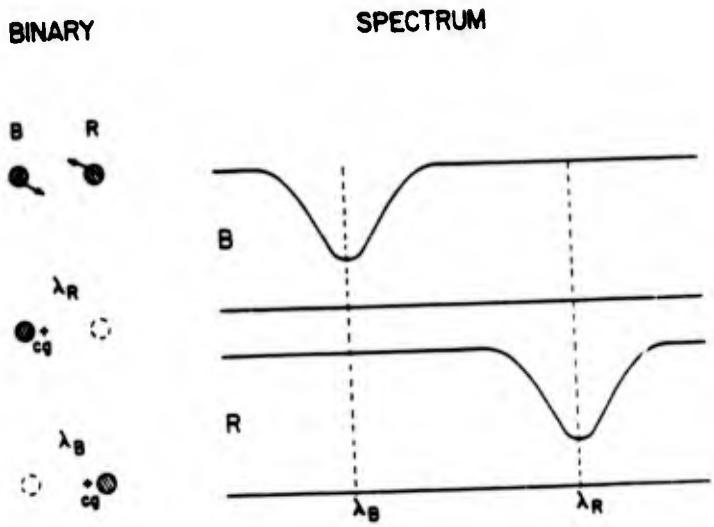

Figure 6. Schematic of spectroscopic binary observations. Observation of the unresolved binary at λ_B and λ_R will show different locations of the photocenters of gravity (cg). These differences in location of cg_B and cg_R can be measured with precisions much smaller than the speckle sizes.

Observations were obtained of the spectroscopic binary α VIR in March 1982 with the 2.3 telescope to explore the sensitivity of the DSI technique to measure the separation and or ientation of spectroscopic binaries. The technique is explained in Figure 6. The small separation Wollaston was used giving an artificial double star with about 3 μrad separatio We used the 0.45 Å Hα filter adjusted to have one of the band passes fall on the Hα line o one of the components. The other band pass was located on the wing of the Hα line on the

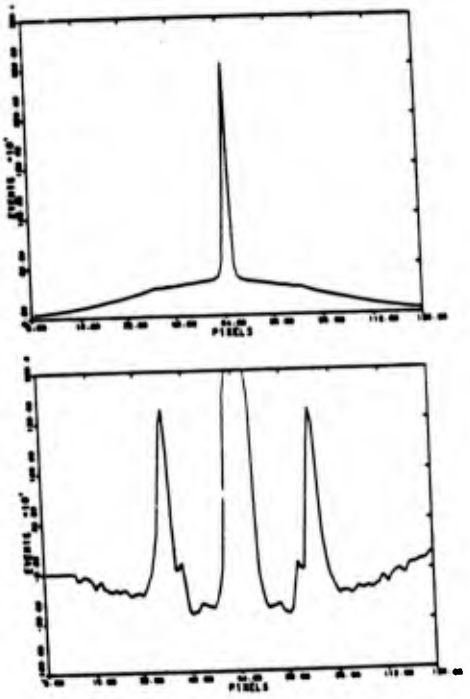

Figure 7. Autocorrelation of the artificial double star image of α VIR. Top before ba ground subtraction, bottom after subtraction.

other component. The specklegrams are of the photon limited case. Figure 7 (top) shows a cut through the 2D autocorrelation function along the direction of the image separation showing (i) the narrow large zero displacement peak, (ii) the large seeing disk background, (iii) narrow peaks due to video clock signal interference, and (iv) the signal of interest. Figure 7 (bottom) shows the same after subtraction of a gaussian background and after subtraction of the clock signal. The artificial double star is well detectable although it is obvious from Figure 7 (bottom) that the gaussian background subtraction is less than perfect. From an analysis of the data covering a total of 20 minutes observing time we arrive at an accuracy of the technique of 2.5 nrad RMS in both α and δ direction. This accuracy was insufficient to unambiguously separate the binary components which equals 13 nrad at maximum separation, mainly because the two specklegrams are only partially separated. In spite of this, the anticipated differential separation of the photon centers of gravity equals about 4 nrad so that the measurement accuracy is tantalizingly close to resolving this binary. We expect to improve the accuracy of the technique by using (i) higher transmission filters, (ii) larger telescopes which give narrower autocorrelation peaks, thus improving the precisions, (iii) the wide separation Wollaston prism which reduces the high background underneath the autocorrelation peak and therefore the noise.

These improvements should combine to give corresponding improvements in precision of at least an order of magnitude.

Conclusion

We are planning to use the techniques of differential speckle interferometry and speckle spectroscopy in the future for a detailed study of stellar atmospheres and envelopes, for a study of stellar rotation[2-3] and spectroscopic binary orbits, and for the examination of cores of active galactic nuclei and Seyfert galaxies. Differential techniques appear to be very sensitive for the study of the behavior of astronomical objects for which spectral and/or polarization variation of structure can be expected.

Acknowledgements

The instrumentation described here was built with the enthusiastic help of C. Poland and R. Young. We appreciate the support received in obtaining the observations by the staffs of KPNO, Steward Observatory, and the MMTO. This work was supported by NSF grant AST 8201092.

References

1. Labeyrie, A. "Stellar Interferometry Methods", Ann. Rev. Astron. Astrophys. 16, 77, 1978.
2. Beckers, J.M. "Differential Speckle Interferometry", Optica Acta 29, 361, 1982.
3. Beckers, J.M. and Hege, E.K. "Experiments in Differential Speckle Interferometry", Proceedings IAU Colloquium 67 "Instrumentation for Astronomy with Large Telescopes", Zelenchukskaya (Ed. C.M. Humphries) p. 199, 1982.
4. Hege, E.K., Hubbard, E.N., Strittmatter, P.A., and Cocke, W.J., "The Steward Observatory Speckle Interferometry System", Optica Acta 29, 701, 1982.
5. Dobrowolski, J.A. "Mica Interference Filters with Transmission Bands of Very Narrow Half-Widths", Journal Optical Soc. of America 49, 794, 1959.
6. Weigelt, G.P. "Speckle Holography Measurements of the Star Zeta Caneri and AOS 3358", Appl. Opt. 17, 2660, 1978.

STATISTICAL ANALYSIS OF A SELF-CALIBRATING SHIFT-AND-ADD IMAGE RECONSTRUCTION TECHNIQUE

J. Freeman, K. Hege*, J. Christou and E. Ribak

Steward Observatory
University of Arizona
Tucson, Arizona 85721

and

F. Roddier
National Optical Astronomy Observatories
Tucson, Arizona 85726

To be Submitted to J. Opt. Soc. Am.

*Visiting Astronomer, Kitt Peak National Observatory, a division of the National Optical Astronomy Observatories, operated by the Association of Universities for Research in Astronomy, Inc., under contract with the National Science Foundatioin.

ABSTRACT

We demonstrate the underlying statistical basis for the Christou, Ribak and Hege technique for recovering a mean speckle image, completely free of atmospheric noise bias. Our analysis of this method, which is a logical extension of the simple shift and add technique pioneered by Bates and Lynds, Worden and Harvey, is a logical extension of an earlier study by Hunt, Fright and Bates of the Bates technique.

I. INTRODUCTION

The following is a brief outline of a statistical analysis of the Weighted Shift and Add Algorithm (WSA).

Our WSA statistical analysis is an extrapolation of the analysis of the Simple Shift and Add Algorithm undertaken by Hunt Wright and Bates (1982). In that paper, the expected SSA intensity profile was found to be

$$S(x) = 2\langle I\rangle + \underline{P_s(x)}\,(S_{max} - \langle I\rangle) - S_{max} \qquad (1)$$

where $\langle I\rangle$ is the average intensity of the specklegram. S_{max} is the maximum intensity found in the frame and $P_s(x)$ is a real function of the complex coherence of the speckles and is independent of individual speckles under the assumption that the speckle process (seeing) remains constant with time. $P_s(x)$ is related to the complex coherence factor $u_x(x)$ by the expression (Goodman, 1975):

$$P_s(x) = \langle I\rangle^2 \left[\, 1 + |u_x(x)|^2 \,\right] \qquad (2)$$

where:

$$0 \le |u_x(x)| \le 1$$

If eq. (2) is substituted into eq. (1) the result is

$$S(x) = (S_{max} - \langle I\rangle)\,|u_x(x)|^2 + \langle I\rangle \qquad (3)$$

Since $|u_x(x)|^2$ is the only spatially variant term in eq. (3), any understanding of the results of the SSA analysis (and hence the WSA analysis, as will be shown) is based on a knowledge of the structure of the complex coherence function $u_x(x)$.

Goodman, in Statistical Properties of Laser Speckle Patterns (Dainty, 1975) uses the complex coherence function extensively. One expression he derives is the conditional probability density:

$$P_x(I_2|I_1) = \frac{\exp\left[\dfrac{|\mu_x(x)|^2 I_1 + I_2}{\langle I\rangle\left(1 - |\mu_x(x)|^2\right)}\right]}{\langle I\rangle\left(1 - |\mu_x(x)|^2\right)}\; I_0\left(\frac{2\sqrt{I_1 I_2}\;|\mu_x(x)|}{\langle I\rangle\left(1 - |\mu_x(x)|^2\right)}\right) \qquad (4)$$

where I_1 and I_2 are two intensities seperated by a distance x in a speckle pattern. Through the use of this probability density we are able to obtain estimates of the complex coherence function.

II. OBSERVATIONS

Using astronomical speckle interferometric data of the standard star Epsilon Orionis taken at the 2.7 m telescope in F-Alpha at SCM, it is easy to build up histograms which are equivalent to plots of eq.(4) at constant radii. These histograms are seen in figs 1-7. By fitting the theoretical distribution $P_I(I_2|I_1)$ with $|u_x(x)|$ as the independent variable, we can obtain estimates of the complex coherence. The smooth lines in figs. 1-7 are the model estimates obtained by such fits. The results of the estimates of the complex coherence are summarized in Table I.

III. DISCUSSION

The development of eq. (4) makes no reference to the concept of "speckles". The term speckle is casually used (e.g. Hunt et al., 1982 or Christou et al., 1982) to describe a distorted, diffraction limited image found in a specklegram. The number of "speckles" is always assumed to be much less than the number of pixels in a specklegram and each "speckle" is also assumed to have an identifiable central maximum. If such "speckles" exist, then the intensities in the area in the specklegram associated with a "speckle" should be qualitatively different than those for any arbitrary point in the field. To check the above assumptions, the matched filter methods developed by Ritak (1982) were used to determine the "speckle" maxima in a series of specklegrams. Then, the probability density histograms were computed for the pixels surrounding those maxima. The computed histograms are seen is figs. 8-11. Comparison of the maxima histograms with the histograms computed for any point in the specklegram reveal no substantial qualitative difference.

This leads us to the conclusion that in a statistical sense, "speckles" exist continously through a specklegram. However, due to exponential photon statistics in a single specklegram, statistical fluctuation at a particular point may so dominate the local area that in effect an isolated speckle may be said to exist.

IV. APPLICATIONS TO WEIGHTED SHIFT AND ADD

At this point we rejoin our derivation of the WSA statistical analysis. WSA (Christou et. al. 1982) differs from SSA (Hunt et al. 1982) in that WSA weights and shifts on a number of points, subject to some amplitude threshold, in the specklegram, and not just the brightest. If we were to shift on pixels of all intensities, the resulting WSA profile W(x) would equal:

$$W(x) = \sum_{i=1}^{N} \int_0^{\infty} S(x)\;\; V_i(x)\; p(V_i)\; dV_i \qquad (5)$$

Where S(x) is given by eq. (3) and $p(V_i)dV_i$ is the differential

probability density describing the existence of local speckle maximum . Assuming an exponential distribution for the speckle intensities, $p(\zeta)$, and integrating over all intensities and summing over the specklegram data set yields:

$$W(x) = \langle I \rangle^2 (|u_A(x)|^2 + 1) \qquad (6)$$

Since $|u_A(0)| = 1$, we would expect the WSA profile to look like some function with amplitude $\langle I \rangle^2$ on top of a constant background of value $\langle I \rangle^2$. In practice, however, the pixels that are shifted on are determined by a local maxima selecting technique, namely the integrand in eq. (5) is subject to a non-zero threshold in practice. This procedure insures that pixels are systematically selected from the upper end of the exponential probability density. Then, the expected WSA profile would approximately equal:

$$W'(x) = W(x)/\langle I \rangle^2 = K |u_A(x)|^2 + 1 \qquad (7)$$

where in first approximation, K is a constant < 1 and whose value is determined by the integration threshold. Examination of the radial average of an actual WSA image (Figure 12) reveals that eq. (7) must be a better model of the process than eq. (6). The profile of Epsilon Orionis was taken from a 128 x 128 image. Table 1 contains a comparison of the value of the normalized WSA intensity profile with the measurements of the complex cohernce function. Notice that to a first order approximation that the numbers are similar.

Christou et al. (1985) have shown that the WSA image for a point source converges to the expected Airy pattern for the particular telescope used. This result coupled with our model leads us to the remarkable conclusion that the square modulus of the complex coherence function must equal the theoretical Airy pattern.

TABLE I

RADIUS	MCD COMPLEX COHERENCE	WSA POINT SOURCE
1.00	.69	.77
1.41	.59	.63
2.00	.40	.34
2.83	.15	.12
3.00	.06	.09
4.00	≈.00	.02
4.24	≈.00	.03

REFERENCES

Dainty, J. C. (1975), ed. Laser Speckle and Related Phenomena Springer-Verlag, New York, 1975.

Goodman, J. W. (1975) "Statistical Properties of Laser Speckle Phenomena" In Laser Speckle and Related Phenomena, J. C. Dainty, ed., Springer-Verlag, New York 1975, p9.

Hunt, B. R., W. R. Fright and R. H. T. Bates (1983) "Analysis of the Shift-And-Add Method for Imaging Through Turbulent Media", J. Opt. Soc. Am 73, p. 4.

Christou, J., E. Ribak, K. Hege and J. Freeman, (1985) "Self-Calibrating Shift-And-Add Techniques", Astron. J., In Preparation.

Ribak, E., K. Hege, J. Christou, and J. Freeman (1985), "Matched Filters can Extend Shift-And-Add Speckle Image Reconstruction Techniques to Poison Noise Dominated Observations", J. Opt., Soc. Am., In Preparation.

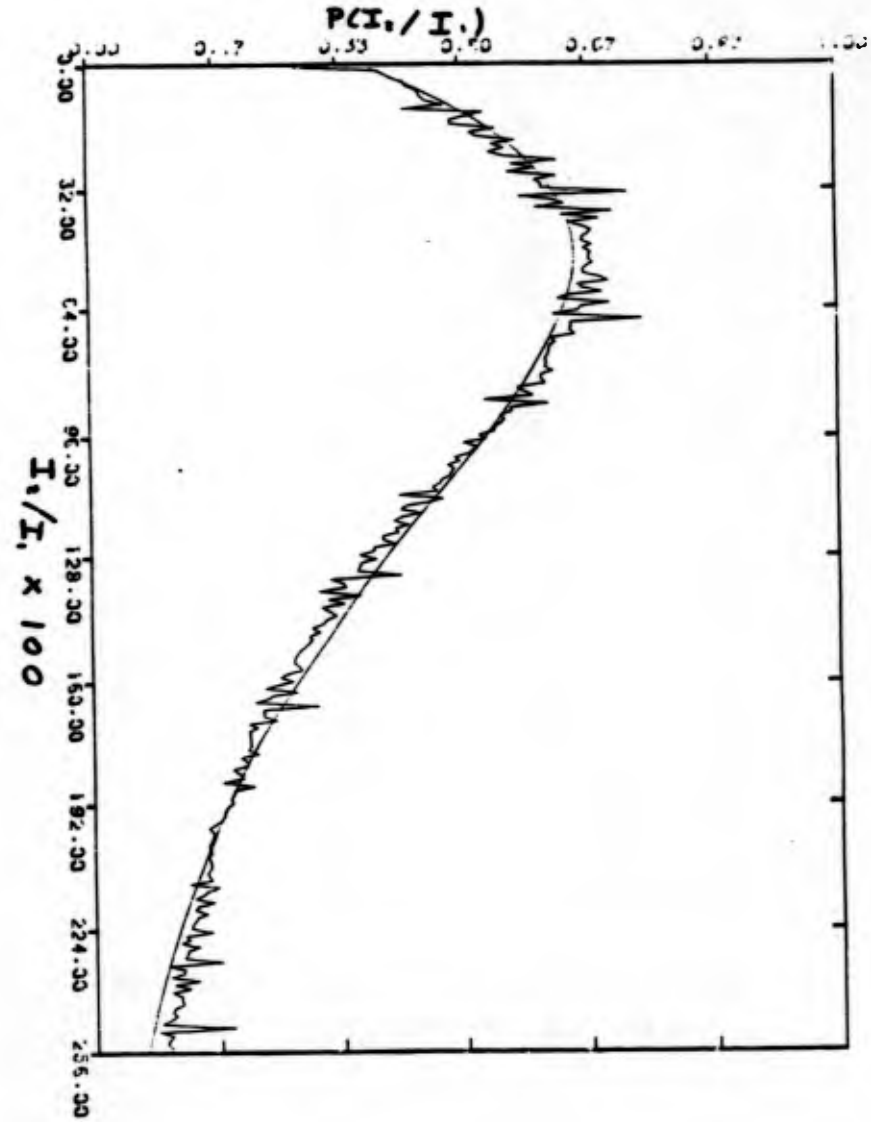

FIG. 1

FIG. 2

RADIUS = 1.41

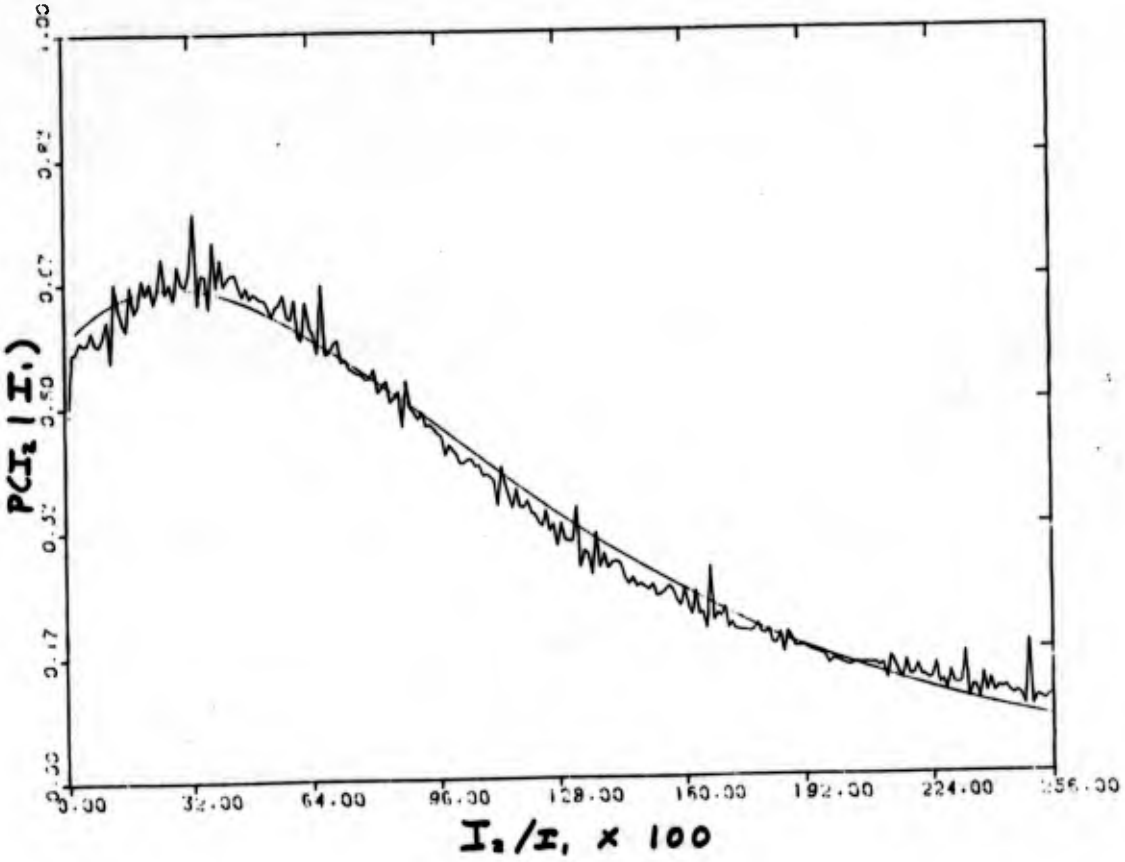

FIG. 3

RADIUS = 2.0

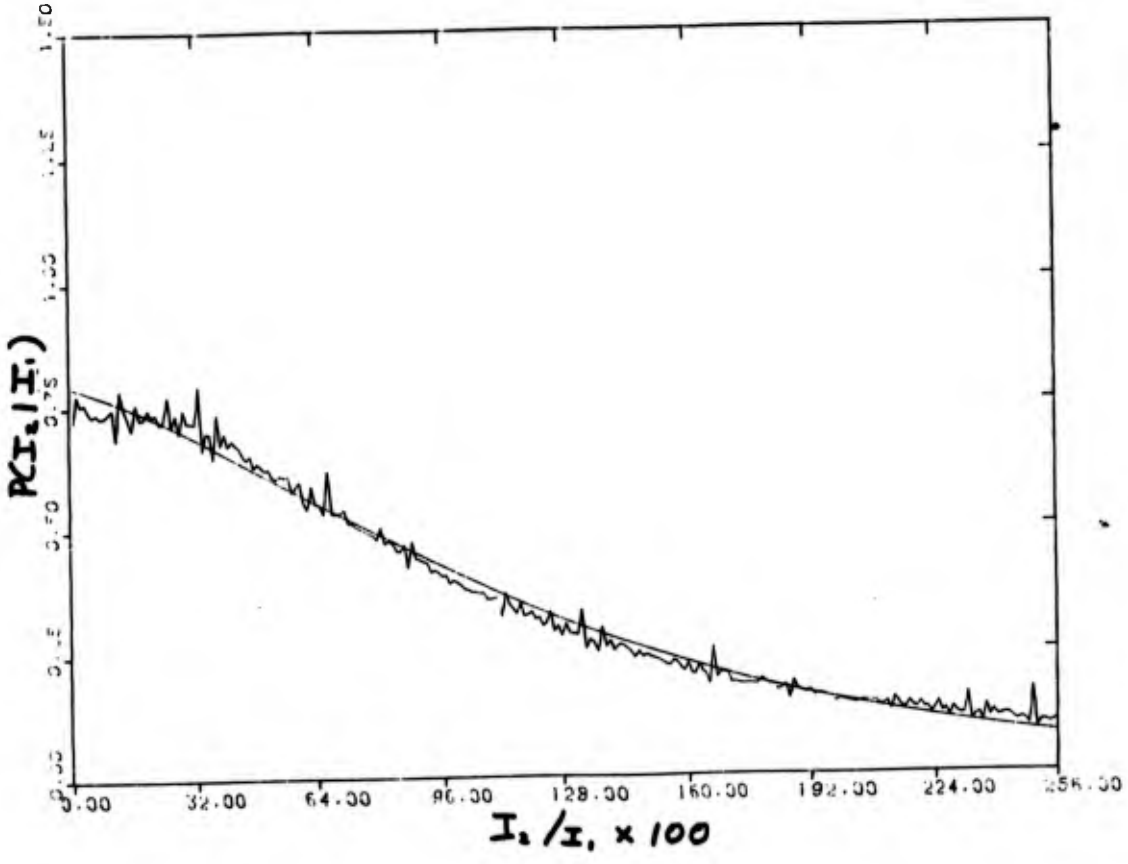

FIG. 4

RADIUS = 2.83

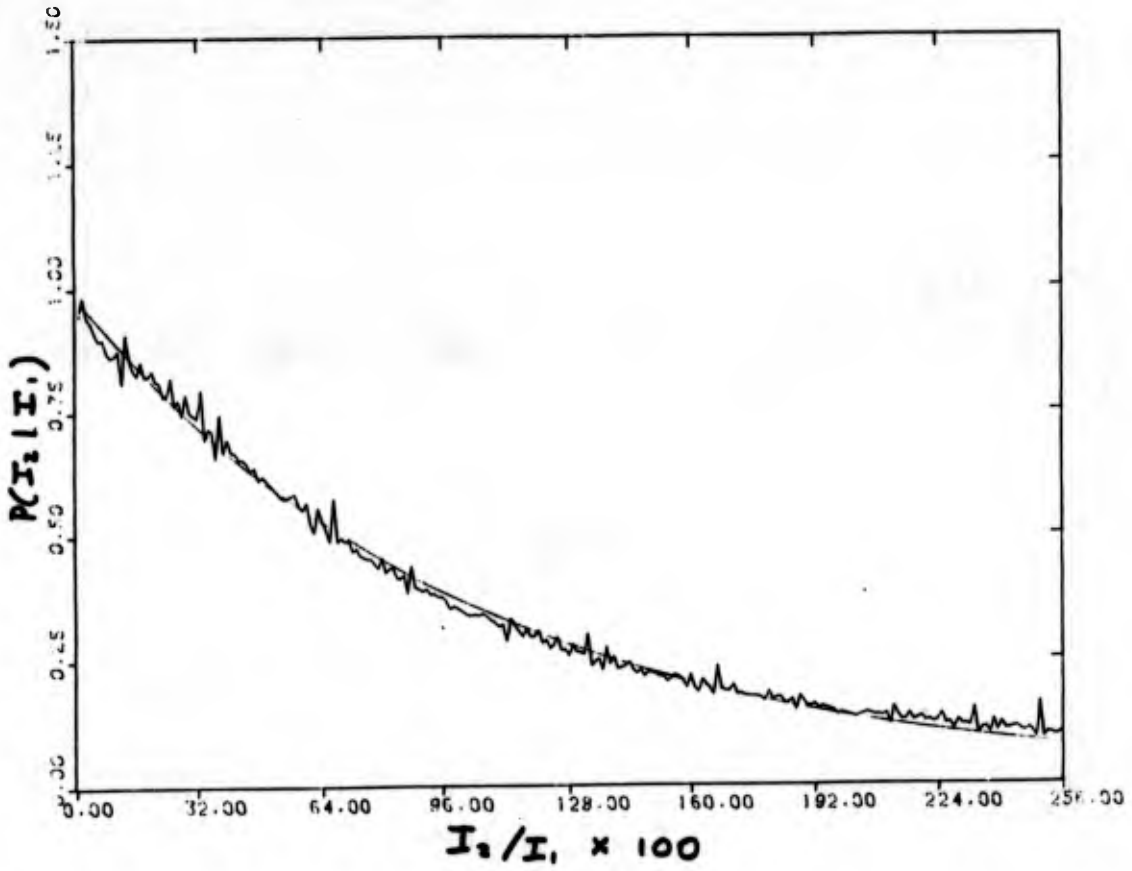

FIG. 5

RADIUS = 3.00

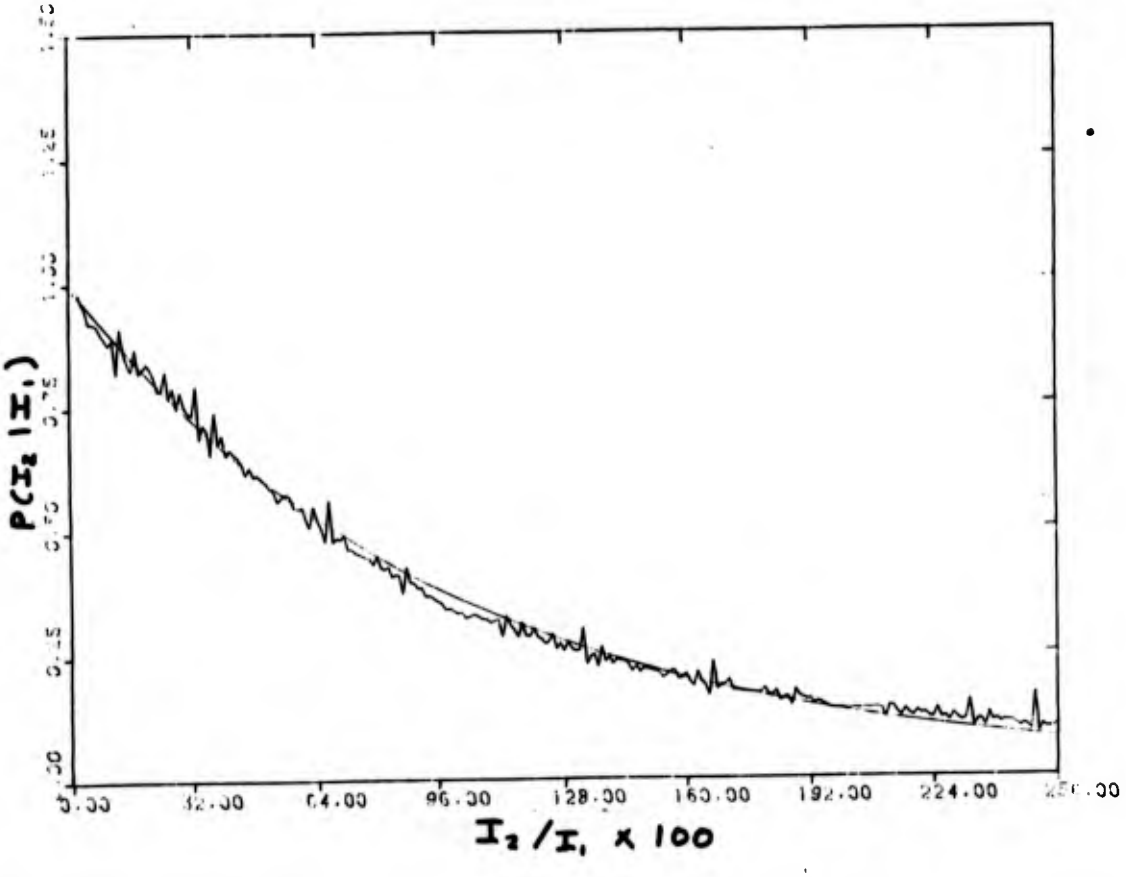

FIG. 6

RADIUS = 4.0

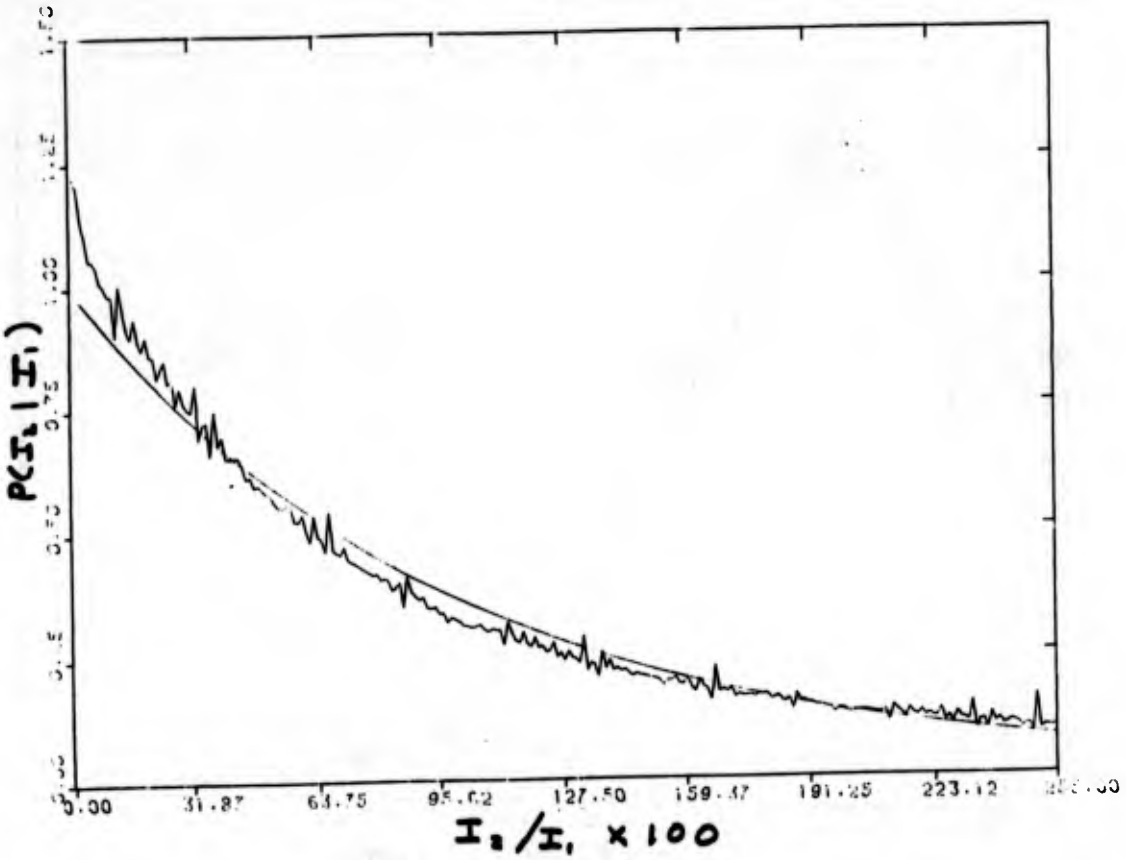

FIG. 7

RADIUS = 4.24

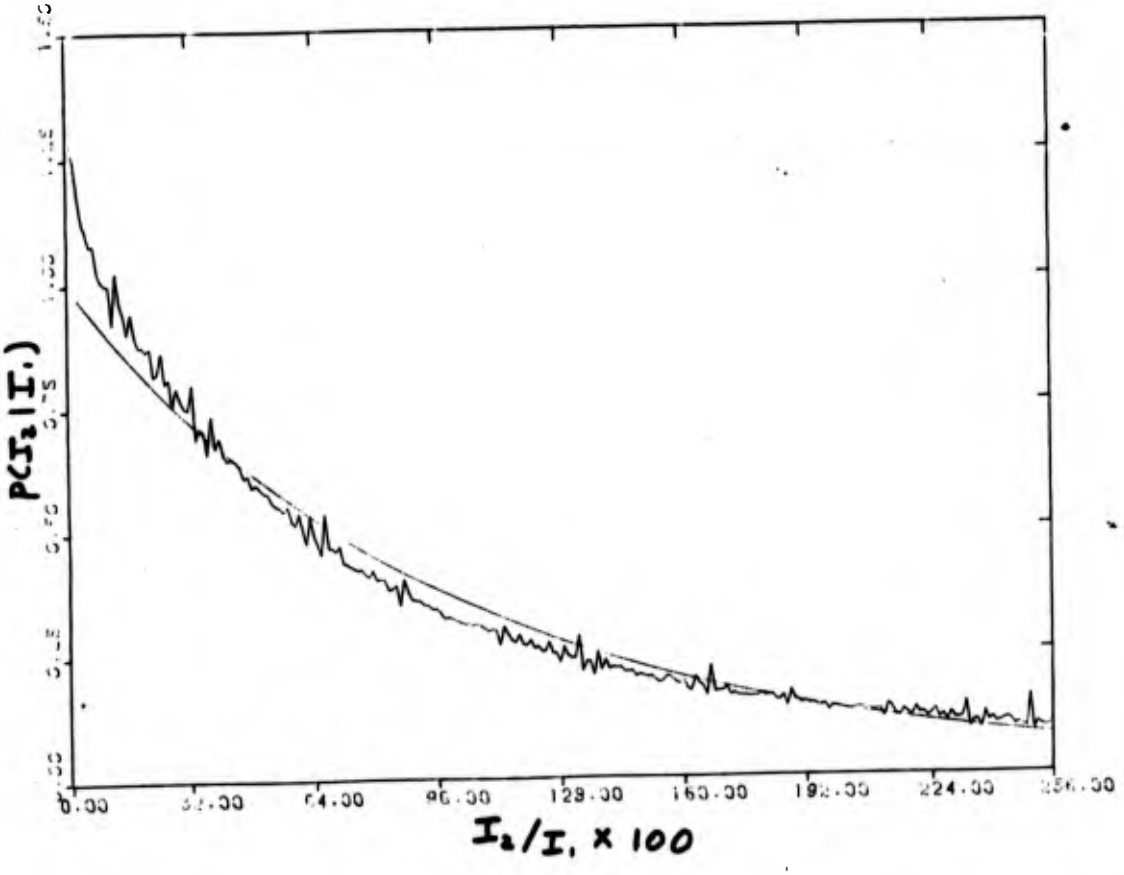

FIG. 8

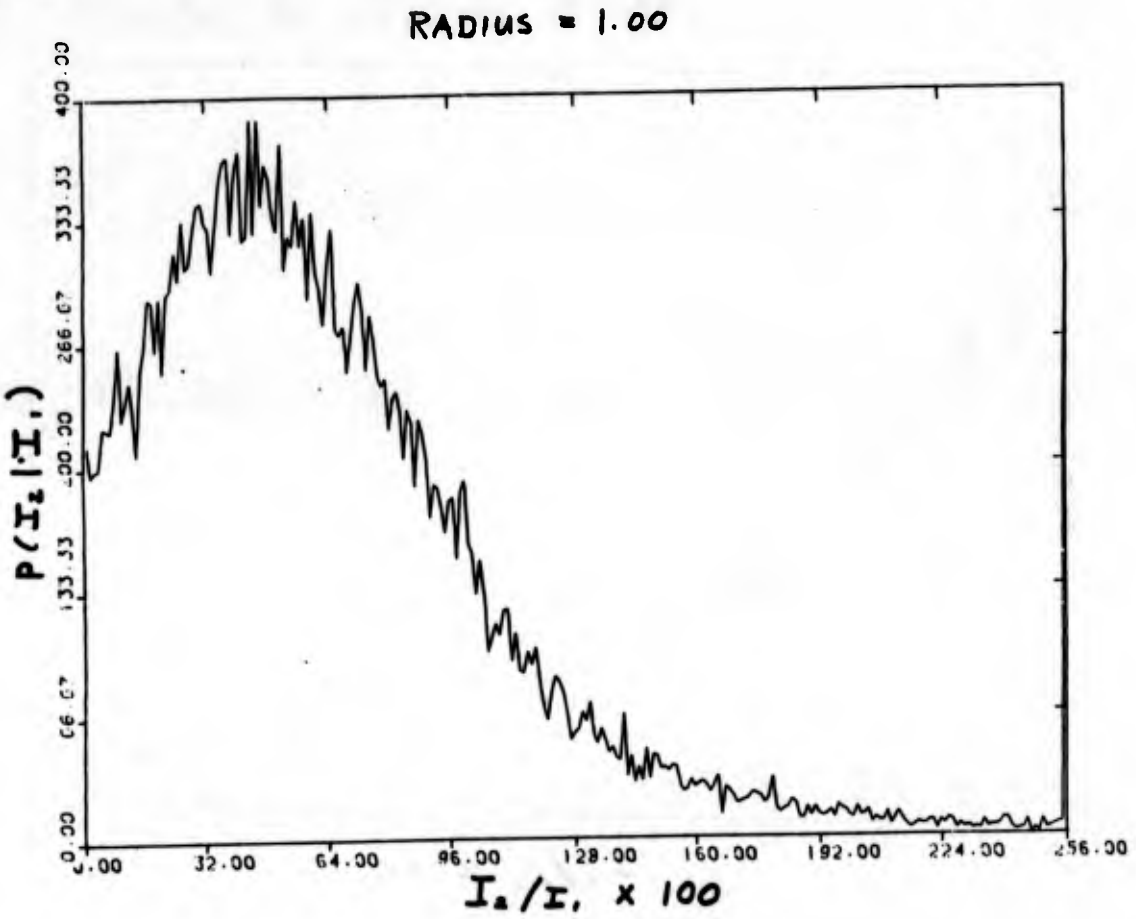
RADIUS = 1.00
400.00
333.33
266.67
200.00
133.33
66.67
0.00
P(I₂|I₁)
0.00
32.00
64.00
96.00
128.00
160.00
192.00
224.00
256.00
I₂/I₁ x 100

FIG. 9

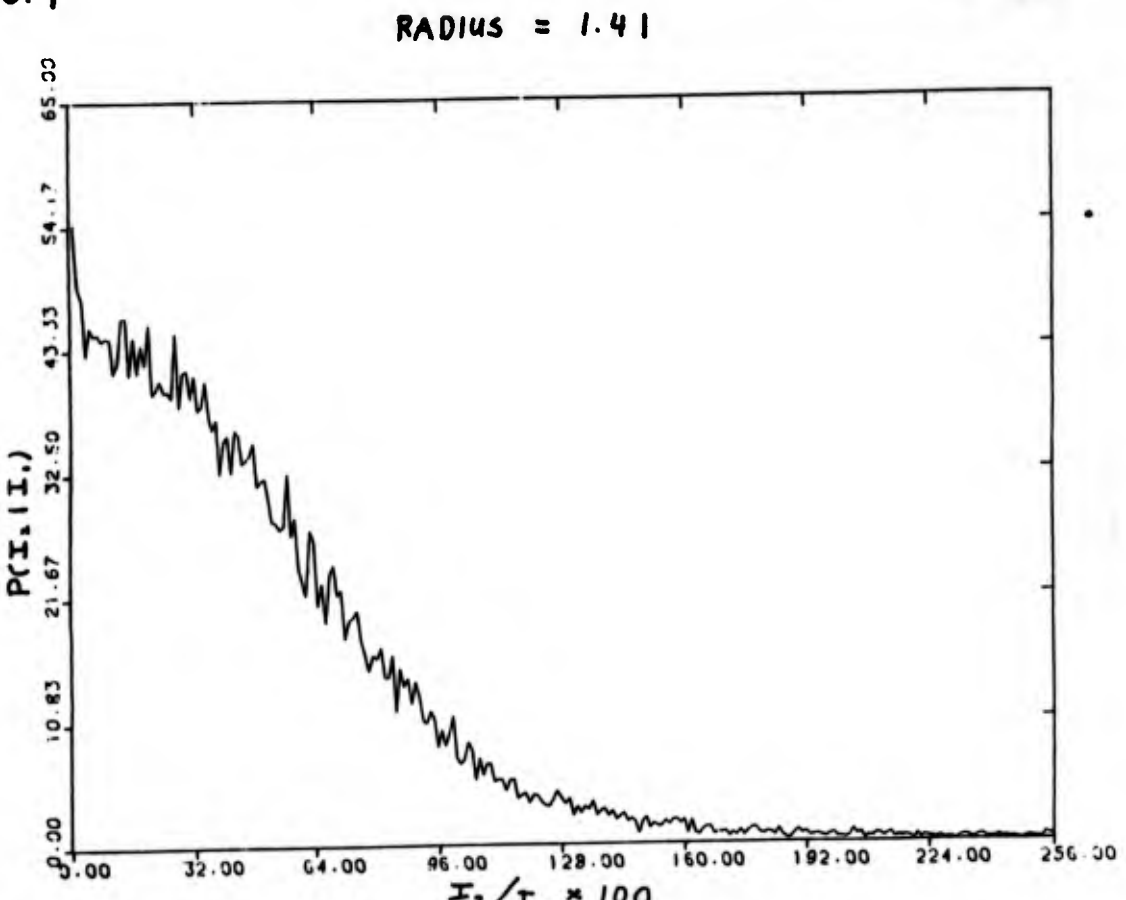
RADIUS = 1.41
65.00
54.17
43.33
32.50
21.67
10.83
0.00
P(I₂|I₁)
0.00
32.00
64.00
96.00
128.00
160.00
192.00
224.00
256.00
I₂/I₁ x 100

FIG. 10

RADIUS = 2.0

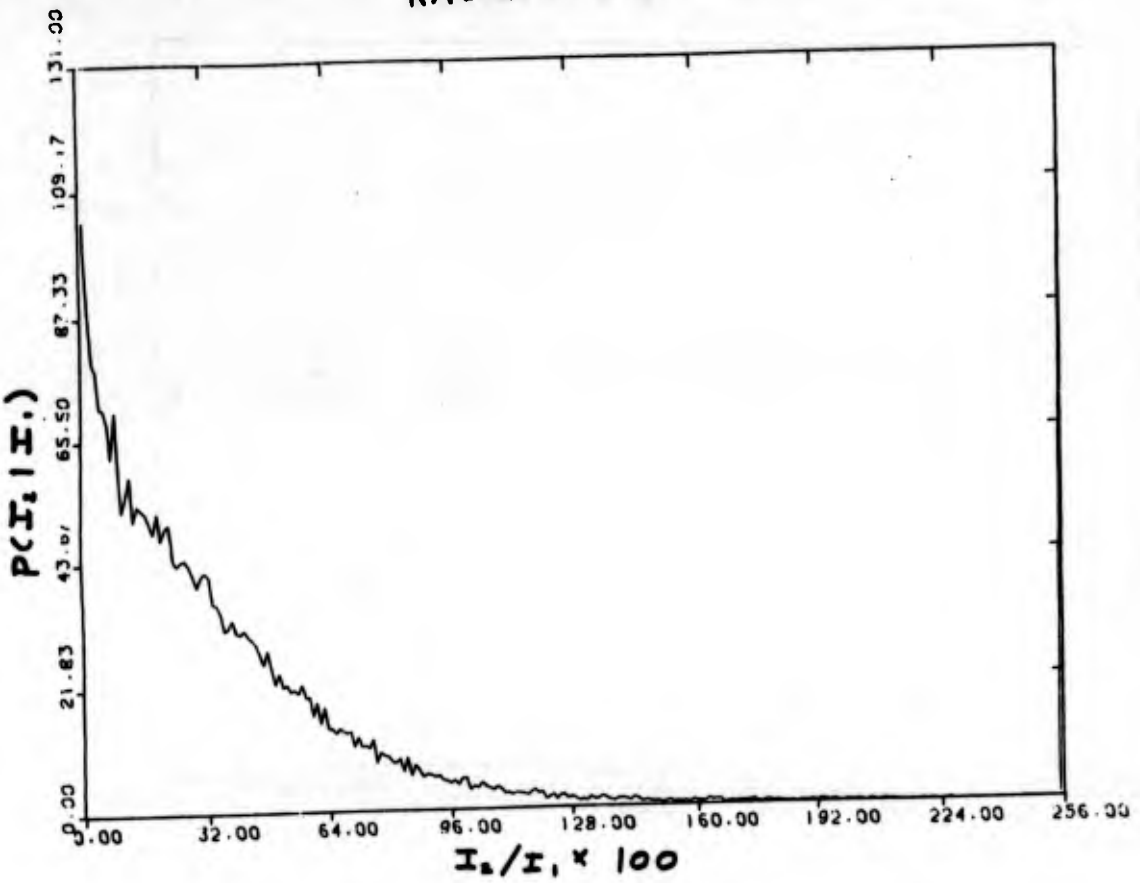

FIG. 11

RADIUS = 2.83

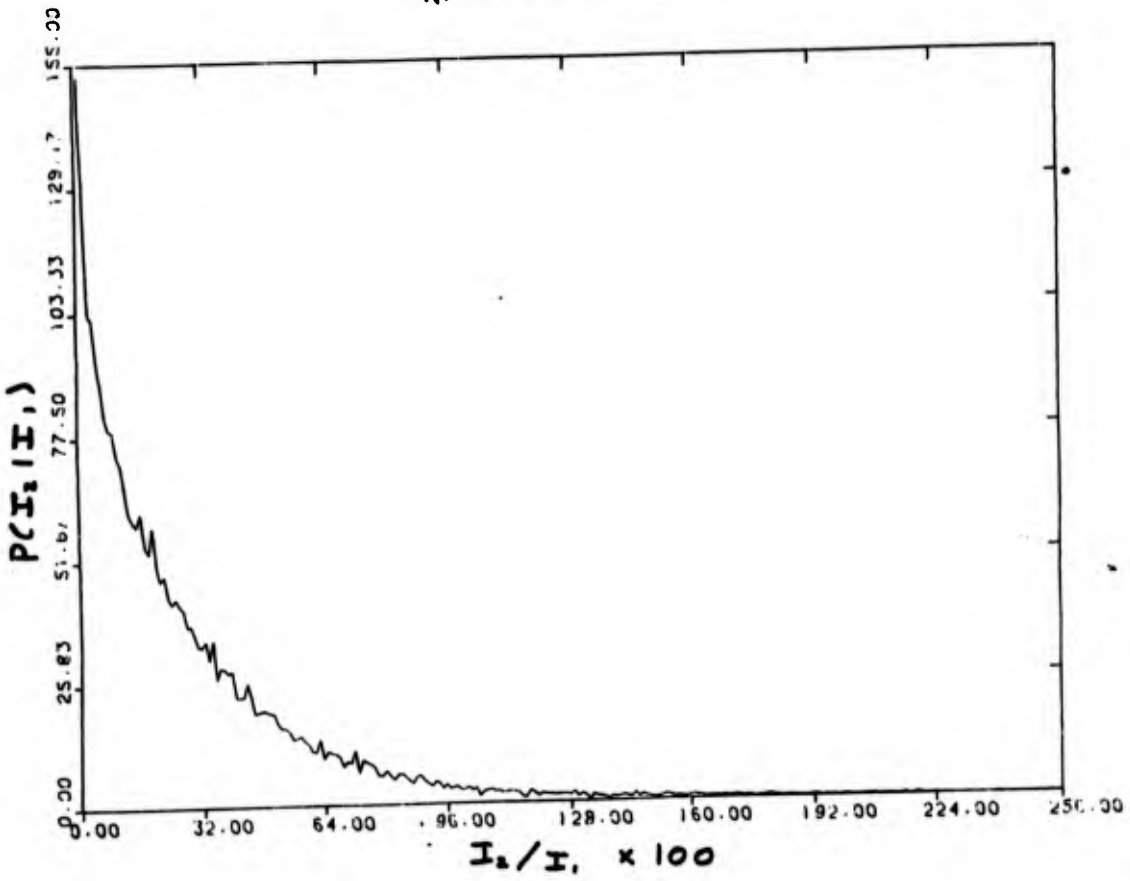

FIG. 12

EPISILON ORI WSA

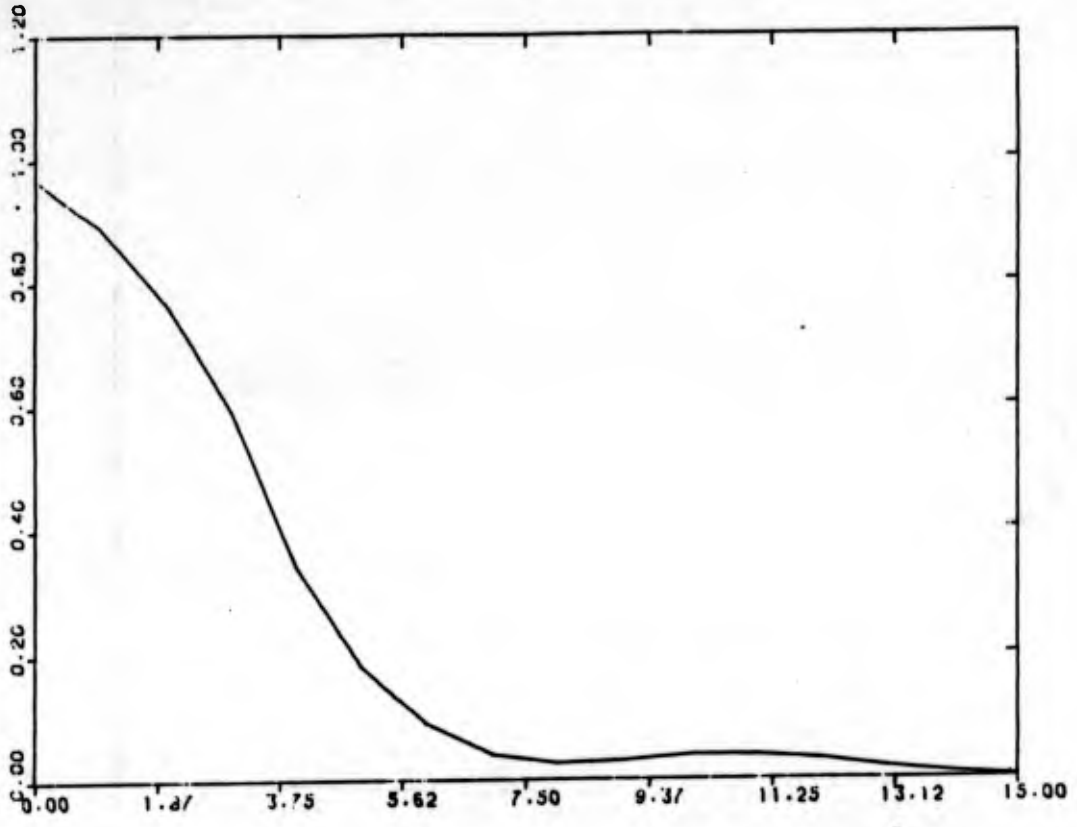

The versatile array

N. J. Woolf, J. R. P. Angel, and D. W. McCarthy, Jr.

Steward Observatory, University of Arizona
Tucson, Arizona 85721

Abstract

We discuss a four element non-degenerate array telescope-interferometer for ground use. The elements are 8 meter mirrors, and the maximum array spacing and two element spacing are 75m and 108m respectively. The array may be used as three separate telescopes, one 11.3m and two 8m for work not requiring highest angular resolution. We discuss the problems of making speckle measures to high enough precision for synthetic images to be produced. We conclude by showing that the high resolution presents opportunities to make types of observation that are neither possible with VLBA nor NNTT.

Introduction

Since the introduction and development of new interferometric speckle techniques by Labeyrie and his collaborators[1], there has been a surge of interesting observational results. These results encourage the design of interferometers of higher resolution and sensitivity. However, the very large change in quality of interferometric data, with modest changes in observing conditions suggests that interferometry makes a poor sole justifier for a giant facility at optical and IR wavelengths. One would like to have a facility in which extraordinary conditions were used for interferometry, and yet the facility provided for alternate high interest work for the, say 2/3 of the time when conditions are more ordinary.

There has been some recent confusion as to the value of using large apertures in interferometers, though they are clearly preferred for the other types of observation. The value of a large aperture in increasing interferometric sensitivity is not very great when the image is enlarged beyond the diffraction pattern by seeing. In that case, the speckle interference patterns add incoherently, and sensitivity increases linearly with aperture diameter, whereas in the diffraction limited case, sensitivity increases as $(\text{diameter})^2$.

In the visible, the apertures may be made coherent by adaptive optics if the object is bright enough (~ 10th magnitude), which is not usually helpful. However beyond a few microns the isoplanatic patch is so large, and the speckle change time so long that the telescope can be made coherent in the IR by using adaptive optics working with the visible light of the object, or a faint field star. For these cases the interferometer with large primary mirrors becomes a very powerful tool, because the sensitivity is increasing as $(\text{diameter})^2$.

A study of the optimum use of collecting area in a visible or IR interferometer shows that greatest sensitivity is obtained by dividing the area into two equal apertures, and moving one so as to sequentially explore the U-V plane. For a practical interferometer, there is a benefit from reducing the types of motion needed for a large aperture, and in keeping the moved apertures to manageable dimensions. In this paper we have chosen to balance these needs by considering an array of four 8m mirrors, in which the exploration of the U-V plane is done by an azimuth motion of the array, coupled with the diurnal apparent motion of the sky.

Eight meter mirrors make good building blocks. They are the largest individual mirrors likely to be available in the near future. In the 0.3 to 1 micron range, CCD spectrographs on this size telescope are limited by photon noise of sky background for resolving powers up to a few times 10^4. With mirrors this large, it is possible to make a few element interferometer with high angular resolution, and with no holes in the U-V plane.

This article breaks into four further sections. First, there is a description of the Versatile Array concept. Second, is a discussion of the expected optical performance of the concept, with estimates of a few of the design parameters. Third, is a discussion of the problem of making interferometric measures with sufficiently small systematic errors that good image reconstruction is possible. Finally, there is a discussion of the application of this device to two major problem areas in astronomy. The first concerns the nature and structure of the innermost regions of energetic extragalactic objects such as quasars and Seyfert galaxies. The second concerns the structure of solar-system-like objects in formation.

The concept

The concept welds together four main ideas. First, due to Low[2], is the idea that a linear array which points at right angles to the array line, and which rotates on a track for azimuth pointing is a very convenient form of interferometer. Second, is an idea from Gursky and Traub[3] that an optimum form for a small number of telescopes in a line is as a non-degenerate array. Third, originating with the 200-inch telescope, and picked up by Angel[4], is the idea that lightweighted castings of borosilicate glass make good inexpensive telescope mirrors. Indeed, though we now know how to get them into better thermal equilibrium with the air and themselves[5], the performance of the 200-inch is itself the clearest indication that this is a good route. Fourth, arising from Beckers' and Hege's[6] work with the MMT, is the realization that an MMT-like focus can, by careful choice of geometry, be operated as a phased focus over the field width for which the atmosphere allows isoplanatism.

Figure 1 shows an optical scheme for the Versatile Array, when used in non-degenerate array form. All parts of the optics rotate together about the elevation axle, whose position is also marked. Two pairs of telescopes, one with a 4m gap, the other with a 16m gap each have a 2-facet MMT-like beam combiner directing the light towards the elevation axle. A flat mirror then directs the light along the axle towards the center of the array. The innermost telescopes are separated by 28m. The three gaps between telescopes, and all optics except the first three mirrors, are in evacuated housings.

At a point midway between the outer telescopes is the combined focus, where path lengths are equal. At this point, it is possible either to combine light from two pairs of mirrors in one of three combinations, or to combine all beams to form one image.

The chopping secondary mirrors are 45 cm diameter, to permit high frequency chopping. The final beams are f/100, giving a focal plane scale of 4mm/arc-second. The unvignetted field is about 20"x1'. The smaller dimension is in the direction of higher resolution.

The practical realization of this scheme requires the following:

1. The entire array must be able to rotate around the azimuth axis during observations.
2. For separate use of the telescopes, separate bearings are desirable.
3. A long mechanical beam linking the telescopes is not rigid enough to define pointing directions, nor to maintain phasing. In consequence an optical servo system is used for these purposes.

A possible mechanical realization of the scheme is shown in plan and elevation in Figure 2. The two closest 8m mirrors are placed on a single mount. Together they constitute an 11.3m telescope, and their erection would constitute phase one of the construction. The two other telescopes are built to a similar mechanical plan. Each is a complete alt-azimuth telescope revolving on a circular track centered on the 11.3m.

As has been pointed out by Labeyrie[7], the bearings of large telescopes provide poor positioning of the telescopes for interferometric precision. Therefore, the optical servo system measures only between the telescopes "tubes".

Along the elevation axle, also within the evacuated housings are laser beams and mirrors. These laser beams are used to control the position of the telescopes, and the direction of their beams to maintain phasing to within atmospherically imposed limits, ~ 20-50 microns.

The telescope elevation axes are kept collinear by the servo system. It also measures the distance between telescopes, and moves the auxiliary optical systems so as to maintain phasing. Pointing of individual telescopes is corrected at low frequencies by rotation of the bearings. Higher frequency corrections and adaptive wavefront correction use the beam combining mirrors.

In the non-degenerate configuration, the center to center separation of the outside mirrors is 72m. If one of the mirrors is brought to the other side of center, this separation is increased to 108m, and is therefore useful for obtaining the highest possible resolution. However, such observations would leave a gap in the U-V plane. The third configuration is to use the system as three separate telescopes. For this purpose, alternate top ends would be needed for all telescopes. A variety of useful top end configurations have been found while studying possible variants for an MMT/NNTT. The versatility of this array arises from two aspects. First, there are these three configurations which, quite apart from their interferometric potential also have the light gathering power of either one 16m telescope or one 11.3 and two 8m telescopes. Second, there is the potential for building the array in stages, as funds become available, providing that an appropriate site if found. It is a particularly interesting facility for a

Fig 1

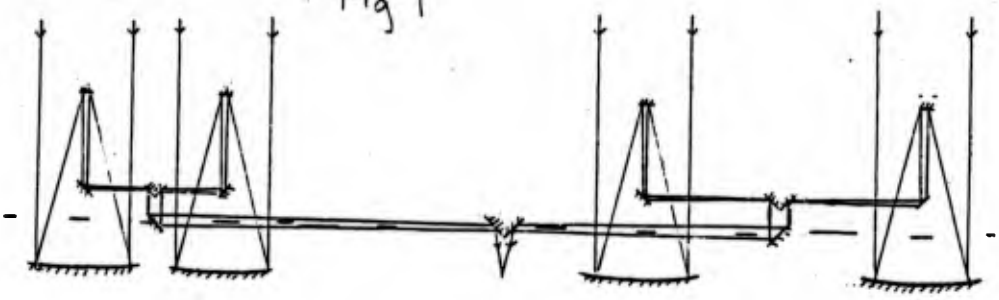

Fig 2

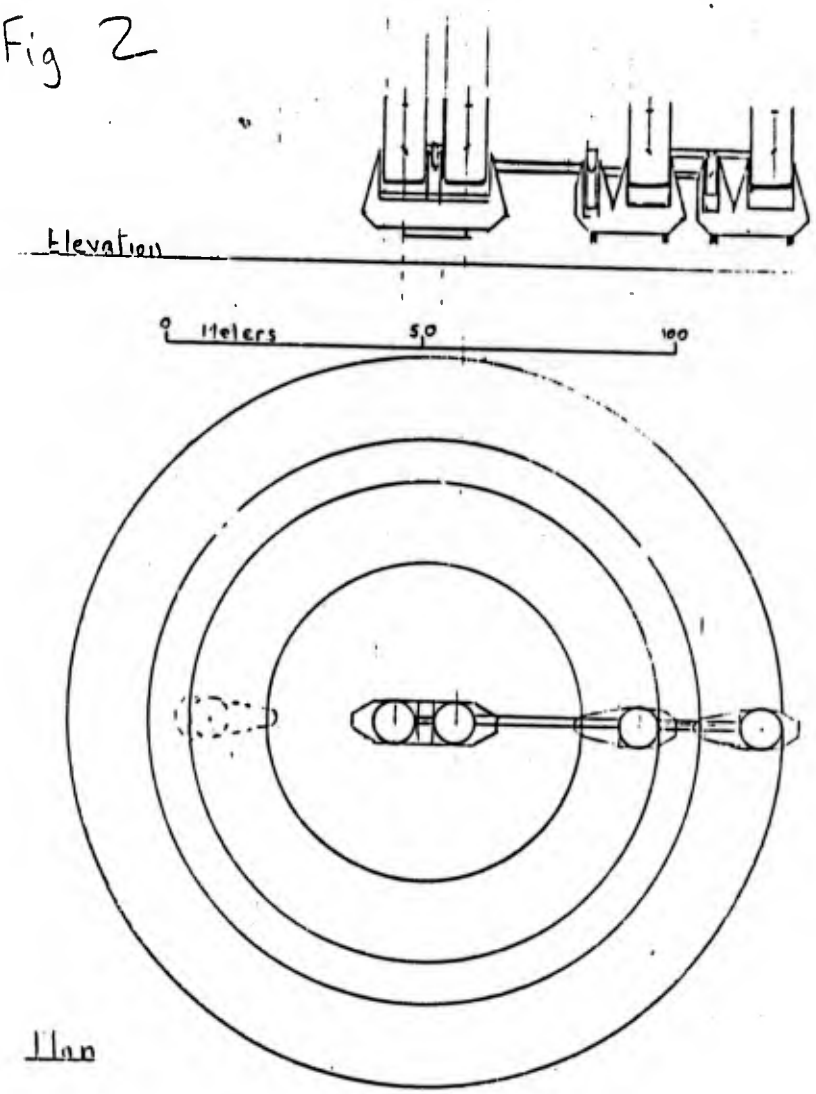

binary star. The measures were normalized by alternating the telescope between the binary, and a nearby unresolved source every few minutes, yet the result shows the visibility function apparently exceeding unity at intermediate spatial frequencies, and the systematic error is far greater than internal error would lead one to expect.

Fig 6

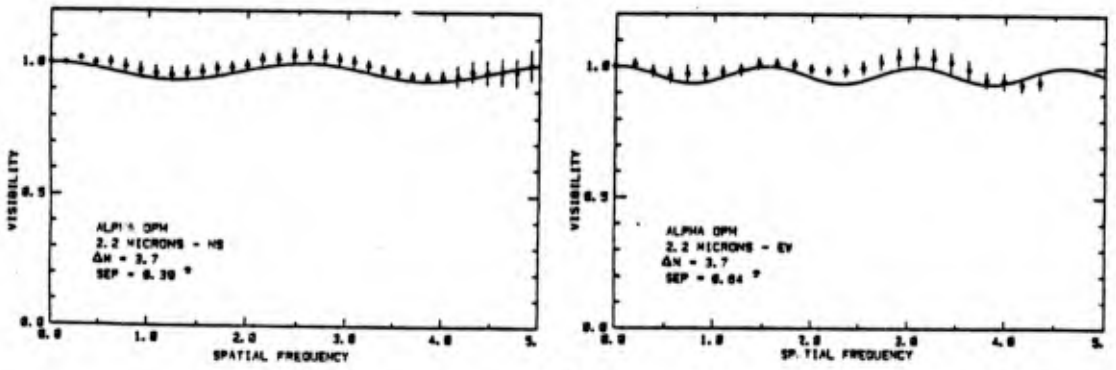

The speckle transfer function must be determined to the required precision of ~ 1%. First, this needs a systematic measure of seeing correct to ~ 0.5%, since the speckle transfer function is reduced below the telescope MTF by ~ $(D/v_o)^2$. Lena[8], has suggested that visible seeing should be monitored during IR speckle measures. Since the instantaneous wavefront disturbances are unlikely to match the Kolmogorov spectrum of the average, this may be inadequate for most telescopes. For the VA it is definitely incorrect. When adaptive optics is used on the separate 8m telescopes, the long wavelength wavefront corrugations are substantially smoothed, but the short wavelength corrugations remain. Thus the visible and IR seeing became decoupled. It is recommended that monitoring the seeing should be performed at the same wavelength as the speckle observations. Indeed, there is a possibility that a variant of the Worden and Welter method[9] in conjunction with frequent reference to a nearby star may be the best method of correcting for seeing.

In addition to seeing modifying the speckle transfer function, it is also modified by the exposure time, if that becomes comparable with, or longer than the speckle change time. This effect can inject random differences in transfer function between the reference star and the object. The use of TV frame rates for visible speckle observations may be one reason why visible region speckle results tend to be less precise than IR measures.

The transfer function may also be affected by a number of factors which might change between reference star and object. These include subtle changes in focus and alignment, as well as phasing for an array. Systematic control of these qualities with open-loop servos's should be an adequate solution. In addition, the transfer function of object and reference may differ if observations are made with a spectral bandwidth near the limit for the conditions, and if the two have different spectral distributions. At visible wavelengths, correction for atmospheric dispersion can also cause errors. For the VA concept these do not exist because the speckle pattern is horizontal.

While none of these problems seem insuperable, it is not surprising that to date speckle suffers from problems like those of Figure 6. Demonstration of these problems being overcome is a necessary step on the way to bulding a large array.

Use of the array

Two current problems illustrate the use of the array, and distinguish it from those problems which can be solved at radio wavelengths by VLBA, and at O/IR wavelengths by NNTT.

poorer than if the two outer mirrors were used alone as an interferometer. The two-mirror 108m spaced mirrors gives better resolution. The four-mirror and 108m configuration angular resolution are shown in Figure 5, which for comparison also shows the resolution of two possible NNTT configurations, and four different assumed values of atmospheric seeing, characterised by the r_o values at 5000Å.

Because the diffraction pattern of the array only produces high angular resolution in one direction, reconstruction of a picture requires combined use of the apparent diurnal rotation of the sky, and the rotation of the array. Observations in at least 14 different position angles are needed to specify the U-V plane.

Like radio astronomy arrays, the extent to which the full angular resolution is realized depends on the latitude of the telescope, and the declination of the source. For a northern hemisphere telescope, complete resolution is only possible if the declination of the object is more northerly than the latitude of the site. However, for a telescope at 32 degrees N, and permitting observations only above 20 degrees elevation, 70% of the N-S resolution is obtainable for objects down to 17 degrees S, and 50% of the N-S resolution is obtained for objects down to 28 degrees S.

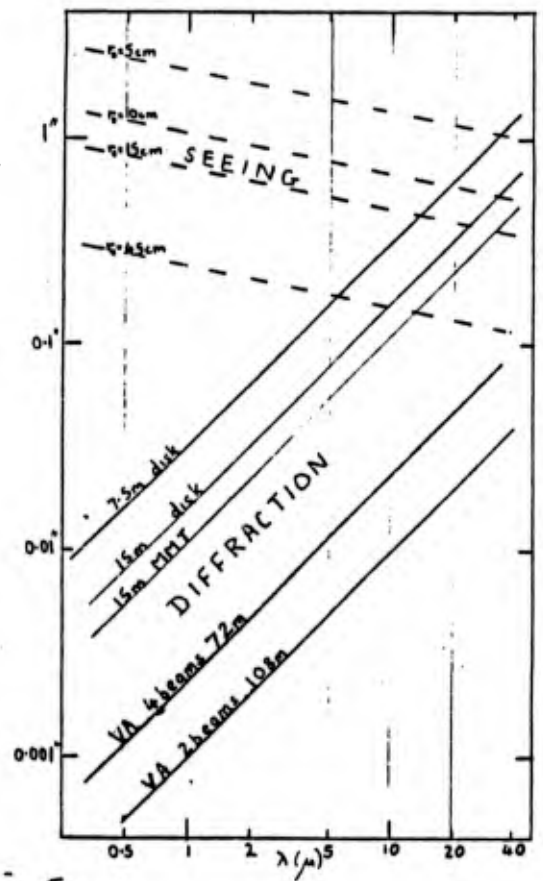

fig 5

It is instructive to compare NNTT with VA, because the configurations have some of the same differences shown at radio wavelengths by the VLA and VLBA. At 5-20 microns, NNTT has comparable resolution to VLA. At 5000Å, VA has comparable resolution to VLBA. The higher resolution of VA is obtained at a price. The individual mirrors are now so far apart that it is impossible to use observations with one mirror to predict where the wavefront is at an adjacent mirror. Because of this, VA cannot be used with complete adaptive optics across the aperture. Thus high angular resolution must be obtained from statistical procedures such as speckle interferometry. There is a concurrent loss sensitivity. In compensation, VA puts 100 times as many pixels into a given area of sky. Because the apertures of the VA cannot be phased, except perhaps at mm and sub-mm wavelengths, VA does not fit the specifications for being a possible NNTT. Both it and NNTT can be used for high resolution spectroscopic mapping. NNTT would use long slit spectroscopy. VA would use speckle spectroscopy, which is a powerful technique for overcoming many systematic problems of speckle.

While overall adaptive optics is not possible with VA, the individual apertures would of course be used adaptively to compress the image into an 8m diffraction pattern whenever observing conditions permitted. Adaptive optics would be used as part of the speckle observational mode. In order to explore the expected appearance of such specklegrams, a number were artifically generated by computer. Figure 4b shows one of these theoretical monochromatic specklegrams on the same scale as Figure 4a. It can be seen that there are usually one or two high peaks, with the highest rising to 70 to 80% of the highest phased array peak. This suggests that speckle with the array will be quite efficient.

Systematic errors with speckle

The use of a system like the VA for high angular resolution mapping would need the systematic errors of individual visibility measures to be brought down to a level where they do not dominate picture noise. This level is about 1%, and is far better precision than has been reported for speckle to date. Figure 6 shows visibility measures of a bright

number of groups to operate together.

The array poses two interesting mechanical problems. The first of these is the mechanism to make the single telescopes revolve. The mechanical demands placed on this motion by the optics servo system is for stiffness, rather than for precision. The second problem concerns the way to shield the telesocpes from storms, and to thermally insulate them from daytime heating. Because of the nature of the azimuth revolution it may be possible to have the housings for the separate telescopes built onto the yokes, while the central telescope is housed in a roll-off shed.

Optical performance

Figure 3 shows the MTF for the array at 2.2 microns, in the directionof highest resolution. Figure 4a shows a cut through the diffraction pattern in the same plane. At right angles to this direction the pattern is like that of a single 8m disk. The resolution in the pattern is like that of a single 8m disk. The resolution in the pattern is somewhat

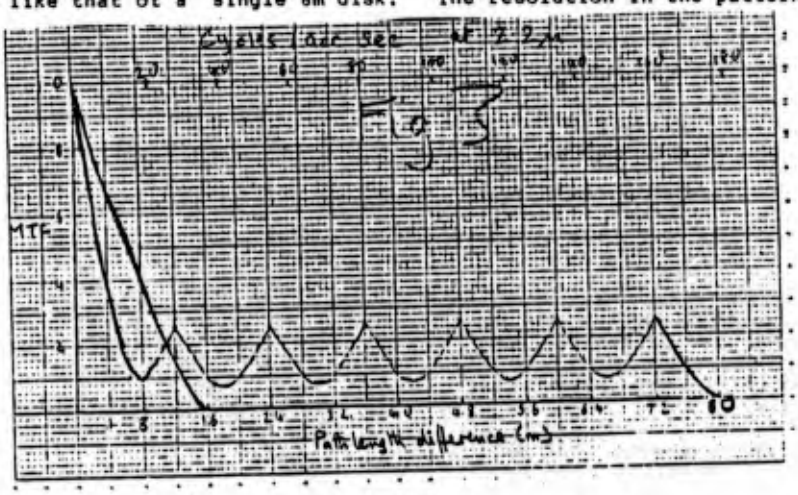

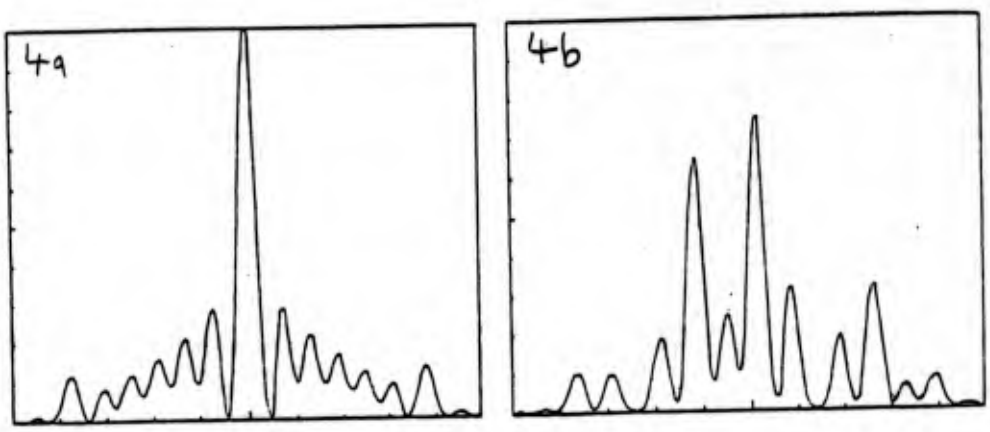

Phased Diffraction Pattern

Typical Speckle Pattern

Planetary system formation has been of great interest for centuries. The nearest planetary systems in formation are likely to be at distances of ~ 3×10^{20} cm. Inner portions of these systems are likely to be warm enought to be detected at 2-3μ, whereas outer regions will require observations in the thermal IR. Thus in the inner parts one is trying to explore inhomogenity on a scale of several parts in 10^{12} cm, the typical separation of inner planet orbits. The angular scale here is ~ 5×10^{-3} arcseconds. The separation of region where outer planets might form is some ten times larger. Reference to Figure 5 shows that this resolution can be obtained with the array. Although even higher resolution can be achieved with VLBA, that technique is only useful for sources of high surface brightness, and in the radio regime there is currently no reason for expecting this.

Quasars and Seyfert galaxies are two examples of extragalactic sources where energy pours out of a minute region. Though matter also pours out of this region, the geometric relation of the parts, and the exploration of how the core is fed with energy is still needed. At VLBA wavelengths it is possible to explore the collimated plasma jets that shoot out of the center. At visible wavelengths it would be extremely interesting to explore the dense gas clouds which produce emission lines. In particular Doppler speckle spectroscopy could distinguish the placement of parts of this gas to some small fraction of the diffraction limited resolution of the array. Discussion of the dimensions of these gas clouds, e.g. by Ulrich[10] lead to predictions of the brightest having angular sizes in the range of 10^{-3} to 10^{-4} arcseconds. The largest of these values is attainable in the visible with an array of this size, using the diffraction limit. Even the smaller of these values is attainable with differential speckle spectroscopy, and corresponds to light travel times of a few light weeks for the nearer Seyfert galaxies. The light emitting clouds and the radio emitting jets presumably correspond to matter doing two very different things, therefore the relationship between their angular structure can be very helpful in discovering the nature of the eneryg sources.

Conclusions

A scheme for obtaining high resolution array which is also a powerful set of telescopes has been discussed. Technical problems to be solved include both mechanical aspects of the array, and the details for obtaining precise specklegrams. The technique appears to make some interesting IR and optical observations available.

NJW and JRPA would like to acknowledge support under NASA grant NAGW-121. NJW would also like to thank the U.S. Air Force for grant F19628-82-K. DWMcC would like to thank the NSF for support under grant -0025.

ADAPTIVE OPTICS

N. J. Woolf
Steward Observatory, University of Arizona

ABSTRACT

Adaptive optics is a technique for correcting atmospheric wavefront disturbances to yield diffraction limited imaging. It is a technique whose advantages are most apparent in the 2-5μ spectral region, where wavefront corrections are derived from study of visible objects. Graphs are presented to show performance needs of adaptive optics systems.

INTRODUCTION

The idea of correcting the wavefront arriving at a ground telescope to get perfect images has been around for some time e.g., Babcock (1953). Of the various ways of getting high angular resolution images, this adaptive optics has the greatest potential for studying faint objects, it has the greatest difficulties of implementation and the greatest cost. There is also a lesser task, which is that of correcting the optical figure of a telescope so as to get seeing limited performance. This latter goal is called active optics. The figure of telescope optics, focus, misalignment, etc., changes on a slow timescale, and can be corrected at frequencies below 0.1 Hz. In constrast, atmospheric fluctuations of wavefront occur at higher frequencies, and adaptive optics may, for some observations, need to operate at frequencies above 1000 Hz. Whereas active optics is usually unable to compensate for any significant fraction of atmospheric disturbances, adaptive optics will readily correct for optical imperfections of the telescope provided only that wavefront errors do not have too high an amplitude or spatial frequency. In general, active optics is likely to be able to work by modifying support forces and positions of existing optical components, whereas adaptive optics will require new optical components capable of high frequency articulation to be inserted into the optical train. Detailed discussions of adaptive optics have been given by Hardy (1978, 1982). Woolf and Angel (1980) have discussed some IR aspects of adaptive optics.

Adaptive optics theory is based on the assumption that atmospheric disturbances obey a Kolmogorov spectrum. The evidence that this is indeed the case has been presented by the author (Woolf 1982). There is a deviation from this spectrum expected at small scales where turbulence turns into heat. This

Proceedings of the IAU Colloquium No. 79: "Very Large Telescopes, their Instrumentation and Programs", Garching, April 9–12, 1984.

has no major effects on seeing. In addition there are deviations at large scales where turbulence is injected. One indication of this is shown in Woolf, McCarthy, and Angel (1983). This may also show itself by images from extremely large telescopes showing less motion in proportion to their size than would otherwise be expected.

Deviations from a Kolmogorov spectrum would be expected to have repercussions on the design of adaptive optics, and therefore require consideration before using the theory. There are two kinds of images which might suggest deviations from a Kolmogorov spectrum. These are, large images with very little motion, and small images with very large amounts of motion. If there is little moton, then the outer scale of turbulence (for the dominant turbulence), must be smaller than the telescope primary. This will occur when the primary mirror temperature is severely out of equilibrium with ambient air. Benard convection cells, or roll convection on the primary will be responsible, depending on the tilt of the mirror. There will be a need to correct high spatial frequencies, at a low temporal rate. In general such problems should be seen as indicators against the use of adaptive optics, and rather for a rigorous program of facility seeing improvement.

Exquisite images, dancing around at high speed have on occasion been reported from large telescopes. If the motions were indeed implying that large scale disturbances had been injected into the atmosphere, there is no known way of preventing these eddys decaying and producing enlarged images. Therefore it seems that these image motions must instead be produced by vibration of the telescope or some optical component ("sailing", rather than "seeing", Woolf and Ulich 1984). In general, sailing is correctible by adaptive optics, but may place a severe load on the amplitude of wavefront correction required. Thus e.g. a 10m telescope showing 1" peak-to-peak image motion requires 50μ peak-to-peak wavefront correction, whereas a typical seeing motion will be ~ 5 times smaller. The comments about mirror seeing correction are also applicable here. Adaptive optics should be considered as a way of making good images better. It is a most expensive way of correcting for poor telescope design or implementation.

BEHAVIOR OF THE ATMOSPHERE

The seeing disturbance of the atmosphere produces a peak-to-peak wavefront error increasing to large distances as $d^{5/6}$, see Figure 1. Correspondingly, the rms slope of the wavefront is proportional to $d^{-1/6}$. In the geometric optics condition this sets the image size. However, the steepest wavefront slopes occur with the least wavefront amplitude. Below ~ $\lambda/6$, wavefront errors are

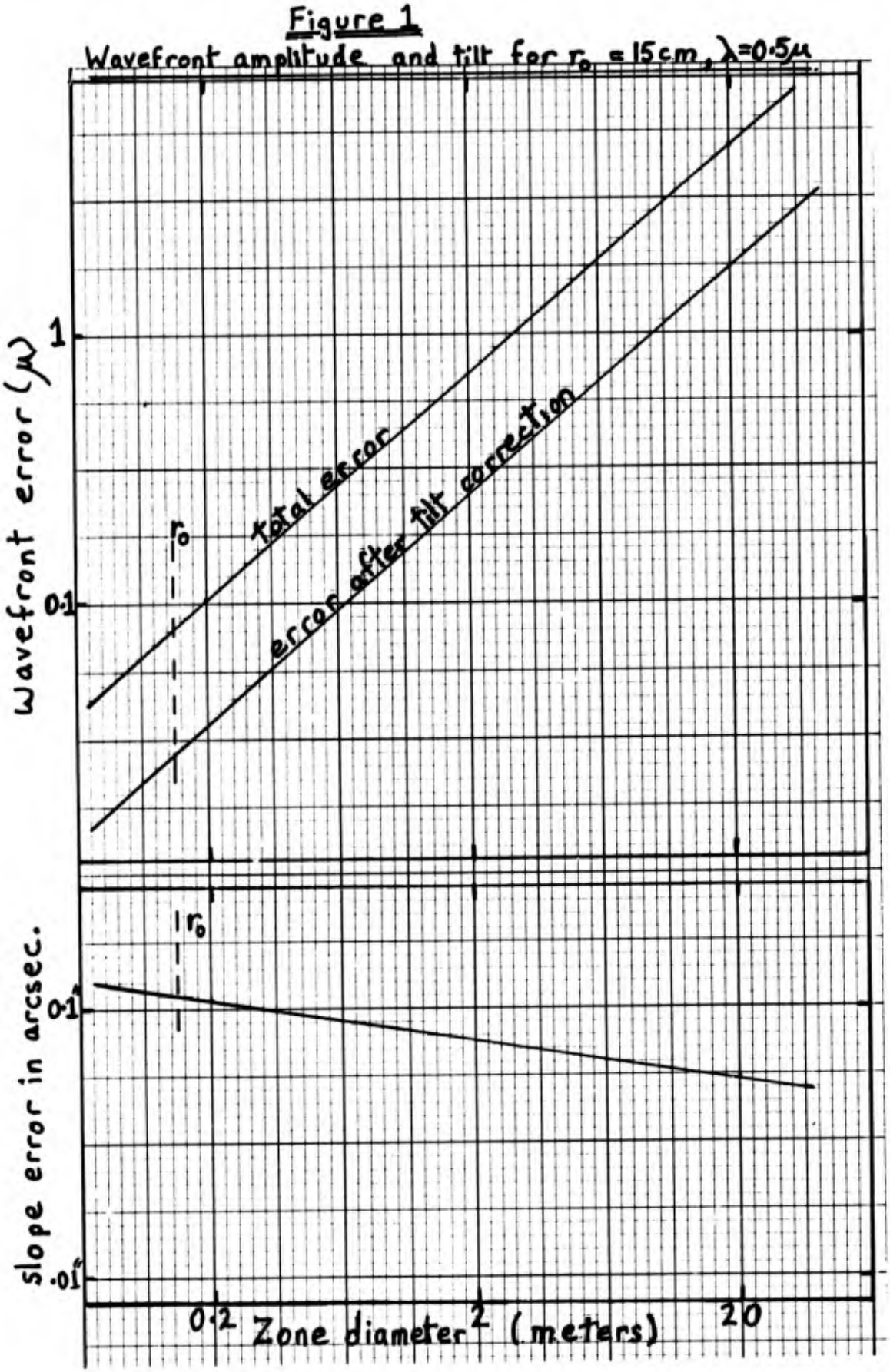
Figure 1
Wavefront amplitude and tilt for r_o = 15cm, λ=0.5μ
Wavefront error (μ)
1
0.1
r_o
total error
error after tilt correction
slope error in arcsec.
1"
.1"
.01"
r_o
0.2
Zone diameter^2 (meters)
20

such that they depress the central diffraction core, but do not affect the image core FWHM. Thus apertures over which wavefront errors are less than $\sim \lambda/6$ are diffraction limited, and larger apertures are seeing limited. The transition dimension r_o is a wavelength dependent length. Thus $\lambda \propto r_o^{5/6}$ or $r_o \propto \lambda^{1.2}$. Since the diffraction limited resolution θ, is proportional to λ/r_o, it is proportional to $\lambda^{-0.2}$.

Adaptive optics deforms a surface in the optical train to correct for wavefront errors in the incoming beam. If the corrections could be inserted at an image plane of the region of the atmosphere which inserts the errors, then a perfect optical system would have been restored. In practice, wavefront errors are inserted from the upper stratosphere down to the focus, and while perfect correction can be applied to one image point, the corrections cease to be adequate beyond a so-called "isoplanatic patch". This area of sky increases to long wavelengths, where less perfect correction of the atmosphere is adequate, and also can be larger if less perfect image correction is acceptable.

It is in principle possible to have correction applied to a number of planes conjugate to those where errors are inserted. In practice it is hard enough to get information adequate to correct one plane and in consequence this isoplanatic patch is set by the ratio of r_o to a characteristic height range of the atmosphere over which wavefront errors are inserted. If this height is 10 km, and r_o = 10 cm, then the isoplanatic angle is 10^{-5} radian or 2". Correspondingly, if r_o is 8 meters at 20μ, the isoplanatic patch is ~ 3'. If one stellar object is used for sensing errors, and another one is to be observed, it is essential for the two objects to be in the same isoplanatic patch.

It is not essential for the two objects to be observed in the same wavelength band. The refractive index of air at visible and IR wavelengths is very similar, further, differential refraction is usually much smaller than the IR isoplanatic patch, thus it is possible to observe an optical object and apply corrections for an IR observation (Woolf and Angel 1980).

THE SIZE OF WAVEFRONT ERRORS

Hardy (1983) has given the size of wavefront errors across an aperture of diameter d:

Total wavefront error	$\approx 0.16\ (d/r_o)^{5/6}$ waves rms.
After tilt removal, residual error	$\approx 0.06\ (d/r_o)^{5/6}$ waves rms.

There is a wavefront error that the active optics will produce if the reference source is faint, producing N photoelectrons/second from the mirror area

Photon noise errors $\approx 0.06\ (7.5/N)^{1/2}$ waves rms.

There is a time delay error if corrections are made at a time Δr later than they are measured. This error increases with the speed $\bar{v}$ at which the disturbed wavefront crosses the telescope, increasing as

$$\Delta r \bar{v}/r_o$$

Finally, there is an isoplanatism error if the reference source is separated from the imaged object by an angle $\Delta\theta$, with the error increasing with $\Delta\theta h/r_o \cos^{8/5} z$, where z is the zenith angle.

The effects of these terms are shown in a series of graphs. Figure 2 shows how it is necessary to control smaller and smaller patches of the entrance pupil to obtain diffraction limited images as the wavelength gets shorter, or the seeing worse. The seeing conditions assumed are r_o = 15 cm at 5000Å for good seeing. Poor seeing is r_o = 6.5 cm, excellent seeing r_o = 34 cm.

The wavefront error effect can be related to the energy concentration in the core of a diffraction pattern.

$$\frac{I}{I_o} \approx 1 - 4\pi^2 \left(\frac{\varepsilon}{\lambda}\right)^2$$ where ε is the rms wavefront error.

Thus for a 0.1 wave total budget, there is about 60% of maximum energy within the core, and for 0.05 wave budget about 90%. The error budgets assume that three equal terms contribute, being typically residual curvature over the corrected patches, correction applied later than the measurement made, and the third being an assumed equal contribution from photon noise and lack of isoplanicity.

Figure 3 shows the total response time for observation and control corresponding to Figure 3. One of the less expensive control options is to use a television camera as sensor, with an overall response time of at least 0.015 second, probably twice as much. Lines corresponding to these response rates are also marked on the figures.

Figure 4 shows the angular field of view corresponding to the isoplanatic patch for these same conditions. Figure 5 asks under what conditions one can expect to find a bright enough star to make corrections within the isoplanatic

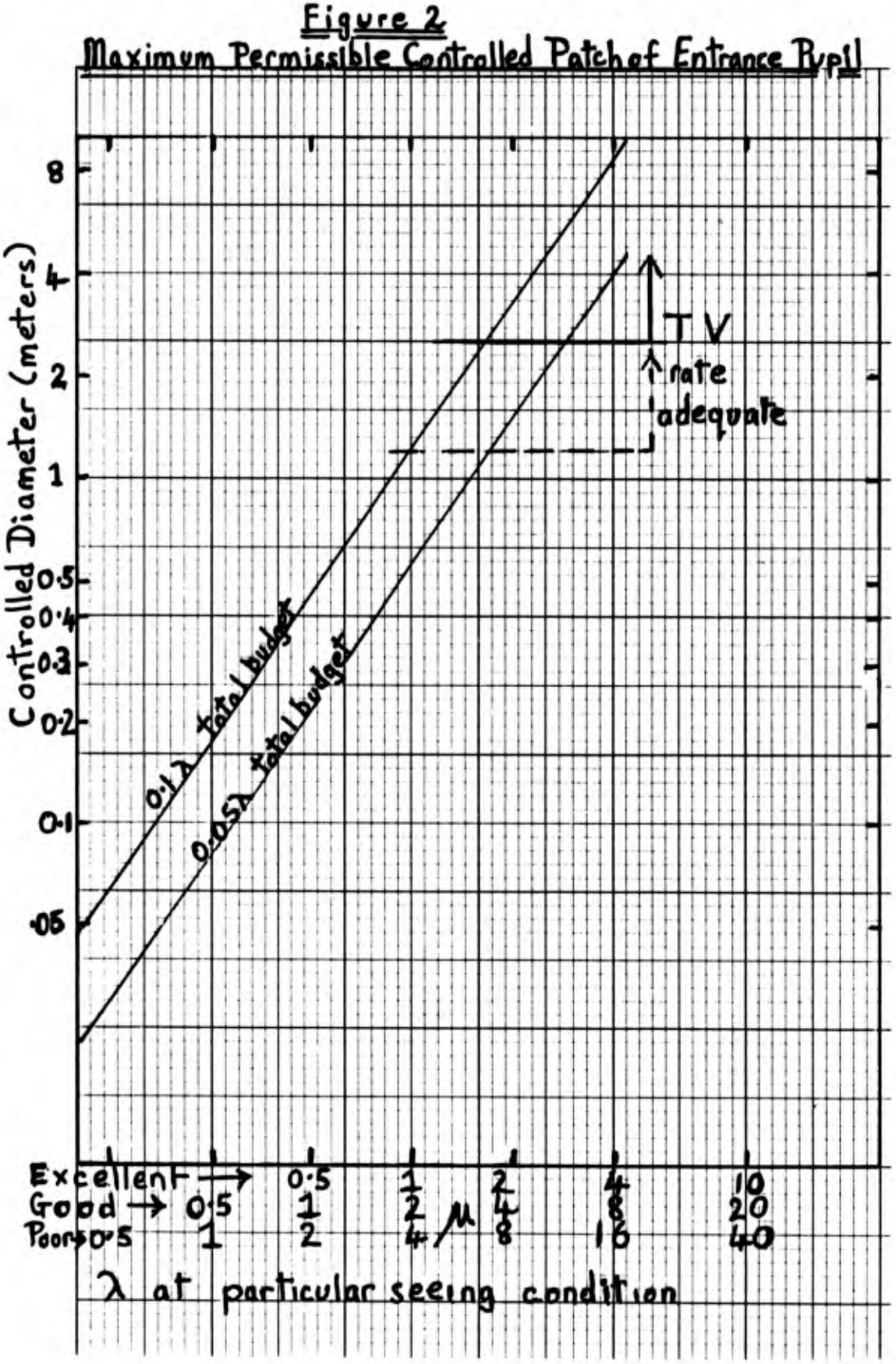
Figure 2
Maximum Permissible Controlled Patch of Entrance Pupil
Controlled Diameter (meters)
8
4
2
1
0·5
0·4
0·3
0·2
0·1
·05
TV rate adequate
0·1λ total budget
0·05λ total budget
Excellent → 0·5 1 2 4
Good → 0·5 1 2 4 8
Poor → 0·5 1 2 4 8 16 40
μ
10
20
λ at particular seeing condition

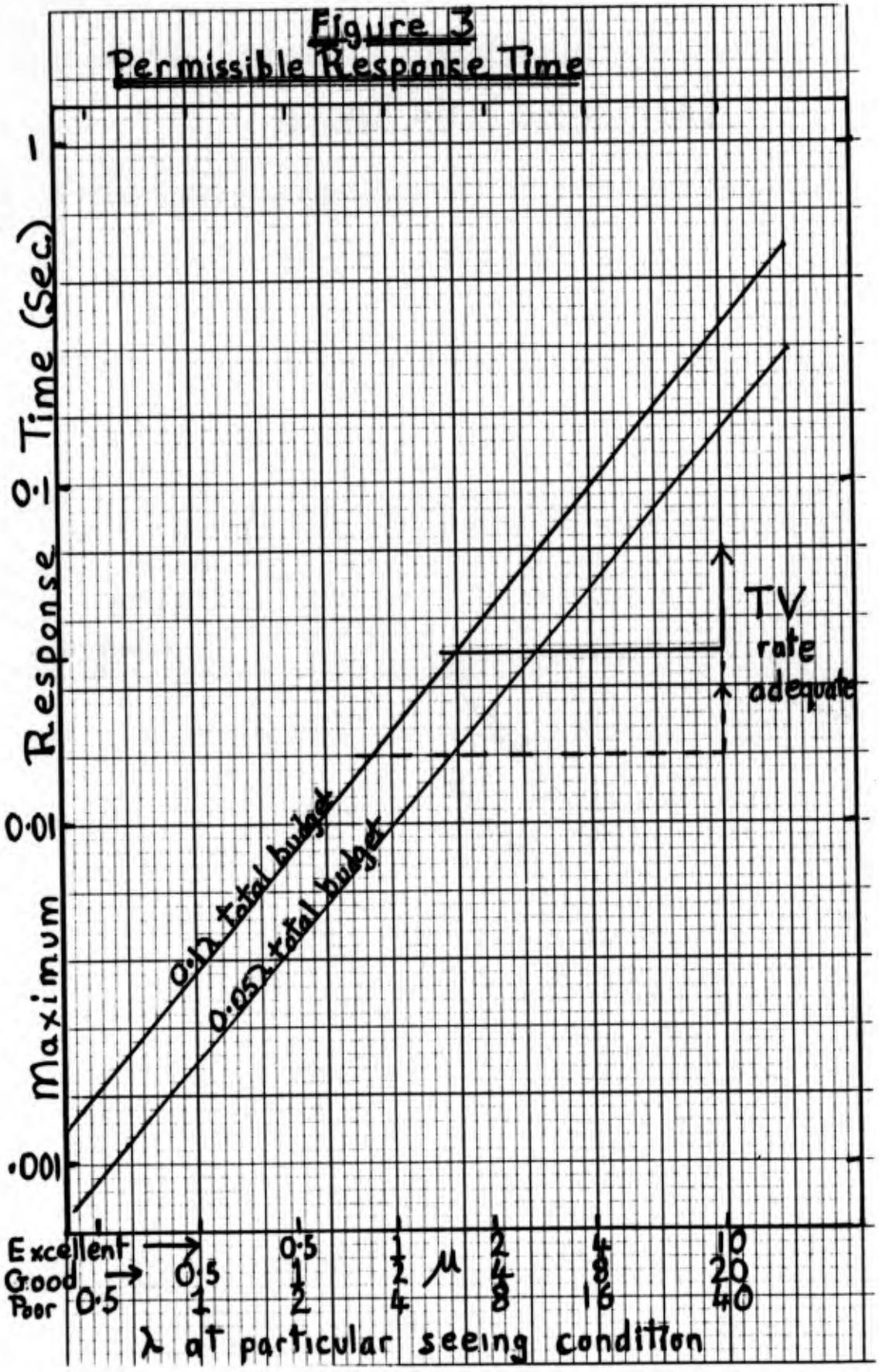
Figure 3
Permissible Response Time
Maximum Response ∴ Time (Sec.)
1
0·01
·001
TV rate adequate
0·1 λ total budget
0·05 λ total budget
Excellent →
Good → 0·5 1 0·5 1 2 4 8 16 32
Poor 0·5 1 2 4 8 16 32 64
λ at particular seeing condition

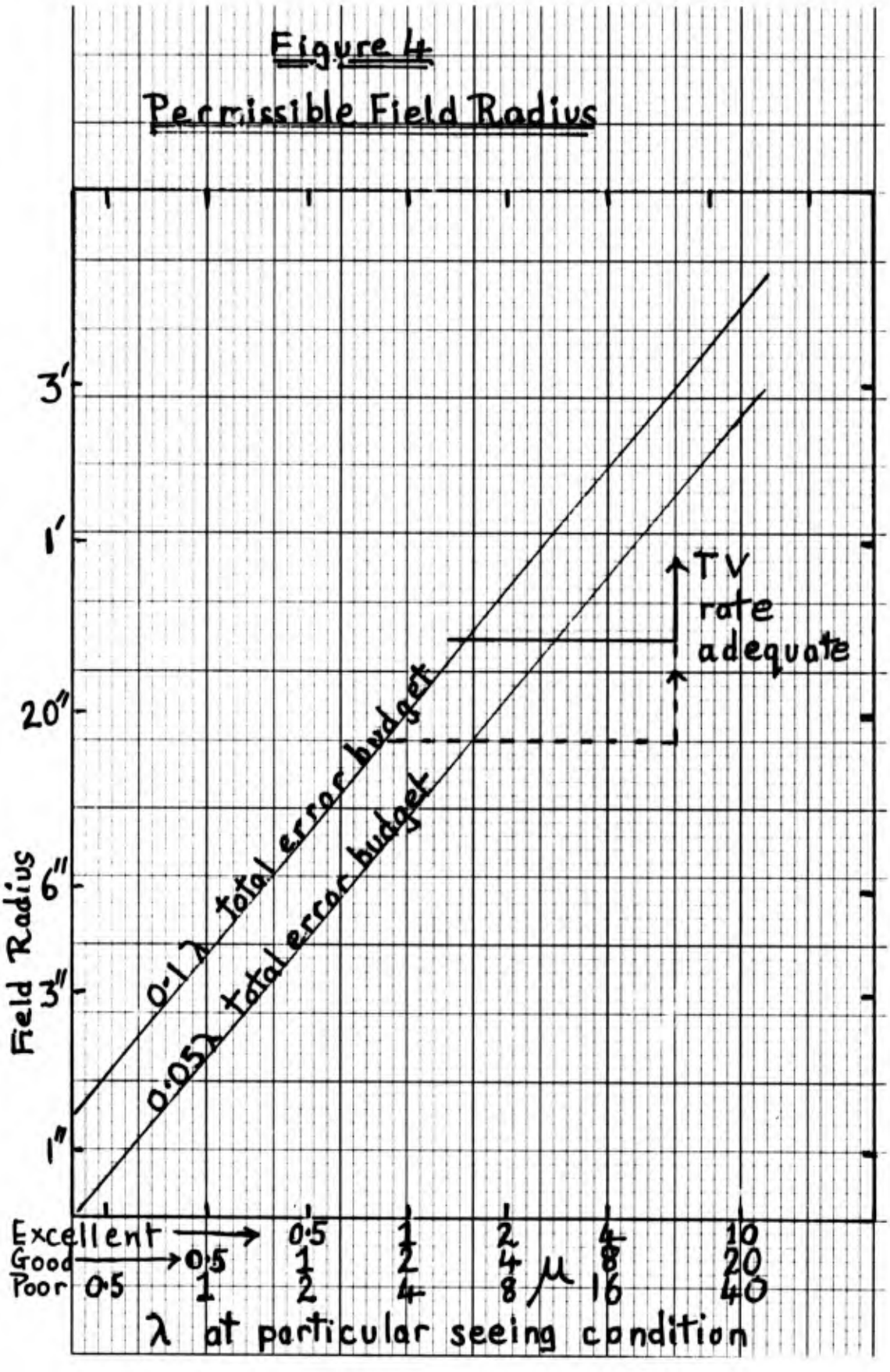
Figure 4
Permissible Field Radius
3'
1'
20"
6"
3"
1"
Field Radius
0·1λ total error budget
0·05λ total error budget
TV rate adequate
Excellent → 0·5 1 2 4 10
Good → 0·5 1 2 4 8 20
Poor 0·5 1 2 4 8 16 40
μ
λ at particular seeing condition

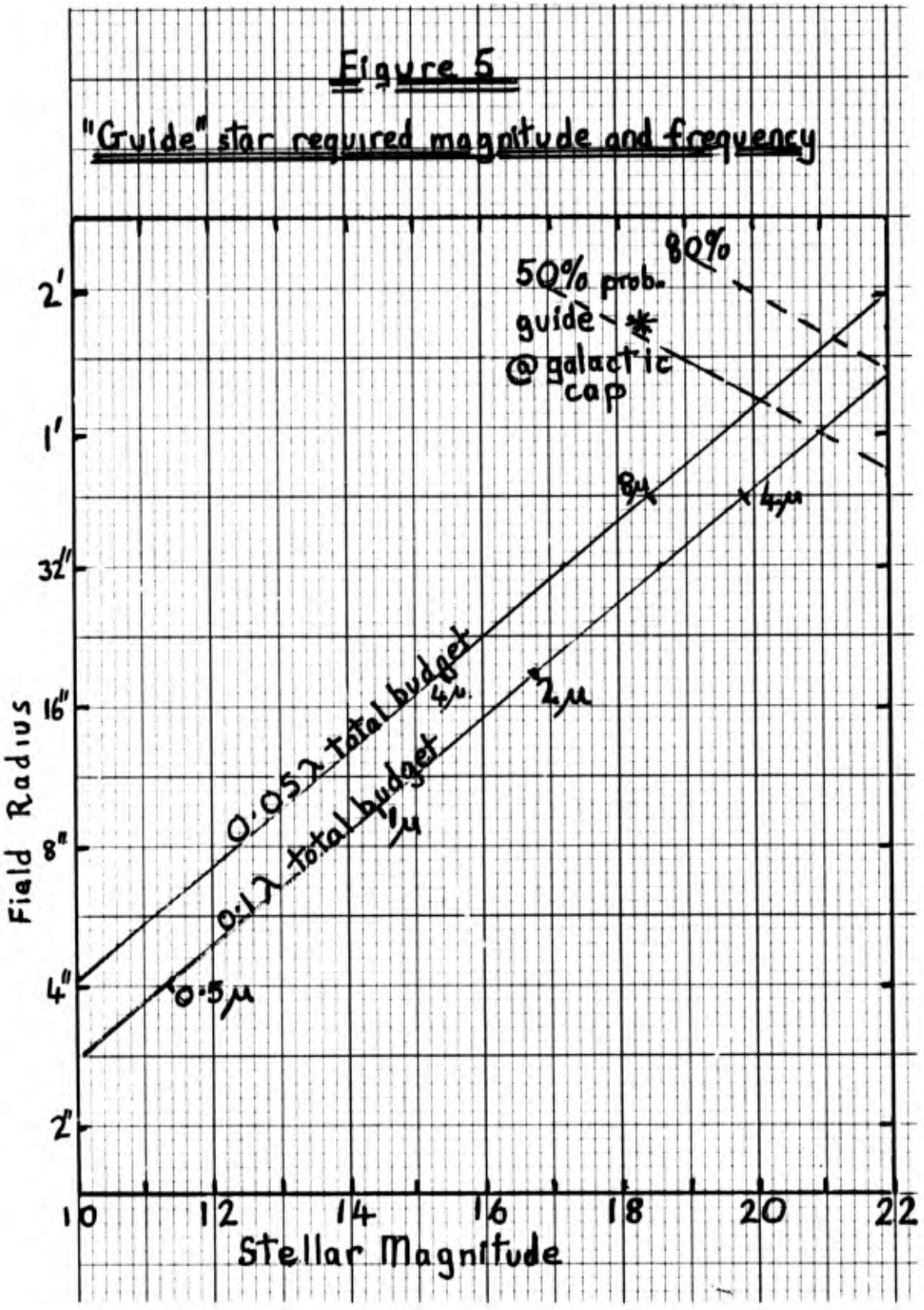
Figure 5
"Guide" star required magnitude and frequency
80%
50% prob.
guide
@ galactic
cap
8μ
4μ
2μ
0.05λ total budget
0.1λ total budget
½μ
¼μ
0.5μ
Field Radius
2'
1'
32"
16"
8"
4"
2"
10
12
14
16
18
20
22
Stellar Magnitude

patch near the galactic poles. Here it is assumed that the correction is obtained from the visual light of the object, but that adaptive optics is used to correct an IR image.

It can be seen that random reference stars will only be suitable for use at long IR wavelengths, or under exceptionally good conditions. In general it seems likely that adaptive optics will need to operate with the visual light of the object. Fortunately even quite faint objects will provide enough light to operate adaptive optics in the IR.

Finally in Figure 6, we have attempted to estimate the cost of fitting an 8m telescope with adaptive optics. The assumption is that each corrected element of surface will cost a total of $\$10^4$. If one corrects many elements, then the correction will need to be at high temporal frequency. The extension to higher and higher frequency is likely to wipe out the mass-production advantages of more channels. This is a very crude reconnaisance of the problem, but does indicate that adaptive optics for visible or near visible wavelengths is likely to be very expensive. In addition, the tiny isoplanatic patch may well also be limiting. In contrast, adaptive optics that can operate down to 2-3μ under the best seeing conditions seems likely to be both useful and to have a reasonable cost.

ADAPTIVE OPTICS AND ALTERNATE TECHNIQUES

Adaptive optics at O-IR wavelengths differs from adaptive optics at radio wavelengths because at O-IR wavelengths, individual telescope apertures tend to be greater than r_o. In consequence, real time correction of the wavefront increases the peak brightness in an image and shrinks its size, so giving greater contrast with thermal or airglow background radiation. This means that greater sensitivity to faint objects is available from adaptive optics than with other techniques. Another way of seeing this is to consider that with adaptive optics, a total observation of 10^4 seconds is coherent for addition of signals. In contrast, speckle techiques operate with coherence times of 10^{-2} to 1 second. In consequence, Fourier components in the image can be determined $\sim 10^2$ to 10^3 times more precisely by adaptive optics for a given observing time.

In contrast however, when real time wavefront correction produces a corrected isoplanatic patch, nothing outside that patch is correctible. When speckle produces a similar sized isoplanatic patch, that merely sets the size of the patch that can be corected in a single analysis process, and does not limit the patch of sky that can be mapped.

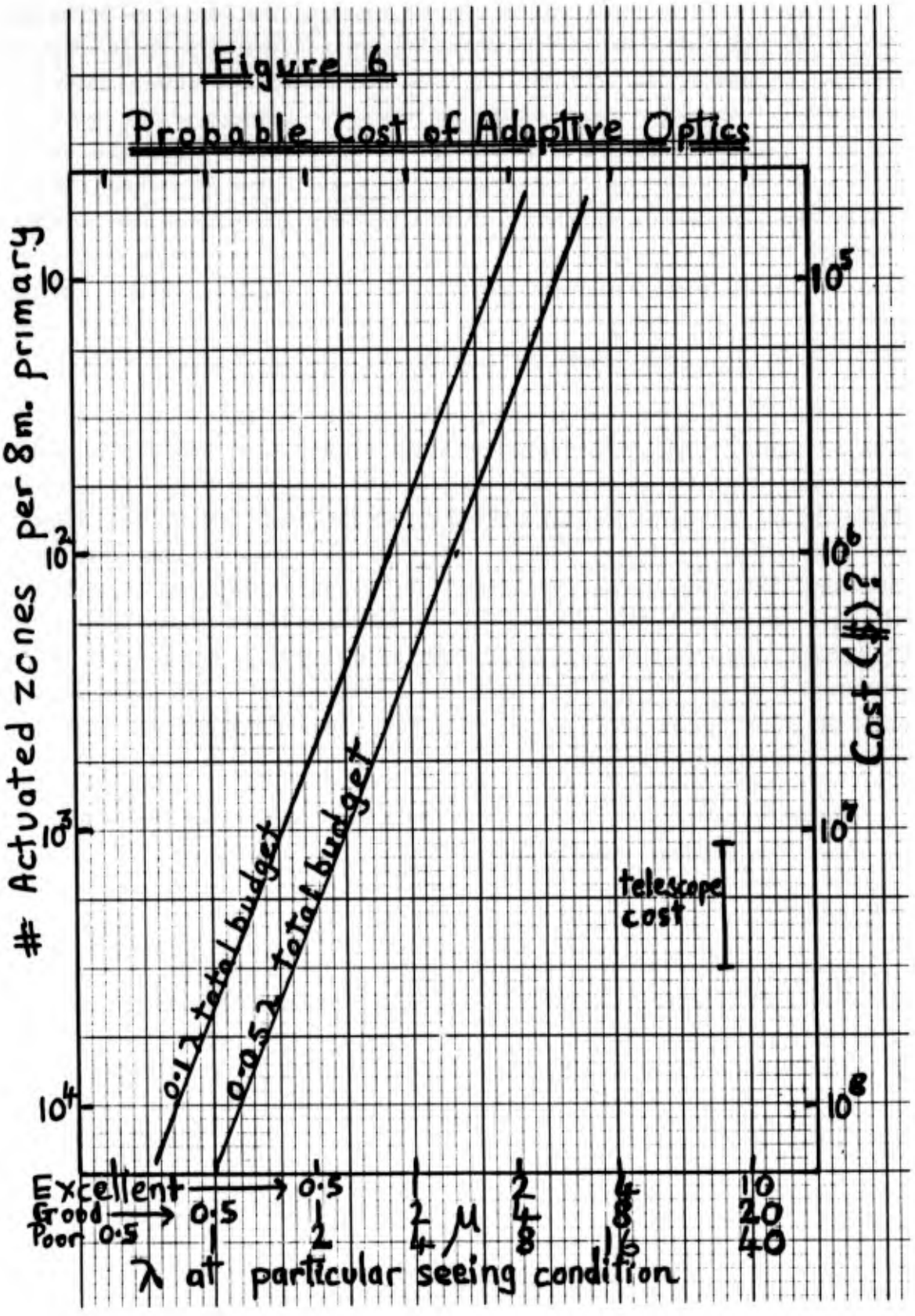
Figure 6
Probable Cost of Adaptive Optics
Actuated zones per 8m. primary
Cost ($)²
0.1 λ total budget
0.25 λ total budget
telescope cost
Excellent
Good
Poor
λ at particular seeing condition

Another question about adaptive optics concerns the correction of images for the thermal infrared. In general, the part of the atmosphere creating seeing disturbances will not be the same as those contributing emissivity fluctuations. Therefore there will be an interaction between seeing correction and sky noise. Even more disturbing is the possibility that the seeing corrections will produce modulation of the telescope's thermal emission, which often exceeds image flux by ~ 10^6. It does not seem profitable to ponder these questions without an empirical test. Adaptive optics of reasonable cost seems likely to permit interesting observations in the 2-5μ region. Tests of such a system in the 10μ window will reveal whether there are background noise problems, and how serious they are.

A further question that is often asked is whether some reduced level of adaptive optics, such as correction of image motion alone should offer major advantages. Here the question revolves around the causes of image degradation. If aberrations or mirror thermal problems dominate, there will be little benefit from correcting for image motion. If telescope shake is dominant, then correcting for image motion may result in results as good as if a stable telescope had been built. However if the dominant image degradation is by atmospheric turbulence, then there is a rather abrupt transition between slight improvement of the image, and seeing the diffraction core. It would seem a waste of effort not to go all the way and fully correct the diffraction pattern at some interesting wavelength.

Adaptive optics also seems interesting for correcting the individual apertures of a Michelson interferometer.

CONCLUSIONS

Adaptive optics is a promising technique for use with Very Large Telescopes. It warrants practical tests. It is expensive, but should pay off by providing higher sensitivity than other techniques for getting high angular resolution. Support is acknowledged under NASA grant NAGW-121. Thanks are also due to Dr. R. N. Wilson for asking questions that permitted substantial improvement of this paper.

REFERENCES

Babcock, H. W. 1953, PASP, 65, 229.
Hardy, J. H. 1978, Proc. IEEE, 66, 651.
Hardy, J. H. 1982, Proc. SPIE, 332, 252.

Woolf, N. J., and Angel, J. R. P. 1980, Optical and IR Telescopes for the 1990's, 1131, ed. A. Hewitt, KPNO.

Woolf, N. J. 1982, Ann. Rev. Astron. Ap., 20, 367.

Woolf, N. J., McCarthy, D. C., Angel, J. R. P. 1982, Proc. SPIE, 332, 50.

Woolf, N. J., and Ulich, B. 1984, in Site Testing for Future Large Telescopes, 163, ed. A. Ardeberg and L. Woltjer.

DISCUSSION

G. Burbidge: I would like to ask again about the costs of making corrections. If I understand you correctly you believe, and I agree, that the cost of correction should only be a fraction ($\lesssim$ 25%) of the total cost. What is the total cost for a 7-8 meter single dish telescope?

N. Woolf: This is a vital question. It is answered at some length in the written version of the paper jointly authored with Angel and Williams. Depending on how the primary is aluminized, what primary focal ratio is chosen, and whether this is the first to a given design, the cost is likely to range between $12 and 30 million for a telescope, housed, but without instrumentation or on-site facilities.

R. Bingham: Has the pattern of turbulence enough duration as it sweeps across the aperture to give some improvement in signal-to-noise ratio if we translate an observed pattern?

N. Woolf: In principle, if a single layer of turbulence were responsible, and one had separated the telescope aberrations by time averaging, one could take advantage of the slow decay of large scale turbulence. It seems likely that in practice the multiplicity of turbulent layers, and the deviation of their wind vectors would make the problem intractable.

GONE WITH THE WIND, OR SAILING AND SEEING WITH A GIANT TELESCOPE

N. J. Woolf and B. L. Ulich
Steward Observatory, University of Arizona

ABSTRACT

Both anecdotal and quantitative information on seeing and wind shake at the MMT are used to discuss the problem of site selection for a giant telescope. An adequately isolated mountain peak is defined, and such peaks are not rare. It is shown that at such a peak, the site contribution to seeing will, in general, be much less than the contribution of the remainder of the atmosphere. In contrast, the typical seeing at a large observatory is usually dominated by the contribution of the facility. Because seeing is mainly a problem of facility design, site selection criteria can strongly weight the major problem of wind shake. Wind oscillatory torques are a major problem for a facility designed for excellent seeing. These torques increase with the square of wind speed. It is not yet clear how the responsibility for these torques should be apportioned between the site and the facility. Extreme care in all relevant factors, but particularly in site selection, will be needed to ensure that excellent telescope images are not spoiled by wind shake.

INTRODUCTION

Most large telescope science output is critically dependent on the degree of blurring of the image. Two pernicious effects are liable to blur a telescope image beyond the limits set by the instruments optical quality. These blurs are produced by refractive fluctuations of the atmosphere, "seeing", and also by wind driven image motion in the telescope, "sailing".

Many astronomers still believe that most "seeing" is caused outside the telescope facility, and that "sailing" can be prevented by the use of windscreens. It is the thesis of this paper that most seeing for most large telescopes is self-induced, and is in part caused by an attempt to shield them from the wind.

The route to this conclusion is painful, since many millions of dollars have been poured into giant telescopes which produce mediocre images. It is likely we would still be building telescopes with poor images but for the novel character of the MMT. Aided by good luck, and driven by a shortage of funds, the design of the MMT facility allowed a reduction of facility seeing below the level of that produced by the remainder of the atmosphere. This then revealed that other large telescopes were not routinely reaching the limits permitted by the atmosphere.

This surprising result has still not been used to full advantage. At this time, the MMT primary mirrors still have an inadequate figure that was meant to match the average seeing anticipated (1 - 2"). Nonetheless it has been possible to explore the reduction of facility induced seeing, and to confirm that a necessary part of the strategy is to expose the telescope to the wind.

The MMT is very rigid, and winds at Mr. Hopkins are low, but despite this the vibration of the MMT is just marginally permissible. Scaling this result to larger sizes suggests that wind vibration will be a major problem with giant lightweight telescopes, and a major task of both telescope design and site selection is to keep sharp images without being lost and Gone With The Wind.

THE MMT EXPERIENCE

Selection of Mt. Hopkins as an observatory site was a relatively casual process. Fred Whipple and Gerard Kuiper reportedly flew in a light plane over the Santa Rita Mountains just south-east of Tucson. The air turbulence was quite bad over Mt. Wrightson, the highest peak of the range, but was much less over Mt. Hopkins, an outlier on the windward side.

Later there were measures of seeing on a 7,200 ft. ridge (Pearlman et al. 1974), using observed image motion in a 15 cm telescope. They state that the expected seeing is 1 - 2". At the 8,550 ft. summit selected as the site for the MMT, similar studies with a small telescope near the ground gave similar results.

In consequence the MMT optics were figured to produce images no better than 0.5" FWHM, and indeed the very first images were about 2" as expected. As part of the process of bringing the telescope into operation, the project scientists, Drs. Hoffmann and Carleton tried sealing off the floor of the observing chamber where the yoke arms came through, and as a temporary expedient they used sheets of flexible plastic. The images noticably improved, but more surprisingly, a few days later it was noticed that the mirrors on one side of the MMT were producing poorer images. The cause was traced to a small crack between two of the plastic sheets on the side allowing warm air to leak into the observing chamber. It alerted us all to the great importance of minute quantities of heat in degrading facility performance.

Later, when Beckers became MMT director, a similar role was played by the local seeing in the laser alignment system then in use. Beckers and Williams (1982) have reported on the range of activities that have been needed to bring MMT seeing to its current state. These are part of a strategy to bring all surfaces in the observing chamber to ambient temperature and so eliminate thermal convection currents within the facility.

The strategy of setting air and facility temperature the same within a fraction of a degree was made possible by the overall design. First, the very open observing chamber allowed wind to flow through the telescope, and so permitted the thermal time constant to be short. Also, the design allowed the telescope tube (OSS) to be treated separately from the yoke, and so only 50 tons of material had to be brought to ambient temperature, compared with some 400 tons for a conventional telescope of this size. Perhaps the most helpful feature was the lightweight primary mirrors of about 7 cm equivalent solid thickness. These have an equilibration time scale of about one hour, as compared with days for large solid blanks.

MMT SEEING

The seeing at a site can be characterized by Fried's parameter r_o measured at a standard wavelength such as 5000A. Overall site performance may be expressed as a single figure by $\langle r_o^2 \rangle$ a measure of the reciprocal of the image area (Woolf 1982). Unfortunately, since this heavily weights rare good seeing, measures tend to be of low precision.

The seeing of the free atmosphere has been measured by 60 balloon soundings by the JOSO group for latitudes between 28 and 43 N (Barletti et al. 1976). The distribution function for their measures at 3 km. elevation have been plotted on probability graph paper in Figure 1.

Beckers (1982a,b) has observed the instantaneous FWHM at the MMT for 91 nights, and has published his observed distribution function. In Figure 1 we have plotted the distribution function for his results, by converting the FWHM to r_o with the formula $\Theta = 0.995\ \lambda/r_o$, appropriate to a seeing image. The corresponding FWHM for a disk diffraction pattern is $\Theta = 1.029\ \lambda/D$. Also shown in Figure 1 are the results corrected for the interferometrically measured optical imperfection of the telescope (see Beckers and Williams). From the figure, the MMT seeing measured by image area is about 30% poorer than the free atmosphere alone, and the seeing is better than 1" some 85% of the time. This surprising results cannot be accepted without query. It is possible for instantaneous images to be far better than average, and indeed from the Steward Observatory 2.3m telescope we have recorded an instantaneous image of Arcturus with a 0.2" FWHM, when the mean value of r_o was 12 cm. Fortunately, there are some other types of seeing measure that check and confirm these results.

Forbes and Woolf (1983) show that image motion can be used to measure seeing, even for giant telescopes. They published one such measure of MMT seeing. Woolf, McCarthy and Angel (1982) have published a further five such measures. Unfortunately, one measure was taken on a night when the telescope was opened at midnight with a 4° C temperature difference from inside to out-

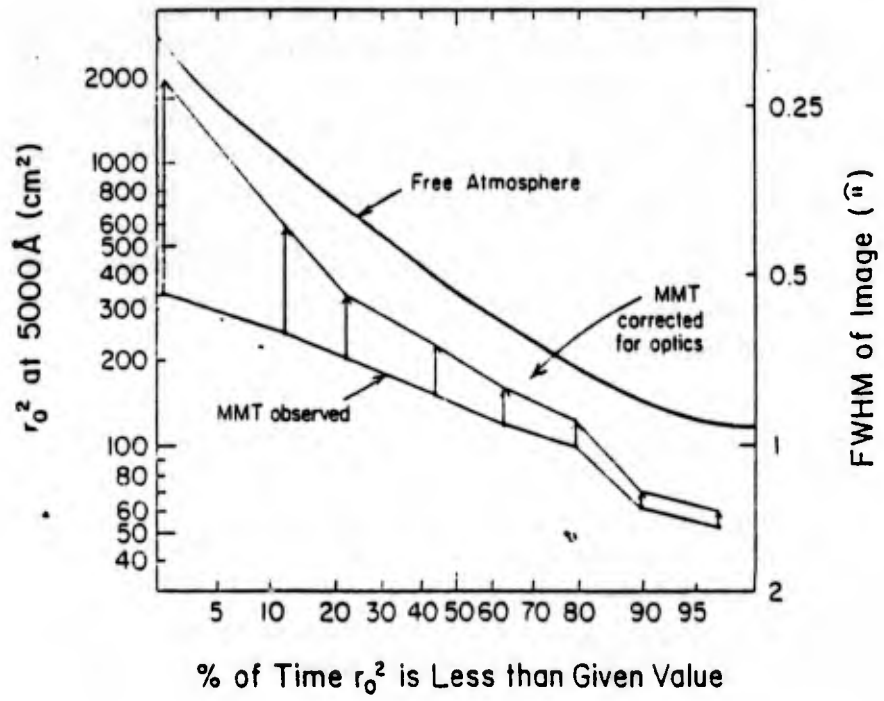

Figure 1.

side, and with appropriately awful seeing. For the other five nights with good measures, the computed values of r_0 are 32.3, 16.0, 15.0, 11.3 and 9.8 cm. These results are consistent with the results of Figure 1. From the Beckers' data, the mean value of $\langle r_0^2 \rangle$ is 320 cm^2 whereas from the image motion the value is 350. The corresponding value for the free atmosphere is about 500 cm^2. A larger number of observations of MMT image motion, by Ulich, are currently being analyzed. Preliminary results are also consistent with the data of Figure 1.

In the Forbes and Woolf paper, there are also five observations of image motion for conventional large telescopes, and a sixth reported by Woolf, McCarthy and Angel. The telescopes are the 3.8, 2.3 and 2.1 m telescopes on Kitt Peak and the CFHT on Mauna Kea. The values are 12.1, 12, 11.5, 10.3, 8.6 and 6 cm with $\langle r_0^2 \rangle$ of 107 cm^2. Further information on large telescope seeing has been measured interferometrically by Dyck and Howell (1983) for the 2.24 m telescope on Mauna Kea. For their observations $\langle r_0^2 \rangle$ averages 133 cm.

There is interferometric information for another telescope on Mauna Kea. This is the planetary patrol 60 cm telescope whose good images played such an important role in selecting the site of the CFHT. For the ten nights studied by

Dainty and Scaddan (1975), after correction to 5000Å $\langle r_0^2 \rangle$ is 170 cm. It should be noted in passing that some of the seeing problems of large telecopes would be expected to be reduced in this small instrument. The results are collected together in Table 1. We believe that the differences between telescopes shown in this table are almost entirely due to facility implementation.

Table 1. Seeing Measures

	Free Atmos.	MMT	Large Tel.	2.24m	60 cm
$\langle r_0^2 \rangle$	500	320	107	133	168

It can be seen that the seeing blur area for conventional large telescopes are about four times larger than set by the free atmosphere, whereas the MMT is about 1.4 times the free atmosphere. While it is, in principle, possible that the MMT site is responsible for this remarkable difference, there is against that the argument that the survey revealed nothing extraordinary about the MMT site. Site measures elsewhere seem to confirm this opinion. Certain additional MMT experiences also confirm the importance of facility degradation.

First, the seeing varies slightly among the MMT primary mirrors. This result shows that the facility still contributes to the seeing. Secondly, a temporary windshield was tried and abandoned. When used, the image size increased from about 0.8" to 1.0" (J. T. Williams, verbal communication). When allowance is made for the optical imperfections, one estimates that the windscreen approximately doubled the seeing blur area. Both results show that free airflow is crucial to the MMT good images.

Another experience is related by Aaronson and Olszewski (1982) "We began observing our first night just after a storm had blown by. Big billowy clouds and fog were still rolling by in the early evening. At Kitt Peak after such conditions the seeing is invariably 10" or worse, and was in fact such that night according to observers we later talked to. However, our seeing was 1-2" all night long, (and the next night as well)." The result shows the importance of a short thermal time constant for the facility.

Finally, we note that the MMT is not totally immune to site seeing effects. One night the wind was blowing from the north (very rare) and it was blowing over a snow bank on the north face of the mountain. When pointed upwind, images were quite good, 1", but downwind to the south they were some three times larger. The observers were so astonished at this phenomenon that they repeated the observation several times. This result shows that the air in the mountain's own wake may be highly disturbed, particularly if the high emissivity and high

latent heat of snow is involved. It is fortunate when the prevailing wind at a site is such that one can look into it much of the time. These anecdotes lead to a more quantitative study of wind and seeing phenomena in the following pages.

SITE SEEING

The first condition for ensuring that the site seeing is not appreciably worse than free air seeing is that the site should be out of the turbulent wake of upstream mountains. This condition may be estimated in two ways. First, eddies die out in several times their own length, which is the scale size of the mountain. Thus eddies are expected to die down over distances of about 20 km. Alternately, one may consider the processes whereby eddies decay into thermal energy, taking a time of about 1/2 hour. For typical windspeeds these two conditions lead to similar conclusions. We may expect that a mountain with no others within 20 - 30 km will be free of upstream problems, unless it creates them itself. Such problems may arise from outlying upwind peaks, or from thermal inversions rising over the site.

Ground inversions occur because the ground is a good radiator. Heat flows by conduction from the air to the ground, where it is then radiated to space, leaving a layer of cold air near the surface. Typically the ground emissivity times the transmission of the atmosphere is quite high, leading to a heat flow of 300 w/m^2 and a ground inversion temperature difference of 10 °C. The thin layer of cold air will be mixed up into the mountain boundary layer, and cause local seeing. The mixing occurs in two forms, first from the overall flow of air across the site creating a thick turbulent layer, but also from the wind at the surface bringing up large bubbles of cold air near the surface.

From the airflow over a mountain, kinematic viscosity would give an enormous Reynolds number. Therefore the flow pattern will be set by eddy viscosity. At the edge of the boundary layer, there will be a transition to laminar flow, such that the Reynolds number will become about 100, or even less. For a turbulent flow, the ratio of boundary layer thickness to characteristic flow dimension will be $1/b = \sqrt{R}$. Thus the boundary layer thickness will be about 1/10 or a little more of the mountain dimension.

The cold air near the surface may be either dragged up to the top of the boundary layer as a part of eddy motion, or small bubbles of it may be elevated by the wind giving them upward velocities that are dissipated by the bubble's negative buoyancy. The bubbles should reach a height H, where

$$H = \frac{v^2}{2g} \cdot \frac{T}{\Delta T}$$

Here v is the wind speed, g the gravitational acceleration, T the absolute temperature, and ΔT the ground inversion temperature difference. Typically this leads to a height of 1.3 meters for a speed of 1 m/sec. These two theoretical conclusions closely parallel experience.

Observations of thermal turbulence over Haleakala, Hawaii, have been reported by Miller, Zieske and Hanson (1976). From the ground up there is a rapid decline in thermal turbulence to a height of about 20 m, where turbulence levels off to some ten times its value in the free atmosphere. The top of the boundary layer above this 3000 m mountain is some 300 to 600 m above the summit. Near the top of this boundary there is a slight rise in the thermal turbulence, followed by a rapid decline to free atmosphere conditions. Similar indications of the overall boundary layer have been reported by Walters and Kunkel (1981). Above a continental mountain, they found that about 300 m up, there were weak falling plumes of cold air.

The surface wind effect has been noticed by both Lynds (1970) and Guryanov (1980). Lynds showed that on Kitt Peak, for winds less than 4.4 m/sec the modal height reached by the cold air of the inversion is 10 m. Our formula predicts this height is appropriate for a speed of 2.8 m/sec. For winds above 4.4 m/sec the modal height was 40 m. The modal wind speed on Kitt peak is about 5.6 m/sec, and for this speed the height predicted is indeed 40 m.

For good atmospheric conditions, the extended region from about 30 m to 500 m has a typical value of C_N^2 of $1\text{-}2\times10^{-16}$ $m^{-2/3}$. The integral effect of this is about 8×10^{-14} $m^{1/3}$ or about one quarter of the overall effect of the free atmosphere. Guryanov found that at 10 m height the typical value of C_N^2 is 3×10^{-15} $m^{-2/3}$, though with a range of about two orders of magnitude. Ten meters of the worst seeing added as much as the rest of the atmosphere, but usually the region above 10 m did not dominate the overall seeing.

From these observations it appears that sites themselves, if chosen with reasonable care will produce seeing only some 30% worse than the free atmosphere. This agrees with the MMT results, and confirms that poorer results at other sites are largely caused by the facilities themselves.

A different potential problem for a site is that a thermal inversion will rise above the summit during the night. The cooling of ground air at a rate of 300 w/m^2 permits a ground inversion to rise at a rate of 0.03 m/sec, or about 1 km during the night. In general, the effect of the cold air insulating the ground prevents growth at this rate, but valleys and plateaus fill with air from higher ground, and any peak that rises less than 500 m from the surrounding region is liable to be occasionally overrun by a local inversion.

If the summit is extended, a ground inversion will grow in depth back from the leading edge to a height about 0.03 l/v where l is the distance back from the edge. For a 1 km summit size this is about 6 m which becomes of appreciable concern for the design of interferometers.

FACILITY SEEING

Beckers and Williams described the steps to improve MMT seeing to its current level. Here we are concerned to demonstrate the interaction of the telescope and the airflow. If the telescope or facility surfaces have temperature that differ from the air by flow by ΔT °C, the facility induced seeing will be about $\Delta T/2$". The air temperature changes during a night. Beckers and Williams show a change of 3.3 °C during a night at the MMT. Dyck and Howell report on Mauna Kea a cooling of 1.6 °C in the first half of the night, but negligable change in the second half. From both these numbers the typical cooing rate is 0.4 °C per hour. In the next section we discuss a telescope image budget for a giant facility which permits a maximum facility seeing (other than for the primary mirrors) of 0.08". Thus, the telescope and observing chamber must not be more than 0.16 °C above wind temperature, and this requires a maximum time constant of 24 minutes.

The specific heat or air is about double that of steel, and so the requirement becomes that the telescope intercepts its own mass of air once every 48 minutes. The density of air is about 10^{-3} tonnes/m^3. Let the surface density of the telescope be S tonnes/m^2. Then the minimum air speed is given by,

$$v = S/2880 \times 10^{-3}, \text{ or } v = s/2.88.$$

As an example, the exposed part of the MMT has a surface density (allowing for spaces) of about 3 tonnes/m^2, corresponding to a minimum necessary windspeed of 1 m/sec. Some parts of the MMT, such as mirror cells, have higher surface density, thus it is not surprising that the windscreen spoiled the seeing. Indeed, one predicts that there should be a deterioration in seeing at low wind speeds, and for such occasions there should be giant exhaust fans to produce a minimum wind speed of about 1 m/sec past all parts of the telescope.

A LARGE TELESCOPE ERROR BUDGET

Site criteria only make sense in terms of an overall telescope error budget. For this, one tries to distribute costs to give the greatest resources to the items that create the most problem. Woolf (1982), pointed out that the best seeing at a site determines the budget. The performance of a telescope can be described as the reciprocal of the mean time to make an observations. For many purposes this performance is proportional to the reciprocal of the image solid angle, i.e.,

$$P = \int_{\text{time}} \frac{dt}{\Omega} \Big/ \int dt \propto \int r_o^2\, dt \Big/ \int dt$$

For the free atmosphere seeing, if the error budget is 0.2", the performance loss over a perfect telescope is 30%, and if the budget is 0.33" FWHM the loss is 50%. These constraints imply a very tight budget. The attached initial budget is not optimized, but it does already provide a guide as to the type of budget to be expected.

Table 2. Error Budget

If error budget is 0.2" FWHM, loss is 30%
If error budget is 0.33" FWHM, loss is 50% -- unacceptable

	FWHM	$(\text{FWHM})^2$
Primary with Adaptive Compensation	0.12"	0.0144
Other Optics + Support	0.08"	0.0064
Optical Design (wide field, wide λ atmos. dispersion compensation)	0.12"	0.0144
Focus - Adaptive	0.04"	0.0016
Misalignment - Adaptive	0.04"	0.0016
Mistracking (Star Tracker)	0.08"	0.0064
Local Seeing	0.08"	0.0064
Mirror Seeing	0.08"	0.0064
Total $\text{FWHM}^2 = \Sigma(\text{FWHM})^2$	0.24"	0.058

33% is in last 3 items

It should be noted that some 33% of the error budget has been set aside for facility seeing, and tracking precision, which is of course affected by wind. This is little flexibility for a radical redistribution of terms. There is a potential problem in that these terms are competing. The image budget seems to show that the telescope must be exposed to the wind, while the tracking budget shows that wind shake must be small. We therefore now address wind problems.

WIND EFFECTS

Wind effects may be conveniently classified as static and dynamic. The static effects are due to the mean wind pressure. The dynamic effects are due to the fluctuations of the wind speed. On mountain tops, as we have discussed, the boundary layer is turbulent, and so the fluctuations in wind pressure are comparable with the wind pressure itself. In general, if the static effects do not have a significant amplitude, the dynamic effects will be unimportant. Likewise, if the static effects are significant, then it is likely that dynamic effects will also be significant.

The static drag on a telescope surface will be D where,

$$D = CA\rho v^2/2$$

A is the projected area, v is the flow velocity, ρ is the air density, and C, the drag coefficient, is a factor between0.5 and 1 for a wide range of likely Reynolds numbers. The factor of +/-33% in this drag coefficient is quite unimportant compared with the uncertain upper limit to the wind speed for operation.

Figure 2 shows wind speeds and pressures on three mountains (Crawford 1983, Pearlman et al. 1972, Kaufman and Vecchione 1981). If we assume that the telescope has an abrupt cut off in operation at a certain level of deformation or mispointing, then the thickness of the telescope members, and thus the mass of the telescope must increase proportionately with the square of the upper cut off speed required. There has been some discussion of the overall cost of a

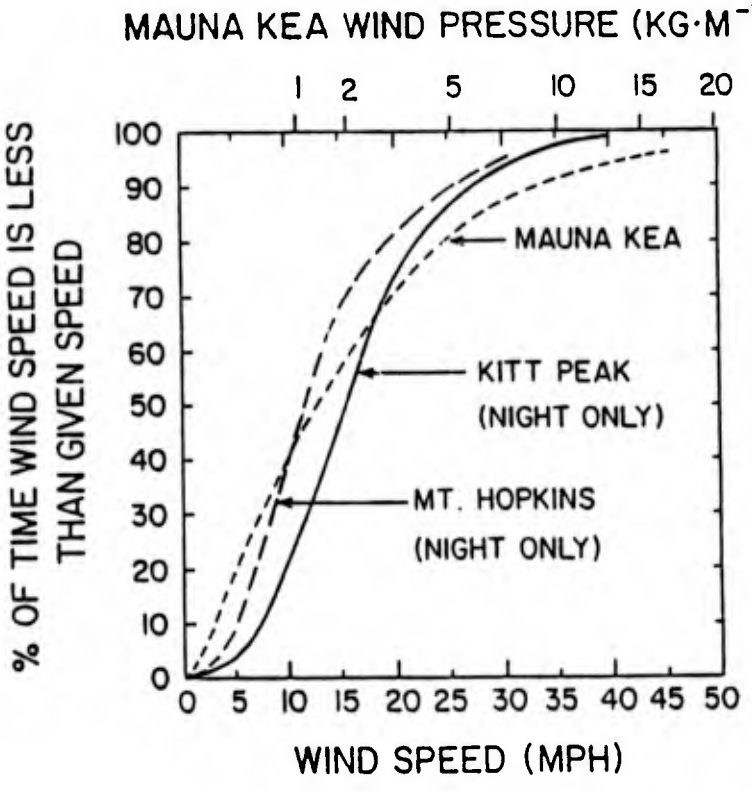

Figure 2.

telescope as being directly proportionnl to the mass. While this a naive oversimplification, if applied here, one would find that the bulk of the funds were spent to gain a very small amount of observing time.

STATIC WIND DEFLECTIONS

The static wind pressure is about 0.05 km/m^2 when the wind is 1 m/sec, or 2 kg/m^2 at a wind of 6 m/sec. Large telescope large parts tend to have surface mass densities of about 1000 kg/m^2 and smaller parts have surface densities of about 100 kg/m^2. Thus for these parts wind forces represent no more than a 2% perturbation to the gravitational deflection. Although good designs do attempt to keep a telescope aligned despite variation of the gravity vector with pointing, the precision of this alignment cannot practically be better than about 5% of the gravity flexure even with tuneable structures like the MMT. For this reason, wind should not play a significant role in the alignment of a telescope.

The one part of a telescope where forces are balanced to a precision considerably higher than 2% is a large primary mirror. Angel, Woolf, Hill and Goble (1983) shows that an 8 m size lightweighted honeycomb mirror can be adequately supported against wind gusts if the support forces are controlled by the fixed point pressures. A thin solid mirror would be some five times thinner, and some 25 times more flexible and on this basis it would be unable to cope with winds of about 5 m/sec and a complex servo system would be required. Alternately Nelson (1977) has proposed that large mirrors should be segmented so that the deformations of the parts of the mirror are not cumulative. In any of these solutions, the critical questions concern the interplay of wind forces, mirror cell deflection and mirror control system. Such detailed considerations are beyond the scope of this paper.

DYNAMIC EFFECTS

To understand the effects of fluctuating wind forces on a telecope, we shall first consider the response of a mechanical system to external torques of various frequencies. Let the mechanical system have a moment of inertia J, a spring constant K and a damping coefficient of B per unit velocity. Let the torque amplitude at frequency f be T, and let the phase shift of the response be ϕ. Then,

$$T\sin(2\pi ft) = (K - 4\pi^2 f^2 J)\sin(2\pi ft-\phi) + 2\pi fB\cos(2\pi ft-\phi)$$

and if the amplitude is A,

$$A = T/\sqrt{(K-4\pi^2 f^2 J)^2 + 4\pi^2 f^2 B^2}$$

and,

$$\tan \phi = 2\pi fB/(K-4\pi^2 f^2 J)$$

The amplitude of the angular error per unit torque is plotted against the frequency in Figure 3 as the upper line. It can be seen that there are three parts to the diagram. At low frequencies, the amplitude is constant at T/K. At high frequencies the amplitude is $T/4\pi f^2 J$, and there is a resonance at a frequency $f = 1/2\pi \sqrt{K/J}$, whose amplitude and width are determined by the damping coefficient.

If a servo system is used to reduce the amplitude of the response at low frequencies, it must be tailored for stability so as to have less than unit gain at frequencies where the phase shift exceeds 180°. For typical electronic filters this implies that the gain goes to unity at about 0.2 of the resonant frequency. The resultant overall response is shown by the dashed modification to the upper curve in Figure 3.

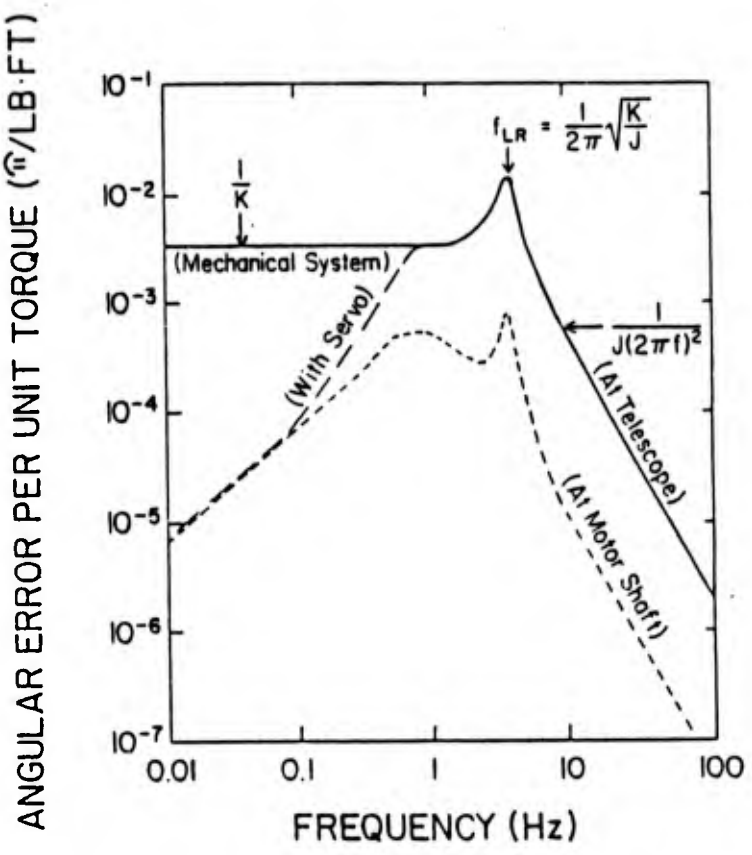

Figure 3.

For comparison, Figure 4 shows the responsivity of the MMT to azimuth torques injected at the motor shaft. The drive was successively modified to increase the spring constant of the drive, first by relocating one drive motor, and then by adding two further drive motors and gearboxes (see Ulich and Davidson 1982, and Ulich 1982). It can be seen that in agreement with our analysis above, the resonant frequency was increased during this process, and the increasing spring constant also lowered the amplitude. The detailed modelling process also permitted the true response of the telescope to be derived from the study at the drive motor shaft.

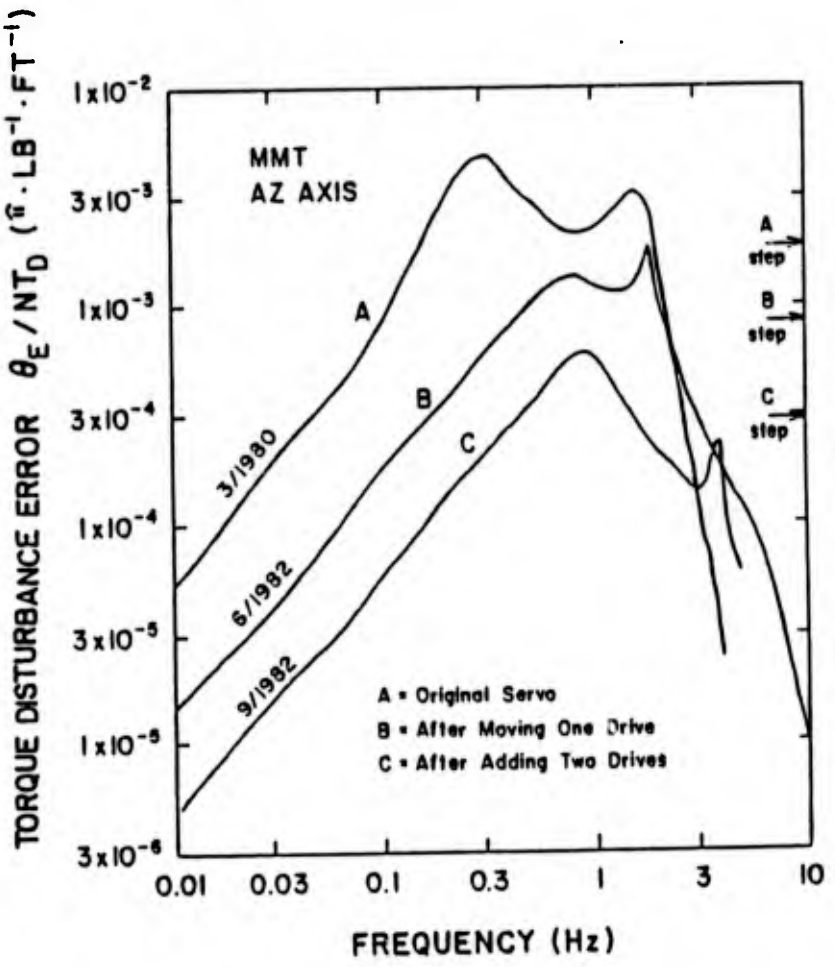

Figure 4.

WIND FORCES AND WIND TORQUES

Wind forces on mountains have been reported by Forbes and Gabor (1982). They find that for frequencies from a few Hz to a few tenths of a Hz, most distributions of force obey a Kolmogorov spectrum, with F(ν) per unit frequency proportional to $\nu^{-5/3}$, or if measured per unit $(Hz)^{1/2}$, R(ν) proportional to to $\nu^{-7/6}$. Whether the ratio of wind force to turbulent wind force varies from

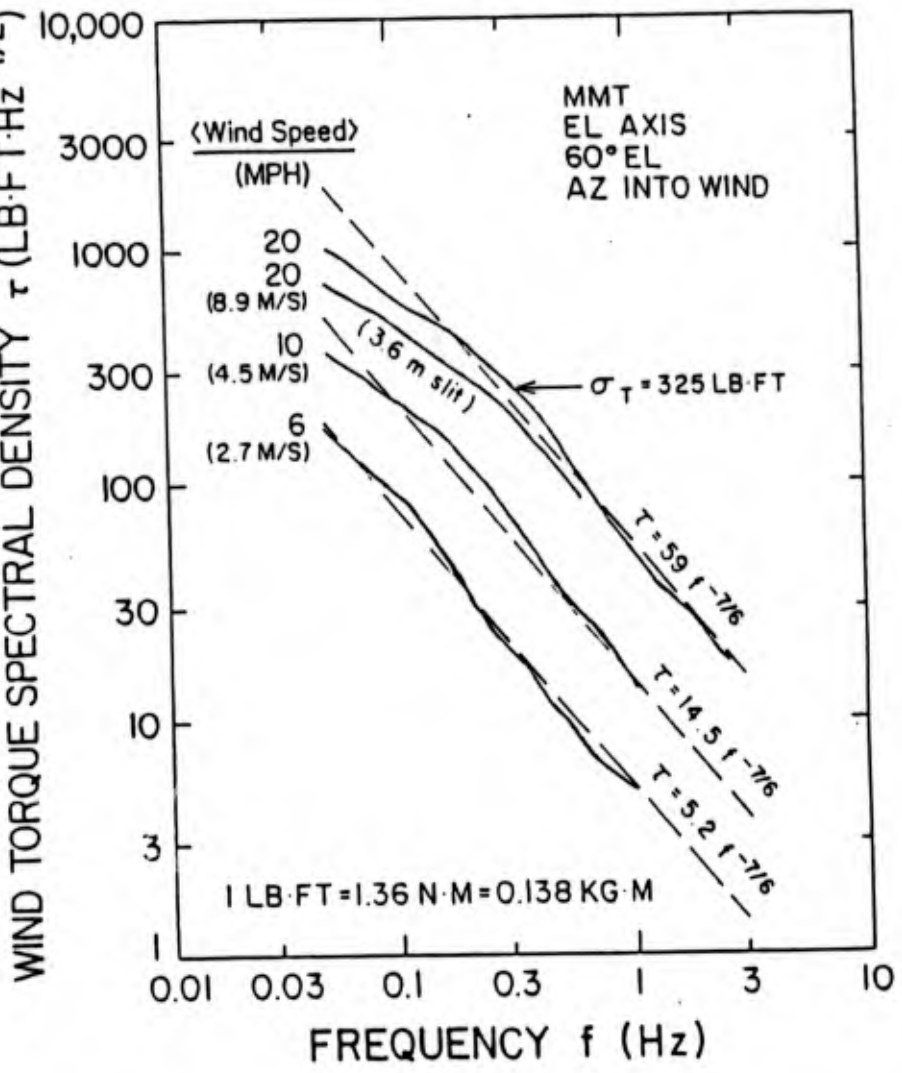

Figure 5.

point to point on a given site, with height, with wind direction, from site to site, or with other factors is currently unknown, though theoretical arguments would suggest that such variations would be likely. At the MMT, Forbes and Gabor show that at 1 Hz the fluctuating force per unit bandwidth is 0.024 of the average wind force.

One of us (BLU) has made observations of wind torques on the MMT on the elevation axis, with the telescope pointed into the wind at the worst elevation angle for shake. These results, in Figure 5 show that the torques follow an approximately Kolmogorov spectrum, and vary with the square of the wind speed.

It is interesting to compare these torques to those one might predict from the work of Forbes and Gabor. The MMT presents an exposed surface of about 16 m^2 and has an average radius about the elevation axis of about 2.5 m. At a wind speed of 9 m/sec and corresponding force of 4 kg/m^2, the maximum possible torque would be about 160 kgm, and the observed 1 Hz fluctuating torque is 7 kgm, which is about a factor 0.04 of the possible torque. This is comparable to the torques one would predict outside the MMT building. Thus for the worst case, the MMT design needed to have the telescope capable of operating in the open. The question whether the same statement should be made for other telescopes and sites cannot yet be answered.

In Figure 6 the pointing error spectral density has been observed, for two different gains of the servo system. The results are in excellent agreement with a convolution of the wind spectrum in Figure 5 with the elevation torque sensitivity curve (similar to Figure 4) for a wind speed of 5.4 m/sec, the rms pointing error is 0.13 arcseconds, comparable with, but beyond our error budget for a large telescope. Recent improvements in the servo system have brought the pointing error to 0.14" in a wind of 10 m/sec. We therefore now study the MMT torque responsivity to see how we may both predict, and appropriately produce the required giant telescope torque responsivity.

TORQUE RESPONSIVITY

The MMT wind induced errors are almost entirely due to drive shaft errors. We have measured the difference between the optical pointing and the encoder angle in high wind. The observations showed substantial tracking errors of a few arc seconds, but the difference between the optical axis and the encoder were not detectable. This indicates that it is much easier to make a very stiff optical support structure than a stiff drive.

The MMT drive spring constant in azimuth is dominated by the motors and gear boxes, as the results of Figure 4 show. The drive was initially so floppy that it was necessary to shield the yoke arms from the wind, but the modifica-

tions to the drive have now increased the spring constant by a factor of four and brought the azimuth locked rotor frequency to about 4 Hz, comparable with the elevation frequency. Further increases in spring constant in azimuth would be possible by adding more gearboxes, but the design of the telescope would not allow a large improvement in elevation.

In elevation, the motors and gearboxes are only responsible for some 40% of the spring constant, and the remainder must be attribed to the mechanical design of the mount. It seems that a modified yoke and bearing system would permit the drive stiffness to be set by the motors and gearboxes to a substantially higher value than at present.

If we then try to predict the effect of increasing drive stiffness for a given telescope, we find that the response to wind will vary as,

$$R \propto f^{-2/3}/K \text{ or } \propto J^{1/3}/K^{4/3}$$

The increase of drive stiffness of the MMT would be a non-trivial cost. The combination of gearboxes and motors currently in use at the MMT costs some $200,000 and a factor of 4 increase in stiffness would therefore represent about a 10% increase in the overall cost of the facility. It would, at least in azimuth, lower the response to wind by a factor of about 6, and thus allow an excellent pointing error of about 0.023" rms in a 10 m/sec wind.

If we now try scaling these results to larger telescopes, we find that linear scaling of structures by a scaling factor S, increases wind torques by S^3, spring constant by S^3, the moment of inertia by S^5, and the locked rotor frequency by 1/S. The corresponding angular wind deflections increase as $S^{2/3}$. If the scaling is done so as to scale the surface density of members separately, by a factor D, then the deflections increase as $S^{5/3}/D$.

As a check that our understanding of these factors is correct, we have taken the simple servo-mechanical model of Figure 3, and assumed a Kolmogorov spectrum of wind torques from the straight lines on Figure 5. We have then calculated that from the observed telescope resonant frequency, spring constant and moment of inertia, the expected wind driven fluctuating point errors would be 0.16" at 10 m/sec, compared with the 0.14" observed.

There has been considerable discussion about making a 15 m telescope with a mass of about 400 tons, and for such a telescope S ~ 3 and D ~ 0.5. Further, in this meeting there has been discussion of operating a telescope in winds up to 13 m/sec. For such a telescope and such conditions the wind shake would be 40 times the MMT value described above, or 6"!

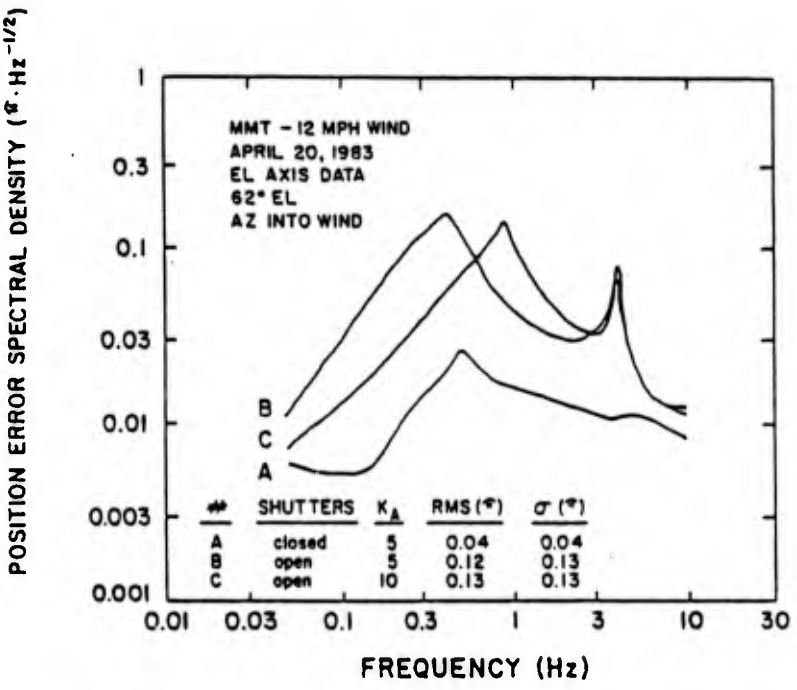

Figure 6.

POSSIBLE SOLUTIONS

There are various ways of dealing with wind shake. The most radical would be to try to create some outer skin for the telescope to accept all wind forces, while keeping an appropriate airflow to control seeing. Practical versions of this have not yet been presented, but are by no means impossible in principle, though they may be costly. The conventional dome is an inadequate solution of this type.

The next possible solution is to have a servo system that moves optical elements to stabilize the image. This requires feedback from an optical image, and the higher the frequency of image motion to be stabilized, the brighter must be the star. Some optical designs with narrow fields of view for e.g. IR imaging, will not find such stars available. Further, some wide field configurations will have only massive optical components, and large dimensions, again creating problems for an optical servo system. One particular mechanical concern for allowing the telescope to move with large amplitudes is the danger of coupled oscillations leading to high amplitudes at high frequencies. For both of these reasons the solution of having an optical servo loop does not appear very attractive as an overall solution, though if amplitudes are somewhat

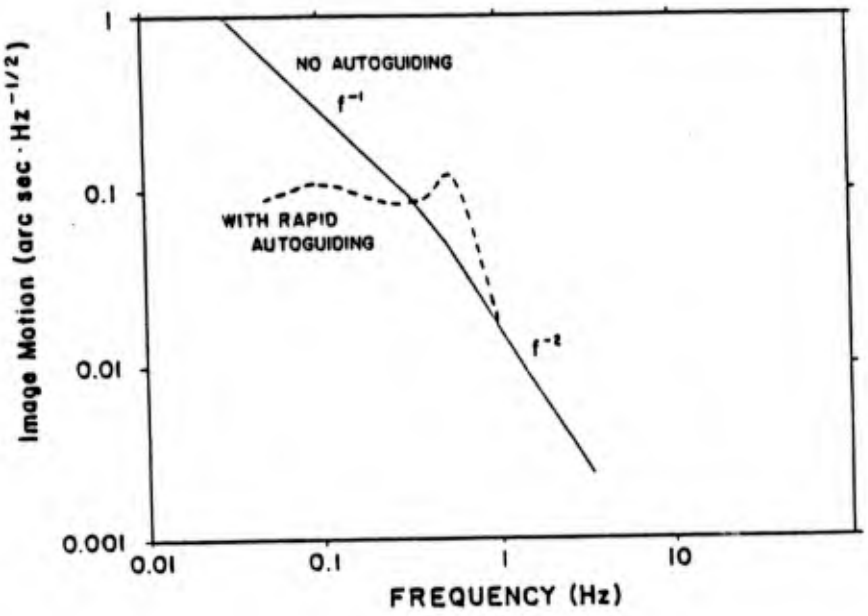

Figure 7.

marginal, an optical loop could be used to make the residual vibration acceptable. Figure 7 shows an attempt to use an optical servo with the MMT. It gave very marginal benefit. The potential factor of 5 that might be gained in drive stiffness is likely to be one major factor in a solution. If we try to increase the surface density of material, we find that for a steel structure, the increase permitted is quite small. A factor of 2 increase to the surface density of the MMT substantially raises the structural cost, and increases the specific heat of the structure to the limit allowed by passive cooling. Active cooling, and a massive telescope is an expensive solution that might solve a part of the problem.

If we consider alternative materials for constructing the telescope, Carbon Fiber Resin Plastic (CFRP or graphite-epoxy) seems the most attractive. This material has a cost fabricated per unit strength a few times higher than steel, but a resonant frequency some 2 - 3 times higher, so that for the same strength structure the vibration amplitude is decreased about 1.8 times. The thermal capacity of CFRP per unit strength is about 2/3 of that of steel, so that for the same structural thermal capacity, a CFRP structure will vibrate with a 2.7 times lower amplitude. When the thermal capacity is not limiting, as in radio telescopes the advantage of CFRP could be very great, but for an optical telescope the potential gains seem more modest.

We find no simple single solution, and must consider whether the wind specifications should indeed allow an 18 m/sec wind in the worst possible direction. Certainly we would like to be able to use a telescope for at least half of the time without worrying about the wind direction. At a low wind site however the 50% wind has a speed of only some 5 m/sec, and for this wind the shake is reduced a factor of 13! Then for higher winds we could select the observing program to reduce the shake to acceptable levels.

We have considered that a modified MMT with stiffer drives should have about a four times smaller amplitude. Thus for a steel telescope of MMT surface density, at a low wind site we find that wind shake is just controllable by steel stiffness and added drive stiffness.

It is also possible that we might find sites where the wind torques are less than at the MMT for the same average wind speed. Currently we cannot say to what extent the turbulence level of the wind really defines the MMT shake, or whether the interaction of the wind with the building and telescope plays an important role. In the first case, there would be value in comparing turbulence at different sites. For the second, it would be irrelevant. Further experiments are required.

While solutions do seem possible, it is clear that site wind levels can play a major role in determining whether good imaging is frequently or rarely possible. Thus site wind becomes a prime topic for consideration in site selection.

REFERENCES

Aaronson, M. and Olszewski, E. 1982, MMT Observers Report, 3/10/82.

Angel, J. R. P., Woolf, N. J., Hill, J. and Goble, L. 1983, Proc. SPIE, 444, in press.

Barletti, R., Cepatelli, G., Paterno, L., Righini, A., Speroni, N. 1976, J. Opt. Soc. Am., 66, 1380.

Beckers, J. M. 1982a, b, MMT Technical Memorandum #9 and #14.

Beckers, J. M. and Williams, J. T. 1982, Proc. SPIE, 332, 16.

Crawford, D. L. 1983, Proc. SPIE, 444, in press.

Dainty, J. C. and Scaddan, R. J. 1975, MNRAS, 170, 519.

Davison, W. and Ulich, B. L. 1982, Proc. SPIE, 332, 9.

Dyck, M. and Howell, R. 1983, PASP, in press.

Forbes, F. and Gabor, G. 1982, Proc. SPIE, 332, 198.

Forbes, F. and Woolf, N. 1983, Proc. SPIE, 444, in press.

Guryanov, A. E. 1980, Soviet Astronomy, 24, 379.

Lynds, C. R. 1970, "The Physics of Seeing Program", Tucson, Kitt Peak National Observatory.

Kaufman, J. M. and Vecchione, M. 1982, Ten Meter Telescope Report 66, University of California, Berkeley.

Miller, M., Zieske, P. and Hanson, D. 1976, SPIE, 75, 30.

Nelson, J. 1977, "Optical Telescopes of the Future", ed. Pacini, Richter and Wilson, p. 133.

Pearlman, M. R., Hogan, D., Goodwin, K. and Kurtenbach, D. 1972, Smithsonian A. O. Special Report #345.

Pearlman, M. R., Bufton, J. L., Hogan, D., Kurtenback, D. and Goodwin, K. 1974, Smithsonian A. O. Special Report, #357.

Ulich, B. L. 1982, Proc. SPIE, 332, 33.

Woolf, N. J., McCarthy, D. W. and Angel, J. R. P. 1982, Proc. SPIE, 332, 57.

Woolf, N. J. 1982, Ann. Rev. Astron. & Ap., 20, 367.

Reprinted from Nature, Vol. 295, No. 5851, pp. 651-657, 25 February 1982

Very large ground-based telescopes for optical and IR astronomy

J. R. P. Angel

Steward Observatory, University of Arizona, Tucson, Arizona 85721, USA

Optical and IR astronomers are taking a hard look at their ground-based facilities and devising new ways of making more economic, bigger and better telescopes. Features of instruments of the 15-m class are likely to include servo control to compensate for atmospheric wavefront errors as well as structural deformation, large honeycomb mirror blanks and mirror surfaces produced by economical techniques developed for aspherics.

WHILE detectors and instrumentation have improved enormously during the past 50 yr, the size of the largest optical telescopes has not increased significantly. Detectors have now reached close to the fundamental noise limit set by photon statistics, and techniques have been developed to observe simultaneously many objects in the telescope's field of view. Further progress in many problems of astrophysics now requires an order of magnitude increase in light grasp.

The main purpose of increasing telescope aperture is to reach fainter objects and to improve accuracy of measurement. The quantum nature of light means that to measure intensity, spectrum or polarization to a certain accuracy, even with ideal detectors and optics, requires the collection of a certain minimum amount of energy. For other types of measurements in which detector noise is dominant, the rate of collecting energy is an additional factor, and gives an added advantage to the large telescope. Given that on average only a few hours each day meet all the requirements for observing, and that the largest telescopes must serve a broad community of observers, it is not practical to integrate for more than around 20 h in a season the light from even an object of exceptional importance. For a given collecting aperture this sets a limit to faintness or accuracy.

The qualitative advantages to larger apertures arise from the improved limit to angular resolution set by diffraction. At long IR wavelengths, where image quality is limited by diffraction, high spatial resolution is achieved directly. At shorter wavelengths various interferometric techniques allow the recovery of information on spatial structure at the diffraction limit. This is <10 m arc s in visible light for the telescopes I now consider.

In the US a programme has been started to develop the critical technology for a national telescope with a collecting area equivalent to 15 m diameter. Closely linked projects for smaller telescopes for California and Texas are under way. Meanwhile, in Arizona, the Multiple Mirror Telescope (MMT), a joint research facility of the University of Arizona and the Smithsonian Institution, is a working prototype of many aspects of the new technology. Most ideas for very large telescopes involve multiple primary mirror elements, and the MMT, the first of this type, has six mirrors of 1.8 m diameter all bringing light to a common focus (Fig. 1).

Why ground-based?

The Earth's atmosphere limits the value of ground-based telescopes in various ways. It is completely opaque to wavelengths below 0.3 μm while the IR spectrum is broken up by molecular absorption bands, being completely blocked over the range 40–300 μm. Background radiation from air scattering of sunlight and moonlight, and from thermal emission in the IR interferes with the observation of faint objects. Refractive index changes caused by thermal gradients in the air prevent one achieving diffraction limited images at shorter wavelengths, and the uncertainty of weather means one cannot be sure of any particular observing period.

These limitations are removed for telescopes above the atmosphere. The Space Telescope, scheduled for launch in 1985, will overcome many of these problems. However, its aperture of 2.4 m diameter has only 1/40 the area of a 15-m telescope, while its cost is an order of magnitude larger. Although technology may become so advanced that one could afford very large telescopes to realize the potential of space, our present needs for huge light grasp can only be met by building on the ground.

In fact, many of the observations that need large aperture can be done efficiently through the atmosphere provided that the design, siting and scheduling of the telescope are optimized. Spectroscopy will be the major application for a very large telescope. Provided the atmospheric background is kept to the minimum, the dominant noise source for this work will often be photon shot noise of the signal itself, or detector noise in IR spectroscopy—these noise sources are not reduced by going to space.

Image quality

The factor that most strongly drives cost is the need for excellent image quality. This is required not so much to resolve detail in extended objects but to minimize the background underlying faint unresolved objects. A giant light bucket with indifferent images would be of relatively little value. If, for example, the spectrograph entrance aperture has to be increased in diameter to capture the light of a degraded image, then the increased background may overwhelm the signal. For the faintest objects doubling the telescope diameter is of no advantage if the image diameter is also doubled.

Our intention of achieving good images is likely to have far-reaching consequences for telescope design. Recent experiments and studies demonstrate that some degree of active correction for atmospheric distortion is generally possible, with potentially very large gains for giant telescopes in the IR. If the means to implement such corrections are an integral part of the telescope design, then they may also be used to correct for slight distortion of the optics which would be intolerable otherwise. Large cost savings may be possible if a correction system were to relax the normal tolerance for accuracy, rigidity and stability, especially if the optics are extremely large.

The distortion at the atmosphere can be thought of in terms of the corrugation of a wavefront that was perfectly plane when incident at the top of the atmosphere. It has ripples and waves on all scales, which can be modelled by random turbulence[1]. (Note, however, that turbulence inside the telescope housing has only small scales, and causes separate problems discussed separately below.) The random wavefront deviation δ in micrometres between points separated by d across the wave is given by

$$\delta(\mu) \simeq (d/d_0)^{5/6} \quad (1)$$

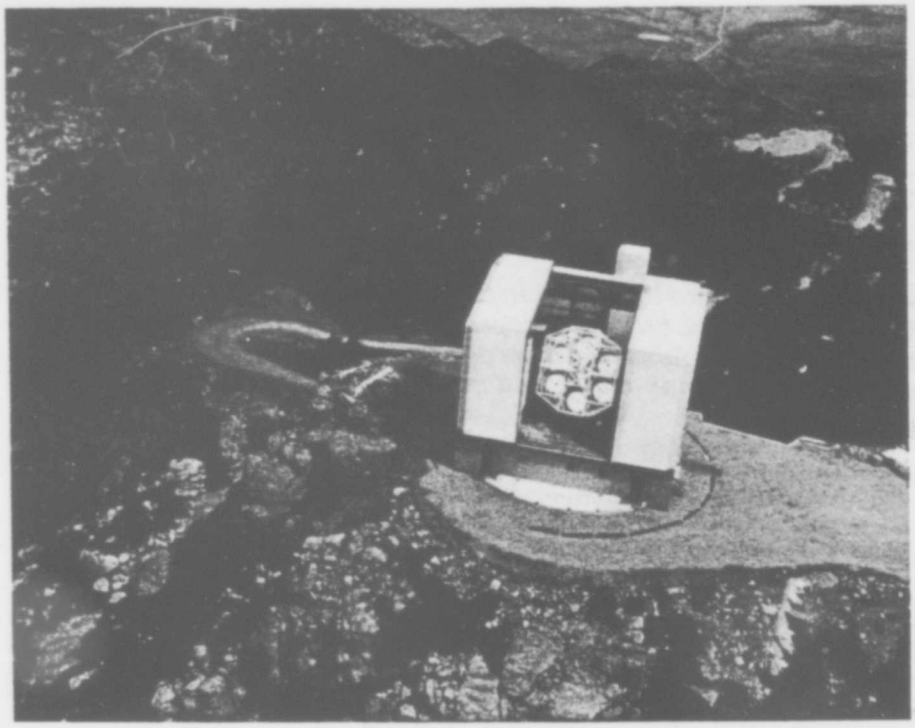

Fig. 1 An aerial view of the Multiple Mirror Telescope in Arizona. The location on top of a sharp, high peak, gives favourable conditions for sharp images. The MMT is jointly owned and operated by the University of Arizona and the Smithsonian Institution.

where d_0 is a measure of the seeing quality and in good conditions may be as large as several metres. The corrugations move at about the wind speed, so that large-amplitude deviations over a scale of 10 m change on a time scale of 1 s, while ripples on a scale of 10 cm vary 100 times faster.

If a true diffraction limited image is to be obtained at any given wavelength, then the deviations across the telescope aperture must not exceed about $\lambda/10$ (see ref. 2). For visible light, the task of correcting the wavefront of a large telescope to this tolerance is extremely difficult. The length scale of ripples with amplitude $>\lambda/10$ is 10–20 cm at best and the time scale is short. Compensation has to be made at an optical surface that can mimic all these rapidly changing small-scale ripples. Considerable progress in making such 'rubber' mirrors has been made by Hardy[3]. Apart from engineering difficulties, however, a fundamental limitation to achieving complete correction of the visible light wavefront is that of deriving the information needed to make the correction. This requires that the source being observed should be bright, or that there should be a bright source no more than a few arc seconds away whose wavefront, similarly distorted, can be used to derive corrections.

Although full correction of the wavefront is generally not possible, correction of the errors on a scale of metres is. Faint field stars within a couple of arc minutes of a target are adequate to provide the necessary much reduced amount of information. From equation (1) we see that the wavefront tilts δ/d are almost as big at large scales as at small, varying only as $d^{-1/5}$, so significant improvement of visible image quality can be expected. Woolf[4] has analysed in detail the improvements that can be made in various conditions: typically, 20–30% reduction in image size can be expected in visible light[4,55]. The better the seeing, the greater the improvement to be made.

In the IR, there is dramatic potential for high quality imaging with large telescopes. At 10 μm, for example, the small-scale ripples that do most damage to visible images are below the $\lambda/10$ threshold, and are not noticed. The seeing disk, resulting only from large-scale waves, will be only a little more than half that of visible light. Woolf has pointed out, though, that if the large-scale errors can be measured and continually corrected with the aid of a nearby visible star, fully diffraction limited performance at 10 μm is achieved in reasonably good seeing conditions. For a filled aperture of 15 m diameter the FWHM of the Airy disk is 0.16 arc s. Because almost every source of interest at 10 μm is fainter than sky background, the advantage of operating a large telescope at this high resolution is enormous.

Thermal control

The frequency of occurrence of different degrees of atmospheric turbulence and hence wavefront distortion has been measured with small, low level, test telescopes by Walker[5]. The results show little difference between the good test sites. From these data and balloon observations of turbulence by Barletti *et al.*[6],

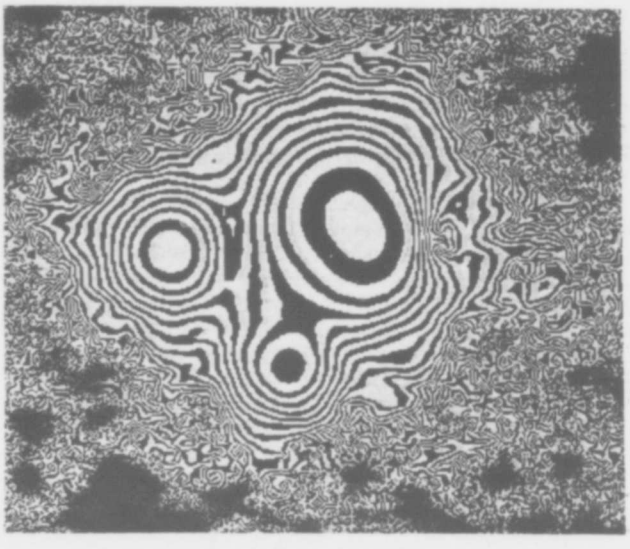

Fig. 2 An example of high resolution imaging from the ground, the QSO PG1115+08. It shows multiple components because of gravitational bending of light rays by an intervening galaxy. The two unresolved round images, separated by 2 arc s, have FWHM of 0.6 arc s. The brightest, elongated image is shown by speckle interferometry to be a double with 0.5 arc s separation[54]. This figure, courtesy of E. K. Hege, was made by Doug Tody at Kitt Peak National Observatory using the IPPS facility with contours space logarithmically by factors of two.

a honeycomb–faceplate sandwich mirror 1.8 m in diameter that will be figured as a parabola and tested alongside the fused silica mirrors in the MMT. We hope to work up to a 7.5-m blank over the next few years.

Ideas for reducing cost are needed in optical figuring. Traditional methods of grinding and polishing are time consuming and expensive for aspherics. One solution was devised by Schmidt, to make the aspheric corrector plates for his camera. A glass blank is polished spherical by conventional methods while being stressed in such a way that on release it takes up the required figure. Lemaitre[33] has demonstrated this method for making on-axis paraboids, making a diffraction limited $f/2$ parabola of 40 cm diameter. Nelson *et al.*[22] have extended the technique to make a precise off-axis parabola 35 cm in diameter, stressing the blank during manufacture with levers at the edge. The major effort of Kitt Peak National Observatory in the field of large telescopes is directed towards making matched off-axis elements 2m in diameter by the same method[34]. Precise tolerance in curvature (~ 1 in 10^5) is needed if a large parabola is to be made from separately figured segments. Another area of concern[35] is how these elements are to be made hexagonal, so they can be fitted together to make a nearly seamless surface of low thermal emission. Trimming a large thin circular mirror could disturb its figure as strain is relieved.

Traditional methods of figuring glass are based on the fact that two rigid blocks rubbed against each other with abrasive between will develop surfaces that are very accurately spherical. Machines to do the rubbing need not have any great precision, they only have to drag one piece across the other in a suitable pattern. A different approach is used in the production of optical surfaces by diamond turning of metal substrates. This is done with an extremely accurate lathe, and a single diamond tool of large radius advanced gradually so as to leave a mirror-like finish with only very shallow grooves. Optical elements up to a metre or so with surface accuracy of the order of micrometres have been produced by this method. Polishing can then give surfaces with better than a wave accuracy and remove the small-scale structure[36].

Unfortunately, metal substrates have not yet been demonstrated that can withstand the repeated temperature cycling of mountain top observatories without gradually losing their shape. Glass, while stable, cannot be finished like metals with a single diamond, but precision direct machining is possible with an abrasive diamond grinding wheel. This can again bring the surface to within a micrometre or so of the final figure, minimizing the work to be done in polishing. Large mirrors or segments would be turned on an air bearing about a vertical axis, and the tool moved across the surface as in Leighton's[37] method of making precision radio telescopes. Parks and Angel[38] have worked out a scheme to make mirror segments in which the grinding tool moves on an arm turned about an axis inclined to the vertical, yielding naturally a very close approximation to a parabola.

Electronic image stabilization

Despite the electronic sophistication available, large telescopes are being built which rely exclusively on massive rigid optics and supports to maintain image quality: only the MMT has used active control to replace force rigidity. The potential for achieving very large collecting areas by this technique at relatively low cost is enormous: the MMT has been built for about one-quarter the cost of its rigid equivalent.

There are various ways that active correction might be made. For single-mirror telescopes (or individual elements of a bigger telescope) we can alter the forces that support the primary, or leave it alone and devise a mechanism to distort the secondary or subsequent mirrors. For high frequency control, Hardy's scheme[3] uses piezo-electric actuators acting on the back of a thin mirror. Merkle *et al.* have demonstrated[39] an electrostatic force system. Magnetic actuators could be used for correction on a less rapid time scale.

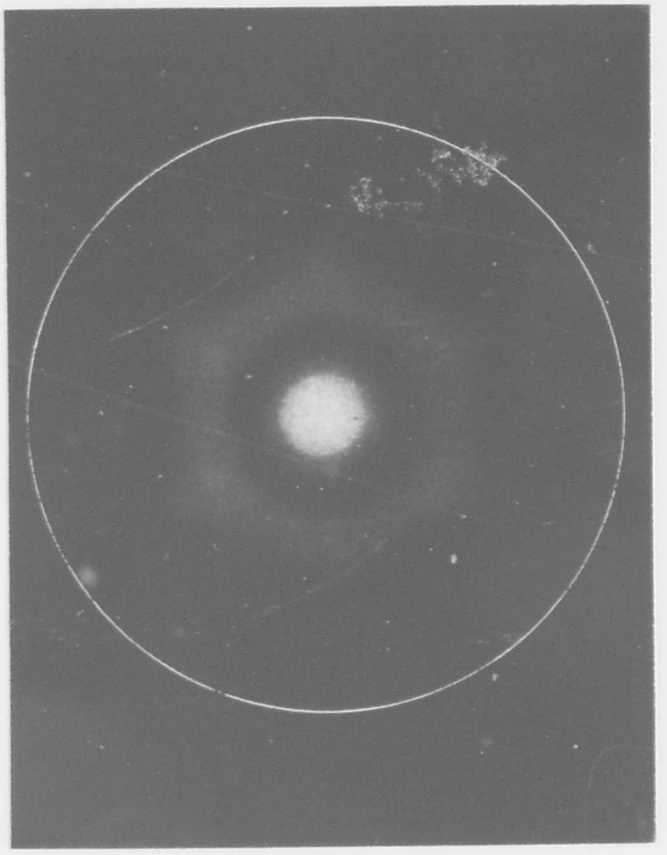

Fig. 5 The diffraction pattern computed by Meinel *et al.* for a phased circular array of six mirrors separated by 0.15% of their diameter. 40% of the total energy is within the first dark ring. The peaks in the continuous hexagonal ring reach 0.11 the intensity of the central peak, the six isolated peaks 0.06. The Airy pattern of one individual mirror, with a first dark ring of diameter shown by the white circle, has a resolution nearly four times poorer then that of the phased pattern.

To achieve a single focus in telescopes that have more than one collecting mirror we need to sense and correct the alignment of each mirror. In the MMT the tilt of individual secondary mirrors is controlled by micrometers driven by stepper motors, giving single steps of 0.05 arc s at the combined focus. Gabor[40] has demonstrated a ball screw actuator suitable for tilting 2-m primary elements with even higher angular precision.

How do we derive the information necessary to make corrections? Elastic deflections arising from differing orientation with respect to the gravitational field are repeatable, and tables of corrections necessary for their compensation can be stored in the control computer. There will remain unpredictable errors, such as wind forces, uncompensated thermal gradients in the structure, and friction in mirror supports, and in the MMT these residual effects amount to about 1 arc s in image motion[9] and a few tens of micrometres in pathlength error as the telescope is moved to different parts of the sky[30]. The residuals which might be achieved in a 15-m class instrument, probably not much worse than in the MMT, are comparable with the random wavefront error already present from atmospheric turbulence.

To realize fully the potential of active optics, one must determine how rays from a star illuminating different parts of the reflecting surface come together at the focus, and feed back corrections to the active elements. This will correct both the structural errors and the large-scale wavefront errors, if done with a frequency response of a few hertz. One method is by

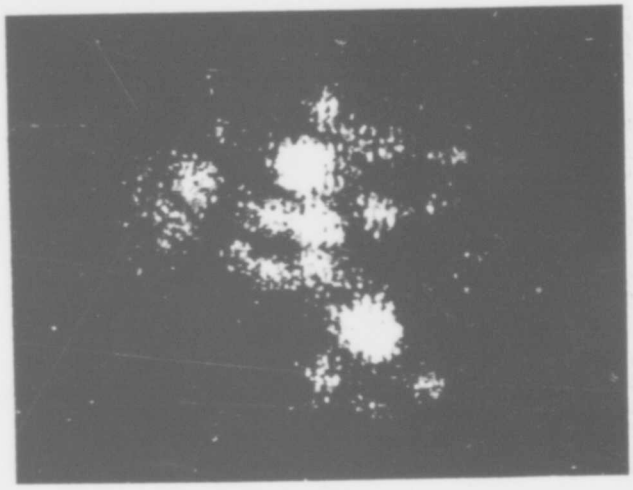

Fig. 6 Interference fringes spaced by 30 m arc s in the highly magnified image of an unresolved star. The image was formed by two of the 1.8-m mirrors of the MMT, with a centre-to-centre spacing of 5 m. (Courtesy of E. K. Hege and P. A. Strittmatter.)

automating the knife edge test: in its basic form the star image is focused on a sharp edge, such as a razor blade, and an auxiliary lens is used behind the edge to form an image of the primary mirror. A tilt of the wavefront in a particular region will then show as a bright or dark patch in the image. Hardy[41] has used a scheme in which an oscillating grating cuts across the star image, and the pupil is imaged on a bank of photomultipliers. Phases of the signals from each photomultiplier then give the tilt error of each part of the pupil. A variant of this idea is where the reference star is imaged on a sharp four-sided pyramid, and each reflected beam passes through a Fabry lens to image the pupil on one of the four sensitive imaging detectors[4]. A complete map across the pupil of tilt of the wavefront in both directions is obtained by intercomparison of the four pupil images. An alternative method that does not use a knife edge uses a lens placed after the combined focus to image the pupil on an array of tilted mirrors. Each mirror directs light from a part of the pupil to a field reimaging lens, and imaging detectors monitor the full field image from each pupil segment. Image locations relative to a reference dot in the combined focal plane then give the tilt of each pupil segment. In both these schemes the problem of maintaining co-alignment of a multiple element telescope reduces to the same problem addressed by offset guiders in today's single element telescopes. An automated system has to be reproduced for each section of the primary that will be independently corrected.

For the wavefront error correction to work, one must either use part of the light from the program star itself, or use a field star close enough for it to share the same large-scale wavefront errors. The angular separation α of shared motion is approximately d/h, where d is the scale of the wavefront error and h is the effective height of the wavefront disturbance. For $d = 2$ m and $h = 4$ km (ref. 42), α is about 2 arc min. Well correlated motion of two stars 50 arc s apart observed with a 1.8 m aperture in conditions of reasonably good seeing (1.2 arc s) is shown in Fig. 4 (ref. 43).

Because much of the work of a large telescope will be with faint objects giving no useful signal for electronic stabilization, the capability for continuous fine tuning of the image relies on finding a guide star within the field of common motion. Fortunately, the development of CCD detectors of excellent red sensitivity means that adequate signals can be obtained. Consider, for example, stars of R magnitude <16, which with a red filter would stand out clearly even in full moonlight. At the sparsest regions near the galactic poles these have a density of 382 per square degree[42], and will thus be found with 75% probability within a 2 arc min radius. The light from such a star collected by a 2-m element will give a signal of 8000 electrons s^{-1} in a CCD, adequate to implement the schemes outlined above with a frequency response of a few hertz.

When rapid wavefront tilt corrections are made to a telescope with continuous primary and secondary surfaces then instantaneous large-scale phase errors are also removed. As discussed earlier, this should allow diffraction-limited performance to be achieved in the IR. Even if the full collecting aperture is made from separate elements it should still be possible to maintain correct phasing from tilt measurement provided that the elements are close to each other, and that no steps are allowed to develop in the wavefront going from element to element. Relative phases between elements can be established by occasional observations of broad band interference in an unresolved reference source[30]. For a system of adjacent segments making a single surface, capacitive sensors such as those developed by Gabor[40] can be used to maintain accurately steps between adjacent mirrors.

The diffraction pattern of MMT type telescopes when multiple circular apertures are combined perfectly in phase has been explored elsewhere[25,45,46]. The intensity at the central maximum of the pattern depends only on the total collecting area; at this point all the radiation is added in phase no matter where it was collected. The width of the central peak depends on the diameter of the full array. An exact calculation of a typical diffraction pattern is shown in Fig. 5. This is for a circular array of six mirrors, separated by 0.15% of their diameter. Such a close array could potentially be maintained in phase from tilt sensing. The power of such a telescope for IR imaging is realized when we consider the potential resolution at 10 μm. Equation (1) shows that the phase errors over individual 6-m mirrors will get to $\lambda/10$ or less in good seeing. An MMT configuration of six such mirrors with active correction of phase differences between mirrors would give images close to the diffraction limit of Fig. 5, that is 0.11 arc s FWHM of the central peak, the same as for a filled aperture of 22-m diameter.

Although active wavefront correction to achieve directly diffraction limited images for visible light is not generally possible, various interferometric techniques can be used to study spatial structures at the diffraction limit. Very large single mount telescopes will allow resolution of ~5 m arc s at 0.5 μm. An example of interferometry between the full surface of two of the 1.8-m mirrors of the MMT is shown in Fig. 6. The centres of the mirrors are separated by 5 m, giving a fringe spacing of 30 m arc s at the observed wavelength of 0.75 μm. A specialized interferometric telescope array, such as Labeyrie is building, will give longer baseline and higher resolution than any single large telescope, but the latter will be able to reach considerably fainter objects[47].

Instrumentation and operation

We have focused on current ideas for making the large telescopes which, nevertheless, have excellent images; it is beyond our scope to review other characteristics, but we can indicate some of the challenges.

The sensitivity of present large telescopes in the wavelength range below 1 μm is being brought close to the theoretical maximum using silicon arrays. CCDs have near unit quantum efficiency and negligible noise for nearly all applications. We must also plan to use these detectors in very large telescopes: the challenge is to handle the inevitably large detector area. Because optics of present telescopes and spectrographs are close to the fastest practical speeds, increases in detector area proportional to the primary collecting area are inevitable. Detector areas from 10 to 1,000 cm^2 will be needed, depending on the number of spatial and/or spectral resolution elements to be resolved in a single exposure. Just as we will probably make large collecting areas from more than one piece of glass, we will probably need to make the detector from more than one piece of

Woolf[7] has derived probability distributions for long exposure (time averaged) image size. He finds the diameter containing half the energy of a point source should be 0.7 arc s at the 50th percentile, 0.3 arc s at the 10th percentile.

The images that are actually recorded at most large telescopes are rarely as good as this, mostly because of thermal disturbance of the air near the telescope and enclosure. The increased size and thermal inertia of a giant telescope means we must be especially careful to understand and control these local effects. Adiabatic effects of turbulence on refractive index are not significant at normal wind speeds, but heating and cooling by convection and radiation are. The sensitivity to heat can be appreciated when we realize that light passing through a single bubble of air with a temperature difference of only 1 °C from its surroundings is spread into a cone of 0.5 arc s diameter. Turbulent thermal boundary layers can cause acute problems.

Local thermal gradients are potentially worse at high desert sites where diurnal changes of air temperature are large, and where radiation cooling at night is strong. The effects of an observatory building on image quality stem both from heat sources within the building and from failure of external surfaces to accommodate the changes in the ambient temperature. In the MMT building, exposed surfaces were of low thermal mass and were backed by good insulation, and the telescope chamber was small and well ventilated[8]. Beckers[9] reports a series of measurements at the MMT of temperature made with thermometers and a 10-μm TV camera, and of internal seeing measured with laser beams in the dome. The use of insulation and surfaces with low emissivity at 10 μm on the telescope and mount as well as the building, means that very good thermal equilibrium with the ambient air is achieved.

The one part of any telescope that cannot be insulated is the mirror. Seeing generated by mirrors has been studied by Lowne[10], who finds experimentally a seeing disk of 0.5 T arc s for a mirror temperature T °C hotter than ambient. Conventional large solid mirrors have time constants of many hours, and so are generally likely to be out of equilibrium by at least 1 °C from the changing night-time air, even if refrigeration is used during the day to set some anticipated mean operating temperature. Mirror seeing will thus frequently spoil potential sub-arc second seeing, unless the thermal time constant is kept to an hour or less. This goal can be achieved using metal mirrors or glass with faceplates no more than a few centimetres thick and air circulated behind. The fact that the MMT has thin-faced honeycomb mirrors may account in part for its frequently excellent seeing, despite substantial diurnal temperature variation at its high site. The image shown in Fig. 2 of the 'triple' QSO, having high resolution of 0.6 arc s, was obtained with one of the MMT honeycomb mirrors, with correction every 1 s for low frequency image motion caused by large scale wavefront tilts[11].

Ideas for very large telescopes

Traditionally telescopes have a single primary mirror made from a rigid massive disk of glass. Mirror supports for optical telescopes are based on the principle that perfect support against gravitational distortion of an elastic solid at any orientation is given by floating it in a liquid of the same density. Mirror cells arrange for the gravity balancing force to be distributed over the mirror back and sides, simulating flotation as far as possible. Thermal distortion of modern mirrors is effectively eliminated through the use of very low expansion materials having coefficient of $<10^{-7}$ per °C. Stiffness is such that the mirror figure is not significantly disturbed by wind in the telescope enclosure.

Mirrors of 4-m diameter are probably the limiting size for an economical telescope using these principles. Considerable increase should be practical if lightweight (thin or honeycomb) blanks are used together with some active compensation for mirror deformation and resultant wavefront distortion. Lewis[12] finds that on site manufacturing of a 10-m blank of 20 cm thickness out of fused silica or ultra low expansion (ULE) glass is practical. Studies of stiffness and designs for supports of thin meniscus mirrors of ULE or Zerodur in the 7–10 m range have been made by Epps *et al.*[13], Mack[14] and Pearson[15]. Pyrex honeycomb mirrors in this size range that would be considerably stiffer and potentially less expensive are under development[16,17]. Flotation support alone of large thin mirrors is unlikely to yield a surface precision much better than 1 arc s, particularly when one considers that wind forces in reasonable size domes will be large. However, with the aid of servo controls, as we have considered above for wavefront correction, slight errors in figure may not be a serious drawback.

The goal of a 15-m diameter primary aperture, which I adopt as representative of a very large telescope, is probably too large to be handled practically if made from a single piece of glass. Certainly the technology would have to be proved in smaller sizes before one could consider seriously such an approach. I thus consider designs that involve several or many separate mirror sections. For nearly all optical observations other than interferometry these separate elements could be in the form of separate telescopes, with data from separate instruments added to yield all the signal-to-noise advantage of the full aperture. Disney[18] has pointed out the advantages of such an array, in which fairly high spectroscopic resolution can be obtained with silicon CCD detectors without reaching the detector noise limit. Heterodyne IR interferometry would be possible with such an array[1], but direct interferometry and those IR observations which need all the light at a single focus[19] are almost impossible to achieve if the telescopes are on fixed separate mounts[20].

The most obvious route to a single focus is to figure all the elements as parts of a single parabolic surface. These must be mounted in a supporting structure as stiff as possible, and a scheme must be devised to manipulate the segments (or smaller elements reflecting images of the segments) to maintain correct orientation and phase. Such an approach has been studied by astronomers at the University of California. Nelson[21,22] and his collaborators are developing methods to prepare separately and bring together 25 off-axis hexagonal elements, to make an approximately hexagonal parabolic surface 10 m across. Angel *et al.*[23] have considered a design of six identical circular off-axis mirrors, each 6-m in diameter.

The MMT[24] takes an intermediate approach between separate telescopes and a segmented single reflecting surface. The experience of this working prototype has led to proposals[4] for much larger versions. A design for a 15-m telescope now being studied in some detail incorporates four 7.5-m honeycomb glass primaries co-aligned in a single telescope mount. Many optical observations would be done with relatively small instruments at the four separate foci but, as in the MMT, auxiliary mirrors would be arranged to bring the light to a combined and phase focus when needed. In this concept structural deformation and wavefront errors could be compensated in the small secondary optics or the primary mirrors.

Both the single-surface concept and the multiple telescope concept have the potential of yielding a telescope which can optimize images yet is versatile enough to undertake optical, thermal IR or interferometric observations. These approaches are being considered for the United States national 15-m telescope by a consortium of the Universities of Arizona, California and Texas with Kitt Peak National Observatory. This effort is concentrating on the key areas of technology that need development, bearing in mind a target cost of around $100 million.

Other concepts for very large telescopes which have received considerable attention are generally less versatile, but may have an important part to play for special tasks. Designs based on the Arecibo radio telescope with a fixed spherical bowl and moving secondary optics[25–28], solve the problems of gravitation distortion of a moving primary surface. Spherical segments of the surface could be produced inexpensively and spherical figure can be maintained easily against thermal deformation by laser metrology from the centre of curvature. However, performance

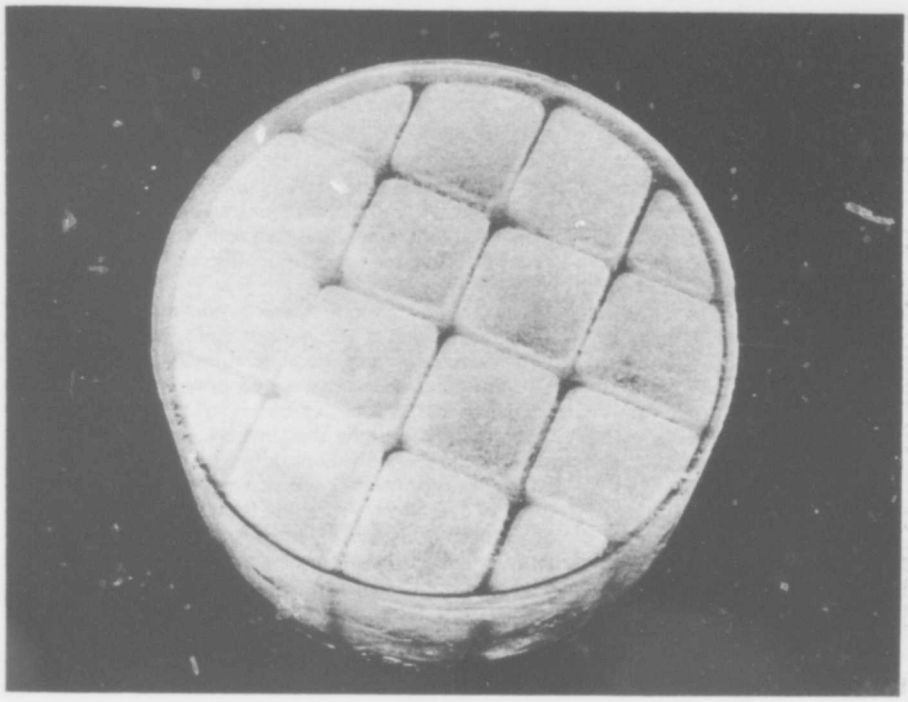

Fig. 3 A honeycomb–faceplate sandwich mirror blank cast from borosilicate glass as a single piece[14]: it is 60 cm in diameter and 35 cm thick, with ribs 6 mm thick on 15-cm squares.

in the thermal IR would be poor because of varying background as the detector tracks across different parts of the sphere. Also sky coverage is limited and it is difficult to correct spherical abberation over a large field of view. Furthermore, it would be expensive to raise such a telescope above the turbulent thermal boundary of the ground. A valuable application for this type of telescope would be for multiple object spectroscopy, in which a small corrector would be used for each point object under study, and many such correctors would be tracked at once across a limited spherical focal surface of some 20–30° (ref. 29). Multiple object spectroscopy is, of course, an important application of any of the giant telescopes discussed here.

A large telescope configuration that might become very important, with more experience with interferometry, has been suggested by Low[30]. Several telescopes would move on circular tracks, so as to remain in a line perpendicular to the object under study. If individual lightweight and stabilized telescopes of 5 m or more in diameter could be moved in this way, then the array would also be a good general purpose telescope. A fundamental question is the image quality that can be achieved in telescopes close to flat ground with no domes.

Making mirror elements

A central issue of any plan for a very large telescope must be a technique to fabricate the huge reflecting surface at acceptable cost and in a reasonable period of time. Without new ideas, mirror costs could take up most of the entire budget. If very low expansion materials are to be used then any structures other than solid sheets are probably ruled out because of very expensive fabrication costs. Costs for material alone are in the range \$50–100 kg^{-1}.

Borosilicate glass honeycomb is an attractive alternative for large mirror elements. The raw material is inexpensive and can be easily fabricated into complex structures by casting at relatively low temperatures. Figure distortion is a problem in solid borosilicate glass mirrors because temperature gradients persist for a long time, but will not be significant in a structure that can rapidly be made isothermal. The Palomar 5-m, the Lick 3-m and the KPNO 2.1-m mirrors are ribbed Pyrex structures with thickness of faceplate and ribs of ~10 cm. Thermal distortion of these mirrors is generally below the 1 arc s level[31]. At Steward Observatory we have undertaken to make large blanks consisting of 3-cm faceplates and still thinner wall honeycomb sandwiched between. These will be ventilated internally with air at ambient temperature, so equilibration will be rapid. A fundamental advantage is that mirror seeing, discussed earlier, will be eliminated. Two 60-cm test mirrors have been made from borosilicate glass: one has a slotted strut type of construction[32] and has been figured to a $\lambda/8$ r.m.s. sphere. The other, a similar honeycomb sandwich but made by a single casting in a complex mould, is shown in Fig. 3. Thermal relaxation and structural properties of both mirrors are being investigated by interferometry. Efforts are now directed towards casting in one piece

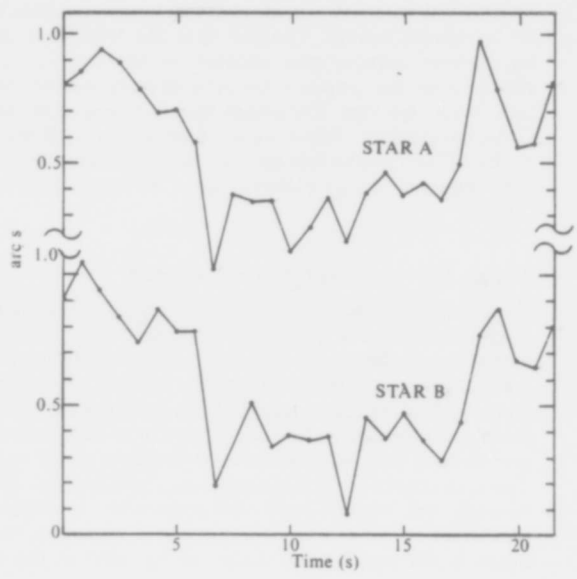

Fig. 4 Atmospheric-induced motion in one coordinate of two stars close to the North Pole separated by 50 arc s. Each data point gives the centre of gravity of an image integrated for 1/6 s. The r.m.s. fluctuation of the difference in positions is 0.11 arc s (ref. 41).

silicon. Many options exist for arranging detector chips in close mosaics, or in multiple smaller instruments. Some of the factors are discussed in ref. 18.

Another challenge is to maintain a sizeable field of view for a very large telescope. With good detectors there will be an important role for precise photometry and objective spectroscopy[48] of many thousands of objects at once in a wide field. With fibres automatically positioned in the focal plane and feeding the light along the slit of a spectrograph, dozens of objects can be observed over a wide field at once, with high spectral resolution if required[49,50]. If the primary focal ratio is made very fast to keep down tube length and dome size in a single-surface telescope, difficulties can arise in obtaining a wide field. However, two-element reflecting correctors offer a remarkable opportunity of obtaining a large corrected field with a fast primary. An optimized design[23] of the Baker–Paul type[51,52] explored in detail by ray tracing has an $f/1$ primary and an $f/2$ corrected focus. The achromatic images are no worse than 0.2 arc s over a 1° field.

The third challenge in a giant telescope is to maximize the operational efficiency. The best use is to match the type of observations to the conditions prevailing. Moonlight and twilight are obvious factors but there are also unpredictable changes in transparency, seeing, water vapour, wind and clouds. Ideally one needs several complementary instruments, ready for use with only a few minutes time lost for interchanging. Astronomers need not be present at the site for observations with standard equipment: they could be called to a local data terminal when their observations were to be made. Experiments in this type of operation have already begun at Kitt Peak National Observatory[53].

Multiple detectors, automated multiple object probes, automatic interchange of instruments, resident observing staff and communication with remotely located astronomers are expensive. When we consider, though, the capital investment in a 15-m class telescope, the costs of development, construction and operation of these instruments will not be disproportionate.

Conclusion

We are seeing the beginning of a new generation of large telescopes for optical astronomy, characterized by innovative methods of mirror fabrication and active feedback to maintain image quality. Large, rigid mirror substrates of honeycombed glass are being developed, along with techniques for inexpensive manufacture of precision aspheric surfaces. Advances in sensors and data processing now make it practical to measure continuously atmospheric distortion and make rapid corrections to the wavefront to improve image quality. Very large telescopes incorporating these mirrors and active control should work better and cost less than if built by conventional means. Remarkable advances over current levels of performance, beyond simply collecting more photons, now seem within reach. A 15-m telescope can potentially, with a modest degree of wavefront correction, give images at 10 μm approaching 0.1 arc s in diameter. This is comparable to the diffraction-limited resolution of the space telescope in visible light. Interferometry with the 15-m telescope at visible wavelengths will allow the exploration of structures in faint objects at 5 m arc s resolution, approaching the resolution achieved at radio wavelengths with interferometry over intercontinental baselines.

These unique advantages for higher spatial resolution argue that the first of the very large instruments should be a phasable design. However, when several very large telescopes are to be built it may be advantageous to design different complementary specialized types. For example, a very large telescope directed towards spectroscopy at shorter wavelengths might take the form of an array of independent smaller telescopes, or of a fixed spherical dish with tracking foci, and could be conveniently located on a lower mountain. Telescopes for thermal IR and submillimetre work need to be as high as possible for low water vapour and put a premium on the largest possible phased aperture. Again, for high resolution interferometry widely spaced large telescope elements are needed that move smoothly along the ground. Each type has a place.

This review has benefited from discussions with colleagues at the University of Arizona and the Smithsonian Institution. In particular, Nick Woolf inspired the discussion of atmospheric effects and has made many suggestions for improving the manuscript. I also thank Jacques Beckers and his staff at the MMT, for it is at this telescope that we are working out many of the basic new ideas common to proposed advanced telescopes. Work was supported by the NSF under grant AST 78-22714 and NASA NAGW-121.

1. Townes, C. *Optical and Infrared Telescopes for the 1990's* (ed. Hewitt, A.) 797 (Kitt Peak National Observatory, Tucson, 1980).
2. Born, M. & Wolf, E. *Principles of Optics* 5th edn (Pergamon, Oxford, 1975).
3. Hardy, J. W. *Optical and Infrared Telescopes for the 1990's* (ed. Hewitt, A.) 535 (Kitt Peak National Observatory, Tucson, 1980).
4. Woolf, N. J. & Angel, J. R. P. *Optical and Infrared Telescopes for the 1990's* (ed. Hewitt, A.) 1062 (Kitt Peak National Observatory, Tucson, 1980).
5. Walker, M. F. *P.A.S.P.* **83**, 401 (1971); *Trans. IAU* XVI A, Pt 1, 219 (1972).
6. Barletti, R., Cepatelli, G., Paterno, L., Righini, A. & Speroni, N. *J. opt. Soc. Am.* **66**, 1380 (1976).
7. Woolf, N. J. *A. Rev. Astr. Astrophys.* **20** (in the press).
8. Carleton, N. P. in *The MMT and the Future of Ground Based Astronomy'*, 37 (ed. Weekes, T. C.) (SAO Spec. Rep. No. 385, 1979).
9. Beckers, J. *MMT tech. Rep. No.* 10. 10 (1981).
10. Lowne, C. M. *Mon. Not. R. astr. Soc.* **188**, 249 (1979).
11. Hege, E. K., Angel, J. R. P., Weymann, R. J. & Hubbard, E. N. *Nature* **287**, 416 (1980).
12. Lewis, W. C. *Workshop on Optical Fabrication and Testing*, Tucson, 5 (Optical Society of America, 1979).
13. Epps, H., Rank, D. & Wampler, J. *Report to the Director of Lick Observatory on the Choice of Primary Mirror for the UC Ten Meter Telescope* (1979).
14. Mack, B. *The Observatory* **101**, 135 (1981).
15. Pearson, E. Internal Rep. Univ. Texas (1981).
16. Angel, J. R. P. & Hill, J. *Proc. ESO Conf.* (1981)
17. Angel, J. R. P., Arganbright, D., Harmonson, L., Hill, J. M. & Woolf, N. *Proc. IAU Colloq.* No. 67 (1981).
18. Disney, M. *Optical and Infrared Telescope for the 1990's* (ed. Hewitt, A.) 649 (Kitt Peak National Observatory, Tucson, 1980).
19. Gillette, F. *Optical and Infrared Telescopes for the 1990's* (ed. Hewitt, A.) 293 (Kitt Peak National Observatory, Tucson, 1980).
20. Learner, R. C. M. *The Observatory* **101**, 137 (1981).
21. Nelson, J. *Optical and Infrared Telescopes for the 1990's* (ed. Hewitt, A.) 11 (Kitt Peak National Observatory, Tucson, 1980).
22. Nelson, J., Gabor, G., Hunt, L., Lubliner, J. & Mast, T. *Appl. Opt.* **19**, 2341 (1980).
23. Angel, J. R. P., Woolf, N. J. & Epps H. *Pap. S. P. I. E. Meet. Advanced Technology Optical Telescopes* Tucson (1982).
24. Beckers, J. *et al. Telescopes of the* 1980's (Annual Reviews Monograph, 1981).
25. Meinel, A. *IAU Symp. No.* 27, 611 (1965).
26. Drake, F. *Optical and Infrared Telescope for the 1990's*, (ed. Hewitt, A.) 649 (Kitt Peak National Observatory, Tucson, 1980).
27. Mertz, L. *Optical and Infrared Telescopes for the 1990's* (ed. Hewitt, A.) 957 (Kitt Peak National Observatory, Tucson, 1980).
28. Aikens, R. *et al. NGT Rep.* No. 2, (Kitt Peak National Observatory, Tucson, 1977).
29. Angel, J. R. P. *Proc. IAU Colloq. No.* 67, (1981).
30. Low, F. J. *Optical and Infrared Telescopes for the 1990's* (ed. Hewitt, A.) 825 (Kitt Peak National Observatory, Tucson, 1980).
31. Bowen, I. *IAU Symp. No.* 27, 1313 (1965).
32. Loytty, E. Y. & DeVoe, C. F. *I.E.E.E. Trans. Aerospace Electron. Syst.* **5**, 300 (1969).
33. Lemaitre, G. *Optical and Infrared Telescopes for the 1990's* (ed. Hewitt, A.) 896 (Kitt Peak National Observatory, Tucson, 1980).
34. Ghozeil, I. *Optical and Infrared Telescope for the 1990's* (ed. Hewitt, A.) 616 (Kitt Peak National Observatory, Tucson, 1980).
35. Brown, D. *Meet. New Techniques and Telescopes in Optical Astronomy* (Royal Astronomical Society, London, 1980).
36. Parks, R. E. *Workshop on Optical Fabrication and Testing*, Tucson (Optical Society of America, 1979).
38. Parks, R. and Angel, J. R. P. *Paper S.P.I.E. Meet. Instrumentation in Astronomy-IV*, Tucson (1982).
37. Leighton, R. B. *Final Techn. Rep. NSF Proj.* AST 73-04908; *Astrophys. J.* **230**, 149 (1978).
39. Merkle, F., Freischlad, K. & Bille, J. in *Scientific Importance of High Angular Resolution at Infrared and Optical Wavelengths*, Munich (1981).
40. Gabor, G. *S.P.I.E. Proc. Instrumentation in Astronomy III* **172**, (1979).
41. Hardy, J. W. *Proc. ESO Conf. on Optical Telescopes of the Future*, Geneva, 455 (1977).
42. Young, A. T. *Astrophys J* **189**, 587 (1974).
43. Angel, J. R. P. *Proc. ESO Conf. Scientific Importance of High Angular Resolution at Infrared and Optical Wavelengths*, Munich (1981).
44. Bahcall, J. & Soneira, R. M. Preprint (Princeton Univ., 1981).
45. Meinel, A. B., Meinel, M. & Woolf, N. J. *Appl. Opt. opt. Engng* **9** (in the press).
46. Sanger, G. thesis, Univ. Arizona (1978).
47. Roddier, F. in *Scientific Importance of High Angular Resolution at Infrared Optical Wavelengths* (eds Ulrich, & Kjar,) (ESO, 1981).
48. Hoag, A. A. & Schroeder, D. J. *P. A. S. P.* **82**, 1141 (1970).
49. Hill, J. M., Angel, J. R. P., Scott, J. S., Lindley, D. & Hintzen, P. *Astrophys. J. Lett.* **242** L69 (1980).
50. Angel, J. R. P. in *The MMT and the Future of Ground-Based Astronomy* (ed. Weekes, T. C.) (SAO Special Report No. 385, 1979).
51. Paul, M. *Rev. Opt.* **14**, 169 (1935).
52. Baker, J. G. *I.E.E.E. Trans. Aerospace Electron. Syst.* **5**, 261 (1969).
53. Janes, C., Robinson, W. & Shechter, P. *KPNO tech. Rep.* (in preparation.).
54. Hege, E. K., Hubbard, E. N., Strittmatter, P. A. & Worden, S. P. *Astrophys. J. Lett.* **248**, L1 (1981).
55. Woolf, N. J., Angel, J. R. P., Antebi, J., Carleton, N. & Barr, L. D. *Paper S. P. I. E. Meet. Advanced Technology of Optical Telescopes*, Tucson (1982).

106204
106196
065216

CONTINUED DEVELOPEMENT OF A PROXIMITY FOCUSED IMAGE INTENSIFIER FOR ASTRONOMICAL APPLICATIONS

Richard N. Cromwell

1. INTRODUCTION

Image intensifiers are currently a primary detector for ground-based optical astronomy. They are used with various electronic readout systems, as in the Wampler-Robinson scanner (image dissector), the IPCS (Plumbicon), and Shectman and Steward Observatory scanners (CCD and Reticon). Photographic plates and film are also still used extensively to record the phosphor output of image intensifiers, especially when large area coverage is required. The image intensifier offers the advantages of reasonably high quantum efficiency, essentially noise-free amplification to very high gain values and suitability for rapid read-out when this is required. The CCD, implementation of which is being carried out at a number of observatories, offers significantly better detective quantum efficiency (DQE) in certain applications--especially for medium to high signal to noise ratio observations at wavelengths longward of 4000-4500 A. With the promise of availability of CCDs such as those from Tektronix, which are expected to have good uv response, low readout noise and 2048 x 2048 pixels, CCDs are sure to be used more and more. However, the performance and availability of such detectors are not yet assured. Moreover, there are a number of astronomical problems for which the image intensifier is likely to remain superior. These include any problems in which it is necessary to read-out rapidly, as for example in speckle interferometry, high-resolution seeing-compensated direct imagery, imaging and spectro polarimetry or photon counting centroided spectroscopy (higher resolution per detector pixel).

Also, in problems where only a few photoelectrons per resolution element are recorded, and therefore where a CCD image would be dominated by readout noise, image intensifiers will provide superior signal-to-noise ratios. It also seems likely that, in the uv spectral range (shortward of 4000 A) the DQE of image intensifiers will remain competitive with that of CCDs for some time to come. At these wavelengths intensifiers may indeed remain the primary detector of choice even for more conventional applications. (It is likely, of course, that for many such applications the CCD will still provide the read-out mechanism.)

While from the astronomical point of view therefore, demand for high quality image intensifiers is likely to remain high, especially for those with good uv response, it is an unfortunate fact of life, that such intensifiers are becoming increasingly hard to obtain and to fund. This is partly for intrinsic reasons (e.g. electrostatic inverter tubes are hard to modify for uv applications) and partly due to market considerations (e.g. the military demand is mainly for rugged red sensitive tubes). It was with these points in mind that Steward Observatory, after reviewing the existing state-of-the-art intensifiers and their suppliers, undertook jointly with the intensifier manufacturer Proxitronic Funk a program to develop a proximity focused image intensifier for astronomy. The proximity tubes manufactured by Proxitronic Funk at that time showed the most promise as a future astronomical detector, and required only a modest amount of additional scientific input and development effort. The tubes exhibit performance characteristics that, when considered as a

combined set, offer advantages over those provided either by magnetically focused or electrostatically focused intensifiers. These characteristics are: the inherent capability of containing uv sensitive photocathodes by virtue of their flat input window (ie, they do not require curved, uv-absorbing, fiberoptic input windows, as are required in electrostatic tubes); total freedom from geometrical distortion; uniformity of photometric response and resolving power, from center to edge of the field; immunity of image deflection due to strong electrostatic or magnetic fields; small, compact size; low unit cost.

We are satisfied that as a result of the development phase just completed we are now able to produce the first fully operational proximity tubes that are of sufficient quality for astronomy. However, we have learned during our study that, not only in these proximity tubes but in many other image intensifiers as well, roughly half of the photoelectrons released from the first photocathode are lost when the electrons strike the first phosphor screen. This is true of every premium quality blue-sensitive image intensifier we have tested, which includes the magnetic focused tubes manufactured by RCA, ITT and EMI, and the proximity focused tube manufactured by Proxitronic Funk. Since our discovery of this problem, much of our effort has gone toward resolving it in the Proxitronic tubes. We just now are beginning to succeed (see the following Section 2 and Ref. 21).

In the present proposal we are requesting a continuation of support for two years of our development of proximity tubes for astronomy. During the first year a major emphasis is placed upon improving the photoelectron counting efficiency, the

specific property of existing intensifiers from several manufacturers that is directly causing their poor DQE. We anticipate that the development phase of the program will be virtually completed within the first year of work and we are therefore also requesting support during the first year for production of up to 16 fully operational tube samples to be used in constructing up to four multi-stage intensifier packages for laboratory and astronomical intruments.

In the second year we wish to continue whatever small refinements we discover are desirable, but intend to concentrate on the production of full-performance intensifiers and complete the construction of six detector packages, which include the four begun during the first year. We feel that the best way to document the suitability of these new intensifiers outside the laboratory is to construct several instruments utilizing them as early as possible and gain valuable experience by routinely scheduling them at the Multiple Mirror Telescope and Steward Observatory 2.3 m telescope in a variety of astronomical applications.

A number of astronomical research projects being carried out at Steward Observatory will benefit from the production of the proposed instruments. Equally important, the astronomical community as a whole will benefit from the availability of the proximity tubes. In Section 2 we summarize the status of the previous development program. Section 3 reviews the image tube laboratory facilities of Steward Observatory.

2. SUMMARY OF PREVIOUS DEVELOPMENT PROGRAM

The Steward Observatory/Proxitronics development of a proximity focused image intensifier for astronomical applications was formally carried out during May 1, 1982 to November 30, 1984. A no-cost six-months extension is now in effect to prepare this status report and proposal for continuation of support.

Considerable progress has been made in the program, with significant improvements in tube characteristics achieved. Our success in accomplishing the major goals set down in the original proposal are illustrated in Table 1.

Three samples of proximity tubes have now been produced by Proxitronic Funk that are suitable for astronomical application (serial numbers 3861, 8137 and 8558). These samples generally meet all the criteria given in Table 1 (with the notable exception of a good DQE, a matter discussed later). These tubes contain either a bialkali photocathode of exceptional blue response (No. 8137) or a multialkali photocathode of reasonable blue-to-red response (Nos. 3861 and 8558) (see Fig. 1). We are very encouraged by the fact that we have been able to produce these first fully operational proximity tube samples that are of sufficient quality for astronomy. The tubes could clearly be utilized in instruments that presently employ the relatively hard-to-get and expensive magnetic intensifiers which have blue-sensitive photocathodes (Refs. 2, 7, 19 and 20). However, during the time we were developing these proximity tubes, we were simultaneously discovering a very important problem: They and two premium quality magnetic intensifiers used in our primary

astronomical instruments produced only roughly half as high a DQE as we had expected. This has been reported in two papers (Refs. 19 and 20). Since our discovery of this problem, much of our effort has gone toward understanding it. We cannot now be satisfied to simply match the DQE of our existing premium blue-sensitive intensifier systems, but we must realize the full factor of nearly 2 improvement in DQE implied by our recent work.

Below, we briefly summarize the most important results of the past program. Much of the material that follows was presented elsewhere (Refs. 20 and 21, copies enclosed), and the following serves as an update to those presentations. Some of the results have not been published elsewhere.

2.1 SIGNIFICANT RESULTS

1. The low counting efficiency (typically 55%) of photoelectrons exhibited by every intensifier tube we have measured, with the single notable exception of tubes manufactured by Varo (Refs. 19, 20 and 21), ultimately led us to recognize that the problem was caused by the phosphor screen. Discussion with other tube manufacturers and review of the literature suggested that phosphor screens could be made to have higher "efficiency" (radiant energy emitted per incident electron energy), and therefore possibly higher counting efficiency, if larger phosphor grains were used (Refs. 22 and 23). Thus, an early experiment was to manufacture tube samples having phosphor screens made of larger grains than standard. Although this experiment proved highly interesting, it did not solve the counting efficiency problem. Ultimately, a number of phosphor

screen manufacturing techniques had to be varied and a number of hypotheses had to be tested before tubes were finally produced that exhibited substantially improved counting efficiencies. The most significant results to date are: 1) The three most recent tube samples have exhibited counting efficiencies of 60, 69 and 70 %, respectively. 2) Coarse-grained screens do not create any advantages over standard-grain screens once the several steps in the manufacturing process are properly optimized. Indeed, only disadvantages with coarse-grain screens are then experienced (lower counting efficiency, lower resolution and more fixed-pattern noise). 3) Several steps standardly taken during the screen manufacturing process were observed to affect both the counting efficiency and the overall gain of the intensifier in a complex and interactive way. These include: the amount and type of screen binding agent used; the aluminum deposition technique; the time, temperature and specific technique used to burn off the lacquer coating between the screen and aluminum coating; the thickness of the screen layer; the temperature, the electron energy and the duration of various electron scrubbing cycles; and the phosphor grain size. We have found no evidence to date that electrons are totally absorbed, nor therefore lost, in the black aluminum overcoating of the Proxitronic screens.

2. A number of important conclusions have been drawn from measurements of the pulse height distribution (PHD) of several samples of tubes of different configurations. We find that: 1) There exists a threshold operating voltage (between photocathode and phosphor) above which any pulse on the output phosphor created by a photoelectron will produce a detectable signal.

This voltage is in the range of 10-12 kV. 2) Neither the shape of the PHD curve nor the counting efficiency change appreciably when the tube is operated above this threshold voltage. Only the average pulse amplitude, or gain, increases with increased voltage above this threshold. 3) The photoelectron counting efficiency, which is simply the total area under the PHD curve, approaches 100% in tubes where the shape of the PHD curve is more symmetrical, or gaussian, in appearance. This is illustrated in the Varo tube and Proxitronic tube PHDs shown in Fig. 2 of Ref. 21. The PHD therefore serves as a useful diagnostic tool in improving the performance, and counting efficiency, of the phosphor screen.

3. The gain in recent experimental samples of Proxitronic tubes (Nos. 8553, 8555 and 8558) has been increased by a factor of 2 to 3 compared to production tubes. This has been accomplished with no significant degradation of resolution or other properties by using the methods mentioned in item 1 above. We anticipate that the improved gain will allow future construction of fiberoptically coupled multi-stage tubes of exceptionally high gain. Such tubes should compete favorably with microchannel plate intensifiers in gain, and should substantially beat them in DQE (Refs. 19 and 20).

4. Bright emission points within the field and beyond-the-edge field emission (i.e. emission outside the active area) have essentially been eliminated as a result of extensive testing, discussion, and improvements in manufacturing techniques. Five samples (Nos. 3861, 7919, 8137, 8555 and 8558) have been produced

to date that exhibit no, or extremely weak, spurious bright points or beyond-the-edge emission even when operated at voltages above their nominal design voltages. This property has allowed us to study the effects of voltage and temperature on the photocathode dark emission. The results are unintluenced by other dark emission phenomena experienced earlier at least at some level in most samples. The relationship of dark emission vs. temperature and voltage published originally (Ref. 20, Fig.9) remains an accurate representation of these later samples, and measurements at our present coldest temperature (-40 ^{o}C) follow a simple linear extrapolation of the earlier published data. For many astronomical applications, the dark emission is acceptably low when the tubes are cooled to -30 ^{o}C. However, it will be desirable to cool to -50 ^{o}C when the very lowest dark emission rates are required (10 electrons/cm^{2}·sec). Bialkali photocathodes in the Proxitronic tubes have about the same dark emission as multialkali photocathodes at a cooled temperature of -60 ^{o}C (estimated via extrapolation of measured data), although their dark emission is roughly 10 times lower than multialkali photocathodes at room temperature.

5. The ion dark emission rate has been systematically reduced during the course of this program by several changes in manufacturing techniques, including reduction of residual gasses in the tubes and subtle alterations in the electrode structures. Virtually all recent samples of tubes have ion dark emission rates of less than 1/cm^{2}·sec when cooled to -40 ^{o}C. Ions in these tubes were measured to release typically 65 electrons from bialkali photocathodes and 190 electrons from multialkali

photocathodes.

6. The ion signal-induced background (SIB) is normally low enough that it is not a problem for astronomical applications. Some (but not all) of the most recent sample tubes with improved counting efficiency and gain exhibited roughly twice the normal ion SIB. It simply isn't known if this is a property inherent in the higher counting efficiency phosphors or not. Because ion SIB is a problem in certain commercial applications of the proximity tubes, we must see that future tubes do not retain this problem. Currently, we are undertaking a modification in the tube structure that is specifically aimed at reducing the ion content, and hence the ion SIB.

7. Early cooling tests of a tube potted in a standard hard plastic potting material resulted in cracking the tube We have since potted many tubes using soft silicone rubber material and have had complete success, both in regard to high-voltage holdoff and temperature cycling to -40 °C.

8. Resolution vs. wavelength, separation and voltage has been well documented for these tubes (Ref. 20).

9. The multialkali tubes demonstrate that their resolution/gain/darkemission/voltage tradeoffs converge to a good performance tube in a 2.5 mm separation, 15 kV operating voltage configuration. Tubes with bialkali photocathodes must be manufactured in a 1.5 mm, 12 kV configuration. Because of the unusually high electric field strength required in the bialkali tube, it is uncertain whether or not the manufacture of such tubes can be commercially viable. However, we are encouraged by

our admittedly limited experience of producing one fully astronomical quality tube (No. 8137) from only two attempts (although this tube has a standard, low counting efficiency phosphor).

10. Three tubes were fabricated having fast X-3 phosphors in order to investigate their suitability in applications with fast readout detectors. Although their gain was quite low (about 100 photons/photoelectron at 15 kV), we found the PHD to be superior to that of the standard P-20 phosphor tubes, and the counting efficiency (64%) to be somewhat better as well. We expect that the same phosphor improvement techniques we are developing for the P-20 phosphors will likely improve the gain and counting efficiency of the X-3 phosphors. If so, tubes using these phosphors could provide an important advantage for detectors requiring fast readout. More investigation is necessary.

11. Development of a good blue response photocathode has been painstakingly slow, but rewarding. Bialkali photocathodes are now reliably and repeatedly produced that compare favorably to the very best blue responses we've measured in the past 10 years. The response of tube No. 8137 in Fig. 1 is an example. The most recent multialkali photocathodes have met our minimum blue response goal, but there is still room for improvement in the 3000-4000 A region (see Fig. 1).

12. Success has been achieved in producing a conductive anti-corona coating over the quartz input window that has high uv transmission. Early attempts to create such a coating using nichrome, a known uv transmitting materi l, were disappointing

because the transmission never exceeded 80%. Surprisingly, we found that tin oxide, which normally absorbs heavily in the uv, can be deposited in a sufficiently thin layer that its transmission exceeds 80% at 3000 A and exceeds 95% longward of 3500 A. Tests of still thinner coatings are underway, although we are satisfied that the problem has already been virtually solved.

13. Study beyond that published in Ref. 20 has been continued of the electric field enhancement of the photocathode responses of proximity tubes. We find that, in the spectral region where the photocathode quantum efficiency is greater than 5%, the enhancement of the response is negligible, even for electric fields corresponding to the maximum operating voltage of the tube. For the long wavelength tail of the photocathode response, however, the response can be enhanced by as much as a factor of 6, and the enhancement steadily, but slowly, increases with increasing field strength.

2.2 PRESENT STATUS

We have accomplished our major objective of producing full astronomical quality proximity focused intensifiers. The manufacturing yield of such devices is almost to the point where they can be successfully commercially produced. All but one of the remaining problems should be entirely eliminated with just another iteration or two of changes in the manufacturing processes. The one remaining significant problem, the low counting efficiency of the phosphor screen, is a fundamental problem for many image intensifiers, and a solution to this

problem is essential. We are just now seeing some progress in this area and are requesting support to continue our investigation.

3. FACILITIES

3.1 STEWARD OBSERVATORY

Under the direction of Dr. Richard Cromwell, Steward Observatory has established a laboratory devoted to thoroughly evaluating image intensifier devices and building intensifier systems. The test facility was organized in the early 1970's as a joint project between Steward Observatory and the Optical Sciences Center of the University of Arizona. A number of techniques and test instruments have been developed for evaluating various characteristics of electronic imaging devices. Tests include measurement of: photocathode quantum efficiency at several monochromatic wavelengths within the spectral range 3000 to 9000 A (absolute accuracy to ± 2% using the latest National Bureau of Standards reference detector (Ref. 1); resolving power across the active field; uniformity of response, including large-scale variations and small-scale variations ("fixed-noise" structure); linearity, gain and intensity transfer characteristics; geometrical distortions, signal-induced background; dark emission (both ion events and thermal electrons); time decay of output events; pulse height distribution; and detective quantum efficiency.

In addition to the laboratory expertise, Steward Observatory

has considerable practical experience in making intensifier systems operate well at the telescope. Special high voltage potting techniques, high voltage connector and cabling structures, conductive coatings for eliminating field emission in intensifiers, magnetic shielding configurations, new designs of focusing permanent magnets and electromagnets, image tube cooling apparatus, custom assembly and selection of multi-stage intensifier configurations, etc., have been developed to satisfy the research requirements at Steward Observatory (Refs. 5, 6, 11, 13, 14, 17, 18, 19 and 20.) Image intensifier systems that were largely designed and built at Steward Observatory for use at its various telescopes are listed in Table II. References in which a description is given of the system are listed. In nearly all of the intensifier systems, the individual tube stages were specially selected and assembled in our laboratory. Several of the acquisition and guiding television systems developed at Steward Observatory have been produced, and have been provided for the U.C.S.D. Minnesota 1.5 m telescope and the Naval Observatory in Flagstaff, the MMT, and Steward Observatory 2.3 m, 1.5 m, and 0.9m reflectors. All the television-related and other recently constructed intensifiers utilize double-conducting window and potting techniques developed at Steward Observatory to eliminate corona and high voltage breakdown problems (Ref. 11).

Several scientists and technical people at Steward Observatory will be contributing part time to the present program insofar as the proposed instruments relate to their specific research programs. Groups particularly involved include the speckle imaging group (led by K. Hege and P. Strittmatter) and

the Space Telescope group (led by R. Angel and R. Allen). Several astronomers, including R. Cromwell, J. Liebert and R. Weymann, will provide valuable feedback as they observe and analyse data obtained with the instruments. During early preparation of instruments and use at the telescopes, a number of people from the Steward Observatory and MMT technical support groups will be providing assistance.

We believe that the experience and facilities of Steward Observatory in image tube testing and implementation are entirely adequate to support this development program.

3.2 PROXITRONIC FUNK

Proxitronic Funk manufactures an expanding line of photomultipliers and image intensifiers at its Benscheim facilities. During 1984 the entire firm was relocated from its site in Darmstadt to a much larger and more modern facility in Benscheim. An important addition in the new facility is a separate workspace and added personnel devoted to research and development work, which may be scheduled independently of the production facilities. This will aid considerably in our present development program and in the company's continuing effort to improve their products. Proxitronic Funk is willing and able to make changes in processing parameters to optimize their products for astronomical use and desires to continue this development in collaboration with Steward Observatory on an exclusive basis. Currently the maximum diameter tube which Paroxitronic manufactures is 25 mm. Larger tubes could be provided in the future on a basis of demand.

4. REFERENCES

1. M. A. Lind, E. F. Zalewski and J. B. Fowler, "The VBS Detector Response Transfer and Intercomparison Package: The Instrumentation", NBS Tech. Note 950, 1977.

2. R. H. Cromwell and R. R. Dyvig, "Evaluation of Image Intensifiers for Astronomy", pp. 677-696 in Photo-Electronic Image Devices (Proc. Fifth Symposium), J. D. McGree, D. McMullan, and E. Kahan, eds., in Advances in Electronics and Electron Physics, Vol. 33B, L. Marton, Ed., New York, Academic Press, 1972.

3. R. H. Cromwell and R. R. Dyvig, "Laboratory Evaluation of Eleven Image Intensifiers", Optical Sciences Center Technical Report 81, August 1973.

4. R. H. Cromwell and G. H. Smith, "Resolving Power, Signal-Induced Background, Noise, and Detective Quantum Efficiency of Image Intensifier Photographs", Proceedings of the SPIE, Vol. 42, 1973.

5. R. H. Cromwell, Unpublished data from Steward Observatory Image Tube Laboratory.

6. E. K. Hege, R. H. Cromwell and N. J. Woolf, "Quantum-Noise Limited REadout of Image Intensifiers Using a Reticon Photodiode Array", in Advances in Electronics and Electron Physics, Vol. 52, pp. 397-413, L. Marton and C. Marton, eds., New York, Academic Press, 1979.

7. R. H. Cromwell, "Evaluation of Image Tubes for Use in Direct Photography of Astronomical Sources", Optical Sciences Center Technical Report 38, 154 pp., April 1969.

8. D. C. Barry and R. H. Cromwell, "Spectroscopic Comparison of Open Clusters. I. The Reddening, Blanketing, and Metallicity of M67", Astrophys. J., 187:107, January 1975.

9. Carswell, R. F., Hilliard, R. L., Strittmatter, P. A., Taylor, D. J. and Weymann, R. J., "A Cross-Dispersed Echelette Spectrograph and a Study of the Spectrum of the QSO 1331+170", Ap. J. 196, 351, 1975.

10. D. C. Benner, U. Fink and R. H. Cromwell, "Image Tube Spectra of Pluto and Triton from 6800 to 9000 A", ICARUS 36, 82-91, 1978.

11. R. H. Cromwell and J. R. P. Angel, "Elimination of Corona and Related Problems with Astronomical Image Tubes", in Advances in Electronics and Electron PHysics, Vol. 52, pp. 183-188, L. Marton and C. Marton, eds., New York, Academic Press, 1979.

12. R. H. Cromwell and E. K. Hege, "Image Intensifier Readout by Photodiode Arrays and Photographic Plates", to be published in the AAS Photo-Bulletin, 1981.

13. J. R. P. Angel, R. H. Cromwell and J. Magner, "An Intensified Storage Vidicon Camera for Finding and Guiding at the Telescope", in Advances in Electronics and Electron Physics, Vol. 52, pp. 347-353, L. Marton and C. Marton, eds., New York, Academic Press, 1979.

14. E. R. Craine and R. H. Cromwell, "Laboratory Tests and Astronomical Application of an Image Intensifier with a 146mm Diameter Photocathode", in Advances in Electronics and Electron Physics, Vol. 52, pp. 339-346, L. Marton and C. Marton, eds., New York, Academic Press, 1979.

15. E. R. Craine, "Optical Infrared Sky Survey Instrumentation", Proceedings of the SPIE, Vol. 172, 169, 1979.

16. G. D. Schmidt, J. R. P. Angel and R. H. Cromwell, "A Reinvestigation of the Scattering Halo of M82 Based on Polarimetric and Isophotal Maps", Astrophys. J., 206:888, June 1976.

17. R. H. Cromwell, C. R. Batishko and A. G. Millikan, "Improved Resolution from Image Tubes", AAS Photo-Bulletin No. 1, 1973.

18. J. R. P. Angel, "A Magnet for Use with a Magnetic Image Intensifier and a Folded Schmidt Spectrograph Camera", Proceedings of the SPIE, Vol. 172, 377, 1979.

19. R. G. Allen, R. H. Cromwell, J. W. Liebert, R. H. Macklin and H. G. Stockman, "The Steward Observatory Intensified Photon-Counting Reticon System," in Instrumentation in Astronomy V, Proc. SPIE 445, 167, 1984.

20. R. H. Cromwell, P. A. Strittmatter, R. G. Allen, E. K. Hege, H. Kuhr, K.-H. Marien, H. W. Funk and K. Frank, "A Proximity Focused Image Intensifier for Astronomy," in Advances in Electronics and Electron Physics, to be published, 1984.

21. R. H. Cromwell, "The Lost Photon Problem in Image Intensifiers," 165th Meeting of the AAS, 1985. Abstract in BAAS Vol 16, No 4, Pg. 904, 1984. Full paper in Preprint No. 565 of the Steward Observatory.

22. G. E. Giakoumakis, C. D. Nomicos and P. C. Euthymiou, "Absolute Efficiency of ZnCdS:Ag Screens excited by an Electron Beam," in J. Appl. Phys. Vol 51, 1980.

23. S. Nevin, ITT Electro-Optical Products Division, Fort Wayne, Indiana, private communication, 1983.

SPIE
San Diego, '85

Differential Speckle Imaging with the Cophased Multiple Mirror Telescope

J.C.Hebden, E.K.Hege
Steward Observatory, University of Arizona, Tucson, Az 85721

and J.M.Beckers
NOAO, 950 N. Cherry Ave., Tucson, Az 85726.

Differential Speckle Interferometry (DSI, Beckers, Opt.Acta, 29, 4. 1982) is a technique which involves obtaining speckle images (specklegrams) of a stellar object at two distinct wavebands simultaneously. Comparison of these images enables differences in the appearance of the object resulting from the differences in the observing wavelength to be derived.

Data has been obtained using the fully-phased six-mirror aperture of the Multiple Mirror Telescope (MMT). DSI observations were made of the M-type supergiant Alpha Orionis at two distinct sky position angles separated by about 90 degrees, as well as of the point source Gamma Orionis. In this attempt to investigate the H-alpha envelope of the supergiant star, specklegrams were obtained in the H-alpha line and in the nearby continuum 6Å away.

The DSI data reduction method consists of performing a frame-by-frame complex deconvolution of the line specklegram by its simultaneously acquired counterpart. Each complex quotient is weighted by the continuum power spectrum and summed over a large number of frames, yielding the differential image

$$FT^{-1}\left[\frac{\sum_N \frac{h(u,v)}{c(u,v)}|c(u,v)|^2}{\sum_N |c(u,v)|^2}\right] = FT^{-1}\left[\frac{\sum_N h(u,v)c^*(u,v)}{\sum_N |c(u,v)|^2}\right]$$

Images from Astronomical Speckle Data: Weighted Shift-and-Add Analysis

J.C.Christou*, E.K.Hege+, J.D.Freeman and E.Ribak
Steward Observatory, University of Arizona, Tucson, Arizona 85721

We have applied a modified version of the Lynds,Worden and Harvey (LWH) analysis (Astrophys.J.,207,174,1976), which we call Weighted Shift-and-Add (WSA) (Bull.Amer.Astron.Soc.,16,885,1984), to astronomical speckle interferometric data.

A specklegram is assumed to be the convolution of a diffraction limited image with a set of delta functions or impulses representing the positions of the speckles. For each specklegram we generate an impulse distribution where each impulse corresponds in location and magnitude to a local maximum. The specklegram is then deconvolved, in the Fourier plane, by the impulse distribution. In order to avoid the zero divide problems of the standard deconvolution we have used a weighted deconvolution procedure. If the specklegram is represented by i(r) and the impulse distribution by imp(r) then the final deconvolved image is

$$I(r) = FT^{-1}\left[\frac{\sum_n \left[FT\{i_n(r)\}/FT\{imp_n(r)\}\right] W_n(r)}{\sum_n W_n(r)}\right]$$

where FT indicates Fourier transform and W(r) is the weighting function which we have set equal to the power spectrum of the impulse distribution.

Unlike the LWH and conventional Shift-and-Add (Bates &

since $|c(u,v)|^2 = c^*(u,v)c(u,v)$, and where N is the ensemble of DSI specklegram pairs, h(u,v) is the Fourier transform of the "line" specklegram and c(u,v) is the Fourier transform of the "continuum" specklegram. This quotient contains a form of inherent Wiener-type filter which suppresses the signal at high spatial frequencies.

"Differential images" of Gamma Orionis exhibit a central maximum whose half power width compares well with the expected (12 msa) diffraction limited result for the 6.86m aperture of the MMT. Results for Alpha Orionis show significant intensity over a diameter of ≈150 msa, about 3 times greater than the measured diameter in the continuum. The rotation of central features within the images, corresponding to the two sky position angles, is a strong validation of this result.

* The MMT is a joint facility of the University of Arizona and the Smithsonian Institution.

Work supported in part by NSF (grants AST-8113212, AST-8201892).

Cady, Optics Commun.,32,365,1988) analyses the WSA technique appears to be self-calibrating for the seeing. It does not have the residual seeing produced background found in results of the other analyses.

Results of this analysis for a number of resolved and unresolved (at the telescope diffraction limit) objects are presented. The results for the unresolved objects agree well with computed point spread functions. Using this analysis we have measured the point spread functions for a number of telescopes including the fully phased MMT++ array.

We are currently investigating the use of Matched Filter techniques (Ribak et al. this conference), to locate speckles for fainter objects. This should allow extension of this technique to approximately $m_v = 16$ as for other speckle analyses.

This work was supported in part by AFGL contract F19628-82-0025, AFOSR contract 82-0028 and NSF grants AST-8113212 and AST-8201092.

* Visiting Astronomer from Dept. of Astronomy, New Mexico State University, Las Cruces, NM88003.

+ Visiting Astronomer, Kitt Peak National Observatory, National Optical Astronomy Observatories operated by the Association of Universities for Research in Astronomy supported by the National Science Foundation.

++ The Multiple Mirror Telescope is a joint facility of the University of Arizona and the Smithsonian Institution.

Use of Matched Filtering to Identify Speckle Locations.

E. Ribak*, E. K. Hege and J. C. Christou
Steward Observatory, University of Arizona, Tucson, Az 85721

While using different realizations of the shift-and-add method (Christou et al., this conference), we find that in many cases the required speckle maxima are not well defined. This is due mainly to Poisson noise, inherent in the detection process, which obliterates the shape of faint speckles. The problem is aggravated for extended objects with sharp local peaks, such as binaries. As a remedy, we use a filter that smoothes out each speckle and defines at the same time its maximum.

Theory says that the best filter to use in such a case would be very close to the speckle itself. In the case that we do not have such a shrewd guess, we can start with a bell function, slightly wider than the expected speckle. When we acquire enough speckles, we can use the shift-and-add result to provide a better filter instead of the initial one. We iterate this procedure until convergence is achieved. While building a new filter, we also combine it with a high-pass filter. The latter suppresses the variable background created by coalescing speckles in a large speckle cloud. Single-photon speckles (or events) can also be discriminated against by using a comparison low-pass filter.

This whole process is carried out in the image plane. We are currently investigating the possibility of performing a part of the process in the Fourier plane, where the filtering convolution and speckle shifting can be faster and more exact for larger images.

Work supported in part by NSF (grants AST-8113212, AST-8201092) and AFOSR (contract 82-0020)

* Weitzmann Fellow.

Statistical Analysis of the Weighted Shift and Add Image Reconstruction Technique

J.D.Freeman, E.Ribak, J.C.Christou* and E.K.Hege+
Steward Observatory, University of Arizona,
Tucson, AZ 85721

The Weighted Shift and Add algorithm (WSA) is an image reconstruction technique whereby diffraction limited images of astronomical objects are obtained from speckle interferometric data (Bull. Amer. Astr. Soc., 16, 174, 1984). To a first order approximation, atmospheric distortion can be thought of as having the effect of reproducing many object distributions throughout the image plane. WSA finds the maxima of these object distributions and stacks them up together to produce the diffraction limited image. A full description of the process can be found in Christou et al. and Ribak et al. (companion papers, this conference, 1985).

This paper attempts to put the understanding of WSA on a firm mathematical basis by a statistical analysis of the algorithm. The approach follows that of the Hunt Fright and Bates statistical analysis (J. Opt. Soc. Am., 73, 456, 1983) carried out for the Simple Shift and Add algorithm (Bates and Cady, Opt. Comm., 32, 365, 1980) despite the fact that to a large degree their analysis is first order approximation. Simply, the expected profile of the WSA image is calculated by finding the expectation value of the stacked speckle pattern by conditioning an average speckle on the intensity distribution of the specklegram. The expected WSA profile is found to be linearly dependent solely on the complex coherence function of a speckle

pattern. The last section of this paper contains a detailed discussion of how the statistical analysis compares with the results obtained by Christou et al.

This work has been supported in part by Air Force Contracts (AFGL F19628-82-K-0025) and (AFOSR 82-0020).

* Visiting Astronomer from Dept. of Astronomy, New Mexico State University, Las Cruces, NM88003.

+ Visiting Astronomer, Kitt Peak National Observatory, National Optical Astronomy Observatories operated by the Association of Universities for Research in Astronomy supported by the National Science Foundation.

The Cauchy/Schwarz Inequality as a Constraint in Power Spectrum Analysis and Image Reconstruction

W. J. Cocke
Steward Observatory
University of Arizona
Tucson, Arizona 85721

ABSTRACT

It is well-known that Cauchy's inequality may be used to derive relations which are very useful in crystallography. We show here that a similar usage may be made in multi-dimensional power spectrum analysis and image reconstruction, in the case where the image or autocorrelation in question is assumed to be non-negative.

Cauchy's inequality is appropriately used for the discrete Fourier transform, whereas for the continuous case Schwarz' inequality gives a completely analogous result. In both cases, the results are inequalities which restrict the phases and moduli of the Fourier transforms, and we show that they are useful diagnostics in phaseless image reconstruction.

As a simple example, consider a power spectrum P_ℓ assumed to be the Fourier transform of a non-negative autocorrelation. A special case of the Cauchy-inequality result shows that $P_\ell^2 \leq \frac{1}{2}P_0(P_0+P_{2\ell})$, where P_0 is the "d.c." level of the power spectrum. If the power spectrum is suppressed at high frequencies, so that $P_{2\ell} = 0$, then the corresponding autocorrelation is non-negative only if $P_\ell \leq P_0/\sqrt{2}$, which is more restrictive that the usual $P_\ell \leq P_0$.

Other useful and more general results are derived. In particular, we exhibit a set of inequalities for the iterative treatment of power spectra which have been damaged by noise and artifacts.